Origin of runaway OB stars
Ursprung von Runaway OB Sternen

Der Naturwissenschaftlichen Fakultät
der Friedrich-Alexander-Universität
Erlangen-Nürnberg

zur

Erlangung des Doktorgrades Dr. rer. nat.

vorgelegt von

Andreas Irrgang

aus Cham

Als Dissertation genehmigt
von der Naturwissenschaftlichen Fakultät
der Friedrich-Alexander-Universität Erlangen-Nürnberg

Tag der mündlichen Prüfung: 06.08.2014

Vorsitzender des Promotionsorgans:	Prof. Dr. Johannes Barth
Gutachter:	Prof. Dr. Ulrich Heber und Prof. Dr. Norbert Przybilla
Gutachter:	Prof. Dr. Artemio Herrero
Gutachter:	Prof. Dr. Rolf-Peter Kudritzki

Zusammenfassung

Runaway-Sterne des Spektraltyps O und B sind massereiche und demzufolge junge Sterne, die sich überraschenderweise von den Sternentstehungsgebieten der Milchstraße, wie zum Beispiel deren Spiralarme, wegbewegen oder bereits wegbewegt haben. Es wird daher vermutet, dass diese Sterne aus ihrer Geburtsumgebung herausgeschleudert worden sind. Mögliche Auswurfszenarien sind dynamische Wechselwirkungen in dicht gepackten Sternhaufen, beispielsweise der sehr nahe Vorbeiflug zweier Doppelsternsysteme, oder eine Supernovaexplosion, die ein Doppelsternsystem zerreißt. Erkenntnisse über den Ursprung von Runaway-Sternen des Spektraltyps O und B können für mehrere, ansonsten eigenständige Forschungsbereiche der Astronomie von großer Bedeutung sein. So könnten diese Sterne etwa Informationen liefern über das Gravitationspotential der Milchstraße und ihres Halos aus dunkler Materie, über Sternentstehung und (Doppel-)Sterentwicklung als auch über stellare Nukleosynthese während Supernovaexplosionen. Insbesondere könnten die Runaway-Sterne den ersten empirischen Nachweis dafür liefern, dass der Prozess des schnellen Neutroneneinfangs in Kernkollaps-Supernovaexplosionen stattfindet. In dieser Arbeit werden 18 Runaway-Sterne des Spektraltyps O und B sowohl spektroskopisch als auch kinematisch untersucht um daraus Schlussfolgerungen über ihre Herkunft zu ziehen.

Das Herzstück unserer kinematischen Untersuchung ist die Berechnung von Sterntrajektorien im Gravitationspotential der Milchstraße. Letzteres wird typischerweise anhand von Modellen abgeleitet, welche die beobachtete Massenverteilung innerhalb der Galaxis beschreiben. Realistische, aber dennoch einfache und vollkommen analytische Massenmodelle sind bereits in der Vergangenheit präsentiert worden. In der Zwischenzeit sind jedoch verbesserte Beobachtungsdaten verfügbar geworden, die zur Kalibrierung der Modelle genutzt werden können. Um diesen neuen Beobachtungen Rechnung zu tragen, werden in dieser Arbeit drei weit verbreitete Modellpotentiale überarbeitet. Die Masse des Halos aus dunkler Materie wird hierbei – innerhalb der Beschränkungen der angewendeten Modelle – auf vollkommen konsistente Weise abgeschätzt. Als erste Anwendung wird überprüft, ob die Große Magellansche Wolke wirklich als Ursprungsort für den extremen Runaway-Stern HE 0437−5439 in Frage kommt.

Grundlage für die spektroskopische Untersuchung ist eine neuartige, eigens entwickelte Strategie. Sie ist objektiver und erheblich effizienter als traditionelle Methoden und ist insbesondere auch auf Spektren von doppellinigen spektroskopischen Doppelsternen anwendbar. Mithilfe von 63 Referenzsternen aus der näheren Sonnenumgebung wird der neue Ansatz anschließend ausgiebig getestet, wobei folgende Ergebnisse erzielt werden: (i) Die vermutlich größte systematische Unsicherheit bei der Parameterbestimmung massereicher Sterne liegt in der Beschreibung der Verbreiterung der Balmerlinien durch den Stark-Effekt. Zwei konkurrierende atomphysikalische Verbreiterungstheorien werden hierzu verglichen und die daraus resultierenden systematischen Unterschiede werden quantifiziert. (ii) Den hoch gesteckten Vergleichstest, der durch den kosmischen Häufigkeitsstandard (CAS) gesetzt wird, besteht die neue Strategie für *differentielle* Analysen. Für *absolute* Elementhäufigkeiten besteht noch Verbesserungsbedarf, insbesondere für späte B-Sterne. Letztere wurden allerdings beim CAS noch nicht berücksichtigt. Die Referenzsterne eignen sich ausgezeichnet, um bei (Runaway-)Sternen Häufigkeitsanomalien mit bisher unerreichter Genauigkeit differentiell nachzuweisen. (iii) Die hohe chemische Homogenität von massereichen Sternen in der näheren Sonnenumgebung wird hier bestätigt und zusätzlich für drei chemische Elemente erstmals nachgewiesen. (iv) In 16

Referenzsternen findet sich bereits die charakteristische Signatur des Wasserstoffbrennens mittels des CNO-Doppelzykluses. Vergleiche mit Vorhersagen der Sternentwicklungstheorie sind erfolgreich und untermauern somit gängige Sternentwicklungsmodelle. (v) Diese Arbeit liefert einen in dieser Form noch nie erbrachten empirischen Befund dafür, dass mikroskopische Turbulenzen innerhalb der Photosphäre von massereichen Sternen von einer Konvektionszone unterhalb der Photosphäre verursacht werden.

Zu guter Letzt werden die überarbeiteten Massenmodelle der Milchstraße und die neue spektroskopische Analysestrategie dazu verwendet, Nachforschungen über den Ursprung von 18 Runaway-Sternen des Spektraltyps O und B anzustellen. Um chemische Besonderheiten aufzudecken, werden die Häufigkeiten relativ zu denen der Referenzsterne bestimmt.

Die chemische Analyse ergibt: (i) Während die Häufigkeitsmuster von neun Objekten normal sind, treten bei vier Runaway-Sternen Anomalien in der chemischen Zusammensetzung auf die möglicherweise auf atmosphärische Diffusionsprozesse hinweisen, also nicht mit dem Ejektionsmechanismus in Zusammenhang stehen. (ii) Mehr oder weniger deutliche Hinweise dafür, dass von einer Supernova ausgestoßenes Material auf der Sternoberfläche angesammelt wurde, finden sich in fünf Objekten. Diese könnten also durch den Doppelstern-Supernova Mechanismus ausgeworfen worden sein. (iii) Der Stern PG 1315−077 entpuppt sich als Doppelsternsystem, in dem beide Komponenten normale chemische Häufigkeiten aufweisen.

Um Informationen über den möglichen Geburtsort innerhalb der galaktischen Scheibe, über die Auswurfgeschwindigkeit oder über die Flugzeit zu erhalten, werden die Trajektorien der Runaway-Sterne zurück zur galaktischen Scheibe gerechnet. Es ergibt sich unter anderem: (i) Das Runaway-Szenario kann für alle Sterne bestätigt werden mit Ausnahme von Stern HD 22586, dessen Flugzeit sein Entwicklungsalter übersteigt. (ii) Die Sterne HD 271791 und HIP 60350 sind möglicherweise nicht an die Milchstraße gebunden und würden in den intergalaktischen Raum entweichen. (iii) Im Rahmen des Runaway Szenarios benötigt das oben erwähnte Doppelsternsystem PG 1315−077 eine sehr hohe Ejektionsgeschwindigkeit. Das supermassereiche Schwarze Loch im Zentrum unserer Galaxis könnte durch seine Gezeitenkräfte ein hierarchisches Dreifachsternsystem zerrissen und das Doppelsternsystem somit ausgeworfen haben.

Ausgehend von dieser Arbeit können in Zukunft einige neue Projekte angegangen beziehungsweise bestehende fortgeführt werden. So lassen sich bespielsweise die Massenmodelle der Milchstraße noch deutlich realistischer gestalten um die künftigen hoch genauen astrometrischen Messungen des *Gaia* Satelliten interpretieren zu können. Des Weiteren eröffnet die Entwicklung der neuen spektroskopischen Analysestrategie die Möglichkeit, die Spektren einer großen Anzahl von massereichen (Runaway-)Sternen in kurzer Zeit und auf homogene Weise zu untersuchen. In jüngster Zeit mehren sich die Anzeichen, dass es unter O- und B-Sternen weit mehr Doppelsterne gibt als bisher angenommen. Daher wird die Anwendung der neuen Methode auf überlagerte Spektren besonders in den Fokus rücken.

Abstract

Runaway stars of spectral type O and B are massive and thus young stars that, surprisingly, are currently leaving or already have left the star-forming regions of the Milky Way, i.e., the spiral arms inside the Galactic disk. They are therefore supposed to be the result of an ejection event that forced them to run away from their original place of birth. Possible ejection scenarios encompass dynamical interactions in dense star clusters, such as close binary-binary encounters, or a supernova explosion disrupting a binary system. Unraveling the origin of runaway OB stars can bring new insights into several distinct fields of astronomy. For example, they can tell us something about the structure and gravitational potential of the Milky Way and its dark matter halo, about star formation and stellar (binary) evolution, and about stellar nucleosynthesis in supernova explosions. In particular, runaway stars could provide the first observational evidence that the rapid neutron capture process is taking place during core-collapse supernovae. In this thesis, a combined spectroscopic and kinematic analysis of 18 runaway OB stars is presented to reveal some clues about their past.

The core of our kinematic investigation is the computation of stellar trajectories in the gravitational potential of the Milky Way. The latter is typically inferred from modeling the observed mass distribution inside the Galaxy. Realistic, yet simple and fully analytical mass models have already been presented in the past. However, improved as well as new observational constraints have become available in the meantime calling for a recalibration of the respective model parameters. Therefore, three widely used model potentials are revisited in this work to match the most recent observations. The mass of the dark matter halo is – within the limitations of the applied models – estimated in a fully consistent way. As a first application, the trajectory of the extreme runaway star HE 0437−5439 is re-investigated to check its suggested origin in the Large Magellanic Cloud.

For the spectroscopic investigation, a novel analysis strategy is presented here. It is more objective and considerably faster than traditional methods and is also applicable to composite spectra of double-lined spectroscopic binary systems. By applying it to a sample of 63 nearby reference stars, the new approach is thoroughly tested and the following results are obtained: (i) It is shown that the use of different Balmer line Stark broadening theories for the spectroscopic analysis introduces a non-negligible source of systematic uncertainty to the parameter determination in massive stars. (ii) For *differential* analyses, the new strategy passes the ambitious benchmark test provided by the cosmic abundance standard (CAS). In contrast, the determination of highly precise *absolute* abundances needs some revision, particularly in the case of late B-type stars. However, the latter were not considered in the CAS study at all. Using abundances relative to the reference stars, it is possible to identify abundance anomalies in other stars (like runaway stars) with unprecedented accuracy. (iii) The high degree of chemical homogeneity of nearby massive stars, which was found in a previous study, is confirmed and extended to three additional chemical species. (iv) The observed signature of hydrogen burning via the CNO bi-cycle, which is detected in 16 of the reference stars, is successfully checked against theoretical predictions. (v) Unprecedented observational support is provided for the assumption that the photospheric microturbulent motion in massive stars is linked to a sub-photospheric convective motion.

Finally, the revised Milky Way mass models and the new spectroscopic analysis strategy are employed to investigate the origin of 18 runaway OB stars. Abundances relative to the reference

stars are determined in order to detect chemical peculiarities.

The abundance analysis reveals: (i) While the abundance patterns of nine objects are normal, peculiar chemical compositions emerge for four runaway stars, which, however, rather hint at atmospheric diffusion processes than being related to a specific ejection mechanism. (ii) More or less clear indications for the capture of supernova ejecta are found for the remaining five targets. They are therefore good candidates for the supernova ejection scenario. (iii) Object PG 1315−077 turns out to be a runaway binary system with normal chemical composition.

Stellar trajectories are traced back to the Galactic plane to deduce a runaway star's possible birthplace in the Galactic disk, its ejection velocity, or its time of flight. Among others, the following results are obtained: (i) All stars are consistent with the runaway scenario except for HD 22586, whose flight time is in excess of its evolutionary age. (ii) The stars HD 271791 and HIP 60350 are possibly gravitationally unbound to the Milky Way. (iii) The ejection velocity of the runaway binary system PG 1315−077 is quite large. It could be the result of the tidal disruption of a hierarchical triplet system by the supermassive black hole at the Galactic center.

This thesis provides the basis for several existing and future projects. For instance, the Milky Way mass models can be further improved to account for the upcoming highly precise astrometric data by the *Gaia* satellite. In addition, the development of the novel strategy for the spectroscopic investigation makes it possible to homogeneously analyze spectra of a large number of massive (runaway) stars in a short time. Since massive binary systems are currently a hot topic in the community, the application to composite spectra is certainly one of the most promising aspects to mention here.

Contents

1 Introduction/Motivation

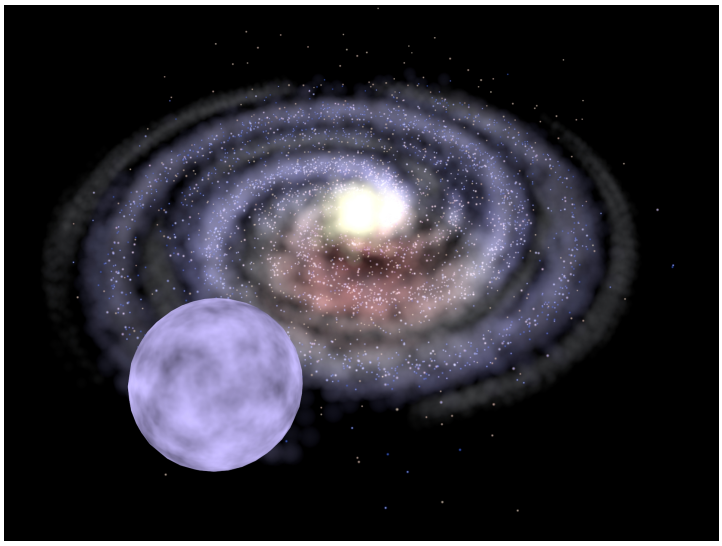

Figure 1.1: Runaway stars of spectral type O and B are massive and thus young stars that, surprisingly, are currently leaving or already have left the star-forming regions of the Milky Way, i.e., the spiral arms inside the Galactic disk. They are therefore supposed to be the result of an ejection event that forced them to run away from their original place of birth. See Appendix A for an animated version of this figure.

The Milky Way is our host galaxy[1] and is yet only one out of a countless number of galaxies that populate the entire universe. Each galaxy itself is formed of billions of constituents that are bound to each other by gravitation. Obviously, the most prominent constituents are the shining objects visible to the eye – the stars. They can be classified, for instance, according to their mass and evolutionary status. Interestingly, the lifetime of stars is decreasing with increasing stellar mass. Low mass stars like the Sun live for billions of years while massive stars of more than three solar masses end their lives after only a few hundred million years and less. Therefore, massive stars are generally expected to be found only within or close to star-forming regions, i.e., the spiral arms within the galactic disk of spiral galaxies such as the Milky Way. However, this view is challenged by a tiny but fascinating class of stars, namely the runaway stars of spectral type O and B. Runaway OB stars are massive and thus young stars that, surprisingly, are currently leaving or already have left the star-forming regions inside the Galactic disk. Some of them are even located in the halo of our Galaxy, thousands of parsecs away from the Galactic disk. They are supposed to be the result of an ejection event that forced them to run away from their original place of birth.

Possible ejection scenarios encompass dynamical interactions in star clusters – either initial dynamical relaxation (Poveda et al. 1967) or close many-body encounters such as binary-binary interactions (Leonard & Duncan 1988, Fig. 1.2) – or a supernova explosion disrupting a binary system (Blaauw 1961, Fig. 1.3). The ejection velocity depends strongly on the details of the encounter or on the configuration of the progenitor binary system. Nevertheless, one may state as a general rule that the more massive and the closer the involved components are, the larger is the velocity with which the runaway star is leaving its former host system. Typical values for the ejection velocity range from a few dozen to several hundred kilometers per second. While the chemical composition at the surface of the runaway star is not changed at all during dynamical interactions, the opposite can be true in the case of the supernova scenario. If the two components are sufficiently close, material ejected by the exploding primary might be accreted

[1] Note that "**G**alaxy" is a synonym to "Milky Way" whereas "**g**alaxy" is a general term.

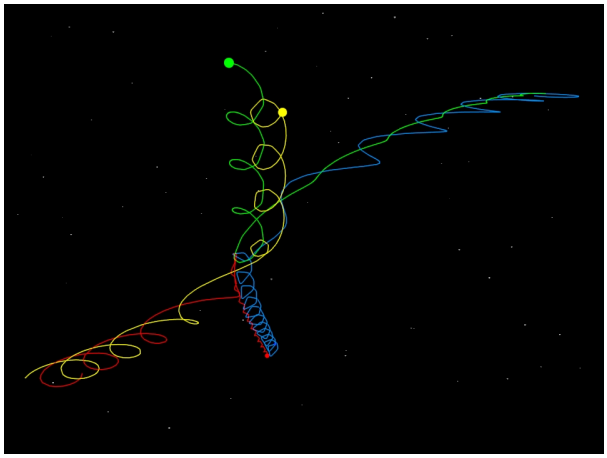

a: Exchange of partners. No ejection.

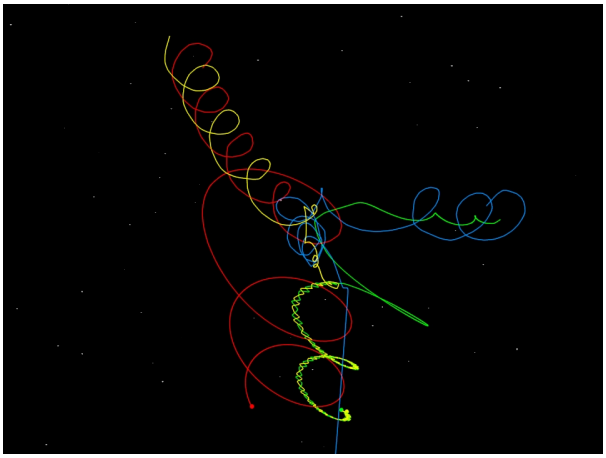

b: Formation of a stable triplet system. Single ejection.

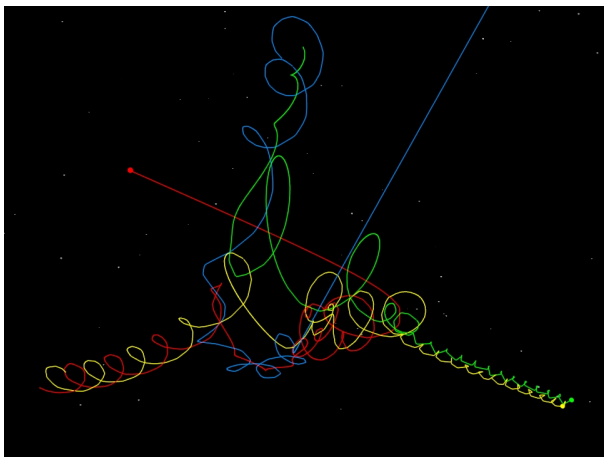

c: Formation of a new binary system. Double ejection.

Figure 1.2: Dynamical binary-binary interactions visualized with the help of trails: Two initially separated binary systems – red and yellow, blue and green – interact via a spatially close encounter resulting in (a) an exchange of partners, (b) formation of a hierarchical triplet system and ejection of the blue star, or (c) formation of a new binary system and ejection of the blue and red stars. See Appendix A for an animated version of this figure.

by its companion leading to a pollution of its atmosphere with characteristic supernova products. This signature, which can survive in massive stars for a long time due to the absence of a large outer convection zone, is expected to be more pronounced in the fastest and thus most extreme runaway stars since those stem from the closest progenitor systems.

Interest in runaway stars has been revived recently by the discovery of a new class of extreme velocity stars (Brown et al. 2005; Edelmann et al. 2005; Hirsch et al. 2005), the so-called hypervelocity stars, traveling at such a high velocity that they escape from the Galaxy. They were first predicted by theory (Hills 1988) to be the result of the tidal disruption of a binary system by a supermassive black hole that accelerates one component beyond the Galactic escape velocity (the Hills mechanism, Fig. 1.4). Because the Galactic center hosts such a supermassive massive black hole, it is the suggested place of origin for the hypervelocity stars. However, this paradigm has been challenged recently by the young hypervelocity star HD 271791 because its kinematics point to a birthplace in the metal-poor rim of the Galactic disk (Heber et al. 2008). Przybilla et al. (2008b) presented a high-precision quantitative spectral analysis that indicated a pollution with supernova ejecta. They conclude that HD 271791 is the surviving secondary of a massive binary system disrupted in a supernova explosion. Because a similar scenario has been proposed for the origin of runaway B stars by Blaauw (1961), Przybilla et al. coined the

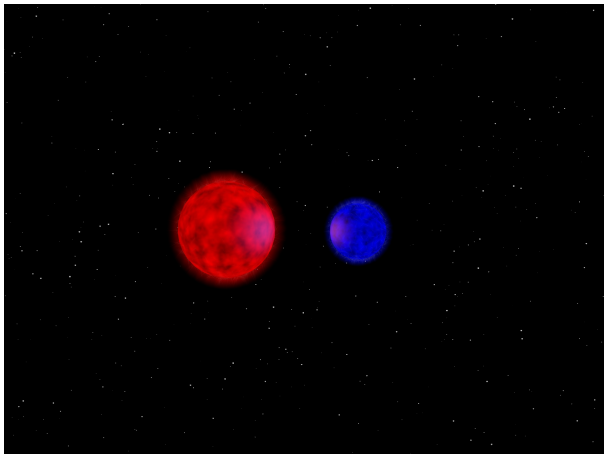

a: Initially bound binary system.

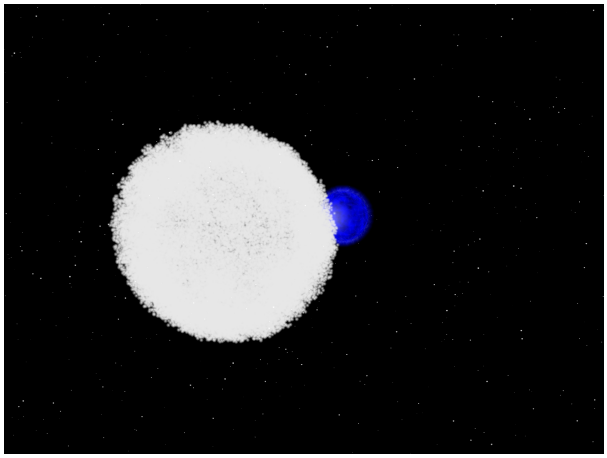

b: Supernova explosion.

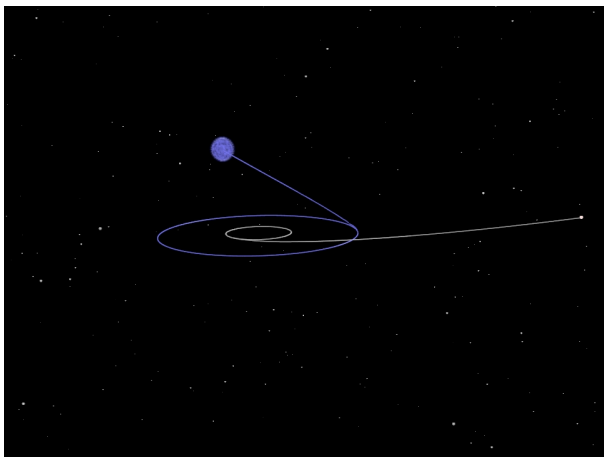

c: Release of the runaway star.

Figure 1.3: Disruption of a binary system by a supernova explosion: The primary component (red) of an initially bound system explodes in a symmetric supernova explosion reducing its mass significantly. The secondary star (blue) is hence so weakly attracted by the supernova remnant (white) that it is able to leave the former binary as a high-velocity runaway star. See Appendix A for an animated version of this figure.

term hyper-runaway star for the most extreme runaways that exceed their local Galactic escape velocity. According to Irrgang et al. (2010), the star HIP 60350 qualifies as a candidate hyper-runaway star. If indeed true, it would be the second one in this extremely rare class of objects.

In the long term, the analysis of runaway OB stars can bring new insights into several distinct fields of astronomy. Once a sufficiently large sample of them will be analyzed, their spatial as well as velocity distribution may be used to constrain the structure, e.g., the location of the spiral arms (Silva & Napiwotzki 2013), and the gravitational potential of the Milky Way. Moreover, runaway stars are decisive for the discussion as to whether or not in-situ star formation outside the Galactic disk, which is believed to be impossible because the halo is almost devoid of interstellar matter and existing clouds are of too low densities to form stars, can be considered as a serious alternative to the standard picture. They are also valuable probes for the dynamics occurring during many-body interactions and supernova explosions. Furthermore, models of stellar and binary evolution have to account for their peculiar characteristics. In addition, quantitative abundance analyses of supernova-induced runaway stars can give hints about complex processes such as envelope ejection and nucleosynthesis in those explosions. The detection of enhanced concentrations of elements fused via the rapid capture of neutrons would be the first

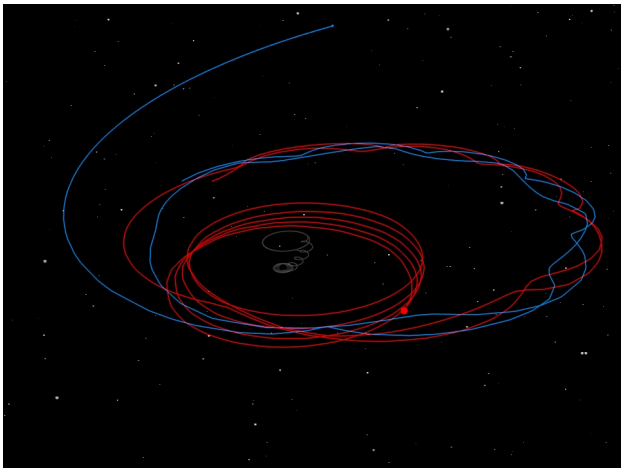

Figure 1.4: The tidal disruption of an initially bound binary system (red and blue trails) by a massive black hole (gray trail) can accelerate one component (blue) at the expense of the other component's (red) potential energy. According to Hills (1988), ejection velocities up to a few thousand kilometers per second are possible with this so-called Hills or slingshot mechanism. See Appendix A for an animated version of this figure.

observational evidence for the assumption that this so-called r process is taking place during supernova explosions. The latter, however, is a very ambitious task and would require high-quality ultraviolet spectra which are hard to obtain and even harder to model.

With the preceding aspects in mind, the immediate goal of this study is to perform a combined kinematic and spectroscopic analysis of a sample of 18 runaway stars in order to unravel their origin. Several spectroscopic analyses have already been published but almost all of them were inconclusive. This is because the expected anomalies are subtle and require a high degree of accuracy that has not been achieved so far. In a rigorous approach, we update the kinematic analysis tool to calculate stellar trajectories by accounting for the most recent observations constraining the Galactic gravitational potential. In a second step, we develop a new spectroscopic analysis technique, investigate its most important systematic uncertainty (the hydrogen line broadening due to the Stark effect), and apply it to a benchmark sample of normal O- and B-type stars, which provides a reference for a differential analysis of runaway stars. In this way, the precision of our abundance analysis is considerably increased enabling us to identify subtle chemical anomalies with higher sensitivity than any previous investigation. The new method is then applied to a sample of the kinematically most extreme halo stars known.

Chapter 2 summarizes textbook knowledge about stars (classification, structure, and evolution), stellar nucleosynthesis, and the structure of the Galaxy to provide the required astrophysical background knowledge. In Chapter 3, the basis for the kinematic investigation is laid by calibrating three Milky Way mass models with the help of updated and new observational constraints. Chapter 4 is a review about quantitative spectroscopy and addresses basic concepts of spectrographs, data reduction, and the modeling of spectra. In Chapter 5, a newly developed method for an objective spectroscopic analysis of massive stars is introduced. The broadening of hydrogen lines via the Stark effect, which turns out to be a major source of uncertainty in the spectroscopic analysis of massive stars, is discussed in Chapter 6. The new spectral analysis method is thoroughly tested in Chapter 7 by applying it to 63 nearby standard stars, which then provides an important benchmark for the subsequent investigation of the main sample, i.e., the 18 runaway stars, in Chapter 8. Finally, the thesis is rounded off by an outlook in Chapter 9.

2 Astrophysical background

This chapter, which is based on the textbooks of Clayton (1983), Carroll & Ostlie (1996), and Karttunen et al. (2007) is intended to give the necessary astrophysical background for this thesis, in particular for those readers that do not work in astronomy. The most important topics are the classification, structure, and evolution of stars with special emphasis on OB-type stars, nucleosynthesis, and the structure of the Milky Way. Several technical terms are introduced, too.

2.1 Luminosity and effective temperature

The examination of distant stars is solely based on their emitted light because no further information is obtainable. Therefore, a proper definition of physical quantities, which describe the features of electromagnetic radiation, is advisable.

First of all, the specific intensity I_ν is defined as the energy $\mathrm{d}E_{\mathrm{A},t,\Omega,\nu}$ per frequency interval $\mathrm{d}\nu$ that passes in time $\mathrm{d}t$ through an area $\mathrm{d}A_\mathrm{p}$ in the direction of the solid angle $\mathrm{d}\Omega$. The subscript p in $\mathrm{d}A_\mathrm{p}$ indicates that the area projected onto the direction of the solid angle $\mathrm{d}\Omega$ is referred to. With θ being the angle between the normal of the area and $\mathrm{d}\Omega$, one has $\mathrm{d}A_\mathrm{p} = \mathrm{d}A\cos(\theta)$, which gives

$$\mathrm{d}E_{\mathrm{A},t,\Omega,\nu} = I_\nu \mathrm{d}A_\mathrm{p}\mathrm{d}t\mathrm{d}\Omega\mathrm{d}\nu = I_\nu \cos(\theta)\mathrm{d}A\mathrm{d}t\mathrm{d}\Omega\mathrm{d}\nu\,. \tag{2.1}$$

The total intensity I is obtained by integrating I_ν over all frequencies:

$$I = \int_0^\infty I_\nu \mathrm{d}\nu\,. \tag{2.2}$$

In practice, I is of little interest due to the lack of spatial resolution (except for the Sun). Summing the geometrically weighted intensity over all possible directions yields an observable quantity called flux F, which is the net amount of energy that flows through an area $\mathrm{d}A$ per time interval $\mathrm{d}t$, that is $\mathrm{d}E_{\mathrm{A},t} = F\mathrm{d}A\mathrm{d}t$:

$$\int_{4\pi} I\cos(\theta)\mathrm{d}\Omega = F = \int_0^\infty F_\nu \mathrm{d}\nu = \int_0^\infty \int_{4\pi} I_\nu \cos(\theta)\mathrm{d}\Omega\mathrm{d}\nu\,. \tag{2.3}$$

The total energy emitted per unit time from the surface S of a star is called luminosity L,

$$L = \int_\mathrm{S} F_S \,\mathrm{d}A\,, \tag{2.4}$$

which simplifies to

$$L = 4\pi R_\star^2 F_S \tag{2.5}$$

in the case of a spherically symmetric star with radius $R_\star$.

Assigning a surface temperature to a star is a nontrivial task. On the one hand, the stellar surface is not a sharp but extended region with a nontrivial temperature structure. On the other hand, the definition of temperature by statistical physics is, in principle, only valid in thermodynamic equilibrium. Since stellar objects are close to but never completely in thermodynamic statistical equilibrium, the temperature assigned to a star depends on the physical quantity used for its determination. One definition of a stellar surface temperature relies on the Stefan-Boltzmann law, which states that the flux emitted by a blackbody is equal to $\sigma_{\mathrm{SB}} T^4$, where σ_{SB} is the Stefan-Boltzmann constant and T the temperature of the emitter. The application of this law to the surface of a star defines the effective temperature T_{eff} according to $F_S = \sigma_{\mathrm{SB}} T_{\mathrm{eff}}^4$, which, in combination with Eq. (2.5), can be used to link the effective temperature T_{eff} to the stellar luminosity and radius:

$$L = 4\pi R_\star^2 \sigma_{\mathrm{SB}} T_{\mathrm{eff}}^4 \,. \tag{2.6}$$

2.2 Classification of stars

Almost all the information that can be obtained about a star stems from its spectrum, which is the distribution of electromagnetic radiation with wavelength. Therefore, any stellar classification scheme is based on spectral features, for instance the strength of certain emission or absorption lines. The most common scheme is the Harvard classification, which was developed at Harvard Observatory in the early 20th century. It is based on absorption lines that are mainly sensitive to the stellar temperature, instead of gravity or luminosity. Among others, lines of hydrogen, helium, magnesium, silicon, calcium, iron, and some other metals[2] are utilized. According to the Harvard scheme, most stars can be divided into one of the seven groups labeled by the capital letters O, B, A, F, G, K, and M. The effective temperature decreases from O to M. This classification was recently extended by the classes L and T, which take the newly discovered coolest stars and brown dwarfs into consideration. Due to historic reasons, O-, B-, and A-type stars are sometimes called early-type stars. Hot objects like O- or B-type stars are characterized by pronounced absorption lines of helium, hydrogen, and metals in high ionization levels[3] such as C II/III, N II/III, O II/III, and Si III/IV. In contrast, the spectra of cool stars with spectral types G to M are dominated by lines of neutral metals and molecular bands. In order to categorize even more objects, additional groups have been introduced, for instance the classes S and C which parallel M in temperature but show different spectral lines. Class WR (Wolf-Rayet) covers objects of extremely high temperature, which exhibit broad emission lines of ionized helium and highly ionized carbon, oxygen, and nitrogen. Subclasses with strong carbon and rather weak nitrogen lines or vice versa are denoted WC or WN, respectively. A typical feature of Wolf-Rayet stars is the radiation-driven stellar wind.

To understand why the visibility of lines is connected to the ionization stage of a chemical element and to the effective temperature, consider the following simplified picture. Each spectral absorption line corresponds to a specific transition in an atom. Photons can only be absorbed by an atom if the latter is in the lower of the two states that are involved in this transition. The strength of an absorption line increases with the number of absorbers and, therefore,

[2] In astronomy, the term "metal" refers to any element other than hydrogen or helium.

[3] The notation X I stands for the neutral atom of species X, X II for the singly ionized atom, X III for the doubly ionized atom and so on.

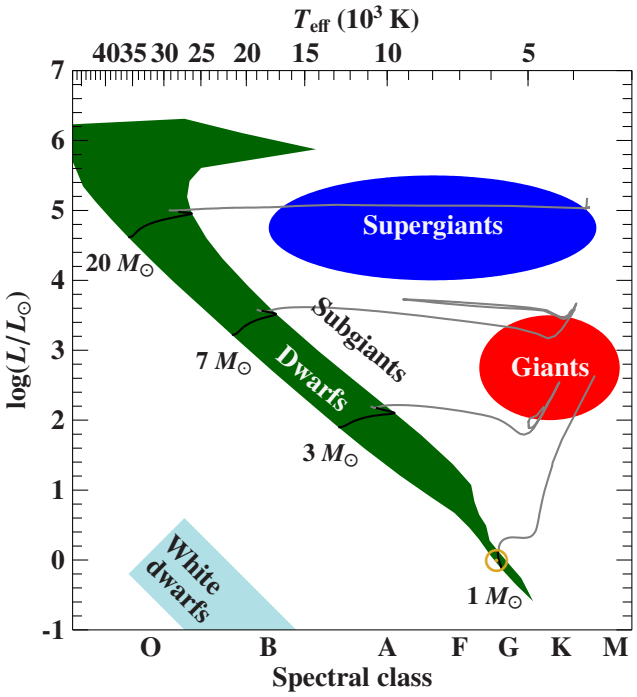

Figure 2.1: Classification of stars with the help of a schematic Hertzsprung-Russell diagram. Position of dwarfs, (super)giants, and white dwarfs are indicated. The location of the Sun is marked by a yellow ⊙. Overlaid are evolutionary tracks by Ekström et al. (2012) for stars with initial masses of 1 $M_\odot$, 3 $M_\odot$, 7 $M_\odot$, and 20 $M_\odot$. The hydrogen-burning (or main-sequence) phase is coded in black color, the subsequent helium-burning phase in gray. This work focuses on OB dwarfs and subgiants, that is stars with effective temperatures ranging from 12 000 K to 35 000 K and masses between 3 $M_\odot$ and 25 $M_\odot$.

depends on the population of the lower state, which, in turn, is a function of the temperature and the excitation and ionization energies of the respective atom. For example, the Balmer lines of hydrogen are relatively weak in class O because a large fraction of the hydrogen atoms is ionized owing to the high temperatures of these objects. With decreasing temperature, the fraction of neutral hydrogen in the first excited state grows and finally reaches a maximum at spectral class A, which shows the strongest and broadest hydrogen lines of all spectral types. However, a further reduction of the temperature drives more and more hydrogen atoms in their ground state and, thus, suppresses the Balmer transitions so that the Balmer lines become weak in stars of spectral types K and M. A quantitative description can be given by the combined application of the equations by Boltzmann (Eq. (4.35)) and Saha (Eq. (4.36)), where the former determines the occupation numbers of excited states within an atom of fixed ionization stage and the latter links different ionization stages by taking into account the available phase space of the released electron.

To gain further insight into the nature of stars and their evolution, it is instructive to study the correlation between spectral class/temperature and luminosity. This was done at the beginning of the 20th century by the astronomers E. Hertzsprung and H. N. Russell, who discovered one of the most fundamental relations of astrophysics: by plotting the spectral class versus luminosity for a sufficient large number of stars, they found a clear pattern, which showed that the evolution of stars is based on fundamental principles. A schematic version of such a so-called Hertzsprung-Russell (HR) diagram is displayed in Fig. 2.1. In a simple picture, three major groups can be distinguished, namely, dwarfs, (super)giants, and white dwarfs. Each of these groups represents a distinct phase in the evolution of stars. The dwarfs are stars that burn hydrogen in their cores to generate energy. This is the first and most important stage in stellar evolution since it is the one that lasts longest. Approximately 80 to 90 percent of all stars are in this phase. This also applies to the Sun, which has an effective temperature of 5785 K (Karttunen et al. 2007). The dwarf phase is followed by the giant or supergiant phase, which

is characterized by advanced burning stages in the stellar core after exhaustion of hydrogen, which causes the star to change its structure and, thus, to expand. The inevitable destiny of most stars is to become a white dwarf, which is a very compact and hence less luminous, high-density object. It is slowly cooling down because no energy is created in its interior. White dwarfs avoid gravitational collapse due to the pressure of the degenerate electron gas. However, for stellar masses above the Chandrasekhar limit of 1.5 $M_\odot$, the gravitational force is so strong that it can compress the matter to such high densities that the electrons are pressed into the nuclei of atoms, which leads to the formation of neutrons out of protons. The resulting object is called a neutron star and is stabilized by the pressure of the degenerate neutron gas. For masses exceeding the larger Tolman-Oppenheimer-Volkoff limit of about 2–3 $M_\odot$, the neutron pressure is not enough to stop the gravitational collapse. The object is turned into a black hole, which is so compact that not even light can escape from it.

In the HR diagram, the dwarfs form a continuous band, which is often referred to as main sequence. The position of a star on the main sequence depends on its initial mass. The massive stars on the upper main sequence are hot and, hence, of spectral type O, B, or A, whereas the less massive stars on the lower main sequence are cooler. The evolutionary tracks of four stars with different initial masses are displayed in Fig. 2.1 to give an impression of how stars evolve in the HR diagram.

2.3 Stellar structure

To get a feeling of how stellar evolutionary tracks are calculated, it is necessary to understand the principle laws that describe the structure of stars. For the sake of simplicity, complex effects like rotation, magnetic fields, gravitational collapse, or mass loss are neglected and only the most simple case of a spherically symmetric star is considered here. The conditions inside a star can then be expressed by the following system of four differential equations which link the radial distribution of mass $M(r)$, pressure $P(r)$, luminosity $L(r)$, temperature $T(r)$, and density $\rho(r)$ to each other:

$$\frac{\mathrm{d}M(r)}{\mathrm{d}r} = 4\pi r^2 \rho(r)\,, \tag{2.7a}$$

$$\frac{\mathrm{d}P(r)}{\mathrm{d}r} = -\frac{GM(r)\rho(r)}{r^2}\,, \tag{2.7b}$$

$$\frac{\mathrm{d}L(r)}{\mathrm{d}r} = 4\pi r^2 \rho(r)\left(\epsilon - T\frac{\mathrm{d}S}{\mathrm{d}t}\right), \tag{2.7c}$$

$$\frac{\mathrm{d}T(r)}{\mathrm{d}r} = -\frac{3}{4ac}\frac{\kappa}{T^3}\frac{L(r)}{4\pi r^2} \quad \text{(radiative)} \quad \text{or} \quad \frac{\mathrm{d}T(r)}{\mathrm{d}r} = \frac{\Gamma_2 - 1}{\Gamma_2}\frac{T(r)}{P(r)}\frac{\mathrm{d}P(r)}{\mathrm{d}r} \quad \text{(convective)}\,. \tag{2.7d}$$

Equation (2.7a) is the mass continuity equation $M(r) = \int_0^r 4\pi \acute{r}^2 \rho(\acute{r})\mathrm{d}\acute{r}$ in its differential form. Equation (2.7b) follows from the application of Newton's second law to an infinitesimal mass element $\mathrm{d}M = \rho \mathrm{d}A\mathrm{d}r$ at radial position r and the balance of gravitational and pressure force,

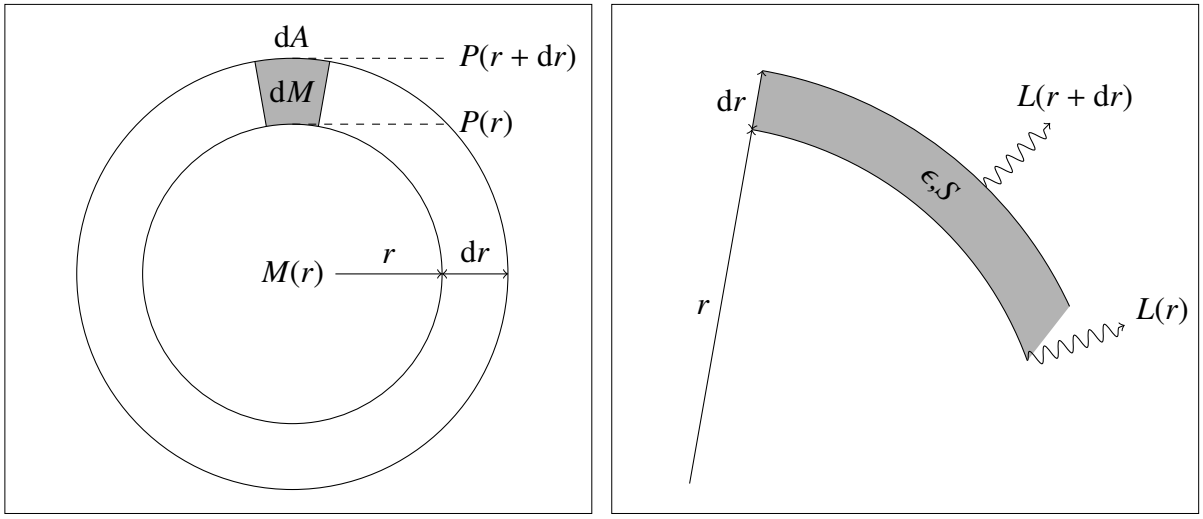

a: Hydrostatic equilibrium. b: Energy conservation.

Figure 2.2: *Left:* The condition of a static stellar structure requires that the inbound gravitational force is balanced by a pressure-induced outbound force, which yields the equation of hydrostatic equilibrium Eq. (2.7b). *Right:* Energy conservation states that the difference in luminosities of two adjacent shells is caused either by energy production or changes in the heat energy in between the shells, which gives Eq. (2.7c).

see Fig. 2.2a:

$$
\begin{aligned}
\mathrm{d}F &= \mathrm{d}M\frac{\mathrm{d}^2 r}{\mathrm{d}t^2} = \rho(r)\mathrm{d}A\mathrm{d}r\frac{\mathrm{d}^2 r}{\mathrm{d}t^2}\,.\\
\mathrm{d}F &= \mathrm{d}F_{\text{gravitation}} + \mathrm{d}F_{\text{pressure}}\\
&= -\frac{GM(r)\mathrm{d}M}{r^2} + P(r)\mathrm{d}A - P\left(r+\mathrm{d}r\right)\mathrm{d}A = -\frac{GM(r)\rho(r)\mathrm{d}A\mathrm{d}r}{r^2} - \mathrm{d}P(r)\mathrm{d}A\,.\\
&\Rightarrow \frac{\mathrm{d}P(r)}{\mathrm{d}r} = -\frac{GM(r)\rho(r)}{r^2} - \rho(r)\frac{\mathrm{d}^2 r}{\mathrm{d}t^2}\,.
\end{aligned}
$$

In equilibrium, the time derivative vanishes and the equation of hydrostatic equilibrium is obtained. Equation (2.7c) is the equivalent of energy conservation. The quantity ϵ is the energy released per unit mass of stellar matter by nuclear reactions per unit time. It is a function of density $\rho(r)$, temperature $T(r)$, and the set of elemental abundances $\{n(x)\}$, $\epsilon = \epsilon\left(\rho(r), T(r), \{n(x)\}\right)$. The quantity $S = S\left(\rho(r), T(r), \{n(x)\}\right)$ is the entropy per unit mass of stellar matter. Therefore, the second term in Eq. (2.7c) reflects that energy can also be absorbed or released in form of heat $\mathrm{d}Q = T\mathrm{d}S$. Combining the definitions of ϵ and S with Fig. 2.2b, one has $4\pi r^2\rho(r)\mathrm{d}r\epsilon = L(r+\mathrm{d}r) - L(r) + 4\pi r^2\rho(r)\mathrm{d}rT\mathrm{d}S/\mathrm{d}t$, which leads immediately to Eq. (2.7c). Equation (2.7d) determines the temperature gradient within the star, which is tightly connected to the transport of energy. In principle, there are four possibilities for the latter: radiative transfer, convection, conduction, and neutrino emission. Due to their weak interaction with matter, neutrinos merely remove energy from the star instead of redistributing it. Hence, neutrino losses are considered as a negative ϵ in Eq. (2.7c) and do not influence the temperature gradient. It can be shown that the effects of conduction are non-negligible solely for extremely high densities,

which are encountered, for instance, in white dwarfs, and are therefore not of interest for this work. In main-sequence stars, energy is transported either by radiative transfer or convection. To discriminate between them, consider a certain amount of gas enclosed in a perfectly elastic balloon that is displaced adiabatically, that is without exchange of heat, by a small distance in radial direction. Due to the negative pressure gradient (see Eq. (2.7b)) inside the star, the balloon will expand to adopt the same pressure as its environment. Since the expansion is assumed to be adiabatic, the new density inside the balloon typically differs from the one outside of it. If the inner density exceeds the outer, the balloon will be pulled back by gravitation, so that convective motion is suppressed. According to the equation of state of a perfect gas, a higher density implies a lower temperature at constant pressure. The adiabatic change of temperature inside the balloon is therefore larger than the non-adiabatic one of the environment in the case of a stable, non-convective configuration. Hence, convection can occur only in the opposite case when the radiative temperature gradient exceeds the adiabatic one. The latter is given by the second formula in Eq. (2.7d) where Γ_2 is the second adiabatic exponent, which couples T and P during adiabatic changes. It is a function of density, temperature, and composition of the gas, and is always larger than one, $\Gamma_2 = \Gamma_2(\rho(r), T(r), \{n(x)\}) > 1$. The radiative temperature gradient is motivated as follows. According to the Stefan-Boltzmann law, the power emitted per unit area by a blackbody is $\sigma_{\mathrm{SB}} T^4$. Consider two adjacent spherical shells with radii r and $r + \mathrm{d}r$ and temperatures T and $T + \mathrm{d}T$. Assuming that each shell absorbs all energy irradiated on it, the net energy gain, that is the difference between absorbed and emitted energy, at $r + \mathrm{d}r$ per unit time is $4\pi r^2 \sigma_{\mathrm{SB}}(T^4 - (T + \mathrm{d}T)^4) = -16\pi r^2 \sigma_{\mathrm{SB}} T^3 \mathrm{d}T + O(\mathrm{d}T^2) \approx -16\pi r^2 \sigma_{\mathrm{SB}} T^3 \mathrm{d}T$. This expression gives the amount of energy that is transferred from r to $r + \mathrm{d}r$ and is, thus, equal to the luminosity: $L(r) \approx -16\pi r^2 \sigma_{\mathrm{SB}} T^3 \mathrm{d}T$. Further assuming that each photon travels a characteristic distance l before it is absorbed, $\mathrm{d}T$ becomes $l\,\mathrm{d}T/\mathrm{d}r$. For later convenience, define the absorption coefficient κ by $l = \kappa^{-1}$ and introduce the radiation constant $a = 4\sigma_{\mathrm{SB}}\, c^{-1}$ where c is the speed of light in vacuum. Putting everything together yields $L(r) \approx -16\pi r^2 a c T^3 (4\kappa)^{-1} \mathrm{d}T/\mathrm{d}r$. Apart from a factor $4/3$, this is identical to the first formula in Eq. (2.7c), which is derived by an exact solution of the respective diffusion equation in combination with a precise definition of the absorption coefficient $\kappa = \kappa(\rho(r), T(r), \{n(x)\})$ (see Clayton 1983, pp. 172–183). To decide which version of Eq. (2.7d) has to be applied, one has to evaluate both expressions. As discussed above, the radiative temperature gradient is valid as long as it is below its adiabatic counterpart. Otherwise, convection occurs, which is then assumed to be governed by the adiabatic version of Eq. (2.7d).

A few words about the absorption coefficient, or opacity, κ are appropriate at this point. As indicated by its name, the opacity is a measure for the ability of photons to travel through a medium: the higher κ the shorter the mean distance that is passed before the photon is absorbed or scattered. The four most important processes that contribute to the opacity are bound-bound absorption, bound-free absorption, free-free absorption, and scattering from free electrons. The first three interactions are true absorption processes in the sense that the number of photons is decreased by one while the photon and its energy are absorbed by an electron. However, depending on the state – bound to an atom or free in the continuum – of initial and final electron, the description of the interaction varies significantly. The scattering from free electrons, which is also called Thomson scattering, is not a true absorption process since the photon number does not vary. Yet, this interaction alters the kinematics of a photon and can be thought of as the absorption of an initial and subsequent emission of a final photon. Hence, it also influences the

opacity of stellar matter. All interactions, especially bound-bound and bound-free absorption, depend on the composition of the medium under investigation. The temperature and density also affect the state of the atoms (for example, with respect to occupation numbers, ionization stages, energy levels) as well as the number and velocity distribution of electrons and are, therefore, crucial for the determination of κ. The computation of opacities is a complex task since it requires the proper knowledge of various cross-sections, which either are directly measured or have to be calculated by means of atomic physics. Finally, a nontrivial average over frequencies, the so-called Rosseland mean (see Clayton 1983, p. 182), has to be performed to compute the mean opacity, which enters Eq. (2.7d), from the frequency-dependent spectral opacity κ_ν.

Because they are the most abundant elements, κ is generally dominated by hydrogen and helium. Computations reveal that hydrogen ionization zones, i.e., regions where a considerable part of hydrogen is ionized and which are characterized by $T \approx 10^4\,\mathrm{K}$ for densities of main-sequence stars, have the largest opacities. On the one hand, cooler environments do not offer enough sufficiently energetic photons to induce bound-free transitions in hydrogen nor is the number of free electrons large enough for scattering to be important. On the other hand, larger temperatures reduce the fraction of neutral hydrogen atoms and, hence, mitigate the effects of bound-bound and bound-free absorption on the opacity. For intermediate temperatures, none of the four absorption processes substantially drops off, which results in a maximum value for κ. This has important consequences for the existence of convection zones. According to Eq. (2.7d), the radiative temperature gradient is proportional to κ, which means that the ionization zone of hydrogen has the steepest temperature gradient and, thus, is the best candidate for convection. In addition to that, Γ_2 happens to be very close to one in a partially ionized state, which further strengthens this effect since it flattens the adiabatic temperature gradient. As illustrated in Fig. 2.1, the effective surface temperatures of O- and B-type stars exceed $10^4\,\mathrm{K}$ so that the hydrogen ionization zone and its associated convection zone are absent in these objects. This does not apply to mid A-type stars and cooler where pronounced convection zones are expected in the stellar envelope.

Another important opacity source are the so-called iron group elements such as chromium, manganese, iron, cobalt, and nickel. Owing to their huge number of atomic transitions, which is several orders of magnitude larger than that of hydrogen, these elements can contribute significantly to the bound-bound and bound-free opacity under certain circumstances. The corresponding peak in the opacity is referred to as the iron opacity bump and affects OB stars in at least two ways. Firstly, it can cause convective motion similarly to the hydrogen ionization zone in cool stars. However, the location and extent of the convective regions are quite different. The hydrogen convection zone typically covers a considerable fraction of the stellar interior and is, thus, crucial for the structure of the star. The iron convection zone, on the other hand, comprises a relatively small amount of mass and lies just below the surface of the star. It is therefore negligible for the stellar structure but – as discussed in Sect. 7.3.5 – important for the stellar atmosphere, which is the region of the star where the emitted spectrum comes from. Secondly, the iron opacity bump is supposed to trigger the pulsation, or variability, of β Cepheid stars and slowly-pulsating B-stars via the so-called κ mechanism. In this scenario, the pulsations are driven by the opacity, which changes with temperature and density and, therefore, acts similar to a valve in a combustion engine.

Before the differential Eqs. (2.7) can be solved to compute the structure of a spherically symmetric star, one has to provide a set of boundary conditions, which typically are $M(0) = 0$,

$L(0) = 0$, $P(R_\star) = P_{R_\star}$ and $T(R_\star) = T_{R_\star}$. In stars of spectral type O and B, the temperature gradient is radiative at the stellar surface. Because the expression κ/T^3 in Eq. (2.7d) becomes very large as T approaches zero, the interior structure is then insensitive to the boundary conditions and one can simply assume that $P_{R_\star} = 0$ and $T_{R_\star} = 0$. Note that $T_{R_\star} = 0$ does not imply $T_{\rm eff} = 0$ since the latter follows from $L(R_\star)$, $R_\star$, and Eq. (2.6). Further requirements to solve the system of equations are the knowledge of expressions for $\epsilon(\rho(r), T(r), \{n(x)\})$, $S(\rho(r), T(r), \{n(x)\})$, $\kappa(\rho(r), T(r), \{n(x)\})$, $\Gamma_2(\rho(r), T(r), \{n(x)\})$, and for the equation of state of the stellar gas $P = P(\rho(r), T(r), \{n(x)\})$, which is used to eliminate the pressure. Finally, after specifying the chemical composition $\{n(x)\}$ of the star, the system is completely determined and numerical integration methods yield the mass, temperature, density, and luminosity as a function of the radius r, whereby $R_\star$ is so far an input parameter. To compute a model with a certain mass instead of a certain radius, one can introduce $M_r = M(r)$ as the independent variable by using Eq. (2.7a) to replace r by M_r in the other three equations. The resulting functions are then $r(M_r)$, $L(M_r)$, $T(M_r)$, and $\rho(M_r)$ with M_r ranging from zero to the total mass M. Once an initial stellar model is at hand, it can be used to compute the evolution of a star with the given mass. To do so, one has to specify the input parameters of the next model by means of the current model, which means, for instance, that one has to take into account the changes in the chemical composition due to nuclear reactions or convective mixing and that one has to update the time derivative of the entropy S, see Eq. (2.7c).

Although the underlying problem is extremely complex, stellar models have proven to be very successful. In particular, the match of stellar evolution theory, which is discussed in the next section, to observation is impressive.

2.4 Stellar evolution

A very important tool to understand the evolution of stars is the well-known virial theorem from statistical physics. It links the total kinetic energy K to the total gravitational potential Φ, provided the system is in hydrostatic equilibrium:

$$K = -\frac{\Phi}{2}\,. \tag{2.8}$$

The most crucial statement that can be drawn from Eq. (2.8) is the fact that gravitational contraction, i.e., a reduction of Φ, from one stable state to another one leads to a rise in kinetic energy by a portion that is one half of the released gravitational energy. Consequently, a contracted mass is heated up. The remaining part of the energy is transformed into radiation.

The formation of stars is triggered by gravitational instabilities of the interstellar gas. If a sufficient amount of matter is somehow compressed to a small enough volume, gravitation can overcome the counteracting pressure and prompt the gas to collapse. In the course of this process, the gravitational pull as well as the outgoing pressure keep on growing. Due to heat-up processes at the center of the instability, the pressure eventually stops the shrinkage and a state close to hydrostatic equilibrium is reached at the central region. However, mass is still accreted from the surrounding medium, which further increases the temperature and pressure. This continues until the central temperature reaches the point where repulsive Coulomb interactions between protons are overcome at sufficiently large rates so that a non-negligible amount of

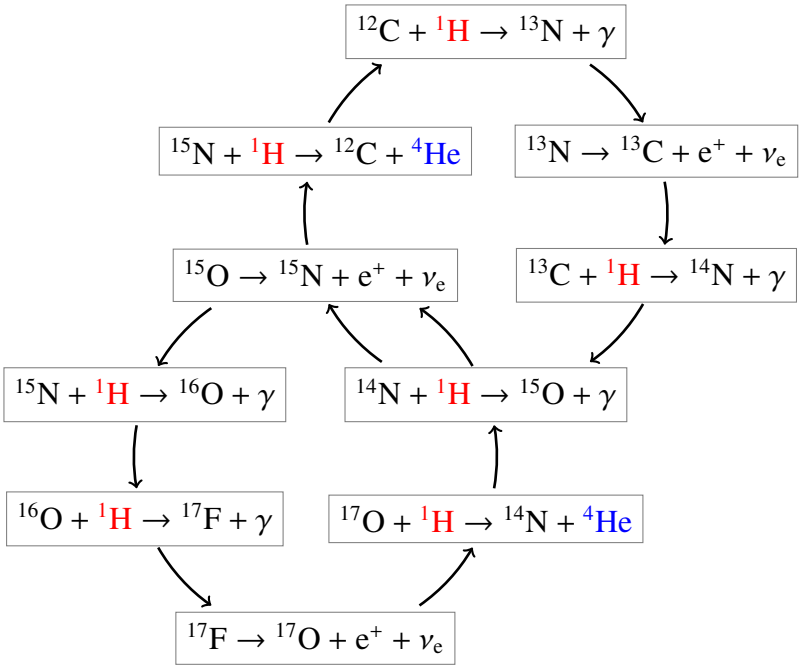

Figure 2.3: Conversion of hydrogen to helium via the carbon-nitrogen-oxygen bi-cycle. Incoming hydrogen atoms are marked red while the reaction product helium is colored in blue. Carbon, nitrogen, and oxygen act as catalysts. The reaction $^{14}N + {}^{1}H \rightarrow {}^{15}O + \gamma$ is the bottleneck in this network.

nuclear fusion reactions occur in the core. This additional release of energy creates a radiation pressure that prevents the newly formed star from accreting even more matter. After some relaxation time, an almost stable state is achieved. Since huge masses – a lower limit is given by the Jeans mass (see Karttunen et al. 2007, p. 125) – are required to make a gas cloud collapse due to its own gravitation, stars are supposed to form only in associations or open clusters, which are groups of stars with a few hundred to a few thousand members. The individual stars result then from the fragmentation of the initial gas cloud into smaller ones, which are at some point compact enough to collapse on their own.

The first nuclear burning stage that continually creates energy in a star is the conversion of hydrogen to helium, which is commonly denoted hydrogen burning. As hydrogen is by far the most abundant element, there is so much fuel available that stars spend most of their life in this main-sequence phase. The lifetime τ of a star is, roughly speaking, proportional to the amount of fuel and inverse proportional to the energy consumption. In a very simple picture, the former can be approximated by the mass M of the star and the latter by its luminosity L, which yields $\tau \propto M/L$. Given the fact that the luminosities of stars on the upper main sequence exceed their counterparts on the lower main sequence by orders of magnitude (see Fig. 2.1), the lifetimes of massive stars are expected to be substantially smaller than those of the cool stars. This assumption is confirmed by stellar evolutionary tracks, which show that stars at the lower end of the main sequence live for billion of years while early-type stars end their life after a few hundred million years or less.

The conversion of hydrogen to helium is not a single reaction but a whole reaction network. For massive stars on the upper main sequence, this network is the carbon-nitrogen-

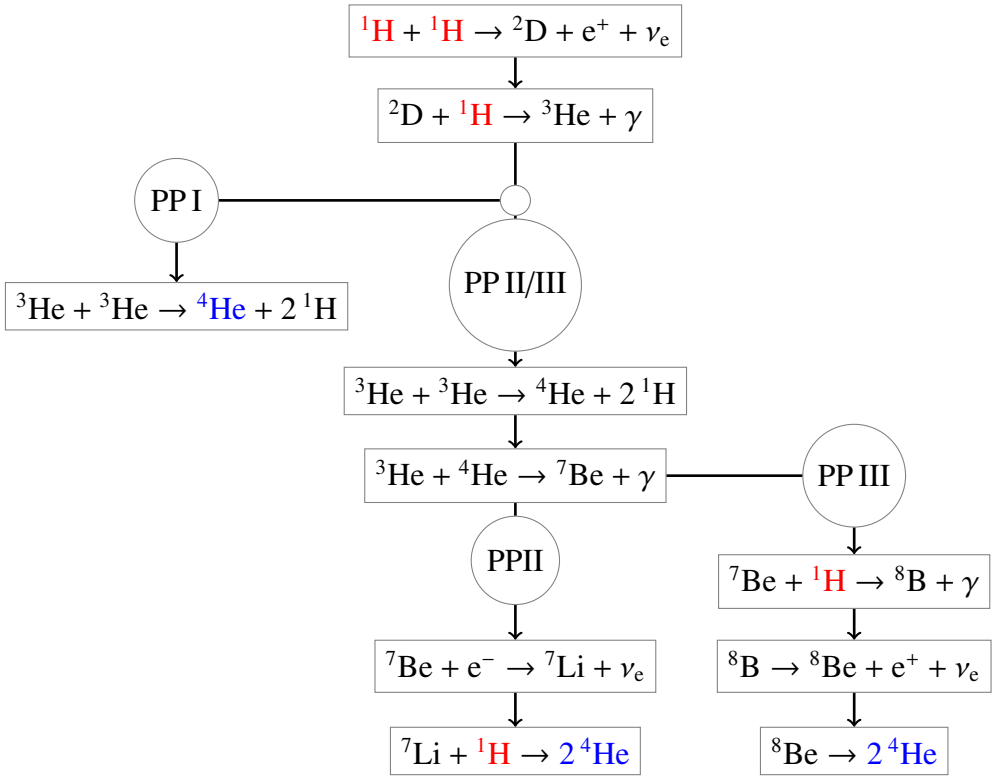

Figure 2.4: Conversion of hydrogen to helium via the proton-proton chain: Incoming protons are marked red while the reaction product helium is colored in blue. Three different reaction channels are distinguished. PP I is the only path that can occur in a pure hydrogen gas and is most effective in cool stellar environments. With increasing temperature, energy generation is dominated by PPII, then by PPIII, and finally by the CNO bi-cycle (Fig. 2.3).

oxygen (CNO) bi-cycle (Fig. 2.3), whereas the proton-proton (PP) chain (Fig. 2.4) dominates in low-mass stars where the temperature in the stellar interior is smaller. Investigations reveal (see Clayton 1983, pp. 366–410) that the energy production in the CNO bi-cycle is extremely sensitive to the temperature. As a consequence, the energy generation is strongly peaked at the center of the star where the temperature reaches its maximum. Therefore, almost the entire luminosity is created in a tiny central region, the core. To transport this huge amount of energy to the outer layers, the temperature gradient has to be as steep as possible, which inevitably leads to convection. In contrast, the temperature dependence of the PP chain is so modest that radiative energy transfer is sufficient. In combination with the discussion about the occurrence of a hydrogen ionization zone in Sect. 2.3, one can conclude that objects on the upper main sequence like OB-type stars have convective cores and radiative envelopes, whereas the situation is vice versa for lower main-sequence stars like the Sun.

During hydrogen burning, the position of the star in the HR diagram (Fig. 2.1) is slightly moving away from its original location, which is characterized by the ignition of hydrogen[4], to the upper right. The reason for this is that the conversion of hydrogen to helium leads to a reduction of free particles. As a consequence, the particle pressure at the center of the star

[4]The curve consisting of all those points is referred to as **z**ero **a**ge **m**ain **s**equence (ZAMS).

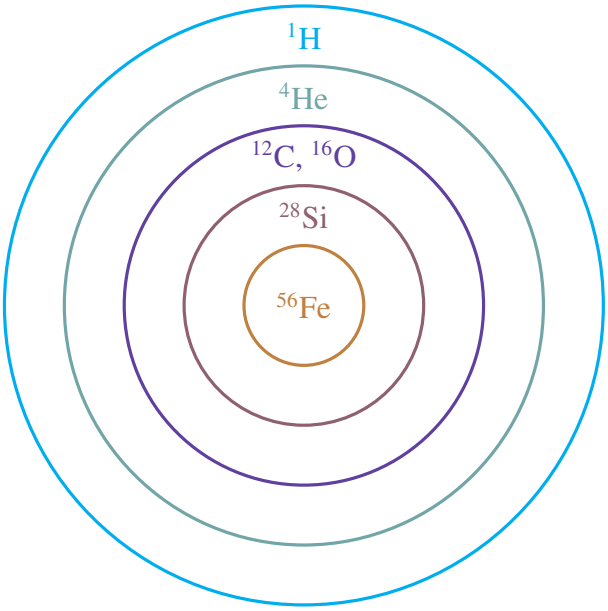

Figure 2.5: Onion-like shell structure of massive stars at the end of their evolution. Each shell represents a nuclear burning stage that was originally located at the center of the star. After depletion of the central fuel, the burning continued as shell burning in the adjacent, heated layers and gradually moved outwards. The drawing is not to scale.

decays, which results in a slow but steady contraction and heating of the core. The temperature of the surrounding shell is then also increased, and is, at some point, capable of burning hydrogen, which leads to a further contraction of the central region. The associated rise of the central temperature steepens the temperature gradient, which, however, throws the energy transfer out of balance. To compensate for this, the outer layers of the star expand to flatten the gradient again. Consequently, the surface and, hence, the luminosity of the star increases although the effective temperature decreases. The development described so far is similar for stars of all masses and takes place gradually, contrary to what follows when the hydrogen fuel at the center is exhausted. In a vastly simplified picture, the depletion of hydrogen leaves behind a non-reactive and continually contracting helium core that is surrounded by a hydrogen burning shell. The central contraction is still accompanied by an expansion of the entire star, which marks the onset of its (super)giant phase in the HR diagram.

In massive stars ($M \gtrsim 8\,M_\odot$), the contraction of the core is slowed down by the ignition of helium burning via the triple alpha reaction $3\,^4\mathrm{He} \rightarrow {}^{12}\mathrm{C}+\gamma$, which is actually composed of two successive reactions, namely the creation of the unstable isotope ^{8}Be by $^4\mathrm{He} + {}^4\mathrm{He} \leftrightarrows {}^8\mathrm{Be}$ and an almost instantaneous catch of a third alpha particle ${}^8\mathrm{Be}+{}^4\mathrm{He} \rightarrow {}^{12}\mathrm{C}+\gamma$. Apart from a much shorter time span, the evolution during central helium burning is quite similar to that of hydrogen burning, which means that there remains again a non-reactive, rapidly contracting core enclosed by an inner helium and outer hydrogen burning shell after the depletion of the central helium fuel. However, the core does not purely consist of carbon at this point but also contains oxygen, neon, and magnesium, which were produced by further alpha particle captures. With rising temperatures, the conditions for carbon and oxygen burning are met yielding magnesium ($^{12}\mathrm{C} + {}^{12}\mathrm{C} \rightarrow {}^{24}\mathrm{Mg} + \gamma$), sulfur ($^{16}\mathrm{O} + {}^{16}\mathrm{O} \rightarrow {}^{32}\mathrm{S} + \gamma$), and silicon ($^{16}\mathrm{O} + {}^{16}\mathrm{O} \rightarrow {}^{28}\mathrm{Si} + {}^4\mathrm{He}$). Finally, silicon is burned to nickel ($^{28}\mathrm{Si} + {}^{28}\mathrm{Si} \rightarrow {}^{56}\mathrm{Ni} + \gamma$), which, in turn, decays to iron ${}^{56}\mathrm{Ni} \rightarrow {}^{56}\mathrm{Co}+\mathrm{e}^+ + \nu_\mathrm{e} \rightarrow {}^{56}\mathrm{Fe}+2\mathrm{e}^+ + 2\nu_\mathrm{e}$. Since ^{56}Fe has the largest binding energy per nucleon of all nuclei, energy is no longer released by further thermonuclear fusion reactions. Therefore, iron marks the natural end of stellar energy generation due to nuclear fusion.

At this point in stellar evolution, the massive star is supposed to have an onion-like struc-

ture as illustrated in Fig. 2.5. Because of exhaustion of the central fuel, the hydrogen burning region migrated to an outer layer, which had been heated up and, thus, had enabled hydrogen to fuse there. The following, advanced burning stages have undergone the same development. However, at the onset of carbon and oxygen burning, the temperature is large enough for another effect, namely photodisintegration, to occur, which is the disintegration of nuclei by the thermal photon bath. Since this fission reaction is endothermic, it reduces the temperature and pressure of the environment. While this effect is negligible in the course of carbon and oxygen burning, its plays a decisive role during silicon burning (see Clayton 1983, pp. 517–533) and especially for the final fate of massive stars. As mentioned above, iron is not capable of producing further energy by nuclear reactions. Instead, the collapse of the already contracting iron core is tremendously accelerated by the removal of photons due to the photodisintegration of iron, which not only reduces the temperature but also the particle and radiative pressure resulting in a runaway process. In this way, the gravitational energy, which is released by the contraction of the core, reconverts a considerable amount of iron to elements prior in the fusion chain. The ongoing collapse of the core raises the central density to values sufficient to form neutrons out of free electrons and protons. The core contraction is then finally stopped or at least sharply slowed down by the emerging degenerate neutron pressure that is a consequence of Pauli's exclusion principle for fermions. The abrupt deceleration leads to some rebound of matter sending away pressure waves into the outer, in-falling material. Although loosing significant amounts of energy via photodisintegration, which is induced by the temperature rise after compression, the shock waves can still leave the iron rich central region. In exterior shells, they regain strength by igniting higher or by fostering existing nuclear burning stages, respectively, or by absorbing neutrinos that were, for instance, copiously released during photodisintegration, electron-positron annihilation, or neutron production. The latter is possible since the densities in the waves reach values that are that high that not even so weakly interacting particles like neutrinos can penetrate these regions without some absorption. The strengthening of the shock waves finally leads to an eruptive explosion during which the outer layers of the star are expelled. According to Fig. 2.5, the ejected envelope mainly consists of hydrogen, helium, carbon, and the so-called alpha elements oxygen, neon, magnesium, silicon, and sulfur. Depending on its mass, the remnant evolves either to a neutron star in the case that the pressure of the degenerate neutron gas can withstand the gravitational force or to a black hole if it cannot.

The events outlined in the previous paragraph describe a type II supernova, which differs from type I due to the presence of hydrogen absorption lines. Supernovae of type I lack this peculiar feature and can further be distinguished into I a, I b, and I c: The latter two resemble type II supernovae as they also originate from the collapse of a massive star's iron core. Albeit, stars of type I b have somehow lost their hydrogen envelope, type I c also their helium envelope prior to the supernova explosion. Type I a supernovae are supposed to result from mass accretion of a carbon-oxygen white dwarf in a close binary system. Accounting for the mass loss during stellar evolution, white dwarfs are the final fate of stars with $M \lesssim 8\,M_\odot$. In contrast to the massive stars, the conditions in the cores prevent low-mass stars from igniting carbon or oxygen burning after helium is depleted. The main reason for this is the huge central density, which results in an additional electron degeneracy pressure that stops the core contraction and, thus, the associated rise of temperature, which is necessary for further nuclear fusion reactions. After expelling its outer layers, which then form a planetary nebula, the remaining compact core is slowly cooling down as a white dwarf. However, if, by some means, the mass of the white dwarf

is increased above a critical threshold, carbon burning can begin after all. The corresponding release of nuclear energy raises the temperature but, by virtue of the matter's degeneracy, does not significantly effect the pressure. Hence, the growing temperature is not compensated by an expansion of the burning region and, consequently, leads to more and more fusion reactions until the degeneracy is removed. Like a thermonuclear runaway, the front of carbon burning moves fast through the white dwarf, releasing more and more energy, which eventually disrupts the entire star. In contrast to other supernovae, explosions of type I a set free a considerable amount of iron, which was fused during the sudden and enormous jump of temperature, and do not leave behind a remnant.

As just mentioned, the destiny of low-mass stars like the Sun is to become a white dwarf after main-sequence hydrogen and giant-phase helium burning. The boundary separating the evolution of massive from non-massive objects is not sharp and depends on the composition of the star, in particular on its metallicity, which is the mass fraction of all elements except for hydrogen and helium.

Having some insights into the complex processes that govern the structure and evolution of stars[5], it is now time to focus on stellar nucleosynthesis.

2.5 Origin of the elements

The theory of stellar elemental synthesis has been developed for almost six decades[6] now and is still far from being complete. For the scope of this work, only the basic ideas are of importance and, hence, presented. Figure 2.6 shows the distribution of elemental abundances in the Sun. Apart from an overall tendency to lower abundances with larger atomic weights, peaks are evident, which are a direct consequence of the nuclear structure of atoms and the circumstances encountered during the evolution of stars. The most abundant element is hydrogen, which was produced in the early phase of the universe right after the Big Bang and is, thus, of primordial origin. The second most abundant element is helium, which is mainly primordial but to some extent also the result of hydrogen burning. All heavier elements have been produced from hydrogen and helium by nuclear fusion reactions in the interiors of stars and subsequently have been ejected into the interstellar matter, e.g. by supernova explosions, to form new generations of stars. Consequently, the metal content of a galaxy increases with time because more and more stars undergo the final stages of their evolution.

As outlined in the previous section, the final nuclear burning stage is silicon burning, which is accompanied by the counteracting process of photodisintegration. Because of the existence of an inverse disintegration reaction, a state of nuclear statistical equilibrium can be achieved after depletion of silicon. In equilibrium, those elements are favored that have the tightest binding and, hence, the lowest energies – the iron-group elements. This principle, commonly denoted as e(quilibrium)-process, gives a good explanation for the peak at the iron group in Fig. 2.6.

But what is the origin of those elements heavier than the iron group? The mechanisms described so far, e-process and nuclear fusion, predict substantially smaller abundances for these

[5] See, e.g., Clayton (1983, Chapters 5 and 6), Carroll & Ostlie (1996, Chapter 13), or Karttunen et al. (2007, Chapter 12) for much more detailed information on this topic.

[6] Starting with Burbidge et al. (1957) and Cameron (1957). A comprehensive review article is given, e.g., by Wallerstein et al. (1997).

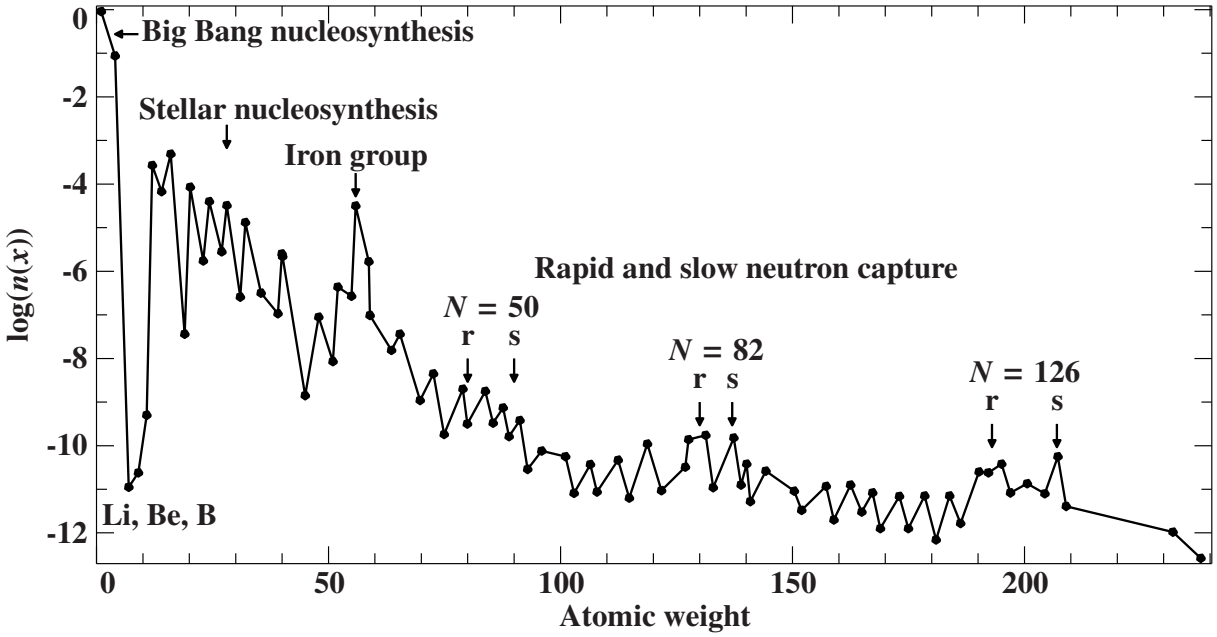

Figure 2.6: Solar abundance curve according to the protosolar values by Asplund et al. (2009). Abundances $n(x)$ are given as fractional particle number with respect to all elements. The letters "r" and "s" mark contribution from the rapid and slow neutron capture process while N is the number of neutrons. The shape of the curve can be well explained by the combined effects of Big Bang and stellar nucleosynthesis.

elements than actually observed. This is owing to the fact that, on the one hand, the binding energy per nucleon is small in heavy elements so that they are not favored in equilibrium, and, on the other hand, the strong Coulomb repulsion between the highly charged nuclei prevents fusion reactions from occurring at significant rates. However, neutron captures are not affected by the Coulomb interaction. Successively adding one neutron after the other to a nucleus can build up massive, neutron-rich atoms that can then transform into other chemical species by β decays. Depending on the available neutron flux, two kinds of neutron capture processes are distinguished: the s(low) process and the r(apid) process.

In the s process, the neutron flux is so small that any β-decay reaction has time to occur before the next neutron is captured. In order to explain the abundance peaks labeled with "s" in Fig. 2.6, one has to bear in mind that the neutron-capture cross sections in the s-process path are not equal. In particular, a shell model of the nucleus[7] shows that atoms with neutron numbers 50, 82, and 126 have relatively small cross sections because their neutron shells are closed. This results in a low probability or a long time, respectively, to capture further neutrons and hence leads to the observed accumulation of their β-decay products. The neutron fluxes necessary for the s process are supposed to occur during hydrogen and helium shell burning in asymptotic-giant-branch stars where protons, carried from hydrogen to helium shells, e.g., by convection, can initiate the following reaction chain: $^{12}\mathrm{C} + \mathrm{p} \rightarrow {}^{13}\mathrm{N} + \gamma \rightarrow {}^{13}\mathrm{C} + \mathrm{e}^{+} + \nu_{\mathrm{e}} + \gamma$ and $^{13}\mathrm{C} + {}^{4}\mathrm{He} \rightarrow {}^{16}\mathrm{O} + \mathrm{n}$. Alternatively, neutrons can be produced in hotter environments via

[7]Despite its conceptual simplicity, the model has been so successful that its inventors were awarded with the Nobel Prize in physics in 1963. For more details, see the Nobel lecture of Goeppert Mayer (1964).

$^{14}\mathrm{N} + {}^{4}\mathrm{He} \rightarrow {}^{18}\mathrm{F} + \gamma$, $^{18}\mathrm{F} \rightarrow {}^{18}\mathrm{O} + \mathrm{e}^{+} + \nu_{\mathrm{e}}$, $^{18}\mathrm{O} + {}^{4}\mathrm{He} \rightarrow {}^{22}\mathrm{Ne} + \gamma$, and $^{22}\mathrm{Ne} + {}^{4}\mathrm{He} \rightarrow {}^{25}\mathrm{Mg} + \mathrm{n}$.

The r process is characterized by a neutron flux that is so large that there is no time for β decays to happen in between two successive neutron capture events. Therefore, the atoms accumulate neutrons, which are, according to the shell model, less and less bound. This process is finally stopped when the photon-induced ejection rate of the least bound neutron equals the neutron-capture rate. However, this kind of steady state is destroyed as soon as the neutron-rich nucleus β decays, resulting in a new nuclear structure with tighter binding so that thermal photons are no longer able to remove neutrons from the nucleus. In the case of closed neutron shells with 50, 82, or 126 neutrons, an additionally added neutron generally has a very low binding energy compared to the previous one. Consequently, several β decays are needed before the capture of neutrons can continue. Since waiting for β decays consumes most of the time in the whole process, atoms will pile up at 50, 82, and 126 neutrons. The rapid capture is stopped when the neutron flux expires. Then, the neutron-rich atoms undergo subsequent β decays until the first stable configuration is reached. The resulting abundance maxima are at smaller atomic weights than their s process equivalents, see Fig. 2.6. In contrast to the s process, an environment that offers a sufficiently large neutron flux is not yet identified for the r process. The most promising site is close to a neutron star, which forms during a supernova explosion, where neutrons are released by weak interactions of matter with neutrinos. Unfortunately, observational evidence for this assumption is still missing (see, for instance, Wallerstein et al. 1995).

One may wonder whether neutron fluxes intermediate to the s and r process exist, whose theoretical description would then be much more complicated. Fortunately, this does not seem to be the case and a combination of the two processes is apparently sufficient to explain the abundances of the elements beyond the iron group.

2.6 Structure of the Milky Way

The Milky Way is a normal barred spiral galaxy that, as illustrated in Fig. 2.7, can be divided into three major parts, namely a central bulge, a rotating disk, and a dark matter halo.

The center of the Milky Way hosts a supermassive black hole of about four million solar masses, which is associated with the radio source Sgr A* and is surrounded by a spherical central bulge. The bulge contains relative old, low-mass stars with ages of a couple of billion years as well as young (ages of a few million years), massive stars, which are, for instance, found in the Quintuplet and Arches clusters in the most central region. The mass density and metal content are high. Since it has common features with both, the disk and the halo, it is a distinct Galactic component.

The bulge is enclosed by a rotating, dichotomous disk with a thick component that is approximately 30 kpc in diameter and 2 kpc in height. The thin disk with a height of about 0.1–0.2 kpc comprises a considerable fraction of the youngest and most metal-rich stars in the Galaxy with ages down to a few million years. Star formation in the Milky Way is widely supposed to be restricted to the disk's spiral arms where the interstellar matter is densest and, thus, offers the best conditions to trigger the collapse of a gas cloud. The resulting associations or open clusters, to which young stars belong right after birth, dissolve relatively quickly. In contrast, the surrounding thick disk consists primarily of older, metal-poorer stars that are similar to those of the halo.

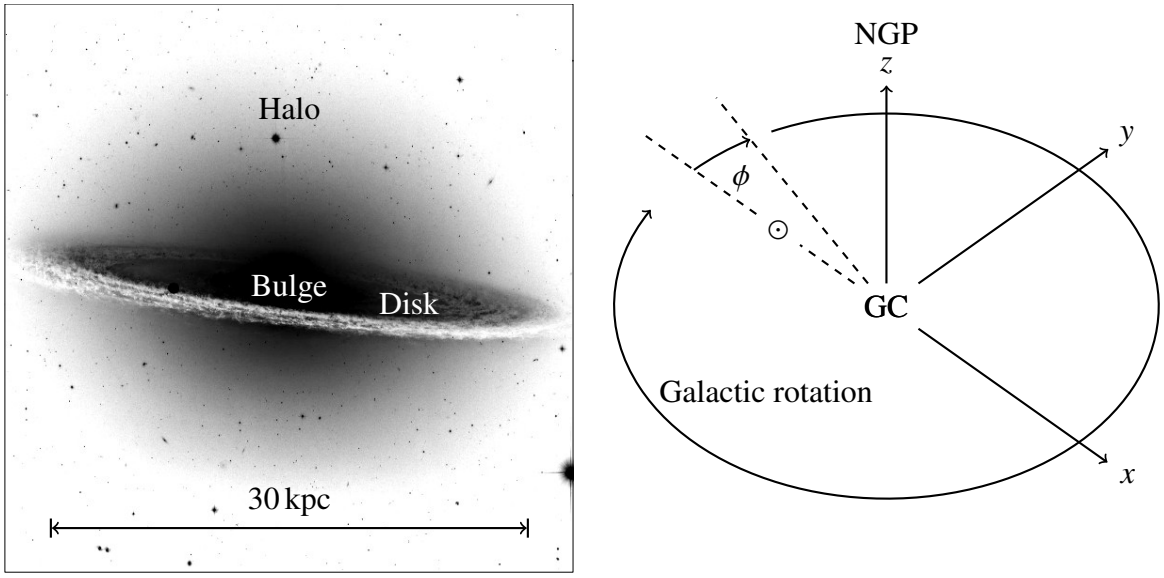

Figure 2.7: *Left:* Schematic structure of the Milky Way showing the three major components bulge, disk, and halo. *Right:* Galactocentric coordinate system as used in this work: a right-handed, cartesian, non-rotating frame of reference with the Galactic center (GC) at the origin, the north Galactic pole (NGP) in positive z-direction, and the Sun ($\odot$) on the negative x-axis at $z \approx 0 \pm 20\,\mathrm{pc}$. The clockwise rotation of the disk is indicated.

Bulge and disk are embedded in a huge spherical halo with a radius of up to a few hundred kiloparsecs. Halo stars can be among the oldest objects in the Milky Way with ages of about thirteen billion years. They are typically found in globular clusters, which are stable, gravitationally bound groups of several ten thousand stars with a regular, radial structure. Due to the lack of dense interstellar material, star formation is probably not taking place in the halo, which explains the low metallicities as well as the large ages of its constituents. Since the visible stellar mass in the halo is by far not sufficient to account for the shape of the observed Galactic rotation curve, the halo is supposed to be dominated by dark matter.

To classify stars according to their kinematics, age, and chemical composition, the concept of stellar populations is sometimes used. Population I stars like the Sun have ages of up to a few billion years, a rather high metallicity, i.e., metal fraction by weight, of 0.01 to 0.04, an almost circular orbit around the Galactic center, a very low velocity component perpendicular to the disk, and are typically members of the thin disk. Population II stars, on the other hand, are old (more than ten billion years), metal poor, on elliptical trajectories which are not aligned to the Galactic plane and which have large vertical velocity components, and usually found in the globular clusters of the halo.

To describe the kinematics of stars in the Milky Way, the choice of a proper coordinate system is advisable. In this work, a right-handed, cartesian, non-rotating frame of reference with the Galactic center at the origin, the north Galactic pole in positive z-direction, and the Sun on the negative x-axis is used and referred to as Galactocentric, see Fig. 2.7. Note that the Sun's planar coordinates x and y will change with time as the disk is (differentially) rotating in clockwise direction from the point of view of the north Galactic pole. Velocity components

in x-, y-, and z-direction are labeled with v_x, v_y, and v_z. Cylindrical coordinates with radius $r = \sqrt{x^2 + y^2}$ and angle $\phi = \arctan(-y/x)$ are sometimes also used.

Trajectories play an important role in the analysis of runaway stars as they allow us to deduce information about the star's spatial origin and the ejection event. However, the computation of stellar orbits requires a reliable model of the Galactic gravitational potential. The construction of three up-to-date Milky May mass models is therefore presented in the following Chapter.

3 Milky Way mass models for orbit calculations*

Tracking large-scale orbits within the Milky Way is an important component in the study of the dynamical properties of stars, globular clusters, or satellite galaxies. Given the object's coordinates and velocity components, this is a straightforward task once the Galactic gravitational potential is available. Owing to a lack of observational constraints, a great deal of the Milky Way's mass distribution – in particular of its dark matter halo – remains unknown. Therefore, different mass models are able to reproduce the observations equally well. For the purpose of numerical orbit calculations, a mathematically simple and analytically closed potential is preferred because it supports fast computations, which is especially favorable when using Monte Carlo methods for error estimation.

The Galactic gravitational potential of Allen & Santillán (1991) perfectly fulfills these criteria and has thus been widely used to calculate trajectories for, e.g., globular clusters (Odenkirchen et al. 1997; Allen et al. 2008; Lane et al. 2012), dwarf spheroidals (Lépine et al. 2011), planetary nebulae (Wu et al. 2011), white dwarfs (Pauli et al. 2003, 2006), horizontal-branch stars (Altmann & de Boer 2000; Kaempf et al. 2005), subluminous B stars (Altmann et al. 2004; Tillich et al. 2011), halo stars (Schuster et al. 2012; Pereira et al. 2012), runaway stars (Irrgang et al. 2010; Silva & Napiwotzki 2011), and hypervelocity stars (Hirsch et al. 2005; Edelmann et al. 2005). However, the model parameters can be recalibrated using new and improved observational constraints. In this context, a simplified expression for the halo component is introduced as well.

As for similar studies, standard constraints encompassing terminal velocities for the inner rotation curve, circular velocities of maser sources for the outer rotation curve, in-plane proper motion of Sgr A*, local mass/surface density, and the velocity dispersion in Baade's window are fitted to determine the respective parameters. To constrain the mass at large radii, in particular that of the dark matter halo, the approach of Przybilla et al. (2010b) is followed here by requiring the dynamically peculiar halo star SDSSJ153935.67+023909.8 (J1539+0239 for short) to be gravitationally bound to the Milky Way (Sect. 3.1).

Despite its simplicity, the resulting revised Allen & Santillán model (hereafter denoted Model I) is capable of meeting all of its imposed conditions. In addition to the fast computation of realistic trajectories, calibration of the potential using the star J1539+0239 allows the halo mass to be estimated in a fully consistent way (Sect. 3.2). To investigate the influence of the applied halo component on the results, the fitting is redone with the original halo mass distribution being replaced by a truncated, flat rotation curve model according to Wilkinson & Evans (1999) (hereafter denoted Model II, Sect. 3.3) and a Navarro et al. (1997) dark matter halo (hereafter denoted Model III, Sect. 3.4).

The spatial origin of the hypervelocity star HE 0437−5439 (Edelmann et al. 2005) is investigated as a first application example (Sect. 3.5). Finally, conclusions are drawn (Sect. 3.6).

3.1 Observations and fitting

In this section, all the details of the fitting process are outlined, i.e., what assumptions are made, what observations are taken into consideration, and how the fitting actually is done.

*This Chapter is heavily based on the paper by Irrgang et al. (2013).

3.1.1 Introductory remarks

All gravitational potentials $\Phi(r, z)$ considered here are the sum of a central spherical bulge component $\Phi_\mathrm{b}(R)$, an axisymmetric disk component $\Phi_\mathrm{d}(r, z)$, and a massive spherical dark matter halo $\Phi_\mathrm{h}(R)$:

$$\Phi(r, z) = \Phi_\mathrm{b}(R(r, z)) + \Phi_\mathrm{d}(r, z) + \Phi_\mathrm{h}(R(r, z)) \,. \tag{3.1}$$

Here, (r, ϕ, z) are cylindrical coordinates and $R = R(r, z) = \sqrt{r^2 + z^2}$ is the spherical radius.

The corresponding density can be derived by virtue of Poisson's equation:

$$4\pi G\rho(r, z) = \nabla^2\Phi(r, z) \,. \tag{3.2}$$

For the sake of simplicity, all potentials are independent of time. Consequently, rotating, nonaxisymmetric features, such as the Galactic bar or the spiral arms, are not implemented here, because they require that more complex models (see, e.g., Pichardo et al. 2003, 2004) are considered. To account for the effects of bar and spiral arms, additional systematic uncertainties are added to the observational data where necessary, see for instance Sect. 3.1.2.

Sticking to the convention of Allen & Santillán (1991), throughout this Chapter, the gravitational potentials are expressed in units of $100\,\mathrm{km^2\,s^{-2}}$, lengths in kpc, and masses in galactic mass units $M_\mathrm{gal} = 100 \times 1000^2\,\mathrm{kpc\,[m]}/G\,\mathrm{[SI]}\,M_\odot \approx 2.325 \times 10^7\,M_\odot$, yielding a gravitational constant G of unity.

3.1.2 Observational constraints

Similar to Dehnen & Binney (1998), observations are divided into eight different groups that are introduced and discussed in the following.

Solar kinematics

Analyzing kinematic observations made in the celestial reference frame in a Galactocentric picture requires a coordinate transformation from one system to the other. Since this transformation obviously depends on the Sun's position and velocity, the interpretation of any data is affected by the values chosen for these parameters. To set up the coordinate transformation, we take J2000.0 equatorial coordinates for the Galactic center (GC) $\alpha_\mathrm{GC} = 17^\mathrm{h}45^\mathrm{m}37\overset{\mathrm{s}}{.}224$, $\delta_\mathrm{GC} = -28^\circ56'10\overset{''}{.}23$ and north Galactic pole (NGP) $\alpha_\mathrm{NGP} = 12^\mathrm{h}51^\mathrm{m}26\overset{\mathrm{s}}{.}282$, $\delta_\mathrm{NGP} = +27^\circ07'42\overset{''}{.}01$, as mentioned in the appendix of Reid & Brunthaler (2004). By monitoring stellar orbits around the central supermassive black hole Sgr A*, Gillessen et al. (2009) restricted the distance $r_\odot$ from the Sun to the GC to the range

$$r_\odot = 8.33 \pm 0.35\,\mathrm{kpc}\,, \tag{3.3}$$

which is the first observational constraint.

The Sun's velocity is a superposition of the in-plane circular motion v_0 of its local standard of rest (LSR) around the GC and its peculiar motion $\vec{v}_\odot = (U, V, W)_\odot$ relative to the LSR. Hereby, U is the component towards the GC, V in direction of Galactic rotation, and W perpendicular to the Galactic plane. Motivated by the McMillan & Binney (2010) discussion of a systematic offset in the V-component of maser motions versus a nonstandard value

of $V_\odot$, the $(U, V, W)_\odot$ values determined by Schönrich et al. (2010) are in this case preferable to others since they allow the use of maser sources to constrain the Galactic rotation curve (see Sect. 3.1.2) without the necessity of modeling an additional net peculiar motion. Thus, $\vec{v}_\odot = (11.1^{+0.69}_{-0.75}, 12.24^{+0.47}_{-0.47}, 7.25^{+0.37}_{-0.36}) \pm (1, 2, 0.5)\,\mathrm{km\,s^{-1}}$ is used here.

Following the argument in McMillan (2011), the proper motion of Sgr A* along Galactic longitude l, $\mu_{\mathrm{SgrA^*}} = -6.379 \pm 0.026\,\mathrm{mas\,yr^{-1}}$ (Reid & Brunthaler 2004) is utilized as an indicator for v_0 instead of Oort's constants A and B. With a spatial motion of Sgr A* of $0 \pm 1\,\mathrm{km\,s^{-1}}$ (McMillan & Binney 2010), this proper motion can be assumed to be solely caused by the solar motion around the GC yielding as second observational constraint:

$$\mu_{\mathrm{SgrA^*}} = -\frac{1}{r_\odot}\,(V_\odot + v_0) = -\frac{1}{r_\odot}\,(V_\odot + v_\mathrm{c}(r_\odot))\ . \tag{3.4}$$

The circular velocity $v_\mathrm{c}(r)$ is hereby linked to the potential via

$$v_\mathrm{c}(r) = \left.\sqrt{\acute{r}\frac{\mathrm{d}\Phi(\acute{r}, 0)}{\mathrm{d}\acute{r}}}\right|_{\acute{r}=r}\ . \tag{3.5}$$

Rotation curve

The Galactic rotation curve deduced from terminal velocities in the inner and intermediate regions and from maser sources in the outer region yield the third, fourth, and fifth groups of observational constraints considered here.

Terminal velocities: the terminal velocity $v_\mathrm{term}(l)$ is the measured peak velocity of the interstellar gas along the line-of-sight at Galactic coordinates $b = 0$ and $-90° < l < 90°$. Assuming a circularly rotating interstellar medium, $v_\mathrm{term}(l)$ can be computed from the circular velocity v_c at $r = r_\odot \sin(l)$ corrected for the observer's projected motion:

$$v_\mathrm{term}(l) = v_\mathrm{c}\,(r_\odot \sin(l)) - (v_\mathrm{c}(r_\odot) + V_\odot)\sin(l) - U_\odot \cos(l)\,. \tag{3.6}$$

For this study, unprocessed terminal velocities are extracted from surveys in H I by Burton & Gordon (1978) and in CO by Clemens (1985). Similar to Dehnen & Binney (1998), a constant uncertainty of $7\,\mathrm{km\,s^{-1}}$ is added in quadrature to the stated uncertainties of the Clemens data to account for non circular motions and the inability of the model potential to reproduce, e.g., spiral arm features. Complementary to the CO measurements, the H I data probe the central region with $|\sin(l)| < 0.3$, which is additionally affected by distortions due to the bar. Therefore, a rather generous uncertainty of $15\,\mathrm{km\,s^{-1}}$ is quadratically added to their measurement errors.

Maser observations: maser sources are associated with high-mass star-forming regions and are consequently good tracers of the kinematic properties of their surrounding interstellar gas. Using very long baseline interferometry techniques, their positions, parallaxes, and proper motions can be measured to very high accuracy even for distant sources giving the opportunity to sample a relatively wide range of Galactocentric radii. Together with heliocentric radial velocities from Doppler shifts, these data hence allow precise determination of the masers' three-dimensional motions. In contrast to Reid et al. (2009), McMillan & Binney (2010) show that

it is fairly justified to adopt their corresponding circular velocity components as probes for the Galactic rotation curve when taking the Schönrich et al. (2010) values for the peculiar motion of the Sun. Following this argument, parallaxes, proper motions, and heliocentric radial velocities for 30 maser sources have been compiled from the literature (Sandstrom et al. 2007; Hirota et al. 2008a,b; Reid et al. 2009; Rygl et al. 2010; Sato et al. 2010; Asaki et al. 2010; Niinuma et al. 2011; Honma et al. 2011). To account for the virial motion of the masers with respect to their high-mass star-forming regions, a constant uncertainty of $7\,\mathrm{km\,s^{-1}}$ (see Reid et al. 2009) is added in quadrature to the measurement errors when computing circular velocities.

Mass and surface densities

The local dynamical mass density $\rho_\odot$ and the surface density $\Sigma_{1.1}$ are together the sixth group of observational constraints. Their derivation is straightforward from the model:

$$\rho_\odot = \rho_\mathrm{b}(r_\odot) + \rho_\mathrm{d}(r_\odot, 0) + \rho_\mathrm{h}(r_\odot) \tag{3.7}$$

$$\Sigma_{1.1} = \int_{-1.1\,\mathrm{kpc}}^{1.1\,\mathrm{kpc}} (\rho_\mathrm{b}(r_\odot, z) + \rho_\mathrm{d}(r_\odot, z) + \rho_\mathrm{h}(r_\odot, z))\,\mathrm{d}z\,. \tag{3.8}$$

Holmberg & Flynn obtained $\rho_\odot = 0.102 \pm 0.010\,M_\odot\,\mathrm{pc}^{-3}$ from Hipparcos data on a volume-complete sample of A and F stars (Holmberg & Flynn 2000) and $\Sigma_{1.1} = 74 \pm 6\,M_\odot\,\mathrm{pc}^{-2}$ from observations of K giant stars (Holmberg & Flynn 2004).

Velocity dispersion in Baade's window

The velocity dispersion of the bulge in Baade's window, σ_BW, is implemented as the seventh constraint probing the inner most region of the Milky Way. Following the reasoning of Dehnen & Binney (1998), it is given as

$$\sigma_\mathrm{BW} = \sigma_\mathrm{b}(0.0175 r_\odot, -0.068 r_\odot) = 117 \pm 15\,\mathrm{km\,s^{-1}}\,, \tag{3.9}$$

where σ_b is estimated from the model potential as

$$\sigma_\mathrm{b}^2(r, z) = \frac{1}{\rho_\mathrm{b}(r, z)} \int_z^\infty \rho_\mathrm{b}(r, \acute{z}) \frac{\partial \Phi(r, \acute{z})}{\partial \acute{z}} \mathrm{d}\acute{z}\,. \tag{3.10}$$

The extreme halo star J1539+0239

The most stringent constraints on the halo mass result from the kinematically most extreme objects. Usually, the very distant satellite galaxy Leo I is considered to be the most important tracer of the halo mass. Its proper motion has recently been measured with the Hubble Space Telescope (HST) for the first time (Sohn et al. 2013) and allowed to determine a limit on the halo mass (Boylan-Kolchin et al. 2013). However, close-by halo stars may provide even more compelling results. The kinematically most extreme halo star is the blue horizontal-branch star

J1539+0239 for which Przybilla et al. (2010b) found a Galactic rest-frame velocity of about $694^{+300}_{-221}\,\mathrm{km\,s^{-1}}$, making it the fastest halo object known so far. Unlike other hypervelocity stars, however, this object is currently approaching the Galactic disk with its pericentric passage of the GC still to occur. As discussed in the next paragraph, this indicates that J1539+0239 is gravitationally bound to the Milky Way, yielding a so far unexploited and – due to the star's immense space motion – significant constraint on the Galaxy's total mass. We show in Sects. 3.2.2, 3.3.2, and 3.4.2 that the limits on the halo mass derived from the kinematics of this star alone are even more stringent than those from Leo I, so we add J1539+0239 to our set of constraints for the potentials and use Leo I as a consistency check. Our approach, which is based on the six-dimensional phase space information of the most extreme objects, is complementary to statistical studies of several thousand stars (see, e.g., Xue et al. 2008; Gnedin et al. 2010) that only make use of line-of-sight velocities.

To justify the assumption that J1539+0239 is bound to the Galaxy, consider the opposite, i.e., a trajectory that passes by the Milky Way only once, never to come back again. Such an orbit could be explained either by a non-Galactic origin, e.g., as a hypervelocity star ejected from another galaxy, or by an extreme dynamical event, e.g., a very close multibody encounter in a globular cluster or satellite galaxy, ejecting a star from its halo environment in a direction pointing not too far away from the GC. Although both scenarios cannot be ruled out by stellar age or space motion arguments, they are unlikely since they require very special circumstances, e.g., an extraordinarily high ejection velocity, a specific ejection direction, or the ejection event occurring at a certain time. Most of these restrictions are weaker or do not apply at all in the case of a bound orbit. For instance, the peculiar motion of J1539+0239 could still be the result of an ejection event. But because the accessible phase space is finite now, there is a non-zero probability of finding a trajectory starting from any initial condition (with matching conserved quantities) sooner or later in a phase-space state very close to J1539+0239, allowing for countless more ejection locations, directions and times. In particular, the GC no longer can be excluded as the star's spatial origin, which opens up the possibility of a dynamical interaction with the central supermassive black hole (Hills 1988). This mechanism is known to be most powerful in terms of acceleration and is the best candidate for explaining extreme velocity objects. Alternatively, as shown by Abadi et al. (2009), the latter may result from the tidal disruption of a dwarf galaxy, a non ejection scenario that is also able to produce bound (but not unbound), high-velocity stars that approach the Galactic disk.

The assumption that J1539+0239 is gravitationally bound to the Milky Way is the eighth and last observational constraint. With E_* denoting the star's total energy, i.e., the sum of kinetic and potential energy, per unit mass, the standard approach to incorporating this is to require $E_* \leq 0$. But the Milky Way is not an isolated system, and beyond some distance, the influence of other objects such as Andromeda is no longer negligible. Since those effects are not included in the presented models, a more rigorous approach is chosen here by defining a bound state as

$$E_* \leq \Phi(0, 200\,\mathrm{kpc})\,, \tag{3.11}$$

theoretically limiting orbits to $R \sim 200\,\mathrm{kpc}$. However, the actual implementation in the least-squares fit is

$$\chi_* = \begin{cases} \dfrac{E_* - \Phi(0, 200\,\mathrm{kpc})}{\Delta E_*} & \text{if } E_* - \Phi(0, 200\,\mathrm{kpc}) > 0, \quad (3.12a) \\ 0 & \text{otherwise.} \quad (3.12b) \end{cases}$$

Hereby, ΔE_* is the error in E_* resulting from uncertainties in determining J1539+0239's distance, radial velocity, and proper motions. Since ΔE_* is large (for instance $E_*/\Delta E_* \sim 0.82$ in the original Allen & Santillán potential), violations of Eq. (3.11) are generously admitted. For the same reason, the particular choice of 200 kpc is not decisive as for instance $-\Phi(0, 200\,\mathrm{kpc})/\Delta E_* \sim 0.16$ while $-\Phi(0, 150\,\mathrm{kpc})/\Delta E_* \sim 0.21$ and $-\Phi(0, 250\,\mathrm{kpc})/\Delta E_* \sim 0.13$ (again in the original Allen & Santillán potential).

3.1.3 Fitting process

The model parameters (see Sects. 3.2–3.4) are simultaneously determined via a χ^2-minimization procedure using the Interactive Spectral Interpretation System (ISIS, Houck & Denicola 2000). Observations of the rotation curve, as well as of J1539+0239, are always taken in raw form from the literature, i.e., as measured in celestial coordinates, in order to exclude inconsistencies during the transformation to the Galactic reference frame originating in different values for the LSR and solar motion. Moreover, any given uncertainty found in the literature is considered here, typically via Gaussian statistics. For instance, to compare the maser measurements to model predictions, their positions and velocities are converted to Galactic coordinates, allowing computation of rotational velocities v_c and Galactrocentric distances r. The corresponding uncertainties in the observational data are then accounted for using Gaussian error propagation. Additionally, the (admittedly small) uncertainties stemming from $\vec{v}_\odot$ are propagated in the same way. As the resulting data points in the (r, v_c)-plane have errors in both directions $(\Delta r, \Delta v_\mathrm{c})$, it is not obvious at which radius to compare the model to observation, i.e., how to compute the χ^2 without neglecting Δr. The solution chosen here is to convert Δr to an error in v_c by estimating the effects of it on the model rotation curve according to $(\Delta v_\mathrm{c})_\mathrm{model} = (\mathrm{d}v_\mathrm{c}/\mathrm{d}r)_\mathrm{model}\Delta r$ and adding it in quadrature to Δv_c.

Very much attention is paid to take all sources of error into consideration in order to assign the correct weighting to each observational constraint in the total χ^2. Unfortunately, systematic effects such as the missing modeling of spiral arms are difficult to quantify and are not sufficiently dealt with by just adding a constant error. Therefore, an unweighted fitting routine, e.g., assuming that a single maser point weighs the same as the proper motion of Sgr A* (see Eq. (3.4)), does not yield a satisfactory result because the fit would be dominated by the large number of data points used while fitting the rotation curve. To account for this, each contribution to the total χ^2 of the above-mentioned eight groups of observational constraints is divided by the number of data points N within the group:

$$\chi^2_\mathrm{w} = \sum_{i=1}^{8} \left(\frac{1}{N_i} \sum_{j=1}^{N_i} \chi^2_{ij} \right) . \tag{3.13}$$

The model parameters given in Tables 3.1–3.3 are those that minimize this weighted χ^2.

3.2 Model I

Model I is a revision of the Allen & Santillán (1991) potential.

3.2.1 Components and characteristics

Bulge and disk

The potential forms $\Phi_\mathrm{b}(R)$ and $\Phi_\mathrm{d}(r,z)$ of bulge and disk are those proposed by Miyamoto & Nagai (1975):

$$\Phi_\mathrm{b}(R) = -\frac{M_\mathrm{b}}{\sqrt{R^2 + {b_\mathrm{b}}^2}} \tag{3.14}$$

$$\Phi_\mathrm{d}(r,z) = -\frac{M_\mathrm{d}}{\sqrt{r^2 + \left(a_\mathrm{d} + \sqrt{z^2 + {b_\mathrm{d}}^2}\right)^2}}\,. \tag{3.15}$$

The parameters $M_\mathrm{b}/M_\mathrm{d}$ determine the contribution of their components to the total potential, and $b_\mathrm{b}/a_\mathrm{d}/b_\mathrm{d}$ are scale lengths.

The related densities ρ_b and ρ_d are (see Eq. (3.2))

$$\rho_\mathrm{b}(R) = \frac{3{b_\mathrm{b}}^2 M_\mathrm{b}}{4\pi(R^2 + {b_\mathrm{b}}^2)^{5/2}} \tag{3.16}$$

$$\rho_\mathrm{d}(r,z) = \frac{{b_\mathrm{d}}^2 M_\mathrm{d}}{4\pi} \frac{a_\mathrm{d} r^2 + \left(a_\mathrm{d} + 3\sqrt{r^2+z^2}\right)\left(a_\mathrm{d} + \sqrt{r^2+z^2}\right)^2}{\left(z^2 + {b_\mathrm{d}}^2\right)^{3/2}\left(r^2 + \left(a_\mathrm{d} + \sqrt{\left(z^2 + {b_\mathrm{d}}^2\right)}\right)^2\right)^{5/2}}\,. \tag{3.17}$$

Integrating these densities over the entire volume to obtain the total masses m_b and m_d of bulge and disk gives the expected identities $m_\mathrm{b} = M_\mathrm{b}$ and $m_\mathrm{d} = M_\mathrm{d}$.

The dark matter halo

Pursuing mathematical simplicity, the halo potential $\Phi_\mathrm{h}(R)$ used here differs slightly from the original one by Allen & Santillán. We assume the halo mass m_h inside a sphere of radius R is given by (see Allen & Martos 1986)

$$m_\mathrm{h}(<R) = \begin{cases} \dfrac{M_\mathrm{h}\left(\frac{R}{a_\mathrm{h}}\right)^\gamma}{1 + \left(\frac{R}{a_\mathrm{h}}\right)^{\gamma-1}} & \text{if } R < \Lambda, \qquad (3.18a) \\ \dfrac{M_\mathrm{h}\left(\frac{\Lambda}{a_\mathrm{h}}\right)^\gamma}{1 + \left(\frac{\Lambda}{a_\mathrm{h}}\right)^{\gamma-1}} = \text{constant}, & \text{otherwise.} \qquad (3.18b) \end{cases}$$

Here, M_h is again a weighting factor and a_h a scale length. Clearly, this specific form is chosen to have the asymptotic behavior $m_\mathrm{h}(<R) \propto R$ for large R motivated by the observed flat rotation curve. To avoid an unphysical, infinite halo mass, a cutoff parameter Λ is incorporated as well. In principle, the exponent γ is a free parameter, too. However, the shortage of halo constraints means the ability of the model to reproduce the observations is not attenuated by setting $\gamma = 2$, reducing the expression's complexity (and avoiding singularities at the origin in the equations of motion for $\gamma < 2$).

The expression $m_\mathrm{h}(< R)$ is the volume integral of the halo density ρ_h over the sphere of radius R. Assuming a spherically symmetric halo density $\rho_\mathrm{h} = \rho_\mathrm{h}(R)$ and using Poisson's equation (Eq. (3.2)), a relation between $m_\mathrm{h}(< R)$ and its respective potential can be derived:

$$\begin{aligned} m_\mathrm{h}(< R) &= 4\pi \int_0^R \acute{R}^2 \rho_\mathrm{h}(\acute{R}) \mathrm{d}\acute{R} = \int_0^R \acute{R}^2 \nabla^2 \Phi_\mathrm{h}(\acute{R}) \mathrm{d}\acute{R} = \int_0^R \acute{R}^2 \frac{1}{\acute{R}^2} \frac{\mathrm{d}}{\mathrm{d}\acute{R}} \left(\acute{R}^2 \frac{\mathrm{d}}{\mathrm{d}\acute{R}} \Phi_\mathrm{h}(\acute{R}) \right) \mathrm{d}\acute{R} \\ &= R^2 \frac{\mathrm{d}}{\mathrm{d}R} \Phi_\mathrm{h}(R) \,. \end{aligned} \tag{3.19}$$

Inserting Eq. (3.18) and directly integrating the result accounting for the boundary condition $\Phi_\mathrm{h}(\infty) = 0$ yields

$$\Phi_\mathrm{h}(R) = \int_\infty^R \frac{m_\mathrm{h}(\acute{R})}{\acute{R}^2} \mathrm{d}\acute{R} = \begin{cases} \dfrac{M_\mathrm{h}}{a_\mathrm{h}} \left(\dfrac{1}{(\gamma - 1)} \ln \left(\dfrac{1 + \left(\frac{R}{a_\mathrm{h}}\right)^{\gamma-1}}{1 + \left(\frac{\Lambda}{a_\mathrm{h}}\right)^{\gamma-1}} \right) - \dfrac{\left(\frac{\Lambda}{a_\mathrm{h}}\right)^{\gamma-1}}{1 + \left(\frac{\Lambda}{a_\mathrm{h}}\right)^{\gamma-1}} \right) & \text{if } R < \Lambda, \quad (3.20a) \\ -\dfrac{M_\mathrm{h}}{R} \dfrac{\left(\frac{\Lambda}{a_\mathrm{h}}\right)^{\gamma}}{1 + \left(\frac{\Lambda}{a_\mathrm{h}}\right)^{\gamma-1}}, & \text{otherwise.} \quad (3.20b) \end{cases}$$

For $\Lambda = 100\,\mathrm{kpc}$ and $\gamma = 2.02$, this is equivalent to the expression given in Allen & Santillán (1991) obtained via integration by parts. The advantage of the above representation is that the dependent variable R appears only once and linearly in the argument of the logarithm (since $\gamma = 2$).

The corresponding density ρ_h is

$$\rho_\mathrm{h}(R) = \begin{cases} \dfrac{M_\mathrm{h}}{4\pi a_\mathrm{h}} \dfrac{\left(\frac{R}{a_\mathrm{h}}\right)^{\gamma-1} \left(\left(\frac{R}{a_\mathrm{h}}\right)^{\gamma-1} + \gamma \right)}{R^2 \left(1 + \left(\frac{R}{a_\mathrm{h}}\right)^{\gamma-1} \right)^2} & \text{if } R < \Lambda, \quad (3.21a) \\ 0 & \text{otherwise.} \quad (3.21b) \end{cases}$$

3.2.2 Results

The properties of the best-fitting Model I are visualized in Figs. 3.1 and 3.2 and summarized in Table 3.1. Given the model's simplicity, the overall agreement with the imposed constraints is very good. In particular, $r_\odot$, μ_{SgrA^*}, $\rho_\odot$, $\Sigma_{1.1}$, and σ_BW are almost perfectly reproduced. The rotation curve, on the other hand, reveals systematic discrepancies between model and observation originating mainly in the inadequate treatment of the Galactic bar and the spiral arms. Moreover, most of the maser sources still seem to lag behind the Galactic rotation curve. Despite these shortcomings, the unweighted χ^2 per degree of freedom (d.o.f.) is about 1.5, thereby confirming the good match.

To see how well the individual parameters are confined by the observational constraints, 90%-confidence limits were computed from the weighted χ^2_w statistics after multiplying it with a factor yielding $\chi^2_\mathrm{w}/\mathrm{d.o.f.} = 1$ at the best fit, i.e., at the minimum χ^2_w. The resulting intervals are given in Table 3.1, too. As illustrated in Fig. 3.3, there is a strong correlation between M_h and a_h that explains the large uncertainties of these two parameters. This degeneracy is a consequence

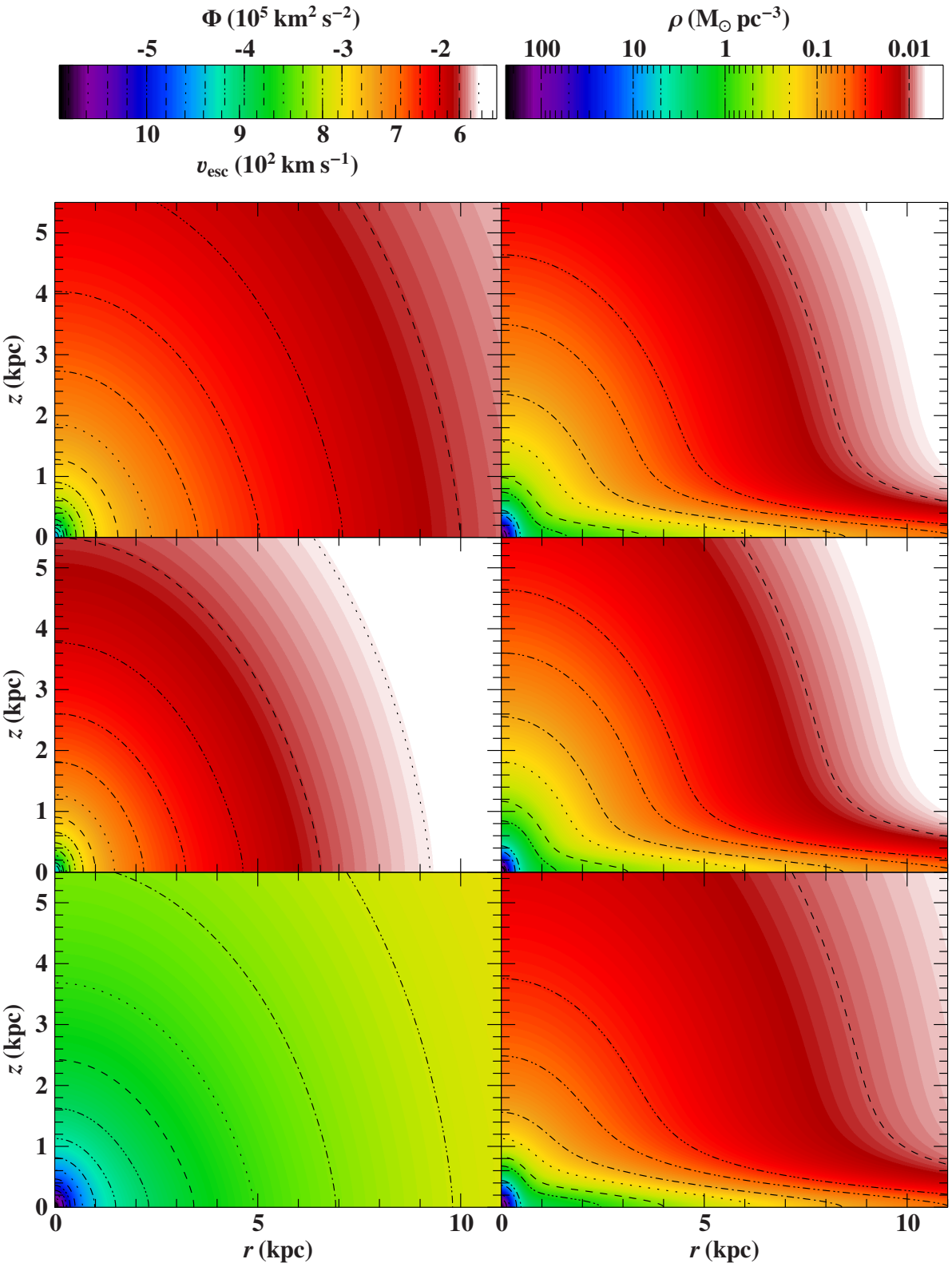

Figure 3.1: Gravitational potential $\Phi(r, z)$, formal escape velocity $v_{\rm esc}(r, z) = \sqrt{-2\Phi}$, and total mass density $\rho(r, z)$ for the best-fit parameters of Model I (*upper panel*), Model II (*middle panel*), and Model III (*lower panel*). Contours are indicated by dashed lines.

Table 3.1: Properties of the best-fitting Model I.

Parameter	Value	Constraint	Value		Derived Quantity	Value
			Observation	Model		
$r_\odot$ (kpc)	8.40 ± 0.08	$r_\odot$ (kpc)	8.33 ± 0.35	8.40	v_0 (km s^{-1})	242.0
M_b (M_gal)	409 ± 63	μ_{SgrA^*} (mas yr^{-1})	-6.379 ± 0.026	-6.384	m_b ($10^9 M_\odot$)	9.5 ± 1.5
M_d (M_gal)	2856^{+376}_{-202}	Terminal velocities from H I	See Fig. 3.2	See Fig. 3.2	m_d ($10^{10} M_\odot$)	$6.6^{+0.9}_{-0.5}$
M_h (M_gal)	$1018^{+27\,933\,(a)}_{-\ \ 603}$	Terminal velocities from CO	See Fig. 3.2	See Fig. 3.2	m_h ($10^{12} M_\odot$)	$1.8^{+2.4}_{-0.8}$
b_b (kpc)	0.23 ± 0.03	Circular velocities from masers	See Fig. 3.2	See Fig. 3.2	$M_{R<50\,\mathrm{kpc}}$ ($10^{12} M_\odot$)	$0.51^{+0.33}_{-0.04}$
a_d (kpc)	$4.22^{+0.53}_{-0.99}$	$\rho_\odot$ ($M_\odot$ pc^{-3}), $\Sigma_{1.1}$ ($M_\odot$ pc^{-2})	0.102 ± 0.010, 74 ± 6	0.102, 74	$M_{R<100\,\mathrm{kpc}}$ ($10^{12} M_\odot$)	$0.97^{+0.96}_{-0.09}$
b_d (kpc)	$0.292^{+0.020}_{-0.025}$	σ_BW (km s^{-1})	117 ± 15	120	$M_{R<200\,\mathrm{kpc}}$ ($10^{12} M_\odot$)	$1.9^{+2.4}_{-0.8}$
a_h (kpc)	$2.562^{+25.963\,(a)}_{-\ \ 1.419}$	χ_*	≤ 0	0.66	$v_{\mathrm{esc},\odot}$ (km s^{-1})	616.4
Λ (kpc)	$200^{+\ 0\,(b)}_{-83}$				A (km s^{-1} kpc^{-1})	15.06
γ	2 (fixed)				B (km s^{-1} kpc^{-1})	-13.74

Notes. The quoted uncertainties for the model parameters and masses are 90%-confidence limits: After normalizing the weighted χ^2_w via multiplication with a factor yielding $\chi^2_\mathrm{w}/\mathrm{d.o.f.} = 1$ at the minimum χ^2_w, 90%-confidence intervals are calculated from this normalized χ^2 statistics and the condition $\Delta\chi^2 = 2.71$. $^{(a)}$ The large uncertainties are due to a strong correlation between M_h and a_h, see Fig. 3.3. $^{(b)}$ Motivated by cosmological studies, the restriction $\Lambda \leq 200$ kpc is imposed.

of the missing constraints on the halo mass distribution. The available observations are only able to constrain the halo mass inside a sphere of radius 14.1 kpc (see Fig. 3.3), which, however, can be reproduced by numerous different combinations of M_h-a_h pairs. A parametrization of the halo using only one independent variable would thus be sufficient to obtain a good fit to the data. From Fig. 3.3, it is also clear that the degeneracy in the two halo parameters does not follow curves of constant halo mass inside 50, 100, or 200 kpc, which explains the relatively large uncertainties of the total masses inside these radii as listed in Table 3.1.

Przybilla et al. (2010b) were the first to exploit the star J1539+0239 as a probe for the mass of the Galaxy and its main contributor, the dark matter halo, and they derived $m_\mathrm{h} \geq 1.7^{+2.3}_{-1.1} \times 10^{12}\ M_\odot$ based on the same model potential as discussed here. Their result, however, was derived solely from the condition that J1539+0239 is bound to the Milky Way while neglecting any other observational constraint that keeps the mass low. In contrast, the mass estimates presented in Table 3.1 are fully consistent with all the observational data mentioned before.

The best-fit parameters yield a total mass (with 90%-confidence limits computed analogously to the model parameters' uncertainties) of $M_\mathrm{total} = 1.9^{+2.4}_{-0.8} \times 10^{12}\ M_\odot \approx m_\mathrm{h}$. This result is a modest revision of the Przybilla et al. (2010b) value, and it confirms their conclusion that a total Galactic mass of about $1 \times 10^{12}\ M_\odot$ such as found by Xue et al. (2008) possibly underestimates the true value. From Eq. (3.18) and the fact that $\Lambda = 200$ kpc at the best fit, it is obvious that M_total is affected by the restriction $\Lambda \leq 200$ kpc. Although the latter is justified by cosmological simulations on galaxy formation, the specific choice for the upper boundary can of course be subject to discussion. But since even the mass corresponding to $\Lambda = 450$ kpc lies within the 90%-confidence interval of M_total, this concern does not seriously change the result. To remove the Λ dependence, consider the quantity $M_{R<50\,\mathrm{kpc}}$, i.e., the total mass within 50 kpc. From the kinematic analysis of a combined sample of field horizontal-branch stars, globular clusters, and satellite galaxies, Sakamoto et al. (2003) have obtained $M_{R<50\,\mathrm{kpc}} = 5.4^{+0.1}_{-0.4} \times 10^{11}\ M_\odot$ agreeing with $M_{R<50\,\mathrm{kpc}} = 5.1^{+3.3}_{-0.4} \times 10^{11}\ M_\odot$ as found in this study.

It is worth noting that J1539+0239 is not at all gravitationally bound to the Milky Way

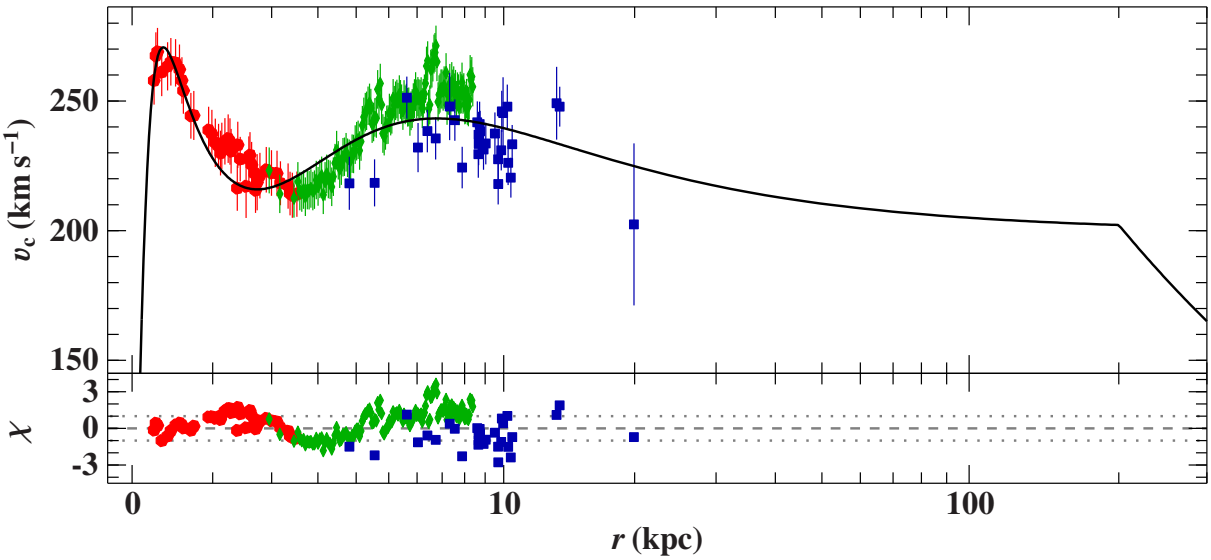

Figure 3.2: Comparison of the best-fitting model rotation curve (solid black line) with terminal velocities from surveys in H I (red circles) and in CO (green diamonds), as well as maser observations (blue squares) for Model I.

in the best-fitting model. This is possible because of the large uncertainty in its position and velocity determination resulting in a small contribution ($\chi_* = 0.66$) to the total χ^2_w. More precise kinematic information on the star would set tighter constraints on the Galactic potential, probably reducing the uncertainties in the mass estimates.

We also model the trajectory of the very distant satellite galaxy Leo I based on the full six-dimensional phase space information (position: $\alpha = 10^h8^m28\overset{s}{.}68$, $\delta = +12°18'19.7''$; distance: 256.7 ± 13.3 kpc; radial velocity: $282.9 \pm 0.5\,\mathrm{km\,s^{-1}}$; proper motion: $\mu_\alpha \cos(\delta) = -0.1140 \pm 0.0295\,\mathrm{mas\,yr^{-1}}$, $\mu_\delta = -0.1256 \pm 0.0293\,\mathrm{mas\,yr^{-1}}$, Sohn et al. 2013). Leo I is found to be formally bound to the Galaxy, showing that J1539+0239 is indeed the dominant constraint on the halo mass.

Table 3.1 also contains some derived quantities that are not directly fitted, such as $v_{\mathrm{esc},\odot}$ or $v_0/r_\odot$. The escape velocity at the Sun's position is about $616\,\mathrm{km\,s^{-1}}$, thereby lying very close to the 90%-confidence limit $498\,\mathrm{km\,s^{-1}} < v_{\mathrm{esc},\odot} < 608\,\mathrm{km\,s^{-1}}$ of Smith et al. (2007). The ratio of v_0 over $r_\odot$ is $28.8\,\mathrm{km\,s^{-1}\,kpc^{-1}}$ and thus somewhat less than the values found by Reid et al. (2009), $30.3 \pm 0.9\,\mathrm{km\,s^{-1}\,kpc^{-1}}$, or McMillan & Binney (2010), $29.9 - 31.6\,\mathrm{km\,s^{-1}\,kpc^{-1}}$, from maser sources alone.

As pointed out before, the halo mass distribution is not well constrained by the observations, so different potential shapes of the halo can yield almost equal matches to the data but differ significantly in other properties, as for instance the total mass. To investigate this behavior, two other representations of the dark matter halo are considered in the following sections.

3.3 Model II

In Model II, the halo is replaced by the truncated, flat rotation curve model used in Wilkinson & Evans (1999) and Sakamoto et al. (2003).

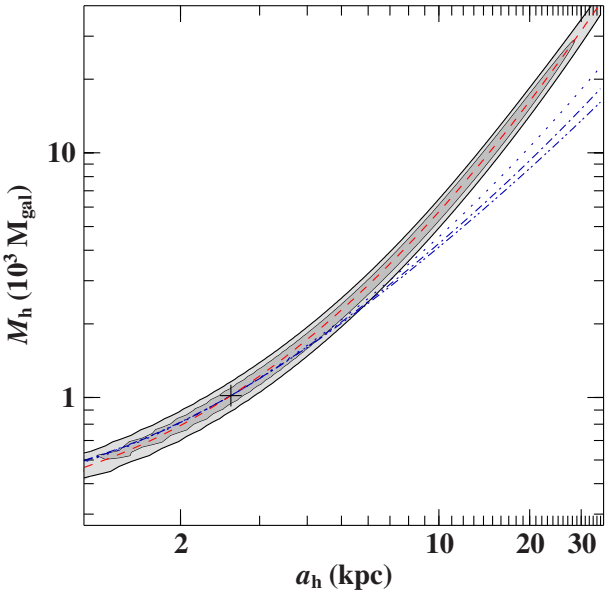

Figure 3.3: Visualization of the correlation between M_h and a_h in Model I: The single parameter 90%-confidence region defined by $\Delta\chi^2 \leq 2.71$ and corresponding to a 74%-joint-confidence region is black-rimmed and shaded in dark gray, while the 3σ region ($\Delta\chi^2 \leq 9$, 99%-joint-confidence region) is the total black-rimmed, gray-shaded area. The cross marks the location of the best fit. The four curves define the loci of constant halo mass inside a sphere of radius 14.1 kpc (red dashed), 50 kpc (blue dotted), 100 kpc (blue dashed-dotted), and 200 kpc (blue dashed-dotted-dotted).

3.3.1 Components and characteristics

While bulge and disk components have the same shape as in Model I, the halo potential reads as (Wilkinson & Evans 1999)

$$\Phi_h(R) = -\frac{M_h}{a_h} \ln\left(\frac{\sqrt{R^2 + {a_h}^2} + a_h}{R}\right). \tag{3.22}$$

The resulting density

$$\rho_h(R) = \frac{M_h}{4\pi} \frac{{a_h}^2}{R^2 \left(R^2 + {a_h}^2\right)^{3/2}} \tag{3.23}$$

is cusped like R^{-2} for $R \ll a_h$ and falls off like R^{-5} for $R \gg a_h$. In this way, the corresponding rotation curve is flat in the inner regions, and the total halo mass $m_h = M_h$ is finite without invoking a cutoff parameter.

3.3.2 Results

The properties of the best-fitting Model II are visualized in Figs. 3.1 and 3.4 and summarized in Table 3.2. While the rotation curve reveals the same systematic shortcomings as found in Model I, the match of the remaining constraints is of comparable quality. The unweighted χ^2 per d.o.f. is 1.7.

Again, there is a tight correlation between the halo parameters M_h and a_h (see Fig. 3.5). To avoid unphysically large halos, the restriction $a_h \leq 200$ kpc has to be imposed based on exactly the same reasoning as the condition $\Lambda \leq 200$ kpc in Model I. Owing to the correlation, this step also sets an upper limit to the parameter M_h, hence to the total halo mass m_h. Unfortunately, the effects on the latter and thus on the total Galactic mass are more severe in this case since its 90%-confidence interval, $M_{total} = 1.7^{+0.2}_{-0.5} \times 10^{12} M_\odot$, covers a_h values only up to 218 kpc. The mass inside 50 kpc, on the other hand, is almost independent of the chosen upper boundary for a_h. According to Sakamoto et al. (2003), this quantity is much more robust than, e.g., the total mass of the Milky Way. The reason for this is the specific form of the applied potential.

Table 3.2: Properties of the best-fitting Model II.

Parameter	Value	Constraint	Value		Derived Quantity	Value
			Observation	Model		
$r_\odot$ (kpc)	8.35 ± 0.08	$r_\odot$ (kpc)	8.33 ± 0.35	8.35	v_0 (km s^{-1})	240.4
M_b (M_gal)	175 ± 28	μ_{SgrA^*} (mas yr^{-1})	-6.379 ± 0.026	-6.383	m_b ($10^9 M_\odot$)	4.1 ± 0.7
M_d (M_gal)	2829 ± 192	Terminal velocities from H I	See Fig. 3.4	See Fig. 3.4	m_d ($10^{10} M_\odot$)	6.6 ± 0.5
M_h (M_gal)	$69\,725^{+\,5\,790\,(a)}_{-20\,931}$	Terminal velocities from CO	See Fig. 3.4	See Fig. 3.4	m_h ($10^{12} M_\odot$)	$1.6^{+0.2}_{-0.5}$
b_b (kpc)	0.184 ± 0.040	Circular velocities from masers	See Fig. 3.4	See Fig. 3.4	$M_{R<50\,\mathrm{kpc}}$ ($10^{12} M_\odot$)	0.46 ± 0.03
a_d (kpc)	$4.85^{+0.41}_{-0.33}$	$\rho_\odot$ ($M_\odot$ pc^{-3}), $\Sigma_{1.1}$ ($M_\odot$ pc^{-2})	0.102 ± 0.010, 74 ± 6	0.102, 75	$M_{R<100\,\mathrm{kpc}}$ ($10^{12} M_\odot$)	$0.79^{+0.06}_{-0.08}$
b_d (kpc)	0.305 ± 0.020	σ_BW (km s^{-1})	117 ± 15	116	$M_{R<200\,\mathrm{kpc}}$ ($10^{12} M_\odot$)	$1.2^{+0.1}_{-0.2}$
a_h (kpc)	$200^{+\,0\,(a)\,(b)}_{-60}$	χ_*	≤ 0	0.80	$v_{\mathrm{esc},\odot}$ (km s^{-1})	575.9
					A (km s^{-1} kpc^{-1})	15.11
					B (km s^{-1} kpc^{-1})	-13.68

Notes. The quoted uncertainties for the model parameters and masses are 90%-confidence limits (see notes on Table 3.1 for details). $^{(a)}$ The large uncertainties are due to a strong correlation between M_h and a_h, see Fig. 3.5. $^{(b)}$ Motivated by cosmological studies, the restriction $a_\mathrm{h} \leq 200$ kpc is imposed.

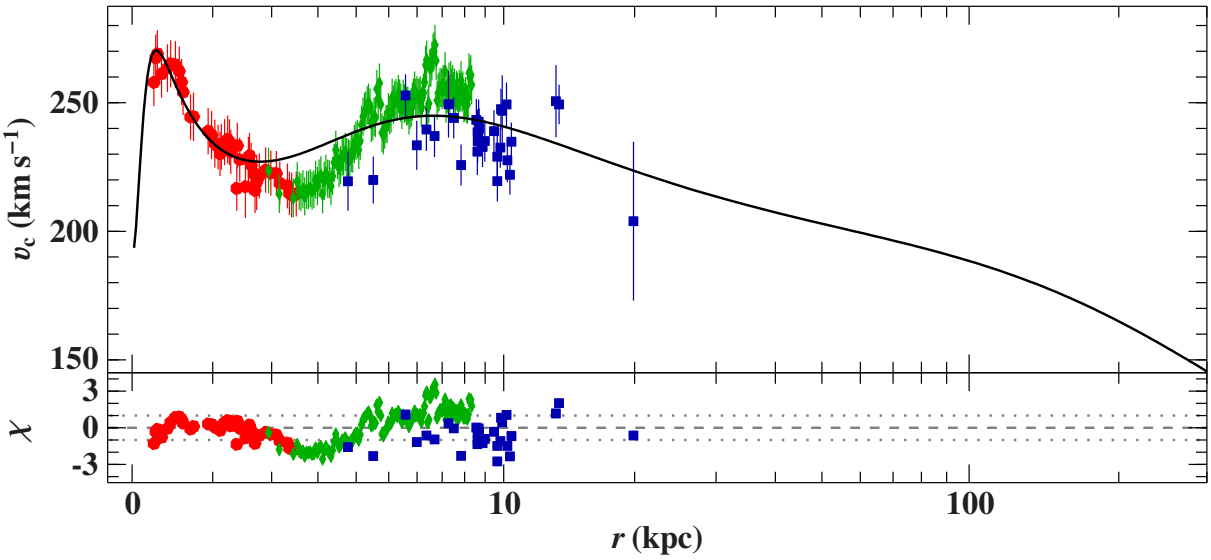

Figure 3.4: Comparison of the best-fitting model rotation curve (solid black line) with terminal velocities from surveys in H I (red circles) and in CO (green diamonds), as well as maser observations (blue squares) for Model II.

It is such that loci of equal masses inside spheres of radii ranging from ~0 to ~50 kpc lie in a very narrow band in the M_h-a_h plane (see Fig. 3.5). Although the correlation follows contours of equal mass within the central ~20 kpc, it therefore nearly follows contours of equal mass within the central 50 kpc, resulting in small uncertainties for the latter. The value derived here, $M_{R<50\,\mathrm{kpc}} = 4.6 \pm 0.3 \times 10^{11} M_\odot$, is slightly lower than in Sakamoto et al. (2003), $M_{R<50\,\mathrm{kpc}} = 5.4^{+0.1}_{-0.4} \times 10^{11}\ M_\odot$.

In general, the gravitational potential of Model II is shallower than in Model I (see Fig. 3.1) implying systematically lower masses, a lower local escape velocity of about 576 km s^{-1} in agreement with Smith et al. (2007), and an unbound orbit for J1539+0239 ($\chi_* = 0.80$). Nevertheless, Leo I is still on a bound orbit.

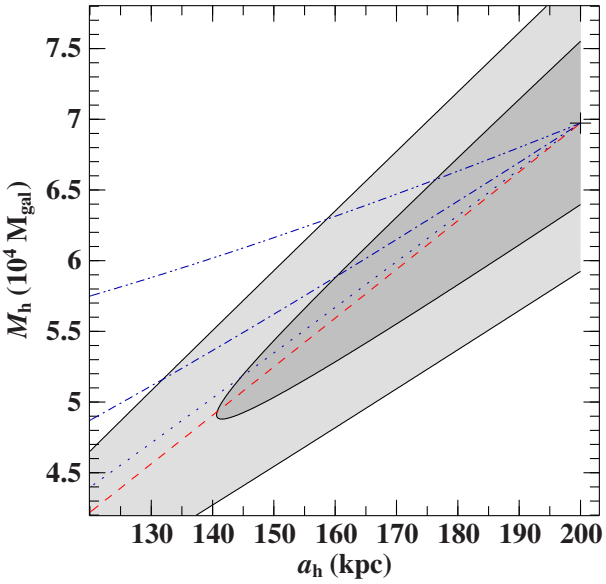

Figure 3.5: Visualization of the correlation between M_h and a_h in Model II. The meaning of the cross, curves, and shaded regions is the same as in Fig. 3.3 except that the red dashed line defines loci of constant halo mass inside a sphere of radius 20 kpc.

3.4 Model III

The third halo potential considered here is based on the universal density profile of dark matter halos suggested by Navarro et al. (1997) from cosmological simulations.

3.4.1 Components and characteristics

Using

$$\rho_h(R) = \frac{M_h}{4\pi} \frac{1}{(a_h + R)^2 R} \tag{3.24}$$

(Navarro et al. 1997) together with Eq. (3.2), one obtains a halo potential of

$$\Phi_h(R) = -\frac{M_h}{R} \ln\left(1 + \frac{R}{a_h}\right). \tag{3.25}$$

The weighting factor M_h is thereby equivalent to the mass inside a sphere of radius ~5.3 times the scale length a_h. The combination of this halo potential with a Miyamoto & Nagai (1975) disk and bulge component (see Sect. 3.2.1) is hereafter denoted Model III. Owing to the use of Eq. (3.24) for $R \to \infty$, the total halo mass is formally logarithmically divergent.

3.4.2 Results

The properties of the best-fitting Model III are visualized in Figs. 3.1 and 3.6 and summarized in Table 3.3. The quality of the fit is similar to Models I and II and yields an unweighted χ^2 per d.o.f. of 1.7.

In contrast to the two previous models, the rotation curve is rising outside the solar circle, reaching its maximum at about 82 kpc, and falling off beyond this point. This is a consequence of the search for a compromise between the opposing constraints of making J1539+0239 bound,

Table 3.3: Properties of the best-fitting Model III.

Parameter	Value	Constraint	Value		Derived Quantity	Value
			Observation	Model		
$r_\odot$ (kpc)	8.33 ± 0.09	$r_\odot$ (kpc)	8.33 ± 0.35	8.33	v_0 (km s^{-1})	239.7
M_b (M_gal)	439 ± 28	$\mu_{\mathrm{SgrA*}}$ (mas yr^{-1})	-6.379 ± 0.026	-6.380	m_b ($10^9 M_\odot$)	10.2 ± 0.7
M_d (M_gal)	3096 ± 197	Terminal velocities from H I	See Fig. 3.6	See Fig. 3.6	m_d ($10^{10} M_\odot$)	7.2 ± 0.5
M_h (M_gal)	$142\,200^{+137\,900}_{-\ 75\,500}$ [a]	Terminal velocities from CO	See Fig. 3.6	See Fig. 3.6	m_h ($10^{12} M_\odot$)	∞ [b]
b_b (kpc)	0.236 ± 0.021	Circular velocities from masers	See Fig. 3.6	See Fig. 3.6	$M_{R<50\,\mathrm{kpc}}$ ($10^{12} M_\odot$)	$0.81^{+0.13}_{-0.15}$
a_d (kpc)	$3.262^{+0.144}_{-0.121}$	$\rho_\odot$ ($M_\odot$ pc^{-3}), $\Sigma_{1.1}$ ($M_\odot$ pc^{-2})	0.102 ± 0.010, 74 ± 6	0.102, 75	$M_{R<100\,\mathrm{kpc}}$ ($10^{12} M_\odot$)	1.67 ± 0.46
b_d (kpc)	0.289 ± 0.022	σ_BW (km s^{-1})	117 ± 15	123	$M_{R<200\,\mathrm{kpc}}$ ($10^{12} M_\odot$)	$3.0^{+1.2}_{-1.1}$
a_h (kpc)	$45.02^{+22.56}_{-16.78}$ [a]	χ_*	≤ 0	0.20	$v_{\mathrm{esc},\odot}$ (km s^{-1})	811.5
					A (km s^{-1} kpc^{-1})	14.70
					B (km s^{-1} kpc^{-1})	-14.08

Notes. The quoted uncertainties for the model parameters and masses are 90%-confidence limits (see notes on Table 3.1 for details). [a] The large uncertainties are due to a strong correlation between M_h and a_h, see Fig. 3.7. [b] Formal divergence, see Sect. 3.4.1.

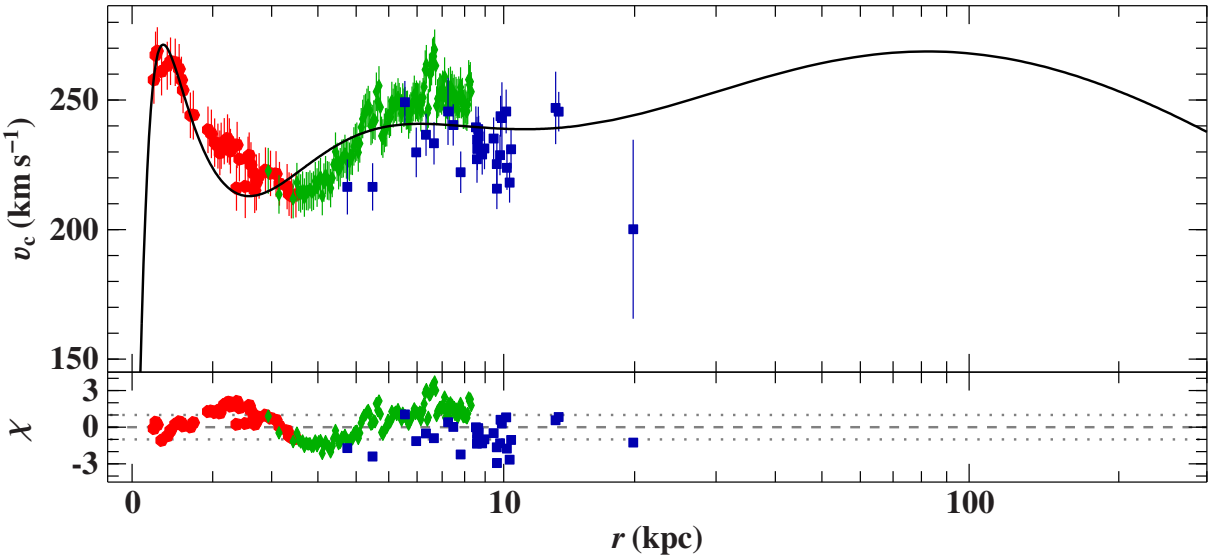

Figure 3.6: Comparison of the best-fitting model rotation curve (solid black line) with terminal velocities from surveys in H I (red circles) and in CO (green diamonds), as well as maser observations (blue squares) for Model III.

i.e., giving the Milky Way a very high total mass, and, at the same time, limiting the mass in the central ~19 kpc (see Fig. 3.7) to match the remaining observations. Unlike Model III, Models I and II were designed to give flat rotation curves, avoiding any analogical behavior. As a result, the masses of Model III systematically exceed those of the others, e.g., by more than a factor of 1.5 in terms of $M_{R<50\,\mathrm{kpc}}$. Moreover, because of using Eq. (3.24) for $R \to \infty$, the total mass M_total is logarithmically infinite. Following Navarro et al. (1997), an alternative measure of the halo mass is given by M_{200}, which is the halo mass inside a sphere of radius r_{200} defined to have a mean interior density of 200 times the critical value for closure $\rho_\mathrm{crit} = 3H^2/8\pi G$. Assuming a Hubble constant H of 73 km s^{-1}Mpc^{-1}, values of $r_{200} = 319^{+61}_{-58}$ kpc and $M_{200} = 4.0^{+1.2}_{-1.8} \times 10^{12} M_\odot$ are derived from Model III agreeing with $r_{200} = 301$ kpc and $M_{200} = 3.4 \times 10^{12} M_\odot$ as used by

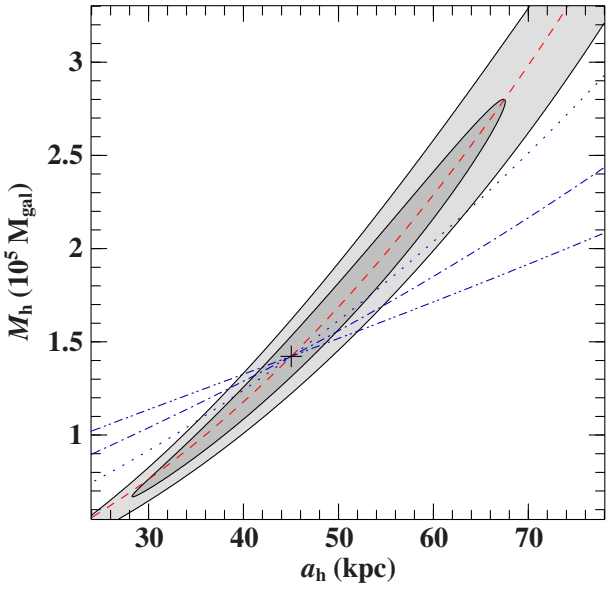

Figure 3.7: Visualization of the correlation between M_h and a_h in Model III. The meaning of the cross, curves, and shaded regions is the same as in Fig. 3.3 except that the red dashed line defines loci of constant halo mass inside a sphere of radius 18.8 kpc.

Abadi et al. (2009). The respective local escape velocity of 812 km s^{-1} significantly exceeds the Smith et al. (2007) value but is comparable to the one in Abadi et al. (2009). Although this is high enough to keep Leo I formally bound, it does not hold J1539+0239 within 200 kpc ($\chi_* = 0.20$).

Kenyon et al. (2008) considered a Galactic potential that only differs from Model III in the bulge component: the expression $R + b_b$ is used instead of $\sqrt{R^2 + {b_b}^2}$. Putting special emphasis on the very central region of the Milky Way, the parameters of their model were tweaked to provide a reasonable match to observations from $R = 5$ pc to $R = 100$ kpc. Compared to Model III, their resulting model is less massive ($M_{200} = 1.6 \times 10^{12} M_\odot$), which is also reflected by lower values for the local escape velocity ($v_{esc,\odot} = 635$ km s^{-1}), the local mass and surface density ($\rho_\odot = 0.046\, M_\odot$ pc^{-3}, $\Sigma_{1.1} = 46\, M_\odot$ pc^{-2}), and the circular motion of the LSR ($v_0 = 220$ km s^{-1}).

3.5 The hypervelocity star HE 0437−5439 revisited

Given the smoothness of the presented potentials, a simple fourth-order Runge-Kutta method with adaptive stepsize control is sufficient to reliably and efficiently solve the equations of motion (as given in Appendix B) numerically. Various trial trajectories, including those of the LSR, were successfully calculated in order to test the self-written ISIS-implementation of the adopted integrator. The hypervelocity star HE 0437−5439 (Edelmann et al. 2005) is analyzed as a first and very interesting application because the spatial origin of this star is still under debate.

When hypervelocity stars were first discovered in 2005 (Brown et al. 2005), dynamical ejection from the supermassive black hole at the GC (Hills 1988) was supposed to be their only origin because these stars move so fast that they are unbound to the Galaxy. This scenario was challenged by the discovery of the third hypervelocity star HE 0437−5439 (Edelmann et al. 2005), a massive B star, because the travel time from the GC to its present position would exceed its lifetime by a factor of 4. Edelmann et al. (2005) notice that the star is much closer to the Large Magellanic Cloud (LMC) than to the Galaxy and might therefore originate in the LMC. This was

Table 3.4: Kinematic input parameters.

Parameter	Value	
	HE 0437−5439	LMC
α (J2000.0)	$4^{\rm h}38^{\rm m}12\overset{\rm s}{.}8^{(a)}$	$5^{\rm h}27\overset{\rm m}{.}6^{(d)}$
δ (J2000.0)	$-54°33'12''^{(a)}$	$-69°52'^{(d)}$
distance (kpc)	$61 \pm 9^{(b)}$	$50.1 \pm 2.4^{(e)}$
$\mu_\alpha \cos(\delta)$ (mas yr^{-1})	0.53 ± 0.25(stat) ± 0.33(sys)$^{(c)}$	$2.03 \pm 0.08^{(f)}$
μ_δ (mas yr^{-1})	0.09 ± 0.21(stat) ± 0.48(sys)$^{(c)}$	$0.44 \pm 0.05^{(f)}$
$v_{\rm rad}$ (km s^{-1})	$723 \pm 3^{(a)}$	$262.2 \pm 3.4^{(d)}$

Notes. Uncertainties are 1σ.
References. $^{(a)}$ Edelmann et al. (2005) ; $^{(b)}$ Przybilla et al. (2008c) ; $^{(c)}$ Brown et al. (2010) ; $^{(d)}$ van der Marel et al. (2002) ; $^{(e)}$ Freedman et al. (2001) ; $^{(f)}$ Kallivayalil et al. (2006) .

corroborated by a sophisticated differential abundance analysis of high-quality, high-resolution spectra by Przybilla et al. (2008c), who shows that the abundance pattern is inconsistent with that of GC stars but consistent with that of LMC B stars to within error limits. A kinematic investigation for the place of birth of HE 0437−5439 would require precise measurements of the star's, as well as LMC's, proper motion. While several studies have been carried out to measure the proper motion of the LMC, no measurements have been available for HE 0437−5439 until recently. Brown et al. (2010) used two epochs of images taken with the Advanced Camera for Surveys (ACS) onboard HST to determine the proper motion of HE 0437−5439 and argue that their measurement rules out a place of birth in the LMC at the 3σ level but is consistent with an origin from the GC. To remedy the time-of-flight versus lifetime problem, HE 0437−5439 needs to be a blue straggler (Edelmann et al. 2005). This would imply that the progenitor was a triple system from which a binary was ejected by the supermassive black hole. Later on its trajectory, the binary system merged to form the blue straggler (Perets 2009). However, the result of Brown et al. (2010) is strongly affected by the treatment of LMC motions, as well as the charge-transfer inefficiency (CTI) correction applied to the data. To demonstrate both issues, the kinematical analysis of HE 0437−5439 is revisited here considering three different cases.

1) To start with, trajectories for 10^4 Monte-Carlo realizations, which simultaneously account for statistical and systematic uncertainties in current positions and velocities via Gaussian distribution, are computed for HE 0437−5439 and LMC independently using the input parameters listed in Table 3.4. The distributions of pericenter distance $d_{\rm p}$, its corresponding point in time $T_{\rm p}$, and relative velocity $v_{\rm p}$ derived from the resulting sample of 10^8 combinations of orbit pairs are insensitive to the choice of the mass model (see run #1a in Table 3.5), and they confirm the results of Brown et al. (2010) ($d_{\rm p} = 13$ kpc, $T_{\rm p} = -23$ Myr) based on the Kenyon et al. (2008) Galactic potential and identical input values. Since $d_{\rm p}$ exceeds the radii of LMC's central region $R_{\rm cen}^{\rm LMC} = 3$ kpc, as well as the outermost regions $R_{\rm out}^{\rm LMC} = 10$ kpc (Brown et al. 2010), an origin in the LMC seems unlikely in this context.

2) Next, the LMC proper motions of Table 3.4 are replaced by $(\mu_\alpha \cos(\delta), \mu_\delta) = (+1.94 \pm 0.29, -0.14 \pm 0.36)$ mas yr^{-1} (Kroupa & Bastian 1997) to explore their influence on the out-

Table 3.5: Results of the kinematic investigation of HE 0437−5439.

Run	Model I			Model II			Model III		
	d_p (kpc)	T_p (Myr)	v_p (km s^{-1})	d_p (kpc)	T_p (Myr)	v_p (km s^{-1})	d_p (kpc)	T_p (Myr)	v_p (km s^{-1})
#1a	13.2 ± 4.5	−22 ± 13	640 ± 70	13.2 ± 4.5	−22 ± 13	640 ± 70	13.1 ± 4.4	−22 ± 13	640 ± 70
#1b	15.6 ± 10.4	−98 ± 15	690 ± 50	15.7 ± 10.3	−98 ± 16	680 ± 50	14.8 ± 10.1	−95 ± 14	730 ± 40
#2	11.0 ± 4.5	−23 ± 12	680 ± 80	10.9 ± 4.5	−23 ± 12	680 ± 80	11.0 ± 4.5	−23 ± 12	680 ± 80
#3a	7.5 ± 3.6	−26 ± 11	680 ± 80	7.5 ± 3.7	−26 ± 12	680 ± 80	7.6 ± 3.7	−26 ± 12	680 ± 80
#3b	16.6 ± 8.6	−95 ± 12	690 ± 30	17.0 ± 8.9	−95 ± 12	690 ± 30	15.8 ± 8.5	−93 ± 12	730 ± 20

Notes. d_p is the distance, T_p the time, and v_p the relative velocity at periastron of HE 0437−5439 with respect to the center of the LMC (runs #1a, #2, and #3a) or to the GC (runs #1b and #3b). Numbers are mean value ± standard deviation σ. The initial conditions of runs #1 are those of Brown et al. (2010). In runs #2 and #3a, Kroupa & Bastian's (1997) LMC proper motions are used. In runs #3, proper motions of HE 0437−5439 are increased by their systematic errors (CTI correction, see text for details).

come. Performing the same Monte-Carlo method as before, all three models give smaller pericenter distances (see run #2 in Table 3.5) and thus closer encounters of the two objects.

3) Assuming the CTI of ACS to be rising linearly in time, Brown et al. (2010) applied 55% of the epoch-2 CTI correction to their epoch-1 images. According to Massey (2010), however, there was a dramatic increase in the CTI between the two epochs that lead to an overcorrection in the epoch-1 data by Brown et al. implying proper motions of HE 0437−5439 that were larger than stated in Brown et al. (2010). The corresponding effects are roughly estimated here by adding the systematic errors to the mean value and omitting them afterwards, i.e., by using $(\mu_\alpha \cos(\delta), \mu_\delta) = (+0.86 \pm 0.25, +0.57 \pm 0.21)$ mas yr^{-1} as input for the Monte-Carlo calculation. The resulting distributions (see run #3a in Table 3.5) are still almost model independent and visualized for Model III in the upper panel of Fig. 3.8. In all three models, about 10% of all orbit pairs yield pericenter passages within the central region, i.e., $d_\mathrm{p} \leq R_\mathrm{cen}^\mathrm{LMC}$, or 76% in the outermost regions of the LMC ($d_\mathrm{p} \leq R_\mathrm{out}^\mathrm{LMC}$). Out of these, 2% (21%) have shorter flight times than the star's age of 18 ± 3 Myr (Przybilla et al. 2008c). Thus, 0.2% (16%) of the trajectories are consistent with an origin in the inner (outer) LMC without invoking additional requirements, such as a blue straggler nature. The decrease in pericenter distances due to CTI effects (Table 3.5: run #2 versus run #3a) is stronger than when they are due to a change in LMC proper motions (Table 3.5: run #1a versus run #2).

For comparison, we now consider the GC as the place of origin. Using the input values of Table 3.5, HE 0437−5439 passed 95 ± 14 Myr ago within $d_\mathrm{p} = 14.8 \pm 10.1$ kpc of the GC (see Model III of run #1b in Table 3.5). While the travel time is in good agreement with Brown et al. (2010) ($T_\mathrm{p} = -98$ Myr), it is difficult to compare d_p since it is not given in Brown et al. (2010). Nevertheless, the upper lefthand panel of Fig. 3 in Brown et al. (2010) suggests that substantially more than 68% of all trajectories have Galactic plane-crossing locations below 15 kpc. Because the Galactic plane-crossing location is an upper limit for d_p, this fraction increases further when we consider the pericenter distance. However, this contradicts our result that less than 60% of all orbits pass the GC within 15 kpc. As seen from run #3b in Table 3.5, the situation does not

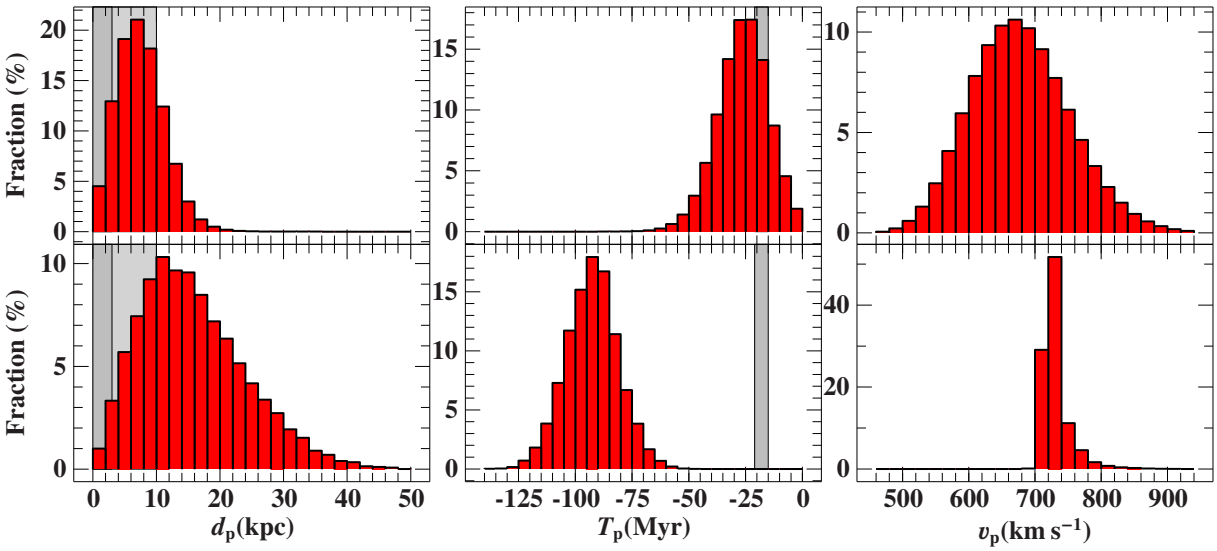

Figure 3.8: Histograms showing the distribution of distances d_p, times T_p, and relative velocities v_p at periastron of HE 0437−5439 with respect to the LMC (*upper panel*, run #3a) and the GC (*lower panel*, run #3b) for Model III. Mean values and standard deviations are given in Table 3.5. The gray-shaded areas mark regions with $d_p \leq R_{cen}^{LMC} = 3$ kpc, $d_p \leq R_{out}^{LMC} = 10$ kpc, and 15 Myr $\leq |T_p| \leq 21$ Myr. The last is the lifetime of HE 0437−5439 assuming a single-star nature (Przybilla et al. 2008c).

change significantly when accounting for the CTI overcorrection. The respective distributions from the 10^4 trajectories of HE 0437−5439 are shown in the lower panel of Fig. 3.8, whereby only ∼2% (27%) of the trajectories have pericenter passages within 3 kpc (10 kpc). All of them exceed the stellar lifetime and therefore require HE 0437−5439 to be a blue straggler.

As a consequence, ruling out an origin in the LMC in favor of the GC is disputable and the question of HE 0437−5439's birthplace remains open.

3.6 Conclusions

The motions of stars provide important information about the mass distribution in various components of the Galaxy. In particular, they trace the dark matter. Oort's (1932) measurements of stellar motions were the first to hint at the presence of dark matter in the Milky Way. Soon, the *Gaia* mission will provide velocity information of a huge number of stars and satellite galaxies with unprecedented precision. Analytical mass models of the Galaxy are utilized to calculate the orbits of stars. Allen & Santillán (1991) derived such a model by making use of observational constraints such as the Galactic rotation curve, the distance to the GC, and the local mass density. During the past twenty years, observational data have greatly improved. Therefore, it was time to revisit the Galactic gravitational potential of Allen & Santillán (1991) and update its parameters by making use of the latest observations. The halo mass is hereby constrained by the most extreme halo star discovered so far (Przybilla et al. 2008c). For comparison, two other widely used halo mass distributions – the truncated, flat rotation curve model (Wilkinson & Evans 1999) and a model derived from numerical cosmological simulations (Navarro et al.

1997) – are fitted as well.

All three Milky Way mass models are analytical, simple, and equally capable of reproducing their imposed restrictions. Major discrepancies only become apparent at Galactocentric distances greater than ∼15 kpc, which is the region where observational constraints are rare and the halo component dominates. In particular, the depth of the gravitational potential is very sensitive to the form of the dark matter halo seriously affecting for instance predictions of the local escape velocity. The significantly different shapes of the halos allow systematic uncertainties in kinematic investigations to be estimated by comparing the results of orbit computations performed in the three models separately.

Finally, the enigmatic hypervelocity star HE 0437−5439 is re-investigated by inspecting its trajectory in the context of the updated potentials. There are several pros and cons of whether the object originated in the LMC as proposed by the discoverers of the star (Edelmann et al. 2005) or from the GC, which is the suspected place of origin of all hypervelocity stars (Brown et al. 2005). The problem with the latter is that the travel time to the GC exceeds the stellar lifetime and that the chemical composition of HE 0437−5439 differs from what is known about stars in the GC. A birthplace in the LMC, on the other hand, would be consistent with both. However, based on their own measurement of the star's proper motion, Brown et al. (2010) claim that the LMC – in contrast to the GC – is ruled out as the place of origin. Therefore, we calculated trajectories for the star by making use of the three mass models under study. Using the same input data as Brown et al. (2010), we could confirm their results regarding the LMC, while those for the GC show discrepancies that are independent of the applied mass model. Our trajectories pass the GC within a considerably larger distance, showing that an origin in the GC is much less likely than suggested by Brown et al. (2010). Moreover, we investigated the influence of LMC proper motions and inspected systematic errors in the star's proper motion measurements stemming from the CTI overcorrection in the ACS images. The latter have not been considered by Brown et al. (2010) but turned out to be crucial. Our calculations show that an origin of HE 0437−5439 in the LMC is at least as likely or unlikely as an origin in the GC. Presently available proper motions are therefore inconclusive, and improved measurements are mandatory for settling this issue.

4 Quantitative spectroscopy

4.1 Spectrographs

Spectroscopy is the practice of obtaining and studying the distribution of electromagnetic radiation with wavelength and is one of the most powerful tools in astronomy. It provides access to a variety of parameters that describe the physical state of stars. The development of larger and larger telescopes and high-resolution spectrographs enables astronomers to acquire spectra of excellent quality, which then allow for analyses of very high precision.

4.1.1 Basics about (long-slit) spectrographs

Although the detailed physics of spectrographs is complicated, the basics are simple and can be explained almost solely in the framework of ray optics. Figure 4.1 shows the schematic construction and ray trace of a typical (long-slit) grating spectrograph. Its integral components and their functions are:

- The slit prevents scattered light from entering the beam and ensures a sharp projection of the light source by the telescope. The slit width b affects the resolution of a spectrum, see Eqs. (4.6) and (4.7).
- The collimator parallelizes the incoming light beam before it reaches the dispersion element. This is necessary to obtain a reasonable interference pattern.
- The dispersion element (grating) separates the light into its constituent wavelengths.
- The camera lens images the resulting spectrum onto the CCD detector.
- The CCD detector creates a digital image of the spectrum.

To minimize the loss of intensity during dispersion, tilted reflection gratings – so-called blaze gratings – are generally used as dispersion elements. As illustrated in Fig. 4.2, these gratings consist of periodic, reflecting grooves that are tilted by the blaze angle Θ relative to the surface normal. Due to this geometry, the maximum of intensity, which corresponds to the classical light path where the angles of incidence and reflection relative to the grooves' surface normal are equal, is shifted towards the direction of the dispersed light. Sticking to the signed definitions of α and β as given in Fig. 4.2, a classical photon follows a trajectory where

$$\alpha + \beta = 2\Theta\,. \tag{4.1}$$

The condition for constructive interference can be derived from Huygens' principle and the fact that the path difference Δs between two light beams has to be an integer multiple n, called order number or simply order, of the wavelength λ. With the definitions of Fig. 4.2, constructive interference occurs when

$$d\,[\sin(\alpha) + \sin(\beta)] = \Delta s \stackrel{!}{=} n\lambda\,. \tag{4.2}$$

The quantities α, d, and n are device-specific and fixed. Thus, Eq. (4.2) allows to determine the angle of reflection β as function of the wavelength λ. An important consequence of this

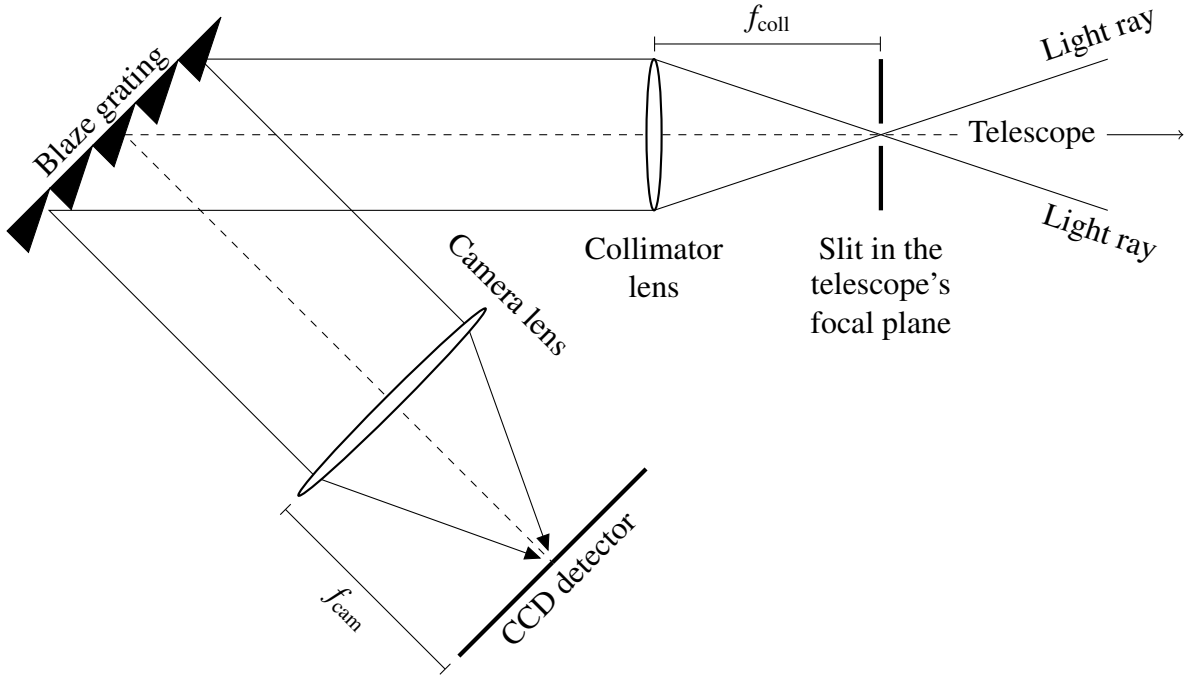

Figure 4.1: Schematic construction and ray trace of a grating spectrograph: The telescope focuses the beam of light at the slit. After the light is parallelized by a collimator lens (with focal length f_{coll}), it is dispersed by the grating. The resulting spectrum is imaged onto a CCD detector by a camera lens (with focal length f_{cam}).

equation is that different diffraction orders overlap in the visible range for $n > 1$, i.e., give the same β for two different wavelengths out of $3800\,\text{Å} \lesssim \lambda \lesssim 7800\,\text{Å}$.

The wavelength where constructive interference occurs on the classical light path is called blaze wavelength $\lambda_{\text{blaze},n}$. It is deduced by inserting Eq. (4.1) in Eq. (4.2) and reads

$$n\lambda_{\text{blaze},n} = d\left[\sin(\alpha) + \sin(\beta)\right]\Big|_{\alpha+\beta=2\Theta} = d\left[\sin(\alpha) + \sin\left(2\Theta - \alpha\right)\right] . \tag{4.3}$$

For a given n, the intensity is at its maximum at the blaze wavelength.

A very important property of a spectrograph is its resolving power, which is defined as the ratio of wavelength λ to its corresponding minimal resolvable wavelength difference $\Delta\lambda$. Within the spectrograph, there are two major processes that cause a smearing of wavelengths and, thus, a limitation of spectral resolution. Firstly, according to the Rayleigh criterion, diffraction by means of a grating is always accompanied by an inherent resolving power

$$(\lambda/\Delta\lambda)_{\text{grating}} = nN . \tag{4.4}$$

Here, n is again the order and N the number of illuminated grooves.

In general, however, it is not the grating that limits the spectral resolving power but the spatial extent of the star's projection in the telescope's focal plane, which is usually given by the slit width b (see Fig. 4.1). Due to the finite size of the slit, the light falling onto the grating in Fig. 4.1 is not entirely parallel but also slightly inclined resulting in a small variation $\Delta\alpha = b/f_{\text{coll}}$ of the incident angle α. For fixed d, n, and reflection angle β, the finite slit width therefore

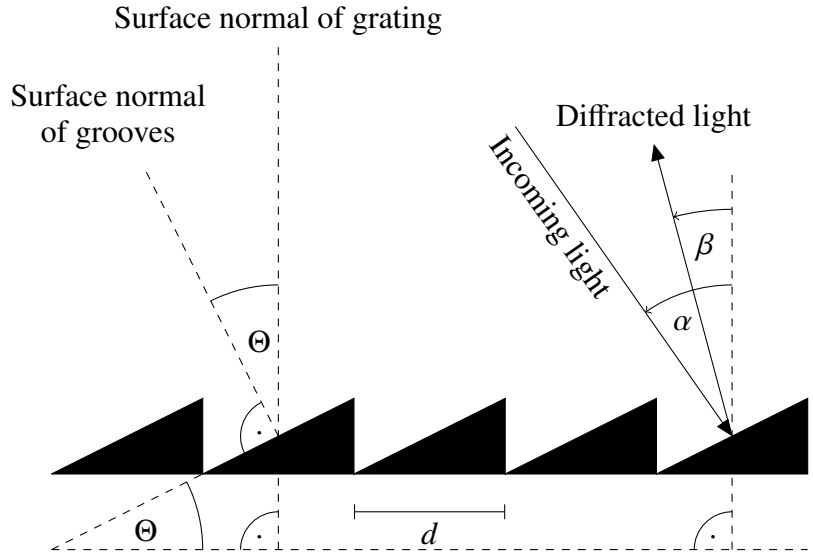

Figure 4.2: Schematic construction of a blaze grating: d is the spacing between two grooves, Θ is the blaze angle, α the signed angle of incidence, and β the signed angle of reflection relative to the grating's surface normal.

implies a smearing of wavelengths $\Delta\lambda$ that is given by

$$\Delta\lambda = \frac{\mathrm{d}\lambda}{\mathrm{d}\alpha}\Delta\alpha \overset{\text{Eq. (4.2)}}{=} \frac{d\cos(\alpha)}{n}\frac{b}{f_{\text{coll}}}\,. \tag{4.5}$$

The linear approximation $\Delta\lambda = \mathrm{d}\lambda/\mathrm{d}\alpha\Delta\alpha$ is valid here because b is small. The corresponding resolving power of a long-slit spectrograph reads then:

$$(\lambda/\Delta\lambda)_{\text{longslit}} = \frac{n\,f_{\text{coll}}}{d\,b\,\cos(\alpha)}\lambda \propto \lambda\,. \tag{4.6}$$

Typically, $(\lambda/\Delta\lambda)_{\text{longslit}} \ll (\lambda/\Delta\lambda)_{\text{grating}}$, so that $(\lambda/\Delta\lambda)_{\text{grating}}$ is called the theoretical resolving power whereas $(\lambda/\Delta\lambda)_{\text{longslit}}$ is the quantity that matters in practice and which is used to describe the quality of a spectrograph.

In most cases, spectra with large resolving powers are desirable since they reveal features that might be hidden or unresolved in their low-resolution equivalents. Consequently, the parameters in Eq. (4.6) are typically chosen such that $\lambda/\Delta\lambda$ is as large as possible. Due to practical and technical issues, this is doable only up to a certain point. Two simple measures that can be taken are the reduction of the slit width b and the usage of high order numbers n. Both actions, however, go along with some difficulties. Owing to diffraction effects in the atmosphere of the Earth, stars are not point-like but have some finite, apparent angular size resulting in an extended projection of the star in the focal plane of the telescope. If the star's image is larger than the slit width, light and thus valuable information is lost, which sets some lower limit on the slit widths. This blurring of stars due to atmospheric effects is called seeing. Note that in the unlikely case of extremely good seeing, where the projection of the star is significantly smaller than the slit width b, one has to substitute the latter by the former in Eq. (4.6) to obtain the actual resolving power. However, in the case that the spectrograph is coupled to the telescope via an optical fiber, the size of the projected star is given by the fiber's diameter, which in turn may replace b in Eq. (4.6) if it is smaller. As mentioned before, making use of $n > 1$ has the drawback of overlapping diffraction orders. But this problem can be solved conveniently by placing a second dispersion element into the light path resulting in a so-called echelle spectrograph.

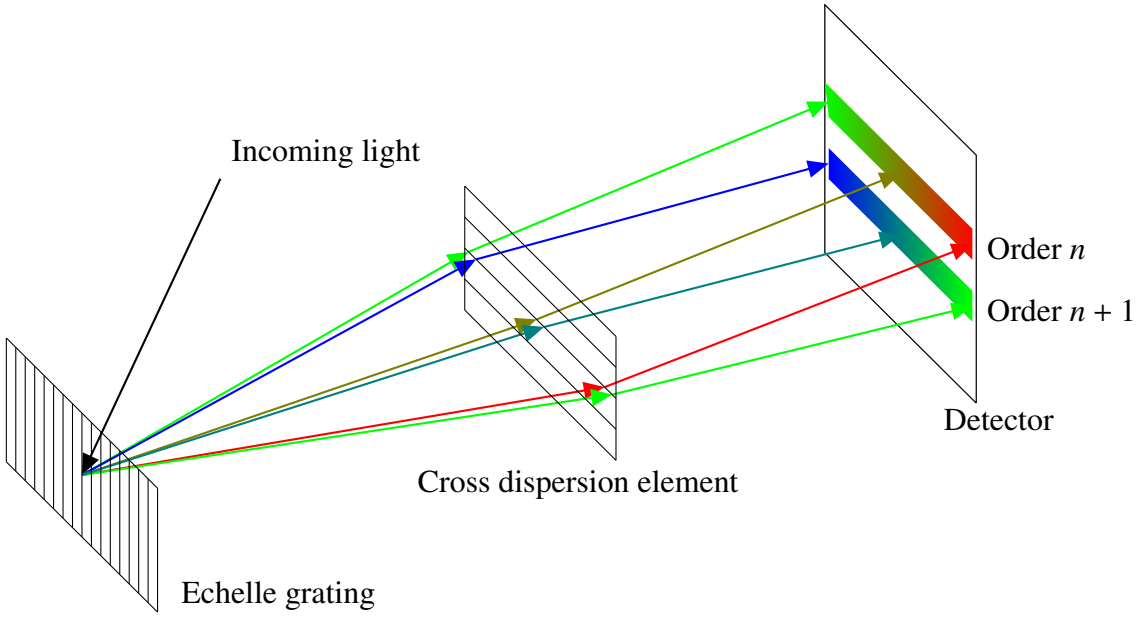

Figure 4.3: Schematic construction of an echelle spectrograph: The incoming light is diffracted by a blaze grating that creates overlapping orders of diffraction. These are separated afterwards by a cross dispersion element that is perpendicular to the first one. For simplicity, slit, camera lens, and collimator lens are not displayed here.

4.1.2 Echelle spectrographs

Echelle spectrographs differ from normal grating spectrographs merely in one additional component: a cross-dispersion element located between the blaze grating and the CCD detector, see Fig. 4.3. The cross disperser's task is to separate the overlapping diffraction orders in the direction that is perpendicular to the initial dispersion. In this way, each diffraction order appears as an isolated, tilted stripe[8] on the detector (see Fig. 4.4a). Echelle spectrographs offer the possibility to make use of very high diffraction orders up to $n \approx 100$ and thus to achieve huge resolving powers $\lambda/\Delta\lambda \approx 100\,000$ on CCD chips of comparatively modest size. To do so, a clever choice of parameters is essential. In particular, the geometry of the spectrograph is usually designed to keep the spectral overlap of neighboring orders small so that each individual order covers an almost unique part of the desired spectral range. Moreover, to minimize the loss of light within each order, the blaze wavelengths $\lambda_{\mathrm{blaze},n}$ defined in Eq. (4.3) are placed at the center of the detector. Under this condition, the spectral resolution of an echelle spectrograph can be approximated by substituting λ in Eq. (4.6) by $\lambda_{\mathrm{blaze},n}$:

$$
\begin{aligned}
(\lambda/\Delta\lambda)_{\mathrm{echelle}} &\approx (\lambda/\Delta\lambda)_{\mathrm{longslit}}\Big|_{n\lambda\approx n\lambda_{\mathrm{blaze},n}=d[\sin(\alpha)+\sin(2\Theta-\alpha)]} \overset{\text{Eq. (4.6)}}{=} \frac{f_{\mathrm{coll}}}{d\,b\,\cos(\alpha)} d\,[\sin(\alpha)+\sin(2\Theta-\alpha)] \\
&= \frac{f_{\mathrm{coll}}\,[\sin(\alpha)+\sin(2\Theta-\alpha)]}{b\,\cos(\alpha)} = \text{constant}\,. \qquad (4.7)
\end{aligned}
$$

[8] The name of the spectrograph – "echelle" is the French word for ladder or stairs – probably originated in this stair-like pattern.

The approximation $\lambda \approx \lambda_{\mathrm{blaze},n}$ is well justified since the spectral range covered by one diffraction order is typically so small that $|\lambda_{\mathrm{blaze},n} - \lambda|/\lambda_{\mathrm{blaze},n} \ll 1$. Equation (4.7) is important in the sense that it shows that the resolving power of echelle spectrographs is independent of λ, which is in contrast to their (long-slit) equivalents for which $\lambda/\Delta\lambda \propto \lambda$ holds (see Eq. (4.6)).

4.1.3 CCD detectors: Imaging the spectrum

The spectrum created by the spectrograph is imaged by a CCD chip. To resolve all spectral features, the spatial distribution of the pixels on the CCD has to be fine enough, which means that the CCD detector's resolving power $(\lambda/\Delta\lambda)^{\mathrm{CCD}}$ has to be equal or larger than the spectral resolution (in the latter case the spectrum is said to be oversampled). Let b_{pixel} be the spatial width of a single pixel of the CCD. According to the Nyquist criterion, the spatial resolving power is then given by $2\,b_{\mathrm{pixel}}$. Substituting $\alpha \to \beta$, $b \to 2\,b_{\mathrm{Pixel}}$, and $f_{\mathrm{coll}} \to f_{\mathrm{cam}}$ in the derivation of Eqs. (4.6) and (4.7), the CCD detector resolution reads

$$(\lambda/\Delta\lambda)^{\mathrm{CCD}}_{\mathrm{longslit}} = \frac{n\,f_{\mathrm{cam}}\,\lambda}{2\,b_{\mathrm{pixel}}\,d\,\cos(\beta)} \propto \lambda \tag{4.8}$$

and

$$(\lambda/\Delta\lambda)^{\mathrm{CCD}}_{\mathrm{echelle}} \approx \frac{f_{\mathrm{cam}}\,[\sin(\beta) + \sin(2\Theta - \beta)]}{2\,b_{\mathrm{pixel}}\,\cos(\beta)} = \text{constant}\,. \tag{4.9}$$

An important implication of Eqs. (4.8) and (4.9) is the fact that the data points, i.e., pixels read from the CCD, have equidistant spacing in wavelength for long-slit spectrographs but a steadily increasing spacing for echelle spectrographs. Let λ_i be the wavelength assigned to pixel i and $\Delta\lambda_i = \lambda_i/(2\,(\lambda/\Delta\lambda)^{\mathrm{CCD}}_i)$ be the corresponding pixel width in the wavelength domain (factor 2 because of Nyquist criterion). Then, $\lambda_{i+1} = \lambda_i + \Delta\lambda_i/2 + \Delta\lambda_{i+1}/2 = \lambda_i + \lambda_i/4/(\lambda/\Delta\lambda)^{\mathrm{CCD}}_i + \lambda_{i+1}/4/(\lambda/\Delta\lambda)^{\mathrm{CCD}}_{i+1}$ and consequently

$$\lambda_{i+1} = \lambda_i + \frac{d\,\cos(\beta)\,b_{\mathrm{pixel}}}{n\,f_{\mathrm{cam}}} = \lambda_i + \text{constant} \tag{4.10}$$

for a long-slit spectrograph and

$$\lambda_{i+1} = \lambda_i \frac{1 + \left(4\,(\lambda/\Delta\lambda)^{\mathrm{CCD}}_{\mathrm{echelle}}\right)^{-1}}{1 - \left(4\,(\lambda/\Delta\lambda)^{\mathrm{CCD}}_{\mathrm{echelle}}\right)^{-1}} = \lambda_i\,\text{constant} \tag{4.11}$$

for an echelle spectrograph.

4.2 Data reduction

The data obtained from a spectrograph cannot be used for a quantitative investigation in their raw form. They have to be processed into a useful format by a procedure called data reduction. Depending on the spectrograph in use, the steps applied during this process might vary a little bit. The principal ideas are nevertheless the same for all devices and are presented in the following:

a: Star. b: Flat-field. c: Thorium-Argon lamp.

Figure 4.4: Raw echelle spectra with 21 diffraction orders of a star, a flat-field, and a Thorium-Argon reference lamp. Dark colors indicate high intensities.

1) Removal of high-energetic cosmic particles: High-energetic cosmic particles cause unwanted signals on the CCD chip. Their occurrence naturally rises with increasing exposure time. In general, these events are confined to single pixels and their signal strength is much larger than that of photons. Due to these characteristics, cosmics can be effectively identified and removed by means of a moving average filter.

2) Subtraction of bias frame: Because of noise, very weak signals could be shifted to negative values during the readout process of the CCD which might cause problems. To avoid this, a constant offset is automatically added to each image before readout. This artificial signal can be removed with the help of bias frames, which are images taken with zero exposure time and closed shutter. In practice, several bias frames are taken, averaged to reduce the noise, and finally subtracted from all the other images.

3) Subtraction of scattered light and dark current: Due to reflections within the spectrograph, scattered light might distort the object's spectrum. This is corrected for by subtracting the inter-order signal that is adjacent to that of the target on the CCD. This action also removes the dark current, an additional signal caused by thermal excitations inside the CCD during the recording, which is anyway minimized by cooling down the detecting device to very low temperatures.

4) Subtraction of background: Some spectrographs offer the possibility to image not only the spectrum of the target but also the region around it. Provided that there is no other compact source close to the target, this can be used to obtain an estimate for the background signal that contaminates the spectrum of the object and, thus, has to be subtracted from it. Background primarily consists of ground based light that is scattered in Earth's atmosphere or of photons that stem from extended sources in the direction of observation.

5) Flat-fielding: The intensity profile along the diffraction orders is dominated by the so-called blaze function which peaks at the blaze wavelength $\lambda_{\mathrm{blaze},n}$ (see Eq. (4.3)) and falls off to the sides. Furthermore, there might be some damaged pixels on the CCD chip resulting in unphysical drops of the photon flux. To get rid of both of these problems, one can take

a spectrum of a source that emits light that is as independent of wavelength as possible, a so-called flat-field (see Fig. 4.4b). The division of the science frame by the flat-field frame replaces the strong wavelength dependency of the spectrograph and the CCD by the smooth one of the flat-field source.

6) Wavelength calibration: To convert the pixel scale into a wavelength scale, i.e., to derive the dispersion relation, one can make use of calibration lamps such as a Thorium-Argon lamp. The emission spectra of these lamps (see Fig. 4.4c) are very well studied so that the wavelengths of almost all lines are precisely known, which allows to assign wavelengths to pixels.

7) Rebinning: The individual orders are extracted from the two-dimensional image spectrum and are converted to a one-dimensional wavelength-flux spectrum.

8) Order merging: In the case of echelle spectrographs, the individual orders are merged to a single spectrum that covers the whole spectral range of the spectrograph. The overlapping region between adjacent orders is normally averaged with the help of a ramp function to give a smooth transition.

9) Normalization: Obtaining flux-calibrated spectra is a difficult task since it requires detailed knowledge about the absorption in the atmosphere of the Earth as well as about the efficiency of the spectrograph, both as function of wavelength. In the case that only relative fluxes are of interest, it is sufficient to normalize the spectrum, that is to set the continuum regions to unity. This facilitates the comparability of different observations but also the comparison with theoretical models. Unfortunately, normalization is a somewhat subjective process and, therefore, a potential source of error.

10) Heliocentric correction: Due to the relative motion v between the target and the Earth, wavelengths λ_0 are shifted to λ according to the Doppler formula

$$\frac{\lambda - \lambda_0}{\lambda_0} = \frac{v}{c} \,. \tag{4.12}$$

Here, c is the speed of light. The relative velocity v can be written as the sum of the target's radial velocity v_{rad} with respect to the Sun and a season-dependent component v_{helio} caused by Earth's rotation and its motion around the Sun:

$$v = v_{\mathrm{helio}} + v_{\mathrm{rad}} \,. \tag{4.13}$$

Given the coordinates of the target, the location of the telescope, and the time of observation, v_{helio} can be precisely calculated and, thus, corrected. According to Eq. (4.12), this can be done only in combination with v_{rad}:

$$\lambda_0 = \frac{\lambda}{1 + v/c} = \frac{\lambda}{1 + (v_{\mathrm{helio}} + v_{\mathrm{rad}})/c} \,. \tag{4.14}$$

Nevertheless, given the facts that $|v_{\mathrm{helio}}| \lesssim 30\,\mathrm{km\,s^{-1}} \ll c$ and $|v_{\mathrm{rad}}| \lesssim 1000\,\mathrm{km\,s^{-1}} \ll c$, the error introduced by the two subsequent corrections

$$\lambda_{\mathrm{helio-corrected}} = \frac{\lambda}{1 + v_{\mathrm{helio}}/c} \tag{4.15}$$

and

$$\lambda_{\text{subsequent}} = \frac{\lambda_{\text{helio-corrected}}}{1 + v_{\text{vrad}}/c} \tag{4.16}$$

is totally negligible:

$$\begin{aligned}\frac{\lambda_0 - \lambda_{\text{subsequent}}}{\lambda_0} &= 1 - \frac{1}{\lambda_0}\frac{\lambda}{(1 + v_{\text{rad}}/c)(1 + v_{\text{helio}}/c)} = 1 - \frac{1 + (v_{\text{helio}} + v_{\text{rad}})/c}{(1 + v_{\text{rad}}/c)(1 + v_{\text{helio}}/c)} \\ &= O\left(\frac{v_{\text{helio}}/c\, v_{\text{rad}}/c}{1 + (v_{\text{helio}} + v_{\text{rad}})/c}\right)\end{aligned} \tag{4.17}$$

Therefore, a heliocentric correction in the form of Eq. (4.15) is applied at the end of data reduction so that Doppler shifts in the spectrum are solely due to the target's motion.

4.3 Model spectra

4.3.1 Radiative transfer

The fundamental equation that governs the radiative transfer in stellar atmospheres is denoted radiative transfer equation and reads

$$\mathrm{d}I_\nu = -\kappa_\nu I_\nu \mathrm{d}s + \eta_\nu \mathrm{d}s\,. \tag{4.18}$$

I_ν is the specific intensity introduced in Sect. 2.1, κ_ν is the (macroscopic) absorption coefficient or opacity introduced in Sect. 2.3, η_ν is the (macroscopic) emission coefficient, and $\mathrm{d}s$ is an infinitesimal distance in direction of solid angle $\mathrm{d}\Omega$. Hence, the radiative transfer equation accounts for the changes of the macroscopic radiation field caused by absorption or emission of photons by the traversed matter. In general, the quantities κ_ν and η_ν are very complicated functions of the variables that define the state of the matter, such as density ρ, temperature T, or chemical composition $\{n(x)\}$. They can be derived from microscopic physics according to

$$\kappa_\nu = \text{number of absorbers} \times \text{atomic cross-section}(\nu) \tag{4.19}$$

and

$$\eta_\nu \propto \text{number of emitters} \times \text{transition probability}(\nu) \tag{4.20}$$

where the frequency-dependent cross-sections and transition probabilities are given by atomic physics. The dimension of κ_ν is length^{-1}, which means that κ_ν^{-1} is the characteristic distance a photon can travel before it is absorbed. As outlined in Sect. 2.3, four different absorption cross-sections are distinguished: bound-bound, bound-free, free-free, and scattering (which is actually not a true absorption process). Bound-bound transitions are responsible for the spectral absorption lines while the other three processes contribute to the continuum behavior.

For later convenience, consider a plane-parallel geometry with distances $\mathrm{d}s$ parametrized by $\mathrm{d}z$ (outbound coordinate in the direction perpendicular to the plane) and $\cos(\theta)$ (θ is the angle to the normal of the plane) via $\mathrm{d}s = \mathrm{d}z/\cos(\theta)$ (see Fig. 4.5). After defining the inbound

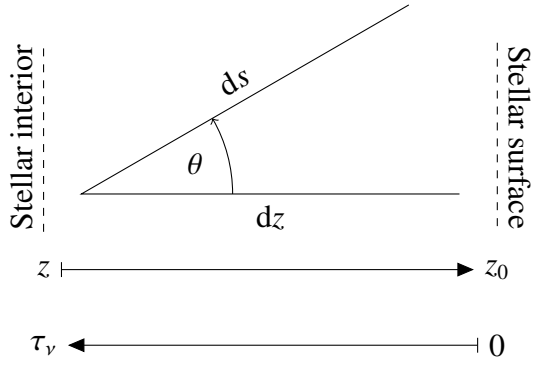

Figure 4.5: Useful quantities to describe the radiative transfer in a plane-parallel atmosphere: z is the outbound coordinate that is perpendicular to the plane, θ is the angle to the normal of the plane, and $\tau_\nu = -\int_{z_0}^{z} \kappa_\nu \mathrm{d}\acute{z}$ is the inbound optical depth.

optical depth $\tau_\nu = -\int_{z_0}^{z} \kappa_\nu \mathrm{d}\acute{z}$, Eq. (4.18) can be rewritten in terms of τ_ν via $\mathrm{d}s = \mathrm{d}z/\cos(\theta) = -\mathrm{d}\tau_\nu/\kappa_\nu/\cos(\theta)$ yielding

$$\cos(\theta)\,\mathrm{d}I_\nu = I_\nu \mathrm{d}\tau_\nu - \frac{\eta_\nu}{\kappa_\nu}\mathrm{d}\tau_\nu\,. \tag{4.21}$$

Introducing the source function $S_\nu = \eta_\nu/\kappa_\nu$, this leads to

$$\cos(\theta)\frac{\mathrm{d}I_\nu}{\mathrm{d}\tau_\nu} = I_\nu - S_\nu\,. \tag{4.22}$$

Once the source function is given, the radiative transfer equation reduces to a first-order differential equation with constant coefficients, which can be solved by multiplying an integrating factor $\exp(-\tau_\nu/\cos(\theta))$:

$$\begin{aligned}
&\cos(\theta)\exp\left(\frac{-\tau_\nu}{\cos(\theta)}\right)\frac{\mathrm{d}I_\nu}{\mathrm{d}\tau_\nu} = I_\nu \exp\left(\frac{-\tau_\nu}{\cos(\theta)}\right) - S_\nu \exp\left(\frac{-\tau_\nu}{\cos(\theta)}\right)\\
\Rightarrow\ &\cos(\theta)\frac{\mathrm{d}}{\mathrm{d}\tau_\nu}\left[I_\nu \exp\left(\frac{-\tau_\nu}{\cos(\theta)}\right)\right] + I_\nu \exp\left(\frac{-\tau_\nu}{\cos(\theta)}\right) = I_\nu \exp\left(\frac{-\tau_\nu}{\cos(\theta)}\right) - S_\nu \exp\left(\frac{-\tau_\nu}{\cos(\theta)}\right)\\
\Rightarrow\ &\cos(\theta)\frac{\mathrm{d}}{\mathrm{d}\tau_\nu}\left[I_\nu \exp\left(\frac{-\tau_\nu}{\cos(\theta)}\right)\right] = -S_\nu \exp\left(\frac{-\tau_\nu}{\cos(\theta)}\right)\\
\Rightarrow\ &I_\nu(\tau_{\nu,1},\cos(\theta)) = I_\nu(\tau_{\nu,2},\cos(\theta))\exp\left(-\frac{\tau_{\nu,2}-\tau_{\nu,1}}{\cos(\theta)}\right) + \int_{\tau_{\nu,1}}^{\tau_{\nu,2}} S_\nu(\acute{\tau_\nu})\exp\left(-\frac{\acute{\tau_\nu}-\tau_{\nu,1}}{\cos(\theta)}\right)\frac{\mathrm{d}\acute{\tau_\nu}}{\cos(\theta)}.
\end{aligned} \tag{4.23}$$

The first term in Eq. (4.23) shows that the intensity I_ν in the direction of positive $\cos(\theta)$ at a high optical depth $\tau_{\nu,2}$ is exponentially weakened by absorption on its way to a low optical depth $\tau_{\nu,1}$. The same is true for the second term, which describes the contributions of the source function along the path from $\tau_{\nu,2}$ to $\tau_{\nu,1}$. Note that Eq. (4.23) is just the formal solution of the radiative transfer equation and is not applicable in reality because the source function S_ν is also a function of the specific intensity I_ν. This is owing to the fact that the radiation field interacts with the surrounding matter and, thus, changes it's state and properties, which in turn determine κ_ν and η_ν and in this way S_ν.

4.3.2 Setting up a model atmosphere

In principle, the structure of a stellar atmosphere, that is the region of the star from where the observed light is emitted, can be deduced from the same set of equations (Eqs. (2.7)) that defines

the entire stellar structure. However, several simplifications can be made:

1) Plane-parallel geometry: The thickness Δr_{atmos} of stellar atmospheres is usually small compared to the radius $R_\star$ of the star: $\Delta r_{\text{atmos}}/R_\star \ll 1$. The curvature of the star is consequently negligible on the length scales of those interactions that occur in the atmosphere.

2) Homogeneity: The atmosphere is supposed to be homogeneous in each layer, i.e., there are no variations perpendicular to its normal. Hence, a single coordinate is sufficient to give the location within the atmosphere. Coordinates in use are either z, which increases towards the outer part of the atmosphere where $z = z_0 = R_\star$, or τ_ν, which increases towards the inner region and vanishes at the surface (see Fig. 4.5). In contrast to z, the optical depth τ_ν is dimensionless and, as seen in Eq. (4.23), a measure of extinction when considering fluxes emanating from the surface ($\tau_{\nu,1} = 0$, $\cos(\theta) > 0$). Due to its frequency dependence, the same value of τ_ν does not correspond to the same geometrical position z when considering different wavelengths. A mean optical depth can be defined by virtue of the Rosseland mean opacity $\kappa_{\text{Rosseland}}$ (see Sect. 2.3): $\tau = -\int_{z_0}^{z} \kappa_{\text{Rosseland}} \mathrm{d}\acute{z}$. This quantity is then a wavelength-independent indicator for extinction.

3) Stationarity: The atmosphere is supposed to be in a steady state, which means that time-dependent effects such as pulsations are neglected.

4) Hydrostatic equilibrium: Owing to stationarity, the equation of hydrostatic equilibrium Eq. (2.7b) is still valid. Since the atmosphere is only a small layer at the outer rim of the star, hydrostatic equilibrium simplifies to

$$\frac{\mathrm{d}P(r)}{\mathrm{d}r} = -\frac{GM(r)\rho(r)}{r^2} \approx -\frac{GM}{R_\star^2}\rho(r) \equiv -g\rho(r) \quad \Rightarrow \quad \frac{\mathrm{d}P(z)}{\mathrm{d}z} = -g\rho(z)\,. \tag{4.24}$$

The (constant) surface gravity

$$g = GMR_\star^{-2} \tag{4.25}$$

is one of the most important parameters that characterize stellar atmospheres. It is typically given as the logarithm with base ten of its value in cgs units, $\log(g\,(\mathrm{cm\,s^{-2}}))$. Because of the approximations made, the mass continuity equation Eq. (2.7a) becomes obsolete.

Note that P is a combination of the pressure caused by the plasma, i.e., the electrons and ionized atoms, and of the radiation: $P = P_{\text{plasma}} + P_{\text{radiation}}$. While P_{plasma} is computed from the equation of state of the plasma, e.g., the ideal gas law, an explicit expression for $P_{\text{radiation}}$ is given by the following (see Clayton 1983, p. 108) where c is again the speed of light:

$$P_{\text{radiation},\nu} = \int_{4\pi} \frac{I_\nu}{c} \cos^2(\theta)\,\mathrm{d}\Omega\,. \tag{4.26}$$

Equation (4.26) can be used to estimate the effects of photon pressure on the atmospheric structure. Under the reasonable assumption that κ_ν and η_ν are isotropic, the application of Eqs. (2.3) and (4.18) in combination with $\mathrm{d}s = \mathrm{d}z/\cos(\theta)$ yields:

$$\begin{aligned}\frac{\mathrm{d}P_{\text{radiation},\nu}}{\mathrm{d}z} &\overset{\text{Eq. (4.26)}}{=} \frac{1}{c}\int_{4\pi} \frac{\mathrm{d}I_\nu}{\mathrm{d}z}\cos^2(\theta)\,\mathrm{d}\Omega \overset{\text{Eq. (4.18)}}{=} -\frac{\kappa_\nu}{c}\int_{4\pi} I_\nu \cos(\theta)\,\mathrm{d}\Omega + \frac{\eta_\nu}{c}\int_{4\pi}\cos(\theta)\mathrm{d}\Omega \\ &\overset{\text{Eq. (2.3)}}{=} -\frac{\kappa_\nu}{c}F_\nu\,.\end{aligned} \tag{4.27}$$

Integration over frequencies results in

$$\frac{\mathrm{d}P_{\mathrm{radiation}}}{\mathrm{d}z} = -\frac{1}{c}\int_0^\infty \kappa_\nu F_\nu \mathrm{d}\nu = -\frac{1}{\rho(z)c}\int_0^\infty \kappa_\nu F_\nu \mathrm{d}\nu \rho(z) \equiv -g_{\mathrm{radiation}}\rho(z)\,, \tag{4.28}$$

which finally leads to

$$\frac{\mathrm{d}P_{\mathrm{plasma}}}{\mathrm{d}z} = -g\rho(z) - \frac{\mathrm{d}P_{\mathrm{radiation}}}{\mathrm{d}z} = -\rho(z)\left(g - g_{\mathrm{radiation}}\right)\,. \tag{4.29}$$

Here, the radiative acceleration $g_{\mathrm{radiation}} = (\rho(z)c)^{-1}\int_0^\infty \kappa_\nu F_\nu \mathrm{d}\nu$ was introduced. For B- or late O-type stars on the main sequence, it is weak compared to the surface gravity g. On the other hand, the stellar winds of massive O-type or Wolf-Rayet stars are a direct consequence of $g_{\mathrm{radiation}} > g$ resulting in a break-down of hydrostatic equilibrium and dynamic outflow of stellar matter into space. Obviously, such atmospheres are harder to handle since hydrodynamic effects such as mass loss have to be taken into account.

5) Radiative equilibrium: A static atmosphere implies energy conservation for each individual point. Therefore, the amount of energy per unit volume absorbed by the matter has to compensate the loss due to emission:

$$\int_0^\infty \int_{4\pi} \kappa_\nu I_\nu \mathrm{d}\Omega \mathrm{d}\nu \stackrel{!}{=} \int_0^\infty \int_{4\pi} \eta_\nu \mathrm{d}\Omega \mathrm{d}\nu\,. \tag{4.30}$$

Substituting $\mathrm{d}s = \mathrm{d}z/\cos(\theta)$ in Eq. (4.18), integrating over the solid angle and frequency, and applying Eq. (4.30) yields:

$$\int_0^\infty \int_{4\pi} \cos(\theta)\frac{\mathrm{d}I_\nu}{\mathrm{d}z}\mathrm{d}\Omega\mathrm{d}\nu = \int_0^\infty \int_{4\pi} (-\kappa_\nu I_\nu + \eta_\nu)\mathrm{d}\Omega\mathrm{d}\nu \stackrel{\text{Eq. (4.30)}}{=} 0\,. \tag{4.31}$$

Switching integration and differentiation in the left-hand side of Eq. (4.31) and making use of Eq. (2.3) leads to:

$$\frac{\mathrm{d}}{\mathrm{d}z}\int_0^\infty \int_{4\pi} \cos(\theta) I_\nu \mathrm{d}\Omega\mathrm{d}\nu \stackrel{\text{Eq. (2.3)}}{=} \frac{\mathrm{d}}{\mathrm{d}z}\int_0^\infty F_\nu \mathrm{d}\nu \stackrel{\text{Eq. (2.3)}}{=} \frac{\mathrm{d}F}{\mathrm{d}z} \stackrel{\text{Eq. (4.31)}}{=} 0 \;\Rightarrow\; F = \text{constant}\,. \tag{4.32}$$

Thus, local energy conservation leads directly to flux conservation in a plane-parallel geometry. According to the Stefan-Boltzmann law, the constant flux can be linked to the effective temperature T_{eff}, which is another important parameter that describes the state of an atmosphere, via $F = \sigma_{\mathrm{SB}} T_{\mathrm{eff}}^4$. Note that Eq. (4.32) is just the plane-parallel version of Eq. (2.7c) since the right-hand side of the latter equation vanishes in stellar atmospheres due to stationarity and temperatures that are too low to produce energy by nuclear reactions.

In summary, the basic system of integro-differential equations that governs the atmospheric structure depends on the input parameters g and $T_{\rm eff}$ and reads:

$$\frac{\mathrm{d}P_{\rm plasma}(z)}{\mathrm{d}z} = -\rho(z)\left(g - \frac{1}{c\rho(z)}\int_0^\infty \kappa_\nu \int_{4\pi} I_\nu \cos(\theta)\,\mathrm{d}\Omega\mathrm{d}\nu\right), \tag{4.33a}$$

$$\int_0^\infty \int_{4\pi} \cos(\theta) I_\nu \mathrm{d}\Omega\mathrm{d}\nu = \sigma_{\rm SB} T_{\rm eff}^4\,, \tag{4.33b}$$

$$\cos(\theta)\frac{\mathrm{d}I_\nu}{\mathrm{d}\tau_\nu} = I_\nu - S_\nu\,. \tag{4.33c}$$

The system of Eqs. (4.33), which couples all frequencies, depths, and angles with each other, is numerically treated in a standard way, namely, by discretization and linearization. Of course, there are several additional equations that contain further constraints such as charge conservation or the equation of state of an ideal gas, which have to be fulfilled, too. Under the assumption of local thermodynamic equilibrium (see Sect. 4.3.3), Eq. (4.33c) can be transformed into Eq. (2.7d) (Clayton 1983, Chap. 3.2) finally showing the complete analogy of Eqs. (2.7) and (4.33).

As already indicated at the end of Sect. 4.3.1, the most serious obstacle to solve the coupled system of Eqs. (4.33) is the source function. The specific form of S_ν is by no means trivial and is determined by macroscopic properties of the plasma such as temperature, density, and composition, as well as microscopic quantities like atomic cross-sections and transition probabilities. Therefore, solving this complex system is not a trivial task. The standard way is an iterative approach. First, one has to choose a trial atmosphere as starting point. That initial guess could be either the result of a previous calculation with a similar surface gravity and effective temperature or an analytical expression based on simplifications that allow the system to be solved exactly, for instance, the gray approximation. The trial atmosphere typically does not fulfill Eqs. (4.33) but provides hints of how to change it to make it work. This is done iteratively, which means that one varies, for example, the temperature profile that is implicitly present in Eq. (4.33c) via S_ν while keeping the remaining parameters fixed. The improved temperatures can, in turn, be inserted into equation Eq. (4.33a) via the ideal gas law to derive a new guess for the density or pressure, respectively. These new functions can again be substituted in Eq. (4.33c) to obtain a new photon flux I_ν, which has to be further altered in order to satisfy Eq. (4.33b). Once the trial functions for all physical quantities are updated, the procedure can start anew. The iterations are continued until a certain convergence criterion is reached, i.e., the differences between the new and old structure are below a given threshold. The resulting atmosphere can then be used to compute a synthetic spectrum.

The predictive power and physical correctness of synthetic spectra naturally depend on the assumptions made. In particular, the question of how to treat the source function is crucial. In the next section, the concepts of local thermodynamic equilibrium and non-local thermodynamic equilibrium will be introduced, which deeply affect the form of S_ν and accordingly the structure of the atmosphere.

4.3.3 Local versus non-local thermodynamic equilibrium

Apart from a precise description of the atomic structure (energy levels, statistical weights, transition probabilities) of the individual chemical species via so-called model atoms, the computation of the source function requires detailed knowledge of the statistical properties of the plasma: What percentage of atoms of a certain element is found in a specific excitation/ionization level? How many particles per volume are there at all? What is their velocity distribution? There are two different approaches to answer these questions.

Local thermodynamic equilibrium (LTE): The principle of thermodynamic equilibrium of statistical physics has proven to be very powerful and is applied in many distinct fields of physics. However, it cannot be valid for stars in a global manner since properties such as the gravitational force, pressure, or temperature depend on the position within the star. Nevertheless, thermodynamic equilibrium can be assumed locally, meaning that each individual volume element or each layer in a plane-parallel geometry, respectively, is in thermodynamic equilibrium and, hence, can be described by a local temperature T. Note that this concept is solely used to obtain the source function and, therefore, applies to the plasma but not to the radiation field, which is still determined by the radiative transfer equation and not via the Planck function. According to statistical physics, LTE implies

- a Maxwellian velocity distribution (with Boltzmann constant k and particle mass m)

$$p(v)\mathrm{d}v = \left(\frac{m}{2\pi kT}\right)^{\frac{3}{2}} \exp\left(-\frac{mv^2}{2kT}\right) 4\pi v^2 \mathrm{d}v\,, \tag{4.34}$$

- a Boltzmann excitation formula (with occupation number density n_i, statistical weight g_i, and energy E_i of the ith excitation level with respect to the ground state of the ion)

$$\frac{n_j}{n_i} = \frac{g_j}{g_i} \exp\left(-\frac{E_j - E_i}{kT}\right), \tag{4.35}$$

- and a Saha ionization equation (with total number density N_I of the ionization stage I, electron mass m_e, electron number density n_e, Planck constant h, partition function $G_I = \sum_{i=0}^{i_\mathrm{max}} g_i \exp(-E_i/kT)$, and ionization potential χ_I of the respective ion)

$$\frac{N_{I+1}}{N_I} = \frac{2}{n_\mathrm{e}} \frac{G_{I+1}}{G_I} \frac{(2\pi m_\mathrm{e} kT)^{\frac{3}{2}}}{h^3} \exp\left(\frac{-\chi_I}{kT}\right). \tag{4.36}$$

In combination with the conservation of charges, which is expressed by $\sum_I N_I Z_I - n_\mathrm{e} = 0$ with Z_I being the charge associated with level I, Eqs. (4.35) and (4.36) yield all occupation number densities n_i and N_I. Together with the information in the model atoms, this set of equations allows the local source function to be calculated.

LTE is a very good approximation as long as particles and photons from regions with different temperatures do not interact, i.e., as long as the interactions remain local, which is, for instance, the case in the interior of stars. However, the assumption of LTE is not valid if, on the one hand, the particle density is so low that the mean free path of particles and photons

can exceed the typical distance between two zones of different temperature, and, on the other hand, the photon flux is so high that there is always a non-negligible fraction of photons that links zones with different temperatures. Departures from LTE become thus more pronounced in stellar atmospheres with a high effective temperature, which implies a high photon flux, and a low surface gravity, which implies a low particle density. In B- and late O-type dwarfs and subgiants, the mean free path of particles is typically small enough to assume that the particle interactions conserve LTE in good approximation. The photon flux, on the other hand, can already be strong enough to cause deviations from LTE occupation numbers, i.e., non-LTE effects.

Non-local thermodynamic equilibrium (non-LTE): In non-LTE, the occupations numbers are no longer determined by the local temperature, i.e., by Eqs. (4.35) and (4.36), but by more general equations, namely the so-called statistical equilibrium or rate equations:

$$n_i \sum_{j \neq i} \left(R_{ij} + C_{ij} \right) = \sum_{j \neq i} n_j (R_{ji} + C_{ji}) \,. \tag{4.37}$$

Here, R_{ij} and C_{ij} are the radiative and collisional rates for transitions from level[9] n_i to level n_j. Consequently, the rate equations demand that the rate with which the state i is depopulated (left-hand side) is equal to that rate with which it is populated (right-hand side). The rates are functions of the radiation field, particle velocity distribution, and atomic cross-sections. Thus, the statistical equations together with the condition that the total number of particles of an element is conserved, $\sum_i n_i = n$, form a complex, non-linear system of coupled equations that has to be solved in order to obtain the occupation number densities and in this way S_ν. Moreover, the Eqs. (4.37) are coupled to the system of Eqs. (4.33) and all of them have to be solved simultaneously. Depending on the chemical elements under consideration, the numerical effort is sometimes so large that the calculation of a synthetic non-LTE spectrum can take days instead of minutes as for LTE. Note that speaking of non-LTE does usually not imply a complete departure from LTE principles since, e.g., the velocity distribution is still assumed to be Maxwellian. Statistical equilibrium is a generalization of local thermodynamic equilibrium and the latter is restored in the limit of high particle densities and low photon fluxes.

As demonstrated in Figs. C.1.1a to C.1.1m, the spectra of O- and B-type stars are affected by non-LTE effects because of their high temperatures.

4.3.4 Hybrid LTE/non-LTE approach

The computation of a single synthetic spectrum in non-LTE is an expensive numerical task and is very time consuming. In addition, the determination of spectroscopic parameters is based on a whole grid of models in a multi-dimensional parameter space ($T_{\rm eff}$, $\log(g)$, $\{n(x)\}$, ...) and, thus, requires the calculation of a huge number of model spectra. To reduce the numerical effort, a hybrid LTE/non-LTE approach is used in this work. It is discussed in detail by Nieva & Przybilla (2007) and Przybilla et al. (2011), who also show that this approach is consistent with full non-LTE calculations for B-type stars. The underlying idea is that non-LTE effects

[9]For simplicity, the levels n_i and n_j in Eq. (4.37) refer to any level in an atom and not only to those of a particular ionization stage like in Eq. (4.35).

are important for the details of radiative transfer but negligible for the atmospheric structure. If this is the case, the system of Eqs. (4.33) can be solved in LTE. The resulting atmosphere is then kept fixed during the simultaneous solution of the radiative transfer Eq. (4.33c) and rate Eqs. (4.37), which implies that any non-LTE feedback on the atmospheric structure is neglected. The following codes are applied for this purpose:

1) ATLAS12 (Kurucz 1996): Computes the atmospheric structure in LTE.

2) DETAIL (Giddings 1981; Butler & Giddings 1985, extended and updated): Based on the fixed ATLAS12 atmosphere, the coupled radiative transfer Eq. (4.33c) and rate Eqs. (4.37) are solved to obtain the radiation field and the occupation number densities in non-LTE. Basically, the problem is solved at this point. However, to speed up the calculations, the frequency grid in DETAIL is relatively rough and approximations for the line broadening are used. The respective output is thus insufficient to reproduce the detailed shape of spectral lines. Nevertheless, the source function S_ν is determined by the resulting non-LTE occupation number densities.

3) SURFACE (Giddings 1981; Butler & Giddings 1985, extended and updated): Using a considerably finer frequency grid and more detailed line profiles than doable with DETAIL, the SURFACE code allows the final radiation field to be precisely determined. By means of the formal solution (Eq. (4.23)), the flux emerging at the stellar surface ($\tau_{\nu,1} = 0$) is

$$I_\nu(0, \cos(\theta)) = I_\nu(\tau_{\nu,2}, \cos(\theta)) \exp\left(-\frac{\tau_{\nu,2}}{\cos(\theta)}\right) + \int_0^{\tau_{\nu,2}} S_\nu(\tau'_\nu) \exp\left(-\frac{\tau'_\nu}{\cos(\theta)}\right) \frac{\mathrm{d}\tau'_\nu}{\cos(\theta)} \,. \tag{4.38}$$

Here, $\tau_{\nu,2}$ corresponds to the inner rim of the computed photosphere where the medium is optically thick at each frequency ν, that is $\tau_{\nu,2} \gg 1$.

Assuming a spherical symmetric star with negligible photospheric curvature, the spectrum $F_\nu(0)$, which is emitted from the stellar surface in direction of an infinite distant observer, results from the integration of the specific intensity $I_\nu(0, \cos(\theta))$ of a plane-parallel atmosphere over one hemisphere[10], see Fig. 4.6:

$$F_\nu(0) = 2\pi \int_0^1 \left(I_\nu(\tau_{\nu,2}, \cos(\theta)) \exp\left(-\frac{\tau_{\nu,2}}{\cos(\theta)}\right) + \int_0^{\tau_{\nu,2}} S_\nu(\tau'_\nu) \exp\left(-\frac{\tau'_\nu}{\cos(\theta)}\right) \frac{\mathrm{d}\tau'_\nu}{\cos(\theta)} \right) \mathrm{d}\cos(\theta) \,. \tag{4.39}$$

To obtain a normalized synthetic spectrum, the continuum flux $F_{\mathrm{cont},\nu}(0)$ has to be computed as well. This is done by considering only continuous absorption and emission coefficients in the source function S_ν. The final model spectrum is then given by:

$$F_{\mathrm{norm},\nu} = \frac{F_\nu(0)}{F_{\mathrm{cont},\nu}(0)} \,. \tag{4.40}$$

[10]Note that the use of the notation F_ν in Eq. (4.39) is consistent with Eq. (2.3) since the solid angle integration in Eq. (4.39) can be expanded to the entire sphere because $I_\nu(0, \cos(\theta)) = 0$ for $\cos(\theta) < 0$. The latter is a boundary condition of the system of Eqs. (4.33) and states that no light enters the star from outside.

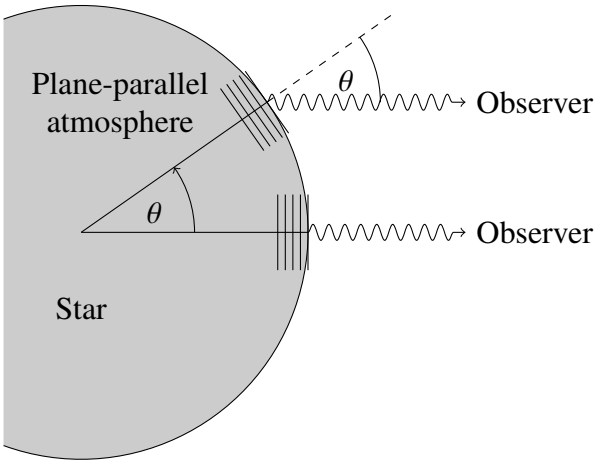

Figure 4.6: The spectrum emitted by a star in direction of an infinite distant observer is the superposition of the fluxes of all individual surface elements visible to the observer. For a spherically symmetric star with negligible photospheric curvature, the spectrum can hence be calculated from integrating the specific intensity $I_\nu(0, \cos(\theta))$ of a plane-parallel atmosphere over one hemisphere, that is from $\theta = 0°$ to $\theta = 90°$, see Eq. (4.39).

Using the relations $|F_\nu \mathrm{d}\nu| = |F_\lambda \mathrm{d}\lambda|$ and $\lambda\nu = c$, this reads in wavelength space

$$F_\lambda = \frac{c}{\lambda^2} F_\nu \,,\; F_{\mathrm{norm},\lambda} = F_{\mathrm{norm},\nu} \,. \tag{4.41}$$

Another simplification in the hybrid LTE/non-LTE approach with respect to full non-LTE calculations is that the population number densities of the individual metals are computed separately, whereby LTE occupation numbers are used for the other "background" metals. This is justified as long as the non-LTE effects of individual metals on the radiation field are small. Owing to their large abundances, this does not apply to hydrogen and helium, whose non-LTE population numbers are considered in all Detail calculations.

The contributions of the background metals to the source function are accounted for either via so-called opacity distribution functions (ODFs) or the concept of opacity sampling (OS), which are both based on simplified LTE principles. In the OS approach, the spectrum is sampled by a large yet limited number of frequency points, for each of which the opacity of the background elements is estimated in LTE. OS is very flexible since the opacities are directly calculated from the current conditions of the atmosphere. In contrast, ODFs are tabulated opacities as function of frequency, temperature, and pressure. They are calculated once for a certain chemical composition and a very fine frequency grid, which is typically much finer than that of OS. ODFs have thus the advantage of providing quick access to the source function since one only has to interpolate pre-tabulated values. On the other hand, they are not very well suited to analyze stars with a non-standard chemical composition.

Finally, the use of OS or ODFs, respectively, is important to allow for metal line blanketing, which is the redistribution of photons from the ultraviolet to longer wavelengths by virtue of several hundred thousands of densely packed metal lines in the ultraviolet.

4.3.5 Principles of line formation

A spectral line is caused by the discrete transition from one atomic state to another one. The wavelength of the associated photon is determined by the energy difference between the upper and lower atomic level. As a consequence, spectral lines are the fingerprints of chemical species since the atomic structure with its corresponding atomic transitions is unique for each element.

Spectral lines are usually observed in absorption because the line opacity $\kappa_{\mathrm{line},\nu}$ exceeds the continuous opacity $\kappa_{\mathrm{cont},\nu}$ by virtue of the additional bound-bound absorption, $\kappa_{\mathrm{line},\nu} > \kappa_{\mathrm{cont},\nu}$. Therefore, the same optical depth $\tau_\nu = -\int_{z_0}^{z} \kappa_\nu \mathrm{d}\acute{z} = 1$ is reached for different geometrical distance $z_0 - z$. The optical depth $\tau_\nu = 1$ marks the boundary between the optically thin ($\tau_\nu < 1$) and optically thick ($\tau_\nu > 1$) region and, thus, defines the region where most of the emitted photons stem from. Hence, the continuum flux arriving at the observer originates in deeper stellar layers than the flux that is associated with spectral lines. According to Eq. (2.7d), which holds qualitatively also in atmospheres, the temperature increases towards the center of the star. Consequently, the continuum is emitted from hot layers with a high flux whereas spectral lines form in the cooler outer layers with less flux.

The shape of spectral lines depends, on the one hand, on atomic properties of the chemical element and, on the other hand, on the state of the surrounding plasma. In the following, all effects and parameters that affect the shape and strength of spectral lines are briefly introduced:

- Natural line width: Excited atomic states are not stable but decay after a characteristic lifetime Δt. Heisenberg's uncertainty principle $\Delta E \Delta t \geq h$ states that the energy difference E_0 between the excited and the de-excited level is not sharp but has an intrinsic spread ΔE, which translates into a range of energies for the absorbed/emitted photon. The corresponding distribution in frequency space, $\Phi_{\mathrm{natural}}(\nu)$, can be derived from a classical damped oscillator yielding a Lorentzian profile:

$$\Phi_{\mathrm{natural}}(\nu) = \frac{\gamma_{\mathrm{rad}}/4\pi^2}{(\nu - \nu_0)^2 + (\gamma_{\mathrm{rad}}/4\pi)^2} \,. \tag{4.42}$$

  The damping constant γ_{rad} is either measured experimentally or obtained theoretically from quantum mechanical calculations of transition probabilities. The central frequency ν_0 is derived from $E_0 = h\nu_0$.

- Pressure broadening: The ions of the plasma are not isolated but interact with each other via the Coulomb force. The resulting perturbations influence the atomic structure of the ions and lead to shifts in their energy levels. This effect becomes more pronounced with increasing pressure since the particles are then closer and the Coulomb forces stronger. In hot stars of type O and B with a large number of charged particles, the relevant interactions are the linear and quadratic Stark effect. The former affects atoms with intrinsic dipole moments such as neutral hydrogen (H I) or singly ionized helium (He II) while all others are subject to the latter. Depending on whether the duration of the interaction is short (impact approximation) or long (quasi-static approximation) relative to the lifetime of the energy level under consideration, the energetic shifts are different. For moderate densities, the short-term perturbations of the impact approximation dominate the pressure broadening, which again can be described in frequency space by a Lorentzian profile $\Phi_{\mathrm{pressure}}(\nu)$ according to Gray (2005, pp. 238–253).

- Thermal Doppler broadening: By virtue of the well-known Doppler effect, the rest-frame frequency ν_0 of a photon, which is absorbed or emitted by a particle that is moving with the line-of-sight velocity v, is shifted to the frequency ν, compare Eq. (4.12):

$$\frac{\nu_0 - \nu}{\nu} = \frac{v}{c} \quad \Rightarrow \quad \nu = \frac{\nu_0}{v/c + 1} \overset{v \ll c}{\approx} \left(1 - \frac{v}{c}\right)\nu_0 \quad \Rightarrow \quad v \approx c\frac{(\nu_0 - \nu)}{\nu_0} \,. \tag{4.43}$$

In thermodynamic equilibrium, the thermal velocity distribution $p(v)$ in an arbitrary one-dimensional spatial direction is a Gaussian curve according to the Maxwell-Boltzmann statistics:

$$p(v) = \frac{1}{\sqrt{\pi}\bar{v}} \exp\left(-\frac{v^2}{\bar{v}^2}\right) . \tag{4.44}$$

Here, $\bar{v} = \sqrt{2kT/m}$ is the dispersion of the line-of-sight velocity for particles of mass m at temperature T. The thermal Doppler profile in frequency space, $\Phi_{\text{thermal}}(\nu)$, follows from Eqs. (4.43) and (4.44) in combination with the condition that $|\Phi_{\text{thermal}}(\nu)\mathrm{d}\nu| = |p(v)\mathrm{d}v|$:

$$\Phi_{\text{thermal}}(\nu) = p(v)\left|\frac{\mathrm{d}v}{\mathrm{d}\nu}\right| \approx \frac{c}{\sqrt{\pi}\bar{v}\nu_0} \exp\left(-\frac{c^2(\nu_0-\nu)^2}{\bar{v}^2\nu_0^2}\right) = \frac{1}{\sqrt{\pi}\Delta\nu_{\text{thermal}}} \exp\left(-\frac{(\nu_0-\nu)^2}{\Delta\nu_{\text{thermal}}^2}\right) . \tag{4.45}$$

It is a Gaussian function parametrized by the thermal Doppler width $\Delta\nu_{\text{thermal}} = \bar{v}\nu_0/c$.

- Non-thermal Doppler broadening: In order to match hydrostatic model spectra to observations, an additional non-thermal velocity component has to be postulated, the so-called microturbulence. It is motivated by small-scale motions which are well below the photon mean-free-path and which are neglected in hydrostatic models. For simplicity, it is standard practice to incorporate the effects of microturbulence by assuming its velocity distribution to be Gaussian with dispersion parameter ξ:

$$p(v) = \frac{1}{\sqrt{\pi}\xi} \exp\left(-\frac{v^2}{\xi^2}\right) . \tag{4.46}$$

In analogy to the thermal Doppler broadening, the corresponding frequency profile is then described by a non-thermal Doppler width $\Delta\nu_{\text{non-thermal}} = \xi\nu_0/c$ and reads

$$\Phi_{\text{non-thermal}}(\nu) = \frac{1}{\sqrt{\pi}\Delta\nu_{\text{non-thermal}}} \exp\left(-\frac{(\nu_0-\nu)^2}{\Delta\nu_{\text{non-thermal}}^2}\right) . \tag{4.47}$$

The physical origin of microturbulent motion in photospheres of O and B stars is not completely understood so far. Therefore, the microturbulence parameter ξ is more or less used as a fudge factor in the spectroscopic analysis to derive consistent abundances from different spectral lines of one element. According to Cantiello et al. (2009), however, the occurrence of microturbulence in photospheres of hot stars might be linked to a sub-surface iron convection zone. This is discussed in more detail in Sect. 7.3.5.

The four previous broadening processes are all uncorrelated and, hence, can be combined via multiple convolutions of the individual line profiles to give the total profile. Using the facts that convolutions are associative and commutative and that the convolution of two Gaussian/Lorentzian functions is again a Gaussian/Lorentzian function, one has:

$$\Phi_{\text{total}} = \Phi_{\text{natural}} * \Phi_{\text{pressure}} * \Phi_{\text{thermal}} * \Phi_{\text{non-thermal}} = \Phi_{\text{Lorentz}} * \Phi_{\text{Gauss}} \equiv \Phi_{\text{Voigt}} . \tag{4.48}$$

The total line profile is thus a so-called Voigt function, which is, by definition, the convolution of a Gaussian and a Lorentzian function. The shape of the Voigt profile can be similar to a Gaussian

profile if the broadening is dominated by a Gaussian-shaped mechanism like thermal or non-thermal Doppler broadening, or can be close to a Lorentzian profile if the natural line width or pressure broadening are the strongest broadening agents. Neutral hydrogen, for instance, is heavily affected by pressure broadening via the Stark effect so that the broad wings of its lines are Lorentzian while the line cores are rather Gaussian because of the temperature induced Doppler broadening. Note that the profile function Φ_{total} describes the frequency dependence of the bound-bound emission and absorption coefficients η_ν and κ_ν and, consequently, influences the source function S_ν but – strictly speaking – is not identical to the shape of spectral lines. However, the line profile function is by far the most important feature when modeling spectral lines so that there is an almost one-to-one correspondence between profile function and spectral line shape.

The broadening mechanisms discussed so far are of microscopic nature. To completely reproduce observations, the following two macroscopic flux redistributions have to be considered as well.

- Rotational broadening and macroturbulence: The equatorial rotational velocity v_{rot} of stars ranges from a few up to several hundred kilometers per second. In particular, unevolved massive stars are found to rotate fast, sometimes even close to their break-up velocity. The projection of the rotational velocity on the line-of-sight direction gives the actually observed velocity $v_{\text{rot,observed}}$. It is commonly expressed via the inclination angle i between rotational axis and line-of-sight: $v_{\text{rot,observed}} = v_{\text{rot}} \sin(i) \equiv v \sin(i)$. The projected rotational velocity leads again to a Doppler shift of photon wavelengths, but this time on macroscopic scales. To account for this, one has to sum up the geometrically weighted fluxes emerging from different parts of the projected disk of the rotating star since resolving the stellar surface is – apart from the Sun and very few other stars – not possible and observed fluxes are, hence, typically integrated ones. Using some minor simplifications, it can be shown (see Gray 2005, pp. 458–467) that the disk integration is sufficiently approximated by the much simpler convolution of the normalized flux with the following rotational profile:

$$\Phi_{\text{rot}}(\lambda) = \begin{cases} \dfrac{2(1-\epsilon)\sqrt{1-\left(\frac{\lambda-\lambda_0}{\Delta\lambda_{\text{L}}}\right)^2} + \frac{1}{2}\pi\epsilon\left(1-\left(\frac{\lambda-\lambda_0}{\Delta\lambda_{\text{L}}}\right)^2\right)}{\pi\Delta\lambda_{\text{L}}\,(1-\epsilon/3)} & \text{if } |\lambda-\lambda_0| \leq \Delta\lambda_{\text{L}}, \quad (4.49a) \\ 0 & \text{otherwise.} \quad (4.49b) \end{cases}$$

  Here, $\Delta\lambda_{\text{L}} = \lambda_0 v \sin(i)/c$ is the largest Doppler shift stemming from the equator of the star and ϵ is the linear limb-darkening coefficient. Limb darkening arises from the fact that the exponential extinction in Eq. (4.38) is not only proportional to the optical depth but also inversely proportional to $\cos(\theta)$. Thus, as one looks toward the limb of the stellar disk ($\theta = 90°$, see Fig. 4.6), one sees systematically higher photospheric layers which are cooler and less bright. For simplicity, a simple linear limb-darkening law in the form $I(\theta) = I_0(1 - \epsilon + \epsilon\cos(\theta))$ is typically assumed to describe the decrease in the continuum intensity when going from the center of the stellar disk ($\theta = 0°$) to the limb ($\theta = 90°$).

  The situation becomes more complicated in the case that rotation is accompanied by macroturbulence, which is the large-scale turbulent motion of cells in stellar atmospheres. According to Aerts et al. (2009), the physical explanation for this macroturbulent motion in massive stars is the collective effect of pulsations. The dimensions of the macrocells are typically so

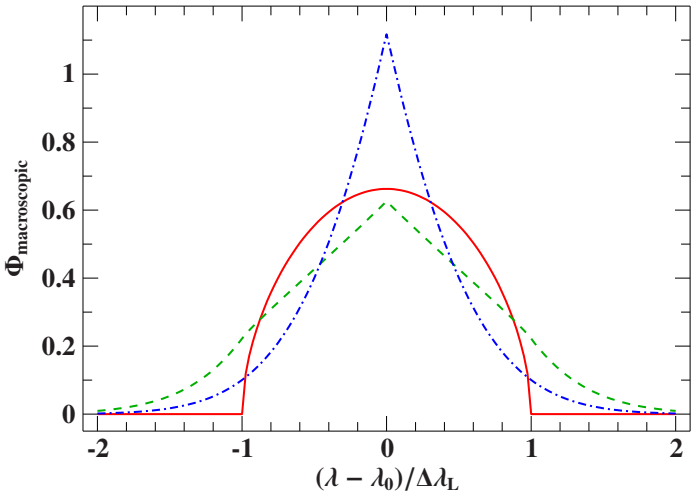

Figure 4.7: Macroscopic broadening profiles $\Phi_{\mathrm{macroscopic}}(\lambda)$ for three different combinations of projected rotational velocity $v\sin(i)$ and macroturbulence ζ but fixed limb darkening $\epsilon = 0.3$. The solid red line is the pure rotational profile of Eq. (4.49) ($\Delta\lambda_\mathrm{L} = \lambda_0 v\sin(i)/c$, $\zeta = 0$), the dashed-dotted blue line a pure macroturbulence profile ($\Delta\lambda_\mathrm{L} = \lambda_0\zeta/c$, $v\sin(i) = 0$), and the dashed green line a mixed profile ($\Delta\lambda_\mathrm{L} = \lambda_0 v\sin(i)/c$, $\zeta = v\sin(i)$).

large that photons remain in them from the time they are created until they escape from the star. Consequently, each macrocell emits a separate spectrum that is Doppler shifted with the cell's specific velocity. A simple but widely used model for the distribution of macrocell velocities on the apparent stellar surface is the symmetric radial-tangential model with macroturbulence parameter ζ (see Gray 2005, pp. 433–437):

$$p(v) = \frac{1/2}{\sqrt{\pi}\zeta\cos(\theta)}\exp\left(-\frac{v^2}{(\zeta\cos(\theta))^2}\right) + \frac{1/2}{\sqrt{\pi}\zeta\sin(\theta)}\exp\left(-\frac{v^2}{(\zeta\sin(\theta))^2}\right). \tag{4.50}$$

Here, the velocity vectors of the macrocells are either along stellar radii (first term in Eq. (4.50)) or tangent to the surface (second term in Eq. (4.50)) and the distribution of speeds is Gaussian. To obtain the contributions of all cells, one has to integrate, on the one hand, over the projected stellar disk and, on the other hand, for each spot on the disk over the distribution of cell velocities as given in Eq. (4.50).

In general, the effects of stellar rotation, limb darkening, and macroturbulence cannot be disentangled but have to be considered simultaneously. Unfortunately, the integration over the projected stellar disk can then no longer be performed or approximated analytically. Instead, the integration has to be done numerically to obtain the joint macroscopic broadening profile $\Phi_{\mathrm{macroscopic}}(\lambda)$ with which the model spectrum is to be convolved. In this work, a dense grid of tabulated profiles (kindly provided by M. Firnstein) is interpolated to access the desired profile as function of the projected rotational velocity $v\sin(i)$, macroturbulence ζ, and linear limb-darkening coefficient ϵ. The profiles for pure rotation, pure macroturbulence, and a mixed state are shown in Fig. 4.7.

- Instrumental profile: Spectral lines are blurred due to the finite resolving power of the spectrograph (Eqs. (4.6), (4.7)) and the detector (Eqs. (4.8), (4.9)). The respective broadening profile, which is used for the convolution with the synthetic flux, is assumed to be Gaussian. Its width is measured by fitting a Gaussian curve to the emission lines of the reference lamp (see Fig. 4.4c). This is well justified because these lines show no significant intrinsic broadening, which implies that their width is dominated by instrumental smearing.

Microscopic broadening mechanisms enter the radiative transfer equation and, in this way, affect the distribution as well as the number of emitted photons, that is the shape as well as the strength

of spectral lines. In contrast, macroscopic broadening is just a redistribution of photons and is, hence, irrelevant for the line strength.

4.4 Spectroscopic parameters and their spectral features

The atmospheres of OB stars, as treated in this work, are characterized by seventeen parameters, which are briefly introduced in the following. The spectral features, from which these parameters are primarily constrained, are also described.

- Effective temperature $T_{\rm eff}$: As outlined in Sect. 4.3.2, the effective temperature, which is a measure for the emitted flux, is a key parameter for the description of the atmospheric structure, see Eqs. (4.33). In particular, the temperature stratification is connected to it because of flux conservation. Hence, the temperature of any photospheric layer rises or falls with increasing or decreasing $T_{\rm eff}$. Since the local temperature is crucial for the excitation and ionization state of the chemical elements, each spectral line is more or less sensitive to $T_{\rm eff}$. The way of how a spectral line changes quantitatively with effective temperature depends on the atomic structure as well as on the conditions of the environment. Qualitatively, the strength of a certain line grows with $T_{\rm eff}$ as long as the population of the lower state of the related atomic transition increases. The maximum population is reached at a certain temperature[11], which is higher for a larger ionization potential as well as for a higher energy with respect to the ground state of the ion. Beyond this maximum, the occupation of the state decreases again because the hotter temperatures drive more and more atoms to energetically higher levels and higher ionization stages. The best indicators for $T_{\rm eff}$ are therefore chemical elements that show spectral lines of at least two different ionization stages since the lines of the lower ionization level weaken with higher temperatures whereas the ones of the higher ionized stage strengthen (see Fig. 4.8). Another indicator for $T_{\rm eff}$ are the widths of those lines for which the thermal Doppler broadening (Eq. (4.45)) is the dominant microscopic broadening effect. This is the case for most metal lines.

- Surface gravity $\log(g\,(\mathrm{cm\,s^{-2}}))$: The surface gravity rules the pressure and density stratification through the hydrostatic equilibrium constraint (Eq. (4.33a)). Thus, all spectral lines are, in principle, affected by $\log(g)$. Since a larger gravity implies a denser plasma and, thus, enhances the probability of electron captures, the surface gravity influences the ionization balance (see Eq. (4.36)). In analogy to $T_{\rm eff}$, spectral lines of different ionization stages are in consequence particularly useful to constrain $\log(g)$. However, the prime indicator for the surface gravity in OB stars are the wings of the hydrogen Balmer lines, which are strongly pressure broadened by means of the linear Stark effect (see Sect. 4.3.5). Unfortunately, the Balmer wings are also sensitive to $T_{\rm eff}$. Increasing the effective temperature in hot stars reduces their line strength and, in this way, narrows their wings, which can be compensated by increasing the pressure broadening via a larger surface gravity. Therefore, the Balmer lines alone are not sufficient to determine both, $T_{\rm eff}$ and $\log(g)$, at the same time and more indicators, such as lines of other chemical elements with varying degree of ionization, have to be taken into account simultaneously (see Fig. 4.8).

[11] For the Balmer lines of hydrogen, this is roughly at 10 000 K.

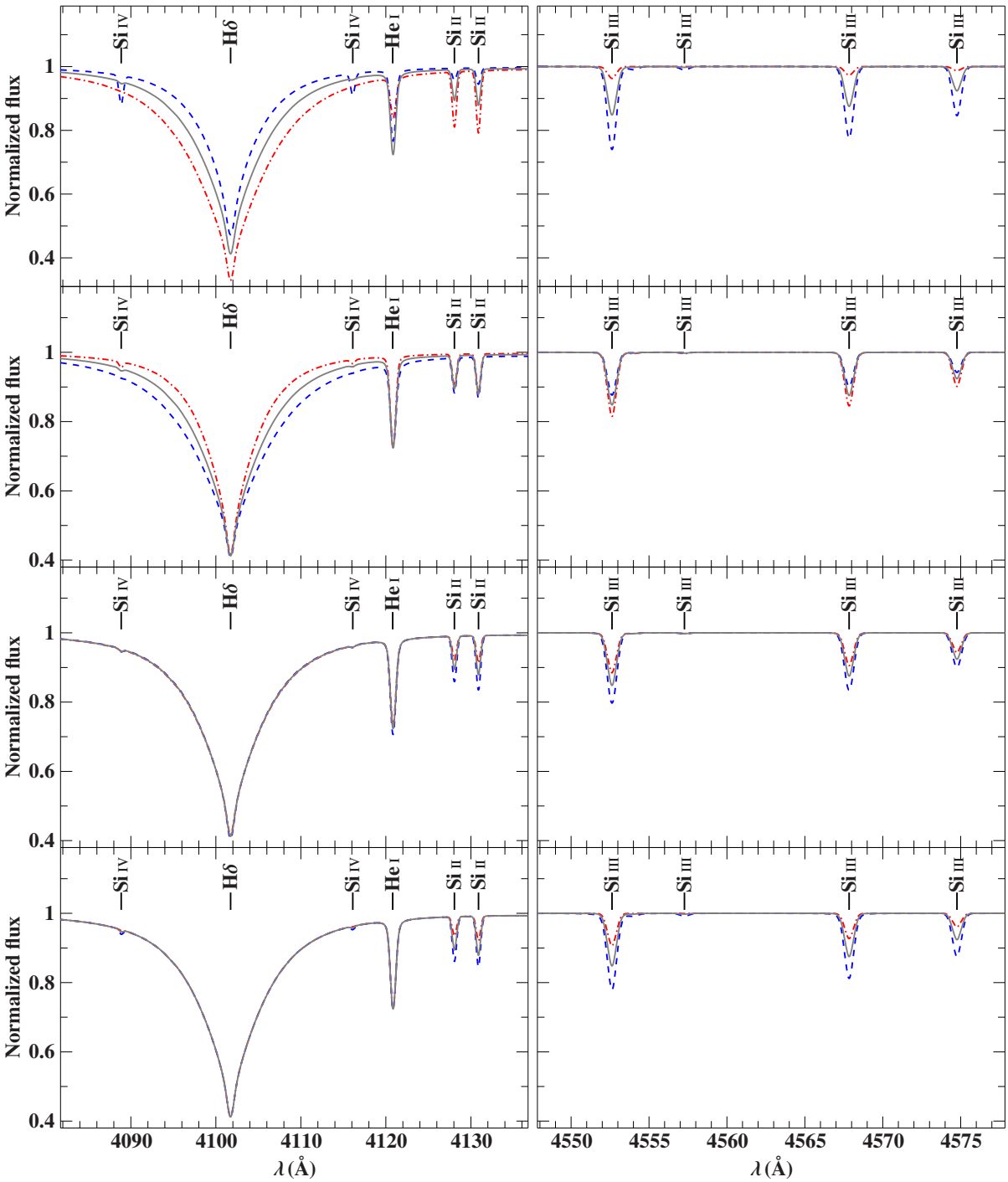

Figure 4.8: Effects of changes in effective temperature, surface gravity, microturbulence, and silicon abundance on lines of hydrogen, helium, and silicon. The parameter under consideration is increased in the blue dashed model and decreased in the red dashed-dotted model with respect to the gray solid reference model ($T_{\rm eff}$ = 20 000 K, $\log(g)$ = 4.0 dex, ξ = 4 km s^{-1}, $\log(n(\mathrm{He}))$ = −1.15 dex, $\log(n(\mathrm{Si}))$ = −4.5 dex) by $\Delta T_{\rm eff}$ = ±5000 K (*top row*), $\Delta \log(g)$ = ±0.4 dex (*second row*), $\Delta\xi$ = ±4 km s^{-1} (*third row*), and $\Delta \log(n(\mathrm{Si}))$ = ±0.6 dex (*bottom row*).

- Microturbulence ξ: As a microscopic broadening agent, the microturbulence parameter basically affects the strength and shape of all spectral lines. Significant effects, however, are expected only if it is the dominant microscopic broadening mechanism, which is typically the case for strong metal lines (see Fig. 4.8). This is owing to the fact that, on the one hand, strong lines form in the cool outer layers of the photosphere where thermal Doppler broadening, which also depends on the specific mass of the chemical element (Eq. (4.45)), is weak. On the other hand and in contrast to hydrogen and many helium lines, natural and pressure broadening is usually small for metal lines.

- Projected rotational velocity $v \sin(i)$ and macroturbulence ζ: These macroscopic broadening parameters describe the blurring of spectral lines (via the profiles of Fig. 4.7) and can be derived from the shape of spectral lines, preferably from those which are intrinsically sharp.

- Radial velocity v_{rad}: This parameter leads to a Doppler shift of the spectrum and can be deduced from Eq. (4.12).

- Chemical elemental abundance $n(x)$ ($x \in \{\mathrm{He, C, N, O, Ne, Mg, Al, Si, S, Ar, Fe}\}$): The abundances of the chemical species enter the continuum as well as the bound-bound opacity and, hence, affect the atmospheric structure as well as individual lines. The higher the abundance, the larger the number of absorbers and, by virtue of Eq. (4.19), the higher the opacity. Since the abundances of the metals are orders of magnitude lower than those of hydrogen and helium, they act only as trace elements, which means that the continuum flux is relatively insensitive to changes in their abundances. In contrast, the strength of individual spectral lines, which increases non-linearly[12] with the number of absorbers, is a good indicator for the abundance (see Fig. 4.8).

[12]The dependency of the line strength on the number of absorbers can be described by a so-called curve of growth, see Gray (2005, pp. 326–330).

5 A new method for an objective spectroscopic analysis of early-type stars*

The chemical evolution of galaxies is dominated by the evolution of early-type stars, since these objects are the progenitors of core-collapse supernovae, and therefore contribute to stellar nucleosynthesis in a pronounced way. In this context, important issues are the effects of rotation, especially for that of rotational mixing, on the evolution of massive stars (e.g., Heger & Langer 2000; Meynet & Maeder 2000), as well as spatial and temporal variations of the chemical composition within the Galactic disk (e.g., Fuhrmann 2008; Przybilla 2008). Quantitative spectroscopic analyses of B- and late O-type stars allow for atmospheric parameters and chemical elemental surface abundances to be inferred with high precision, which directly addresses both of the aforementioned topics (see Nieva & Przybilla 2012). Due to the high frequency of binary systems among early-type stars (see, e.g., Sana et al. 2012; Chini et al. 2012), analysis techniques, which are also able to deal with spectra of double-lined spectroscopic binary systems (SB2) are desirable.

Quantitative spectroscopy is based on the comparison of synthetic and observed spectra. Owing to the multi-dimensionality of the parameter space involved (which include the following for B- and late O-type stars: effective temperature $T_{\rm eff}$, surface gravity $\log(g\,(\mathrm{cm\,s^{-2}}))$, microturbulence ξ, macroturbulence ζ, projected rotational velocity $v\sin(i)$, radial velocity $v_{\rm rad}$, metallicity Z, and elemental abundances $\{n(x)\}$), investigations are time-consuming since an iterative approach is required (for details see Nieva & Przybilla 2010). Starting from initial estimates for the entire set of parameters, individual variables are refined by using spectral indicators that are sensitive to as few parameters as possible to reduce the complexity of the problem. In early-type stars of solar metallicity, for instance, Stark-broadened hydrogen and helium lines are primarily affected by changes in $T_{\rm eff}$, $\log(g)$, and n(He) while they are comparatively insensitive to all others. Consequently, these features allow for the temperature, surface gravity, and helium abundance to be constrained. The use of multiple ionization equilibria, which requires that spectral lines of different ionization stages of the same element indicate equal abundances, yields further constraints on $T_{\rm eff}$ and $\log(g)$ but also on ξ and $n(x)$. Matching the strength of spectral lines and their shape allows for ζ and $v\sin(i)$ to be derived. Because of the highly non-trivial coupling of different parameters, the adjustment of individual variables involves re-evaluation of most of the available indicators, leading to an iterative procedure.

Although those iterative steps can be automated to speed up the investigation (see Lefever et al. 2010), the underlying strategy is still prone to miss the global best solution. On the one hand, not all parameters are varied at the same time but many of them separately so that correlations between them are neglected (see Mokiem et al. 2005). On the other hand, parameters are constrained from selected spectral indicators or windows instead of exploiting the information encoded in the entire spectrum. A global analysis method, which is a method simultaneously probing all parameters while considering the maximum useful spectral range, is therefore our goal.

Automated fitting techniques are suitable for this purpose. Moreover, automation is far less subjective, since the matching of theory and observation is based on a mathematical measure,

*This Chapter is heavily based on the paper by Irrgang et al. (2014b).

such as a χ^2 criterion instead of visual inspection. This is particularly important when one wants to analyze larger samples in a homogeneous manner. The size of the corresponding multi-parameter space, however, requires calculations of numerous synthetic spectra, which is computationally expensive and, therefore, a major obstacle for automated fitting. To minimize the number of calculations involved, synthetic atmospheres may be computed on demand in the course of the fitting process, as realized by Mokiem et al. (2005). In this way, spectra are computed only if they are actually used. Nevertheless, even very efficient fitting algorithms can take from several dozens to hundreds of iterations to find the best solution, which implies a non-negligible run-time of the fitting process. This drawback can be overcome by making use of pre-calculated model grids in which interpolation between grid points can be used to evaluate the fitting function. Unfortunately, sufficient sampling of the whole multi-parameter space is typically not possible, given its large dimension. Consequently, grid-based fitting methods are usually restricted to small subspaces by either keeping some parameters fixed when computing tailored grids (see Castro et al. 2012) or limiting the allowed parameter range, thus reducing the advantages of global automated fitting.

However, due to some unique properties of spectra of early-type stars, such as the low density of spectral lines and the continuous opacity that is dominated by hydrogen and helium, many parameters – in particular, the elemental abundances of the trace elements – are independent of each other. Exploiting this fact, it is possible to probe the entire parameter space by computing only a tiny fraction of it. Based on this idea, we have developed a grid-based global fitting method that facilitates quick and precise determinations of the atmospheric parameters of B- and late O-type stars, which takes non-LTE effects into consideration (Sect. 5.1). Furthermore, it is shown that the accuracy of the analysis is generally not limited by statistics, such as the signal-to-noise ratio (S/N) of the observed spectrum, but rather by systematics, such as the uncertainties in atomic data (Sect. 5.2). For demonstration purposes, the method is then applied to three well-studied early-type stars in Orion and to three SB2 systems yielding atmospheric and fundamental stellar parameters (Sect. 5.3). A discussion of the results obtained (Sect. 5.4) is rounded off by a summary (Sect. 5.5).

5.1 Setting up the fitting function

5.1.1 Input physics: models and codes

Synthetic spectra are calculated by following the hybrid, non-LTE approach discussed by Przybilla et al. (2006) and Nieva & Przybilla (2006, 2007, 2008), which is outlined in Sect. 4.3.4. The structure of the atmosphere, such as the stratification of temperature and density, is based on line-blanketed, plane-parallel, homogeneous, and hydrostatic LTE-model atmospheres calculated with Atlas12 (Kurucz 1996). Deviations from local thermodynamic equilibrium are then accounted for by applying updated versions of Detail and Surface (Giddings 1981; Butler & Giddings 1985). The Detail code solves the coupled radiative transfer and statistical equilibrium equations numerically to obtain population numbers in non-LTE, which in turn are input to the Surface code to compute the final synthetic spectrum that uses more detailed line-broadening data. Comprehensive, state-of-the-art model atoms (see Table 5.1) allow spectral lines to be modeled with high fidelity for chemical elements accessible in the optical spectra

Table 5.1: Model atoms for non-LTE calculations.

Ion	Model atom
H	Przybilla & Butler (2004)
He I/II	Przybilla (2005)
C II-III	Nieva & Przybilla (2006, 2008)
N II	Przybilla & Butler (2001)[(a)]
O I/II	Przybilla et al. (2000), Becker & Butler (1988)[(a)]
Ne I/II	Morel & Butler (2008)[(a)]
Mg II	Przybilla et al. (2001)
Al II/III	Przybilla (in prep.)
Si II/III/IV	Przybilla & Butler (in prep.)
S II/III	Vrancken et al. (1996), updated
Ar II	Butler (in prep.)
Fe II/III	Becker (1998), Morel et al. (2006)[(b)]

Notes. [(a)] Updated, see Nieva & Przybilla (2012) for details. [(b)] Corrected, see Nieva & Przybilla (2012) for details.

of most B- and late O-type stars. Although partly based on LTE concepts, the hybrid method outlined above is consistent with full non-LTE calculations for B-type stars (see Nieva & Przybilla 2007; Przybilla et al. 2011) but is considerably faster and, most importantly, is able to handle more realistic representations of model atoms. For the first time here, we consistently use the concept of LTE opacity sampling to treat background line opacities (employing the realization of Kurucz 1996) in all computational steps, instead of relying on pre-calculated opacity distribution functions.

5.1.2 Probing the parameter space

Stellar atmospheres are described by a variety of physical quantities. The implementation of those parameters in synthetic model computations varies depending on their nature. Within the scope of this work, it is instructive to distinguish between primary atmospheric parameters, which are quantities whose effects can be modeled solely by solving the coupled radiative and structural equations describing an atmosphere, and secondary ones, which are quantities whose effects can be incorporated after an atmosphere has been built. For OB-type stars near the main sequence and their evolved progeny, BA-type supergiants, primary parameters are $T_{\rm eff}$, $\log(g)$, ξ, Z, and $\{n(x)\}$, while ζ, $v\sin(i)$, and $v_{\rm rad}$ are secondary ones. By definition, the effective parameter space for which model atmospheres have to be calculated is therefore spanned by the primary parameters. Given a grid-based fitting method that interpolates a regular multi-dimensional mesh of synthetic spectra, the dimension of this parameter space is the product of the individual dimensions of the primary parameters. Due to this multiplicity, each chemical element included in the analysis drastically increases the number of required models. For instance, calculating a grid with ten elements at nine abundances each implies a factor of 9^{10}, which has to be multiplied with the dimension given by the remaining primary parameters. Since it is infeasible to compute such a large number of models in a reasonable time, a simplification is necessary. To this end, one can exploit the unique properties of (nearby) early-type stars: Due to their young ages, the metallicity of these stars is very well approximated by the cosmic standard (Nieva &

Przybilla 2012), in general, so that $Z = 0.014$ can be assumed throughout. In massive stars, the latter implies that all metals can be considered as trace elements, which implies that moderate changes of their abundances do not significantly affect the atmospheric structure. This occurs because their respective bound-free opacities are small compared to hydrogen and helium and because line blanketing is relatively insensitive to abundance changes of a specific metal. Altering the abundance of an individual metal has therefore little to no effect on spectral lines of the other metals, except in the case of line blends. However, the density of lines is low in optical spectra of early-type stars, so that intrinsic blends are actually rare (With some more restrictions, this even applies to the ultraviolet region.). Moreover, many of these line blends are caused by macroscopic flux redistributions, which can be, for example, via macroturbulence, stellar rotation, or the finite resolving power of the spectrograph, and are thus not an issue, since they do not affect the microscopic physics governing radiative transfer. Consequently, instead of calculating 9^{10} combinations of abundances, it is sufficient to compute models for nine prechosen abundance values for each of the ten species. All of these models contain only lines of one specific trace element, while standard abundances are assumed for the other metals to account for their background opacities. Those 10×9 spectra serve as a basis from which each of the 9^{10} combinations can be constructed, such as via multiplication of the normalized base spectra. Note that helium cannot be treated as a trace element, since corresponding abundance changes have serious impacts on the atmospheric structure, for instance, via the mean molecular weight or its contribution to the continuum opacity. Hence, the number of required synthetic models is the product of the dimensions of $T_{\rm eff}$, $\log(g)$, ξ, n(He), and the base dimensions of the trace elements.

5.1.3 Numerical implementation of the model

From the considerations of the previous subsection, the fitting function is constructed as follows: for each trace element of interest, a multi-dimensional regular mesh spanned by effective temperature (12 000 to 34 000 K, step size: 1000 K), surface gravity (range depending on temperature but typically within 3.0 to 4.6 dex, 0.2 dex), microturbulence (range depending on temperature but typically within 0 to 20 km s^{-1}, 2 km s^{-1}), helium abundance (solar value minus 0.3 dex to solar value plus 0.5 dex, 0.2 dex), and abundance of the species itself (typically solar value minus 0.8 dex to solar value plus 0.8 dex, 0.2 dex) has been calculated in advance. This grid can easily be extended whenever needed. Spectra for arbitrary parameters within the mesh are approximated by linear interpolation. At this point, synthetic models contain only spectral lines of hydrogen, helium, and the element under consideration. To combine the normalized spectra of the individual trace elements, each of them is divided by a model with the same specifications but which contains only hydrogen and helium lines. Multiplying the resulting "corrected spectra" with each other and with the hydrogen-helium model leads to a model that takes all of the primary parameters into account. This simplification is well justified as long as spectral lines of different metals are not blended due to microscopic flux redistributions, such as microturbulence, natural line width, and thermal- or pressure broadening. Furthermore, even for blends of weak spectral lines, the method is a good approximation as interaction effects are tiny in that case. Secondary atmospheric parameters are incorporated afterwards: macroturbulence and stellar rotation via convolution of the synthetic spectrum with a joint profile function, which is obtained from numerical stellar disk integration (see Fig. 4.7 and Sect. 4.3.5) with a

linear limb-darkening law (using coefficients by Claret & Bloemen 2011), and radial velocity by shifting the entire wavelength scale according to the Doppler formula.

5.1.4 Extension to composite spectra

Multiplicity is an important issue for massive stars, as the majority of them probably resides in systems of two (or more) components (see Sana et al. 2012; Chini et al. 2012). While visual binaries or systems with a much fainter secondary can be treated as single stars in the spectroscopic analysis, this is clearly not the case for double-lined spectroscopic binary systems where features of both stars are visible in the spectrum. Stars classified as chemically peculiar objects based on low-resolution and/or low-S/N spectra might actually be unrecognized SB2 systems where the depths of the absorption lines have been altered due to continuum emission of a companion.

The fitting method presented here is also capable of dealing with composite spectra in a simplified manner. To do so, models for the normalized single-star spectra are created separately for the primary (f_p) and secondary (f_s) component following the procedure given in Sect. 5.1.3. To obtain the model for their normalized composite spectrum (f_comp), these individual contributions have to be summed up while taking their weights into account. The latter are given by the components' continuum fluxes ($f_\mathrm{p,cont}$, $f_\mathrm{s,cont}$) and by the ratio of their projected, effective[13] surface areas, which is parametrized by one additional free parameter $A_\mathrm{eff,s}/A_\mathrm{eff,p}$:

$$f_\mathrm{comp} = \frac{f_\mathrm{cont,p}\, f_\mathrm{p} + A_\mathrm{eff,s}/A_\mathrm{eff,p}\, f_\mathrm{cont,s}\, f_\mathrm{s}}{f_\mathrm{cont,p} + A_\mathrm{eff,s}/A_\mathrm{eff,p}\, f_\mathrm{cont,s}} \,. \tag{5.1}$$

Note that this approach conflates all binary interactions, such as mutual distortions and their respective effects on the emitted spectra into the parameter $A_\mathrm{eff,s}/A_\mathrm{eff,p}$. Consequently, the geometric interpretation of $A_\mathrm{eff,s}/A_\mathrm{eff,p}$ as the ratio of the effective surface areas of secondary to primary component is only valid as long as those interactions are negligible, such as for well detached systems. Otherwise, $A_\mathrm{eff,s}/A_\mathrm{eff,p}$ is a combination of the ratio of effective surface areas and a fudge factor that accounts for all missing interaction effects. Of course, the ability of $A_\mathrm{eff,s}/A_\mathrm{eff,p}$ to compensate these shortcomings is limited and certainly fails for very close or contact systems where a much more sophisticated method is necessary (see, for instance, Palate & Rauw 2012; Palate et al. 2013). Nevertheless, the approach outlined here offers a very fast and efficient way to derive atmospheric parameters and elemental abundances of SB2 systems from the analysis of a single epoch composite spectrum.

5.1.5 Comparison with observation

To compare models with observations, the synthetic spectra are finally convolved with the instrumental profile, which is a Gaussian curve whose width is a function of the spectral resolving power $\lambda/\Delta\lambda$.

[13] Spectra received from different surface elements on the star are assumed to be identical in Eq. (5.1). Consequently, effects like limb darkening are neglected, and $A_\mathrm{eff,p}$ and $A_\mathrm{eff,s}$ are more effective than absolute surface areas. However, if those effects are qualitatively similar in the primary and secondary component, they probably cancel each other out when taking the ratio of surface areas yielding $A_\mathrm{eff,s}/A_\mathrm{eff,p} \approx A_\mathrm{s}/A_\mathrm{p}$.

The goodness of fit of a model is then derived from its absolute χ^2:

$$\chi^2 = \sum_i \chi_i^2 = \sum_i \left(\frac{f_i - f_{\mathrm{model},i}}{\delta_i} \right)^2 . \tag{5.2}$$

Here, f_i, $f_{\mathrm{model},i}$ and δ_i are the observed flux, model flux and uncertainty in the observed flux at data point i, respectively. The sum is taken over all pixels i in the spectrum, which either excludes only those lines that have well-known shortcomings, are missing in our models, or are of non-photospheric origin, such as telluric lines and diffuse interstellar bands. The lower the value of χ^2, the better the quality of the fit[14]. Other ways of measuring the fitness exist but may have different properties. One reason to choose a standard i-based over a line-based χ^2 criterion (as, for instance, done by Simón-Díaz et al. 2011b; Castro et al. 2012) is that it gives lines with more data points a larger weight than those with less information. Moreover, the corresponding χ^2 distribution is well studied, which allows statistical uncertainties of the input parameters to be deduced from the χ^2 statistics (see Sect. 5.2.3).

The analysis is carried out completely within the Interactive Spectral Interpretation System (ISIS, Houck & Denicola 2000), which simplifies the investigation tremendously. Apart from many useful functions and tools, various minimization algorithms, such as the simplex or gradient methods are available. As shown in the next section, the χ^2 landscape of our problem is generally very well behaved so that the absolute minimum is found after a relatively small number of steps, which allows for quick and efficient analyses.

5.2 Formal tests and discussion of uncertainties

5.2.1 Noise estimation

Calculating χ^2 requires proper knowledge of the measurement uncertainties δ_i, which either are systematic in nature and, for instance, caused by an incorrect continuum normalization, or, more importantly, have statistical fluctuations, such as noise n_i. The latter can be estimated from an observed spectrum, which does not need to be flux calibrated, in an easy, fast, and robust way when assuming that the noise n_i of data point i obeys a Gaussian probability distribution $p(n_i)$ with a mean value of zero and a priori unknown standard deviation σ_i:

$$p(n_i) = \frac{1}{\sqrt{2\pi}\sigma_i} \exp\left(-\frac{n_i^2}{2\sigma_i^2} \right) . \tag{5.3}$$

For small regions (several data points), the measured flux f_i as a function of the wavelength λ can be approximately written as the sum of a linear function $a + b\lambda_i$, which represents the first two terms in a Taylor expansion of the pure signal and a noise component n_i:

$$f_i = a + b\lambda_i + n_i . \tag{5.4}$$

To estimate the noise level σ_i, consider the quantity Δ_i defined as

$$\begin{aligned} \Delta_i &\equiv f_i - (w_{i-2} f_{i-2} + w_{i+2} f_{i+2}) \\ &= n_i - w_{i-2} n_{i-2} - w_{i+2} n_{i+2} + a + b\lambda_i - w_{i-2}(a + b\lambda_{i-2}) - w_{i+2}(a + b\lambda_{i+2}) . \end{aligned} \tag{5.5}$$

[14] A reduced χ^2 lower than 1 indicates overestimated uncertainties.

Here, w_{i-2} and w_{i+2} are weight factors and chosen such that only the noise terms in Eq. (5.5) remain:[15]

$$\Delta_i = n_i - w_{i-2}n_{i-2} - w_{i+2}n_{i+2}\,. \tag{5.6}$$

The reason for comparing f_i to the (weighted) average of data points $i-2$ and $i+2$ instead of $i-1$ and $i+1$ is that adjacent pixels are likely correlated. For example, this is due to detector cross-talk or actions taken during data reduction like the wavelength calibration. Assuming that there is no correlation with the next neighbor but one implies that Eq. (5.3) is valid for points i, $i-2$, and $i+2$, and the probability distribution $p(\Delta_i)$ reads:

$$p(\Delta_i) = \int_{-\infty}^{\infty}\int_{-\infty}^{\infty}\int_{-\infty}^{\infty} p(n_i)p(n_{i-2})p(n_{i+2})\delta\left(\Delta_i - (n_i - w_{i-2}n_{i-2} - w_{i+2}n_{i+2})\right)\mathrm{d}n_i\mathrm{d}n_{i-2}\mathrm{d}n_{i+2}\,. \tag{5.7}$$

Here, δ is the Dirac delta function. For adjacent data points, it is well justified to assume $\sigma_i = \sigma_{i-2} = \sigma_{i+2} \equiv \sigma$, so that $p(\Delta_i)$ simplifies to

$$p(\Delta_i) = \frac{1}{\sqrt{2\pi}\tilde{\sigma}}\exp\left(-\frac{\Delta_i^2}{2\tilde{\sigma}^2}\right), \quad \tilde{\sigma} = \sigma\sqrt{w_{i-2}^2 + w_{i+2}^2 + 1}\,. \tag{5.8}$$

Consequently, the distribution of $\Delta_i = f_i - (w_{i-2}f_{i-2} + w_{i+2}f_{i+2})$ is a Gaussian with a standard deviation $\tilde{\sigma}$ defined by Eq. (5.8). Extending the assumption of a constant noise level $\sigma_i = \sigma$ to a statistically significant number of data points allows σ, which is the statistical component of the uncertainty δ_i in Eq. (5.2), to be derived from the measurable distribution of Δ_i. If the reduced χ^2 at the best fit is larger than 1, it might also be necessary to consider a systematic component of δ_i (see footnote 16).

5.2.2 Performance and reliability of the method

Before fitting real spectra, several formal tests were carried out to examine the properties of the automated method. With this aim, mock spectra were constructed from synthetic ones by adding Gaussian-distributed noise that corresponded to different S/N. A spectral range [3940 Å, 7000 Å] was chosen to match the minimum wavelength coverage of standard high-resolution spectrographs. Regions in that interval that are generally affected by telluric features were excluded. The spectral resolving power was set to $\lambda/\Delta\lambda = 45\,000$, which is very close to the resolution of the echelle spectra which are analyzed in this study.

Table 5.2 lists the results of this exercise for ten exemplary cases. The input parameters and, thus, the global minimum were recovered with excellent accuracy after only a run-time of few minutes on a standard 3.1 GHz single-core processor and independent of the choice of the starting parameters within the grid, which shows that our method is fast and reliable.

It is important to stress here that all mock spectra were constructed from complete Surface models, which, in contrast to the fitting function, treat every microscopic line blend correctly

[15] Note: $\lambda_{i+1} = \lambda_i + \Delta\lambda_i^{\mathrm{pixel}}/2 + \Delta\lambda_{i+1}^{\mathrm{pixel}}/2$ with $\Delta\lambda_i^{\mathrm{pixel}} = \Delta\lambda_i/2$ because of Nyquist's sampling theorem. For long-slit spectrographs, $\lambda/\Delta\lambda \propto \lambda$ (Eq. (4.6)) so that $\Delta\lambda_i$ = constant which implies $w_{i-2} = 1 - w_{i+2} = 1/2$ to arrive at Eq. (5.6) from Eq. (5.5). For echelle spectrographs, $\lambda/\Delta\lambda$ = const. $\equiv R_{\mathrm{echelle}}$ (Eq. (4.7)), which yields $\lambda_{i+1} = k\lambda_i$ with $k = (4R_{\mathrm{echelle}} + 1)/(4R_{\mathrm{echelle}} - 1)$ which leads to $w_{i-2} = 1 - w_{i+2} = (k^2 - 1)/(k^2 - k^{-2}) \approx 0.5$.

Table 5.2: Comparison of input parameters (*"In" row*) and corresponding parameters obtained from fits (*"Out" row*) for ten exemplary mock spectra computed from complete SURFACE models, which simultaneously account for all lines considered in the fitting function.

	S/N	$T_{\rm eff}$	$\log(g)$	$v_{\rm rad}$	$v\sin(i)$	ζ	ξ	$\log(n(x))$										
		(K)	(cgs)	($\rm km\,s^{-1}$)				He	C	N	O	Ne	Mg	Al	Si	S	Ar	Fe
In	300	15 000	3.750	−18.0	15.0	7.0	2.00	−1.06	−3.70	−4.30	−3.20	−4.00	−4.70	−5.60	−4.60	−4.80	−5.60	−4.60
Out	305	15 000	3.750	−18.0	14.8	8.0	2.10	−1.06	−3.71	−4.28	−3.20	−4.01	−4.70	−5.60	−4.61	−4.81	−5.68	−4.61
Stat.	+3	+20	+0.003	+0.1	+0.1	+0.2	+0.04	+0.01	+0.02	+0.04	+0.02	+0.02	+0.02	+0.02	+0.02	+0.01	+0.07	+0.01
	−3	−20	−0.004	−0.1	−0.1	−0.1	−0.03	−0.01	−0.02	−0.04	−0.02	−0.02	−0.02	−0.02	−0.02	−0.01	−0.08	−0.01
Sys.	...	+300	+0.100	+0.1	+0.2	+0.7	+0.79	+0.15	+0.07	+0.05	+0.04	+0.04	+0.06	+0.02	+0.12	+0.04	+0.08	+0.06
		−300	−0.100	−0.1	−0.1	−1.2	−1.09	−0.09	−0.09	−0.08	−0.08	−0.02	−0.07	−0.02	−0.18	−0.04	−0.14	−0.10
Start	...	19 000	3.700	−15.0	10.0	10.0	3.00	−0.85	−3.60	−4.20	−3.20	−4.00	−4.60	−5.80	−4.40	−4.90	−5.60	−4.60
In	300	15 000	4.250	36.0	17.0	16.0	2.00	−1.06	−3.70	−4.30	−3.20	−4.00	−4.70	−5.60	−4.60	−4.80	−5.60	−4.60
Out	295	14 860	4.215	36.0	17.0	16.1	1.90	−1.04	−3.68	−4.32	−3.22	−4.00	−4.72	−5.60	−4.61	−4.80	−5.50	−4.65
Stat.	+2	+30	+0.008	+0.1	+0.1	+0.3	+0.07	+0.01	+0.02	+0.07	+0.01	+0.02	+0.02	+0.02	+0.02	+0.01	+0.10	+0.01
	−2	−20	−0.006	−0.1	−0.1	−0.2	−0.03	−0.01	−0.01	−0.07	−0.01	−0.02	−0.01	−0.02	−0.01	−0.01	−0.11	−0.01
Sys.	...	+300	+0.100	+0.1	+0.1	+0.2	+0.62	+0.15	+0.07	+0.06	+0.07	+0.06	+0.06	+0.02	+0.11	+0.04	+0.08	+0.08
		−300	−0.100	−0.1	−0.1	−0.3	−0.86	−0.12	−0.08	−0.09	−0.07	−0.04	−0.06	−0.02	−0.11	−0.04	−0.14	−0.10
Start	...	19 000	3.700	35.0	10.0	10.0	3.00	−0.85	−3.60	−4.20	−3.20	−4.00	−4.60	−5.80	−4.40	−4.90	−5.60	−4.60
In	100	20 000	3.750	19.0	25.0	18.0	2.0	−1.06	−3.70	−4.30	−3.20	−4.00	−4.70	−5.60	−4.60	−4.80	−5.60	−4.60
Out	100	19 960	3.734	18.9	23.5	22.0	1.94	−1.05	−3.68	−4.28	−3.19	−4.02	−4.71	−5.56	−4.57	−4.78	−5.59	−4.59
Stat.	+1	+120	+0.015	+0.3	+1.1	+1.7	+0.3	+0.02	+0.04	+0.04	+0.04	+0.04	+0.06	+0.05	+0.07	+0.03	+0.06	+0.05
	−1	−120	−0.017	−0.3	−1.1	−0.9	−0.7	−0.02	−0.03	−0.04	−0.03	−0.04	−0.05	−0.04	−0.05	−0.03	−0.08	−0.04
Sys.	...	+400	+0.100	+0.1	+0.2	+0.7	+0.8	+0.09	+0.08	+0.08	+0.11	+0.04	+0.11	+0.08	+0.14	+0.05	+0.05	+0.05
		−400	−0.100	−0.1	−0.2	−0.7	−1.7	−0.07	−0.06	−0.07	−0.11	−0.04	−0.09	−0.07	−0.12	−0.05	−0.05	−0.05
Start	...	19 000	3.700	10.0	10.0	10.0	3.0	−0.85	−3.40	−4.10	−3.10	−4.20	−4.80	−5.60	−4.20	−4.70	−5.70	−4.50
In	250	20 000	4.250	25.0	5.0	26.0	2.00	−1.06	−3.70	−4.30	−3.20	−4.00	−4.70	−5.60	−4.60	−4.80	−5.60	−4.60
Out	254	19 990	4.251	25.0	0.0	26.9	2.26	−1.07	−3.73	−4.31	−3.22	−4.02	−4.72	−5.58	−4.64	−4.81	−5.61	−4.60
Stat.	+2	+20	+0.003	+0.1	+1.8	+0.1	+0.12	+0.01	+0.02	+0.02	+0.02	+0.02	+0.02	+0.02	+0.02	+0.01	+0.03	+0.02
	−2	−20	−0.004	−0.1	−0.0	−0.1	−0.07	−0.01	−0.02	−0.02	−0.02	−0.02	−0.02	−0.02	−0.02	−0.01	−0.04	−0.02
Sys.	...	+400	+0.100	+0.1	+3.4	+0.1	+1.04	+0.08	+0.09	+0.07	+0.11	+0.04	+0.12	+0.06	+0.13	+0.06	+0.05	+0.01
		−400	−0.100	−0.1	−0.0	−0.1	−1.66	−0.06	−0.07	−0.07	−0.12	−0.03	−0.13	−0.06	−0.11	−0.05	−0.05	−0.03
Start	...	17 000	4.000	20.0	10.0	10.0	3.00	−0.85	−3.40	−4.10	−3.10	−3.80	−4.40	−5.90	−4.70	−4.80	−5.50	−4.70
In	400	25 000	3.750	−25.0	40.0	28.0	2.00	−1.06	−3.70	−4.30	−3.20	−4.00	−4.70	−5.60	−4.60	−4.80	−5.60	−4.60
Out	396	24 930	3.738	−25.0	39.7	28.5	2.02	−1.07	−3.72	−4.31	−3.21	−4.00	−4.70	−5.61	−4.61	−4.81	−5.63	−4.61
Stat.	+2	+20	+0.002	+0.1	+0.1	+0.1	+0.04	+0.01	+0.01	+0.01	+0.01	+0.02	+0.02	+0.01	+0.01	+0.01	+0.04	+0.01
	−2	−20	−0.003	−0.1	−0.1	−0.3	−0.04	−0.01	−0.01	−0.02	−0.01	−0.02	−0.02	−0.01	−0.01	−0.01	−0.04	−0.01
Sys.	...	+500	+0.100	+0.1	+0.3	+1.3	+0.71	+0.06	+0.01	+0.03	+0.07	+0.01	+0.05	+0.04	+0.02	+0.02	+0.10	+0.03
		−500	−0.100	−0.1	−0.1	−1.5	−0.02	−0.07	−0.06	−0.03	−0.08	−0.02	−0.08	−0.06	−0.06	−0.03	−0.12	−0.03
Start	...	23 500	3.800	−20.0	10.0	10.0	8.00	−1.10	−3.50	−4.10	−3.30	−4.10	−4.50	−6.00	−4.20	−4.70	−5.40	−4.30
In	275	25 000	4.250	25.0	70.0	0.0	2.00	−1.06	−3.70	−4.30	−3.20	−4.00	−4.70	−5.60	−4.60	−4.80	−5.60	−4.60
Out	274	25 010	4.259	25.0	69.8	3.6	2.00	−1.05	−3.71	−4.29	−3.21	−3.99	−4.68	−5.60	−4.61	−4.82	−5.59	−4.61
Stat.	+1	+30	+0.003	+0.2	+0.1	+3.7	+0.06	+0.01	+0.02	+0.01	+0.01	+0.03	+0.03	+0.02	+0.02	+0.02	+0.05	+0.02
	−1	−30	−0.003	−0.1	−0.1	−2.8	−0.11	−0.01	−0.02	−0.01	−0.01	−0.03	−0.03	−0.02	−0.02	−0.02	−0.07	−0.02
Sys.	...	+500	+0.100	+0.1	+0.5	+3.5	+1.41	+0.06	+0.08	+0.03	+0.12	+0.02	+0.09	+0.04	+0.12	+0.07	+0.12	+0.05
		−500	−0.100	−0.1	−0.1	−3.6	−2.00	−0.06	−0.10	−0.03	−0.11	−0.04	−0.10	−0.04	−0.11	−0.06	−0.15	−0.04
Start	...	19 000	3.700	30.0	10.0	10.0	3.00	−0.85	−3.80	−4.40	−3.40	−4.20	−4.80	−5.90	−4.50	−4.70	−5.80	−4.90
In	125	30 000	4.250	−15.0	0.0	18.0	2.00	−1.06	−3.70	−4.30	−3.20	−4.00	−4.70	−5.60	−4.60	−4.80	−5.60	−4.60
Out	120	30 110	4.259	−15.0	5.8	16.4	1.84	−1.04	−3.72	−4.31	−3.21	−4.02	−4.69	−5.61	−4.61	−4.81	−5.47	−4.60
Stat.	+2	+40	+0.007	+0.1	+0.4	+0.4	+0.17	+0.02	+0.03	+0.02	+0.01	+0.03	+0.04	+0.03	+0.02	+0.03	+0.15	+0.02
	−2	−60	−0.013	−0.1	−0.5	−0.4	−0.14	−0.02	−0.02	−0.02	−0.02	−0.03	−0.04	−0.03	−0.02	−0.03	−0.24	−0.02
Sys.	...	+610	+0.100	+0.1	+1.1	+0.1	+0.36	+0.03	+0.05	+0.05	+0.05	+0.03	+0.04	+0.06	+0.03	+0.07	+0.15	+0.08
		−610	−0.100	−0.1	−1.2	−0.1	−0.32	−0.03	−0.06	−0.05	−0.03	−0.02	−0.04	−0.06	−0.03	−0.06	−0.17	−0.08
Start	...	32 000	4.400	−15.0	1.0	0.0	7.00	−1.15	−3.70	−4.10	−3.10	−4.20	−4.70	−5.90	−4.70	−4.60	−5.40	−4.80
Mock spectrum as a proxy to the observed spectrum of object #1 in Table 5.4:																		
In	250	23 880	4.127	23.0	5.0	4.0	2.00	−0.99	−3.73	−4.30	−3.29	−4.00	−4.57	−5.79	−4.66	−4.88	−5.49	−4.71
Out	232	23 800	4.109	23.0	4.7	4.0	2.02	−0.99	−3.74	−4.30	−3.30	−4.02	−4.57	−5.80	−4.66	−4.90	−5.51	−4.73
Stat.	+2	+50	+0.006	+0.1	+0.5	+2.2	+0.08	+0.01	+0.01	+0.01	+0.01	+0.02	+0.02	+0.01	+0.02	+0.01	+0.02	+0.01
	−2	−50	−0.007	−0.1	−2.9	−0.4	−0.11	−0.01	−0.01	−0.01	−0.01	−0.02	−0.02	−0.01	−0.02	−0.02	−0.02	−0.01
Sys.	...	+480	+0.100	+0.1	+0.4	+1.3	+0.43	+0.05	+0.04	+0.03	+0.08	+0.04	+0.08	+0.01	+0.06	+0.02	+0.06	+0.02
		−480	−0.100	−0.1	−0.6	−1.5	−0.90	−0.05	−0.03	−0.02	−0.08	−0.04	−0.07	−0.02	−0.05	−0.03	−0.06	−0.02
Start	...	19 000	3.700	20.0	10.0	10.0	3.00	−0.90	−3.50	−4.30	−3.30	−4.20	−4.50	−5.80	−4.50	−4.90	−5.50	−4.70
Mock spectrum as a proxy to the observed spectrum of object #2 in Table 5.4:																		
In	250	19 250	4.052	31.0	7.0	17.0	2.00	−1.00	−3.64	−4.23	−3.21	−4.06	−4.60	−5.71	−4.48	−4.89	−5.57	−4.63
Out	242	19 240	4.058	31.0	4.8	18.0	2.07	−1.00	−3.64	−4.23	−3.22	−4.06	−4.62	−5.70	−4.51	−4.89	−5.57	−4.65
Stat.	+2	+20	+0.005	+0.1	+0.4	+0.1	+0.05	+0.01	+0.01	+0.02	+0.02	+0.02	+0.02	+0.02	+0.02	+0.01	+0.03	+0.02
	−2	−20	−0.005	−0.1	−0.5	−0.1	−0.07	−0.01	−0.02	−0.02	−0.01	−0.02	−0.02	−0.02	−0.02	−0.01	−0.03	−0.02
Sys.	...	+390	+0.100	+0.1	+0.9	+0.1	+0.84	+0.08	+0.08	+0.08	+0.11	+0.03	+0.10	+0.05	+0.13	+0.04	+0.05	+0.01
		−390	−0.100	−0.1	−3.2	−0.1	−1.43	−0.08	−0.09	−0.08	−0.11	−0.03	−0.11	−0.06	−0.12	−0.05	−0.05	−0.03
Start	...	17 000	3.700	20.0	10.0	10.0	3.00	−0.85	−3.50	−3.90	−3.40	−3.80	−4.40	−5.40	−4.00	−4.70	−5.40	−4.80
Mock spectrum as a proxy to the observed spectrum of object #3 in Table 5.4:																		
In	200	29 210	4.284	30.0	31.0	0.0	3.20	−1.05	−3.71	−4.13	−3.40	−4.01	−4.58	−5.73	−4.66	−4.97	−5.83	−4.62
Out	197	29 190	4.273	30.1	30.8	0.0	3.12	−1.04	−3.74	−4.13	−3.41	−4.04	−4.63	−5.76	−4.66	−5.00	−5.87	−4.62
Stat.	+1	+30	+0.005	+0.1	+0.1	+1.8	+0.08	+0.01	+0.02	+0.01	+0.01	+0.03	+0.03	+0.03	+0.02	+0.03	+0.21	+0.02
	−1	−30	−0.005	−0.1	−0.1	−0.0	−0.08	−0.01	−0.02	−0.01	−0.01	−0.03	−0.03	−0.03	−0.02	−0.02	−0.13	−0.02
Sys.	...	+590	+0.100	+0.1	+0.1	+4.6	+0.50	+0.04	+0.03	+0.05	+0.04	+0.04	+0.05	+0.06	+0.04	+0.06	+0.32	+0.09
		−590	−0.100	−0.1	−0.1	−0.0	−0.57	−0.03	−0.04	−0.05	−0.03	−0.03	−0.05	−0.05	−0.04	−0.05	−0.13	−0.07
Start	...	31 000	4.300	20.0	10.0	10.0	7.00	−1.05	−3.60	−4.20	−3.20	−4.10	−4.60	−5.80	−4.40	−4.90	−5.60	−4.60

Notes. See Sect. 5.2.2 for details. Starting parameters for the fitting algorithm are given in the *"Start" row*. The S/N estimates in the *"Out" row* are based on the method outlined in Sect. 5.2.1. The abundance $n(x)$ is given as fractional particle number of species x with respect to all elements. Statistical uncertainties (*"Stat." row*) correspond to $\Delta\chi^2 = 6.63$ and are 99%-confidence limits. Systematic uncertainties (*"Sys." row*) cover only the effects induced by additional variations of 2% in $T_{\rm eff}$ and 0.1 dex in $\log(g)$ (see Sect. 5.2.3 for details) and are formally taken to be 99%-confidence limits.

Table 5.3: Same as Table 5.2 but for three exemplary mock composite spectra.

	S/N	$T_{\rm eff}$	$\log(g)$	$v_{\rm rad}$	$v\sin(i)$	ζ	ξ	$A_{\rm eff,s}/A_{\rm eff,p}$	$\log(n(x))$										
		(K)	(cgs)	($\rm km\,s^{-1}$)					He	C	N	O	Ne	Mg	Al	Si	S	Ar	Fe
Mock spectrum as a proxy to the observed spectrum of object #5 in Table 5.4 (sharp and well-separated features):																			
In p	220	16680	4.098	−84.7	7.9	11.4	2.10	…	−0.96	−3.55	−4.16	−3.25	−4.04	−4.73	−5.86	−4.45	−4.91	−5.58	−4.66
Out f	215	16680	4.098	−84.7	6.9	12.2	2.17	…	−0.97	−3.56	−4.19	−3.25	−4.03	−4.74	−5.91	−4.47	−4.91	−5.60	−4.68
Stat.	$^{+1}_{-1}$	$^{+80}_{-90}$	$^{+0.023}_{-0.020}$	$^{+0.1}_{-0.1}$	$^{+1.4}_{-1.1}$	$^{+0.7}_{-1.3}$	$^{+0.14}_{-0.16}$	…	$^{+0.02}_{-0.03}$	$^{+0.03}_{-0.03}$	$^{+0.04}_{-0.04}$	$^{+0.02}_{-0.03}$	$^{+0.02}_{-0.02}$	$^{+0.03}_{-0.03}$	$^{+0.04}_{-0.06}$	$^{+0.03}_{-0.03}$	$^{+0.02}_{-0.02}$	$^{+0.07}_{-0.10}$	$^{+0.02}_{-0.03}$
Sys.	…	$^{+340}_{-340}$	$^{+0.100}_{-0.100}$	$^{+0.1}_{-0.1}$	$^{+0.7}_{-0.6}$	$^{+0.8}_{-0.8}$	$^{+0.27}_{-0.29}$	…	$^{+0.06}_{-0.07}$	$^{+0.07}_{-0.07}$	$^{+0.06}_{-0.07}$	$^{+0.02}_{-0.02}$	$^{+0.02}_{-0.02}$	$^{+0.03}_{-0.03}$	$^{+0.02}_{-0.03}$	$^{+0.02}_{-0.03}$	$^{+0.02}_{-0.03}$	$^{+0.05}_{-0.06}$	$^{+0.06}_{-0.06}$
Out i	…	16660	4.096	−84.7	6.6	12.4	2.20	…	−0.97	−3.56	−4.18	−3.26	−4.03	−4.75	−5.90	−4.47	−4.91	−5.60	−4.68
Stat.	…	$^{+70}_{-70}$	$^{+0.017}_{-0.022}$	$^{+0.1}_{-0.1}$	$^{+1.4}_{-1.0}$	$^{+0.9}_{-1.3}$	$^{+0.13}_{-0.15}$	…	$^{+0.02}_{-0.02}$	$^{+0.03}_{-0.03}$	$^{+0.03}_{-0.04}$	$^{+0.02}_{-0.02}$	$^{+0.02}_{-0.02}$	$^{+0.03}_{-0.03}$	$^{+0.04}_{-0.05}$	$^{+0.03}_{-0.03}$	$^{+0.02}_{-0.02}$	$^{+0.07}_{-0.11}$	$^{+0.02}_{-0.03}$
Sys.	…	$^{+340}_{-340}$	$^{+0.100}_{-0.100}$	$^{+0.1}_{-0.1}$	$^{+0.6}_{-0.5}$	$^{+0.4}_{-0.8}$	$^{+0.27}_{-0.26}$	…	$^{+0.05}_{-0.06}$	$^{+0.06}_{-0.06}$	$^{+0.05}_{-0.06}$	$^{+0.01}_{-0.01}$	$^{+0.01}_{-0.01}$	$^{+0.03}_{-0.03}$	$^{+0.02}_{-0.02}$	$^{+0.02}_{-0.02}$	$^{+0.02}_{-0.02}$	$^{+0.04}_{-0.06}$	$^{+0.05}_{-0.05}$
Start	…	15000	4.100	−80.0	10.0	10.0	3.00	…	−0.85	−3.60	−4.20	−3.20	−4.00	−4.60	−5.80	−4.40	−4.90	−5.60	−4.60
In s	…	13490	4.274	125.0	28.3	15.6	0.79	0.642	−0.96	−3.55	−4.16	−3.25	−4.04	−4.73	−5.86	−4.45	−4.91	−5.58	−4.66
Out f	…	13200	4.210	125.3	29.3	14.2	0.30	0.662	−0.91	−3.46	−4.21	−3.29	−4.12	−4.79	−5.73	−4.50	−4.97	…	−4.76
Stat.	…	$^{+200}_{-250}$	$^{+0.050}_{-0.070}$	$^{+0.5}_{-0.5}$	$^{+0.8}_{-1.3}$	$^{+1.7}_{-2.9}$	$^{+0.33}_{-0.30}$	$^{+0.020}_{-0.018}$	$^{+0.10}_{-0.07}$	$^{+0.13}_{-0.12}$	$^{+0.26}_{-0.52}$	$^{+0.06}_{-0.08}$	$^{+0.13}_{-0.14}$	$^{+0.06}_{-0.06}$	$^{+0.13}_{-0.16}$	$^{+0.05}_{-0.06}$	$^{+0.11}_{-0.10}$	…	$^{+0.07}_{-0.09}$
Sys.	…	$^{+260}_{-360}$	$^{+0.100}_{-0.100}$	$^{+0.2}_{-0.2}$	$^{+0.2}_{-0.6}$	$^{+0.9}_{-1.2}$	$^{+0.15}_{-0.22}$	$^{+0.036}_{-0.033}$	$^{+0.19}_{-0.17}$	$^{+0.12}_{-0.12}$	$^{+0.01}_{-0.06}$	$^{+0.04}_{-0.07}$	$^{+0.10}_{-0.11}$	$^{+0.03}_{-0.04}$	$^{+0.03}_{-0.04}$	$^{+0.02}_{-0.02}$	$^{+0.10}_{-0.09}$	…	$^{+0.09}_{-0.13}$
Out i	…	13360	4.258	125.3	28.7	15.1	0.15	0.650	…	…	…	…	…	…	…	…	…	…	…
Stat.	…	$^{+80}_{-90}$	$^{+0.028}_{-0.029}$	$^{+0.5}_{-0.5}$	$^{+1.3}_{-1.1}$	$^{+2.1}_{-2.5}$	$^{+0.34}_{-0.15}$	$^{+0.015}_{-0.014}$	…	…	…	…	…	…	…	…	…	…	…
Sys.	…	$^{+270}_{-270}$	$^{+0.100}_{-0.113}$	$^{+0.2}_{-0.3}$	$^{+0.3}_{-0.3}$	$^{+1.6}_{-1.3}$	$^{+0.29}_{-0.15}$	$^{+0.031}_{-0.032}$	…	…	…	…	…	…	…	…	…	…	…
Start	…	15000	4.100	120.0	10.0	10.0	3.00	0.800	−0.85	−3.60	−4.20	−3.20	−4.00	−4.60	−5.80	−4.40	−4.90	−5.60	−4.60
Mock spectrum as a proxy to the observed spectrum of object #6 in Table 5.4 (extremely blended features):																			
In p	350	20600	3.485	−11.2	54.2	9.4	6.04	…	−1.02	−3.79	−4.38	−3.39	−4.02	−4.74	−5.87	−4.66	−4.99	−5.59	−4.79
Out f	350	20740	3.502	−11.3	54.4	1.9	5.80	…	−1.02	−3.76	−4.37	−3.39	−4.03	−4.74	−5.87	−4.68	−5.02	−5.57	−4.76
Stat.	$^{+2}_{-2}$	$^{+30}_{-20}$	$^{+0.005}_{-0.003}$	$^{+0.2}_{-0.2}$	$^{+0.2}_{-0.2}$	$^{+4.4}_{-1.9}$	$^{+0.07}_{-0.12}$	…	$^{+0.02}_{-0.03}$	$^{+0.01}_{-0.01}$	$^{+0.02}_{-0.01}$	$^{+0.02}_{-0.02}$	$^{+0.01}_{-0.03}$	$^{+0.04}_{-0.02}$	$^{+0.01}_{-0.02}$	$^{+0.02}_{-0.01}$	$^{+0.01}_{-0.04}$	$^{+0.03}_{-0.04}$	$^{+0.01}_{-0.01}$
Sys.	…	$^{+420}_{-420}$	$^{+0.100}_{-0.100}$	$^{+0.1}_{-0.1}$	$^{+0.3}_{-0.1}$	$^{+3.1}_{-1.9}$	$^{+0.24}_{-0.49}$	…	$^{+0.03}_{-0.04}$	$^{+0.02}_{-0.02}$	$^{+0.05}_{-0.05}$	$^{+0.09}_{-0.07}$	$^{+0.03}_{-0.04}$	$^{+0.05}_{-0.05}$	$^{+0.03}_{-0.03}$	$^{+0.03}_{-0.03}$	$^{+0.02}_{-0.05}$	$^{+0.03}_{-0.04}$	$^{+0.04}_{-0.04}$
Out i	…	20790	3.506	−11.3	54.4	3.1	5.74	…	−1.01	−3.79	−4.38	−3.41	−4.03	−4.74	−5.87	−4.68	−5.01	−5.59	−4.79
Stat.	…	$^{+30}_{-30}$	$^{+0.004}_{-0.004}$	$^{+0.1}_{-0.1}$	$^{+0.1}_{-0.1}$	$^{+0.1}_{-3.1}$	$^{+0.05}_{-0.02}$	…	$^{+0.01}_{-0.01}$	$^{+0.01}_{-0.01}$	$^{+0.01}_{-0.01}$	$^{+0.01}_{-0.01}$	$^{+0.02}_{-0.02}$	$^{+0.02}_{-0.02}$	$^{+0.02}_{-0.01}$	$^{+0.02}_{-0.02}$	$^{+0.02}_{-0.02}$	$^{+0.02}_{-0.03}$	$^{+0.02}_{-0.02}$
Sys.	…	$^{+420}_{-420}$	$^{+0.100}_{-0.100}$	$^{+0.1}_{-0.1}$	$^{+0.4}_{-0.1}$	$^{+2.8}_{-3.1}$	$^{+0.46}_{-0.46}$	…	$^{+0.01}_{-0.01}$	$^{+0.01}_{-0.01}$	$^{+0.02}_{-0.02}$	$^{+0.04}_{-0.04}$	$^{+0.01}_{-0.01}$	$^{+0.02}_{-0.01}$	$^{+0.02}_{-0.02}$	$^{+0.02}_{-0.02}$	$^{+0.01}_{-0.01}$	$^{+0.02}_{-0.02}$	$^{+0.02}_{-0.02}$
Start	…	20000	3.500	−10.0	50.0	10.0	8.00	…	−1.05	−3.60	−4.20	−3.20	−4.00	−4.60	−5.80	−4.40	−4.90	−5.60	−4.60
In s	…	18610	3.227	−9.1	134.0	59.5	2.90	0.936	−1.02	−3.79	−4.38	−3.39	−4.02	−4.74	−5.87	−4.66	−4.99	−5.59	−4.79
Out f	…	18520	3.200	−9.6	118.0	87.0	3.82	1.085	−1.00	−3.89	−4.40	−3.46	−4.05	−4.75	−5.86	−4.68	−5.01	−5.68	−4.89
Stat.	…	$^{+60}_{-40}$	$^{+0.003}_{-0.002}$	$^{+0.4}_{-0.7}$	$^{+1.6}_{-0.5}$	$^{+0.5}_{-3.0}$	$^{+0.16}_{-0.12}$	$^{+0.008}_{-0.005}$	$^{+0.02}_{-0.02}$	$^{+0.04}_{-0.04}$	$^{+0.03}_{-0.05}$	$^{+0.04}_{-0.05}$	$^{+0.04}_{-0.02}$	$^{+0.05}_{-0.05}$	$^{+0.03}_{-0.06}$	$^{+0.03}_{-0.04}$	$^{+0.03}_{-0.03}$	$^{+0.06}_{-0.05}$	$^{+0.04}_{-0.05}$
Sys.	…	$^{+580}_{-500}$	$^{+0.124}_{-0.124}$	$^{+0.3}_{-0.1}$	$^{+1.3}_{-0.8}$	$^{+2.0}_{-1.6}$	$^{+0.52}_{-0.36}$	$^{+0.069}_{-0.131}$	$^{+0.06}_{-0.03}$	$^{+0.07}_{-0.06}$	$^{+0.09}_{-0.10}$	$^{+0.11}_{-0.13}$	$^{+0.06}_{-0.03}$	$^{+0.10}_{-0.06}$	$^{+0.06}_{-0.05}$	$^{+0.04}_{-0.04}$	$^{+0.07}_{-0.03}$	$^{+0.04}_{-0.04}$	$^{+0.06}_{-0.07}$
Out i	…	18410	3.197	−9.9	120.3	84.9	3.71	1.066	…	…	…	…	…	…	…	…	…	…	…
Stat.	…	$^{+70}_{-20}$	$^{+0.010}_{-0.005}$	$^{+0.7}_{-0.7}$	$^{+4.8}_{-0.5}$	$^{+3.0}_{-3.3}$	$^{+0.15}_{-0.09}$	$^{+0.015}_{-0.008}$	…	…	…	…	…	…	…	…	…	…	…
Sys.	…	$^{+410}_{-390}$	$^{+0.119}_{-0.111}$	$^{+0.2}_{-0.2}$	$^{+0.7}_{-0.6}$	$^{+1.4}_{-1.5}$	$^{+0.62}_{-0.71}$	$^{+0.054}_{-0.061}$	…	…	…	…	…	…	…	…	…	…	…
Start	…	20000	3.500	−10.0	100.0	50.0	8.00	1.000	−1.05	−3.60	−4.20	−3.20	−4.00	−4.60	−5.80	−4.40	−4.90	−5.60	−4.60
Mock spectrum as a proxy to the observed spectrum of object #4 b in Table 5.4 (but with individual metal abundances for the two components):																			
In p	340	29710	3.669	104.0	23.7	41.2	14.92	…	−1.17	−3.79	−4.38	−3.39	−4.02	−4.74	−5.87	−4.66	−4.99	−5.59	−4.79
Out f	353	29730	3.678	103.9	24.9	39.3	15.02	…	−1.17	−3.81	−4.39	−3.41	−4.03	−4.75	−5.88	−4.68	−5.00	…	−4.86
Stat.	$^{+3}_{-2}$	$^{+20}_{-40}$	$^{+0.003}_{-0.003}$	$^{+0.1}_{-0.1}$	$^{+0.3}_{-0.3}$	$^{+0.1}_{-0.1}$	$^{+0.12}_{-0.09}$	…	$^{+0.01}_{-0.01}$	$^{+0.01}_{-0.01}$	$^{+0.01}_{-0.01}$	$^{+0.01}_{-0.01}$	$^{+0.02}_{-0.02}$	$^{+0.02}_{-0.02}$	$^{+0.03}_{-0.03}$	$^{+0.01}_{-0.01}$	$^{+0.02}_{-0.02}$	…	$^{+0.05}_{-0.04}$
Sys.	…	$^{+600}_{-600}$	$^{+0.100}_{-0.100}$	$^{+0.1}_{-0.1}$	$^{+0.9}_{-1.0}$	$^{+0.3}_{-0.1}$	$^{+0.48}_{-0.61}$	…	$^{+0.04}_{-0.04}$	$^{+0.02}_{-0.01}$	$^{+0.04}_{-0.04}$	$^{+0.05}_{-0.05}$	$^{+0.02}_{-0.02}$	$^{+0.03}_{-0.03}$	$^{+0.04}_{-0.03}$	$^{+0.04}_{-0.04}$	$^{+0.07}_{-0.06}$	…	$^{+0.07}_{-0.06}$
Out i	…	29700	3.673	103.9	24.7	39.6	14.98	…	−1.17	−3.81	−4.39	−3.41	−4.04	−4.74	−5.86	−4.68	−5.00	…	−4.80
Stat.	…	$^{+10}_{-20}$	$^{+0.004}_{-0.003}$	$^{+0.1}_{-0.1}$	$^{+0.2}_{-0.1}$	$^{+0.1}_{-0.1}$	$^{+0.08}_{-0.05}$	…	$^{+0.01}_{-0.01}$	$^{+0.01}_{-0.01}$	$^{+0.01}_{-0.01}$	$^{+0.01}_{-0.01}$	$^{+0.02}_{-0.02}$	$^{+0.02}_{-0.02}$	$^{+0.03}_{-0.03}$	$^{+0.01}_{-0.01}$	$^{+0.02}_{-0.02}$	…	$^{+0.04}_{-0.04}$
Sys.	…	$^{+600}_{-600}$	$^{+0.100}_{-0.100}$	$^{+0.1}_{-0.1}$	$^{+0.8}_{-1.2}$	$^{+0.3}_{-0.1}$	$^{+0.50}_{-0.63}$	…	$^{+0.04}_{-0.03}$	$^{+0.02}_{-0.02}$	$^{+0.03}_{-0.04}$	$^{+0.05}_{-0.05}$	$^{+0.02}_{-0.02}$	$^{+0.03}_{-0.03}$	$^{+0.03}_{-0.03}$	$^{+0.04}_{-0.04}$	$^{+0.07}_{-0.06}$	…	$^{+0.03}_{-0.02}$
Start	…	31000	3.800	100.0	40.0	10.0	9.00	…	−1.05	−3.60	−4.20	−3.20	−4.10	−4.60	−5.80	−4.40	−4.90	−5.60	−4.60
In s	…	28070	4.343	−110.9	35.5	62.6	6.04	0.218	−1.17	−3.76	−4.50	−3.59	−4.07	−4.61	−5.70	−4.71	−4.94	−5.60	−4.69
Out f	…	27740	4.253	−110.2	28.2	67.7	6.50	0.221	−1.23	−3.86	−4.50	−3.64	−4.28	−4.45	−5.73	−4.85	−4.96	…	−4.64
Stat.	…	$^{+120}_{-\ 80}$	$^{+0.019}_{-0.019}$	$^{+1.0}_{-0.9}$	$^{+3.0}_{-3.3}$	$^{+3.0}_{-5.9}$	$^{+0.70}_{-0.40}$	$^{+0.001}_{-0.002}$	$^{+0.05}_{-0.04}$	$^{+0.08}_{-0.07}$	$^{+0.05}_{-0.05}$	$^{+0.03}_{-0.03}$	$^{+0.20}_{-0.18}$	$^{+0.31}_{-0.60}$	$^{+0.09}_{-0.09}$	$^{+0.06}_{-0.06}$	$^{+0.08}_{-0.08}$	…	$^{+0.05}_{-0.05}$
Sys.	…	$^{+710}_{-880}$	$^{+0.334}_{-0.523}$	$^{+1.3}_{-0.6}$	$^{+4.0}_{-2.5}$	$^{+0.6}_{-0.2}$	$^{+1.10}_{-2.00}$	$^{+0.022}_{-0.012}$	$^{+0.14}_{-0.11}$	$^{+0.06}_{-0.05}$	$^{+0.05}_{-0.07}$	$^{+0.08}_{-0.03}$	$^{+0.04}_{-0.03}$	$^{+0.17}_{-0.26}$	$^{+0.06}_{-0.05}$	$^{+0.07}_{-0.03}$	$^{+0.04}_{-0.03}$	…	$^{+0.11}_{-0.07}$
Out i	…	26870	4.220	−110.7	33.5	65.0	4.74	0.231	…	…	…	…	…	…	…	…	…	…	…
Stat.	…	$^{+120}_{-140}$	$^{+0.015}_{-0.018}$	$^{+0.8}_{-1.0}$	$^{+2.5}_{-2.7}$	$^{+2.3}_{-2.9}$	$^{+0.29}_{-0.30}$	$^{+0.001}_{-0.002}$	…	…	…	…	…	…	…	…	…	…	…
Sys.	…	$^{+870}_{-850}$	$^{+0.366}_{-0.526}$	$^{+1.3}_{-0.9}$	$^{+3.8}_{-2.7}$	$^{+0.6}_{-0.5}$	$^{+0.74}_{-1.76}$	$^{+0.016}_{-0.010}$	…	…	…	…	…	…	…	…	…	…	…
Start	…	23500	3.800	−100.0	30.0	10.0	8.00	0.300	−1.05	−3.60	−4.20	−3.20	−4.10	−4.60	−5.80	−4.40	−4.90	−5.60	−4.60

Notes. Same as Table 5.2. The letter "p" denotes the primary and "s" the secondary component. The letter "f" indicates that all abundances were allowed to vary freely during the fitting process, whereas "i" denotes the assumption of an identical chemical composition of both components. Argon lines are not visible for all temperatures.

by simultaneously computing lines of all chemical species under consideration. Additionally, models off the grid points were chosen to check that our mesh is sufficiently spaced for the linear interpolation scheme applied. Because the differences of input and output values in Table 5.2 are often covered by the very small statistical uncertainties (see Sect. 5.2.3) that result from the high S/N assigned to the mock spectra, we conclude that inaccuracies introduced by simplifications in our approach are negligible.

In a second step, three mock composite spectra were created with the help of Eq. (5.1). The parameters chosen here are motivated by real SB2 systems and anticipate the results presented in Sect. 5.3. They cover a sharp-lined, well-separated and, thus, easy to analyze system and a very difficult configuration with heavily blended spectral features. Similar to the previous tests, most of the input parameters are recovered with very high precision or at least within the derived uncertainties, as seen in Table 5.3. In particular, the degree of accuracy in the inferred parameters of both components of the extremely blended composite spectrum is astonishing, hence, making us quite confident that our method is also highly suitable for investigations of SB2 systems.

Although our method is able to model individual abundances if necessary, we generally prefer to assume an identical chemical composition for the two components within the binary system. In this way, the number of free parameters and, consequently, the numerical complexity of the problem is significantly reduced. In the cases where the parameters of the secondary component are only poorly constrained due to their little impact on the composite spectrum, it is even necessary to impose these constraints, which compensate for the lack of spectral indicators to derive reasonable atmospheric parameters. Note that the assumption of an equal chemical composition is well justified for SB2 systems containing B-type or late O-type stars. On the one hand, the components of SB2 systems are in general similar regarding to their masses (otherwise, the flux contribution of the fainter companion would not be visible in the spectrum), ages (the whole system formed at once), and pristine chemical composition (both components formed from the same building material). On the other hand, processes causing chemical anomalies are rare among B- and late O-type stars and primarily affect helium (Smith 1996). Since chemical peculiarities are possibly even less frequent in detached binary systems (Pavlovski & Southworth 2013), elemental abundances are expected to evolve in the same way in both components. To estimate the influence of this approximation on the spectral analysis, Table 5.3 lists the results obtained from fitting the three mock composite spectra with adjustable abundances and an equal chemical composition. Even for the system with different individual abundances, the results derived by assuming an identical chemical composition are very satisfying. In particular, this is with respect to the primary component, which dominates the spectrum and in this way also the estimates for the system abundances and their respective confidence limits. As a consequence, the actual abundances of the secondary component may sometimes lie outside of the uncertainty intervals determined for the binary system as a whole. Nevertheless, it is obvious that the decision of whether or not to use separate abundances during the fitting process depends on the individual object and has to be checked, for example, a posteriori by inspecting the final match of the model to the observation.

5.2.3 Discussion of statistical and systematic uncertainties

The accuracy of spectral analyses is generally limited by the quality of the obtained data and the ability of the model to reproduce the observation. As shown in this subsection, shortcomings in the model, which may be due to inaccurate atomic data or deficient line broadening theory, are the main obstacles to overcome to perform more precise investigations.

Statistical uncertainties result from the noise in the observed spectrum and can be deduced from the χ^2 statistics in the standard way: starting from the best fit with a reduced χ^2 of about one[16], the parameter under consideration is increased/decreased, while all remaining parameters are fitted, until a certain increment $\Delta\chi^2$ from the minimum χ^2 is reached (for details, see Bevington & Robinson 1992). Here, each $\Delta\chi^2$ corresponds to a confidence level; for example, $\Delta\chi^2 = 6.63$ is equivalent to the 99%-confidence interval (see the magenta line in Fig. 5.1 for an illustration). The resulting uncertainties are, of course, only trustworthy if the δ_i of Eq. (5.2) are reasonably estimated. The method outlined in Sect. 5.2.1 can do so, as shown by the tests with mock spectra with known noise level (see Tables 5.2 and 5.3). Moreover, those tests, which use the same models as the fitting routine and, thus, exclude all sources of systematic errors apart from microscopic line blends, give an estimate of the statistical uncertainties that can be expected in real data with a similar S/N.

Systematic uncertainties are much harder to cope with. Sources of systematic errors occur almost everywhere in the course of the analysis (see the discussion in Nieva & Przybilla 2010). At the same time, their effects are by no means trivial, and it is extremely difficult and sometimes even impossible to quantify them. In particular, this is true for atomic data (such as energy levels, oscillator strengths, and photo-ionization cross sections), which affect individual spectral lines and the atmospheric structure. Monte Carlo simulations in the style of Sigut (1996, 1999) offer the possibility of estimating the effects on spectra caused by variations in these input data. However, a thorough error analysis has to take all sources of systematic errors into consideration at the same time to account for correlations as well, which is an unfeasible task.

Our analysis strategy is designed to keep systematic uncertainties as small as possible. For instance, an inaccurate local continuum definition can introduce considerable uncertainties to the determination of metal abundances, especially in fast-rotating stars or low-resolution spectra where metal line blends lower the actual continuum. In our routine, these effects are allowed by re-normalizing the observed spectrum with the help of the synthetic ones. Here, the latter are used to properly locate the continuum regions, which are sufficiently frequent in optical spectra of early-type stars. For these, a correction factor is obtained by dividing the (smoothed) observed data with the model data. Interpolating this factor to the whole wavelength grid gives the local continuum correction term for all spectral lines. For this approach to work, a high degree of completeness in terms of modeled lines is necessary, which is verified by high-resolution, high S/N spectra of slow rotators, as seen in Figs. C.2.2a–C.2.2i.

Another crucial part of our strategy is that we are simultaneously fitting the maximum useful range of the optical spectrum. In this way, parameters are determined not just from one or two spectral indicators but from all available ones. As the systematic errors of the individual

[16]This condition is generally not met because there are always some lines that our models still cannot reproduce on the small scales given by the high S/N of the available observations. In that case, the δ_i values corresponding to these lines are increased until their χ_i values (see Eq. (5.2)) approach ± 1 at the best fit eventually yielding a reduced χ^2 of about 1.

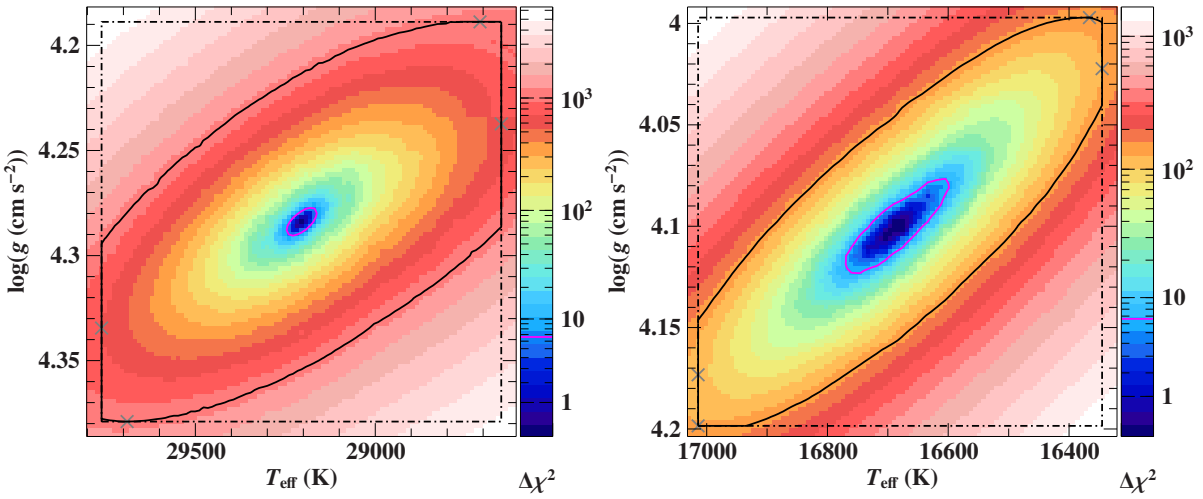

Figure 5.1: Examples of a color coded $\Delta\chi^2$ map as a function of effective temperature and surface gravity for the single star HD 37042 (*left*) and for the primary component of the SB2 system HD 119109 (*right*). The magenta line is the $\Delta\chi^2 = 6.63$ contour line, therefore, indicating the statistical (single parameter) 99%-confidence interval for abscissa and ordinate. The four corners of the black dashed-dotted rectangle are defined by the four combinations that result from adding or subtracting the respective total uncertainty, which is a quadratic sum of statistical and systematic uncertainty, to each coordinate of the best fit location. The point of minimum $\Delta\chi^2$ on each edge of the rectangle is marked by a gray cross. The solid black line surrounds the region within the rectangle with $\Delta\chi^2$ values lower or equal the maximum of the four $\Delta\chi^2$ values given by the gray crosses. In this way, areas within the rectangle where the models fit the observation worst are excluded, while it is ensured that each edge of the rectangle contributes at least one point to the solid line at the same time. This construction is our approach to combine statistical and systematic uncertainties.

indicators are typically independent of each other, which can be exemplified by ionization equilibria of different metals or oscillator strengths of various multiplets, there is a good chance that their effects on the parameter determination average out because some lines systematically give higher and others lower abundances, thus reducing the impact of systematics.

To crudely estimate the systematic uncertainties, we start from the assumption that they mainly appear as inaccuracies in the determination of effective temperature and surface gravity. From our extensive experience with the applied synthetic spectra, we find it realistic but conservative to assign errors of ±2% in $T_{\rm eff}$ and ±0.1 dex in $\log(g)$. The ranges given by these errors are formally treated as 99%-confidence intervals. The precision in fixing the microturbulence and the abundances of the chemical elements is then estimated from propagating the errors in $T_{\rm eff}$ and $\log(g)$. Here, a fit of all remaining parameters is performed for each pixel (that is for each combination of temperature and surface gravity) surrounded by the solid black line in Fig. 5.1. In the case of a binary system, this procedure is carried out for the secondary component as well. The resulting (combined) ranges of parameter values are then taken to be 99%-confidence intervals. This approach is valid as long as uncertainties induced by variations in $T_{\rm eff}$ and $\log(g)$ dominate other sources of systematic errors. While this is likely to be true for ξ and $n(x)$, it is clearly not the case for $v_{\rm rad}$, $v\sin(i)$, and ζ. Determination of radial ve-

locities is generally limited by the accuracy of the wavelength calibration and ranges between 0.1–2 km s^{-1} for common spectrographs. Projected rotational velocity and macroturbulence are incorporated via convolution with corresponding profile functions. Because of simplifications (for example in the treatment of limb darkening or the assumption of radial-tangential macroturbulence) during the derivation of the latter (see Gray 2005, pp. 433–437), their validity may be limited to a few km s^{-1}.

The comparison of statistical and systematic uncertainties, as listed in Table 5.2, shows that our method's total uncertainty is dominated by systematic effects down to at least a S/N of 100. However, this by no means implies that high S/N data are an unnecessary luxury. They are indispensable to detect weak features, such as contributions from a faint companion star, which would otherwise be hidden by noise. Moreover, shortcomings in the models are much more likely to remain unrecognized in low S/N spectra. This is particularly true if they can be partly compensated by tuning some fitting parameters, which, in turn, would cause erroneous results. Instead, this comparison shows that the accuracy of the presented spectral analysis technique is currently limited by modeling and not by observation.

5.3 Application to three single and three binary B- and late O-type stars

5.3.1 The test stars

To illustrate the capabilities of our new method, we re-analyzed three well-studied early-type stars from the Orion region and performed a spectral analysis of three SB2 systems based on very high quality single epoch spectra. For one of the binaries, two additional spectra covering different orbital phases were also investigated. Table 5.4 lists the relevant information about the test stars. We focused on targets which cover a wide range of effective temperatures, have moderate projected stellar rotations, and show a variety of binary configurations.

5.3.2 Atmospheric parameters and abundances

Atmospheric parameters and abundances are determined by fitting synthetic to observed spectra, as outlined in detail in Sect. 5.1. Comparisons of final, best-fitting models with observations are shown for a large portion of the used spectral range in Figs. C.2.2a–C.2.2i for the Orion stars and in Figs. C.2.3a–C.2.3i for the SB2 systems. The overall match of metal lines is almost perfect for the cooler stars of the sample and still very good for the hotter ones where our model atoms begin to be partially incomplete because they were not optimized for this temperature regime. This is particularly true with respect to O II lines. Consequently, more regions have to be excluded from the analysis for higher effective temperatures due to (blends with) missing spectral lines.

Note that we generally exclude several He I lines from the analysis owing to recurrent issues with their detailed spectral line shapes, which is apparent only in high-resolution spectra with high S/N. This specifically affects the diffuse He I lines that show small but perceptible systematic deficiencies in their forbidden components, which can be attributed to shortcomings in their line-broadening theory. These issues are independent of $T_{\rm eff}$ and $\log(g)$ and cannot

Table 5.4: Test stars: ID, spectroscopy, photometry.

#	Object	Instrument	S/N	V	$U-B$	$B-V$	$b-y$	m_1	c_1	H_p	B_t	V_t	References
								(mag)					
Single stars:													
1	HD 35299	FIES[(a)]	250	5.694	−0.874	−0.210	−0.094	0.088	0.057	5.6235	5.430	5.650	(1), (3), (4), (5)
2	HD 35912	FIES[(a)]	240	6.408	−0.743	−0.177	−0.080	0.102	0.211	6.3397	6.166	6.352	(1), (3), (4), (5)
3	HD 37042	FIES[(a)]	205	6.380	−0.930	−0.090	−0.004	0.049	−0.080	...	6.066	6.193	(2), (3), (5)
SB2:													
4 a	HD 75821	FEROS	350	5.097	−0.980	−0.214	−0.074	0.056	−0.079	5.0175	4.829	5.070	(1), (3), (4), (5)
4 b	HD 75821	FEROS	340	5.097	−0.980	−0.214	−0.074	0.056	−0.079	5.0175	4.829	5.070	(1), (3), (4), (5)
4 c	HD 75821	FEROS	340	5.097	−0.980	−0.214	−0.074	0.056	−0.079	5.0175	4.829	5.070	(1), (3), (4), (5)
5	HD 119109	FEROS	220	7.461	−0.510	0.005	0.048	0.061	0.366	7.4667	7.437	7.460	(1), (3), (4), (5)
6	HD 213420	FIES	350	4.505	−0.738	−0.090	−0.007	0.059	0.191	4.4912	4.375	4.493	(1), (3), (4), (5)

Notes. The fourth column is the mean S/N of the spectrum obtained with one of the two high-resolution spectrographs FIES ($\lambda/\Delta\lambda = 45\,000$, Frandsen & Lindberg 1999) or FEROS ($\lambda/\Delta\lambda = 48\,000$, Kaufer et al. 1999). Photometric data: Johnson-Cousins magnitudes U, B, and V were compiled from references (1) and (2), Strömgren colors $b-y$, m_1, and c_1 from (3), the HIPPARCOS magnitude H_p from (4), and Tycho magnitudes B_t and V_t from (5). For reasons of clarity, uncertainties are not given here but can be found in the respective references. [(a)] Spectra have been taken from the IACOB database (Simón-Díaz et al. 2011a) by courtesy of S. Simón-Díaz and were first presented and analyzed in Simón-Díaz (2010).

References. (1) Mermilliod (1991); (2) Ducati (2002); (3) Hauck & Mermilliod (1998); (4) van Leeuwen (2007); (5) Høg et al. (2000).

be resolved, even if these lines are fitted individually. With a sufficient number of alternative, highly trustworthy He I lines present in the optical spectral range, we generally refrain from fitting the diffuse lines to avoid a possible source of systematic error and use them instead as a consistency check. Nevertheless, given the fact that the synthetic profiles of these lines match the observed ones quite well, except for the forbidden components (see Figs. C.2.2a–C.2.2i), this decision is probably too restrictive. The diffuse He I lines could therefore be considered for spectral fitting as well with resulting changes in parameters that are well below the stated systematic uncertainties.

Furthermore, we ignore the temperature-sensitive cores of the Balmer lines during the fitting process by excluding those parts of these lines where their normalized flux is smaller than a cutoff, which is typically chosen to be 0.8. The reason for this is that they are formed in the outer stellar atmosphere, where deviations from the LTE stratification are more pronounced (see Nieva & Przybilla 2007; Przybilla et al. 2011) and where the assumption of hydrostatic equilibrium also becomes less and less valid in the accelerating (weak) stellar wind. Moreover, by simultaneously fitting the entire useful spectral range, there are enough other indicators for $T_{\rm eff}$ such as (multiple) ionization equilibria available so that it is sufficient to use the Balmer line cores as a consistency check (Figures C.2.2a–C.2.2i and Figs. C.2.3a–C.2.3i show how well this works.). As a side product, we also reduce the otherwise overwhelming influence of these lines on the parameter determination.

Table 5.5 lists the atmospheric parameters and abundances of the test stars. Instead of the "classical" notation for the abundance, $\log(x/\mathrm{H}) + 12$, we have chosen $n(x)$, which is the fractional particle number of species x with respect to all elements. The motivation for this is that the helium abundance is variable from star to star, which, in turn, causes the hydrogen abundance to vary since hydrogen and helium abundances are coupled via the fixed number of total

Table 5.5: Atmospheric parameters and abundances of the test stars.

#	$T_{\rm eff}$	log(g)	$v_{\rm rad}$	$v \sin(i)$	ζ	ξ	$A_{\rm eff,s}/A_{\rm eff,p}$	log($n(x)$)										
	(K)	(cgs)	(km s^{-1})					He	C	N	O	Ne	Mg	Al	Si	S	Ar	Fe
1	23 880	4.127	23.0	5.2	4.4	2.02	…	−0.98	−3.73	−4.30	−3.29	−4.00	−4.56	−5.79	−4.66	−4.88	−5.49	−4.71
Stat.	+70 −70	+0.008 −0.008	+0.1 −0.1	+0.7 −2.2	+2.0 −0.7	+0.11 −0.23	…	+0.01 −0.02	+0.02 −0.02	+0.01 −0.01	+0.02 −0.02	+0.02 −0.02	+0.02 −0.03	+0.01 −0.02	+0.02 −0.02	+0.02 −0.01	+0.02 −0.02	+0.02 −0.02
Sys.	+480 −480	+0.100 −0.100	+0.1 −0.1	+0.5 −0.3	+0.8 −1.5	+0.68 −1.39	…	+0.04 −0.06	+0.02 −0.02	+0.03 −0.02	+0.09 −0.08	+0.04 −0.04	+0.10 −0.10	+0.03 −0.03	+0.07 −0.06	+0.06 −0.06	+0.07 −0.06	+0.03 −0.02
1[(a)]	24 000	4.20	…	8	…	0	…	−1.06	−3.67	−4.23	−3.32	−3.92	−4.43	…	−4.54	…	…	−4.55
	±200	±0.08	…	±1	…	±1	…	…	±0.07	±0.07	±0.07	±0.09	±0.07	…	±0.08	…	…	±0.10
2	19 250	4.052	30.7	7.3	17.1	1.99	…	−1.00	−3.64	−4.23	−3.21	−4.06	−4.60	−5.71	−4.48	−4.89	−5.57	−4.63
Stat.	+60 −50	+0.007 −0.007	+0.2 −0.1	+0.4 −0.5	+0.5 −1.1	+0.14 −0.26	…	+0.01 −0.02	+0.03 −0.02	+0.02 −0.02	+0.02 −0.02	+0.02 −0.02	+0.02 −0.03	+0.03 −0.02	+0.03 −0.03	+0.02 −0.01	+0.03 −0.03	+0.02 −0.02
Sys.	+390 −390	+0.100 −0.100	+0.1 −0.1	+0.7 −1.8	+0.2 −0.1	+1.08 −1.56	…	+0.08 −0.09	+0.07 −0.07	+0.08 −0.08	+0.10 −0.11	+0.03 −0.03	+0.11 −0.13	+0.06 −0.07	+0.13 −0.14	+0.05 −0.05	+0.04 −0.05	+0.01 −0.03
2[(a)]	19 000	4.00	…	15	8	2	…	−1.06	−3.71	−4.28	−3.25	−3.99	−4.54	…	−4.56	…	…	−4.52
	±300	±0.10	…	±1	±1	±1	…	…	±0.09	±0.07	±0.09	±0.11	±0.05	…	±0.07	…	…	±0.08
3	29 210	4.284	29.9	30.9	0.0	3.22	…	−1.04	−3.71	−4.13	−3.40	−4.01	−4.58	−5.73	−4.66	−4.97	…	−4.62
Stat.	+30 −50	+0.006 −0.007	+0.2 −0.1	+0.1 −0.1	+1.1 −0.0	+0.10 −0.11	…	+0.01 −0.02	+0.02 −0.02	+0.01 −0.01	+0.02 −0.01	+0.03 −0.03	+0.02 −0.03	+0.03 −0.02	+0.03 −0.01	+0.03 −0.03	…	+0.02 −0.02
Sys.	+580 −590	+0.100 −0.100	+0.1 −0.1	+0.2 −0.1	+2.6 −0.0	+0.47 −0.59	…	+0.04 −0.04	+0.01 −0.03	+0.05 −0.05	+0.04 −0.02	+0.02 −0.02	+0.05 −0.05	+0.05 −0.05	+0.04 −0.03	+0.07 −0.05	…	+0.08 −0.06
3[(a)]	29 300	4.30	…	30	10	2	…	−1.06	−3.71	−4.00	−3.29	−3.91	−4.40	…	−4.49	…	…	−4.50
	±300	±0.09	…	±2	±3	±1	…	…	±0.11	±0.08	±0.08	±0.09	…	…	±0.03	…	…	±0.09
4p a	29 420	3.620	17.7	24.0	37.4	13.58	…	−1.10	−3.81	−4.47	−3.60	−4.10	−4.60	−5.68	−4.70	−4.91	…	−4.59
Stat.	+20 −20	+0.003 −0.003	+0.2 −0.2	+0.7 −0.4	+0.2 −1.3	+0.12 −0.11	…	+0.01 −0.01	+0.02 −0.01	+0.02 −0.01	+0.01 −0.01	+0.01 −0.02	+0.02 −0.01	+0.02 −0.01	+0.01 −0.01	+0.02 −0.03	…	+0.03 −0.02
Sys.	+590 −590	+0.100 −0.100	+1.5 −2.0	+2.9 −5.0	+0.5 −0.1	+0.75 −1.04	…	+0.01 −0.02	+0.02 −0.01	+0.04 −0.02	+0.02 −0.03	+0.01 −0.02	+0.02 −0.01	+0.03 −0.02	+0.04 −0.04	+0.04 −0.05	…	+0.05 −0.04
4s a	32 900	4.687	56.6	0.0	69.1	14.34	0.218	…	…	…	…	…	…	…	…	…	…	…
Stat.	+80 −80	+0.012 −0.014	+0.9 −0.6	+7.8 −0.0	+1.4 −1.1	+0.72 −0.53	+0.002 −0.007	…	…	…	…	…	…	…	…	…	…	…
Sys.	+ 910 −1770	+≥0.063 − 0.305	+14.8 −18.3	+34.8 − 0.0	+0.8 −0.2	+1.66 −2.61	+0.314 −0.095	…	…	…	…	…	…	…	…	…	…	…
4p b	29 710	3.669	104.0	23.7	41.2	14.92	…	−1.17	−3.76	−4.50	−3.59	−4.07	−4.61	−5.70	−4.71	−4.94	…	−4.69
Stat.	+40 −40	+0.005 −0.004	+0.2 −0.1	+0.5 −0.5	+0.4 −0.6	+0.12 −0.12	…	+0.01 −0.01	+0.02 −0.01	+0.02 −0.02	+0.01 −0.01	+0.02 −0.01	+0.02 −0.02	+0.02 −0.02	+0.01 −0.01	+0.02 −0.03	…	+0.03 −0.03
Sys.	+600 −600	+0.100 −0.100	+0.1 −0.1	+1.2 −1.5	+0.1 −0.1	+0.27 −0.24	…	+0.03 −0.03	+0.02 −0.01	+0.06 −0.05	+0.05 −0.05	+0.02 −0.01	+0.03 −0.03	+0.04 −0.04	+0.05 −0.05	+0.07 −0.07	…	+0.05 −0.06
4s b	28 070	4.343	−110.9	35.5	62.6	6.04	0.218	…	…	…	…	…	…	…	…	…	…	…
Stat.	+140 −170	+0.016 −0.021	+0.8 −1.0	+2.7 −2.8	+3.5 −3.4	+0.23 −0.35	+0.003 −0.002	…	…	…	…	…	…	…	…	…	…	…
Sys.	+610 −870	+0.310 −0.434	+0.6 −0.4	+2.6 −1.9	+0.4 −0.6	+0.78 −0.80	+0.014 −0.011	…	…	…	…	…	…	…	…	…	…	…
4p c	29 630	3.622	−17.2	22.4	37.2	14.68	…	−1.17	−3.78	−4.57	−3.58	−4.00	−4.60	−5.71	−4.70	−4.92	…	−4.65
Stat.	+20 −20	+0.003 −0.003	+0.2 −0.1	+0.4 −0.5	+0.2 −0.1	+0.12 −0.12	…	+0.01 −0.01	+0.01 −0.02	+0.02 −0.02	+0.01 −0.01	+0.01 −0.02	+0.02 −0.01	+0.02 −0.03	+0.01 −0.01	+0.03 −0.02	…	+0.03 −0.03
Sys.	+600 −600	+0.100 −0.100	+0.5 −1.0	+1.4 −8.9	+1.1 −0.1	+0.48 −0.19	…	+0.03 −0.02	+0.01 −0.02	+0.03 −0.03	+0.05 −0.04	+0.02 −0.02	+0.03 −0.02	+0.03 −0.04	+0.05 −0.05	+0.06 −0.05	…	+0.05 −0.04
4s c	30 630	4.750	83.5	68.9	38.3	9.73	0.228	…	…	…	…	…	…	…	…	…	…	…
Stat.	+140 −150	+… −0.013	+1.0 −1.0	+0.1 −2.8	+4.1 −4.2	+0.50 −0.47	+0.003 −0.003	…	…	…	…	…	…	…	…	…	…	…
Sys.	+ 780 −1130	+… −0.358	+ 4.4 −36.2	+42.1 − 0.8	+37.7 −22.1	+0.97 −0.73	+0.204 −0.034	…	…	…	…	…	…	…	…	…	…	…
5p	16 680	4.098	−84.7	7.9	11.4	2.10	…	−0.96	−3.55	−4.16	−3.25	−4.04	−4.73	−5.86	−4.45	−4.91	−5.58	−4.66
Stat.	+100 − 90	+0.027 −0.021	+0.1 −0.2	+1.9 −1.3	+1.0 −2.2	+0.17 −0.19	…	+0.02 −0.02	+0.03 −0.03	+0.03 −0.04	+0.02 −0.03	+0.02 −0.03	+0.04 −0.03	+0.05 −0.04	+0.03 −0.03	+0.02 −0.03	+0.06 −0.08	+0.03 −0.03
Sys.	+330 −340	+0.100 −0.100	+0.1 −0.1	+1.2 −0.2	+0.5 −1.7	+0.25 −0.29	…	+0.06 −0.06	+0.06 −0.06	+0.06 −0.06	+0.01 −0.02	+0.01 −0.02	+0.04 −0.03	+0.03 −0.03	+0.01 −0.03	+0.02 −0.03	+0.04 −0.05	+0.04 −0.05
5s	13 490	4.274	125.0	28.3	15.6	0.79	0.642	…	…	…	…	…	…	…	…	…	…	…
Stat.	+90 −80	+0.030 −0.025	+0.5 −0.4	+1.1 −1.5	+3.1 −2.0	+0.32 −0.31	+0.015 −0.013	…	…	…	…	…	…	…	…	…	…	…
Sys.	+270 −280	+0.100 −0.102	+0.1 −0.2	+0.2 −0.3	+1.6 −0.7	+0.23 −0.23	+0.027 −0.028	…	…	…	…	…	…	…	…	…	…	…
6p	20 590	3.485	−11.2	54.2	9.4	6.04	…	−1.02	−3.79	−4.38	−3.39	−4.02	−4.74	−5.87	−4.66	−4.98	−5.59	−4.78
Stat.	+30 −40	+0.004 −0.005	+0.3 −0.2	+0.1 −0.1	+0.1 −2.2	+0.09 −0.08	…	+0.01 −0.02	+0.02 −0.02	+0.01 −0.02	+0.02 −0.01	+0.02 −0.02	+0.02 −0.03	+0.02 −0.02	+0.02 −0.02	+0.01 −0.02	+0.02 −0.03	+0.02 −0.02
Sys.	+420 −410	+0.100 −0.100	+0.1 −0.1	+0.3 −0.1	+1.7 −3.2	+0.60 −0.61	…	+0.01 −0.02	+0.02 −0.01	+0.02 −0.03	+0.06 −0.04	+0.02 −0.01	+0.02 −0.02	+0.02 −0.03	+0.03 −0.03	+0.01 −0.03	+0.01 −0.03	+0.02 −0.02
6s	18 610	3.227	−9.1	134.0	59.5	2.90	0.936	…	…	…	…	…	…	…	…	…	…	…
Stat.	+50 −70	+0.004 −0.006	+1.1 −1.0	+0.1 −0.6	+4.3 −4.7	+0.18 −0.18	+0.014 −0.015	…	…	…	…	…	…	…	…	…	…	…
Sys.	+460 −370	+0.148 −0.130	+0.3 −0.2	+0.5 −0.8	+2.2 −1.8	+0.96 −0.82	+0.069 −0.060	…	…	…	…	…	…	…	…	…	…	…
$\odot$[(b)]								−1.06	−3.57	−4.17	−3.31	−4.07	−4.40	−5.55	−4.49	−4.88	−5.60	−4.50
								+0.01 −0.01	+0.05 −0.05	+0.05 −0.05	+0.05 −0.05	+0.10 −0.10	+0.04 −0.04	+0.03 −0.03	+0.04 −0.04	+0.03 −0.03	+0.13 −0.13	+0.04 −0.04

Notes. Same as Table 5.2. Numbering according to Table 5.4. Argon lines are not visible for all temperatures. Owing to the assumption of a homogeneous chemical composition, abundances of the secondary components "s" are tied to the ones of the primaries "p" during the analysis. [(a)] Values and uncertainties from Nieva & Simón-Díaz (2011) or in the case of oxygen and silicon from Simón-Díaz (2010). [(b)] Protosolar nebula values and uncertainties from Asplund et al. (2009).

Table 5.6: Filter response curves and reference magnitudes used for synthetic photometry.

System	Johnson-Cousins			Strömgren				Hipparcos	Tycho		SDSS				
Passband	U	B	V	u	v	b	y	H_p	B_t	V_t	u'	g'	r'	i'	z'
Reference object	Vega			Vega				Vega	Vega		BD+17°4708				
$\mathrm{mag}_x^{\mathrm{ref}}$	0.041	0.023	0.027	1.444	0.195	0.034	0.03	0.038	0.04	0.023	10.56	9.64	9.35	9.25	9.23
References for $r_x(\lambda)$ and $\mathrm{mag}_x^{\mathrm{ref}}$	(1)			(2)				(1)	(1)		(3), (4)				

Notes. Flux-calibrated spectra for the two reference objects Vega and BD+17°4708 are taken from the CALSPEC database (`http://www.stsci.edu/hst/observatory/cdbs/calspec.html`).
References. (1) Bessell & Murphy (2012); (2) Bessell (2011); (3) `http://www.sdss.org/DR7/instruments/imager/`; (4) Smith et al. (2002).

particles. As a consequence, the quantity $\log(x/\mathrm{H})$ can change even if x stays constant. For a better comparison of metal abundances in stars with different helium content, we therefore prefer the notation that gives abundances relative to all elements.

5.3.3 Mass fractions and stellar parameters

Mass fractions of hydrogen (X), helium (Y), and metals (Z) are directly computed from the deduced atmospheric abundances. The stellar parameters mass M, age τ, and luminosity L are derived from T_{eff}, $\log(g)$, and $v\sin(i)$ by fitting single-star evolutionary tracks that account for stellar rotation ($M \leq 15\,M_\odot$: Georgy et al. 2013; otherwise: Ekström et al. 2012). The unknown inclination term $\sin(i)$ is replaced by its spherically averaged value $\pi/4$ when matching $v\sin(i)$ to the equatorial velocity v_{rot} predicted by the evolutionary tracks. Using the gravitational constant G, the stellar radius $R_\star$ follows then from the definition of the surface gravity Eq. (4.25). This information can be used to derive the spectroscopic distance d to the star by comparing observed and synthetic photometric magnitudes.

For an arbitrary photometric passband x with system response function $r_x(\lambda)$, the corresponding magnitude mag_x can be expressed as

$$\mathrm{mag}_x = -2.5\log\left(\frac{\int_0^\infty r_x(\lambda)f(\lambda)\lambda\mathrm{d}\lambda}{\int_0^\infty r_x(\lambda)f^{\mathrm{ref}}(\lambda)\lambda\mathrm{d}\lambda}\right) + \mathrm{mag}_x^{\mathrm{ref}}\,. \tag{5.9}$$

Here, λ is the wavelength, $f(\lambda)$ the object's flux arriving at the detector, and f^{ref} the respective flux of the reference object – which is typically Vega – with defined magnitude $\mathrm{mag}_x^{\mathrm{ref}}$. Note that photon-counting detectors are assumed here explaining the additional factor λ under the integral signs (for details see for instance the appendix E.4 in Bessell et al. 1998). We make currently use of available photometric observations in the Johnson-Cousins, Strömgren, Hipparcos, Tycho, and SDSS system. Table 5.6 contains all the relevant information on our implemented passbands in order to calculate a magnitude from a given input spectrum.

Equation (5.9) can now be used to derive the spectroscopic distance d to an object from its observed magnitude mag_x and a synthetic spectrum $F(\lambda)$, which describes the calibrated flux emanating from its surface. Under the assumption of a spherically symmetric object and photon

conservation, the energy penetrating a sphere of radius d (centered at the object's position) per unit time is identical to that emitted by the object, i.e.,

$$4\pi d^2 f(\lambda) = 4\pi R_\star^2 F(\lambda)\,. \tag{5.10}$$

Replacing the stellar radius $R_\star$ in Eq. (5.10) by means of Eq. (4.25) and substituting $f(\lambda)$ in Eq. (5.9) by the resulting expression yields a synthetic magnitude that can be matched to observation by an appropriate choice of the distance because the stellar mass M, flux $F(\lambda)$, and surface gravity $\log(g)$ are already fixed by spectroscopy.

To account for interstellar extinction, i.e., the absorption of photons along the line-of-sight, the synthetic flux is multiplied with a reddening factor $10^{-0.4A(\lambda)}$ where $A(\lambda)$ is the extinction in magnitude at wavelength λ. The final expression for the synthetic magnitude therefore reads as

$$\mathrm{mag}_x = -2.5\log\left(\frac{GM\int_0^\infty r_x(\lambda)10^{-0.4A(\lambda)}F(\lambda)\lambda\mathrm{d}\lambda}{d^2 g\int_0^\infty r_x(\lambda)f^{\mathrm{ref}}(\lambda)\lambda\mathrm{d}\lambda}\right) + \mathrm{mag}_x^{\mathrm{ref}}\,. \tag{5.11}$$

Fitzpatrick (1999) provides expressions for $A(\lambda)$ as a function of the color excess $E(B-V)$ and the extinction parameter $R_V = A(V)/E(B-V)$. Owing to the fact that R_V is normally set to its value for the diffuse interstellar medium, namely 3.1 (see for example Fitzpatrick 1999), interstellar extinction introduces typically only one additional parameter to the distance determination.

Photometric colors, i.e., the difference of two magnitudes, are independent of d by virtue of Eq. (5.11). Consequently, at least two complementary observed magnitudes are necessary in order to constrain the two free parameters d and $E(B-V)$. The Johnson-Cousins system with the visual magnitude V and colors $U-B$ and $B-V$ as observed quantities meets this condition, as does the combination of Strömgren colors $b-y$, $c_1 = (u-v)-(v-b)$, and $m_1 = (v-b)-(b-y)$ with an arbitrary absolute magnitude. To minimize dependencies on individual magnitudes and colors, the use of all available measurements is recommended, e.g., via a simultaneous fit.

In the case of SB2 systems, the flux contribution of the secondary component has to be considered as well. This is achieved by replacing $R_\star^2 F(\lambda)$ in Eq. (5.10) with $R_{\star,\mathrm{p}}^2 F_\mathrm{p}(\lambda)+R_{\star,\mathrm{s}}^2 F_\mathrm{s}(\lambda)$ with "p" denoting the primary component and "s" the secondary. This sum can be rewritten in terms of the spectroscopic fitting parameter $A_{\mathrm{eff,s}}/A_{\mathrm{eff,p}} = R_{\star,\mathrm{s}}^2/R_{\star,\mathrm{p}}^2$ (see Sect. 5.1.4) yielding the following substitutions in Eq. (5.11): $F(\lambda) \rightarrow F_\mathrm{p}(\lambda) + A_{\mathrm{eff,s}}/A_{\mathrm{eff,p}}F_\mathrm{s}(\lambda)$, $M \rightarrow M_\mathrm{p}$, $g \rightarrow g_\mathrm{p}$.

Error propagation for mass fractions and stellar parameters is analogous to the estimation of systematic uncertainties in Sect. 5.2.3. That is, for each pixel surrounded by the solid black line in Fig. 5.1, they are derived as outlined in this subsection. Minimum and maximum values of the resulting distributions are again interpreted as to define 99%-confidence intervals.

The test stars' positions in the $(T_\mathrm{eff}, \log(g))$ diagram are compared to evolutionary tracks in Fig. 5.2 and the resulting mass fractions and stellar parameters are given in Table 5.7. Note that the usage of single-star tracks to deduce stellar parameters of binary stars is, of course, justified only if the two binary components have not yet interacted and is otherwise an approximation.

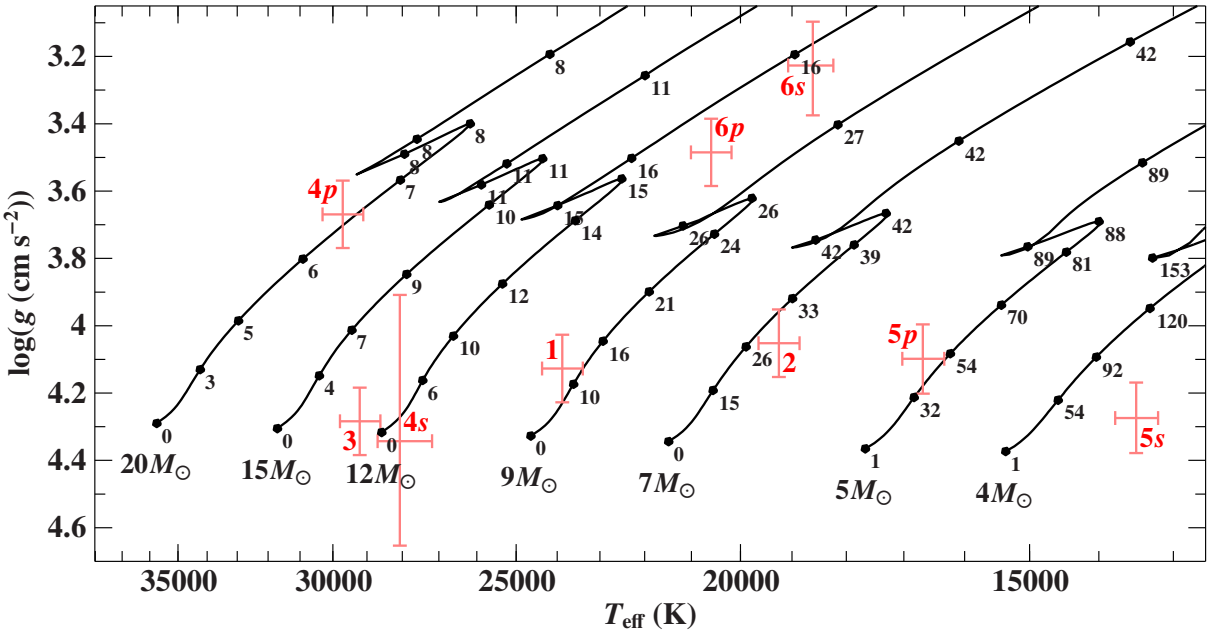

Figure 5.2: Position of the test stars in a $(T_{\rm eff}, \log(g))$ diagram. Overlaid are evolutionary tracks for non-rotating stars ($\Omega/\Omega_{\rm crit} = 0$) of metallicity $Z = 0.014$ and different initial masses ($M \leq 15\,M_\odot$: Georgy et al. 2013; otherwise: Ekström et al. 2012). Black filled circles and numbers mark the age in Myr. Red numbers correspond to those of Table 5.4. Error bars indicate 99%-confidence limits.

5.4 Discussion of the results

5.4.1 Single B- and late O-type stars in Orion

Focusing on a wide range of effective temperatures, we have selected three slowly rotating stars (HD 35299, HD 35912, and HD 37042) from the sample of Nieva & Simón-Díaz (2011) to check our method against previous studies.

As shown in Table 5.5, our atmospheric parameters have excellent agreement with those derived by Nieva & Simón-Díaz. Similarly, the results for the abundances of helium, carbon, and nitrogen are perfectly consistent with each other within the error bars, even though helium was kept fixed at the solar value in the study of Nieva & Simón-Díaz. The same applies to oxygen and silicon abundances by Simón-Díaz (2010). On the other hand, there are systematic discrepancies apparent for neon, magnesium, and iron that can be attributed either to differences in the synthetic models or in the analysis strategy. For instance, several Mg II lines, such as λ4481 Å have shown to be very sensitive to the replacement of pre-calculated opacity distribution functions, as used by Nieva & Simón-Díaz, with the more flexible concept of opacity sampling that is coherently used here throughout all computational steps, which explains the deviations in magnesium. The disagreements in neon and iron presumably arise from the underlying analysis techniques and in particular from how the microturbulence parameter is constrained. Nevertheless, it is extremely satisfying to see that the results of the two approaches match so well despite being based on contrary conceptional designs.

Table 5.7: Stellar parameters and mass fractions of the test stars.

#	M	τ	$\log(L/L_\odot)$	$R_\star$	d	Π^{-1}	$E(B-V)$	X	Y	Z
	($M_\odot$)	(Myr)		($R_\odot$)	(pc)		(mag)			
1	$9.3^{+0.5}_{-0.4}$	12^{+4}_{-7}	$3.75^{+0.08}_{-0.08}$	$4.4^{+0.6}_{-0.6}$	380^{+60}_{-60}	270^{+80}_{-60}	$0.012^{+0.029}_{-0.024}$	$0.677^{+0.024}_{-0.022}$	$0.311^{+0.022}_{-0.025}$	$0.012^{+0.002}_{-0.001}$
2	$6.7^{+0.3}_{-0.3}$	29^{+6}_{-8}	$3.30^{+0.08}_{-0.08}$	$4.0^{+0.6}_{-0.5}$	400^{+70}_{-70}	400^{+490}_{-150}	$0.006^{+0.047}_{-0.038}$	$0.685^{+0.042}_{-0.045}$	$0.301^{+0.043}_{-0.041}$	$0.014^{+0.002}_{-0.002}$
3	$12.9^{+2.0}_{-0.7}$	1^{+2}_{-1}	$4.08^{+0.14}_{-0.08}$	$4.3^{+0.9}_{-0.3}$	450^{+90}_{-60}	...	$0.175^{+0.014}_{-0.016}$	$0.709^{+0.016}_{-0.019}$	$0.279^{+0.020}_{-0.016}$	$0.012^{+0.001}_{-0.001}$
4p a	$20.7^{+2.9}_{-1.8}$	7^{+2}_{-1}	$4.96^{+0.17}_{-0.13}$	$11.7^{+2.3}_{-1.8}$	1040^{+470}_{-260}	1000^{+2300}_{-500}	$0.038^{+0.051}_{-0.049}$	$0.739^{+0.005}_{-0.003}$	$0.252^{+0.003}_{-0.005}$	$0.009^{+0.001}_{-0.001}$
4s a	$15.2^{+1.5}_{-1.2}$	0^{+1}_{-0}	$4.29^{+0.11}_{-0.11}$	$4.6^{+0.2}_{-0.3}$	...	...	...	...	...	...
4p b	$20.2^{+1.8}_{-1.5}$	7^{+1}_{-1}	$4.92^{+0.12}_{-0.12}$	$10.9^{+1.7}_{-1.6}$	960^{+240}_{-200}	1000^{+2300}_{-500}	$0.034^{+0.050}_{-0.048}$	$0.770^{+0.010}_{-0.011}$	$0.220^{+0.011}_{-0.010}$	$0.010^{+0.001}_{-0.002}$
4s b	$11.5^{+2.0}_{-0.5}$	0^{+10}_{-0}	$3.93^{+0.42}_{-0.07}$	$3.9^{+2.9}_{-0.1}$	...	...	...	...	...	...
4p c	$21.1^{+3.1}_{-1.9}$	7^{+2}_{-2}	$4.98^{+0.17}_{-0.13}$	$11.8^{+2.4}_{-1.8}$	1040^{+420}_{-230}	1000^{+2300}_{-500}	$0.037^{+0.049}_{-0.049}$	$0.769^{+0.009}_{-0.011}$	$0.222^{+0.010}_{-0.009}$	$0.010^{+0.001}_{-0.001}$
4s c	$13.0^{+0.6}_{-0.7}$	0^{+1}_{-0}	$4.08^{+0.07}_{-0.07}$	$4.2^{+0.1}_{-0.2}$	...	...	...	...	...	...
5p	$5.2^{+0.2}_{-0.2}$	48^{+10}_{-16}	$2.90^{+0.09}_{-0.09}$	$3.4^{+0.5}_{-0.5}$	470^{+70}_{-60}	550^{+1700}_{-240}	$0.156^{+0.018}_{-0.016}$	$0.660^{+0.031}_{-0.028}$	$0.327^{+0.028}_{-0.032}$	$0.014^{+0.001}_{-0.001}$
5s	$3.5^{+0.4}_{-0.2}$	49^{+47}_{-48}	$2.18^{+0.11}_{-0.13}$	$2.3^{+0.3}_{-0.4}$	...	...	...	...	...	...
6p	$10.4^{+1.3}_{-1.2}$	20^{+10}_{-4}	$4.18^{+0.15}_{-0.15}$	$9.7^{+1.6}_{-1.6}$	510^{+110}_{-100}	530^{+210}_{-120}	$0.109^{+0.032}_{-0.028}$	$0.700^{+0.004}_{-0.005}$	$0.290^{+0.004}_{-0.006}$	$0.011^{+0.001}_{-0.001}$
6s	$11.1^{+0.5}_{-2.1}$	18^{+14}_{-2}	$4.29^{+0.12}_{-0.22}$	$13.4^{+2.4}_{-3.2}$	...	...	...	...	...	...
$\odot^{(a)}$								0.716	0.270	0.014

Notes. Numbering according to Table 5.4. Except for the distance d and color excess $E(B-V)$, uncertainties cover only the effects induced by variations of 2% in $T_{\rm eff}$ and 0.1 dex in $\log(g)$ (see Sect. 5.3.3 for details) and are formally taken to be 99%-confidence limits. Errors in distance and color excess also account for uncertainties in photometric magnitudes and colors. Negative values for $E(B-V)$ imply that synthetic spectra have to be de-reddened instead of reddened in order to best reproduce the photometric observations. Owing to the assumption of a homogeneous chemical composition, abundances of the secondary components "s" are tied to the ones of the primaries "p" during the analysis. Parallaxes Π are from Hipparcos (van Leeuwen 2007), while their original formal errors, which are assumed to be 1σ, are converted to 99%-confidence intervals here. $^{(a)}$ Protosolar nebula values from Asplund et al. (2009).

5.4.2 Spectroscopic binaries

As a first application to SB2 systems, we have analyzed the composite spectra of three binary systems. While the lines of the two components are sharp and very well separated in our spectrum of HD 119109, the opposite is true for HD 213420 (see Figs. C.2.3a–C.2.3i). In the case of HD 75821, we have further derived parameters from spectra taken at three distinct orbital phases to investigate its influence on the results.

HD 119109 (#5): To our knowledge, there is no hint for binarity in the literature for this system so far. Nevertheless, our spectrum shows that this is doubtlessly a SB2 system owing to the many lines that appear twice in the spectrum (see Figs. C.2.3a–C.2.3i). Given the high quality of our observation and the opportune orbital phase, parameters of both components can be reliably deduced. The system turns out to be composed of two relatively unevolved (see Fig. 5.2), coeval ($\tau_{\rm p} = 48^{+10}_{-16}$ Myr, $\tau_{\rm s} = 49^{+47}_{-48}$ Myr) late-type B-stars of masses $M_{\rm p} = 5.2 \pm 0.2\,M_\odot$ and $M_{\rm s} = 3.5^{+0.4}_{-0.2}\,M_\odot$ when using single-star evolutionary tracks. The corresponding squared ratio of radii, $(R_{\star,{\rm s}}/R_{\star,{\rm p}})^2 = 0.45^{+0.29}_{-0.18}$, is consistent with the surface ratio $A_{\rm eff,s}/A_{\rm eff,p} = 0.642^{+0.015({\rm stat.})+0.027({\rm sys.})}_{-0.013({\rm stat.})-0.028({\rm sys.})}$, as is the spectroscopic distance, $d = 470^{+70}_{-60}$ pc, with the parallax, $\Pi^{-1} = 550^{+1700}_{-240}$ pc. The chemical composition resembles that of the single stars studied

in Sect. 5.4.1.

Using published radial velocity measurements, Tetzlaff et al. (2011) have proposed that this object is a runaway star with high probability based on its peculiar space motion. This conclusion should be considered as uncertain as long as the actual system velocity of this binary is unknown.

HD 213420 (#6): This well-known binary system with a period of about 880 days and a radial velocity semi-amplitude of $9\,\mathrm{km\,s^{-1}}$ (Pourbaix et al. 2004) is a clear SB2 system, given the broad absorption features superimposed to He I λ4438 Å, λ6678 Å, C II λ4267 Å, Mg II λ4481 Å, Si III λ4553 Å, λ4568 Å, and S II λ5454 Å (see Figs. C.2.3a–C.2.3i). Although the signatures of the secondary component are weak and thus only detectable in the case of a high S/N, they are apparently sufficient to determine reasonable atmospheric parameters for the companion because the resulting stellar parameters paint a consistent physical picture: In addition to the finding that the ages of both components (with masses $M_\mathrm{p} = 10.4^{+1.3}_{-1.2}\,M_\odot$, $M_\mathrm{s} = 11.1^{+0.5}_{-2.1}\,M_\odot$) are in perfect agreement ($\tau_\mathrm{s} = 20^{+10}_{-\ 4}$ Myr, $\tau_\mathrm{p} = 18^{+14}_{-\ 2}$ Myr), the spectroscopic parameter $A_\mathrm{eff,s}/A_\mathrm{eff,p} = 0.936^{+0.014+0.069}_{-0.015-0.060}$ lies within the uncertainty interval of the squared ratio of the evolutionary-track radii, $(R_{\star,\mathrm{s}}/R_{\star,\mathrm{p}})^2 = 1.9^{+1.9}_{-1.1}$. The spectroscopic distance of the system, $d = 510^{+110}_{-100}$ pc, finally fits to its parallax, $\Pi^{-1} = 530^{+210}_{-120}$ pc. Apart from a slight tendency to a lower metallicity (see Table 5.7), the chemical composition agrees with the reference stars of Sect. 5.4.1.

HD 75821 (#4): This eclipsing binary has a period of about 26.3 days and a radial velocity semi-amplitude of $92\,\mathrm{km\,s^{-1}}$ (Mayer et al. 1997).

The spectrum best suited for the spectral analysis is the second one (b) in Table 5.5, since the spectral line separation is largest in this case, which reveals several pure and unblended features of the companion (see Figs. C.2.3a–C.2.3i). Reliable atmospheric and stellar parameters for both components are, hence, determinable whereby the latter assume that single-star evolutionary tracks are appropriate. Starting from this premise, the system consists of two coeval components ($\tau_\mathrm{p} = 7^{+1}_{-1}$ Myr, $\tau_\mathrm{s} \leq 10$ Myr): a massive primary ($M_\mathrm{p} = 20.2^{+1.8}_{-1.5}\,M_\odot$), which is slightly evolved, and a less massive secondary ($M_\mathrm{s} = 11.5^{+2.0}_{-0.5}\,M_\odot$), which is almost unevolved (see Fig. 5.2). The spectroscopic distance $d = 960^{+240}_{-200}$ pc lies well within the 99%-uncertainty range of the parallax, $\Pi^{-1} = 1000^{+2300}_{-\ 500}$ pc. Finally, the spectroscopically deduced effective surface ratio $A_\mathrm{eff,s}/A_\mathrm{eff,p} = 0.218^{+0.003+0.014}_{-0.002-0.011}$ agrees well with the squared ratio of the evolutionary-track radii, $(R_{\star,\mathrm{s}}/R_{\star,\mathrm{p}})^2 = 0.13^{+0.41}_{-0.04}$, and is further consistent with the photometric light curve (Mayer et al. 2014). The elemental abundances of the system are in line with the single stars except for the relatively low helium, nitrogen, and oxygen content (see Table 5.5).

The heavily blended and, hence, almost vanishing imprints of the companion on the first (a) and third (c) spectrum are insufficient to properly constrain the secondary component's atmospheric parameters. Instead, unphysical values and large systematic uncertainties, which are induced by variations of T_eff and $\log(g)$ of the primary, are derived for the secondary's T_eff and $\log(g)$. These error margins are, on the one hand, a direct consequence of strong correlations among certain parameters and, on the other hand, related to the fact that contributions of the secondary component barely affect the spectrum at the corresponding orbital phases. In a simplified picture, increasing the primary's T_eff and decreasing its $\log(g)$ at the same time causes the He II lines to become considerably deeper than actually observed, while the He I lines still fit nicely. To compensate for this, $A_\mathrm{eff,s}/A_\mathrm{eff,p}$ and, hence, the influence of the secondary component, has

to be significantly increased to fill the He II lines with the continuum which thus weakens them again. However, this makes some spectral lines of the secondary component substantially too strong, which, in turn, is corrected for by smearing them out via a larger $v \sin(i)$ or ζ that finally leads to a more uncertain determination of $v_{\rm rad}$, given the high degree of line blending at these particular orbital phases.

However, the primary's properties and the surface ratio $A_{\rm eff,s}/A_{\rm eff,p}$ are nicely recovered in all three orbital phases, which gives us confidence that the presented method is generally able to determine them from one single spectrum.

5.5 Summary

In this Chapter, a novel objective method to analyze single or composite spectra of early-type stars is presented. It is based on fitting synthetic spectra to observation by using the standard concept of χ^2 minimization, which requires the wavelength-dependent noise of the spectrum to be known. Therefore, a simple but precise way of estimating the local noise has been developed (see Sect. 5.2.1). To facilitate fast and efficient analyses, we make use of pre-calculated grids of synthetic spectra, instead of computing them on demand during the fitting procedure. To sample the entire multi-dimensional parameter space at once, we exploit the unique spectral properties of early-type stars, such as the low density of lines, which reduces the number of models required by several orders of magnitude. In this way, a simultaneous fit of all parameters is possible which has the great advantage that cumbersome iterations by hand or the risk of missing the global best solution are avoided. Moreover, parameters are not only constrained from a subset of available lines but from all useful features in the spectrum. The extension to composite spectra of double-lined binary systems proves extremely valuable in the future, given the high frequency of SB2 systems among early-type stars (see Sana et al. 2012; Chini et al. 2012). In contrast to spectral disentangling techniques like those of Simon & Sturm (1994) or Hadrava (1995), the method presented here allows for – at least – parameters of the primary and the components' effective surface ratio to be inferred from single-epoch spectra alone.

Statistical and systematic uncertainties of our method are discussed (see Sect. 5.2.3). The former are based here on a clearly defined mathematical measure, namely the χ^2 statistics, while the latter on experience. We show that systematic effects generally dominate in the high-quality regime of our observations. The analysis of a larger sample of stars thus enables us to identify possible shortcomings in our models and to derive results with significantly reduced statistical scatter.

As a case study, we have determined parameters of three well-known stars in the Orion region that turn out to be in excellent agreement with previous studies. Additionally, three binary systems have been analyzed with all of them yielding very conclusive results. Consequently, we are now in a position to homogeneously analyze large samples of early-type stars in relatively short times. The results of a comprehensive investigation of 63 nearby mid B-type to late O-type stars are presented in Chapter 7.

6 Impact of different Balmer line Stark broadening theories on the analysis*

The optical spectra of B-type and late O-type stars are dominated by pronounced absorption lines of hydrogen. Because these spectral features are attributed to the Balmer series of atomic transitions, they are denoted Balmer lines. The cores of these lines are primarily affected by the star's effective temperature $T_{\rm eff}$, while their conspicuously broad wings are the main spectral indicator for the surface gravity $\log(g\,(\mathrm{cm\,s^{-2}}))$ owing to the density-dependent Stark broadening in the stellar plasma. Because the determination of fundamental stellar parameters such as distance, mass, age, or evolutionary stage is based on the surface gravity, the significance of the Balmer lines for our understanding of the nature of stars is enormous.

Tables for Stark-broadened Balmer line profiles and detailed information on their derivation are available in the literature. The most commonly used are those of Vidal et al. (1973, VCS tables) which have successfully reproduced observations for various conditions in stellar atmospheres. The VCS tables used in this work were calculated by Schöning (priv. comm.) who modified the VCS program (Vidal et al. 1971a) to be able to treat Balmer series members up to a quantum number of 30. To provide reliable tables in low density media like solar flares and to account for the progress in high-resolution spectroscopy, Stehlé & Hutcheon (1999, SH tables) produced extensive tabulations of hydrogen line profiles based on improved input physics. A study by Cowley & Castelli (2002) revealed no perceptible changes in the Balmer profiles in low-mass stars when switching from VCS to SH broadening tables.

However, the situation is different for early-type stars. The purpose of this Chapter is to quantify the uncertainties in spectroscopic analyses resulting from the use of the broadening profiles either by VCS or SH (Sect. 6.1), to discuss the implications on the determination of stellar parameters (Sect. 6.2), to present (currently inconclusive) attempts to prefer one set of tables to the other (Sect. 6.3), and to summarize our conclusions (Sect. 6.4).

6.1 Comparison of VCS with SH

The two theories differ principally in their treatment of the broadening by the ions, in this case protons. In the VCS unified theory (Vidal et al. 1971b), the ions are quasistatic with a distribution given by that of Hooper (1968). By contrast, the dynamical treatment of the ions by SH relies on the Model Microfield Method first developed by Brissaud & Frisch (1971). Here the proton field jumps at temporal frequencies determined from the same Hooper distribution. Thus the wings are similar in both cases with the line centers having considerably less structure in the SH calculations as the Stark components are smeared out by the ionic motions. The convolution and renormalization of the profiles with the Doppler profile then leads to the differences in the wings described below.

The SH profiles are in good agreement with the benchmark Monte Carlo simulations of Cardenoso & Gigosos (1997) and, e.g., the experiment of Acon et al. (2001) but the errors are still of the order of several per cent. Unfortunately, the more accurate values of Gigosos & Cardenoso (1996) are only available for the first three members of the sequence.

*This Chapter is heavily based on the paper by Irrgang et al. (2014a).

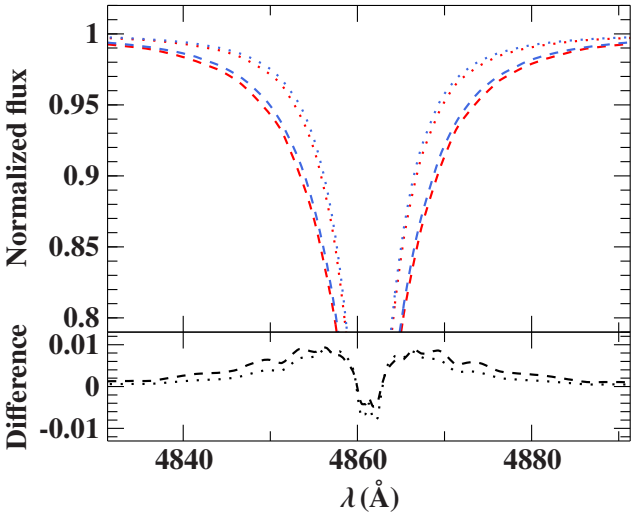

Figure 6.1: Comparison of synthetic Hβ line profiles computed with broadening tables by VCS (red) and SH (blue) revealing significant deviations in the wings. The surface gravity $\log(g\,(\mathrm{cm\,s^{-2}}))$ is 3.6 (dotted) and 4.2 (dashed) while all other parameters are kept fixed (T_{eff} = 25 000 K, $\log(n(\mathrm{He}))$ = −0.95, ξ = 0). The trends shown here are representative for all Balmer lines and combinations of model parameters.

Table 6.1: *Top*: Differences Δ (with respect to the parameters given in the *"Input" row*) obtained from fitting a synthetic input spectrum with VCS broadened Balmer lines with the same models except for SH broadened Balmer lines (*"Δ(VCS → SH)" row*) and vice versa (*"Δ(SH → VCS)" row*). *Bottom*: Average and standard deviation of SH minus VCS based results obtained from fitting spectra of 63 mid B-type to late O-type stars. Results on individual objects are given in Table D.2.

	T_{eff}	$\log(g)$	v_{rad}	$v\sin(i)$	ζ	ξ	$\log(n(x))$										
	(K)	(cgs)		(km s^{-1})			He	C	N	O	Ne	Mg	Al	Si	S	Ar	Fe
Input	15 000	4.250	0.0	10.0	10.0	2.00	−1.06	−3.70	−4.30	−3.20	−4.00	−4.70	−5.60	−4.60	−4.80	…	−4.60
Δ(VCS → SH)	1.1%	0.127	0.0	0.2	−0.7	0.04	−0.01	0.02	0.01	0.03	0.02	0.01	0.02	−0.01	0.02	…	0.02
Δ(SH → VCS)	−1.0%	−0.125	0.0	−0.4	0.9	−0.02	0.00	−0.03	−0.02	−0.03	−0.02	0.00	−0.01	0.01	−0.02	…	−0.03
Input	15 000	3.750	0.0	10.0	10.0	2.00	−1.06	−3.70	−4.30	−3.20	−4.00	−4.70	−5.60	−4.60	−4.80	…	−4.60
Δ(VCS → SH)	1.2%	0.126	0.0	0.3	−0.7	0.05	−0.01	0.02	0.01	0.03	0.01	0.01	0.01	0.00	0.02	…	0.02
Δ(SH → VCS)	−1.2%	−0.126	0.0	−0.3	0.8	−0.04	0.01	−0.02	−0.02	−0.03	−0.01	−0.01	−0.02	0.00	−0.02	…	−0.04
Input	20 000	4.250	0.0	10.0	10.0	2.00	−1.06	−3.70	−4.30	−3.20	−4.00	−4.70	−5.60	−4.60	−4.80	−5.60	−4.60
Δ(VCS → SH)	1.1%	0.128	0.0	0.4	−1.2	0.22	−0.02	0.01	0.01	0.01	0.01	−0.01	0.01	−0.02	0.01	0.02	0.02
Δ(SH → VCS)	−1.2%	−0.134	0.0	−0.9	1.6	−0.20	0.03	−0.01	−0.02	−0.02	−0.02	0.00	−0.01	0.00	−0.01	−0.03	−0.03
Input	20 000	3.750	0.0	10.0	10.0	2.00	−1.06	−3.70	−4.30	−3.20	−4.00	−4.70	−5.60	−4.60	−4.80	−5.60	−4.60
Δ(VCS → SH)	1.0%	0.117	0.0	0.3	−0.8	0.15	−0.02	0.01	0.02	0.01	0.01	−0.01	0.01	0.00	0.01	0.02	0.02
Δ(SH → VCS)	−1.1%	−0.121	0.0	−0.5	1.0	−0.16	0.03	−0.01	−0.02	−0.02	−0.01	0.01	−0.02	−0.01	−0.02	−0.02	−0.03
Input	25 000	4.250	0.0	10.0	10.0	4.00	−1.06	−3.70	−4.30	−3.20	−4.00	−4.70	−5.60	−4.60	−4.80	−5.60	−4.60
Δ(VCS → SH)	0.9%	0.123	0.0	0.2	−1.0	0.20	−0.02	0.00	0.02	0.02	0.01	0.00	0.01	0.01	0.02	0.01	0.02
Δ(SH → VCS)	−1.0%	−0.128	0.0	−0.4	1.0	−0.20	0.02	0.00	−0.01	−0.02	−0.02	0.00	−0.01	−0.01	−0.02	−0.04	−0.01
Input	25 000	3.750	0.0	10.0	10.0	4.00	−1.06	−3.70	−4.30	−3.20	−4.00	−4.70	−5.60	−4.60	−4.80	−5.60	−4.60
Δ(VCS → SH)	1.0%	0.107	0.0	0.1	−0.6	0.12	−0.02	0.01	0.01	0.02	0.01	0.00	0.01	0.01	0.02	0.00	0.02
Δ(SH → VCS)	−1.1%	−0.111	0.0	−0.2	0.6	−0.12	0.01	−0.01	−0.01	−0.01	−0.01	0.00	−0.01	−0.01	−0.02	0.04	−0.01
Input	30 000	4.250	0.0	10.0	10.0	4.00	−1.06	−3.70	−4.30	−3.20	−4.00	−4.70	−5.60	−4.60	−4.80	…	−4.60
Δ(VCS → SH)	0.9%	0.118	0.0	0.2	−0.8	0.17	−0.01	0.01	0.01	0.01	0.01	0.01	0.00	0.01	0.02	…	0.00
Δ(SH → VCS)	−1.0%	−0.117	0.0	−0.4	0.8	−0.15	0.00	−0.02	−0.01	−0.01	−0.01	0.00	−0.01	−0.01	−0.02	…	−0.01
Input	30 000	3.750	0.0	10.0	10.0	4.00	−1.06	−3.70	−4.30	−3.20	−4.00	−4.70	−5.60	−4.60	−4.80	…	−4.60
Δ(VCS → SH)	0.9%	0.088	0.0	0.1	−0.5	0.13	−0.01	0.01	0.01	0.00	0.00	0.00	0.00	0.01	0.00	…	0.00
Δ(SH → VCS)	−1.0%	−0.086	0.0	−0.1	0.4	−0.09	0.00	−0.01	0.00	0.00	0.00	0.00	−0.01	0.00	−0.01	…	0.00
Δ(VCS → SH)	1.2%	0.129	0.0	0.0	−0.6	0.12	−0.02	0.01	0.01	0.02	0.01	0.00	0.02	0.01	0.02	0.04	0.02
	±0.5%	±0.027	±0.4	±1.3	±3.2	±0.13	±0.02	±0.02	±0.01	±0.02	±0.02	±0.02	±0.02	±0.02	±0.02	±0.02	±0.03

Notes. The abundance $n(x)$ is given as fractional particle number of species x with respect to all elements. Argon lines are not visible for all temperatures.

To estimate the impact of the different sets of broadening tables on the line profiles, we compute synthetic spectra following the hybrid strategy as outlined in Sect. 4.3.4. This approach has been checked against full non-LTE calculations for instance in Nieva & Przybilla (2007) and Przybilla et al. (2011) and was found to be valid. Similarly, the hydrogen model atom used here (see Przybilla & Butler 2004) has been thoroughly tested making us very confident that the following model-versus-observation comparisons are not significantly affected by shortcomings in the synthetic spectra.

Figure 6.1 shows a comparison of synthetic Hβ line profiles computed with broadening tables by VCS and SH, respectively. The striking deviations in the wings are representative for all Balmer lines and independent of the specific choice of model parameters. Investigations based on VCS will therefore give systematically lower surface gravities than those relying on SH because the line profiles of the latter are always narrower thus requiring larger $\log(g)$ values to compensate for this tendency.

To quantify the impact of this trend on atmospheric parameters, tests with model spectra have been conducted. For eight different combinations of effective temperature and surface gravity, which roughly cover the zero- and terminal-age main sequence of mid B-type to late O-type stars, synthetic spectra with VCS broadened Balmer lines have been fitted with the same models except for SH broadened Balmer lines and vice versa. The resulting differences in the model parameters are given in Table 6.1 (top). As expected, there is an offset (of about 0.117 dex) in the surface gravity when switching from VCS to SH broadening tables. Moreover, the effective temperature is increased by approximately 1%. The effects on the other parameters are either nonexistent ($v_{\rm rad}$), small to negligible ($\{n(x)\}$), or of little relevance for physical interpretations (ζ, $v\sin(i)$, ξ).

In order to investigate the influence of this discrepancy on spectroscopic analyses of real observations, a sample of 63 mid B-type to late O-type stars – containing also eight SB2 systems – has been analyzed with VCS as well as SH broadened Balmer line models employing the method of Chapter 5. While the star sample is characterized and discussed in detail with regard to atmospheric and fundamental properties in Chapter 7, we focus here solely on the Stark-broadening issue and its consequences on derived quantities. Table D.2 lists therefore the differences in atmospheric parameters obtained from fitting the observed spectra – typically restricted to the spectral range [3940 Å, 7000 Å] – with models using SH or VCS broadening tables, respectively. In full agreement with the previous tests, the surface gravities and effective temperatures of the SH based analyses exceed their VCS counterparts on average by 0.129 ± 0.027 dex and 1.2 ± 0.5% with the offset in $\log(g)$ tending to be slightly smaller for higher temperatures. Likewise, the differences in the remaining parameters (see bottom of Table 6.1 for the average and standard deviation of the full sample) follow closely the trends and expectations raised by the previous tests, i.e., these parameters are hardly affected when switching from VCS to SH broadening.

6.2 Implications for stellar parameters

In general, the stellar parameters mass M, age τ, luminosity L, and radius $R_\star$ cannot be measured directly but have to be derived from comparing the star's position in a $(T_{\rm eff}, \log(g))$ diagram with theoretically predicted evolutionary tracks (see Fig. 6.2). The basic relationships

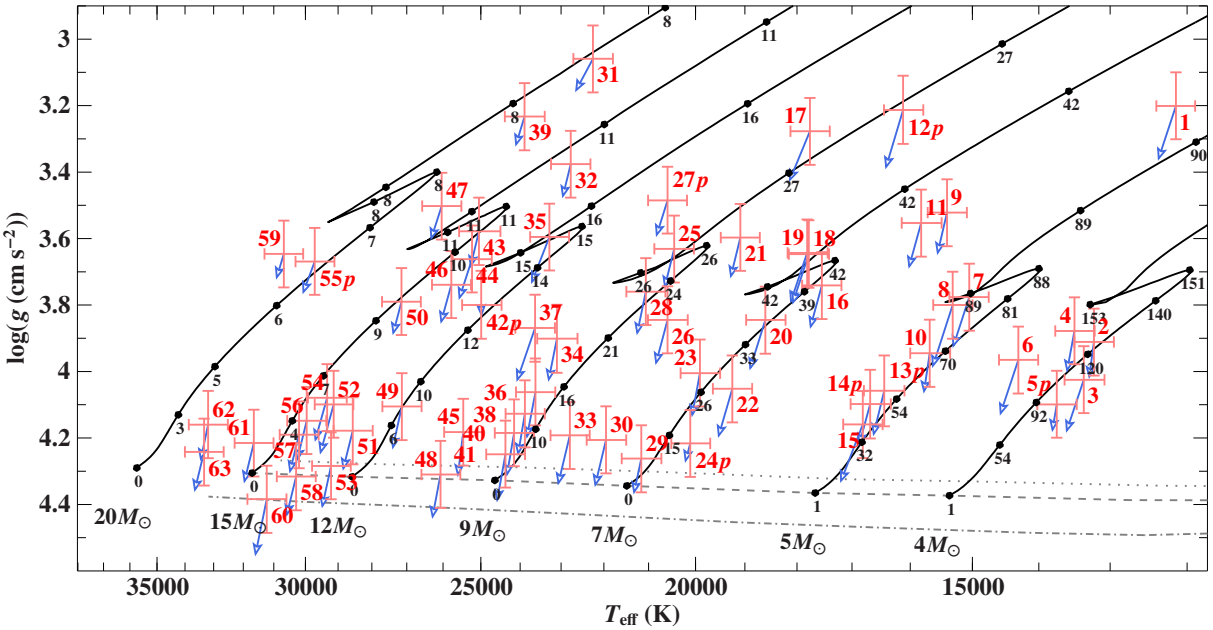

Figure 6.2: Position of the 63 sample stars in a $(T_{\rm eff}, \log(g))$ diagram. Overlaid are evolutionary tracks for non-rotating stars ($\Omega/\Omega_{\rm crit} = 0$) of metallicity $Z = 0.014$ and different initial masses ($M \leq 15\,M_\odot$: Georgy et al. 2013; otherwise: Ekström et al. 2012). Black filled circles and numbers mark the age in Myr. Red numbers correspond to those of Table 7.1. Primary components of a SB2 system are denoted by "p". Error bars indicate 99%-confidence limits. Blue arrows illustrate the shift caused by using SH instead of VCS broadened Balmer lines during the spectral analysis. The gray lines mark the loci of the zero-age main sequence for $\Omega/\Omega_{\rm crit} = 0$, $Z = 0.014$ (dashed), $\Omega/\Omega_{\rm crit} = 0.6$, $Z = 0.014$ (dotted), and $\Omega/\Omega_{\rm crit} = 0$, $Z = 0.006$ (dashed-dotted) according to Georgy et al. (2013).

to convert these quantities (except for τ) into each other are the definition of the luminosity (Eq. (2.6)) and the surface gravity (Eq. (4.25)). Combining atmospheric and stellar parameters with photometric measurements allows the spectroscopic distance d and the color excess $E(B-V)$ to be estimated (see Sect. 5.3.3).

The impact of the two different sets of Balmer line broadening tables on the determination of mass and age with the help of evolutionary tracks by the Geneva group is shown in Fig. 6.2. The systematic shift of SH based analyses towards higher effective temperatures and surface gravities typically lowers the inferred value for the stellar mass especially in the high temperature regime where evolutionary tracks of different masses lie close to each other. The effects on the age also depend on the position in the $(T_{\rm eff}, \log(g))$ plane due to the behavior of the isochrone curves. For instance, early B-type stars on the main sequence are judged younger while late B-type stars beyond the main sequence are older. Finally, the increase in the surface gravity leads to substantially smaller stellar radii by virtue of Eq. (4.25) and therefore to lower luminosities because it outweighs the higher temperature in Eq. (2.6).

Equation (5.11) implies that d is proportional to $\sqrt{M}$, $\sqrt{F}$, and $1/\sqrt{g}$. Distance estimates based on atmospheric parameters with SH broadened Balmer lines are therefore systematically lower than those with VCS given that the respective lower masses and higher surface gravi-

ties dominate the increased flux caused by the higher temperature. Making use of measured parallaxes, this fact can in principle be exploited to argue for or against one of the two sets of broadening tables (see Sect. 6.3.3).

6.3 Evaluation criteria

As outlined before, the two sets of Balmer line broadening tables considered here differ substantially in the wings of the spectral lines and thus yield discrepant results for the atmospheric parameters $T_{\rm eff}$ and $\log(g)$ which, in turn, affect the derived stellar parameters. Motivated by these diverging predictions, we have examined four evaluation criteria in order to compare the consistency of the two sets of tables.

6.3.1 Quality of spectral fits

The most basic criterion is the quality of the spectral fit, i.e., the capability of the model to reproduce an observed spectrum. A standard χ^2 criterion is used to objectively measure the goodness of fit. The entire spectral range instead of only the regions around the Balmer lines is hereby considered. This is due to the fact that every spectral line is more or less affected when switching from VCS to SH broadened Balmer lines because of associated changes in the effective temperature and surface gravity. Comparing the individual χ^2 values with each other, we find that – without any correlation with $T_{\rm eff}$ or $\log(g)$ – VCS models surpass SH models for 37 out of 63 reference stars while the converse is true for the remaining 26 objects. Furthermore, the relative χ^2 differences are on average below 1% showing that these numbers are statistically insignificant.

6.3.2 Evolutionary status

The evolutionary status of an object is used as second evaluation criterion. As already mentioned in Sect. 6.2, it is deduced from the star's position in a $(T_{\rm eff}, \log(g))$ diagram in combination with theoretically predicted evolutionary tracks. As expected and seen in Fig. 6.2, the vast majority of the reference stars is still on the main sequence and only few stars are more evolved. Using SH instead of VCS broadened Balmer lines during the spectral analysis shifts the stars towards the ZAMS and thus into a less evolved stage. In general, this fact does not help much to discriminate between the two sets of tables since we lack independent and sufficiently accurate clues to the stars' individual evolutionary status. Nevertheless, the ZAMS, which is a function of metallicity and initial stellar rotation, naturally separates physical from unphysical states hence offering the possibility to reveal inconsistencies between spectroscopically derived atmospheric parameters and theoretical evolutionary tracks. Figure 6.2 shows that the number of stars that tend to lie in the unphysical region below the ZAMS is noticeably larger when using SH broadening tables. Although this fact argues for the VCS broadening tables, one has to stress that this is again only a slight tendency given the size of the error bars in Fig. 6.2, the unknown uncertainty in the position of the evolutionary tracks and thus also of the ZAMS, and the fact that some of the reference stars may for instance be unrecognized blue stragglers and hence not non-interacting, main-sequence stars as assumed so far.

6.3.3 Spectroscopic distances versus parallaxes

In contrast to the evolutionary status, the spectroscopic distance can be checked against an independent measurement, namely the Hipparcos parallax. For the latter, both reductions – the new one by van Leeuwen (2007) as well as the original one by Perryman & ESA (1997) – are considered here. Figure 6.3 shows this comparison for a selected subset of the 63 reference stars. The following selection criteria have been applied:

1) Stars lying in the unphysical region below the ZAMS in the $(T_{\rm eff}, \log(g))$ diagram (see Fig. 6.2) are omitted since their precise mass and nature and, hence, their spectroscopic distance are uncertain.

2) Objects known or suspected to be single-lined spectroscopic binary systems are excluded because the small but perhaps non-negligible flux contribution of the secondary component is unknown and, thus, cannot be accounted for in the spectroscopic distance determination.

3) For the reduction by van Leeuwen, we regard a parallax measurement as reliable only if it exceeds its respective uncertainty by at least a factor of 5. This limit is lowered to 2.5 in the case of the Perryman & ESA reduction to compensate for its larger formal uncertainties that would otherwise exclude too many stars.

4) Stars are considered only if they have not shown any potential issues – such as strange line profiles – during the spectroscopic analysis.

By definition of the unit of parsec, distances d in parsec can be converted to parallaxes Π in units of milliarcsecond according to the identity relation $\Pi(d) = 1000/d$. Stars for which the measured parallax Π is in agreement with the spectroscopic distance d fall thus on the identity relation in Fig. 6.3. In order to quantify the goodness of the match between measured parallaxes (with 1σ uncertainty δ_Π) and spectroscopic distances (with 1σ uncertainty δ_d), one may therefore measure the minimum deviation of the individual data points in Fig. 6.3 from the identity curve. To weight the deviations in both coordinates with their respective uncertainties, we extend the standard χ measure to two dimensions by defining for each star i the following quantity $\chi_{2{\rm D},i}$:

$$\chi_{2{\rm D},i} = \mathrm{sign}\left(\Pi(d_i) - \Pi_i\right) \sqrt{\left(\frac{d_i - d_{{\rm min},i}}{\delta_{d,i}}\right)^2 + \left(\frac{\Pi_i - \Pi(d_{{\rm min},i})}{\delta_{\Pi,i}}\right)^2}\,. \tag{6.1}$$

Here, $(d_{{\rm min},i}, \Pi(d_{{\rm min},i}))$ is that point on the identity relation that minimizes the square root in Eq. (6.1), i.e., that yields for the point (d_i, Π_i) the smallest weighted distance to the identity curve. The sign term ensures that points above the identity relation in Fig. 6.3 are assigned a positive $\chi_{2{\rm D}}$ while points below a negative one. Asymmetric distance errors δ_d^+ and δ_d^- are accounted for by using δ_d^+ if $d_{{\rm min},i} > d_i$ and δ_d^- otherwise.

For the new Hipparcos reduction, it is obvious from Fig. 6.3 that the Balmer line broadening issue cannot be resolved with the currently available observational data nor is it possible to give any clear preference. The reason for this is that the absolute discrepancies between spectroscopic distances and measured parallaxes are very similar in both cases as can be seen from the average $\chi^2_{2{\rm D}}$ values which are 4.08 for VCS and 3.72 for SH. These numbers are a consequence

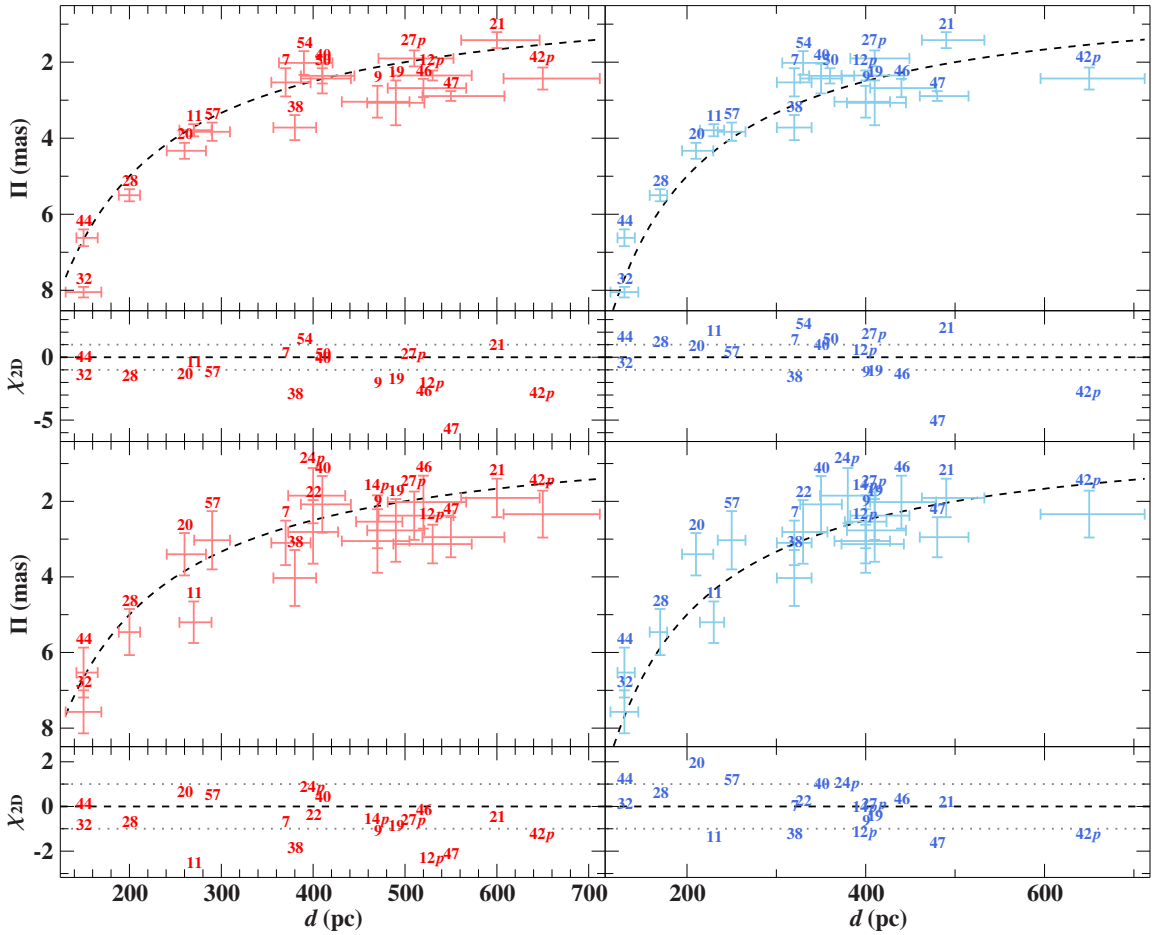

Figure 6.3: Comparison of HIPPARCOS parallaxes Π (*top*: new reduction by van Leeuwen 2007, *bottom*: original reduction by Perryman & ESA 1997) with spectroscopic distances d derived via VCS (*left*) or SH (*right*) analyses. The identity relation is symbolized by the dashed line. Numbers label stars according to Table 7.1. SB2 systems are denoted by "p". Parallax uncertainties are the original formal values while the 99%-confidence uncertainties in the distance (see Sect. 5.3.3) have been converted to 1σ errors here. Residuals χ_{2D} are defined by Eq. (6.1).

of the fact that VCS based distance estimates typically exceed the parallactic distance while their SH counterparts lie below it.

The situation is not much more conclusive in the case of the original reduction. This is mainly because the formal uncertainties for the parallaxes are significantly larger than in the new reduction. Therefore, the average χ^2_{2D} values for both, VCS (1.37) as well as SH (0.95), are substantially reduced making it impossible to draw any statistically significant conclusion. Nevertheless, from these numbers and visual inspection of Fig. 6.3, we note that there is at least a slight tendency towards SH.

6.3.4 Eclipsing binaries

Double-lined eclipsing binaries are probably the most promising candidates to solve the Balmer line broadening issue because they allow for an almost direct determination of absolute stellar

masses and radii via a combined investigation of the binary system's photometric light curve and radial velocity curve. The resulting surface gravity (see Eq. (4.25)) can then be compared to predictions from spectroscopic analyses that rely either on VCS or SH broadening tables.

Among our sample of 63 stars, there is one known eclipsing binary system, namely KX Vel (HD 75821, #55). Based on the latest study by Mayer et al. (2014), this system's primary component has a $\log(g)$ of 3.46 ± 0.03. However, given the low number of data points in the radial velocity as well as light curve, the surface gravity is not as tightly constrained as the small formal uncertainty suggests. In particular, the minimum of the eclipse is not completely sampled making the results for the inclination of the system and for the ratio of radii uncertain (see Mayer et al. 2014 for details) and also a thorough error estimation impossible. The above number compares with the spectroscopically deduced surface gravity of $\log(g) = 3.669^{+0.005(\mathrm{stat.})+0.100(\mathrm{sys.})}_{-0.004(\mathrm{stat.})-0.100(\mathrm{sys.})}$ (see test object #4 in Chapter 5) based on VCS broadened Balmer lines and its SH counterpart $3.768^{+0.004+0.100}_{-0.006-0.100}$ again tending to favor the VCS broadening tables. However, given the incomplete sampling of the eclipse and thus the relatively poor constraints on the geometric properties of the binary system, this result is far from being conclusive. More and better studied eclipsing binary systems are therefore necessary to draw final conclusions.

6.4 Summary

The spectroscopic parameter determination for early-type stars relies heavily on the detailed shape of the Balmer lines. In particular, the wings of these lines are the dominating spectral indicator with respect to the surface gravity due to Stark broadening. The major result of this Chapter is that the frequently used broadening tables by Vidal et al. (1973) and Stehlé & Hutcheon (1999) give considerably different wings for the Balmer lines. The corresponding effects on the atmospheric parameters are most serious for the effective temperature ($\sim$0.7–1.7%) and for the surface gravity ($\sim$0.11–0.16 dex) while all other parameters remain relatively unaffected. In particular, the uncertainty in the surface gravity can have far reaching consequences for the derived stellar parameters and spectroscopic distances. Attempts to argue for one of the two presented sets of broadening tables by means of the quality of the spectral fits, the evolutionary status, the Hipparcos parallaxes, and an eclipsing binary system have been inconclusive so far. However, with the successful launch of the *Gaia* satellite, very high precision parallaxes for a large number of stars will become available in a few years offering a realistic chance to solve this issue. In the meantime, eclipsing binaries are the objects to focus on. We will soon analyze the spectra of several eclipsing systems, whose geometric parameters are well constrained by radial velocity as well as light curves, using our newly developed method which is capable of dealing with composite spectra. Finally, we note that other factors such as the contribution of the He II broadening, which depends on both, the broadening theory and the helium abundance, may play a role at higher temperatures. At the same time, at lower densities the fine structure splitting of the hydrogen energy levels, omitted by both VCS and SH may also be important (Olchawa et al. 2004).

7 Spectroscopic analysis of 63 nearby mid B- to late O-type stars – A testbed for the new analysis method and a reference sample for differential abundance analyses

Abundances of the chemical elements are the key to understand the evolution of entire galaxies and of their individual constituents, the stars. While recently born stars are chemically identical to the surrounding interstellar matter from which they have formed, the situation changes over time as nuclear burning proceeds in the stellar cores to fuse light elements to heavier ones. Via mixing processes, a fraction of the burning products may reach the stellar atmospheres even on the main sequence where they become detectable and, thus, serve as tracers for stellar evolution (e.g. Heger & Langer 2000; Meynet & Maeder 2000; Chieffi & Limongi 2013). In particular, this applies to massive stars where excesses in the nitrogen-over-carbon and nitrogen-over-oxygen ratios with regard to their pristine values are clear signatures of hydrogen burning via the CNO cycles (Przybilla et al. 2010a; Maeder et al. 2014). By ending their lives in core-collapse supernova explosions, it is also the massive stars that have the largest impact on the galactochemical evolution because they release large amounts of energy and processed matter to the interstellar medium (e.g. Woosley & Weaver 1995; Hirschi et al. 2005; Nomoto et al. 2006) and, therefore, increase the metal content in subsequent generations of stars.

With the Sun as the best studied star (e.g. Asplund et al. 2009; Lodders et al. 2009; Caffau et al. 2011), the solar chemical composition is widely used as reference for differential abundance analyses. However, by a detailed abundance analysis of a sample of 29 early B-type stars, Nieva & Przybilla (2012) found that the Sun is atypical for its present-day environment and might be an immigrant from a region closer to the Galactic center. Therefore, it is not an ideal point of reference. Instead of the solar values, Nieva & Przybilla (2012) propose to use the abundances derived from their star sample, the so-called cosmic abundance standard (CAS), as present-day reference. An advantage of early B-type stars is that these objects are young with respect to Galactic evolutionary and dynamical scales, which implies that there is not much time for migration – except for the small subset of kinematically peculiar objects like runaway stars. Consequently, the majority of early B-type stars is characteristic of the chemical composition of their surroundings. Moreover, their photospheres are in radiative equilibrium, unaffected by strong stellar winds, convection, or chromospheres. Hence, their atmospheric structure can be modeled with high fidelity owing to the comparatively simple input physics.

So far, iterative procedures have been used in most previous quantitative spectral abundance studies of early B-type stars (e.g. Gies & Lambert 1992; Kilian 1992; Cunha & Lambert 1994; Morel et al. 2006). They can be very time consuming depending on the amount of atmospheric parameters considered in the iterations, and they may still be subject to some pitfalls. Nevertheless, iterative methods have been highly successful to determine the abundance pattern of early-type stars recently, if high-quality spectra were available and all spectral indicators carefully chosen, guided by experience. Przybilla et al. (2008a) used such a detailed procedure and showed that early B-type stars in the solar neighborhood have very homogeneous metal abundances and can define the present day cosmic abundance standard (Nieva & Przybilla 2012).

In Chapter 5, we have developed a new method for an objective, χ^2-based spectroscopic analysis technique tailored for early-type stars. The method takes advantage of the relatively low density of lines in the optical spectra of early-type stars, which results in very few intrinsic line blends. This characteristic makes the spectral analysis extremely flexible with respect to individual abundances since synthetic spectra with arbitrary combinations of metal abundances can be created from a small set of base spectra. Like in other cases, the new method fits synthetic spectra to observation using the standard concept of χ^2 minimization. However, in order to sample the entire multi-dimensional parameter space at once, a simultaneous fit of all parameters is made avoiding cumbersome iterations by hand or the risk of missing the global best solution. Moreover, parameters are not only constrained from a subset of available lines, but from all useful features in the spectrum. The novel strategy has been validated for three single stars and three SB2 systems in Chapter 5.

In this Chapter, we shall explore the potential of our new approach in order to verify whether (i) the cosmic abundance standard and (ii) its homogeneity can be recovered, (iii) the parameter space in effective temperature and surface gravity can be extended[17], (iv) other parameters (in particular fundamental stellar parameters like mass, radius, luminosity and age) can consistently be determined (see also Nieva & Przybilla 2014), and (v) its ability to single out chemical peculiarities at high sensitivity. To this end, we have acquired high-quality spectra of 63 mid B- and late O-type dwarfs and subgiants, in the majority apparently single stars but eight double-lined spectroscopic binaries are also included. The present sample partly overlaps with the samples of Nieva & Simón-Díaz (2011) and Nieva & Przybilla (2012). The aim of this investigation is to provide a set of comparison stars for differential analyses of, for instance, runaway B-stars to detect small abundance anomalies that may reveal their origin (e.g. Przybilla et al. 2008b; Irrgang et al. 2010).

7.1 The reference sample

Most of our 63 reference stars are nearby mid B- to late O-type stars with visual magnitudes V smaller than 7 mag. Therefore, it has been possible to obtain high-resolution spectra ($\lambda/\Delta\lambda \geq 40\,000$) with high signal-to-noise ratio (S/N $\geq$ 200) from a few nights observing time at 2.2 to 2.5 m telescopes: with CAFE and FOCES on the Calar Alto 2.2 m telescope, with FEROS on the MPG/ESO 2.2 m telescope, and with FIES on the 2.5 m Nordic Optical Telescope (see Table 7.1 for details). The quality of the spectroscopic observations is, thus, excellent and allows us to detect spectral features that are otherwise unresolved or hidden by noise, such as contributions from a fainter companion. About a dozen less bright ($V \sim 9$–10 mag) objects with smaller S/N has been added to the sample in order to increase the range of the atmospheric parameters. Table 7.1 lists information on the reference stars' spectroscopic, photometric, and astrometric data used in this work.

[17]The star sample employed to establish the CAS (Nieva & Simón-Díaz 2011; Nieva & Przybilla 2012) concentrated on main-sequence dwarfs in the effective temperature range $18\,500 \leq T_{\rm eff} \leq 32\,000$ K (see also Nieva 2013), with only a few outliers. The choice of the boundaries was, on the one hand, motivated observationally, because of the possible occurrence of chemically peculiar Bp stars at lower temperatures (e.g. Smith 1996) and due to the onset of pronounced stellar winds in hotter and more luminous objects (e.g. Kudritzki & Puls 2000). On the other hand, it was motivated from the modeling perspective, because the model atoms employed in the studies were thoroughly tested within this parameter range and since non-LTE effects on the atmospheric structure are negligible (Nieva & Przybilla 2007; Briquet et al. 2011; Przybilla et al. 2011).

Table 7.1: Reference stars: ID, spectroscopy, photometry, astrometry.

#	Object	S/N	Flag	V	$U-B$	$B-V$	$b-y$	m_1	c_1	H_p	B_t	V_t	Π	$\mu_\alpha \cos\delta$	μ_δ	References
				(mag)									(mas)	(mas yr^{-1})		
CAFE: $\lambda/\Delta\lambda = 55\,000$																
18	HD 197511	120	g	5.380	−0.640	−0.100	−0.016	0.064	0.318	5.3772	5.260	5.383	2.56	1.94	1.84	(1),(6),(7),(8)
26	HD 212883	140		6.463	−0.750	−0.130	−0.041	0.071	0.182	6.4133	6.299	6.463	2.18	−0.48	−5.48	(1),(6),(7),(8)
19	HD 217811	150		6.384	−0.587	−0.009	0.039	0.061	0.288	6.3861	6.370	6.408	3.07	0.35	−5.82	(1),(6),(7),(8)
FEROS: $\lambda/\Delta\lambda = 48\,000$																
10	HD 3175	290		9.280	−0.610	−0.170	−0.073	0.114	0.370	9.2622	9.120	9.284	1.02	−4.80	−5.78	(1),(6),(7),(8)
2	HD 8323	285		9.529	−0.425	−0.085	−0.027	0.094	0.570	9.5211	9.424	9.534	0.31	−3.53	−15.72	(1),(6),(7),(8)
33	HD 19374	270		6.100	−0.800	−0.120	−0.034	0.078	0.088	6.0935	5.969	6.098	3.92	−24.32	7.46	(1),(6),(7),(8)
3	HD 21532	240		9.940	−0.480	−0.100	−0.047	0.120	0.501	9.8513	9.724	9.836	...	9.05	1.58	(1),(6),(7),(8)
13	HD 21996	310	b	9.400	−0.610	−0.140	−0.070	0.106	0.322	9.3243	9.196	9.294	2.15	0.27	1.29	(1),(6),(7),(8)
5	HD 24626	310	b	5.103	...	−0.137	−0.067	0.111	0.490	5.0631	4.931	5.071	9.42	32.21	−0.83	(1),(6),(7),(8)
57	HD 34816	320		4.286	−1.010	−0.273	−0.110	0.073	−0.061	4.2020	3.966	4.239	3.83	−3.30	−4.91	(1),(6),(7),(8)
36	HD 35337	340	d	5.243	...	−0.217	−0.100	0.087	0.063	5.1642	4.964	5.194	1.98	0.06	−1.60	(1),(6),(7),(8)
54	HD 36960	290		4.790	−1.010	−0.250	−0.106	0.072	−0.056	4.6889	4.436	4.702	2.02	−0.66	0.01	(3),(6),(7),(8)
45	HD 37209	300		5.740	−0.910	−0.220	−0.090	0.080	0.046	5.6299	5.468	5.713	2.12	−0.22	0.05	(3),(6),(7),(8)
40	HD 37481	280		5.950	−0.908	−0.228	−0.094	0.085	0.058	5.8817	5.678	5.910	2.43	0.61	−0.17	(1),(6),(7),(8)
6	HD 39764	320		4.865	−0.564	−0.150	−0.071	0.114	0.414	4.8321	4.687	4.845	9.75	−4.72	31.32	(1),(6),(7),(8)
44	HD 44743	470	e	1.976	−0.970	−0.240	−0.090	0.052	−0.002	1.8911	1.747	1.933	6.62	−3.23	−0.78	(1),(6),(7),(8)
50	HD 46328	220	e	4.330	−0.990	−0.240	−0.093	0.064	−0.022	4.2586	4.030	4.286	2.36	−2.91	6.22	(2),(6),(7),(8)
46	HD 50707	365	e	4.830	−0.960	−0.210	−0.087	0.071	−0.014	4.7485	4.536	4.773	2.68	−5.46	3.58	(2),(6),(7),(8)
32	HD 52089	375		1.502	−0.924	−0.213	−0.081	0.078	−0.002	1.4160	1.350	1.500	8.05	3.24	1.33	(1),(6),(7),(8)
31	HD 54764	240	f g	6.040	−0.791	0.050	0.104	0.017	−0.004	6.0568	6.042	6.041	1.46	−2.55	0.54	(1),(6),(7),(8)
52	HD 55857	245	g	6.080	−1.000	−0.230	−0.102	0.077	−0.072	6.0324	5.804	6.062	0.96	−3.87	6.43	(5),(6),(7),(8)
59	HD 55879	295		6.014	−0.989	−0.175	−0.044	0.045	−0.103	5.9606	5.782	5.968	1.15	−2.78	1.44	(1),(6),(7),(8)
23	HD 55958	285	g	6.560	−0.760	−0.185	−0.081	0.100	0.185	6.5187	6.343	6.535	2.33	−5.18	4.53	(1),(6),(7),(8)
20	HD 56779	290		5.021	−0.692	−0.176	−0.076	0.097	0.256	4.9692	4.806	4.983	4.33	−10.42	5.64	(1),(6),(7),(8)
37	HD 64722	305	e g	5.692	−0.900	−0.154	−0.046	0.075	0.023	5.6423	5.491	5.656	2.44	−4.17	8.03	(1),(6),(7),(8)

Table 7.1: continued.

#	Object	S/N	Flag	V	$U-B$	$B-V$	$b-y$	m_1	c_1	H_p	B_t	V_t	Π	$\mu_\alpha \cos\delta$	μ_δ	References
								(mag)					(mas)	(mas yr^{-1})		
35	HD 70839	390	e g	5.965	−0.822	−0.083	−0.003	0.062	0.055	5.9362	5.826	5.937	1.84	−2.58	4.49	(1),(6),(7),(8)
8	HD 73105	310	c	6.800	−0.600	−0.110	…	…	…	6.7567	6.646	6.760	2.98	−11.98	9.93	(1),(7),(8)
55	HD 75821	350	b	5.097	−0.980	−0.214	−0.074	0.056	−0.079	5.0175	4.829	5.070	1.00	−3.69	3.36	(1),(6),(7),(8)
21	HD 85953	310	f	5.926	−0.735	−0.155	−0.059	0.087	0.230	5.8925	5.736	5.907	1.42	−13.69	0.67	(1),(6),(7),(8)
4	HD 90994	325		5.071	−0.504	−0.139	−0.062	0.111	0.481	5.0315	4.890	5.039	8.06	−39.23	−22.83	(1),(6),(7),(8)
15	HD 110956	220	d	4.640	−0.637	−0.164	−0.072	0.105	0.300	4.5756	4.420	4.594	8.48	−33.03	−14.84	(1),(6),(7),(8)
14	HD 119109	225	b	7.461	−0.510	0.005	0.048	0.061	0.366	7.4667	7.437	7.460	1.81	−1.80	−2.96	(1),(6),(7),(8)
7	HD 137366	310		…	…	…	…	…	…	6.3571	6.238	6.366	2.53	−6.17	−20.85	(7),(8)
61	HD 149438	590		2.825	−1.023	−0.252	−0.093	0.039	−0.090	2.7374	2.536	2.759	6.88	−9.89	−22.83	(1),(6),(7),(8)
1	HD 179761	270		5.138	−0.405	−0.069	−0.010	0.084	0.629	5.1207	5.035	5.117	4.59	6.95	−3.28	(1),(6),(7),(8)
34	HD 289002	60		10.450	−0.570	0.180	…	…	…	…	10.587	10.420	…	−0.3	−1.0	(1),(8),(9)
Fies: $\lambda/\Delta\lambda = 45\,000$																
28	HD 3360	300	f	3.661	−0.849	−0.196	−0.090	0.087	0.134	3.6112	3.421	3.628	5.50	17.38	−9.86	(1),(6),(7),(8)
25	HD 35039	280	a d	4.731	−0.790	−0.169	−0.069	0.083	0.173	4.6616	4.489	4.678	3.51	1.23	1.13	(1),(6),(7),(8)
38	HD 35299	250	a	5.694	−0.874	−0.210	−0.094	0.088	0.057	5.6235	5.430	5.650	3.72	2.08	−2.64	(1),(6),(7),(8)
22	HD 35912	240	a	6.408	−0.743	−0.177	−0.080	0.102	0.211	6.3397	6.166	6.352	2.53	−0.90	0.69	(1),(6),(7),(8)
30	HD 36285	200	a	6.315	−0.823	−0.195	−0.086	0.093	0.115	6.2637	6.078	6.282	1.37	1.42	−1.03	(1),(6),(7),(8)
24	HD 36430	270	a b	6.217	−0.739	−0.180	−0.085	0.111	0.202	6.1602	5.995	6.180	1.40	1.33	0.53	(1),(6),(7),(8)
63	HD 36512	230	a e	4.618	−1.068	−0.264	−0.112	0.061	−0.095	4.5203	4.281	4.565	1.14	−0.10	−4.87	(1),(6),(7),(8)
49	HD 36591	300	a	5.339	−0.911	−0.194	−0.074	0.074	0.002	5.2744	5.103	5.314	2.09	−1.95	0.80	(1),(6),(7),(8)
29	HD 36629	220	a	7.650	−0.660	0.020	0.067	0.067	0.149	7.6540	7.638	7.648	0.66	2.57	−2.19	(2),(6),(7),(8)
48	HD 36959	240	a	5.670	−0.910	−0.240	−0.092	0.085	0.039	5.5912	5.275	5.511	1.21	0.48	−1.50	(3),(6),(7),(8)
58	HD 37020	200	a c	6.730	−0.880	0.040	0.092	0.029	−0.048	4.8593	6.501	6.550	…	…	…	(4),(6),(7),(8)
53	HD 37042	205	a	6.380	−0.930	−0.090	−0.004	0.049	−0.080	…	6.066	6.193	…	2.7	2.1	(2),(6),(8),(9)
41	HD 37744	275	a	6.213	−0.900	−0.208	−0.081	0.079	0.043	6.1451	5.959	6.171	2.39	1.64	2.12	(1),(6),(7),(8)
16	HD 160762	385	c	3.800	−0.702	−0.179	−0.065	0.079	0.292	3.7497	3.581	3.763	7.17	−7.48	4.53	(1),(6),(7),(8)
60	HD 166033	110		9.599	−0.697	0.147	…	…	…	…	8.655	8.597	…	0.8	−0.2	(1),(8),(9)

Table 7.1: continued.

#	Object	S/N	Flag	V	$U-B$	$B-V$	$b-y$	m_1	c_1	H_p	B_t	V_t	Π	$\mu_\alpha \cos\delta$	μ_δ	References
								(mag)					(mas)	(mas yr^{-1})		
43	HD 172427	135	e	9.460	−0.440	0.480	…	…	…	…	9.973	9.582	…	−0.8	−3.2	(1),(8),(9)
39	HD 172488	170	g	7.620	−0.400	0.540	…	…	…	7.7743	8.248	7.756	3.41	−8.81	−22.82	(1),(7),(8)
12	HD 180163	350	b	4.388	−0.651	−0.149	−0.048	0.068	0.356	4.3591	4.203	4.373	2.35	−0.60	−1.26	(1),(6),(7),(8)
11	HD 184171	370		4.739	−0.658	−0.142	−0.057	0.095	0.376	4.6931	4.546	4.709	3.79	1.16	−3.47	(1),(6),(7),(8)
17	HD 207330	460	d g	4.235	−0.733	−0.122	−0.037	0.075	0.247	4.2016	4.065	4.208	2.95	2.77	−2.00	(1),(6),(7),(8)
27	HD 213420	350	b	4.505	−0.738	−0.090	−0.007	0.059	0.191	4.4912	4.375	4.493	1.90	−1.98	−5.36	(1),(6),(7),(8)
42	HD 214993	450	b e	5.253	−0.868	−0.137	−0.034	0.052	0.050	5.2003	5.042	5.205	2.43	−1.59	−5.33	(1),(6),(7),(8)
47	HD 218376	330		4.850	−0.864	−0.028	0.048	0.010	−0.012	4.8322	4.756	4.829	2.89	6.94	−1.95	(1),(6),(7),(8)
51	HD 227460	120		9.502	−0.691	0.150	…	…	…	…	9.665	9.537	…	−5.0	−7.3	(1),(8),(9)
56	HD 227586	180		8.820	−0.664	0.211	0.210	−0.009	0.004	…	8.990	8.819	…	−3.7	−7.1	(1),(6),(8),(9)
62	HD 344783	140		9.767	−0.567	0.432	…	…	…	…	10.219	9.885	…	−4.7	−5.8	(1),(8),(9)
Foces: $\lambda/\Delta\lambda = 40\,000$																
9	HD 209008	320		5.995	−0.568	−0.120	−0.035	0.081	0.411	5.9625	5.838	5.973	3.04	13.22	0.78	(1),(6),(7),(8)

Notes. The numbering of stars (first column) is related to the derived effective temperature, see Table D.3. The third column is the mean S/N of the spectrum, which was obtained with one of the four high-resolution spectrographs Cafe (Aceituno et al. 2013), Feros (Kaufer et al. 1999), Fies (Frandsen & Lindberg 1999), and Foces (Pfeiffer et al. 1998). Photometric data: Johnson-Cousins magnitudes U, B, and V were compiled from references (1), (2), (3), (4), and (5), Strömgren colors $b-y$, m_1, and c_1 from (6), the Hipparcos magnitude H_p from (7), and Tycho magnitudes B_t and V_t from (8). Astrometric data: Parallax Π and proper motions in right ascension $\mu_\alpha \cos\delta$ and declination μ_δ were compiled from (7) or (9) if not available in (7). For reasons of clarity, uncertainties are not given here but can be found in the respective references.

Flags. (a) Spectra were taken from the IACOB database (Simón-Díaz et al. 2011a) by courtesy of S. Simón-Díaz and were first presented and analyzed in Simón-Díaz (2010). (b) SB2 system. (c) SB1 system. (d) Candidate SB1 system. (e) (Candidate) β Cepheid variable according to Stankov & Handler (2005) or Pigulski & Pojmański (2008). (f) Slowly-pulsating B-Star. (g) Detection of strange, e.g., asymmetric, line profiles with unknown origin that may render the spectral analysis uncertain.

References. (1) Mermilliod (1991); (2) Ducati (2002); (3) Morel & Magnenat (1978); (4) Walker (1969); (5) Feinstein (1967); (6) Hauck & Mermilliod (1998); (7) van Leeuwen (2007); (8) Høg et al. (2000); (9) Zacharias et al. (2013).

The sample presented here comprises a number of stars that are already very well studied. Among others, this applies to 13 stars in the Orion OB1 association that were analyzed, for example, by Nieva & Simón-Díaz (2011) and to 6 of the targets which were investigated by Nieva & Przybilla (2012) to establish the CAS. The development of our new analysis method was motivation for us to re-analyze these objects anyway. Beginning with the reduction of their raw data, all reference stars are treated here in a homogeneous manner to avoid unnecessary complications in the interpretation of the results, which can be introduced by mixing heterogeneous studies.

The selection of targets was focused on mid B- to late O-type stars on or close by to the main sequence, that is dwarfs or subgiants, since our synthetic spectra are optimized for this parameter range, for instance, with respect to the completeness of modeled spectral lines. Furthermore, preference was given to slowly rotating stars (with projected rotational velocity $v \sin(i) \lesssim 50\,\mathrm{km\,s^{-1}}$) that show sharp spectral features and only few line blends. However, compromises had to be made in this respect to obtain a diversity of effective temperatures and surface gravities, such that a few objects evolved already beyond the terminal-age main sequence and some faster rotators (with $v \sin(i)$ up to $\sim$150 km s^{-1}) were included.

Despite – but sometimes also owing to – the high quality of our observational data, several ambiguous objects were removed from the original sample, e.g., due to the presence of unusual or asymmetric line shapes. Because of the high fraction of binary systems among early-type stars (see Sana et al. 2012; Chini et al. 2012), it is likely that many of these objects are unrecognized SB2 systems that were observed in an unfavorable orbital phase. Nevertheless, seeking a sample of objects with unambiguous nature, we consider here only those objects that are either clearly identified as SB2 system by virtue of their composite spectrum (8 objects) or that are without any indication for significant flux contributions of a fainter companion (55 objects).

The three-dimensional spatial distribution of the reference stars is shown in Fig. 7.1 (anticipating spectroscopic distances and radial velocities[18] from Sect. 7.2.2). One third of the targets clusters in or around the Orion association of roughly 400 pc distance while about another third is more or less uniformly spread over ±600 pc in the direction of Galactic rotation at Galactocentric radii similar to the Sun. The remaining objects are more than 700 pc away from us[19]. Four distant objects below the Galactic disk enter the sample which are actually known runaway stars (Conlon et al. 1990). Velocities are plotted with respect to the local standard of rest, that is the rest frame of a hypothetical star at the Sun's position that is circularly orbiting the Galactic center. According to Schönrich et al. (2010), the Sun is moving with $(v_x, v_y, v_z)_\odot = (11.1, 12.24, 7.25)$ km s^{-1} relative to the local standard of rest.

7.2 Spectroscopic analysis

7.2.1 Method

The spectroscopic analysis is carried out using our recently developed strategy which is briefly summarized in the following (see Chapter 5 for details).

[18] The center-of-mass velocity $v_{\rm com} = (M_{\rm p} v_{\rm vrad,p} + M_{\rm s} v_{\rm vrad,s})/(M_{\rm p} + M_{\rm s})$ is used in the case of a SB2 system.

[19] Note that on the level of accuracy and precision achieved here, effects of the Galactic abundance gradients (see Sect. 8.2) may become notable.

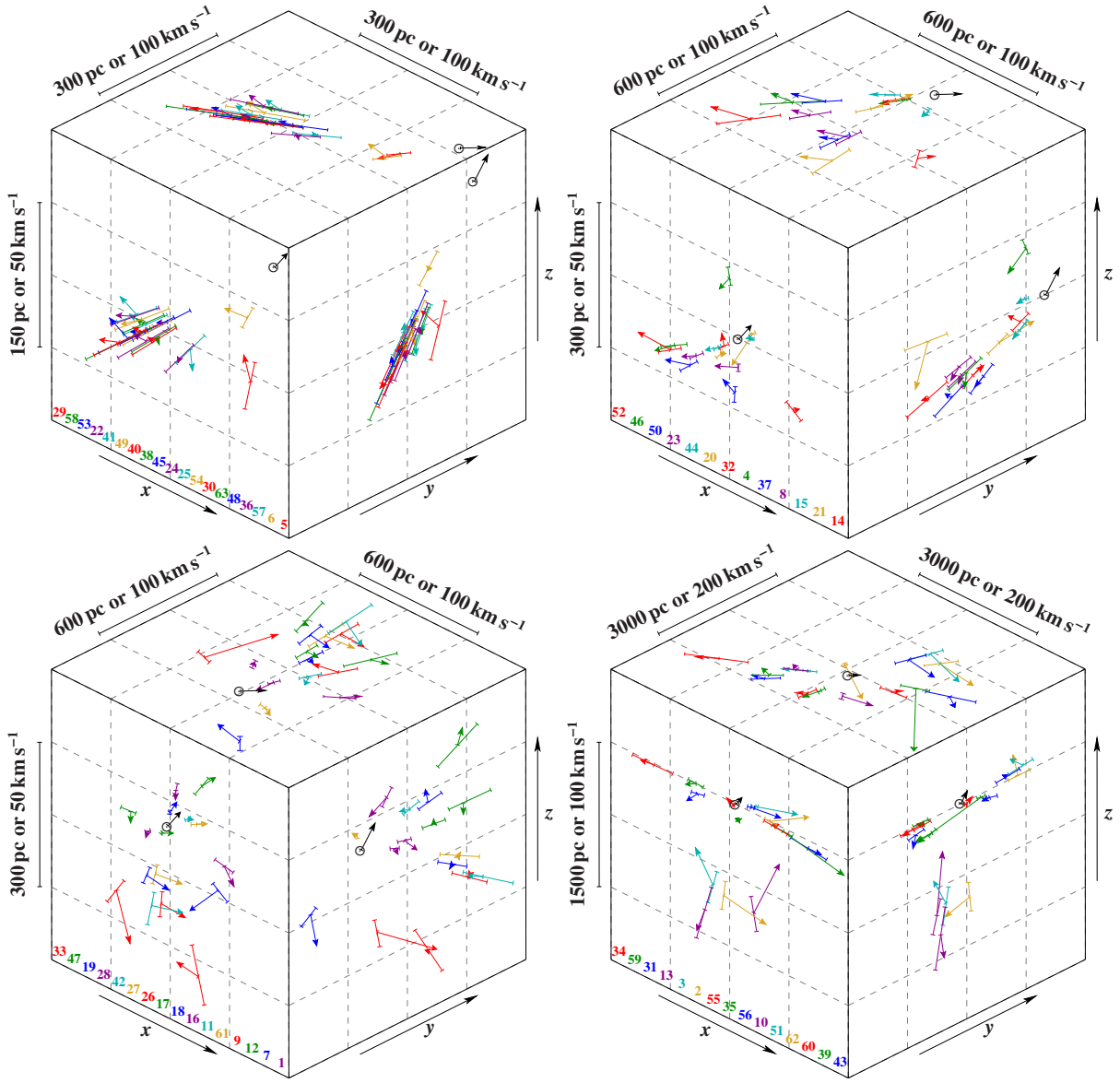

Figure 7.1: Three-dimensional spatial distribution of the reference stars in the coordinate system defined by Fig. 2.7. Position uncertainties are given by error bars while the vectors symbolize the velocities relative to the local standard of rest. Scales for distances and velocities are given by the black bars. The Sun's position is marked by a black ⊙. Numbers correspond to those of Table 7.1 and are sorted in ascending order with respect to the x-coordinate. Colors are intended to guide the eye and do not have any further meaning. For the sake of clarity, the total sample has been split up in four subsets according to right ascension α and distance d: $d < 700$ pc combined with $3^{\mathrm{h}}10^{\mathrm{m}} \leq \alpha < 6^{\mathrm{h}}$ (*top left*), $6^{\mathrm{h}} \leq \alpha < 15^{\mathrm{h}}$ (*top right*), or $15^{\mathrm{h}} \leq \alpha \leq 24^{\mathrm{h}}$, $0^{\mathrm{h}} \leq \alpha < 3^{\mathrm{h}}10^{\mathrm{m}}$ (*bottom left*), and $d \geq 700$ pc (*bottom right*).

The model spectrum's underlying atmospheric structure such as the stratification of temperature and density is computed with Atlas12 (Kurucz 1996) which assumes a plane-parallel, homogeneous, hydrostatic, and line-blanketed atmosphere in local thermodynamic equilibrium

(LTE). To consider non-LTE effects, which are important in photospheres of B- and O-type stars owing to the high photon fluxes, we perform line-formation calculations with updated versions of Detail and Surface (Giddings 1981; Butler & Giddings 1985). Detail solves the coupled radiative transfer and statistical equilibrium equations using an Accelerated Lambda Iteration scheme (Rybicki & Hummer 1991). The resulting non-LTE population numbers are then input for the Surface code, which computes a final synthetic spectrum based on more detailed line-broadening data.

Based on this hybrid non-LTE approach and model atoms according to Table 5.1, an extensive grid of model spectra has been calculated, which serves as base from which arbitrary models within the multi-parameter space spanned by effective temperature $T_{\rm eff}$, surface gravity $\log(g\,(\mathrm{cm\,s^{-2}}))$, microturbulence ξ, macroturbulence ζ, projected rotational velocity $v\sin(i)$, radial velocity $v_{\rm rad}$, and elemental abundances $\{n(x)\}$ ($x \in \{\mathrm{He, C, N, O, Ne, Mg, Al, Si, S, Ar, Fe}\}$) can be created. The concept of using base spectra allowed us to cover the whole parameter space of mid B- to late O-type dwarfs and subgiants with reasonable numerical effort, that means with computing a large yet doable number of models (about 200 000). A fitting procedure that simultaneously fits all atmospheric parameters by matching the entire useful spectral range became therefore feasible and is the core of our new analysis technique.

To be able to optimize all parameters at the same time is a huge advantage over traditional methods – which work in subspaces of the multi-dimensional parameter space by keeping several parameters fixed when fitting the remaining ones – since it offers a very efficient way to find the global best solution, instead of possibly only a local one. Moreover, because almost the entire spectral range is fitted at once, it is ensured that each parameter is constrained by the maximum number of spectral indicators that are available. Therefore, our method, which is also applicable to composite spectra of SB2 systems, is less prone to subjective decisions like the choice of starting values for the parameters or the allocation of spectral indicators to fitting parameters.

In general, our strategy focuses on the suppression of influences with random character such as the aforementioned subjectivity. The small star-to-star scatter in the deduced abundances (see Sect. 7.2.4) can be seen as an indication for the success of our efforts in this direction.

We want to emphasize the similarities and differences with the CAS work of Nieva & Przybilla (2012) at this point, as many comparisons will be made later. First, we expect all issues related to the details of the data reduction in the two works to be of minor importance, see also Sect. 7.2.3. On the other hand, one fundamental difference lies in the way how line blanketing and line blocking are considered in the model atmosphere calculations and for the non-LTE level population determination. While the CAS work employed opacity distribution functions (e.g. Kurucz 1993a) with the Atlas9 code (Kurucz 1993b) and with Detail, we used here the opacity sampling technique of Kurucz (1996) throughout both steps with Atlas12 and Detail. Some ions – the non-LTE model atoms were the same in both instances – turned out to react sensitively to this change therefore yielding different abundances, e.g. Mg II (see Sect. 7.3.1). Both approaches employ χ^2 minimization for the analysis, but the weighting of the spectral indicators is very different. Per ion, individual spectral lines were considered with equal weight in the CAS work. Therefore, a higher weight was given globally to the few lines of a minority ion like O I over the numerous lines of the majority species O II in the course of establishing ionization balance. Here, the weighting is per pixel. Consequently, a few broad spectral features like the Balmer lines contribute significantly to the global χ^2, whereas they were one among many

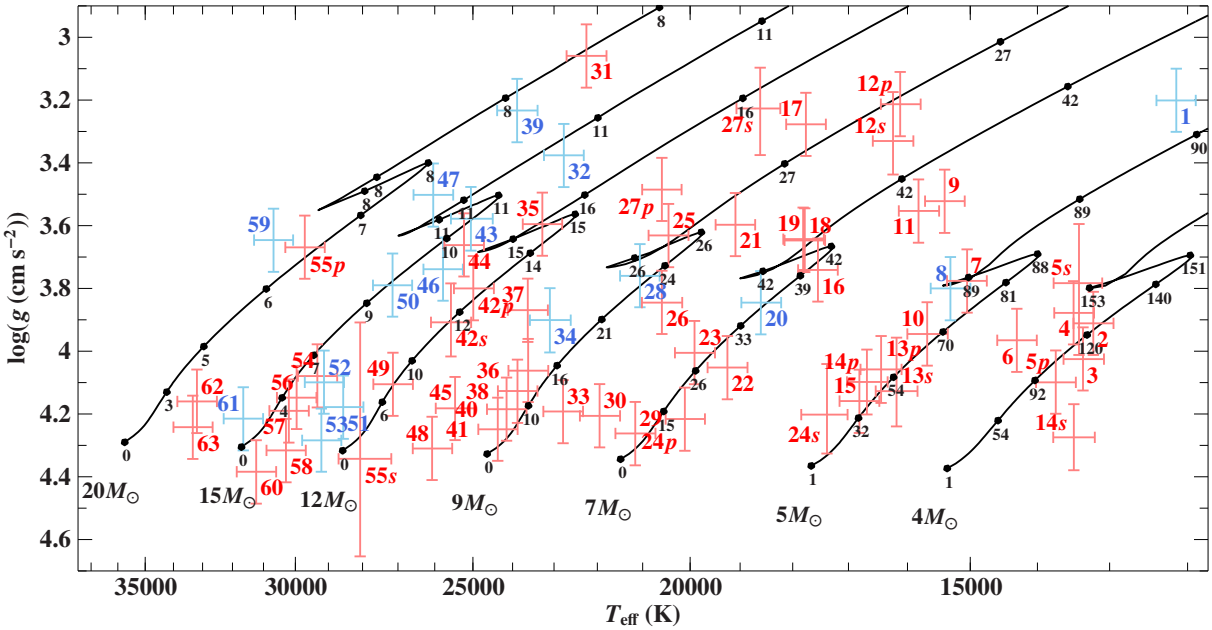

Figure 7.2: Position of the 63 reference stars in a $(T_{\rm eff}, \log(g))$ diagram. Overlaid are evolutionary tracks for non-rotating stars ($\Omega/\Omega_{\rm crit} = 0$) of metallicity $Z = 0.014$ and different initial masses ($M \leq 15\,M_\odot$: Georgy et al. 2013; otherwise: Ekström et al. 2012). Black filled circles and numbers mark the age in Myr. Colored numbers correspond to those of Table 7.1 with "p" denoting the primary and "s" the secondary component of a SB2 system. Stars labeled in blue show indications for CNO-burning product mixing (see Sect. 7.3.3). Error bars indicate 99%-confidence limits.

equal indicators in the CAS work. Finally, we want to note that while there is large overlap between the linelists considered for the analysis here and in the CAS work, some differences exist.

7.2.2 Results

Table D.3 lists the derived atmospheric parameters and the elemental abundances of our reference stars together with their uncertainties. The positions of the stars in a $(T_{\rm eff}, \log(g))$ diagram are compared to evolutionary tracks for non-rotating stars by the Geneva group (Ekström et al. 2012; Georgy et al. 2013) in Fig. 7.2. A rather good coverage of the main-sequence band is achieved in the mass range between 4 $M_\odot$ to about 20 $M_\odot$ and from near the ZAMS to the terminal-age main sequence. Note that the latter is shifted to lower gravities in the case of rotating stars, such that some of the apparently more evolved stars in Fig. 7.2 may still be core-hydrogen burning.

The fundamental parameters mass M, age τ, luminosity L, and radius $R_\star$ are derived with the help of the Geneva evolutionary tracks. The determination of spectroscopic distances d and color excesses $E(B-V)$ is described in Sect. 5.3.3. With respect to Chapter 6, we note that Balmer line Stark broadening tables by Schöning (priv. comm.), which are based on the VCS unified theory (Vidal et al. 1971b), are used here. The fundamental stellar parameters in combination with the mass fractions for hydrogen (X), helium (Y), and metals (Z) are summarized in Table D.4.

7.2.3 Instrumental impact

For three apparently single stars in the sample, spectra of two different observing runs are available which allow us to estimate the impact of the instrument and the data reduction on the outcome of the spectroscopic investigation. For HD 37209 (#45) and HD 37481 (#40), both observations were performed with the FEROS spectrograph at an interval of 30 days. Despite small but still perceptible variations in the line profiles that may hint at variability, the results obtained from the two independent spectra are almost identical in the case of HD 37209 (see Table D.3). For HD 37481, the deviation is somewhat larger but still well within the derived systematic uncertainties (see Table D.3). The reason for the increased discrepancy might lie in a possible variability of HD 37481, which manifests as small mutable bumps in the line profiles. For HD 36960 (#54), the two spectra – one taken with FIES in November 2008 and one with FEROS in November 2011 – do not show any spectral line variations and give the same results within their uncertainties (see Table D.3) making us confident that the present study is not prone to instrumental effects nor to the details of data reduction. The spectra with higher S/N and larger spectral coverage are used in the further course of this work.

7.2.4 Abundances versus atmospheric parameters

In Figs. 7.3 and 7.4, we plot the derived abundances as function of the atmospheric parameters $T_{\rm eff}$ and $\log(g)$ as well as microturbulence and $\sqrt{(v\sin(i))^2+\zeta^2}$ (the combined projected rotational and macroturbulent velocity). The abundances do not correlate with the surface gravity. Neither are there any significant trends of the abundances of neon, magnesium, sulfur, argon, and iron with effective temperature. However, slight trends become apparent for helium, whose abundances are close to solar but appear to be somewhat above solar at the low temperature end and subsolar at the high temperature end. Obvious trends at the level of 0.2–0.3 dex are apparent for carbon, nitrogen, oxygen, aluminum, and silicon. The oxygen abundance seems to peak near 20 000 K whereas aluminum appears to increase with rising temperature. The abundances of carbon, nitrogen, and silicon exhibit a common behavior, namely an increase with decreasing temperatures below 20 000 K.

To quantify these systematic trends, we fit cubic spline functions $cspline(a_{15}, a_{20}, a_{25}, a_{30})$ – defined by the four anchor points (15 000 K, a_{15}), (20 000 K, a_{20}), (25 000 K, a_{25}), and (30 000 K, a_{30}) – to the red data points in the left column of Fig. 7.3. Outliers are accounted for by performing the χ^2 fit twice whereby objects are omitted in the second run that deviate more than 3χ from the best fit of the first run. The resulting values for the fitting parameters a_{15}, a_{20}, a_{25}, and a_{30} are listed in Table 7.2.

A biased determination of the microturbulence parameter ξ during the spectral analysis could be a possible explanation for the correlations of abundances with temperature. This is because an underestimated value for the microturbulence can be compensated, at least to some extent, by an increase in the abundances. Consequently, if the microturbulences of the cooler objects in our sample are, for some reason, systematically judged too low, one would expect exactly those trends with temperature as found for helium, carbon, nitrogen, or silicon – but not those for oxygen and aluminum. Nevertheless, staying in this picture, one would also expect that only the cool stars have underestimated and, therefore, low microturbulences because none of the hotter objects has increased abundances. However, this is in contradiction to the left

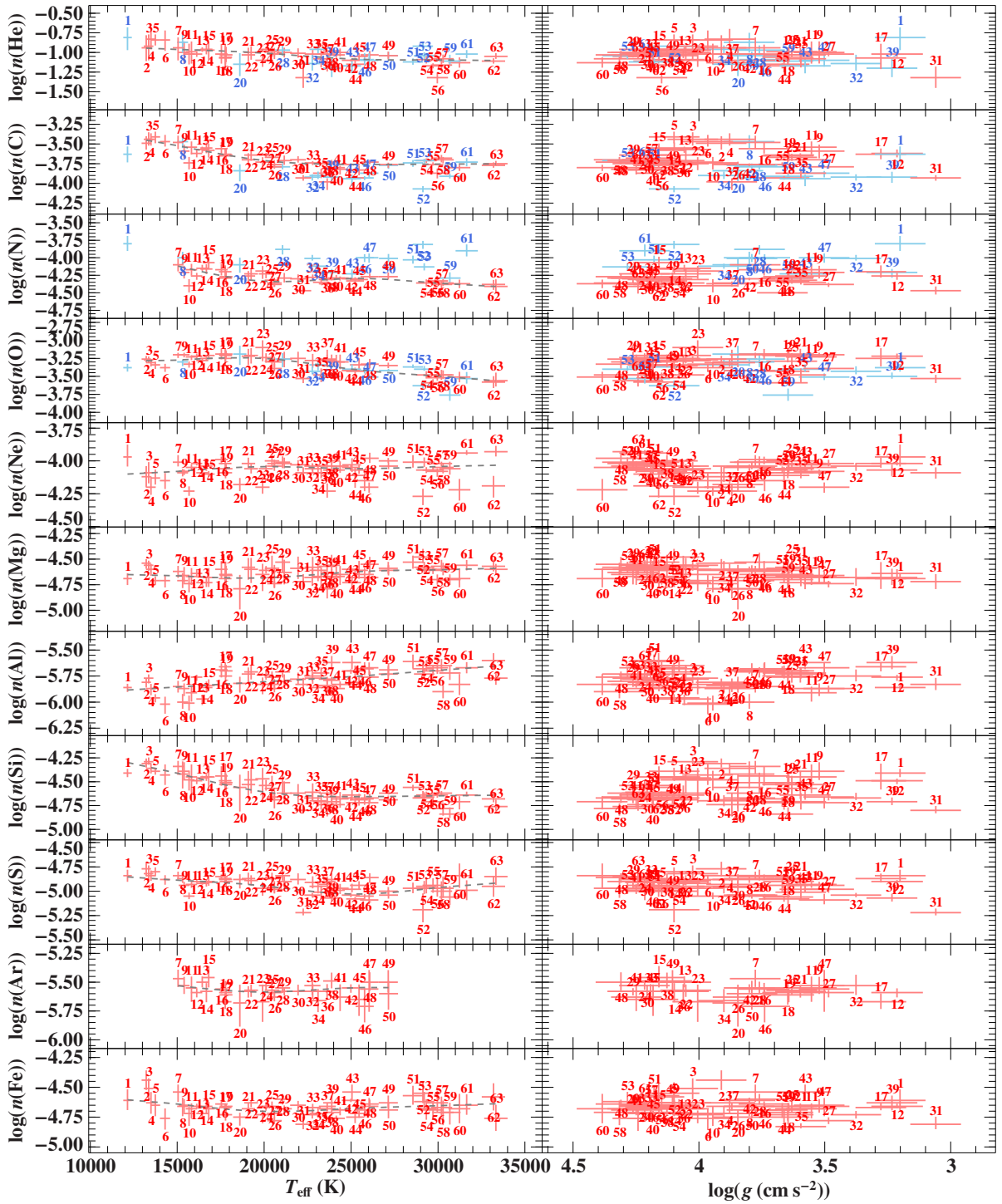

Figure 7.3: Elemental abundances as a function of temperature (*left column*) and surface gravity (*right column*). Numbering according to Table 7.1, values from Table D.3. Error bars cover statistical as well as systematic effects and are 99%-confidence limits. The gray dashed lines represent cubic spline functions used to quantify systematic trends with temperature (see Sect. 7.2.4). Argon and nitrogen lines are not visible for all temperatures. Helium, nitrogen, carbon, and oxygen abundances of stars showing signatures of CNO mixing (see Sect. 7.3.3) are plotted in blue.

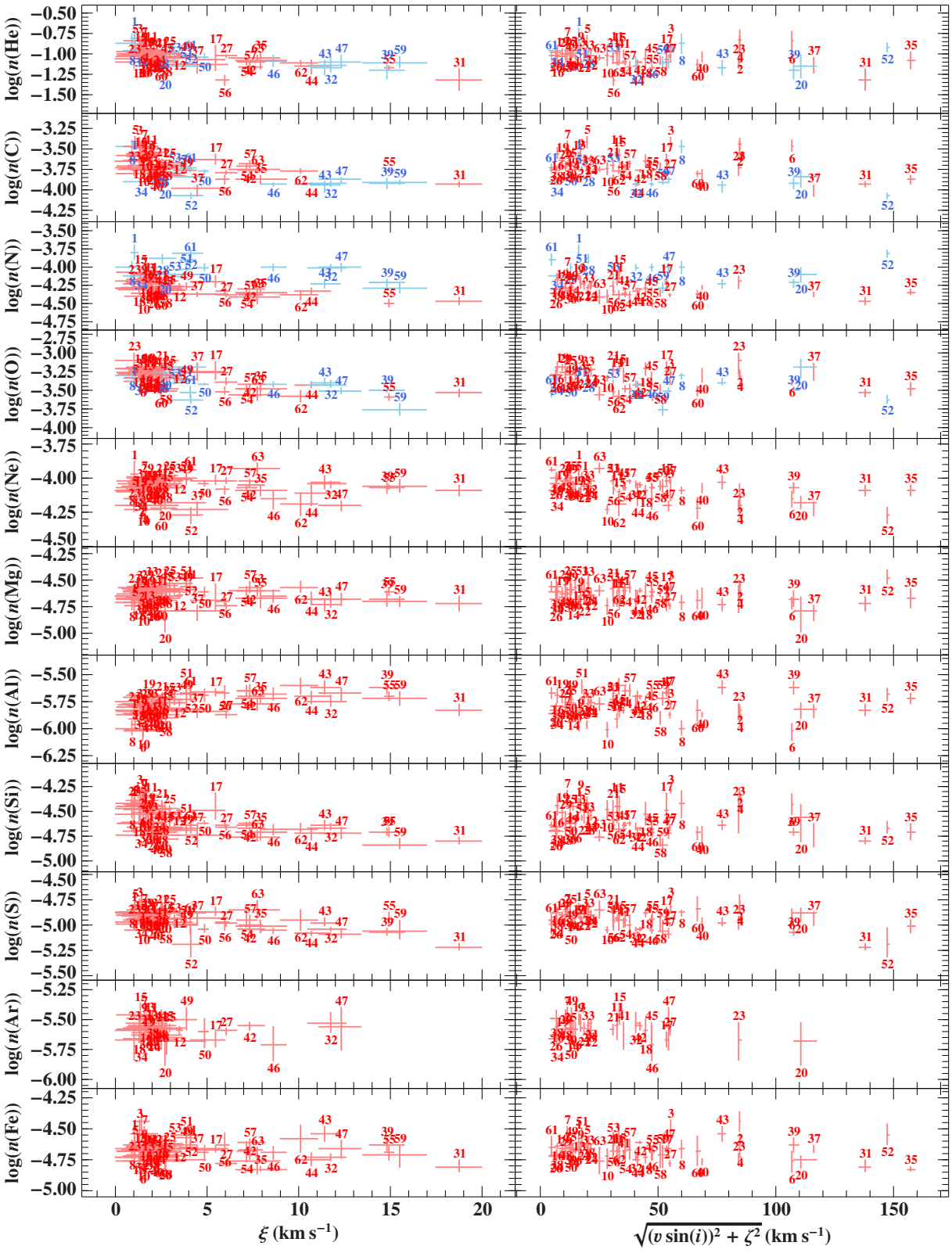

Figure 7.4: Same as Fig. 7.3 but for microturbulence (*left column*) and $\sqrt{(v\sin(i))^2+\zeta^2}$ (*right column*).

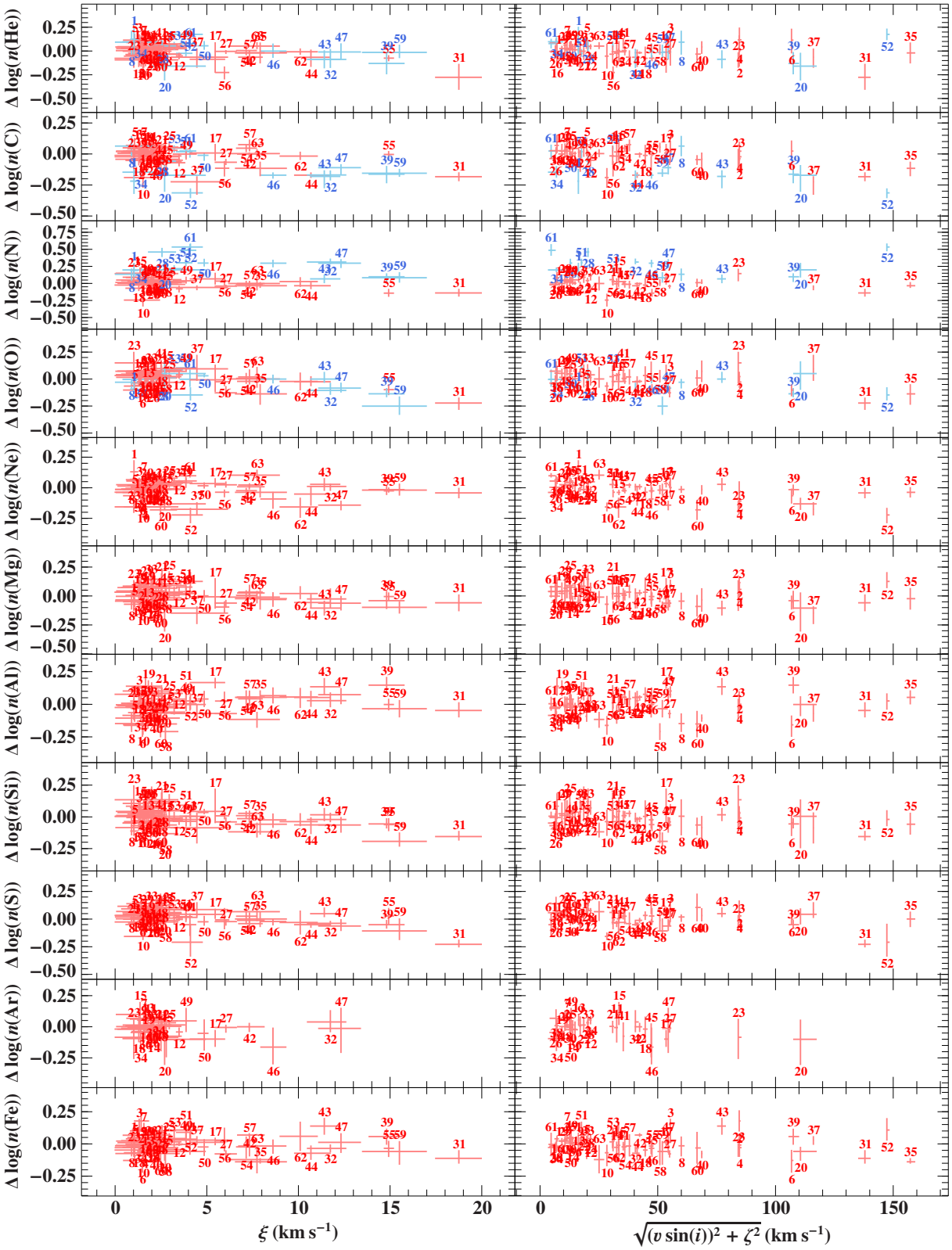

Figure 7.5: Same as Fig. 7.4 but abundances are corrected for the trends with temperature by subtracting the spline functions $cspline_x(a_{15}, a_{20}, a_{25}, a_{30})$ defined by the anchor points given in Table 7.2: $\Delta \log(n(x)) = \log(n(x)) - cspline_x(a_{15}, a_{20}, a_{25}, a_{30})$.

Table 7.2: Anchor points (15 000 K, a_{15}), (20 000 K, a_{20}), (25 000 K, a_{25}), and (30 000 K, a_{30}) for the cubic spline functions $cspline(a_{15}, a_{20}, a_{25}, a_{30})$.

	He	C	N	O	Ne	Mg	Al	Si	S	Ar	Fe	X	Y	Z
a_{15}	−0.96	−3.52	−4.12	−3.28	−4.08	−4.66	−5.86	−4.41	−4.89	−5.53	−4.64	0.665	0.319	0.013
δ_{15}	$^{+0.03}_{-0.03}$	$^{+0.03}_{-0.03}$	$^{+0.04}_{-0.04}$	$^{+0.02}_{-0.02}$	$^{+0.01}_{-0.02}$	$^{+0.02}_{-0.02}$	$^{+0.02}_{-0.02}$	$^{+0.02}_{-0.02}$	$^{+0.01}_{-0.01}$	$^{+0.03}_{-0.03}$	$^{+0.02}_{-0.02}$	$^{+0.011}_{-0.011}$	$^{+0.010}_{-0.010}$	$^{+0.001}_{-0.001}$
a_{20}	−1.01	−3.71	−4.33	−3.25	−4.04	−4.68	−5.80	−4.61	−4.95	−5.59	−4.70	0.691	0.296	0.013
δ_{20}	$^{+0.02}_{-0.02}$	$^{+0.02}_{-0.02}$	$^{+0.02}_{-0.02}$	$^{+0.02}_{-0.03}$	$^{+0.01}_{-0.01}$	$^{+0.02}_{-0.02}$	$^{+0.02}_{-0.02}$	$^{+0.02}_{-0.02}$	$^{+0.02}_{-0.01}$	$^{+0.02}_{-0.02}$	$^{+0.01}_{-0.01}$	$^{+0.005}_{-0.005}$	$^{+0.004}_{-0.005}$	$^{+0.001}_{-0.001}$
a_{25}	−1.08	−3.76	−4.30	−3.40	−4.06	−4.63	−5.76	−4.66	−5.03	−5.55	−4.68	0.734	0.255	0.011
δ_{25}	$^{+0.02}_{-0.02}$	$^{+0.01}_{-0.02}$	$^{+0.01}_{-0.01}$	$^{+0.02}_{-0.02}$	$^{+0.01}_{-0.01}$	$^{+0.02}_{-0.02}$	$^{+0.02}_{-0.02}$	$^{+0.01}_{-0.01}$	$^{+0.01}_{-0.01}$	$^{+0.03}_{-0.03}$	$^{+0.01}_{-0.01}$	$^{+0.002}_{-0.002}$	$^{+0.002}_{-0.002}$	$^{+0.001}_{-0.001}$
a_{30}	−1.09	−3.76	−4.36	−3.50	−4.04	−4.60	−5.69	−4.65	−4.96	−5.56	−4.65	0.735	0.254	0.011
δ_{30}	$^{+0.02}_{-0.02}$	$^{+0.02}_{-0.01}$	$^{+0.02}_{-0.02}$	$^{+0.03}_{-0.02}$	$^{+0.01}_{-0.01}$	$^{+0.02}_{-0.02}$	$^{+0.02}_{-0.02}$	$^{+0.01}_{-0.01}$	$^{+0.03}_{-0.03}$	$^{+0.18}_{-0.18}$	$^{+0.03}_{-0.03}$	$^{+0.005}_{-0.005}$	$^{+0.005}_{-0.005}$	$^{+0.001}_{-0.001}$

Notes. Uncertainties δ cover statistical as well as systematic effects and are 99%-confidence limits.

column of Fig. 7.4 showing that low microturbulences are found for a variety of temperatures and abundances. Moreover, the finding that the abundances do not correlate at all with microturbulence once they have been corrected for their trends with temperature (see Fig. 7.5) clearly indicates that the observed trends are not caused by an incorrect determination of ξ.

A physical explanation for the anomalous abundances observed in our late B-type stars might be the occurrence of diffusion caused by the competition between gravitational settling and selective radiative levitation (see for instance Hempel & Holweger 2003). Owing to a stronger inherent radiative pressure, which is no longer selective but affecting the plasma as a whole, diffusion is expected to be suppressed in hotter objects like mid or early B-type and O-type stars. Furthermore, any kind of mixing such as convective, turbulent, or rotationally-induced circulation is supposed to reduce or even to completely inhibit diffusion. If the observed abundance trends are indeed related to diffusion, one would, therefore, expect that all cool objects in the presented sample rotate slowly so that meridional circulation is weak or absent. As visualized in the right column of Fig. 7.4, this is not the case. For example, HD 8323 (#2), HD 90994 (#4), and HD 39764 (#6) are relatively fast rotators ($\sqrt{(v\sin(i))^2 + \zeta^2} > 80\,\mathrm{km\,s^{-1}}$) but do not show any deviation from the derived abundance trends with temperature. To further strengthen this argument, we also note from the right column in Fig. 7.5 that our abundances do not correlate with rotational line broadening at all – just as expected in the absence of diffusive processes. In addition, no deficiencies in the diffusion indicators oxygen and magnesium (Hempel & Holweger 2003) are detected. We conclude that it is very unlikely that diffusion is responsible for our late-type stars' anomalous abundances.

Because previous studies did not find any correlations of abundances with temperature (Nieva & Simón-Díaz 2011; Nieva & Przybilla 2012), the most simple explanation is that the detection of the trends is related to the new analysis method and/or to the changes in the modeling, such as the usage of opacity sampling instead of opacity distribution functions. Preliminary tests with the stars' spectral energy distributions indicate that our effective temperatures are probably underestimated in the case of late B-type stars. Similarly, the negative $E(B-V)$ values for the cool stars in Table D.4 are unphysical and imply that the respective synthetic spectra lack photons towards the ultraviolet region, which can be compensated by using models with a higher effective temperature. By doing so, many of the observed abundance trends

would also vanish. However, the reason why we probably underestimate the effective temperatures of late B-type stars is currently unknown and further investigations are planned to solve this complex problem. For the moment, we note that the correlations introduce an additional uncertainty to the absolute abundances that is of the order of 0.2–0.3 dex, which is still good, albeit no longer high-precision. Since relative abundances are not affected by this issue, the new method/modeling still allows us to perform differential analyses to identify chemical peculiarities with very high sensitivity.

7.2.5 Double-lined spectroscopic binary systems

Close inspection of the spectra revealed that eight objects in our sample are actually double-lined spectroscopic binaries. In all cases, the parameters derived for the secondary are consistent with those of the primary. In particular, both binary components were found to be coeval to within error margins indicating that our analysis provides reliable results also in the case of SB2 systems.

HD 75821 (#55), HD 119109 (#14), HD 213420 (#27): These SB2 systems have already been discussed in detail in Sect. 5.4.2.

HD 24626 (i Eri, #5): This is a known SB2 System (Chini et al. 2012). We confirm this finding because He I and Si II lines appear to be asymmetric. The spectral analysis reveals that the primary is among the coolest stars in our sample and gives a mass of $3.9^{+0.3}_{-0.2}\,M_\odot$ and an age of 100^{+18}_{-31} Myr. The gravity of the secondary is not well constrained leading to relatively large uncertainties for its mass ($4.0^{+0.7}_{-0.1}\,M_\odot$) and age ($163^{+28}_{-54}$ Myr), which are nevertheless consistent with those of the primary to within the error limits.

HD 180163 (η Lyr, #12): Classified as single-lined spectroscopic binary system (SB1) by Abt & Levy (1978), η Lyr turns out to be a SB2 system owing to the fact that almost every line in our spectrum is clearly composed of two distinct features. Both binary components are already quite evolved stars with masses of $M_\mathrm{p} = 8.7^{+0.5}_{-1.2}\,M_\odot$ and $M_\mathrm{s} = 7.7^{+1.0}_{-0.8}\,M_\odot$. The ages derived for the primary ($29^{+14}_{-\ 2}$ Myr) and secondary (39^{+16}_{-10} Myr) are consistent with each other. The spectroscopically deduced effective surface ratio $A_\mathrm{eff,s}/A_\mathrm{eff,p} = 0.758^{+0.042(\mathrm{stat.})+0.064(\mathrm{sys.})}_{-0.030(\mathrm{stat.})-0.038(\mathrm{sys.})}$ agrees well with the squared ratio of the evolutionary-track radii $(R_{\star,\mathrm{s}}/R_{\star,\mathrm{p}})^2 = 0.7^{+0.9}_{-0.4}$.

HD 21996 (#13): This object is also a SB2 system because of line asymmetries best visible for O I and Si II. The spectral analysis shows that both components are very similar main-sequence stars that are relatively unevolved. The derived masses ($M_\mathrm{p} = 5.2 \pm 0.3\,M_\odot$, $M_\mathrm{s} = 4.9^{+0.4}_{-0.3}\,M_\odot$), ages ($\tau_\mathrm{p} = 55^{+\ 8}_{-15}$ Myr, $\tau_\mathrm{s} = 51^{+13}_{-23}$ Myr), and geometric properties ($A_\mathrm{eff,s}/A_\mathrm{eff,p} = 0.796^{+0.062+0.097}_{-0.054-0.074}$, $(R_{\star,\mathrm{s}}/R_{\star,\mathrm{p}})^2 = 0.8^{+0.9}_{-0.4}$) are fully consistent with each other.

HD 36430 (#24): Morrell & Levato (1991) found the radial velocity of this object to be variable and concluded that it is probably a binary of low amplitude. We see small yet perceptible asymmetries in the profiles of, e.g., Si II/III lines that stem from a fainter companion making this object a SB2 system. It is relatively unevolved and consists of a $6.7^{+0.3}_{-0.4}\,M_\odot$ primary and a $5.3^{+0.5}_{-0.3}\,M_\odot$ secondary component. The derived ages ($\tau_\mathrm{p} = 14^{+10}_{-12}$ Myr, $\tau_\mathrm{s} = 30^{+20}_{-25}$ Myr) and surface ratios ($A_\mathrm{eff,s}/A_\mathrm{eff,p} = 0.707^{+0.029+0.137}_{-0.026-0.127}$, $(R_{\star,\mathrm{s}}/R_{\star,\mathrm{p}})^2 = 0.8^{+0.9}_{-0.4}$) paint a consistent picture.

HD 214993 (#42): This is also a SB2 system given that the recurrent line asymmetries in our

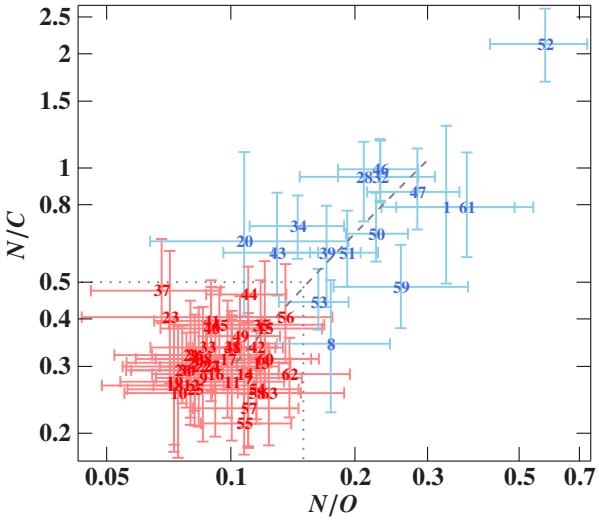

Figure 7.6: Nitrogen-over-carbon (N/C) versus nitrogen-over-oxygen (N/O) mass fractions as tracers for mixing of the stellar photospheres with CNO-burning products from the core. Numbering according to Table 7.1, values computed from Table D.3. Error bars cover statistical as well as systematic effects and are 99%-confidence limits. The gray dotted line represents the border between normal stars (colored in red) and those that show CNO-burning product mixing (blue). The gray dashed line is the predicted nuclear path given by Eq. (7.1), see Sect. 7.3.3 for details.

spectrum are so well reproduced when an additional component is considered. Both stars are somewhat evolved main sequence stars with almost identical masses ($M_\mathrm{p} = 12.0^{+0.9}_{-0.7}\,M_\odot$, $M_\mathrm{s} = 11.8^{+0.9}_{-0.7}\,M_\odot$) and ages ($\tau_\mathrm{p} = 14 \pm 2\,\mathrm{Myr}$, $\tau_\mathrm{s} = 12 \pm 2\,\mathrm{Myr}$). The spectroscopic surface ratio $A_\mathrm{eff,s}/A_\mathrm{eff,p} = 0.813^{+0.074+0.108}_{-0.016-0.060}$ fits nicely to the squared ratio of the evolutionary-track radii $(R_{\star,\mathrm{s}}/R_{\star,\mathrm{p}})^2 = 0.8^{+0.7}_{-0.4}$.

7.2.6 Signatures of CN anomalies

In order to identify abundance anomalies of carbon and nitrogen, which serve as tracers for the mixing of the photosphere with nuclear-processed material from the stellar core (see Sect. 7.3.3 for a detailed discussion), we plot the nitrogen-over-carbon (N/C) versus nitrogen-over-oxygen (N/O) mass fractions in Fig. 7.6. Sixteen stars (labeled in blue in the (T_eff, $\log(g)$) diagram of Fig. 7.2) show the presence of CNO-processed material with $N/O > 0.15$ or $N/C > 0.5$.

The high nitrogen abundances derived here for HD 3360 (#28), HD 46328 (#50), HD 50707 (#46), HD 52089 (#32), and HD 149438 (#61) have already been noticed previously (Morel et al. 2008). In addition, we find that HD 179761 (#1), the coolest object in our sample, is rich in nitrogen as well as HD 218376 (#47), one of the hottest stars, and HD 55879 (#59), one of the most evolved stars. HD 55857 (#52) displays the strongest CNO anomaly because its N/C and N/O ratios are the largest in our sample. Milder anomalies ($0.15 < N/O < 0.2$ or $0.5 < N/C < 0.8$) become apparent for HD 73105 (#8), HD 56779 (#20), HD 289002 (#34), HD 172488 (#39), HD 172427 (#43), HD 227460 (#51), and HD 37042 (#53).

7.2.7 Notes on individual objects

Several of the sample stars have come to attention because they showed some form of irregularity in the course of the analysis. In the following, we briefly describe peculiarities and/or provide additional background information for these stars. Extended discussions of several stars in common with Nieva & Simón-Díaz (2011) and Nieva & Przybilla (2012) can be found in Nieva & Przybilla (2014).

HD 3175 (#10), HD 8323 (#2), HD 21532 (#3), HD 21996 (#13): These cool stars, which are

among the more distant objects, are well-known runaway stars at high Galactic latitudes (e.g. Conlon et al. 1990). HD 21996, HD 8323, and HD 21532 show normal abundances whereas HD 3175 is at the low end of the abundance distribution for almost all elements (Fig. 7.3). Note that the projected trajectory of HD 3175 onto the Galactic plane points inward (see Fig. 7.1), which might indicate that the star originates in an outer, lower-metallicity region of the Galaxy.

HD 3360 (ζ Cas, #28): ζ Cas is a slowly-pulsating magnetic B-star (Neiner et al. 2003). All line profiles behave normal in our spectrum.

HD 35039 (o Ori, #25): o Ori is a candidate single-lined spectroscopic binary system (SB1) according to Abt & Levy (1978). Their system velocity ($\gamma = 27.9 \pm 0.3\,\mathrm{km\,s^{-1}}$) and semi-amplitude ($K = 4.1 \pm 0.4\,\mathrm{km\,s^{-1}}$) are in line with our radial velocity measurement ($v_{\mathrm{rad}} = 29.0 \pm 0.1(\mathrm{stat.}) \pm 0.1(\mathrm{sys.})\,\mathrm{km\,s^{-1}}$). No hints for a companion can be found in the available spectrum.

HD 35337 (8 Lep, #36): Quite similar to HD 35039, 8 Lep ($v_{\mathrm{rad}} = 19.8 \pm 0.1 \pm 0.1\,\mathrm{km\,s^{-1}}$) is a candidate SB1 system with $\gamma = 21.6 \pm 1.5\,\mathrm{km\,s^{-1}}$ and $K = 14.9 \pm 4.1\,\mathrm{km\,s^{-1}}$ (Abt et al. 1990).

HD 36591 (#49): According to Morrell & Levato (1991), the star has a constant radial velocity and is a member of a visual pair with common proper motions while it is classified as a SB2 system by Chini et al. (2012). However, we find no indications for a contribution of a companion in our spectrum. Therefore, we analyze it as a single object.

HD 36959 (#48), HD 36960 (#54): These stars form a visual binary (Lindroos 1985).

HD 37020 (Θ^1 Ori A, #58): Θ^1 Ori A is an eclipsing SB1 system (Stickland & Lloyd 2000). The available spectrum, which shows no evidence for a secondary component, is contaminated with emission lines of the Orion Nebula, which mostly affect hydrogen and helium lines. The Orion Nebula also explains the star's relatively high reddening of $E(B-V) = 0.279^{+0.038}_{-0.039}$ mag.

HD 37042 (Θ^2 Ori B, #53): Based on radial velocity measurements that scatter around our value, $v_{\mathrm{rad}} = 29.9^{+0.2+0.1}_{-0.1-0.1}\,\mathrm{km\,s^{-1}}$, the motion of Θ^2 Ori B was interpreted to be variable (Morrell & Levato 1991) as well as constant (Abt et al. 1991). Since the line profiles in our spectrum are normal – except for the superimposed emission lines of the Orion Nebula which is also responsible for a somewhat increased reddening of $E(B-V) = 0.175^{+0.014}_{-0.016}$ mag – we treat the star as a single object in our analysis.

HD 37209 (#45): This star is part of a common proper-motion pair (Abt & Cardona 1984) with a much fainter companion – the brightness difference is more than 3 mag (Eggleton & Tokovinin 2008). The two available spectra reveal small but still perceptible variations in the line profiles that may hint at variability.

HD 37481 (#40): Small mutable bumps in the line profiles are visible in our two spectra making this object a candidate variable star.

HD 37744 (#41): Morrell & Levato (1991) report a constant radial velocity that is consistent with the value determined here. Small but recurrent deformations of the metal line profiles in the available spectrum may be caused by variability.

HD 39764 (λ Col, #6): According to Oudmaijer & Parr (2010), λ Col is the primary compo-

nent of a visual binary system with a substantially fainter (the difference in the K band exceeds 5 mag) and, therefore, spectroscopically invisible companion. Jerzykiewicz & Sterken (1993) argue that the observed light variation is either due to rotational modulation or pulsation, which possibly explains the small asymmetries in the profiles of some Mg II and Si II lines that we detect in our spectrum.

HD 46328 (#50): This β Cepheid variable possesses a magnetic field (Hubrig et al. 2006, 2009; Silvester et al. 2009).

HD 52089 (ϵ CMa, #32): ϵ CMa is known to be magnetic (Hubrig et al. 2009; Bagnulo et al. 2012).

HD 54764 (#31): This slowly pulsating B-star (Waelkens et al. 1998) has an optical companion (Lindroos 1985) and is the most evolved object in the present sample (see Fig. 7.2). The spectrum exhibits strange line profiles, which have already been reported by Lefever et al. (2007). In addition, the high projected rotational velocity ($v \sin(i) = 131.4^{+0.1+0.4}_{-0.8-0.1}$ km s^{-1}) and high luminosity render the analysis with the available model atmospheres uncertain and possibly explain the star's conspicuously low helium and metal abundances (see Fig. 7.3). The distant position of the star within the Galactic disk is reflected by a color excess of $E(B-V) = 0.242^{+0.024}_{-0.023}$ mag.

HD 55857 (#52): The variability claimed for this object could not be confirmed by Stankov & Handler (2005). Nevertheless, the rotationally broadened lines of this very fast rotator ($v \sin(i) = 147.3^{+0.1+0.4}_{-0.1-0.1}$ km s^{-1}) exhibit clear bump-like features in their profiles. It is uncertain to what extent our spectroscopic analysis and in particular the derived CNO-burning signature (enrichment in helium and nitrogen, depletion in carbon and oxygen, see Fig. 7.3 and Sect. 7.3.3) is affected by this.

HD 55879 (#59): This evolved star of high luminosity is near the border of the parameter space where model calculations are feasible with Atlas12, similar to HD 54764. The comparatively low abundances deduced for oxygen and silicon might be related to this.

HD 55958 (#23): The claimed variability was rejected by Stankov & Handler (2005) but is supported here by the detection of bumps clearly visible in the line profiles of our spectrum.

HD 56779 (#20): The remarkably large macroturbulence ($\zeta = 76.8^{+1.9+6.2}_{-2.0-2.9}$ km s^{-1}), tiny bumps in the line profiles, and the study by Jerzykiewicz & Sterken (1977) make this a candidate variable star.

HD 64722 (#37): Pronounced line-profile deformations in the form of bumps are visible in our spectrum of this fast rotating ($v \sin(i) = 116.1 \pm 0.1 \pm 0.1$ km s^{-1}) β Cepheid variable.

HD 70839 (#35): Very much like HD 64722, this fast rotating ($v \sin(i) = 153.7^{+0.1+0.6}_{-0.1-0.1}$ km s^{-1}) β Cepheid variable exhibits distinctive bumps in the profiles of various lines, which are possibly the reason why it was (mis)classified as SB2 system by Chini et al. (2012).

HD 73105 (#8): This star is a SB1 system with an orbital period of approximately 2.4 days and a system velocity $\gamma = 22.0 \pm 3.0$ km s^{-1} (Jilinski et al. 2010). The radial velocity derived here, $v_{\rm rad} = 21.6 \pm 0.2 \pm 0.2$ km s^{-1}, implies that our spectrum was taken near conjunction, which makes it unsuitable to check whether this system qualifies as SB2 system. A high macroturbulence ($\zeta = 42.6^{+0.7+0.3}_{-1.0-0.1}$ km s^{-1}) is required to reproduce the triangle-shaped spectral lines.

HD 85953 (#21): The spectrum of this slowly-pulsating B-star exhibits normal line profiles and yields no chemical peculiarities.

HD 110956 (#15): This star might either be single (Eggleton & Tokovinin 2008) or part of a SB1 system (Chini et al. 2012). No signatures of a possible companion are visible in our spectrum.

HD 149438 (τ Sco, #61): τ Sco is magnetic (Donati et al. 2006) and is very likely the product of a binary merger (Nieva & Przybilla 2014). No anomalies are detected in the line profiles.

HD 160762 (ι Her, #16): ι Her is a well-known spectroscopic binary with an orbital period of 113.8 days (Eggleton & Tokovinin 2008). The absence of any asymmetries in the extremely sharp spectral lines qualifies this object as a SB1 system.

HD 166033 (#60): There are no indications in the available spectrum that the derived surface gravity is not trustworthy although it places the star slightly below the zero-age main sequence (see Fig. 7.2). Strong diffuse interstellar bands in combination with a comparatively high color excess $E(B-V) = 0.396^{+0.120}_{-0.116}$ mag show that this object is clearly affected by interstellar reddening. Weak nebular [N II] emission lines are visible in the vicinity of Hα.

HD 172427 (#43): This β Cepheid variable reveals prominent diffuse interstellar bands in its spectrum. The high color excess of $E(B-V) = 0.727^{+0.073}_{-0.066}$ mag is, therefore, expected and explained by its distant ($d = 1960^{+520}_{-470}$ kpc) position within the Galactic disk (see Fig. 7.1).

HD 172488 (#39): Similar to HD 172427, this distant ($d = 1290^{+270}_{-300}$ kpc) star, which is located in the Galactic disk, is substantially reddened by interstellar extinction ($E(B-V) = 0.771^{+0.050}_{-0.046}$ mag). Analogously to HD 54764, its atmospheric parameters are very close to the feasibility limit of Atlas12. Furthermore, we observe line profile deformations that pretty much resemble those of variable stars.

HD 197511 (51 Cyg, #18): Indications for non-radial pulsations in the form of clearly moving bumps were detected by Telting et al. (2006) in their very high S/N spectra of 51 Cyg. Although the S/N of our spectrum is lower, we still can confirm the finding of small but perceptible bumps.

HD 207330 (#17): The profiles of this candidate SB1 system (Abt & Cardona 1984) look strange for a number of (silicon) lines in our spectrum. Furthermore, a macroturbulence in excess of the projected rotational velocity ($\zeta = 41.6^{+0.6+0.4}_{-0.2-0.1}$ km s^{-1}, $v\sin(i) = 33.7^{+0.3+0.4}_{-0.4-0.9}$ km s^{-1}) is required to match the overall spectral shape.

HD 218376 (1 Cas, #47): The spectrum of 1 Cas yields atmospheric parameters that are in the vicinity of the feasibility limit of Atlas12 (see also HD 54764). Furthermore, we note that a relatively high macroturbulence $\zeta = 46.9^{+0.2+0.3}_{-1.6-0.1}$ km s^{-1} is required to model the observed line profiles in this somewhat reddened ($E(B-V) = 0.222^{+0.026}_{-0.020}$ mag), nitrogen-rich star.

HD 227460 (#51), HD 289002 (#34): These stars are among the faintest, most distant ones in our sample and are, therefore, stronger affected by interstellar reddening than many others.

HD 227586 (#56): This faint, reddened star is remarkable because of its low helium abundance and the fact that macroturbulent broadening alone is sufficient to model the observed line shapes in the available spectrum.

Table 7.3: Abundance comparisons.

	He	C	N	O	Ne	Mg	Al	Si	S	Ar	Fe	X	Y	Z
$\overline{\log(n(x))}$	−1.04	−3.69	−4.28	−3.36	−4.06	−4.64	−5.78	−4.58	−4.96	−5.56	−4.67	0.706	0.281	0.012
Stat./Sys.	±0.07	±0.12	±0.12	±0.12	±0.02	±0.04	±0.07	±0.12	±0.06	±0.04	±0.03	±0.035	±0.033	±0.002
σ_Δ	0.06	0.05	0.07	0.07	0.07	0.07	0.08	0.06	0.06	0.06	0.07	0.035	0.034	0.002
CAS$^{(a)}$	−1.05	−3.71	−4.25	−3.28	−3.95	−4.48	…	−4.54	…	…	−4.52	0.710	0.276	0.014
$\sigma^{(a)}$	±0.01	±0.04	±0.04	±0.05	±0.05	±0.05	…	±0.05	…	…	±0.03	…	…	±0.002
$\odot^{(b)}$	−1.06	−3.57	−4.17	−3.31	−4.07	−4.40	−5.55	−4.49	−4.88	−5.60	−4.50	0.716	0.270	0.014
	±0.01	±0.05	±0.05	±0.05	±0.10	±0.04	±0.03	±0.04	±0.03	±0.13	±0.04	…	…	…

Notes. For each element x, the sample's "mean" abundance $\overline{\log(n(x))} = \overline{\{a_{15}, a_{20}, a_{25}, a_{30}\}}$ is the average over its four anchor points listed in Table 7.2. The standard deviation $\sigma(\{a_{15}, a_{20}, a_{25}, a_{30}\})$ added in quadrature to the four anchor points' mean 1σ uncertainty $\overline{\{\delta_{15}, \delta_{20}, \delta_{25}, \delta_{30}\}}/2.576$ defines the respective 1σ uncertainty in the *"Stat./Sys." row* covering statistical as well as systematic effects. The quantity σ_Δ is the standard deviation of the distributions plotted in Fig. 7.7. The CAS and solar values are given for comparison. $^{(a)}$ CAS and standard deviations from Nieva & Przybilla (2012). $^{(b)}$ Protosolar nebula values and uncertainties from Asplund et al. (2009).

7.3 Discussion

We want to discuss the results of our investigation with the new strategy by focusing on five major topics. The first is the reliability of absolute abundances derived in this study, the second is the chemical homogeneity of the sample of reference stars, the third is the mixing of CNO-burning products as an empirical test for stellar evolution theory, the fourth is the application of the reference stars for differential abundances analyses, and the fifth is to investigate the distribution of the microturbulent velocities in the Hertzsprung-Russell diagram as a tracer for sub-surface iron convection zones predicted by recent evolutionary models.

7.3.1 Abundances

In the first step, we compare our abundances to the benchmark values given by the cosmic abundance standard (CAS, Nieva & Przybilla 2012). Because of the trends with effective temperature shown by some elements (see Sect. 7.2.4), we define the sample's "mean" abundance of an element as the average over its four anchor points used to describe the trends (Table 7.2). The corresponding standard deviation added in quadrature to the four anchor points' average 1σ uncertainty defines the respective total 1σ uncertainty. Note that these estimators are chosen since they closely resemble the sample's average and standard error of the mean if the systematic trends were absent.

Table 7.3 compares the CAS with the "mean" abundances derived in this study. There is nice agreement for helium, carbon, nitrogen, oxygen, and silicon whereas neon, magnesium, and iron appear to be less abundant beyond the stated margins of uncertainty. As discussed in Sect. 7.2.1, these deviations are caused by differences either in the model calculations or in the analysis strategy. Because several changes have been made, it is difficult to identify the exact reasons. The only obvious case is magnesium, for which many spectral lines were found to

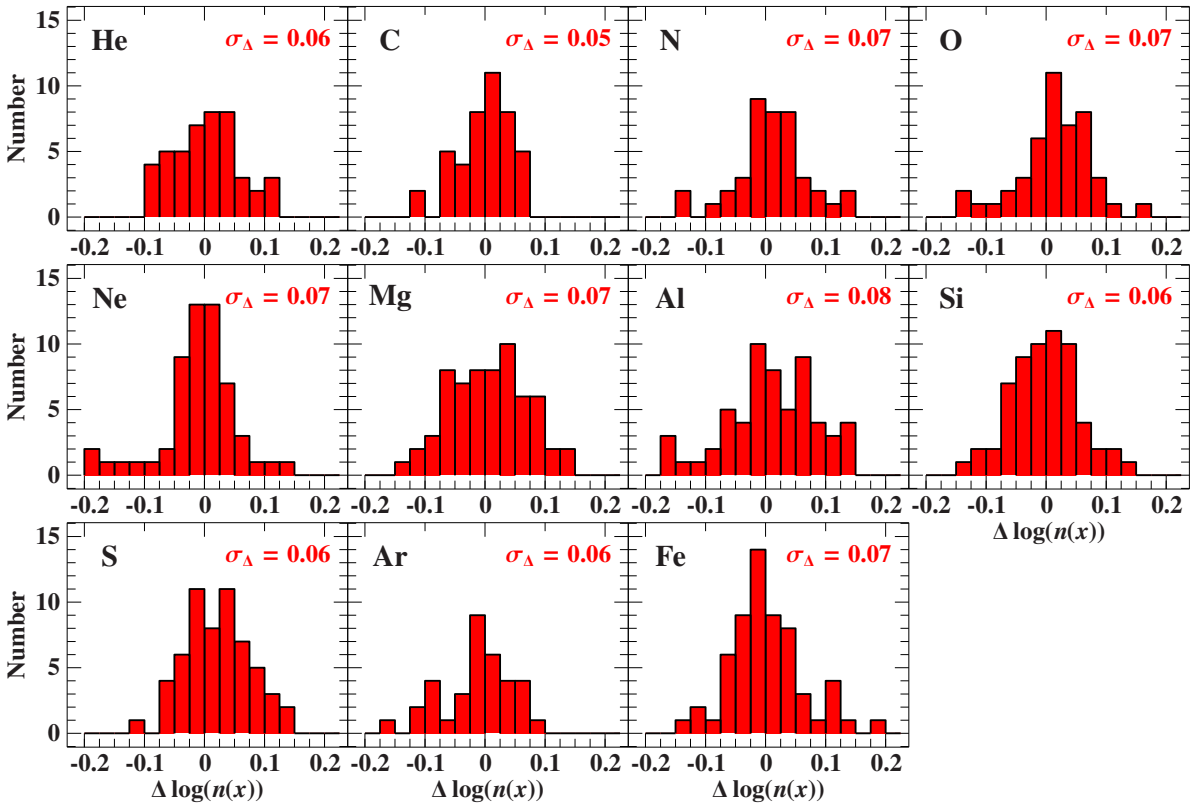

Figure 7.7: Distributions of abundances relative to the fitted cubic spline functions defined by the anchor points in Table 7.2: $\Delta\log(n(x)) = \log(n(x)) - cspline_x(a_{15}, a_{20}, a_{25}, a_{30})$. The corresponding standard deviation σ_Δ reflects therefore the 1σ scatter around the spline curves. Analogously to the fitting of the spline functions in Sect. 7.2.4, objects, which show indications for CNO mixing, or outliers, for which a $3\sigma_\Delta$ criterion is applied in addition to the 3χ-criterion of Sect. 7.2.4, are not considered here.

be very sensitive to the change from the opacity distribution functions to the opacity sampling approach. Nevertheless, the small discrepancies with respect to the CAS at a level of 0.1 dex and the detection of systematic abundance trends with temperature on a similarly low level lie within the systematic uncertainties of about 0.1 to 0.15 dex estimated by Nieva & Przybilla (2012) for the abundance determinations.

7.3.2 Chemical homogeneity in the solar neighborhood

Nieva & Przybilla (2012) found a high degree of chemical homogeneity in the solar neighborhood based on the small star-to-star abundance scatter – expressed as standard deviation σ in Table 7.3 – in their sample of early B-type stars. Hence, it is worthwhile to investigate whether this holds for our extended sample of stars and the extended set of elements – helium, aluminum, sulfur, and argon, in addition to the elements considered by Nieva & Przybilla (2012)[20]. To do so, we assume that the abundance trends with temperature (see Sect. 7.2.4) are indeed systematic and not physical. If so, the distributions of abundances relative to the cubic spline curves,

[20]Note that helium was kept fixed to the protosolar value by Nieva & Przybilla (2012).

which were used to quantify the systematic trends, have to be considered in order to determine the star-to-star abundance spread of the presented sample, see Fig. 7.7. The resulting scatter is listed as σ_Δ in Table 7.3 and is very close to its equivalent σ. In consequence, the histograms in Fig. 7.7 here and in Fig. 12 of Nieva & Przybilla (2012) are rather similar, despite some apparent differences which relate to choices of the displayed abundance ranges and bin widths. This means that we can confirm the large degree of homogeneity of the solar neighborhood found by Nieva & Przybilla (2012) from our extended sample with the same accuracy.

7.3.3 Mixing of CNO-burning products

Core hydrogen burning via the CNO bi-cycle (see Fig. 2.3) is the dominant process for energy production during the main-sequence lifetime of massive stars. Created deep in the stellar interior, the corresponding burning products remain typically hidden from observers unless they are brought to the surface, e.g., via rotationally-induced mixing (see for instance Heger & Langer 2000; Meynet & Maeder 2000). In some cases, signatures of CNO burning can be detected even in the photosphere of relatively unevolved objects like dwarfs or subgiants. Therefore, our sample is suited to directly test stellar evolution theories.

According to Przybilla et al. (2010a), the mass fractions of carbon (C), nitrogen (N), and oxygen (O) at the surface of stars in the mass range considered here are expected to follow a nuclear path that is defined by the conversion of ^{12}C to ^{14}N at the onset of the CN cycle, which dominates the burning of hydrogen at the beginning. In the $(N/C, N/O)$ diagram (Fig. 7.6), this path can be approximated by a straight line with the following analytical expression for its slope:

$$\frac{\mathrm{d}(N/C)}{\mathrm{d}(N/O)} = \frac{(N/C)}{(N/O)}\left(1 + \frac{6}{7}\frac{N}{C}\right) = 3.766\,. \tag{7.1}$$

The right-hand side of this equation has been evaluated using the sample's mean abundances (for unmixed stars) presented in Sect. 7.3.1.

The abundances derived in this study are in excellent agreement with the theoretical considerations leading to Eq. (7.1), see Fig. 7.6. The vast majority of the sample stars clusters around the pristine N/C and N/O ratios. On the other hand, sixteen objects in the sample have $N/O > 0.15$ or $N/C > 0.5$, i.e., they exhibit indications for CNO-burning product mixing. Most of them scatter around the predicted nuclear path, which shows that hydrogen burning in these stars is indeed well described by the nuclear reactions at the beginning of the CN cycle. In contrast, the chemical composition in the photosphere of HD 55857 (#52) reflects an advanced stage of CNO burning since nitrogen is not only enhanced at the expense of carbon but also of oxygen. Likewise, the abundance of the burning end product helium is significantly increased in this object. Thus, it is a good candidate for more detailed tests of stellar evolution models in the future.

7.3.4 Differential analyses

While our new analysis technique is not yet able to provide absolute abundances over the entire atmospheric parameter range investigated here at the same high precision than Nieva & Przybilla (2012) over their more restricted parameter range, we shall demonstrate that it is a

powerful tool to pinpoint abundance anomalies at a level as small as 0.1 to 0.2 dex by means of differential analyses.

Independent of the question as to whether or not the temperature trends are physical, the quantity σ_Δ in combination with the cubic spline functions $cspline(a_{15}, a_{20}, a_{25}, a_{30})$ can be used to identify chemically peculiar objects via a differential abundance analysis. Defined as the standard deviation of the distribution of abundances relative to the spline curves, σ_Δ reflects the amount of scatter around the spline functions that is expected for normal stars. Objects deviating more than about $3\sigma_\Delta$ from the reference curve are thus tendentially peculiar. In the present sample, the most obvious case is HD 55857 (#52), which is already mentioned in Sect. 7.3.3, due to its anomalous abundances of carbon ($\Delta\log(n(\mathrm{C})) \approx -6.2\,\sigma_\Delta$), nitrogen ($\Delta\log(n(\mathrm{N})) \approx 7.6\,\sigma_\Delta$), oxygen ($\Delta\log(n(\mathrm{O})) \approx -2.0\,\sigma_\Delta$), neon ($\Delta\log(n(\mathrm{Ne})) \approx -3.2\,\sigma_\Delta$), and sulfur ($\Delta\log(n(\mathrm{S})) \approx -3.5\,\sigma_\Delta$).

7.3.5 The microturbulent velocity – a tracer for sub-photospheric convection?

Introduced initially as a fudge factor to the spectroscopic analysis to derive consistent abundances from spectral absorption lines with different equivalent widths, the microturbulence parameter ξ has been recently suggested to be a tracer of a sub-surface convection zone by Cantiello et al. (2009). The microturbulent motion in the photosphere is thought to be triggered by a sub-photospheric convection driven by opacity peaks associated with iron. Using a stellar evolution code and the mixing length theory to parameterize the convective motion, Cantiello et al. determined the occurrence and properties of the iron convection zone as a function of stellar parameters. From their models of B- and O-type stars, they predict that this zone and, thus, also the microturbulent velocity becomes more pronounced when going from the zero-age main sequence to cooler surface temperatures and to higher luminosities (see Fig. 9 in Cantiello et al. 2009). Both predictions are exceptionally well confirmed by our empirically derived ξ values as visualized in Fig. 7.8, which shows that there is excellent quantitative agreement between derived microturbulences and predicted average convection velocities. This finding strongly supports the idea that there is a physical connection between photospheric microturbulent and sub-photospheric convective motion on and slightly beyond the main sequence.

7.4 Summary

In this Chapter, atmospheric and fundamental stellar parameters of 63 mid B- to late O-type dwarfs and subgiants were derived in a homogeneous manner. This was in order to test our novel, objective spectroscopic analysis method as well as some changes in the modeling strategy in a practical application.

As a first result, we note that the new approach yields absolute abundances that partly differ from the cosmic abundance standard (Nieva & Przybilla 2012), which we consider to be the benchmark. This applies, on the one hand, to the sample's mean abundances for the elements magnesium, neon, and iron, which are 0.11–0.16 dex lower than expected from the CAS. On the other hand, systematic abundance trends with temperature, which are of the order of 0.1–0.3 dex over the entire range of $T_{\rm eff}$-values considered here, were found, which calls for

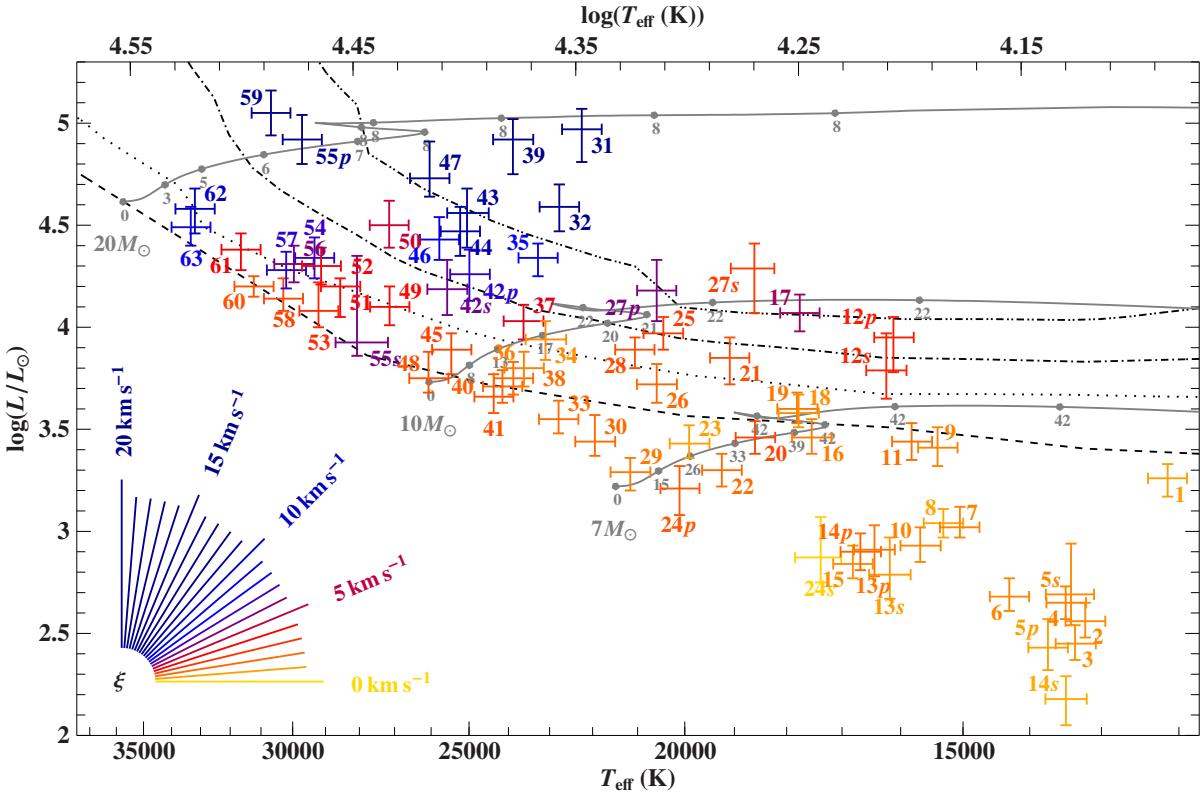

Figure 7.8: Position of the 63 reference stars in a ($T_{\rm eff}$, log($L/L_\odot$)) diagram. Numbers and lines as in Fig. 7.2. The microturbulence ξ is color coded according to the description in the lower left corner. The four non-solid, gray lines are contour lines for the average convective velocity in the upper layers of the iron convection zone. They were extracted from Fig. 9 in Cantiello et al. (2009). Note that the contour lines had to be shifted to roughly account for the two different metallicities used for the computation of evolutionary tracks (here: $Z = 0.014$, Cantiello et al.: $Z = 0.02$).

further studies to clarify their origin. Nevertheless, the high degree of chemical homogeneity of nearby early B-type stars is confirmed from an enlarged sample of stars and extended to three additional chemical species (aluminum, sulfur, and argon) once the aforementioned abundance trends are accounted for. The degree of homogeneity is reflected by a star-to-star scatter that ranges from 0.05 dex to 0.08 dex depending on the element under consideration. We conclude that the new method/modeling is not yet suited to derive high-precision, absolute abundances at the CAS level. Nevertheless, we demonstrate that the abundances of our sample of stars provide a powerful basis for differential analyses of other stars to identify tale-telling anomalies to high accuracy. The signature of CNO-burning product mixing is found in 16 objects, including several relatively unevolved objects. The stars' position in the ($N/C, N/O$) diagram is checked against the theoretically predicted nuclear path, which reveals good agreement between theory and observation. In Chapter 8, we shall carry out differential analyses of runaway stars using the sample presented here.

Finally, the current results allow to stringently test model predictions for the physical origin of the microturbulence in early-type stars like the ones proposed by Cantiello et al. (2009).

While information on the distribution of accurate and precise microturbulent velocities in the upper Hertzsprung-Russell diagram has been scarce so far, the present sample provides such data for a large number of hot stars across and slightly beyond the main sequence. Indeed, the results derived here perfectly match the predictions by Cantiello et al. and, therefore, provide strong observational support for the assumption that the photospheric microturbulent motion in early-type stars is linked to a sub-photospheric convective motion.

8 Runaway stars

Runaway stars are kinematically peculiar objects that formed either by dynamical interactions (initial dynamical relaxation: Poveda et al. 1967; close many-body encounters such as binary-binary interactions: Leonard & Duncan 1988; slingshot mechanism: Hills 1988) or by a supernova explosion disrupting a binary system (Blaauw 1961). Depending on the details of the ejection event, the velocity $v_{\rm ej}$ with which the runaway star is ejected from its former host system can range from modest values of a few dozen kilometers per second to extreme values of several hundred kilometers per second. Runaway stars with low ejection velocities remain close to their place of birth and are, hence, primarily identified via their peculiar velocity vector that points away from star-forming regions. In contrast, runaway stars with extreme ejection velocities are so fast that they can migrate into the Galactic halo even during the relatively short main-sequence lifetime of early-type stars. Since the halo is usually populated by old, low-mass stars only, any OB type star in the halo qualifies as runaway candidate. Consequently, photometric surveys can be used to find members of the extreme class of runaway stars by searching for hot and thus blue objects above or below the Galactic disk. Halo runaway stars are not only relatively easy to detect but are also particularly interesting because they probe the most extreme ejection events, which are typically also the most interesting ones as exemplified by the star HD 271791 (Heber et al. 2008).

The B-type subgiant HD 271791 is the first known hyper-runaway star, which is, by definition, a runaway star that is gravitationally unbound to the Milky Way but – unlike the hypervelocity stars – does not originate in the Galactic center. A detailed quantitative abundance analysis revealed enhancements of oxygen, neon, aluminum, silicon, and sulfur with respect to iron in the atmosphere of HD 271791 (Przybilla et al. 2008b). This signature can be explained by the accretion of material that is ejected during a core-collapse supernova explosion where the exploding star's outer layers are expelled. In the simple picture of Fig. 2.5, the ejected layers mainly consist of helium, carbon, oxygen, and silicon. In the course of the supernova explosion, these can be partly converted to neon, magnesium, and sulfur via subsequent captures of helium nuclei, which are commonly denoted α-particles. Further reaction chains can also produce aluminum and argon to some extent. Iron, on the other hand, is not expected to be released in significant amounts since the central iron core collapses to a neutron stars or a black hole. An enhancement relative to iron in the so-called α-elements oxygen, neon, magnesium, silicon, and sulfur or in the chemical species carbon, aluminum, and argon is thus a clear indication for the supernova scenario as runaway ejection event. The amount and the specific pattern of the enhancement depend, among others, on the geometry of the pre-supernova binary system, the details of the primary component's supernova explosion, and the interaction of the secondary star with the ejected material and are impossible to predict. However, the closer the progenitor binary system, the larger the geometrical cross section of the secondary and the higher is the probability to accrete supernova ejecta. The best candidates to exhibit supernova pollution are consequently the most extreme runaway stars because these stem from the closest binary systems where the orbital velocity is largest. The discovery of α-element enhancement in the atmosphere of HD 271791 shows that runaway stars represent a so far unexploited indicator for stellar nucleosynthesis.

In this Chapter, the analysis of 18 rather extreme runaway stars is presented. Unlike other studies (Conlon et al. 1990; Hoogerwerf et al. 2001; Silva & Napiwotzki 2011), we investigate

not only the kinematic properties of the runaway stars but also perform a quantitative spectroscopic analysis to distinguish between the different ejection channels and to reveal their origin. Motivated by the findings about HD 271791, we particularly search for stars that show signatures of α-element enhancement in order to identify more candidates for the supernova ejection scenario. Stars of spectral type O and B are especially useful for this purpose. First of all, these stars are luminous making it relatively easy to acquire high-quality spectra even if they are far away. Additionally, their young ages facilitate the kinematic investigation since the uncertainty in the results of the numerical orbit calculation, which is introduced by uncertainties in the initial conditions, scales with the orbit integration time. Moreover, pronounced convection zones are not expected to occur in the stellar envelope of massive stars (see Sect. 2.3). This is important for the abundance analysis because the anyway small pollution with supernova ejecta at the surface could otherwise be washed out due to convective mixing with layers below the photosphere. Stars of spectral type F to M in the Harvard classification are therefore less promising candidates although the extent and, hence, the mass of the convection zone decreases towards spectral type F[21]. The disadvantage of A-type stars is that their surface abundances are often affected by diffusion processes (gravitational settling versus selective radiative levitation) making it very difficult to check their abundance patterns for supernova signatures. In contrast, the luminosity in hotter objects like B-type or late O-type stars is so large that the radiative pressure affects the stellar plasma as a whole and, in this way, suppresses diffusion. Early O-type stars and the even hotter Wolf-Rayet stars, on the other hand, are so luminous that radiative driven stellar winds occur which render the spectral modeling and thus the analysis more complicated. Moreover, strong stellar winds lead to mass loss which removes the accreted supernova material again. Finally, the frequency of stars decreases with stellar mass. Accordingly, it is unlikely to find a lot of O stars in general and in particular among the runaway stars, which are either the less massive secondary components of a disrupted binary or the less massive objects in a stellar encounter.

This Chapter is structured as follows: The sample of 18 runaway stars is introduced in Sect. 8.1, the combined kinematic and spectroscopic analysis method is outlined in Sect. 8.2, the flagship runaway star HD 271791 is revisited in Sect. 8.3, the individual results for the remaining stars are discussed in Sect. 8.4, and a summary is given in Sect. 8.5.

8.1 The runaway sample

This work mainly focuses on extreme runaway stars in the Galactic halo because these objects are supposed to be the most promising candidates to find a signature for supernova pollution in the case that the runaway star is indeed ejected via the disruption of a binary system by the explosion of the primary component. Therefore, the targets of prime interest are more distant and consequently considerably fainter than the nearby reference stars of Chapter 7. To obtain high-resolution spectra with sufficient S/N ratio, observations were performed not only at 2.2 to 2.5 m telescopes but also at the 8.2 m ESO Very Large Telescope. Owing to the limited available observing time, compromises had to be made with respect to the quality of the spectra on the one hand and the number of observed targets on the other hand. To this end, high-resolution ($\lambda/\Delta\lambda \geq 30\,000$) spectra with good quality ($60 \leq \mathrm{S/N} \leq 300$) were obtained for 18 halo

[21] Indeed, Israelian et al. (1999) report the detection of α-element enhancement in an F-type star.

Table 8.1: Runaway stars: ID, spectroscopy, photometry, astrometry.

#	Object	S/N	Flag	V	$U-B$	$B-V$	$b-y$	m_1	c_1	H_p	B_t	V_t	$\mu_\alpha \cos\delta$	μ_δ	References
								(mag)					(mas yr^{-1})		
Cafe: $\lambda/\Delta\lambda = 55\,000$															
2	HD 78584	115		8.180	−0.630	−0.170	…	…	…	8.1178	7.965	8.128	15.26	6.05	(1),(6),(7)
Feros: $\lambda/\Delta\lambda = 48\,000$															
7	HIP 13800	270		10.307	−0.639	−0.106	−0.041	0.096	0.338	10.2863	10.118	10.120	4.88	−3.22	(1),(4),(6),(7)
14	HD 22586	190	c d	8.030	−0.910	−0.190	−0.054	0.066	0.022	7.9732	7.800	7.975	7.52	10.02	(1),(4),(6),(7)
1	EC 09452−1403	60		13.81	−0.48	−0.06	…	…	…	…	…	…	−2.8	3.0	(2),(8)
17	HD 204076	190	c d	8.790	−0.840	−0.150	−0.052	0.068	0.068	8.7544	8.619	8.753	10.11	−11.76	(1),(4),(6),(7)
11	PHL 2018	150		11.770	…	…	−0.091	0.102	0.216	…	11.470	11.899	0.7	−1.3	(4),(7),(8)
8	HD 218970	275		9.750	−0.730	−0.190	−0.089	0.109	0.241	9.6807	9.524	9.754	46.48	32.39	(1),(4),(6),(7)
Fies: $\lambda/\Delta\lambda = 45\,000$															
18	HD 100340	170		10.125	−0.971	−0.242	−0.108	0.090	−0.007	10.0318	9.805	10.088	3.36	10.92	(1),(4),(6),(7)
6	HIP 60350	140		11.600	…	…	−0.073	0.112	0.320	11.5675	11.431	11.798	−13.51	16.34	(4),(6),(7)
Foces: $\lambda/\Delta\lambda = 40\,000$															
3	HD 69686	200		7.120	…	…	−0.076	0.114	0.389	7.0450	6.890	7.053	−86.17	7.21	(4),(6),(7)
Uves: $\lambda/\Delta\lambda = 30\,000$															
13	HIP 3013	280	c d	10.876	−0.829	−0.196	−0.097	0.092	0.181	10.8257	10.541	10.730	9.45	−0.79	(1),(4),(6),(7)
10	PG 0122+214	120		12.842	…	…	−0.112	0.115	0.240	…	12.361	13.231	−0.9	−2.0	(5),(7),(8)
9	HD 271791	300		12.258	…	…	−0.047	0.068	0.238	12.2770	12.150	12.266	−1.50	6.89	(4),(6),(7)
4	PG 0934+145	120		13.507	…	…	−0.048	0.083	0.347	…	…	…	0.8	1.9	(5),(8)
5	PG 1315−077	180	a	12.09	−0.87	0.23	−0.079	0.141	0.344	…	…	…	−7.5	−2.2	(3),(5),(8)
15	PHL 159	260	c d	10.760	…	…	−0.073	0.088	0.144	10.7315	10.617	10.809	−5.79	−7.69	(4),(6),(7)
16	PHL 346	235	b d	11.470	…	…	−0.068	0.070	0.094	…	11.222	11.441	4.1	−6.0	(4),(7),(8)
12	PG 2345+241	200	c d	12.463	…	…	−0.037	0.063	0.249	…	12.066	12.378	−2.4	−3.5	(5),(7),(8)

Notes. The numbering of stars (first column) is related to the derived effective temperature, see Table D.6. The third column is the mean S/N of the spectrum, which was obtained with one of the five high-resolution spectrographs Cafe (Aceituno et al. 2013), Feros (Kaufer et al. 1999), Fies (Frandsen & Lindberg 1999), Foces (Pfeiffer et al. 1998), and Uves (Dekker et al. 2000). Photometric data: Johnson-Cousins magnitudes U, B, and V were compiled from references (1), (2), (3), (4), or (5), Strömgren colors $b-y$, m_1, and c_1 from (4) or (5), the Hipparcos magnitude H_p from (6), and Tycho magnitudes B_t and V_t from (7). Astrometric data: Proper motions in right ascension $\mu_\alpha \cos\delta$ and declination μ_δ were compiled from (6) or (8) if not available in (6). For reasons of clarity, uncertainties are not given here but can be found in the respective references.

Flags. (a) SB2 system. (b) β Cepheid variable according to Stankov & Handler (2005). (c) Candidate β Cepheid variable based on spectral line profiles. (d) Asymmetric line profiles that may render the spectral analysis less certain.

References. (1) Mermilliod (1991); (2) Kilkenny et al. (1997); (3) Holmgren et al. (1992); (4) Hauck & Mermilliod (1998); (5) Wesemael et al. (1992); (6) van Leeuwen (2007); (7) Høg et al. (2000); (8) Zacharias et al. (2013).

runaway stars at visual magnitudes V in the range $7 < V < 14$ mag. The stars' spectroscopic, photometric, and astrometric data is listed in Table 8.1. We note that (statistically significant) Hipparcos parallaxes are not available for these targets.

The current sample is compiled from literature and, thus, contains only runaway stars that are already well-known. However, most of the previous studies use photometric instead of spectroscopic methods to derive the atmospheric parameters $T_{\rm eff}$ and $\log(g)$, which then, for instance, enter the distance determination and, therefore, the kinematic investigation. Since elemental abundances are not measurable via photometry at all, the discussion about the origin of these stars is based solely on the deduced kinematic properties, which may also suffer from the limited accuracy in the photometric analysis. This deficiency is overcome here by performing a combined kinematic and spectroscopic analysis, which encompasses a quantitative abundance determination, to unravel the nature of some of the most extreme runaway stars known to date.

The current sample is not representative of runaway stars in general because of the limited number of objects and immanent selection effects. Examples for the latter are the focus on extreme runaway stars and practical constraints from the observational perspective. Moreover, stars with large projected rotational velocities ($v \sin(i) > 150\,\mathrm{km\,s^{-1}}$) were mainly avoided since the strong smearing and blending of spectral lines can render the abundance analysis much less reliable. As a consequence, the targets are discussed individually in the course of this work instead of investigating at the properties of the entire sample.

The three-dimensional spatial distribution of the runaway stars is shown in Fig. 8.1 (anticipating spectroscopic distances from Sect. 8.2)[22]. Apart from the selection effect of choosing objects above or below the Galactic disk, the objects seem to be more or less randomly distributed around the Sun.

8.2 Combined spectroscopic and kinematic analysis

The spectroscopic analysis of the runaway stars is based on exactly the same method (see Chapter 5) as used for the reference stars in Chapter 7. By considering differential instead of absolute quantities, systematic effects and their respective uncertainties are consequently expected to cancel out. In particular, this applies to those elemental abundances that show a systematic trend with temperature (see Sect. 7.2.4). It is thus advisable to express the abundances relative to the standard derived from the reference stars when searching for chemical peculiarities in the runaway stars. As previously mentioned, the iron abundance is expected to be unaffected by the pollution with supernova ejecta. Candidates for the supernova ejection channel can therefore be identified by making use of the quantity

$$\begin{aligned}\left[\frac{n(x)}{n(\mathrm{Fe})}\right] &\equiv \log\left(\frac{n(x)}{n(\mathrm{Fe})}\right) - \log\left(\frac{n(x)}{n(\mathrm{Fe})}\right)_{\rm reference} \\ &= \log(n(x)) - \log(n(x))_{\rm reference} - (\log(n(\mathrm{Fe})) - \log(n(\mathrm{Fe}))_{\rm reference}) \\ &= \log(n(x)) - \mathrm{cspline}_{\rm x}(a_{15}, a_{20}, a_{25}, a_{30}) - (\log(n(\mathrm{Fe})) - \mathrm{cspline}_{\rm Fe}(a_{15}, a_{20}, a_{25}, a_{30})) \\ &= \Delta\log(n(x)) - \Delta\log(n(\mathrm{Fe}))\,,\end{aligned} \tag{8.1}$$

[22] In contrast to Fig. 7.1, velocities are with respect to the Galactic rest frame instead of relative to the local standard of rest.

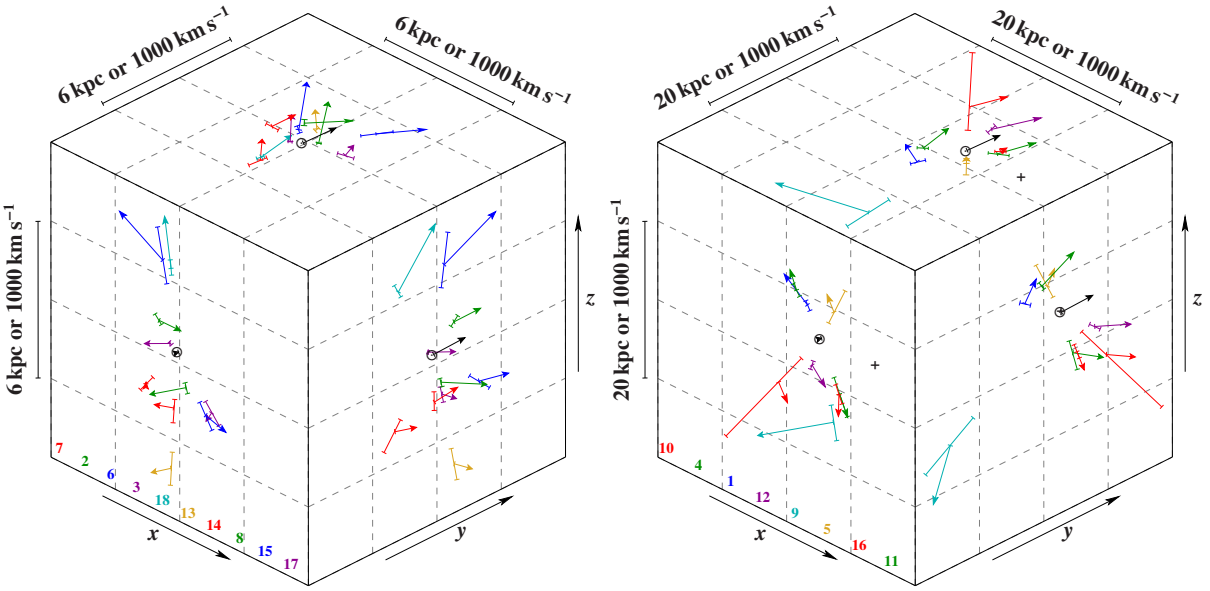

Figure 8.1: Three-dimensional spatial distribution of the runaway stars in the coordinate system defined by Fig. 2.7. Position uncertainties are given by error bars while the vectors symbolize the velocities in the Galactic rest frame. Scales for distances and velocities are given by the black bars. The positions of the Sun and the Galactic center (*right panel only*) are marked by a black $\odot$ and a black +, respectively. Numbers correspond to those of Table 8.1 and are sorted in ascending order with respect to the x-coordinate. Colors are intended to guide the eye and do not have any further meaning. For the sake of clarity, the total sample has been split up in two subsets according to the distance d: $d < 5$ kpc (*left*) and $d \geq 5$ kpc (*right*).

which is larger than zero if the abundance ratio of element x over iron is enhanced with respect to the reference stars. Unfortunately, the differential approach is not appropriate for all quantities. For instance, systematic effects such as the probably underestimated effective temperatures for late B-type stars (see Sect. 7.2.4) or the Balmer line Stark broadening issue (see Chapter 6) affect the absolute value of the spectroscopic distance and, in this way, the kinematic investigation. In that case, the systematic uncertainties do not cancel out but have to be propagated in order to derive reliable final uncertainties, which typically lowers the significance of the results.

The runaway stars' atmospheric parameters, which are based on VCS tables for the Balmer line Stark broadening, and the corresponding stellar parameters are summarized in Tables D.6 and D.5 while their positions in a $(T_{\rm eff}, \log(g))$ diagram are shown in Fig. 8.2. The discussion of the individual results is postponed to Sect. 8.4. It is very important to stress here that the stellar parameters are based on single-star evolutionary tracks although the ejected runaway star is supposed to be a former member of a binary or multiple system in each of the ejection scenarios. This is owing to the fact that the configuration of the pre-ejection system is completely unknown making it impossible to model its evolution. Therefore, the most pragmatic approach is to deduce stellar parameters under the assumption of single-star evolution and to keep in mind that the results, in particular the stars' lifetimes, are only rough estimates in the case that the progenitor binary system has interacted. Note that there are two other effects that play also an important role for the determination of stellar parameters, namely the rotation and metallicity of a star. On the one hand, stellar rotation leads to a centrifugal force and, thus, to a lower surface

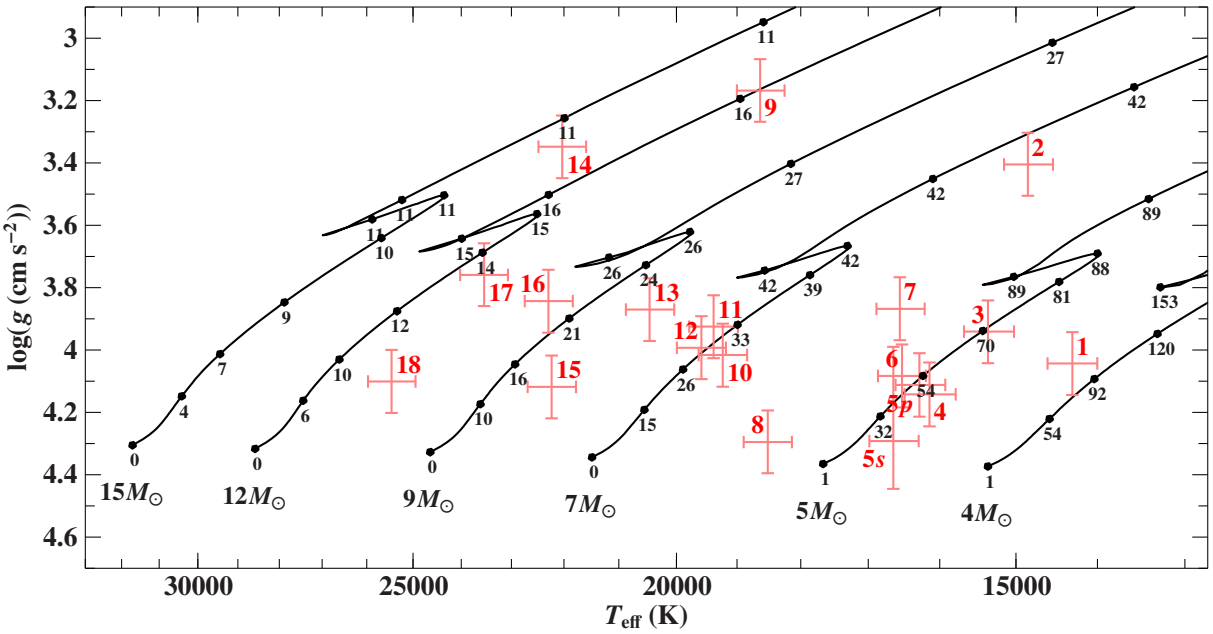

Figure 8.2: Position of the 18 runaway stars in a $(T_{\rm eff}, \log(g))$ diagram. Overlaid are evolutionary tracks for non-rotating stars ($\Omega/\Omega_{\rm crit} = 0$) of metallicity $Z = 0.014$ and different initial masses (Georgy et al. 2013). Black filled circles and numbers mark the age in Myr. Red numbers correspond to those of Table 8.1 with "p" denoting the primary and "s" the secondary component of a SB2 system. Error bars indicate 99%-confidence limits.

gravity. Evolutionary tracks that account for rotation are consequently systematically shifted upwards in the $(T_{\rm eff}, \log(g))$ diagram, see for instance the loci of the zero-age main sequence in Fig. 6.2. On the other hand, rotational mixing increases the stellar lifetime because it continually provides new fuel to the central burning region. Evolutionary tracks for rotating stars are hence not only shifted but also stretched with respect to their non-rotating counterparts. We use the projected rotational velocity as a proxy for the true rotation (see Sect. 5.3.3) in order to choose among the available tracks with different rotation. The metallicity enters, for example, the energy generation rate, the mean molecular weight, or the opacity of the stellar matter and is therefore crucial for the entire structure and evolution of a star. According to Fig. 6.2, stars on the zero-age main sequence become hotter and more compact if the metallicity is decreased. We account for metallicity effects in the stellar parameter determination by estimating the metallicity of a runaway star from its derived surface abundances which is then used to interpolate the evolutionary tracks with different metallicities by Georgy et al. (2013) accordingly.

The spectroscopic analysis provides the distance d to the star and its radial velocity $v_{\rm rad}$. This information, combined with equatorial positions and proper motions in right ascension (α, $\mu_\alpha \cos\delta$) and declination (δ, μ_δ), gives the full six-dimensional kinematics of the object at present time[23], from which the current Galactic rest-frame velocity $v_{\rm Grf} = \sqrt{\vec{v}\cdot\vec{v}}$ follows. A model for the gravitational potential $\Phi(\vec{x})$ of the Milky Way (see Chapter 3) yields the star's local escape velocity $v_{\rm esc}(\vec{x}) = \sqrt{-2\Phi(\vec{x})}$, which can be used to infer whether or not a star is bound

[23]The Galactocentric coordinate system introduced in Fig. 2.7 is used in the following to express coordinates $\vec{x} = (x, y, z)$ and velocities $\vec{v} = (v_x, v_y, v_z)$.

Table 8.2: Galactic abundance gradients used in this work.

Element x	He	C	N	O	Ne	Mg	Al	Si	S	Ar	Fe
m_x (dex kpc^{-1})	0	−0.103	−0.085	−0.033	−0.056	−0.034	−0.046	−0.068	−0.049	−0.051	−0.058
Uncertainty	±0	±0.018	±0.020	±0.005	0.007	±0.007	±0.013	±0.009	±0.008	±0.006	±0.009
Reference	...	(1)	(2)	(3)	(4)	(3)	(5)	(5)	(3)	(4)	(3)

Notes. The helium abundance is assumed to be primordial and, hence, only negligibly affected by stellar nucleosynthesis giving a flat gradient. Uncertainties are (interpreted as) 1σ.

References. (1) Esteban et al. (2005); (2) Carigi et al. (2005); (3) Firnstein (2010); (4) Maciel & Köppen (1994); (5) Lemasle et al. (2013).

to the Milky Way by comparing v_{Grf} to v_{esc}. Moreover, stellar trajectories can be computed for the future and the past. By tracing back the orbit to the Galactic plane, one can determine the possible birthplace of a runaway star in the Galactic disk[24], which is, for instance, characterized by the Galactocentric radius $r = \sqrt{x^2 + y^2}$. Additionally, the flight time τ_{flight} and the ejection velocity v_{ej}, defined as the velocity at disk intersection relative to the rotating Galactic disk, are then accessible. Both of them are important quantities to check if a runaway scenario is realistic at all. On the one hand, the derived evolutionary age of a runaway star has to be larger than its flight time to be consistent with the ejection hypothesis. On the other hand, the ejection velocity imposes constraints on the ejection event and, hence, allows to argue for or against one of the ejection mechanisms. Uncertainties in the input parameters d, v_{rad}, $\mu_\alpha \cos\delta$, and μ_δ are propagated via a Monte Carlo method that simultaneously and independently varies the initial parameters (i.e., the components of position and velocity), assuming for each a Gaussian distribution. Tables D.7, D.8, and D.9 list the results obtained from 100 000 Monte Carlo runs for the three different Milky Way mass models discussed in Chapter 3. If not stated otherwise, the following results mentioned in the text will always refer to Model I and uncertainties will be 99%-confidence limits.

A first and expected finding of the kinematic analysis is that most of the runaway stars do not originate in regions with Galactocentric radii r similar to the Sun (see Eq. (3.3)) but were ejected from inside or outside the solar circle. The sample of nearby comparison stars, which is used to define the reference standard for the differential abundance analysis, is only characteristic of the solar neighborhood ($r \approx r_\odot \pm 0.6\,\mathrm{kpc}$) and, thus, might not be representative of the runaway stars' pristine chemical composition because the Galactic chemical evolution is not uniform but a spatial function. The star-formation rate roughly scales with the density of the interstellar medium, which culminates at the center of the Milky Way and decreases radially outwards. Consequently, the chemical enrichment by supernova explosions of massive stars is highest at the Galactic center and falls off towards the outer rim of the Galactic disk, which then causes a downward gradient in the abundance of a chemical species x with increasing Galactocentric radius r. It is common practice in literature to describe this abundance gradient as a linear function with respect to the logarithmic abundances relative to hydrogen:

$$\log\left(\frac{n(x)}{n(\mathrm{H})}\right)(r) = \log\left(\frac{n(x)}{n(\mathrm{H})}\right)_\odot + m_x(r - r_\odot)\,. \tag{8.2}$$

[24]The disk-crossing coordinates are labeled in the following by the subscript "d".

Under the reasonable assumption that the hydrogen abundance is only negligibly affected by stellar nucleosynthesis and is thus independent of r, this yields:

$$\log\left(n(x)\right)(r) = \log\left(n(x)\right)_{\odot} + m_x(r - r_{\odot})\,. \tag{8.3}$$

Using the abundances from the reference stars as a proxy for the chemical composition in the solar environment, the reference abundances in Eq. (8.1) should hence be corrected as follows to account for the Galactic abundance gradients:

$$\log\left(n(x)\right)_{\text{reference}} \rightarrow \log\left(n(x)\right)_{\text{reference}} + m_x(r - r_{\odot})\,. \tag{8.4}$$

Equation (8.1) transforms then into

$$\left[\frac{n(x)}{n(\text{Fe})}\right] \rightarrow \left[\frac{n(x)}{n(\text{Fe})}\right]_{\text{corr}} \equiv \left[\frac{n(x)}{n(\text{Fe})}\right] - (m_x - m_{\text{Fe}})(r - r_{\odot})\,. \tag{8.5}$$

The abundance gradients used in this work are listed in Table 8.2. Unfortunately, a homogeneous study, which encompasses all ten metals considered here, is not available in the literature. Therefore, gradients from different sources and, thus, abundance tracers have to be mixed. The values by Firnstein (2010) are derived from the spectroscopic analysis of the descendents of OB-type dwarfs, namely BA-type supergiants, by employing the same codes (Atlas, Detail, Surface) as this study making it our preferred reference. The gradients for carbon (Esteban et al. 2005) and nitrogen (Carigi et al. 2005) are derived from H II regions, which are ionized clouds of gas powered by massive stars that directly trace the interstellar medium. Maciel & Köppen (1994) use the emission lines of planetary nebulae, i.e., the expelled outer layers of intermediate mass stars, to determine the gradients for neon and argon while Lemasle et al. (2013) exploit Cepheids, i.e., pulsating stars of spectral type F and G, to deduce the aluminum and sulfur gradients.

Note that the correction for the abundance gradients has its caveats and is used here solely to give an idea of how the differential abundance analysis might be affected by a non-uniform Galactochemical evolution. On the one hand, the published gradients exhibit a non-negligible spread. For instance, the sulfur gradient was found to be $-0.067 \pm 0.006\,\text{dex}\,\text{kpc}^{-1}$ by Maciel & Köppen (1994), $-0.049 \pm 0.008\,\text{dex}\,\text{kpc}^{-1}$ by Firnstein (2010), and $-0.095 \pm 0.015\,\text{dex}\,\text{kpc}^{-1}$ by Lemasle et al. (2013). Moreover, the scatter of the individual data points, from which the gradients were derived via linear regression, is even larger. On the other hand, the runaway stars sample a very wide range of Galactocentric radii which is not fully covered by any of the available tracers (BA-type supergiants: $6\,\text{kpc} < r < 12\,\text{kpc}$; H II regions: $6\,\text{kpc} < r < 11\,\text{kpc}$; planetary nebulae: $4\,\text{kpc} < r < 13\,\text{kpc}$; Cepheids: $4\,\text{kpc} < r < 15\,\text{kpc}$) so that the published gradients have to be extrapolated[25]. Finally, the various abundance tracers probe somewhat different epochs of Galactochemical evolution.

8.3 The hyper-runaway star HD 271791 revisited

In this and the following section, the results of the combined spectroscopic and kinematic analysis, which are summarized in Tables D.5, D.6, D.7, D.8, and D.9, are discussed individually

[25]The extrapolated values at $r = 1\,\text{kpc}$ and $r = 20\,\text{kpc}$ are used for $r < 1\,\text{kpc}$ and $r > 20\,\text{kpc}$, respectively.

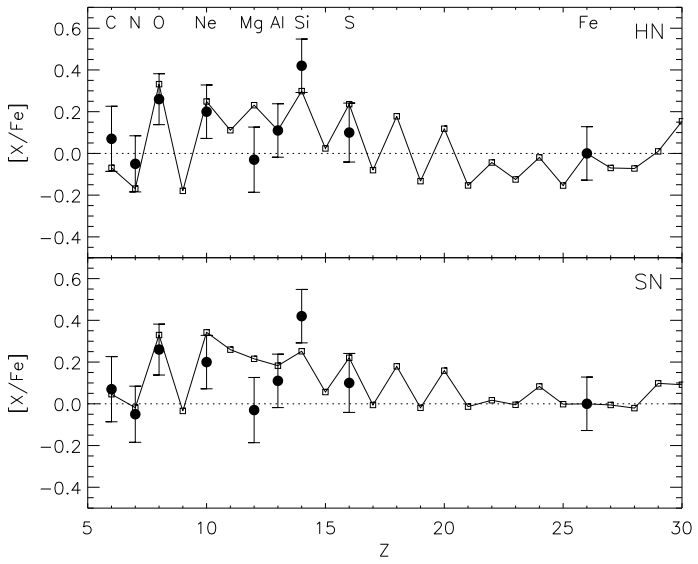

Figure 8.3: Elemental abundance pattern of HD 271791 (filled circles; relative to iron) as function of atomic number according to Przybilla et al. (2008b, Fig. 3). The ordinate is the same as Eq. (8.1) apart from the fact that solar abundances by Grevesse & Sauval (1998) are used as reference. The open squares show the predicted pattern for a supernova (*lower panel*) and a more energetic hypernova (*upper panel*) based on a simplified accretion model. Error bars are combined statistical and systematic 1σ uncertainties. See Przybilla et al. (2008b) for details.

for each of the 18 runaway stars. We start with HD 271971 because the detection of α-element enhancement in its atmosphere was the motivation for this thesis. The remaining stars are sorted in ascending order with respect to their ejection velocity.

HD 271791 (#9): In many respects, this subgiant is the most extreme object in the sample. This is particularly true for its kinematic properties. Although being a well-known runaway star for more than two decades (Kilkenny & Stone 1988), the extraordinary status of HD 271791 was recognized only a few years ago by Heber et al. (2008), who showed that this star is so fast that it is gravitationally unbound to the Milky Way. In contrast to other hypervelocity stars, the kinematics of HD 271791 is not compatible with an origin in the Galactic center and, thus, rules out the most powerful ejection scenario, namely the Hills mechanism. Motivated by this finding, Przybilla et al. (2008b) performed a quantitative abundance analysis and found a peculiar abundance pattern that hints at the accretion of α-elements and hence at the supernova mechanism as ejection event. Based on a simple accretion model, a scenario for the pre-supernova binary system was proposed that is capable of reproducing the observed abundances, see Fig. 8.3. However, according to Gvaramadze (2009), the configuration of the proposed progenitor system is barely consistent with the large Galactic rest-frame velocity of $v_{\rm Grf}$ = 530–920 km s^{-1} (Heber et al. 2008) in the framework of the supernova ejection scenario. Instead, Gvaramadze (2009) suggests that HD 271791 was part of a binary system that remained bound after the supernova explosion of the primary and was ejected later on by a strong dynamical encounter between this binary and another massive binary or a very massive star.

HD 271791 was included in this study as a final test for the novel spectroscopic analysis method and because a new spectrum was available that has a better S/N ratio than that analyzed by Przybilla et al. (2008b). The obtained abundance pattern is shown in Fig. 8.4 and confirms the previous finding that the abundances (relative to iron) of neon, aluminum, silicon, and sulfur are enhanced with respect to the reference. In contrast to Przybilla et al. (2008b), we find no enhancement in oxygen but in magnesium instead. The latter, however, vanishes when the ef-

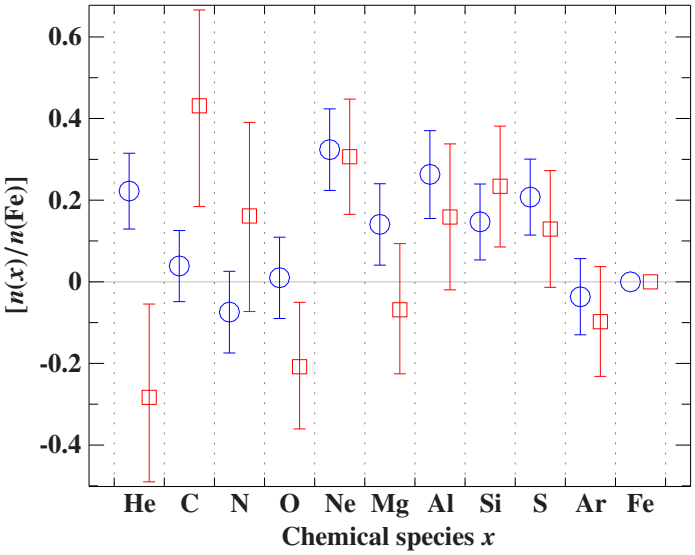

Figure 8.4: Elemental abundance pattern of HD 271791 as derived in this work. The blue circles give the abundances over iron relative to the reference stars according to Eq. (8.1) while the red squares additionally account for the Galactic abundance gradients by virtue of Eq. (8.5). Error bars are combined statistical and systematic 1σ uncertainties. The blue data points should be compared to the filled circles in Fig. 8.3.

fects of the Galactic abundance gradients are taken into account, which are large for HD 271791 since it originates in the outer rim of the Milky Way at $r_\mathrm{d} \approx 17$ kpc. While the enhancement in the above mentioned elements is not seriously affected by this correction, the opposite is true for carbon, nitrogen, and oxygen. However, these elements are anyway not reliable tracers for the accretion of supernova ejecta in the case of HD 271791 as they can be affected by either the rotational mixing of CNO-burning products (HD 271791 is a relatively fast rotator and the most evolved star in the sample, see Fig. 8.2) or the accretion from the wind of the pre-supernova primary, which is supposed to be a Wolf-Rayet star of subclass WC (Przybilla et al. 2008b). Moreover, the use of integrated yields in the accretion model by Przybilla et al. certainly oversimplifies reality and a more sophisticated model might lead to different predictions for the expected abundance pattern. Note that the consideration of the abundance gradients not only changes the abundance pattern but also increases the error bars in Fig. 8.4. This is due to additional sources of uncertainty introduced by the correction. The significance of the corrected abundance pattern is therefore lower than that of the original one. Nevertheless, HD 271791 still exhibits clear indications for the pollution with supernova products.

Distance and proper motions are the key ingredients for the kinematic study but are usually prone to relatively large uncertainties which then propagate through the entire analysis. This is exemplified in Fig. 8.5 by showing nine trajectories that result from variations in the kinematic input data. The outcome of tracing back the orbit to the Galactic plane is almost identical in all three Milky Way mass models. The reason for this is HD 271791's large current Galactic rest-frame velocity of $v_\mathrm{Grf} = 710^{+480}_{-380}$ km s^{-1}, which renders the kinematic analysis almost trivial because the orbit is only negligibly affected by the gravitational potential. Since our spectroscopic distance $d = 19.9^{+4.6}_{-4.2}$ kpc is consistent with the value by Heber et al. (2008, $d = 21 \pm 4$ kpc), we obtain pretty much the same results and conclusions as they do. HD 271791 was ejected from the outer rim of the Galactic disk ($r_\mathrm{d} = 17.1^{+60.6}_{-\ 9.4}$ kpc) about $\tau_\mathrm{flight} = 28^{+91}_{-14}$ Myr ago with an outstandingly high ejection velocity of $v_\mathrm{ej} = 580^{+480}_{-260}$ km s^{-1}. Since the ejection direction was roughly aligned with the rotation of the Galactic disk, the star's Galactic rest-frame velocity at the moment of ejection was additionally boosted leading to velocities which are mainly in excess of the local escape velocity. Consequently, HD 271791 is probably unbound

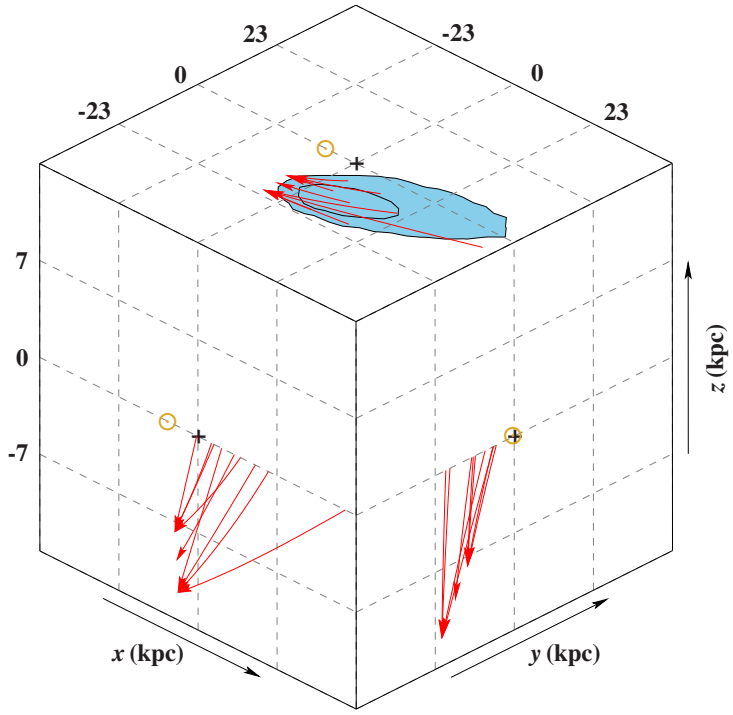

Figure 8.5: Three-dimensional orbits of HD 271791 in the coordinate system defined by Fig. 2.7. The nine trajectories (red lines; arrows indicate the star's current position) are traced back to the Galactic plane and sample the mean kinematic input data as well as variations in the distance, proper motions, and radial velocity. The black rimmed, blue shaded areas mark the 1σ and 2σ region for the intersection with the plane. The positions of the Sun and the Galactic center are marked by a yellow $\odot$ and a black +, respectively. Based on Milky Way mass Model I.

to the Milky Way. The problem outlined by Gvaramadze (2009) is still present, namely that only the very lower end of the derived range for the ejection velocity is compatible with the disruption of a binary system by a supernova explosion. Another issue arises from the revised lifetime ($\tau = 17^{+4}_{-1}$ Myr instead of $\tau = 25 \pm 5$ Myr as derived by Heber et al. 2008 from evolutionary tracks for rotating stars), which is now smaller than the flight time and is therefore in contradiction with the runaway scenario. However, within the error margins, HD 271791 could still be ejected from the disk very soon after its formation. Moreover, we emphasize again that our age determinations rely on single-star evolutionary tracks and are thus only rough estimates if the star was part of an interacting binary system.

All in all, we conclude from HD 271791 that our spectroscopic analysis method is capable of finding peculiar abundance patterns if they are present in the target. Combined with the developed tools for the kinematic investigation, we can now start to study runaway stars for most of which no quantitative spectroscopic non-LTE abundance analysis is available so far.

8.4 Individual results

HIP 13800 (#7): This object is a candidate runaway star already from its discovery by Feige (1958). The spectroscopic and kinematic analysis by Keenan et al. (1986a) indicated that the star has a normal chemical composition and that its kinematic properties are consistent with a Galactic disk runaway scenario.

Based on our more sophisticated analysis techniques and high-quality observational data, we come to exactly the same conclusion as Keenan et al. (1986a). The derived abundance pattern in Fig. 8.6 closely resembles that of the nearby reference stars except for a slight tendency towards a higher baseline metallicity. Correspondingly, the element-over-iron abundance ratios lack any

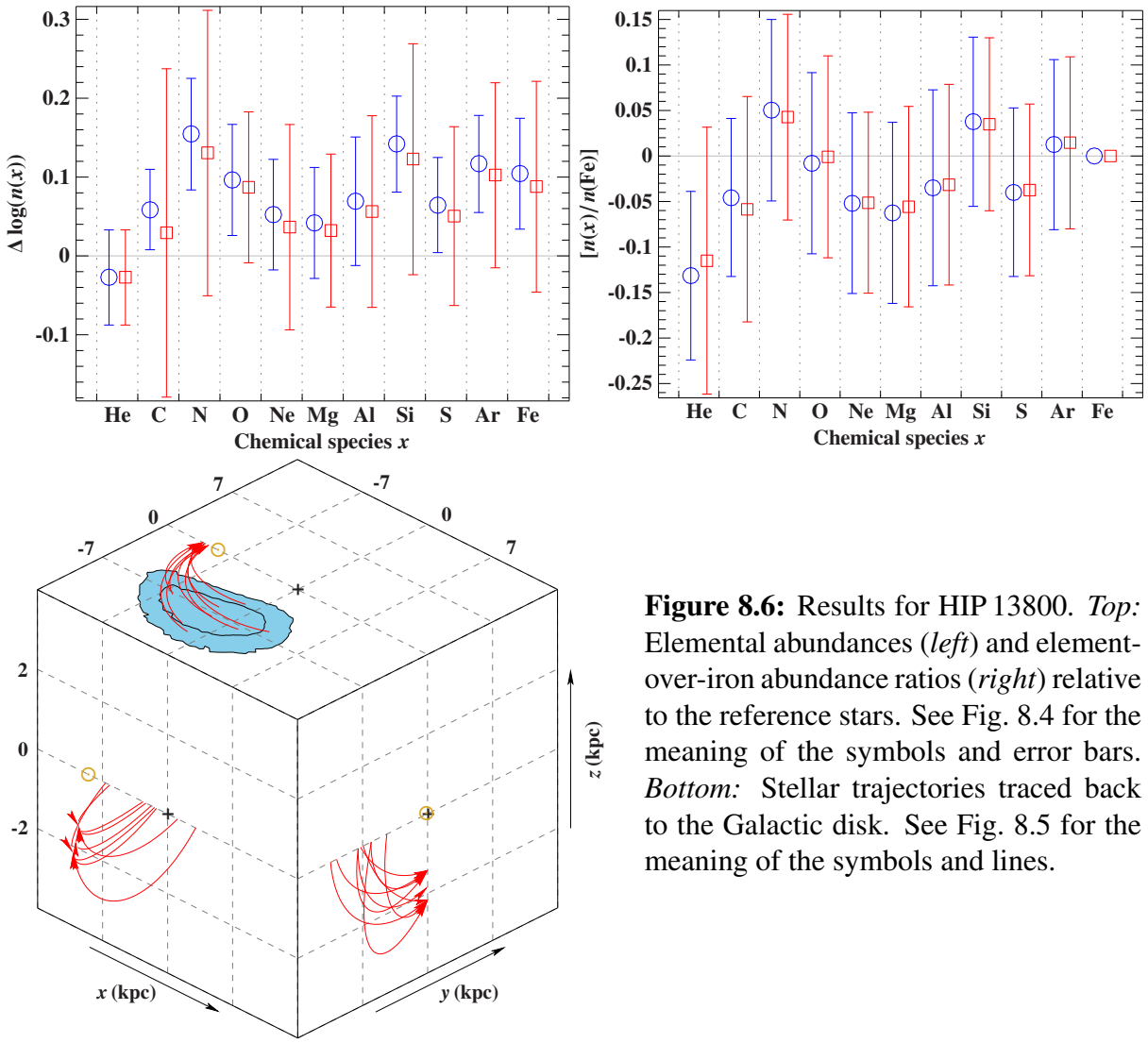

Figure 8.6: Results for HIP 13800. *Top:* Elemental abundances (*left*) and element-over-iron abundance ratios (*right*) relative to the reference stars. See Fig. 8.4 for the meaning of the symbols and error bars. *Bottom:* Stellar trajectories traced back to the Galactic disk. See Fig. 8.5 for the meaning of the symbols and lines.

hint for accretion of supernova ejecta. The kinematic investigation suggests that HIP 13800 was ejected with a rather moderate velocity of $v_{\rm ej} = 100^{+130}_{-\ 40}\,{\rm km\,s^{-1}}$ from a Galactocentric radius of $r_{\rm d} = 8.1^{+5.0}_{-4.6}\,{\rm kpc}$ about $\tau_{\rm flight} = 56 \pm 23\,{\rm Myr}$ ago. Since the flight time is very close to the star's evolutionary age of $\tau = 55^{+20}_{-\ 5}\,{\rm Myr}$, HIP 13800 could have been ejected during the initial dynamical relaxation of a newly formed star cluster (Poveda et al. 1967).

HD 78584 (#2): This long-known candidate runaway star (Abt et al. 1972) is the only object in the sample that shows a significant negative radial velocity of $v_{\rm rad} = -121.4^{+0.7+0.1}_{-0.8-0.1}\,{\rm km\,s^{-1}}$. To our knowledge, no quantitative spectroscopic analysis has been carried out for this star so far. The only published kinematic investigation was performed by Hoogerwerf et al. (2001) and aimed at identifying parent groups for runaway stars, which was not successful for this specific target.

On the one hand, HD 78584 is quite similar to HD 271791 in many respects. It is also a fast rotating ($v\sin(i) = 108.9^{+0.2+0.5}_{-0.1-0.1}\,{\rm km\,s^{-1}}$), evolved subgiant (see Fig. 8.2) that stems from the metal-poor outer rim of the Galactic disk ($r_{\rm d} = 14.5^{+1.0}_{-0.8}\,{\rm kpc}$, Fig. 8.7). This spatial origin is in

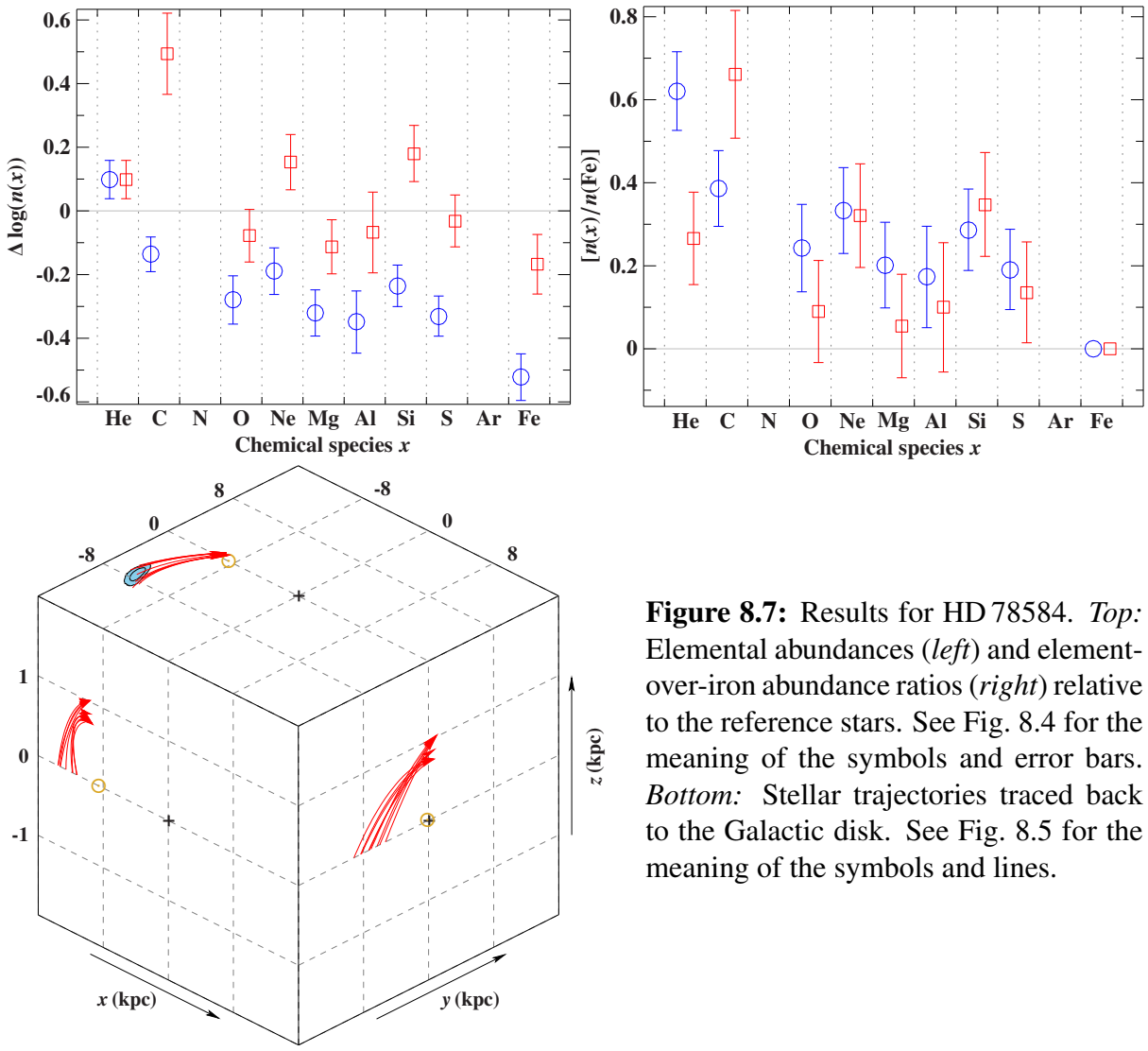

Figure 8.7: Results for HD 78584. *Top:* Elemental abundances (*left*) and element-over-iron abundance ratios (*right*) relative to the reference stars. See Fig. 8.4 for the meaning of the symbols and error bars. *Bottom:* Stellar trajectories traced back to the Galactic disk. See Fig. 8.5 for the meaning of the symbols and lines.

nice agreement with the low iron abundance derived from the spectroscopic analysis (Fig. 8.7). The enrichment in helium might be the result of rotational mixing of CNO-burning products. Unfortunately, this conjecture cannot be checked because the most important mixing indicator, the nitrogen abundance, could not be determined. In addition to helium, the star exhibits enhanced abundances at least for carbon, neon, and silicon. Indications for the supernova ejection scenario arise from the element-over-iron abundance ratios in Fig. 8.7, which shows that all elements are tendentially enhanced with respect to iron.

On the other hand, the kinematic properties of HD 78584 are very different from HD 271791. Unlike the latter, HD 78584 is currently quite close to the Sun ($d = 1.56^{+0.32}_{-0.23}$ kpc) and is moving with a Galactic rest-frame velocity of only $v_{\mathrm{Grf}} = 280^{+30}_{-20}\,\mathrm{km\,s^{-1}}$. Within the supernova scenario, the corresponding moderate ejection velocity of $v_{\mathrm{ej}} = 120^{+40}_{-20}\,\mathrm{km\,s^{-1}}$ can easily result from standard binary systems. No special requirements such as an extraordinary close pre-supernova binary system have to be invoked as in the case of HD 271791. Owing to the smaller geometrical cross section in wide binary systems, it is, however, unclear whether HD 78584 was indeed able to accrete a detectable amount of supernova ejecta. The extremely high carbon abundance

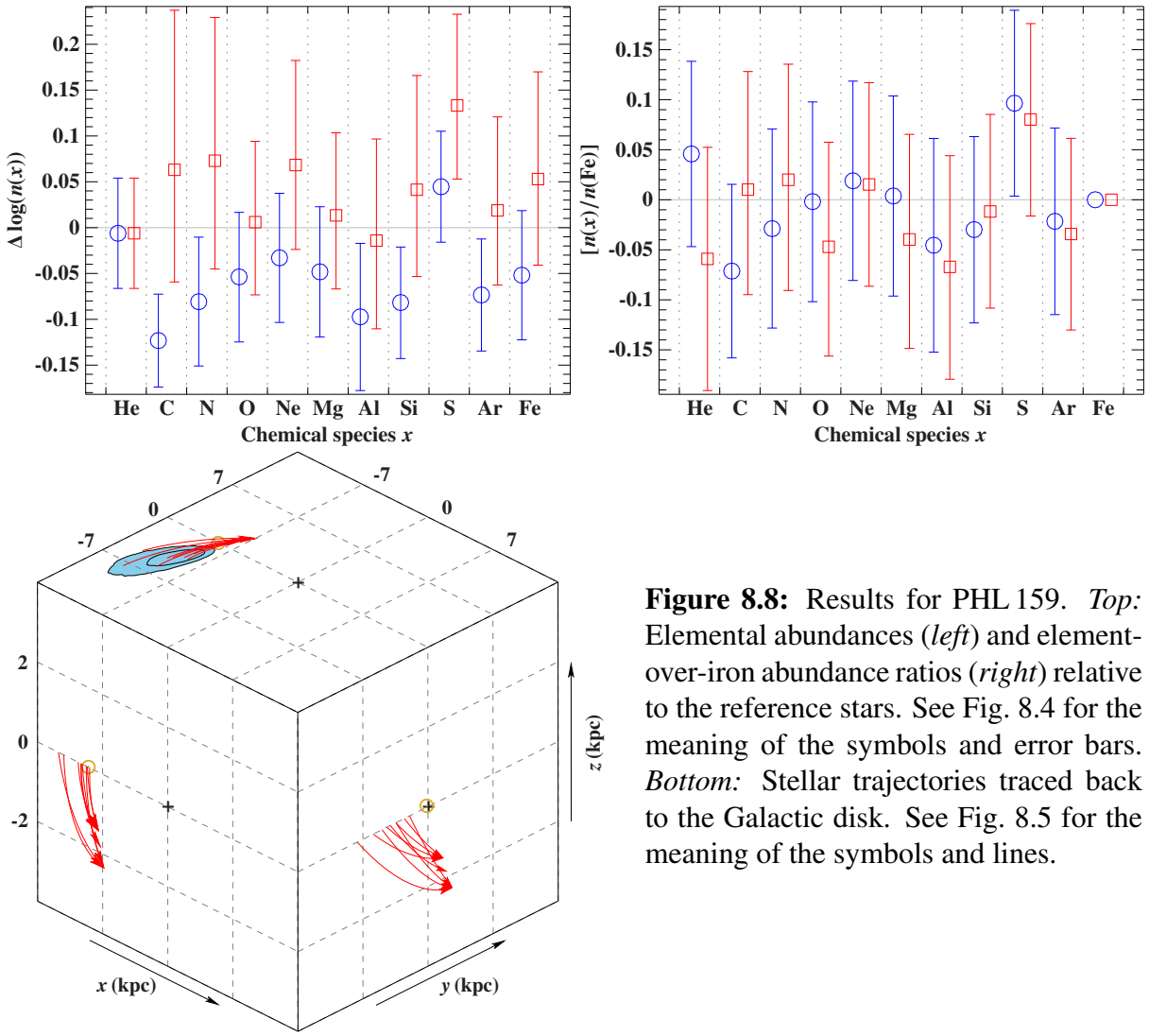

Figure 8.8: Results for PHL 159. *Top:* Elemental abundances (*left*) and element-over-iron abundance ratios (*right*) relative to the reference stars. See Fig. 8.4 for the meaning of the symbols and error bars. *Bottom:* Stellar trajectories traced back to the Galactic disk. See Fig. 8.5 for the meaning of the symbols and lines.

may also be a challenge for the supernova scenario.

Finally, the runaway scenario itself is without doubt a realistic option for HD 78584 since the star's lifetime ($\tau = 50^{+7}_{-6}$ Myr) exceeds its time of flight ($\tau_{\rm flight} = 39^{+13}_{-10}$ Myr).

PHL 159 (#15): This early-type star below the Galactic disk (Brown & Kilkenny 1979) was already spectroscopically and kinematically analyzed by Ramspeck et al. (2001). Based on LTE models and a high-resolution spectrum with good wavelength coverage, they derived an effective temperature of 18 500 ± 1000 K, a surface gravity of 3.59 ± 0.10 dex, and some non-standard abundances, e.g., for magnesium and oxygen. The resulting spectroscopic distance of 5.3 kpc gave a flight time of ∼31 Myr, which was close to the estimated stellar age of 28 ± 2 Myr so that the star could have formed in the disk.

Our atmospheric parameters ($T_{\rm eff} = 22\,230^{+80+450}_{-60-450}$ K, $\log(g) = 4.118^{+0.007+0.100}_{-0.007-0.100}$ dex) are considerably different from those by Ramspeck et al. (2001). The same holds then for derived quantities like the stellar age ($\tau = 16^{+\ 5}_{-16}$ Myr) or the spectroscopic distance ($d = 3.10^{+0.77}_{-0.65}$ kpc). Because of the small projected rotational velocity, $v \sin(i) = 23.1^{+0.3+0.1}_{-0.2-0.1}$ km s^{-1}, the spectral lines

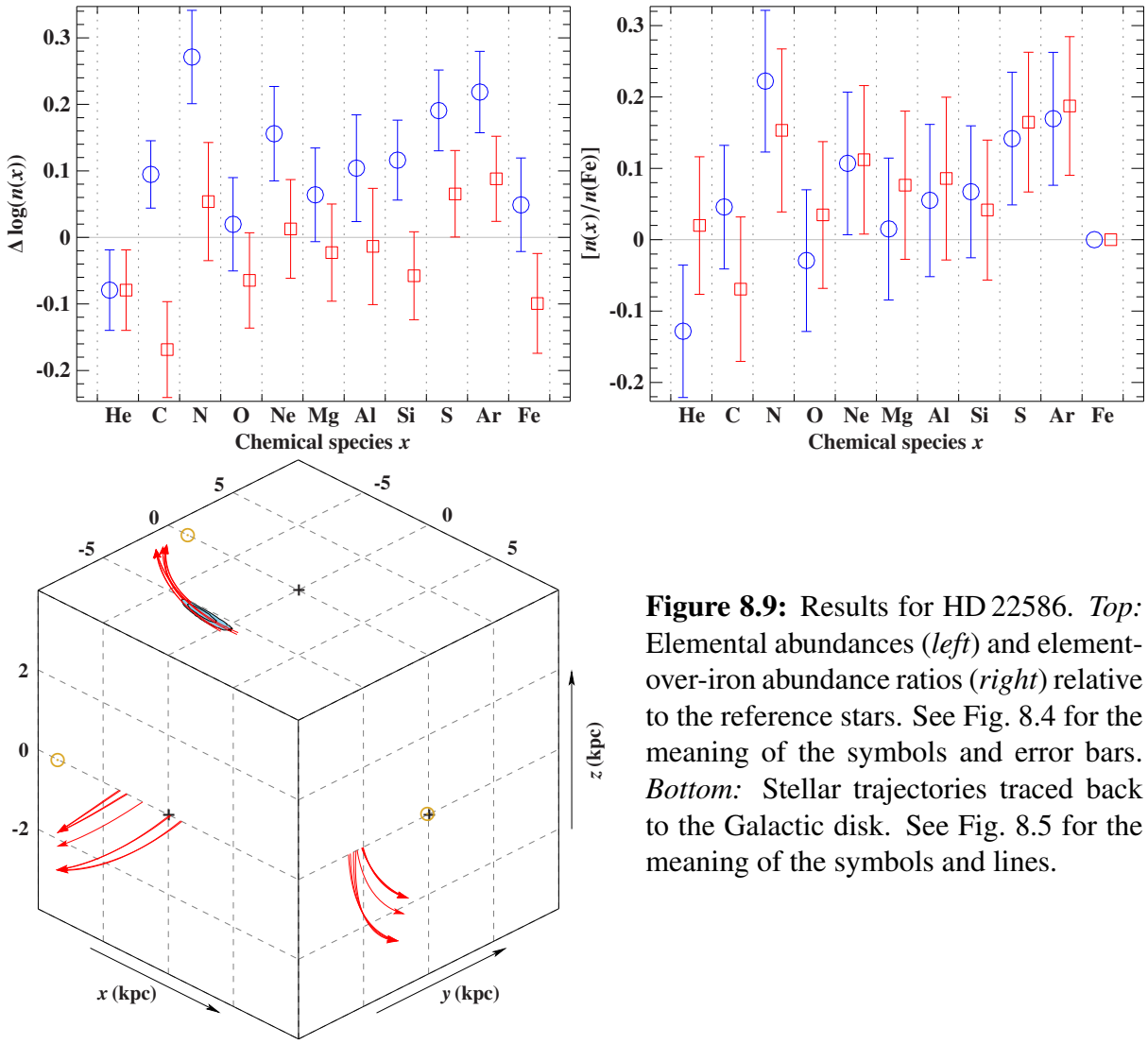

Figure 8.9: Results for HD 22586. *Top:* Elemental abundances (*left*) and element-over-iron abundance ratios (*right*) relative to the reference stars. See Fig. 8.4 for the meaning of the symbols and error bars. *Bottom:* Stellar trajectories traced back to the Galactic disk. See Fig. 8.5 for the meaning of the symbols and lines.

are sharp and clear bump-like features, which are characteristic for β Cepheid variables, become visible. The abundances and element-over-iron abundance ratios in Fig. 8.8 are very similar to those of the reference stars apart from an offset due to the star's possible birthplace outside of the solar circle ($r_\mathrm{d} = 10.2^{+6.4}_{-2.1}$ kpc). Within the error margins, the flight time ($\tau_\mathrm{flight} = 25^{+30}_{-10}$ Myr) is compatible with the evolutionary lifetime if PHL 159 was ejected ($v_\mathrm{ej} = 140^{+40}_{-20}$ km s^{-1}) very soon after its formation, for instance, by the initial dynamical relaxation of its host cluster.

HD 22586 (#14): This target, which was first mentioned by Hill (1970) to be an early-type star that is away from the Galactic plane, is the brightest runaway star in our sample and has been analyzed several times in the past with somewhat different results. For instance, the atmospheric parameters obtained by Keenan et al. (1986a, $T_\mathrm{eff} = 25\,300$ K, $\log(g) = 3.7$ dex) are not consistent with those derived by Magee et al. (2001, $T_\mathrm{eff} = 20\,000 \pm 2000$ K, $\log(g) = 3.6 \pm 0.2$ dex). However, both studies infer a more or less standard chemical composition as well as ages and flight times that do not exclude a Galactic disk runaway origin.

According to our analysis, HD 22586 is somewhat evolved and already in its subgiant phase

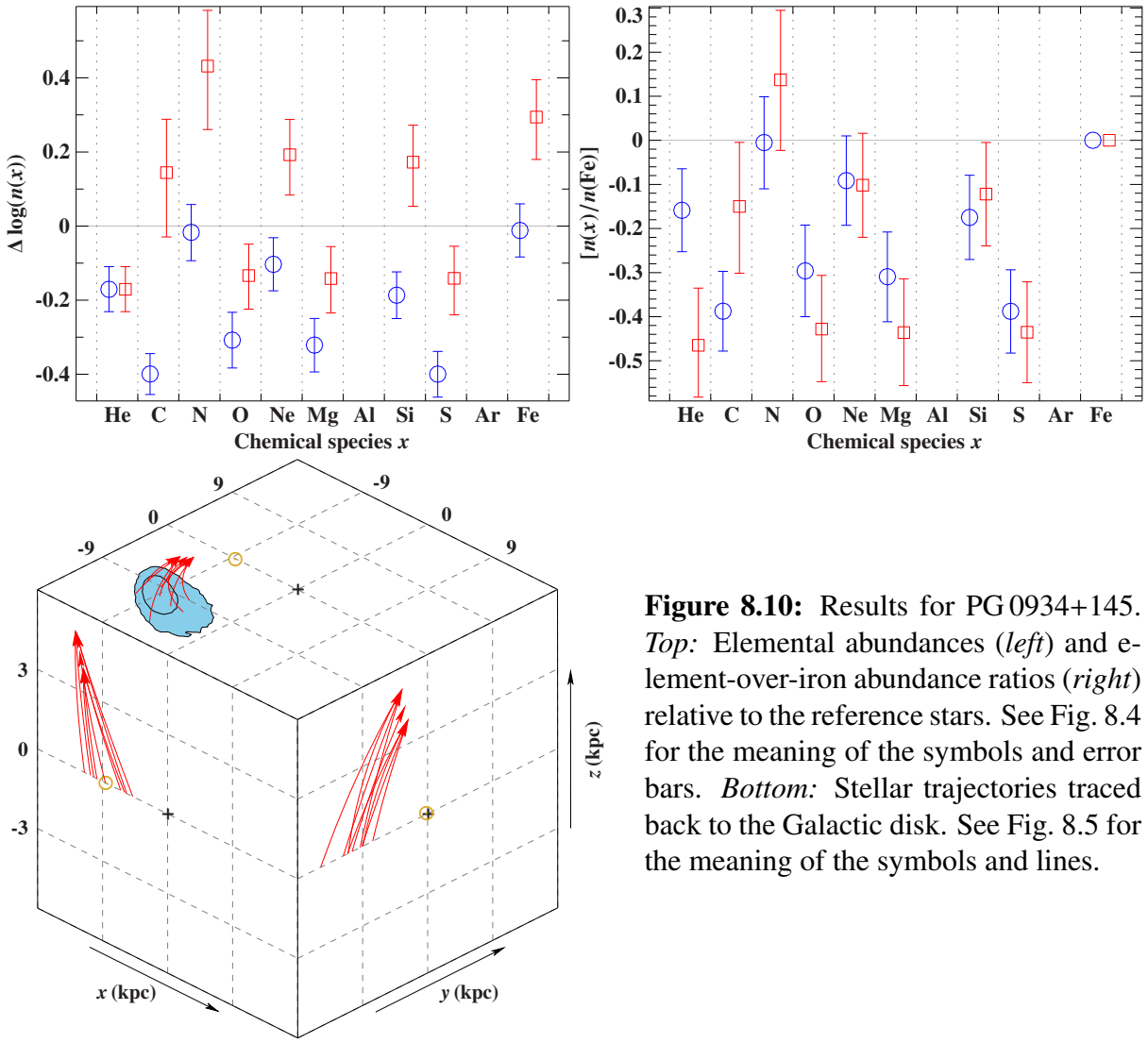

Figure 8.10: Results for PG 0934+145. *Top:* Elemental abundances (*left*) and element-over-iron abundance ratios (*right*) relative to the reference stars. See Fig. 8.4 for the meaning of the symbols and error bars. *Bottom:* Stellar trajectories traced back to the Galactic disk. See Fig. 8.5 for the meaning of the symbols and lines.

(Fig. 8.2, $T_{\rm eff} = 22\,030^{+30+450}_{-30-440}$ K, $\log(g) = 3.348^{+0.002+0.100}_{-0.004-0.100}$ dex). In agreement with the kinematically predicted origin at a Galactocentric radius of $r_{\rm d} = 5.8^{+0.7}_{-0.6}$ kpc, the abundance pattern reveals a metallicity that is larger than that of the reference stars. The existence of a Galactic abundance gradient is also sufficient to explain the high nitrogen abundance, which, otherwise, could also be due to rotationally induced mixing of CNO-burning products to the surface of this medium-fast rotator ($v \sin(i) = 86.3^{+0.1+0.3}_{-0.4-0.1}$ km s^{-1}). The element-over-iron abundance ratios reveal a slight signature for the accretion of supernova ejecta, which, of course, is not statistically significant. Although variability was ruled out for HD 22586 by Hambly et al. (1994), we report the detection of small yet perceptible line asymmetries which closely resemble those found in the spectra of β Cepheid variable stars. Based on the computed trajectories, the star's flight time $\tau_{\rm flight} = 27 \pm 5$ Myr exceeds its evolutionary lifetime of $\tau = 18^{+2}_{-7}$ Myr so that HD 22586 seriously challenges the standard Galactic disk runaway scenario ($v_{\rm ej} = 150^{+30}_{-10}$ km s^{-1}).

PG 0934+145 (#4): This star was already analyzed spectroscopically and kinematically by Rolleston et al. (1999). From their high-resolution spectrum with limited spectral range, they

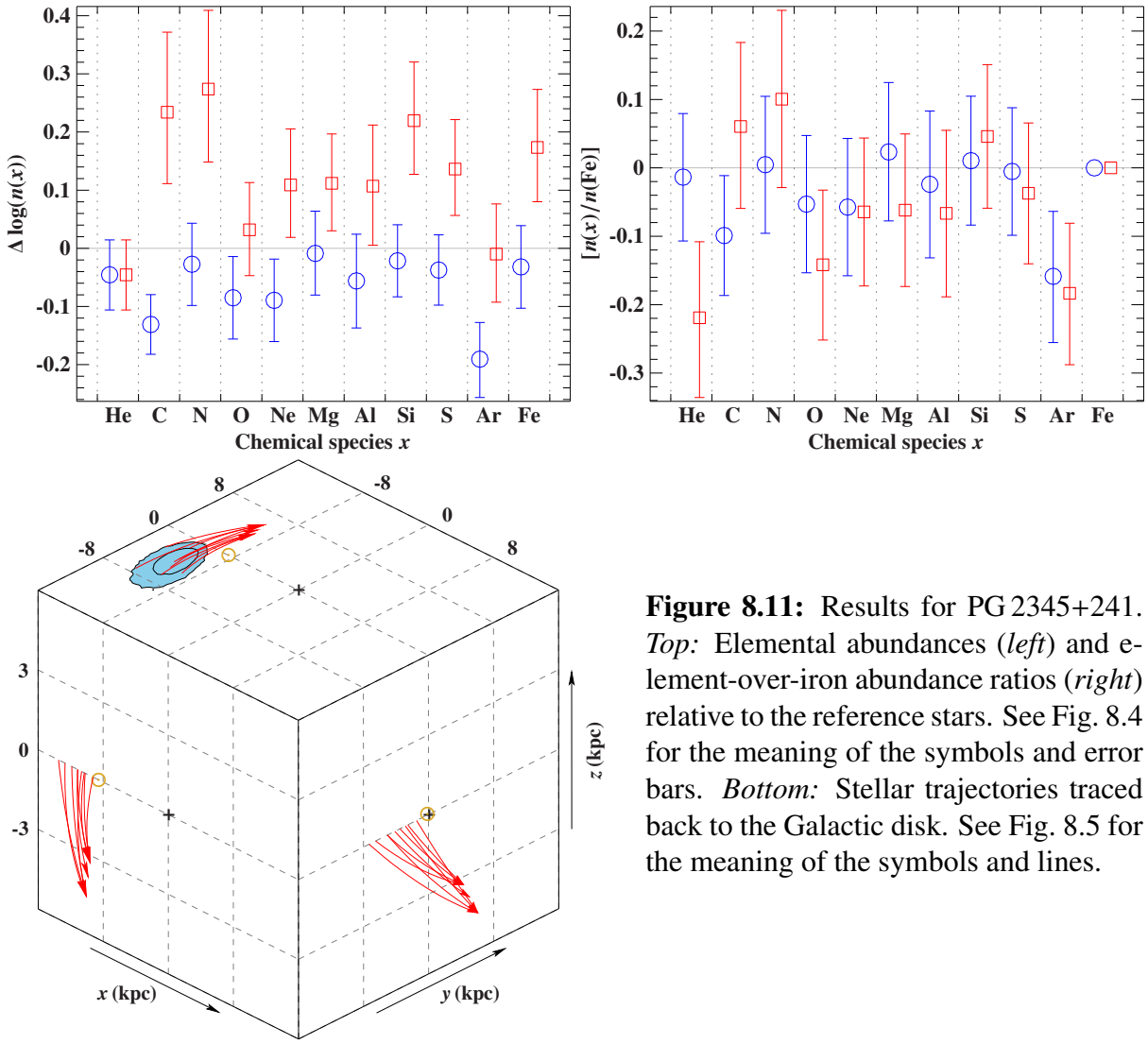

Figure 8.11: Results for PG 2345+241. *Top:* Elemental abundances (*left*) and element-over-iron abundance ratios (*right*) relative to the reference stars. See Fig. 8.4 for the meaning of the symbols and error bars. *Bottom:* Stellar trajectories traced back to the Galactic disk. See Fig. 8.5 for the meaning of the symbols and lines.

obtained an effective temperature of 16 600 ± 1000 K, a surface gravity of 4.0 ± 0.2 dex, and abundances that are low for helium, carbon, magnesium, and silicon while nitrogen appeared to be normal. The kinematic investigation gave strong evidence that PG 0934+145 originated in the Galactic disk.

Our results ($T_{\rm eff}$ = 16 140$^{+130+320}_{-130-330}$ K, log(g) = 4.142$^{+0.020+0.100}_{-0.019-0.100}$ dex) confirm the study by Rolleston et al. (1999) in all aspects. In particular, this applies to the observed depletion in helium, carbon, magnesium, and silicon, which is here additionally found for oxygen, sulfur, and, with restrictions, neon (Fig. 8.10). Nitrogen and iron abundances, on the other hand, closely resemble those of the reference stars. This peculiar abundance pattern is not caused by the accretion of supernova ejecta but might be related to diffusion processes such as selective levitation driven by the radiation field that transfers more momentum to chemical elements with many spectral lines like iron whereas weakly affected elements like helium might sink due to gravitation. Diffusion is suppressed by rotational mixing. Therefore, the target has to be a slow rotator, which imposes the necessary but not sufficient condition that the projected rotational velocity has to be small. This is indeed true for PG 0934+145 with $v \sin(i)$ = 20.2$^{+1.7+0.1}_{-1.8-1.5}$ km s^{-1},

which has the additional advantage that the abundance analysis is very reliable because of the sharp spectral features. Finally, the kinematic investigation is in agreement with a Galactic disk origin of PG 0934+145 ($\tau = 72^{+12}_{-20}$ Myr, $\tau_{\rm flight} = 32^{+30}_{-13}$ Myr, $v_{\rm ej} = 170^{+150}_{-\ 50}$ km s^{-1}).

PG 2345+241 (#12): The high-resolution spectroscopic analysis by Rolleston et al. (1999) gave $T_{\rm eff} = 18\,800 \pm 1000$ K, $\log(g) = 4.2 \pm 0.2$ dex, and a normal metallicity. The resulting estimate for the evolutionary lifetime (19 Myr) was larger than the flight time (14 Myr).

Our spectroscopic analysis reveals asymmetries in the line profiles which cannot be resolved by using a composite model spectrum. Instead, the peculiar shape of the spectral lines resembles that of β Cepheid stars. The abundances obtained in this study (see Fig. 8.11) indicate a standard chemical composition, too. Moreover, no hints for the accretion of supernova ejecta are detectable in the element-over-iron abundance ratios. The atmospheric parameters ($T_{\rm eff} = 19\,580^{+100+400}_{-100-390}$ K, $\log(g) = 3.993^{+0.009+0.100}_{-0.011-0.100}$ dex) yield a stellar age of $\tau = 32^{+4}_{-7}$ Myr which is slightly larger than the flight time $\tau_{\rm flight} = 30^{+17}_{-\ 9}$. With an ejection velocity of $v_{\rm ej} = 180^{+50}_{-30}$ km s^{-1}, PG 2345+241 is consequently a good candidate for the dynamical ejection during the initial relaxation of a newborn star cluster located at a Galactocentric radius of $r_{\rm d} = 11.9^{+3.7}_{-2.1}$ kpc.

PG 0122+214 (#10): The only spectroscopic analysis published for this star is that by Ramspeck et al. (2001), which is based on a high-resolution spectrum with a wavelength coverage of [3600 Å, 5130 Å] and on LTE models. The corresponding atmospheric parameters ($T_{\rm eff} = 18\,300 \pm 1000$ K, $\log(g) = 3.86 \pm 0.10$ dex) gave an age estimate of 35 ± 6 Myr, which was lower than the kinematically derived flight time of 51 ± 24 Myr and, hence, challenged the runaway scenario although the values were still consistent within their uncertainties. Apart from helium, which was found to be normal, abundances could not be derived by Ramspeck et al. (2001) because of the highly broadened spectral lines ($v \sin(i) = 117$ km s^{-1}).

The spectroscopic investigation in this study also suffered from the high projected rotational velocity ($v \sin(i) = 117.6^{+0.2+1.2}_{-0.2-0.7}$ km s^{-1}), which, in combination with the rather small S/N ratio of about 120, caused many weak metal lines to get lost in the noise. This particularly affected the chemical species nitrogen, aluminum, sulfur, and iron, whose abundances are thus less reliable. Nevertheless, we note that the abundance pattern (Fig. 8.12) is compatible with an origin in the outer rim of the Galaxy and does not show any hints for α-element enhancement. Our atmospheric parameters ($T_{\rm eff} = 19\,230^{+70+390}_{-50-390}$ K, $\log(g) = 4.016^{+0.012+0.100}_{-0.008-0.100}$ dex) imply an age of $\tau = 46^{+5}_{-7}$ Myr and a spectroscopic distance of $d = 12.64^{+15.79}_{-\ 6.93}$ kpc. The huge uncertainty in the distance is due to the poor quality of the available photometric data and renders the entire kinematic investigation insignificant. For instance, the ejection velocity, $v_{\rm ej} = 200^{+350}_{-\ 80}$ km s^{-1}, or the Galactocentric radius at disk intersection, $r_{\rm d} = 17.6^{+45.8}_{-13.3}$ kpc, are not constrained at all (see also Fig. 8.12). Similarly, the flight time $\tau_{\rm flight} = 56^{+137}_{-\ 27}$ Myr is so uncertain that any comparison with the star's lifetime is inconclusive. Dynamical ejection from the Galactic disk remains therefore as a possible explanation for PG 0122+214's current position in the halo of the Milky Way.

HD 204076 (#17): It is known for decades that this object is an early-type star below the Galactic plane (Hill 1970). Photometric observations revealed small brightness variations that are typical of β Cepheid variables (Rufener & Bartholdi 1982; Hambly et al. 1994). An abun-

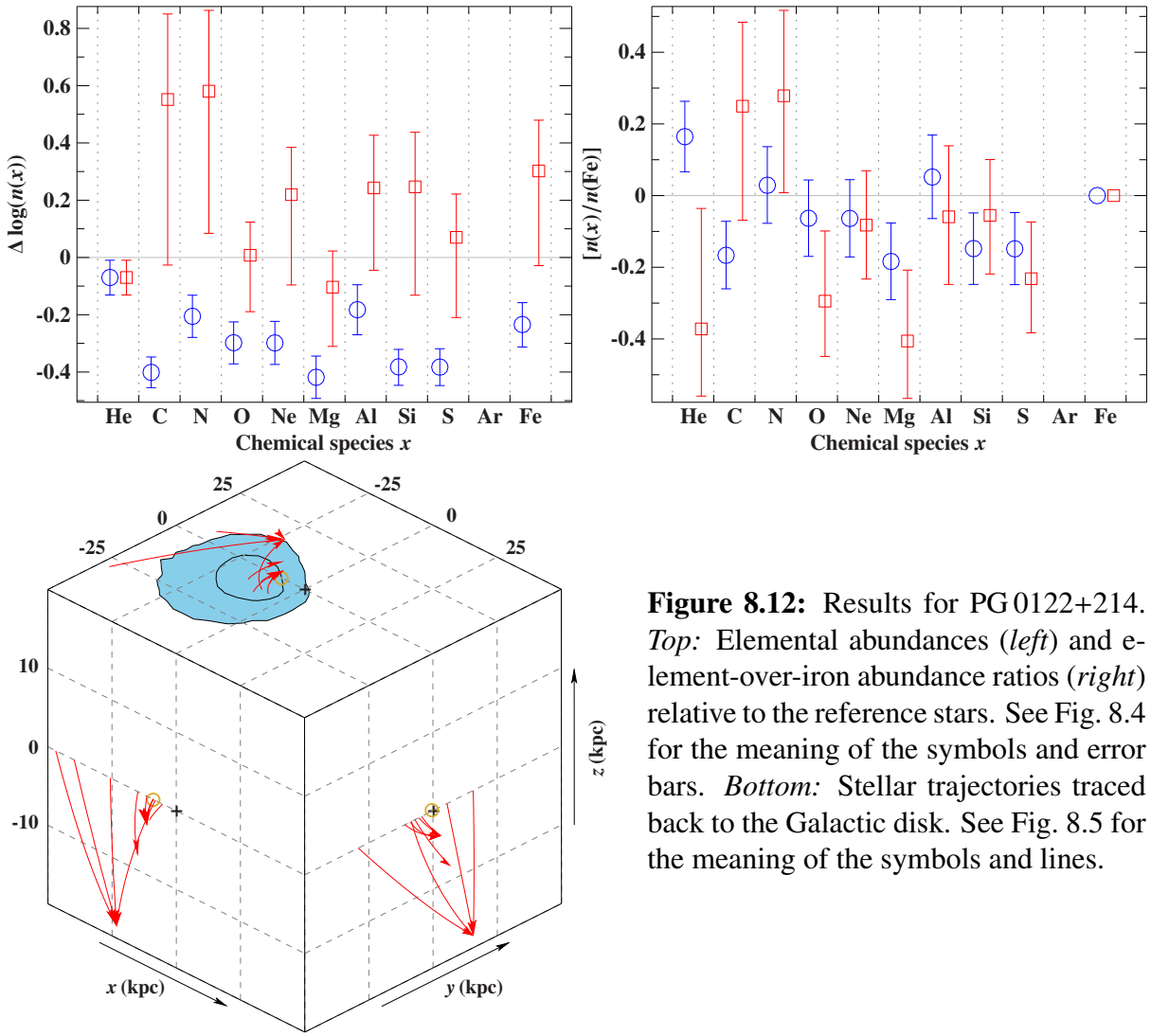

Figure 8.12: Results for PG 0122+214. *Top:* Elemental abundances (*left*) and element-over-iron abundance ratios (*right*) relative to the reference stars. See Fig. 8.4 for the meaning of the symbols and error bars. *Bottom:* Stellar trajectories traced back to the Galactic disk. See Fig. 8.5 for the meaning of the symbols and lines.

dance analysis with respect to carbon, nitrogen, and oxygen showed that all of these elements are probably enriched in HD 204076 (Keenan et al. 1982). A thorough kinematic investigation is still missing for this object.

The line profiles in the available spectrum show obvious bumps and, hence, strengthen the assumption that HD 204076 is a pulsating β Cepheid star. All abundances are larger than those of the reference stars (see Fig. 8.13), which can be partly explained by the star's suggested birthplace well inside the solar circle ($r_\mathrm{d} = 5.3^{+0.6}_{-0.7}$ kpc). The peculiarities for sulfur and argon, however, remain after the correction for the Galactic abundance gradients. Considering the element-over-iron abundance ratios, almost all chemical species are enhanced relative to iron at least at the 1σ level. The kinematic analysis reveals that this target is the runaway star with the second lowest current Galactic rest-frame velocity in the sample, $v_\mathrm{Grf} = 160^{+20}_{-30}\,\mathrm{km\,s^{-1}}$. The flight time ($\tau_\mathrm{flight} = 15^{+3}_{-2}$ Myr) is smaller than the estimated stellar age ($\tau = 18 \pm 2$ Myr). We conclude that HD 204076 qualifies as a candidate for the ejection ($v_\mathrm{ej} = 220 \pm 60\,\mathrm{km\,s^{-1}}$) from the Galactic disk via the supernova channel.

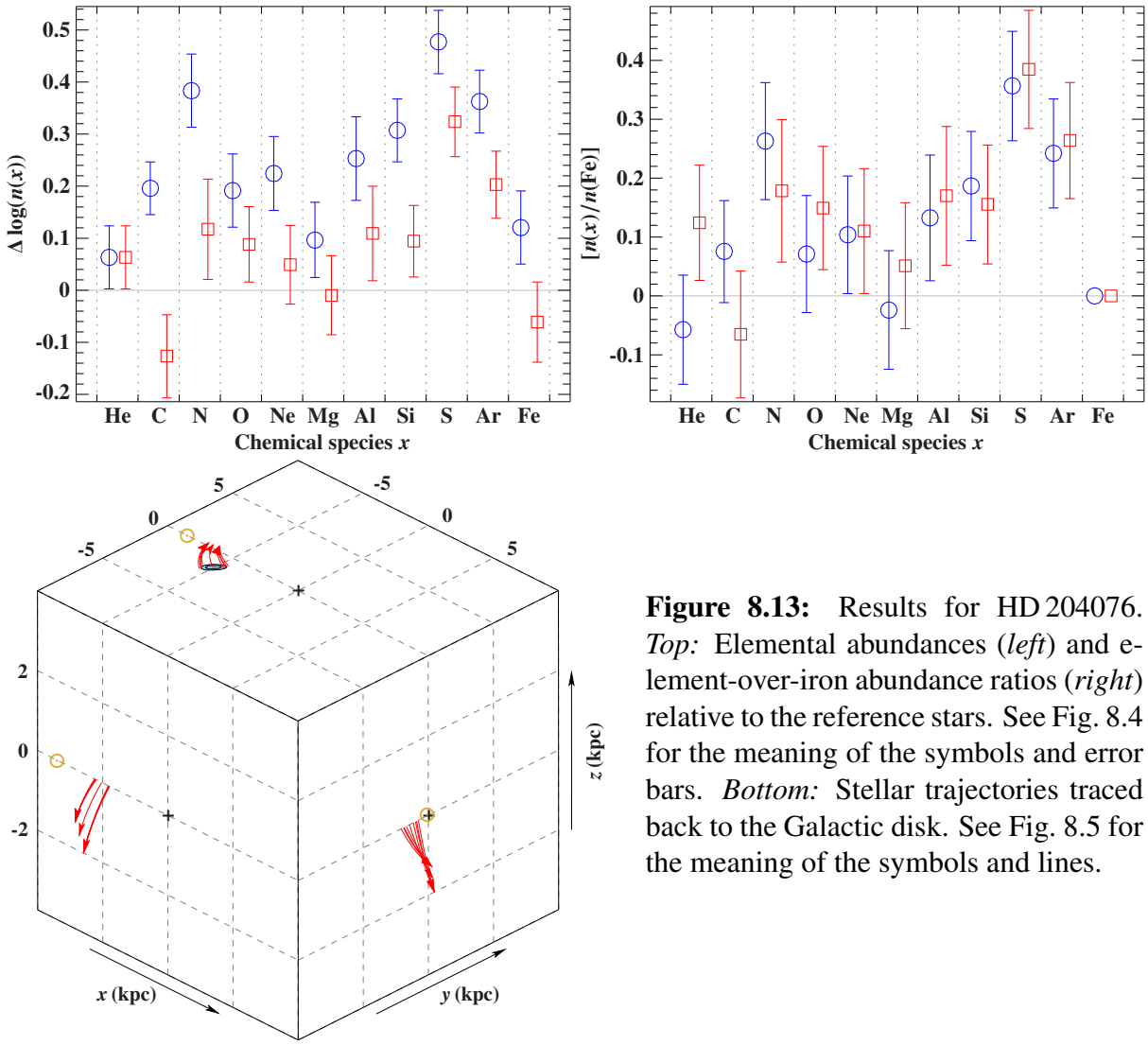

Figure 8.13: Results for HD 204076. *Top:* Elemental abundances (*left*) and element-over-iron abundance ratios (*right*) relative to the reference stars. See Fig. 8.4 for the meaning of the symbols and error bars. *Bottom:* Stellar trajectories traced back to the Galactic disk. See Fig. 8.5 for the meaning of the symbols and lines.

HD 69686 (#3): This nearby runaway star was discovered only a few years ago by Huang et al. (2009), who performed a spectroscopic analysis based on low-resolution, high S/N spectra with a relatively small spectral coverage of about [4000 Å, 5000 Å], which gave atmospheric parameters ($T_{\rm eff}$ = 14 760 ± 200 K, log(g) = 3.93 ± 0.03 dex), an enrichment in helium by a factor of ∼2, but no metal abundances. Although their subsequent kinematic investigation was perfectly consistent with a Galactic disk origin ($r_{\rm d} \approx 5.3$ kpc, $\tau = 73 \pm 10$ Myr, $\tau_{\rm flight} \approx 37$ Myr, $v_{\rm ej} = 192\,{\rm km\,s^{-1}}$), Huang et al. argue that HD 69686 formed well below the Galactic plane ($z \approx -1.8$ kpc) due to indications for a co-moving group of stars, which would hint at star formation in a high velocity cloud of the halo but not at the runaway scenario. However, radial velocity measurements and, hence, the three-dimensional velocities were not available for the candidate group members so that their co-moving nature could not be confirmed.

Our spectroscopic analysis yields similar atmospheric parameters ($T_{\rm eff} = 15\,360^{+\,60+310}_{-130-310}$ K, log(g) = $3.941^{+0.009+0.100}_{-0.005-0.100}$ dex) like the study by Huang et al. but a standard helium content. The abundance pattern shows an overall higher baseline metallicity with no signature for α-element enhancement (see Fig. 8.14). The kinematic investigation is based on a distance of

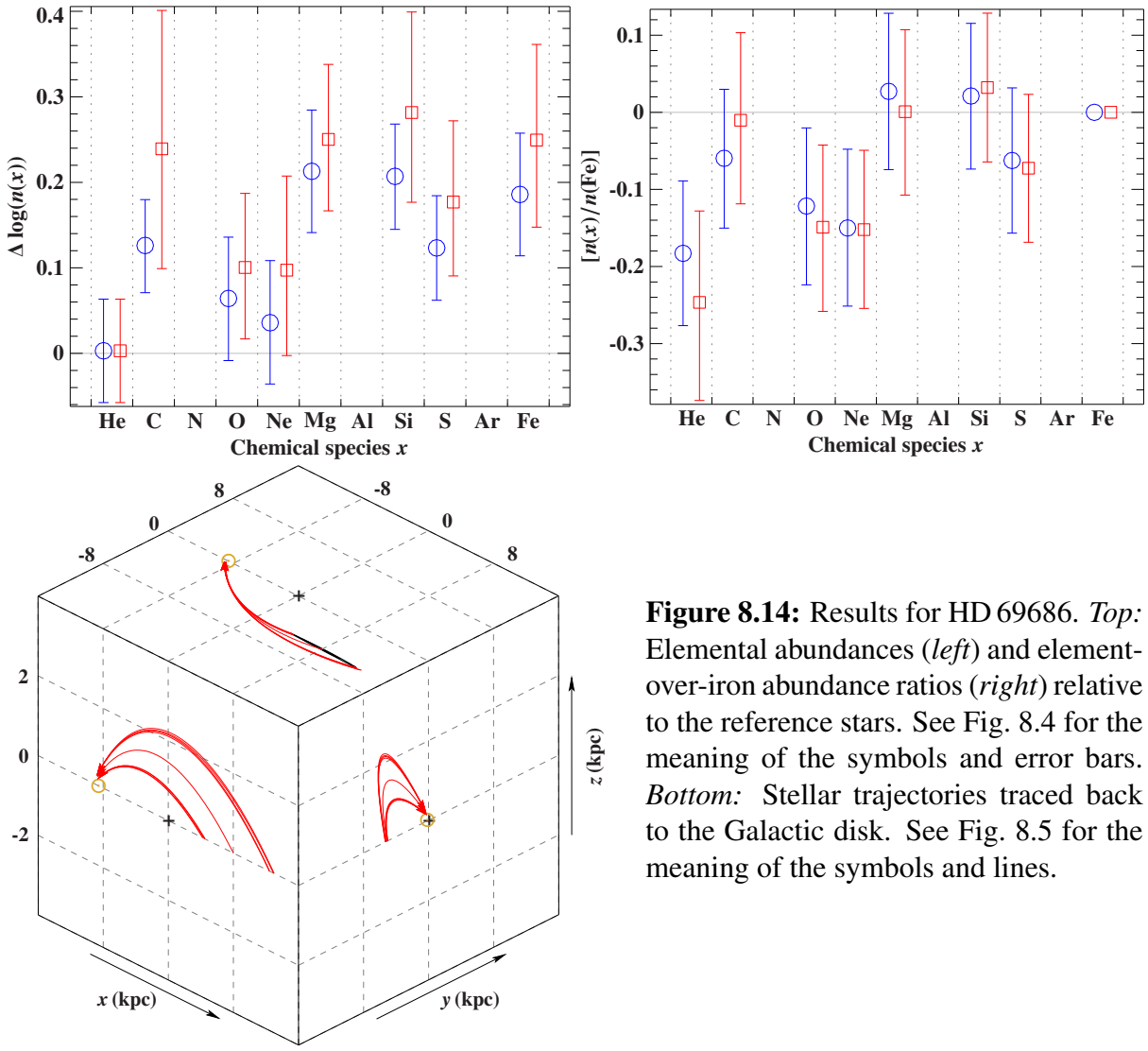

Figure 8.14: Results for HD 69686. *Top:* Elemental abundances (*left*) and element-over-iron abundance ratios (*right*) relative to the reference stars. See Fig. 8.4 for the meaning of the symbols and error bars. *Bottom:* Stellar trajectories traced back to the Galactic disk. See Fig. 8.5 for the meaning of the symbols and lines.

$d = 470 \pm 90$ pc, which is somewhat off from the Huang et al. value of 380 ± 20 pc. This discrepancy propagates then through the orbit computations explaining the differences between the results obtained by Huang et al. (2009) and those given here ($r_{\rm d} = 9.5^{+4.3}_{-2.9}$ kpc, $\tau = 81^{+\ 9}_{-13}$ Myr, $\tau_{\rm flight} = 51^{+15}_{-11}$ Myr, $v_{\rm ej} = 220^{+10}_{-30}$ km s^{-1}). The latter are still in perfect agreement with a runaway hypothesis although the increased metallicity indicates an origin closer to the Galactic center than suggested from the stellar trajectories. HD 69686's high metal content might also argue against its formation in the metal-poor Galactic halo as proposed by Huang et al. (2009).

EC 09452−1403 (#1): This faint star was already spectroscopically and kinematically analyzed by Rolleston et al. (1997) and Lynn et al. (2004). However, the S/N ratio of the available spectra were too low to perform an abundance analysis. Their derived atmospheric parameters ($T_{\rm eff} = 14\,000 \pm 2100$ K, $\log(g) = 4.3 \pm 0.2$ dex) placed the star very close to the zero-age main sequence (see Fig. 8.2), which caused minor flight time versus age problems.

Although the S/N ratio of our spectrum of EC 09452−1403 is the lowest in this study, it is still sufficient to determine reliable abundances for most of the chemical species considered

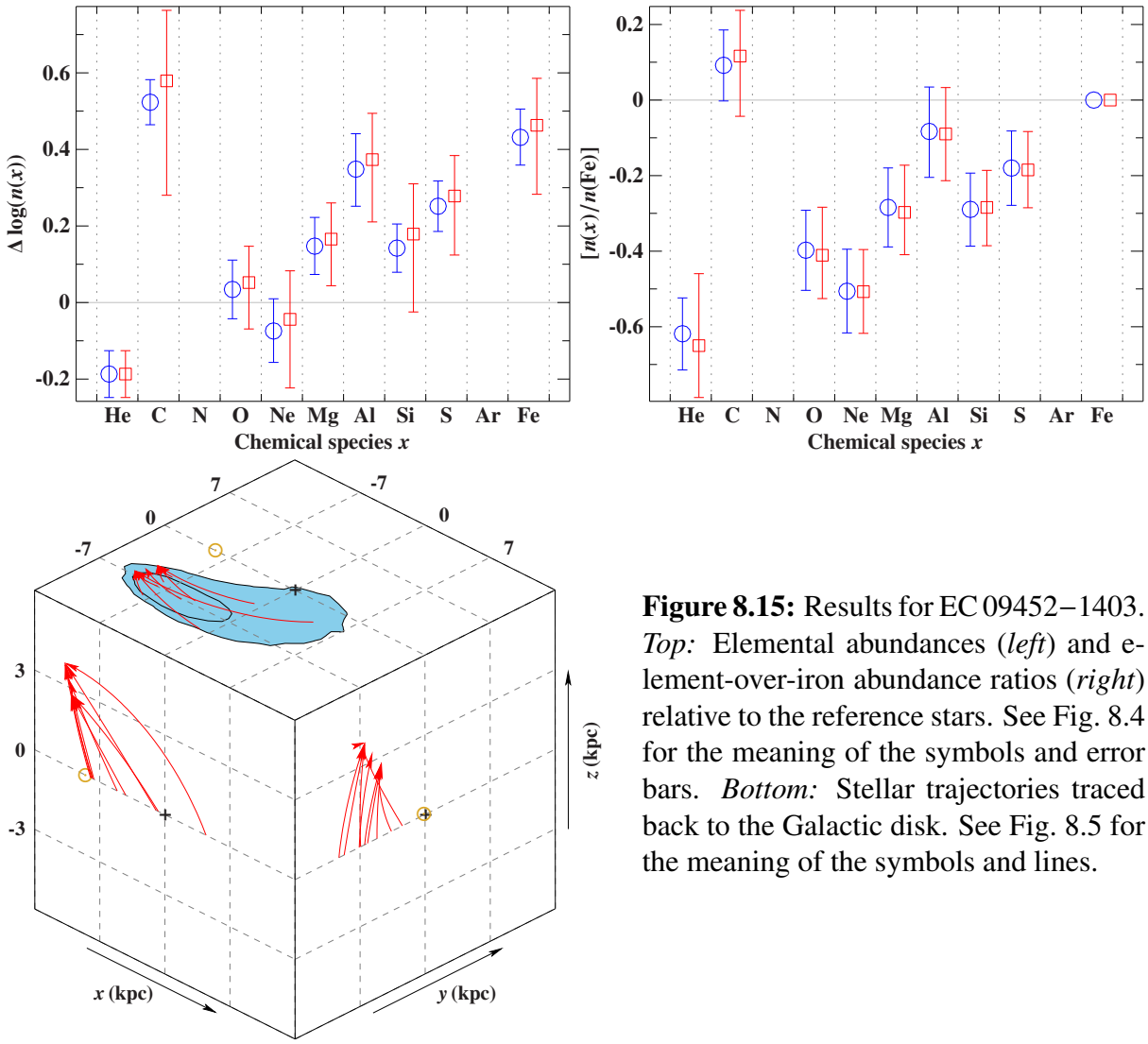

Figure 8.15: Results for EC 09452−1403. *Top:* Elemental abundances (*left*) and element-over-iron abundance ratios (*right*) relative to the reference stars. See Fig. 8.4 for the meaning of the symbols and error bars. *Bottom:* Stellar trajectories traced back to the Galactic disk. See Fig. 8.5 for the meaning of the symbols and lines.

here. The abundances and element-over-iron abundance ratios relative to the reference stars are shown in Fig. 8.15 and indicate (strong) enrichments in carbon, magnesium, aluminum, sulfur, and iron whereas helium is noticeably depleted. Owing to the peculiar helium and iron abundance, accretion of supernova ejecta is not very likely in this case. Instead, the strange abundance pattern might be the result of diffusion caused by selective radiative levitation, which can be present in late B-type stars like EC 09452−1403. However, the high projected rotational velocity $v \sin(i) = 85.0^{+1.7+0.7}_{-1.4-1.1}\,\mathrm{km\,s^{-1}}$ argues against diffusion because the latter is suppressed by mixing processes such as rotationally-induced circulation. Another possible explanation is the star's birthplace. According to Fig. 8.15 and Table D.7, most of the orbits intersect the disk at Galactocentric radii similar to the Sun ($r_\mathrm{d} = 8.9^{+3.9}_{-7.8}\,\mathrm{kpc}$) so that the correction for the Galactic abundance gradients is small. Nevertheless, a non-negligible fraction of the trajectories is consistent with an origin close to the Galactic center where the metallicity is high and the observed metal abundances of EC 09452−1403 would be expected. The low helium abundance, on the other hand, would still remain unexplained in this picture.

Our derived atmospheric parameters ($T_\mathrm{eff} = 14\,300^{+90+290}_{-70-290}\,\mathrm{K}$, $\log(g) = 4.043^{+0.011+0.100}_{-0.009-0.100}\,\mathrm{dex}$)

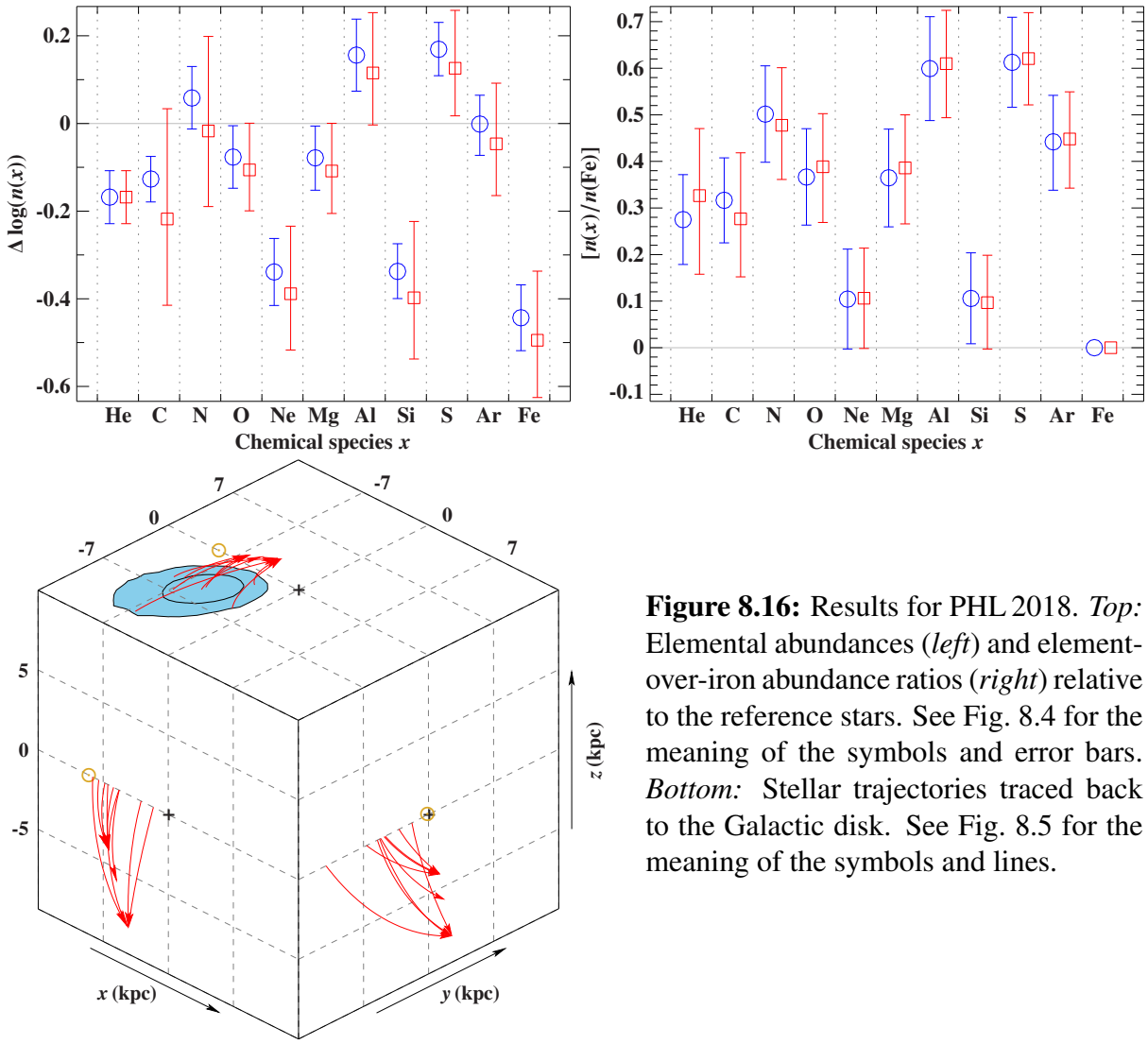

Figure 8.16: Results for PHL 2018. *Top:* Elemental abundances (*left*) and element-over-iron abundance ratios (*right*) relative to the reference stars. See Fig. 8.4 for the meaning of the symbols and error bars. *Bottom:* Stellar trajectories traced back to the Galactic disk. See Fig. 8.5 for the meaning of the symbols and lines.

give an evolutionary age ($\tau = 102^{+17}_{-26}$ Myr) that is well in excess of the travel time ($\tau_{\rm flight} = 22^{+43}_{-13}$ Myr) showing that EC 09452−1403 is without doubt a runaway star. The ejection velocity $v_{\rm ej} = 240^{+280}_{-\ 50}\,{\rm km\,s^{-1}}$ is compatible with all three ejection mechanisms.

PHL 2018 (#11): Not much is known about this early-type star in the Galactic halo. Based on a high-resolution spectrum with yet very limited wavelength coverage, Conlon et al. (1992) were so far the only ones to perform a spectroscopic and kinematic investigation. They derived an effective temperature of 18 500 ± 1000 K, a surface gravity of 3.7 ± 0.2 dex, a projected rotational velocity of 150 ± 20 km s^{-1}, and normal abundances for helium, magnesium, and silicon. Since the star's maximum age exceeded the minimum flight time, Conlon et al. (1992) concluded that a formation in the disk and subsequent ejection is possible for PHL 2018.

Our analysis revealed a huge projected rotational velocity of $v\sin(i) = 241.4^{+0.4+1.0}_{-0.9-0.3}\,{\rm km\,s^{-1}}$, which renders the abundance determination very difficult for those metals that show only weak spectral features. In particular, all lines of neon, argon, and iron are smeared out so much that they are hardly distinguishable from the continuum in the available spectrum with a S/N

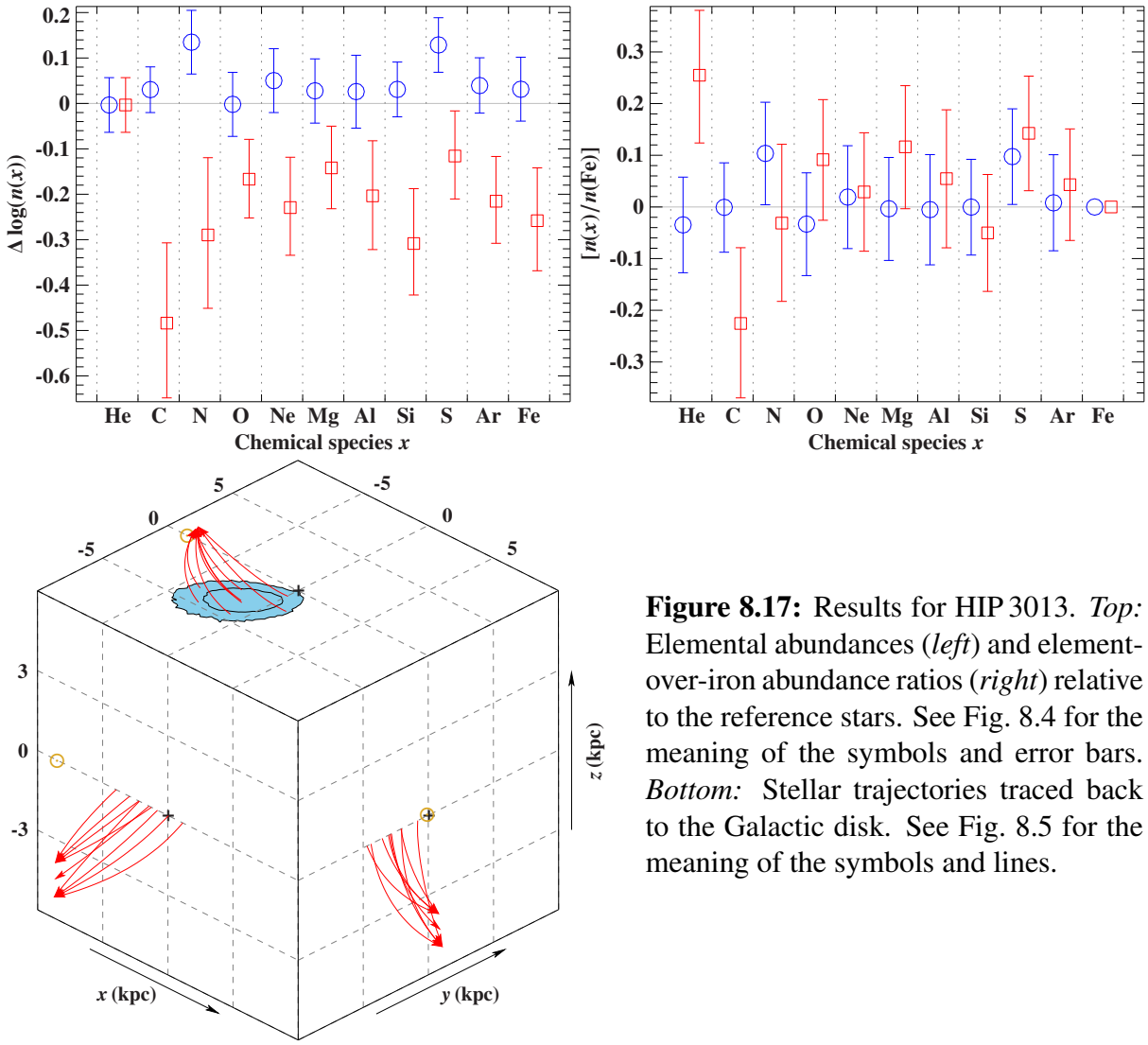

Figure 8.17: Results for HIP 3013. *Top:* Elemental abundances (*left*) and element-over-iron abundance ratios (*right*) relative to the reference stars. See Fig. 8.4 for the meaning of the symbols and error bars. *Bottom:* Stellar trajectories traced back to the Galactic disk. See Fig. 8.5 for the meaning of the symbols and lines.

ratio of about 150. Moreover, an indication for the corruption of our entire abundance analysis by the huge stellar rotation is given by the deduced value for the microturbulence, $\xi = 5.76^{+0.33+2.27}_{-0.23-2.87}$ km s^{-1}, which does not fit to the trend presented in Section 7.3.5. Owing to these problems, we refrain from using the derived abundance pattern shown in Fig. 8.16 for any interpretation. Our atmospheric parameters ($T_{\rm eff} = 19\,380^{+60+400}_{-70-390}$ K, $\log(g) = 3.925^{+0.007+0.100}_{-0.012-0.100}$ dex) give an age of $\tau = 35 \pm 6$ Myr that is in excess of the flight time $\tau_{\rm flight} = 29^{+23}_{-\ 9}$ Myr. PHL 2018 is therefore a clear candidate runaway star that was ejected with a velocity of $v_{\rm ej} = 270^{+150}_{-\ 60}$ km s^{-1} from a Galactocentric radius of $r_{\rm d} = 7.5^{+9.4}_{-4.6}$ kpc.

HIP 3013 (#13): This object, which was found by Cowley (1958) to be an early-type star below the Galactic disk, is an exceptionally well-studied runaway candidate. The results by Conlon et al. (1992) argue for a formation in the halo of the Milky Way whereas Magee et al. (2001), Ramspeck et al. (2001), and Martin (2004, 2006) favor the runaway scenario to explain the unusual current location of HIP 3013. In all studies, the atmospheric chemical composition of the star did not differ significantly from standard values.

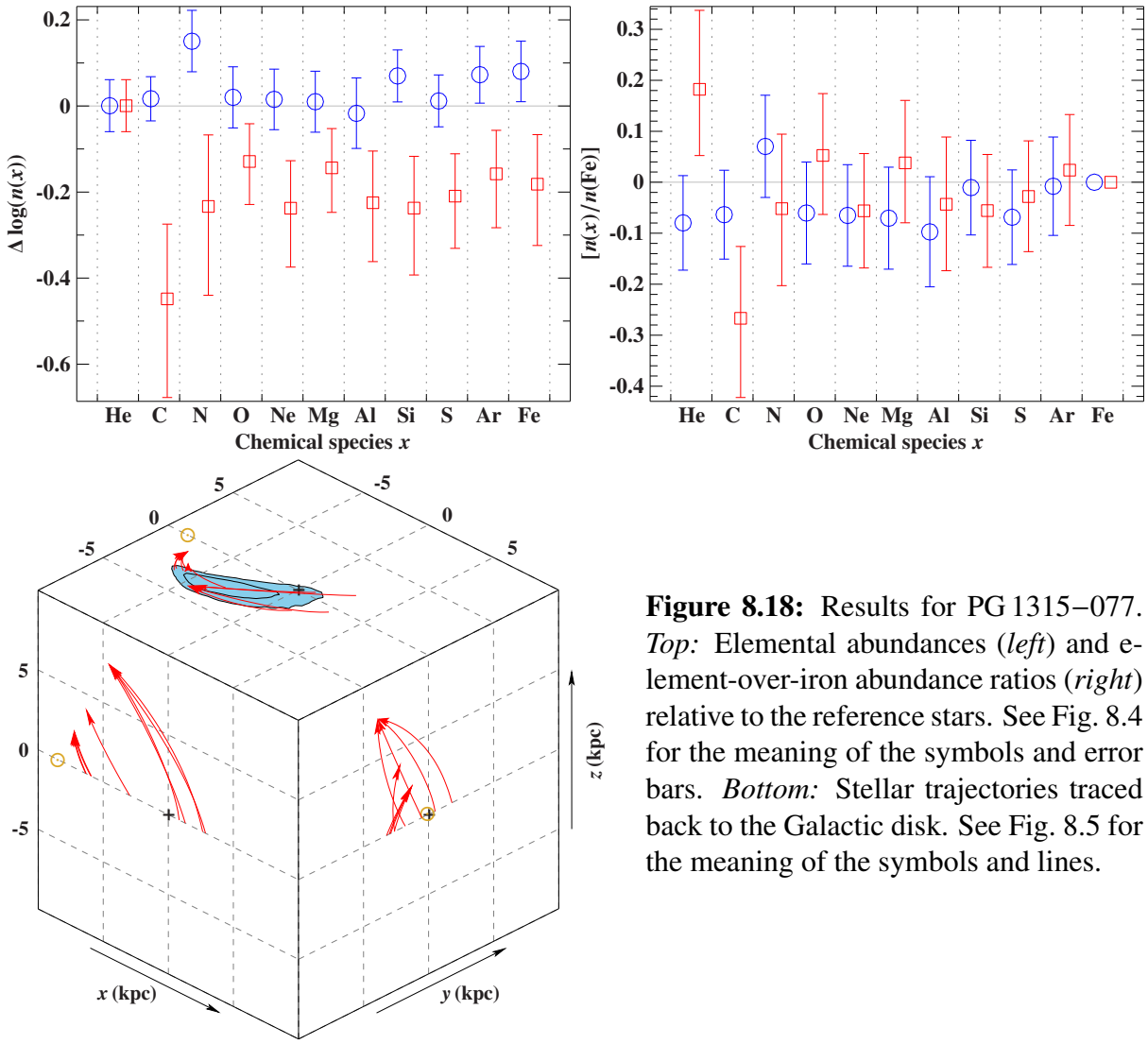

Figure 8.18: Results for PG 1315−077. *Top:* Elemental abundances (*left*) and element-over-iron abundance ratios (*right*) relative to the reference stars. See Fig. 8.4 for the meaning of the symbols and error bars. *Bottom:* Stellar trajectories traced back to the Galactic disk. See Fig. 8.5 for the meaning of the symbols and lines.

This finding is confirmed here. No signatures for a pollution with supernova-ejected material are visible in the abundance pattern nor in the element-over-iron abundance ratios (see Fig. 8.17). Instead, the abundances are very similar to those of the nearby reference stars, which is somewhat surprising since the kinematic investigation suggests a spatial origin well inside the solar circle ($r_\mathrm{d} = 3.4^{+4.0}_{-2.8}$ kpc) where the baseline metallicity is expected to be higher. Small spectral line asymmetries are detected that might hint at variability in the form of β Cepheid variations. The comparison of age ($\tau = 28 \pm 3$ Myr) and flight time ($\tau_\mathrm{flight} = 28^{+6}_{-4}$ Myr) implies that HIP 3013 must have been ejected ($v_\mathrm{ej} = 290^{+240}_{-110}$ km s^{-1}) very soon after its formation, e.g., by the initial dynamical relaxation of its host cluster, to fit into the runaway picture.

PG 1315−077 (#5): This object was considered by Hambly et al. (1993) to be a good candidate for star formation in the halo based on their combined spectroscopic and kinematic investigation. Using medium-resolution spectra ($\lambda/\Delta\lambda \approx 10\,000$), an effective temperature of $19\,000 \pm 1000$ K and a surface gravity of 4.3 ± 0.2 dex was determined. Consequently, the star is very close to the zero-age main sequence (see, e.g., Fig. 8.2), which resulted in a very low

age of ~ 1 Myr. This was then in contradiction to their estimated flight time of about 20 Myr.

The high-quality spectrum available for this study reveals recurrent asymmetries in the spectral lines of, e.g., C II, Si II/III, S II, or Fe II, which can be nicely recovered by employing a composite model spectrum. We therefore conclude that PG 1315−077 is very likely a SB2 system. The atmospheric parameters derived for the primary and secondary ($T_{\rm eff,p} = 16\,280^{+\ 30+330}_{-100-340}$ K, $T_{\rm eff,s} = 16\,640^{+\ 60+340}_{-120-330}$, $\log(g)_{\rm p} = 4.112^{+0.014+0.100}_{-0.020-0.100}$ dex, $\log(g)_{\rm s} = 4.292^{+0.008+0.153}_{-0.009-0.302}$ dex) shift the components of the system to cooler temperatures and lower surface gravities than derived by Hambly et al. (1993), which also increases the derived age of the binary system ($\tau_{\rm p} = 53^{+11}_{-16}$ Myr, $\tau_{\rm s} = 16^{+40}_{-16}$ Myr). We use the center-of-mass velocity $v_{\rm com} = (M_{\rm p}v_{\rm vrad,p} + M_{\rm s}v_{\rm vrad,s})/(M_{\rm p} + M_{\rm s})$ for the kinematic analysis, which suffers from the large uncertainty in the spectroscopic distance, $d = 5.06^{+4.30}_{-2.16}$ kpc, caused by the relatively poor photometric data. The flight time ($\tau_{\rm flight} = 25^{+12}_{-\ 9}$ Myr) is consistent with our revised age whereas the kinematically deduced birthplace of PG 1315−077 ($r_{\rm d} = 3.9^{+3.1}_{-3.8}$ kpc) is at smaller Galactocentric radii than suggested by the abundance pattern, which is almost identical to that of the nearby reference stars (Fig. 8.18) and, thus, does not show any signature for α-element enhancement. We conclude that PG 1315−077 is a runaway binary system that is most likely ejected by dynamical interactions involving, for instance, a hierarchical triplet system. The large ejection velocity $v_{\rm ej} = 330^{+410}_{-130}$ km s^{-1} would then require a close encounter with at least one very massive star or an ejection from the Galactic center by the powerful Hills mechanism.

HD 218970 (#8): Cowley (1958) recognized that this object is an early-type star that is probably located below the Galactic disk. The low-resolution spectroscopic and kinematic investigation by Conlon et al. (1988) revealed more or less normal abundances as well as kinematic properties that are in agreement with the disk runaway scenario. Martin (2004) used high-resolution spectra to derive abundances for silicon and sulfur with both of them showing substantial enhancements relative to a control sample. The subsequent kinematic analysis (Martin 2006) fitted into the runaway picture.

HD 218970's atmospheric chemical composition (see Fig. 8.19) differs significantly from the respective reference stars in this study, too. Overabundances in carbon, nitrogen, oxygen, magnesium, aluminum, silicon, and sulfur are found whereas helium, neon, and iron appear to be normal. The consideration of the Galactic abundance gradients changes only the interpretation of the carbon content, which then meets the expectations for a star that stems from a Galactocentric radius of $r_{\rm d} = 6.2^{+0.5}_{-0.6}$ kpc. Since the same statements hold for the element-over-iron abundance ratios, we conclude that the abundance pattern of HD 218970 exhibits clear signatures for the accretion of supernova ejecta even though neon is not enhanced. From the kinematic point of view, we note that this star has the third largest current Galactic rest-frame velocity ($v_{\rm Grf} = 490^{+70}_{-40}$ km s^{-1}) in our sample, which is the result of a high ejection velocity ($v_{\rm ej} = 340^{+70}_{-50}$ km s^{-1}) in combination with an additional boost from the Galactic rotation. A comparison of the star's age ($\tau = 7^{+10}_{-\ 7}$ Myr) with its flight time ($\tau_{\rm flight} = 7 \pm 1$ Myr) indicates that HD 218970 was ejected soon after its formation, which is possible in the supernova scenario if the primary component of the binary system was sufficiently massive and thus short-lived. Consequently, HD 218970 qualifies as an excellent candidate for the supernova ejection channel.

HD 100340 (#18): This B-type star above the Galactic plane (Cowley 1958) does not show brightness variability on a timescale of hours (Hambly et al. 1994) and is therefore probably

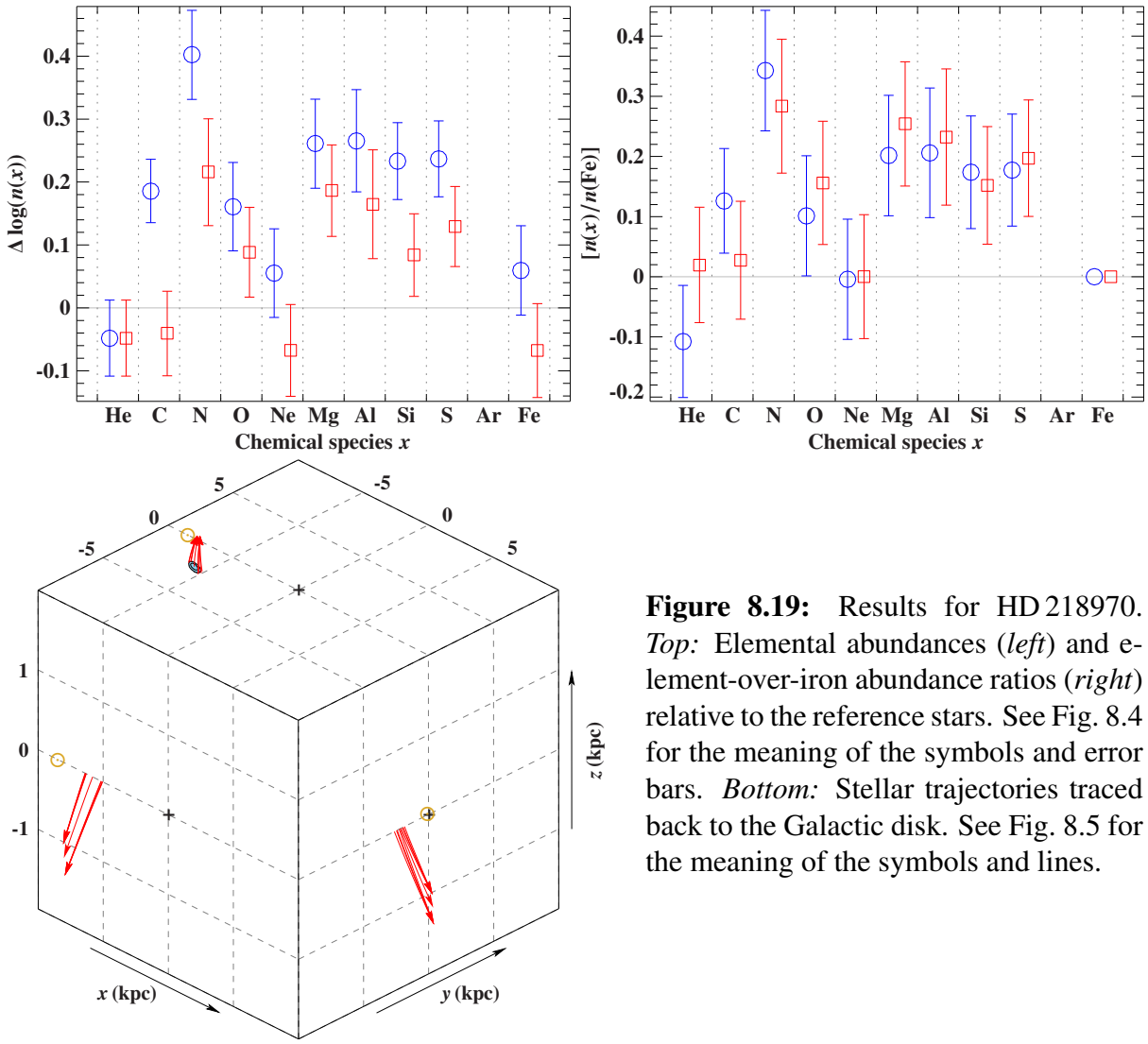

Figure 8.19: Results for HD 218970. *Top:* Elemental abundances (*left*) and element-over-iron abundance ratios (*right*) relative to the reference stars. See Fig. 8.4 for the meaning of the symbols and error bars. *Bottom:* Stellar trajectories traced back to the Galactic disk. See Fig. 8.5 for the meaning of the symbols and lines.

not pulsating. The spectroscopic and kinematic study by Keenan et al. (1987) gave an effective temperature of 25 000 K, a surface gravity of 3.8 dex, and a normal chemical composition. The resulting distance of 5.3 ± 0.9 kpc implied a flight time of 17 Myr, which was larger than the estimate for the maximum stellar lifetime (12 Myr) and, thus, in contradiction with a runaway scenario. Ryans et al. (1999) solved this discrepancy by using a lower spectroscopic distance of 3 kpc, which was the consequence of a revised surface gravity of 4.1 dex.

Our spectroscopic distance $d = 3.47^{+0.39}_{-0.28}$ kpc is similar to that of Ryans et al. (1999). The abundance analysis suffers from the smearing and blending of spectral lines caused by the high projected rotational velocity of $v \sin(i) = 163.4^{+0.1+2.6}_{-0.1-0.1}$ km s^{-1}. In particular, the results for neon and sulfur are not reliable because only weak lines are available for them making their abundances prone to other effects such as the continuum normalization. Neglecting neon and sulfur for a moment, the abundances and the element-over-iron abundance ratios in Fig. 8.20 are quite similar to those of the reference stars. Moreover, the supernova indicators magnesium and silicon do not show any peculiarities. From the kinematic point of view, we note that HD 100340 has the fourth largest current Galactic rest-frame ($v_{\rm Grf} = 440^{+70}_{-60}$ km s^{-1}) as well as ejection ve-

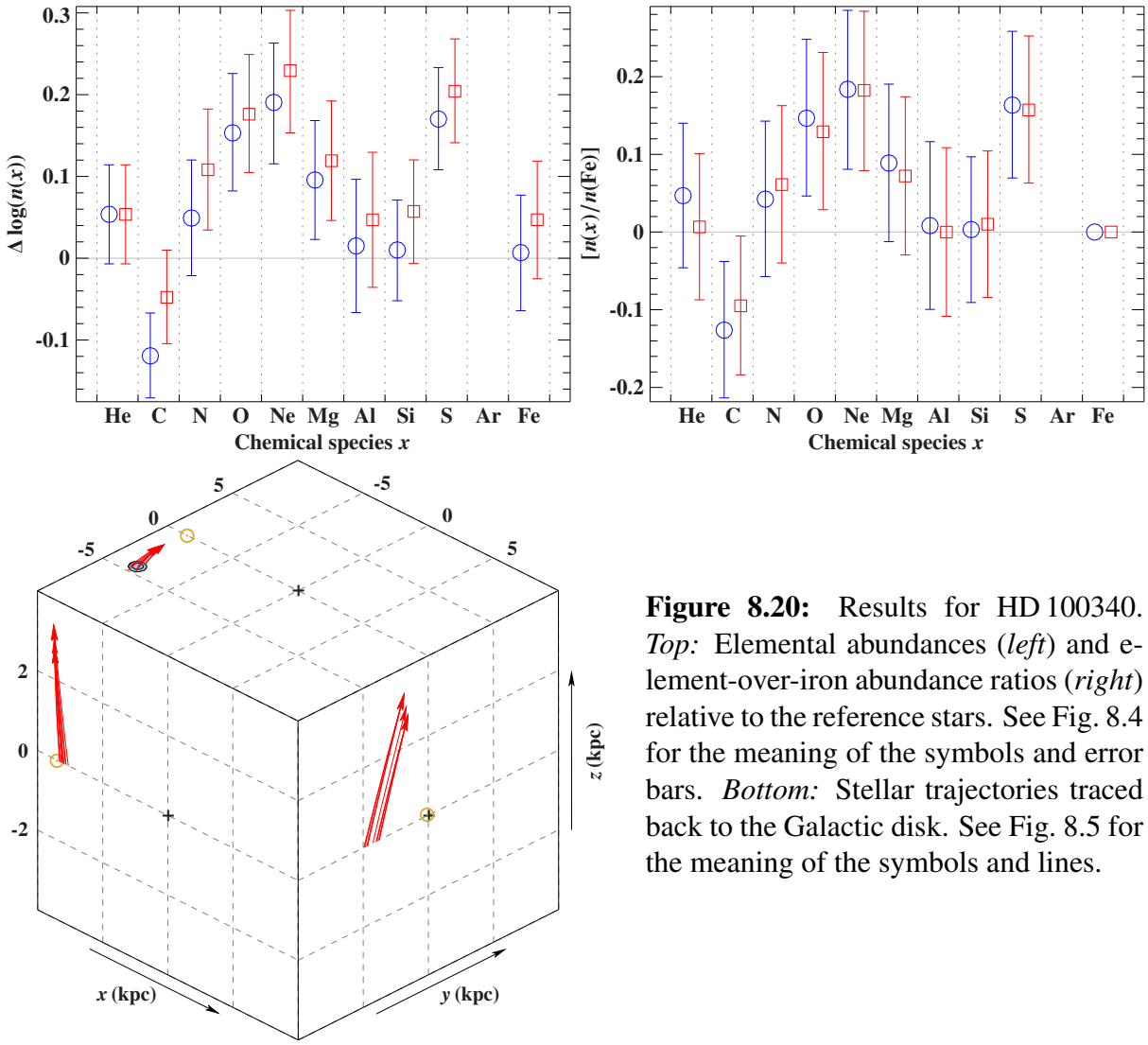

Figure 8.20: Results for HD 100340. *Top:* Elemental abundances (*left*) and element-over-iron abundance ratios (*right*) relative to the reference stars. See Fig. 8.4 for the meaning of the symbols and error bars. *Bottom:* Stellar trajectories traced back to the Galactic disk. See Fig. 8.5 for the meaning of the symbols and lines.

locity ($v_{\rm ej} = 350 \pm 40\,{\rm km\,s^{-1}}$) in our sample. The flight time ($\tau_{\rm flight} = 9^{+2}_{-1}\,{\rm Myr}$) is in agreement with the star's evolutionary lifetime ($\tau = 9^{+4}_{-9}\,{\rm Myr}$) so that HD 100340 could be ejected shortly after its formation, e.g., by a close dynamical encounter involving at least one very massive component.

PHL 346 (#16): This early-type star below the Galactic disk (Kilkenny et al. 1977) is a β Cepheid pulsator (Waelkens & Rufener 1988). Moreover, this object was brought into focus by the analysis of Keenan et al. (1986b) who suggested that PHL 346 is an early B-type star with normal chemical composition that cannot have originated in the Galactic disk but must have formed in the halo. Triggered by this finding, this target was included in several studies about runaway stars (Conlon et al. 1992; Ryans et al. 1996; Ramspeck et al. 2001). All of them confirmed that PHL 346 is chemically not peculiar. However, Ryans et al. (1996) and Ramspeck et al. (2001) pointed out that a runaway scenario from the Galactic disk cannot be excluded at all as explanation for PHL 346's current location in the halo.

As expected for a pulsating star, the line profiles in the available spectrum are not symmetric

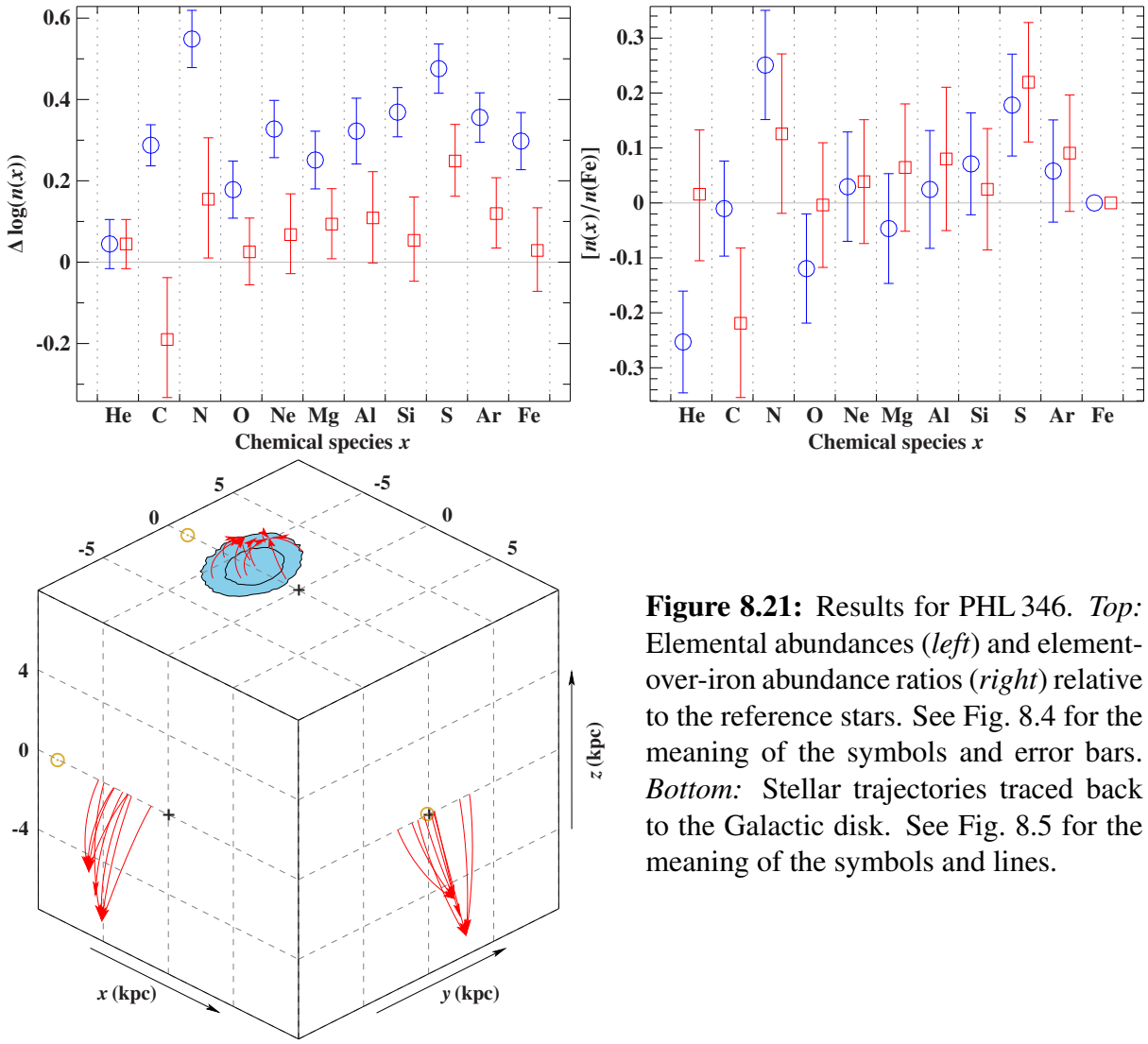

Figure 8.21: Results for PHL 346. *Top:* Elemental abundances (*left*) and element-over-iron abundance ratios (*right*) relative to the reference stars. See Fig. 8.4 for the meaning of the symbols and error bars. *Bottom:* Stellar trajectories traced back to the Galactic disk. See Fig. 8.5 for the meaning of the symbols and lines.

but slightly distorted by bumps. Fortunately, the spectroscopic analysis is not affected by this issue. The differential abundance analysis (see Fig. 8.21) indicates that the baseline metallicity of PHL 346 is about 0.3 dex larger than that of the reference stars. This result agrees very well with the kinematic investigation, which suggests that the star stems from the inner part of the Galaxy ($r_\mathrm{d} = 3.8^{+3.4}_{-2.5}$ kpc). After taking the Galactic abundance gradients into consideration, the abundance pattern appears to be perfectly normal except for sulfur. In particular, there is no hint for the accretion of supernova material in the element-over-iron abundance ratios. From the calculation of stellar trajectories, we infer a flight time of $\tau_\mathrm{flight} = 26^{+11}_{-\ 6}$ Myr. Within error margins, this is compatible with the star's estimated lifetime of $\tau = 21^{+2}_{-3}$ Myr. Therefore, we also come to the conclusion that the runaway scenario should be considered as a serious option for PHL 346. In the case of an ejection event, it is remarkably to note that despite its low current Galactic rest-frame velocity of $v_\mathrm{Grf} = 170^{+100}_{-\ 30}$ km s^{-1}, the star was ejected with one of the largest velocities ($v_\mathrm{ej} = 380^{+180}_{-130}$ km s^{-1}) in the sample. This is possible because the ejection direction was roughly opposite to the Galactic rotation. So instead of receiving an additional boost like HD 271791 or HD 218970, PHL 346 was slowed down by the rotation of the Galactic disk.

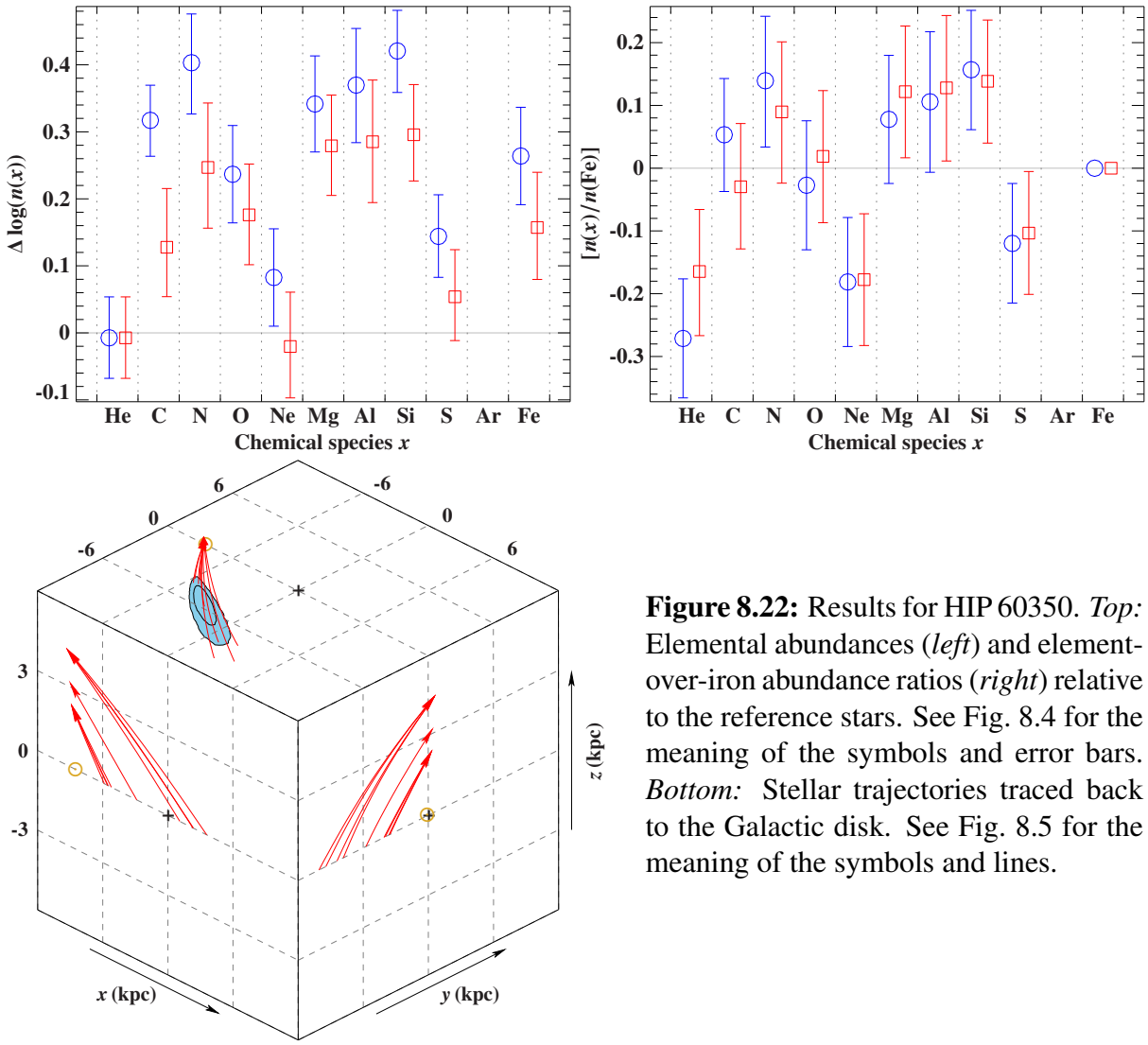

Figure 8.22: Results for HIP 60350. *Top:* Elemental abundances (*left*) and element-over-iron abundance ratios (*right*) relative to the reference stars. See Fig. 8.4 for the meaning of the symbols and error bars. *Bottom:* Stellar trajectories traced back to the Galactic disk. See Fig. 8.5 for the meaning of the symbols and lines.

HIP 60350 (#6): This object is one of the most extreme runaway stars in the literature and is already known for decades (Tobin 1986). Several spectroscopic and kinematic studies were published (e.g., de Boer et al. 1988; Maitzen et al. 1998; Tenjes et al. 2001) in the past, the latest one by us (Irrgang et al. 2010) based on a medium-resolution spectrum ($\lambda/\Delta\lambda$ = 15 000) with a peak S/N ratio of 140. The two major conclusions from that paper were that HIP 60350 is a candidate hyper-runaway star and that its abundance pattern does not exclude the supernova mechanism as ejection scenario. However, the significance of the results suffered from the quality of the data as well as from the iterative analysis strategy.

For the present study, we obtained a new high-resolution spectrum with decent S/N ratio which was then analyzed with the global method outlined in Chapter 5. In this way, we could revise our previous results, which affects mainly the abundance analysis. The resulting abundance pattern (Fig. 8.22) shows a standard helium abundance, modest enhancements in neon and sulfur, and clear enrichments in the remaining metals when compared to the standard values of the nearby reference stars, which indicates an origin closer to the Galactic center than the Sun. The element-over-iron abundance ratios (Fig. 8.22) reveal no significant signature for

α-element capture although magnesium, aluminum, and silicon appear marginally enhanced. In particular, the low values for neon and sulfur do not fit at all in the supernova accretion picture.

Similar to HD 271791, the kinematic investigation of HIP 60350 is rather trivial given the high current Galactic rest-frame velocity of $v_{\rm Grf} = 570^{+110}_{-\ 80}\,{\rm km\,s^{-1}}$ making this object the second most extreme runaway star in our sample and a candidate hyper-runaway star since 22% of the Monte Carlo runs in Milky Way mass Model I yield unbound orbits. Like HD 271791, HIP 60350 was ejected in direction of Galactic rotation and thereby received an additional boost to the already high ejection velocity of $v_{\rm ej} = 400^{+180}_{-\ 70}\,{\rm km\,s^{-1}}$. Since this value exceeds our previous one, $v_{\rm ej} = 389 \pm 111\,{\rm km\,s^{-1}}$ (Irrgang et al. 2010), it is even harder to construct a realistic pre-supernova binary system as it already was in Irrgang et al. (2010). As indicated by the abundances, the star was probably ejected from inside the solar circle at a Galactocentric radius of $r_{\rm d} = 6.6^{+3.2}_{-1.0}\,{\rm kpc}$. The flight time $\tau_{\rm flight} = 16^{+7}_{-6}\,{\rm Myr}$ is well below the age estimate of $\tau = 53^{+13}_{-19}\,{\rm Myr}$. We conclude that HIP 60350 is a runaway star from the Galactic disk, which was rather ejected by a close dynamical encounter than by the disruption of a binary system via a supernova explosion.

8.5 Summary

In this Chapter, a combined spectroscopic and kinematic investigation of 18 runaway stars is presented. Special attention is given to the abundance analysis because it is the most valuable tool to distinguish between the two basic ejection mechanisms, namely dynamical many-body interactions and the disruption of a binary system by the supernova explosion of its primary component. In order to detect chemical peculiarities, a differential abundance analysis is performed, which means that the abundances of the runaway stars are directly compared to those of the nearby reference stars. By doing so, systematic shortcomings in the modeling are expected to cancel out and the significance of the results is considerably larger than in the case of absolute abundance determinations. The inhomogeneous Galactochemical evolution within the Milky Way is accounted for by making use of published Galactic abundance gradients to estimate the runaway stars' pristine chemical composition.

In a first step, the flagship runaway star HD 271791 is re-analyzed. The claimed detection of α-element enhancement is confirmed here at the same level of significance as in the literature. More or less obvious signatures for the capture of supernova ejecta are also found for HD 78584, HD 218970, HD 22586, and HD 204076 whereby HD 218970 is the statistically most significant candidate. The abundance patterns of PG 1315−077, HIP 13800, PG 0122+214, PG 2345+241, HIP 3013, PHL 159, PHL 346, HD 69686, and HD 100340 are rather normal while unusual patterns emerge in the cases of EC 09452−1403, PG 0934+145, HIP 60350, and PHL 2018.

Five stars in the sample (HD 271791, PG 0122+214, HD 22586, PHL 159, and PHL 346) have flight times in excess of their evolutionary age and hence challenge the runaway scenario. However, taking the respective error bars into consideration, this discrepancy is resolved for four of them. The remaining object (HD 22586) can be explained either by in-situ star formation in the halo, e.g., triggered by the collision of interstellar gas clouds, or by binary interactions like mass transfer which then lead to a rejuvenation of the runaway star making it appear younger than it actually is. The latter is equivalent to our earlier statement that the stellar lifetimes are derived from single-star evolutionary tracks and should therefore be interpreted with caution in

the case of the runaway stars.[26]

In addition to these five stars, there are eight stars (HIP 13800, HD 218970, PG 0122+214, PHL 2018, PG 2345+241, HIP 3013, HD 204076, and HD 100340) that were ejected very soon after their formation. This is expected because we primarily selected unevolved runaway stars of spectral type B that are already far away from the Galactic disk. However, traveling these large distances takes some time and many runaway stars, especially those which were not ejected shortly after their birth, will never reach the halo during the limited main-sequence lifetime of a massive star.

In terms of the ejection velocity and the current Galactic rest-frame velocity, HD 271791, which is probably unbound to the Milky Way and consequently a hyper-runaway star, is by far the most extreme runaway star considered here. The second star in this ranking is HIP 60350, which is the only other hyper-runaway candidate in this study. Both stars have in common that they were ejected in direction of Galactic rotation and, in this way, received an additional boost which brought them close to or even above the local escape velocity of the Milky Way. In contrast, PHL 346 has one of the lowest current Galactic rest-frame velocities in the sample although it was ejected with a similar velocity than HIP 60350. However, the ejection direction was opposite to the Galactic rotation.

The object PG 1315−077, whose ejection velocity is also quite high, turns out to be a double-lined spectroscopic binary system that could originate in the Galactic center as the result of the tidal disruption of a hierarchical triplet system by the central supermassive black hole.

[26]Moreover, errors in the determination of crucial parameters like the surface gravity or the proper motions can have serious effects on the outcome of the analysis.

9 Future work

The various projects we reported here (Milky Way mass models, novel spectroscopic analysis method, Balmer line Stark broadening issue, a reference sample of nearby stars, origin of runaway stars) pave the way to tackle many new challenges.

In order to meet the precision of the upcoming astrometric measurements by the *Gaia* satellite, the Milky Way mass models introduced in Chapter 3 need to be improved. The rotating bar or the spiral arms are not considered in the kinematic analysis so far. Moreover, the Galactic halo is populated by a number of satellite galaxies like the Sagittarius Dwarf Galaxy or the Magellanic Clouds. Stellar trajectories that reach far into the halo can certainly be affected by their presence. Finally, the Milky Way is not an isolated system but part of a group of nearby galaxies, the so-called Local Group. Its most massive members are the Milky Way and the Andromeda Galaxy. The gravitational force of the latter might thus also lead to a small yet perceptible perturbation of stellar orbits. The implementation of satellite or neighbor galaxies is more or less straightforward because their effects on the observational constraints used to calibrate the mass distribution of the Milky Way (see Sect. 3.1.2) are negligible. Hence, gravitational potentials, for instance in the form of Eq. (3.14), can simply be added to the currently available Galactic potentials by making use of published data (e.g. McConnachie 2012). To account for the motion of the satellite galaxies, their trajectories in the plain Milky Way mass Models I–III can be exploited. In contrast, the implementation of the rotating Galactic bar and the spiral arms is much more challenging because it breaks the time invariance as well as the axial symmetry of the original gravitational potential. On the one hand, this implies that the observational constraints need to be resolved with respect to time and position, which largely increases the number of required observations. On the other hand, the models become more complex which complicates their calibration. Even without adding new features, the available Milky Way mass models can be continuously improved by regular re-calibrations based on revised and new observational data.[27]

With respect to the spectroscopic analysis, we note that we have acquired a lot of high-quality spectra in the course of this work, actually too many to digest all of them in this thesis. In particular, we have obtained data for about 60 less extreme runaway OB stars in the solar neighborhood. A brief inspection of the available spectra already revealed some highlights warranting more detailed analyses: (i) the detection of an extreme CNO-mixing signature in a B-type star on the main sequence, which is at odds with standard evolutionary models, (ii) the discovery of at least two mid B-type stars of λ Boo type, which are decidedly weak in iron but not in most of the other elements and were previously found only in late B-type to early F-type stars (Griffin et al. 2012), (iii) the realization that many of the nearby runaway stars are actually unrecognized binary systems.

Future perspectives in terms of the new analysis method described in Chapter 5 are certainly the application to low-resolution spectra and the focus on double-lined spectroscopic binary systems. Going to lower resolutions has the advantage that high S/N spectra can be obtained already at relatively small telescopes. This is particularly interesting in the case of faint but fast-rotating stars where the lines are anyway smeared out by stellar rotation. The greatest potential of our new analysis strategy is the option to treat composite spectra in a way that is

[27] Eventually, the standard Runge-Kutta method, which is currently used for solving the equations of motions, could be replaced by a more sophisticated numerical integration technique to speed up the calculations.

a lot more efficient than traditional spectral disentangling techniques. Binary systems are a hot topic in the field today since precision spectroscopy reveals that a large fraction of O- and B-type stars resides in binary (or even multiple) systems rendering many published analyses unreliable. The determination of highly precise surface abundances for a statistically significant number of binary systems could bring new insights into stellar evolution. The novel method also allows to further explore systematic effects, e.g., a rigorous investigation of non-LTE effects (versus LTE) following up on the examples given in Appendix C.1 or the mining in existing large spectroscopic surveys like VLT-FLAMES (Evans et al. 2006) or SDSS (Yanny et al. 2009).

Regardless of the specific future application, there are two open problems in the current spectroscopic analysis that have to be solved as soon as possible. On the one hand, there are clear indications that a remaining systematic bias affects the temperature determination for late B-type stars, see, e.g., the systematic abundance trends with temperature discussed in Sect. 7.2.4, which so far prevent us from deriving highly precise absolute abundances and, thus, a revised cosmic abundance standard. The exact reason for this is unknown at the moment and detailed investigations, e.g., with respect to the spectral energy distribution and the parallel fitting of photometric and spectroscopic data, are planned to diagnose the problem. On the other hand, the uncertainty in the determination of the surface gravity introduced by the different Balmer line Stark broadening tables (see Chapter 6) is very unpleasant. We hope to solve this issue in the near future by means of a comprehensive study of several eclipsing binary systems where the stellar masses and radii are accessible from the analyses of the systems' light and radial velocity curves. In general, the spectroscopic analysis would benefit from some revisions in the applied model atoms. Based on the detailed study of the reference stars in Chapter 7, we could identify some shortcomings in the modeling like missing spectral lines or lines that are systematically too weak or too strong, respectively. This information can now be used to improve the model atoms.

Besides steadily increasing the number of analyzed reference and runaway stars, there are at least two other important tasks in the medium to long term. Firstly, the spectroscopic analysis of those runaway stars that show indications for the accretion of supernova ejecta should be extended to the ultraviolet region where spectral lines of the r-process elements become visible. Finding overabundances in these elements would considerably strengthen the supernova runaway scenario and, what is more, would be strong observational support for the assumption that stellar nucleosynthesis via the rapid capture of neutrons occurs indeed during core-collapse supernova explosions. Secondly, the accuracy of the available astrometric data will be increased by a factor of about thousand with respect to the Hipparcos mission once the final data reduction of the *Gaia* satellite will be released in a few years (first results may already be available at the end of 2015). This will allow for a comparison of our spectroscopic distances with extremely precise parallaxes from which valuable conclusions about the validity of our atmospheric parameter determination can be drawn, for instance with regard to the Balmer line Stark broadening issue. Moreover, the kinematic investigation is currently limited by the uncertainties in the distance and the proper motions. With the astrometric data from *Gaia*, which will also cover Galactic clusters, this will not be a problem any more and kinematic analyses of unprecedented accuracy will become possible. Therefore, we might be able to identify parent clusters even for extreme runaway stars.

A Animations

Animated GIF files of Figs. 1.1, 1.2, 1.3, and 1.4 are available at `http://www.sternwarte.uni-erlangen.de/~irrgang/animations/`. The animations were created using the free open source tool Blender[28]. GIMP[29], a free image editor, is used to create animated GIF files out of individual frames.

To make the animations as realistic as possible, all trajectories (except for the Milky Way runaway star) were calculated numerically starting from reasonable physical conditions. To solve the equations of motion, a fourth-order Runge-Kutta-Fehlberg algorithm was applied. Although the trajectory for the star escaping from the spiral galaxy (Fig. 1.1) was not calculated, the animation is still quite realistic when considering a very fast runaway star.

In the binary-binary interactions (Fig. 1.2), three stars of five solar masses and one star (the blue sphere) of one solar mass were involved. The radii of the stars were scaled under the assumption that they have solar density and then multiplied by a factor of ten for the sake of visualization. The run-times of these animations correspond to approximately five years in real time.

The binary system in the supernova animation (Fig. 1.3) consists of a 15 solar mass primary and a five solar mass secondary component. The orbital period is 1.5 days. Radii were chosen such that the major object is a compact Wolf-Rayet star while the minor one is a slightly evolved main sequence star. Numerically, the supernova explosion was implemented by instantaneously reducing the primary's mass to 1.4 solar masses (canonical mass of a neutron star) and neglecting all other effects.

To have time and length scales appropriate for an animation, the mass of the supermassive black hole in the slingshot scenario (Fig. 1.4) had to be reduced from a few millions to 500 solar masses while, at the same time, the masses of the two stars were set to a rather high value of 25 solar masses. In this way, the gravitational force between the stars is of the same order of magnitude as the black hole's tidal force enabling the latter to disrupt the binary system. Holding this balance of forces while increasing the mass of the black hole requires the binary system to be moved further away from the black hole, which makes the system inappropriate for visualization. Again, stellar radii were scaled from solar density and increased by a factor of ten. Run-time of this event in real time is about 27 years.

[28] `http://www.blender.org/`
[29] `http://www.gimp.org/`

B Equations of motion

The motion of test particles in an axisymmetric gravitational potential $\Phi(r, z)$ can be conveniently derived from the Lagrangian $\mathcal{L}$ of the system:

$$\mathcal{L}\left(r, z, \dot{r}, \dot{\phi}, \dot{z}\right) = \frac{1}{2}\left(\dot{r}^2 + \left(r\dot{\phi}\right)^2 + \dot{z}^2\right) - \Phi(r, z)\,. \tag{B.1}$$

Introducing canonical momenta $p_r = \partial\mathcal{L}/\partial\dot{r} = \dot{r}$, $p_\phi = \partial\mathcal{L}/\partial\dot{\phi} = r^2\dot{\phi}$, and $p_z = \partial\mathcal{L}/\partial\dot{z} = \dot{z}$, the corresponding Lagrange's equations – written as a system of first-order differential equations – read as

$$\dot{r} = p_r\,, \tag{B.2}$$

$$\dot{\phi} = \frac{p_\phi}{r^2}\,, \tag{B.3}$$

$$\dot{z} = p_z\,, \tag{B.4}$$

$$\dot{p}_r = \frac{{p_\phi}^2}{r^3} - \frac{GM_\mathrm{b} r}{\left(r^2 + z^2 + {b_\mathrm{b}}^2\right)^{3/2}} - \frac{GM_\mathrm{d} r}{\left(r^2 + \left(a_\mathrm{d} + \sqrt{z^2 + {b_\mathrm{d}}^2}\right)^2\right)^{3/2}} - \frac{\partial\Phi_\mathrm{h}(R)}{\partial R}\frac{r}{\sqrt{r^2 + z^2}}\,, \tag{B.5}$$

$$\dot{p}_\phi = 0\,, \tag{B.6}$$

$$\dot{p}_z = -\frac{GM_\mathrm{b} z}{\left(r^2 + z^2 + {b_\mathrm{b}}^2\right)^{3/2}} - \frac{GM_\mathrm{d} z\left(a_\mathrm{d}/\sqrt{z^2 + {b_\mathrm{d}}^2} + 1\right)}{\left(r^2 + \left(a_\mathrm{d} + \sqrt{z^2 + {b_\mathrm{d}}^2}\right)^2\right)^{3/2}} - \frac{\partial\Phi_\mathrm{h}(R)}{\partial R}\frac{z}{\sqrt{r^2 + z^2}}\,, \tag{B.7}$$

whereby

$$\frac{\partial\Phi_\mathrm{h}(R)}{\partial R} = \begin{cases} \dfrac{GM_\mathrm{h}}{a_\mathrm{h} R}\dfrac{(R/a_\mathrm{h})^{\gamma-1}}{1 + (R/a_\mathrm{h})^{\gamma-1}} & \text{if } R < \Lambda \text{ \& Model I,} \quad \text{(B.8a)} \\ \dfrac{GM_\mathrm{h}}{R^2}\dfrac{(\Lambda/a_\mathrm{h})^{\gamma}}{1 + (\Lambda/a_\mathrm{h})^{\gamma-1}} & \text{if } R \geq \Lambda \text{ \& Model I,} \quad \text{(B.8b)} \\ \dfrac{GM_\mathrm{h}}{\sqrt{R^2 + {a_\mathrm{h}}^2}R} & \text{if Model II,} \quad \text{(B.8c)} \\ \dfrac{GM_\mathrm{h}}{R^2}\ln\left(1 + \dfrac{R}{a_\mathrm{h}}\right) - \dfrac{GM_\mathrm{h}}{(a_\mathrm{h} + R)R} & \text{if Model III.} \quad \text{(B.8d)} \end{cases}$$

With lengths expressed in kpc, masses in galactic mass units M_gal, and time in Myr, the gravitational constant G has to be replaced by the factor $\sim 1.04598 \times 10^{-4}$ thereby converting units from $100\,\mathrm{km^2\,s^{-2}}$ to $\mathrm{kpc^2\,Myr^{-2}}$.

C Spectra

C.1 LTE versus non-LTE

Figures C.1.1a to C.1.1m visualize the effects of non-LTE in the spectral range $\lambda\lambda$ 3940–8000 Å: Normalized non-LTE fluxes f_{NLTE} (computed with the hybrid approach outlined in Sect. 4.3.4) are compared to LTE fluxes f_{LTE} for effective temperatures T_{eff} of 15 000 K (magenta), 20 000 K (blue), 25 000 K (green), 30 000 K (red) and surface gravities $\log(g\,(\mathrm{cm\,s^{-2}}))$ of 4.25 (*five panels to the left*) and 3.75 (*five panels to the right*). No macroscopic broadening mechanisms apart from a spectral resolving power $\lambda/\Delta\lambda = 48\,000$ are applied. Note that only the strongest spectral lines are labeled and that the list of modeled lines is not complete, e.g., because several O II lines are missing for high temperatures.

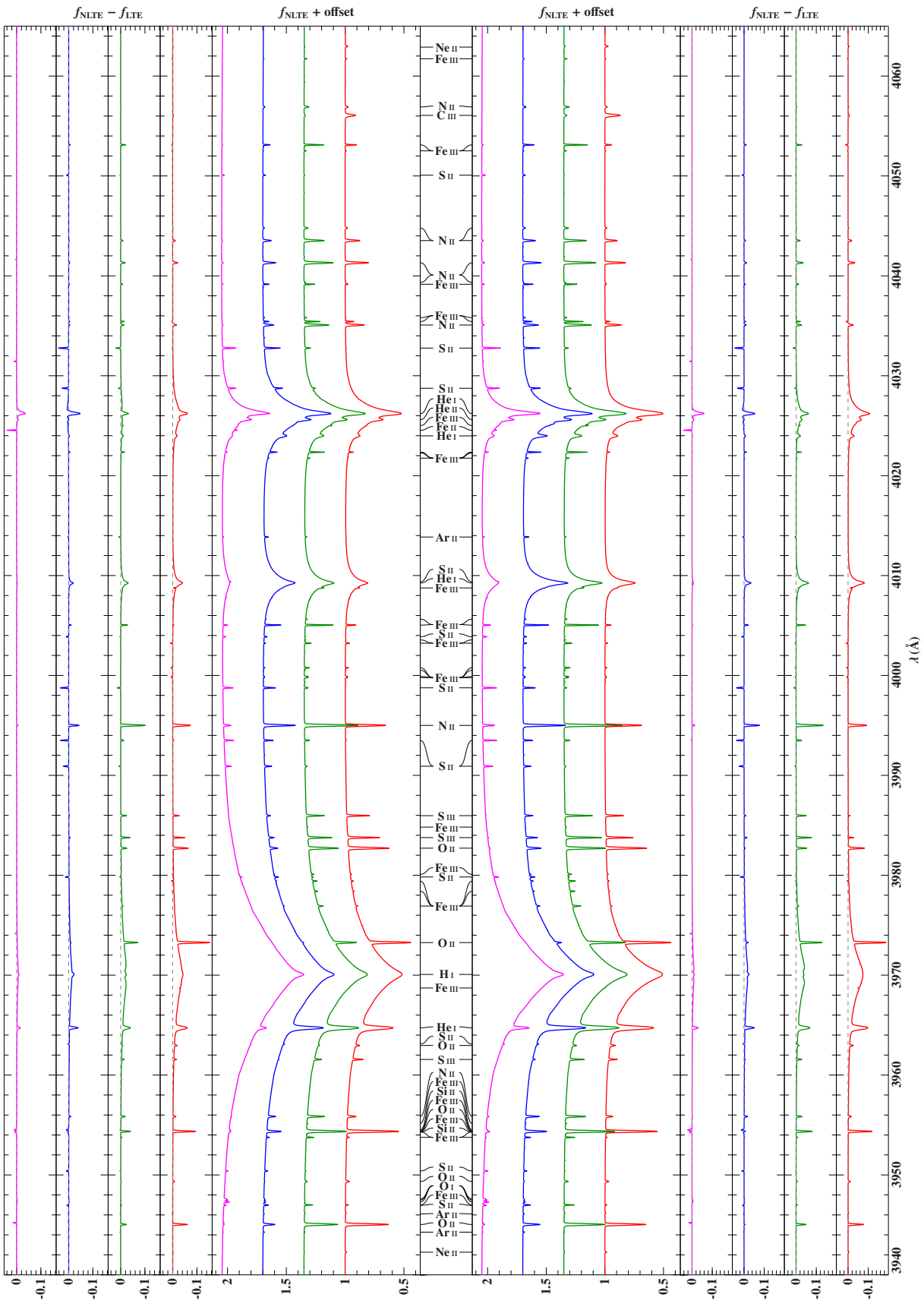

Figure C.1.1a: See Sect. C.1.

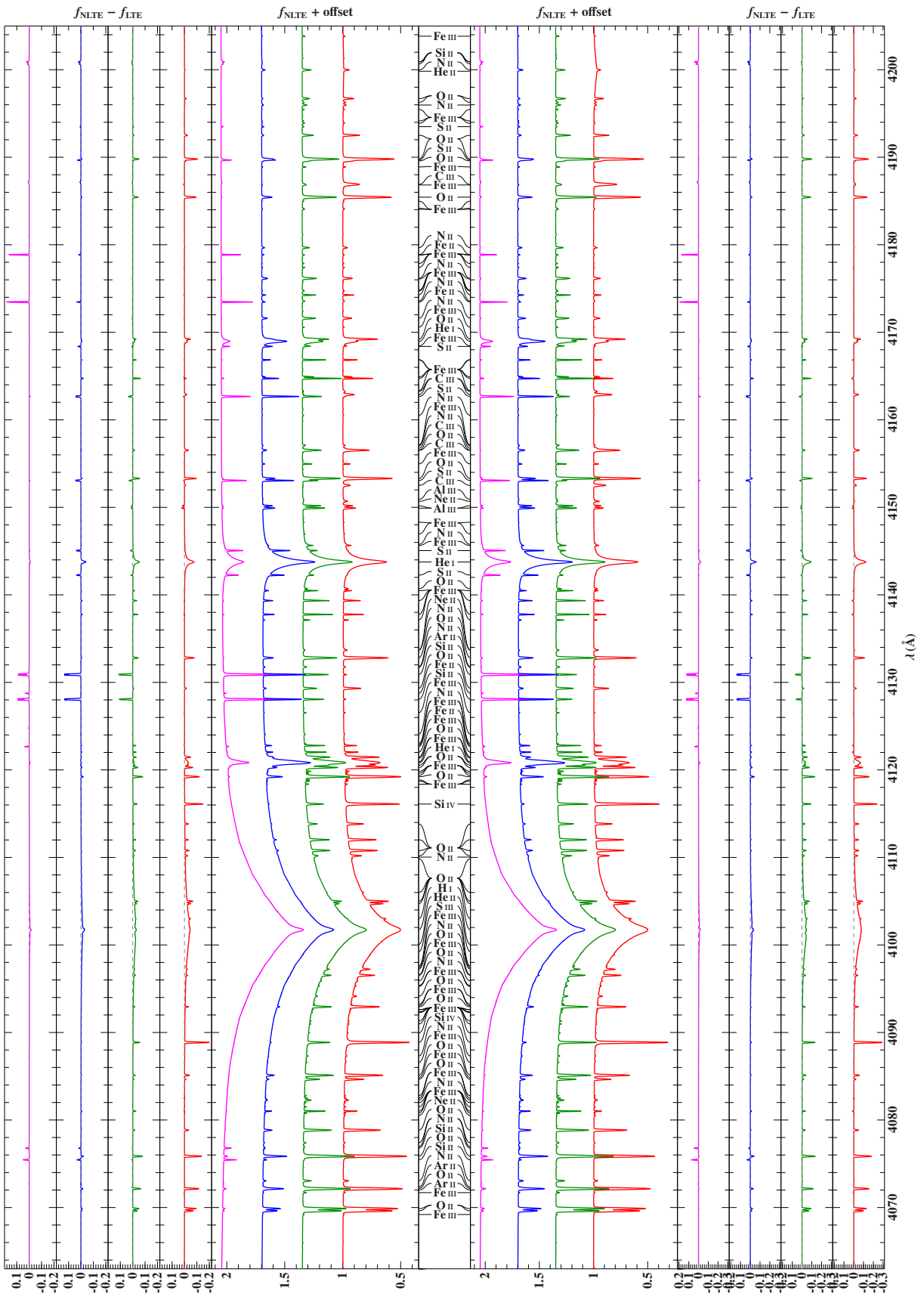

Figure C.1.1b: See Sect. C.1.

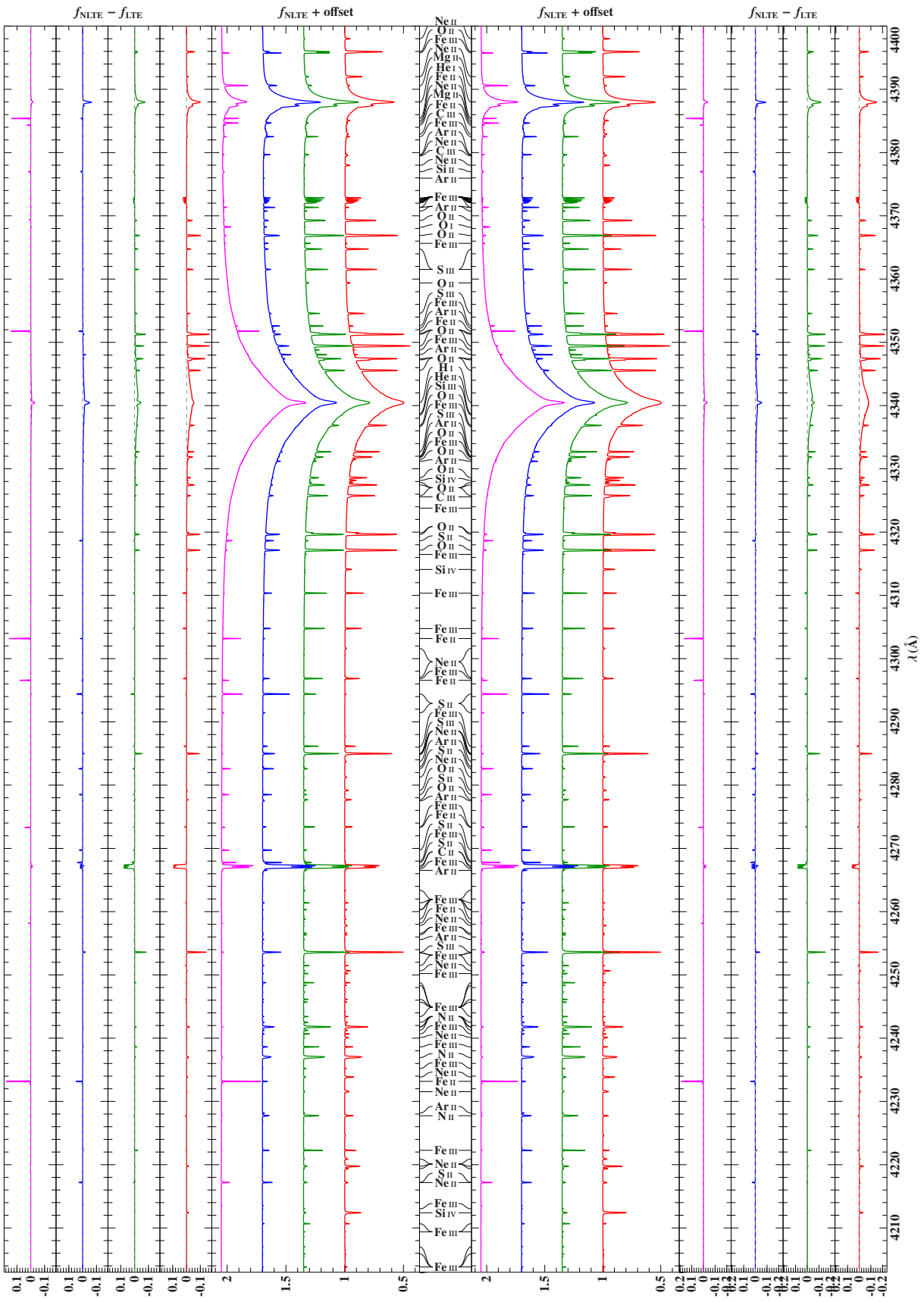

Figure C.1.1c: See Sect. C.1.

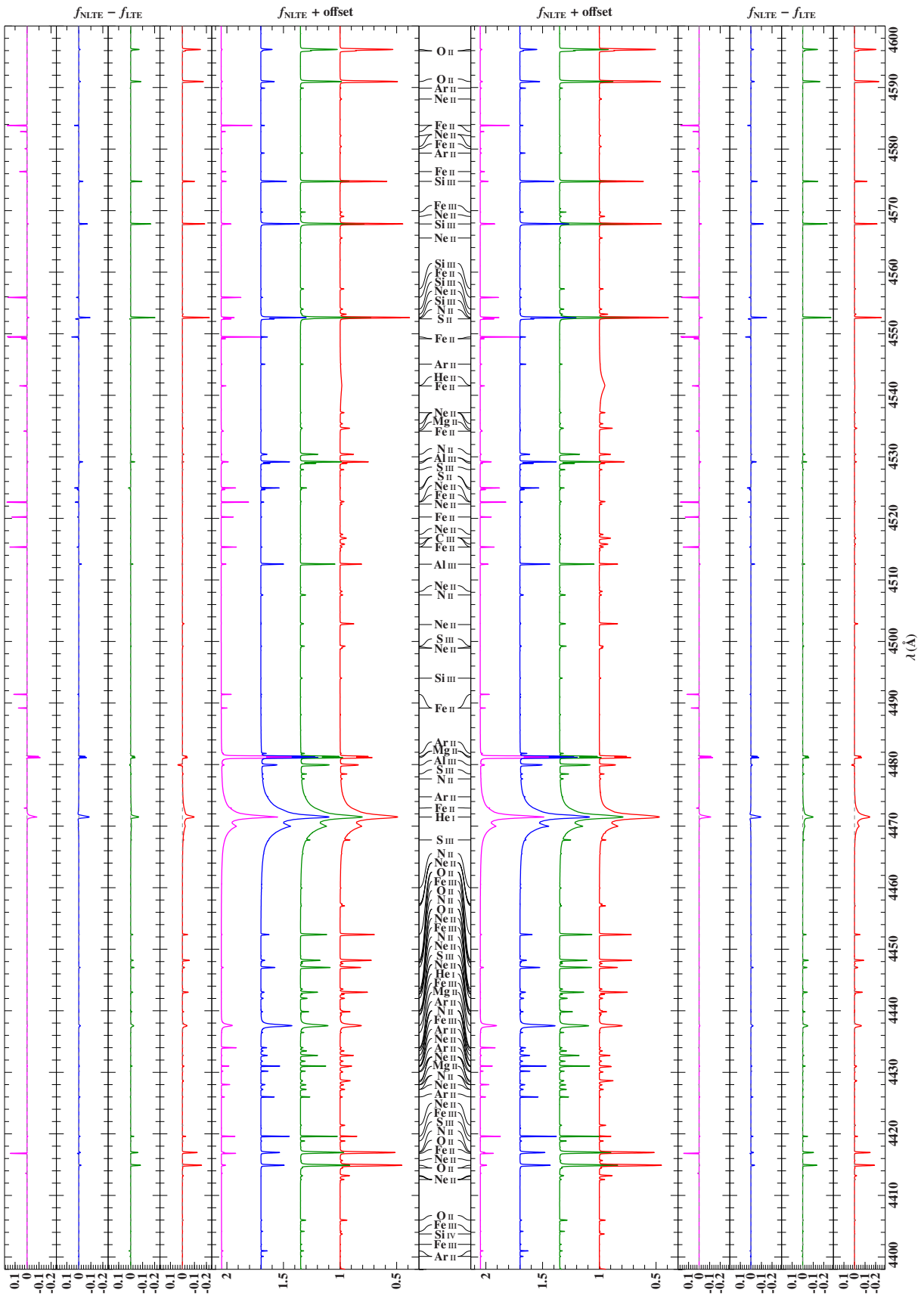

Figure C.1.1d: See Sect. C.1.

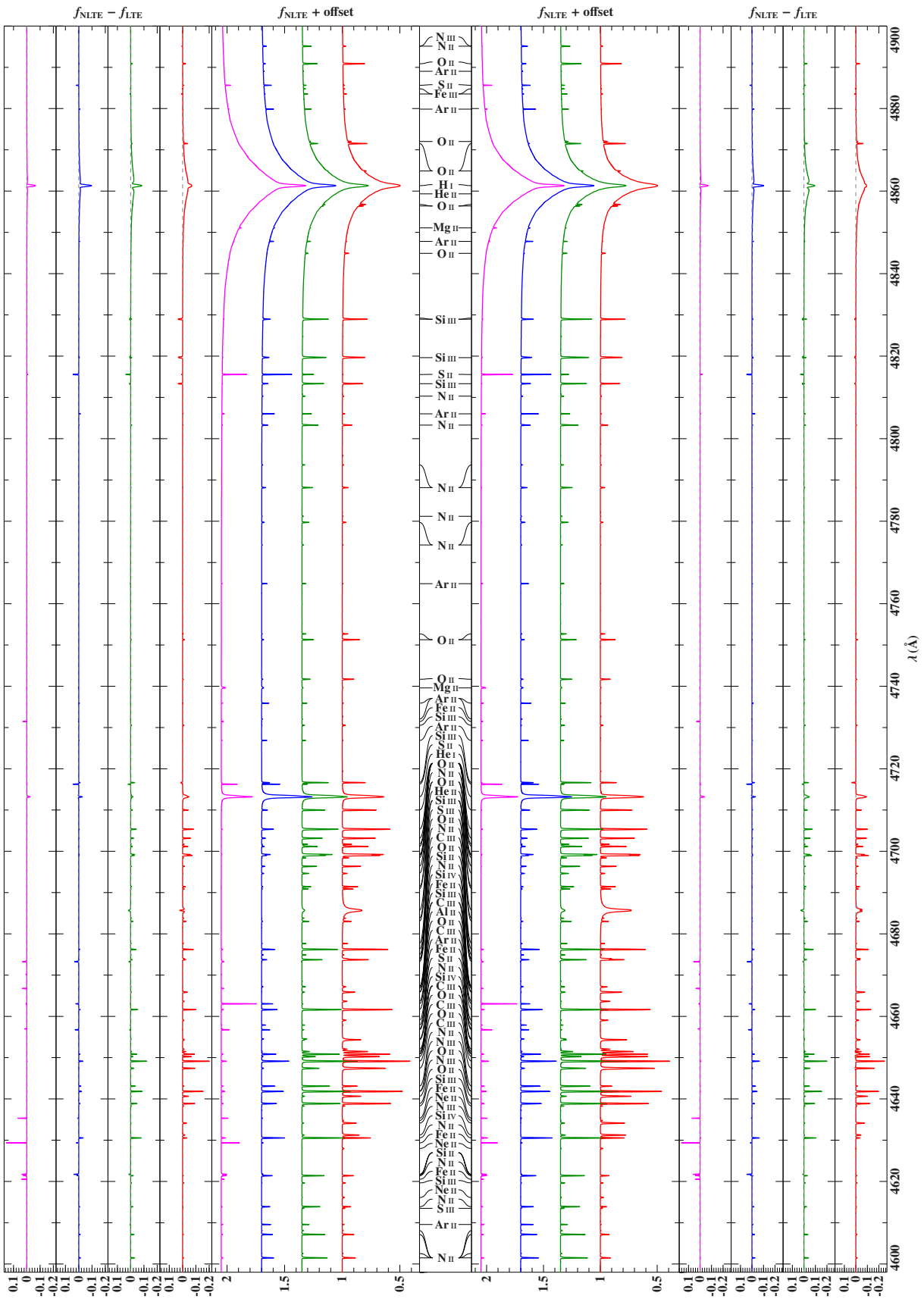

Figure C.1.1e: See Sect. C.1.

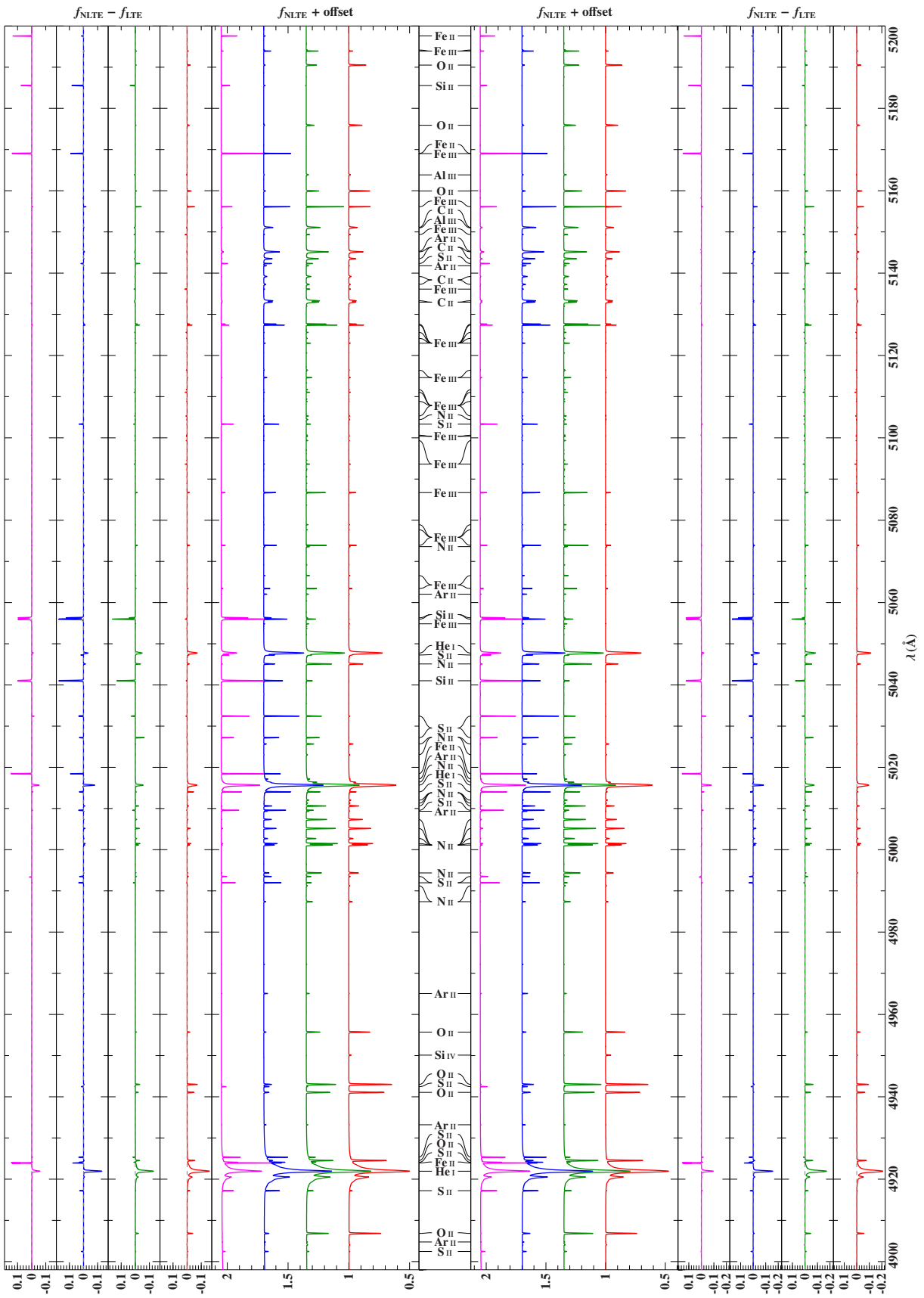

Figure C.1.1f: See Sect. C.1.

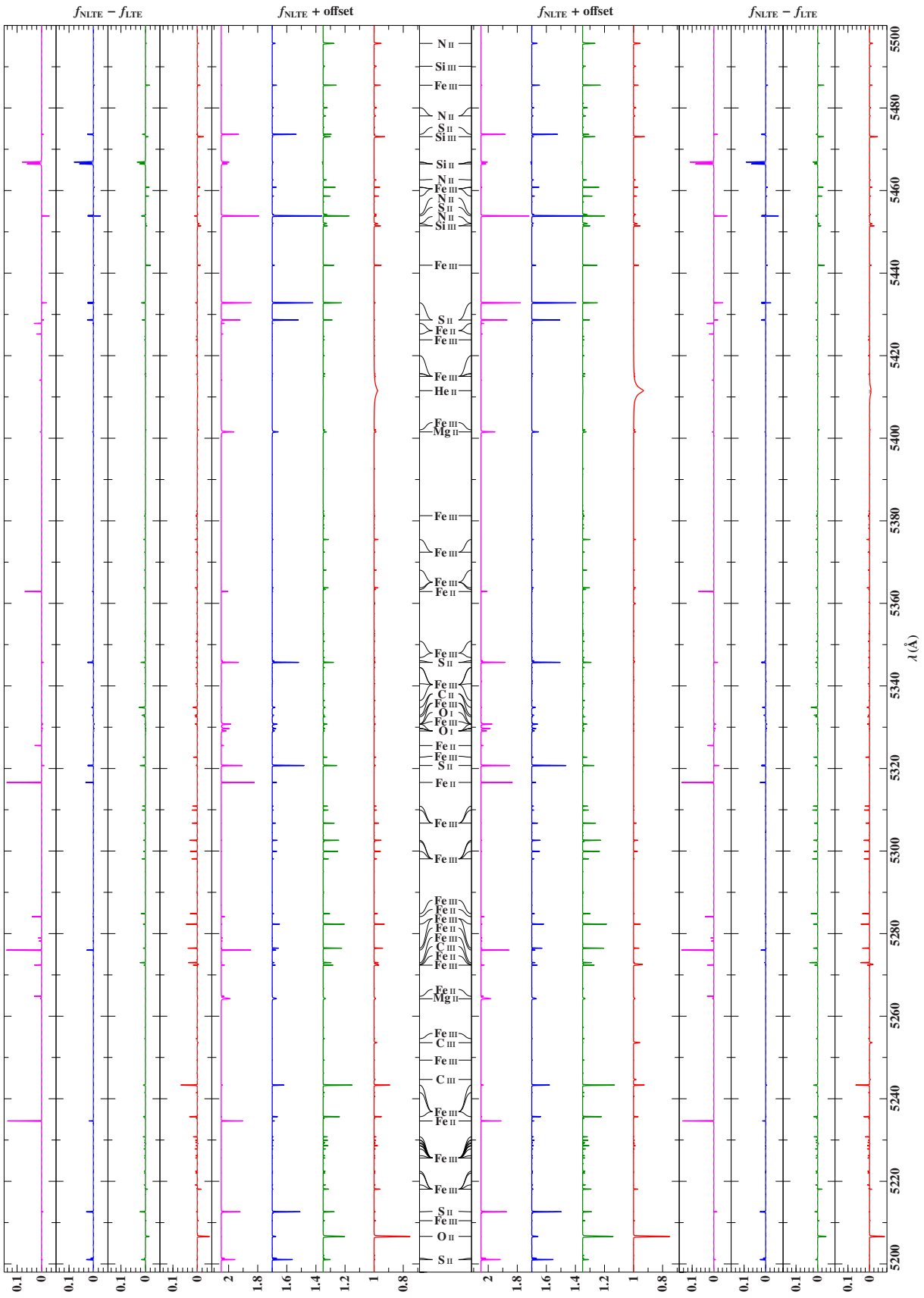

Figure C.1.1g: See Sect. C.1.

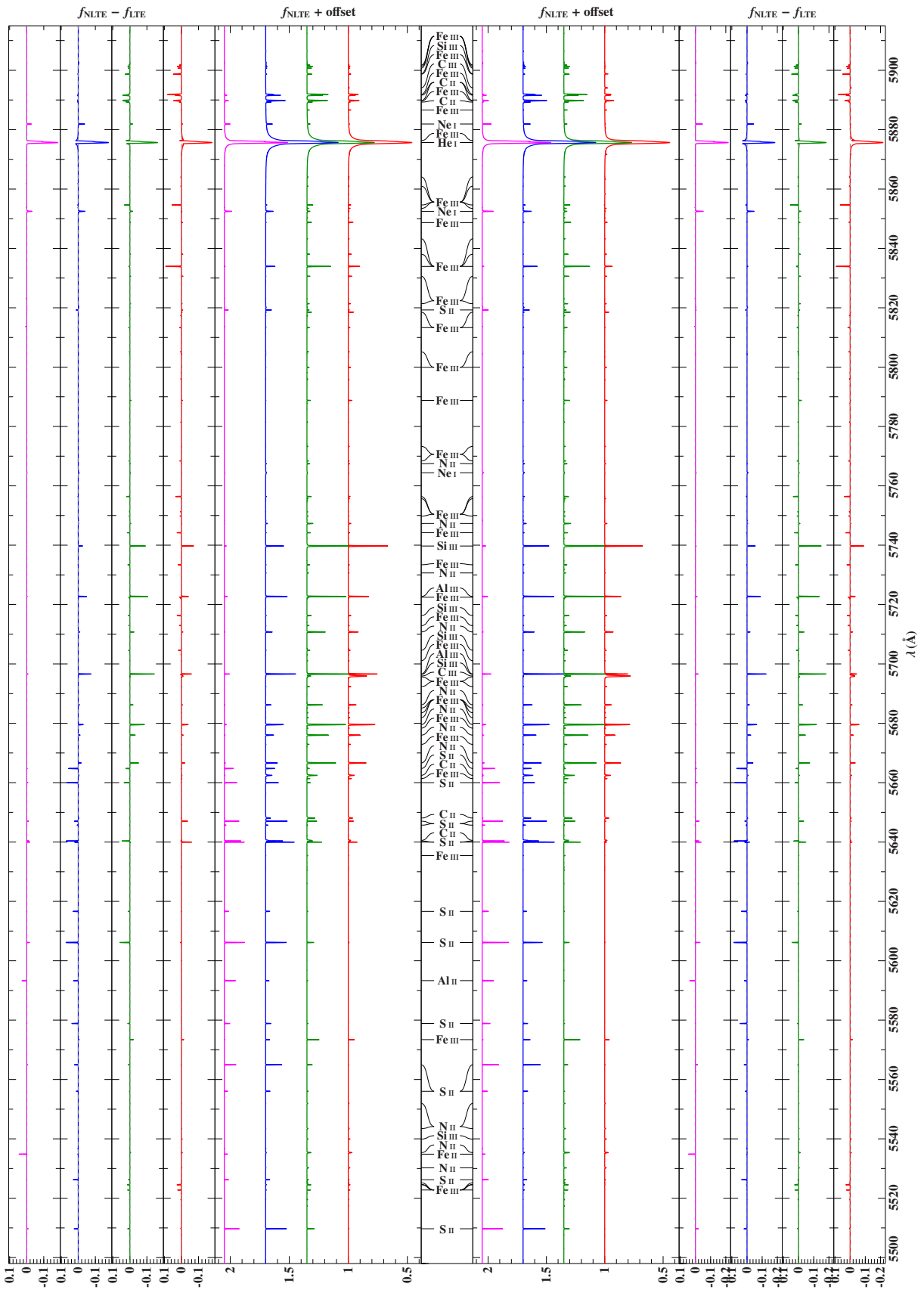

Figure C.1.1h: See Sect. C.1.

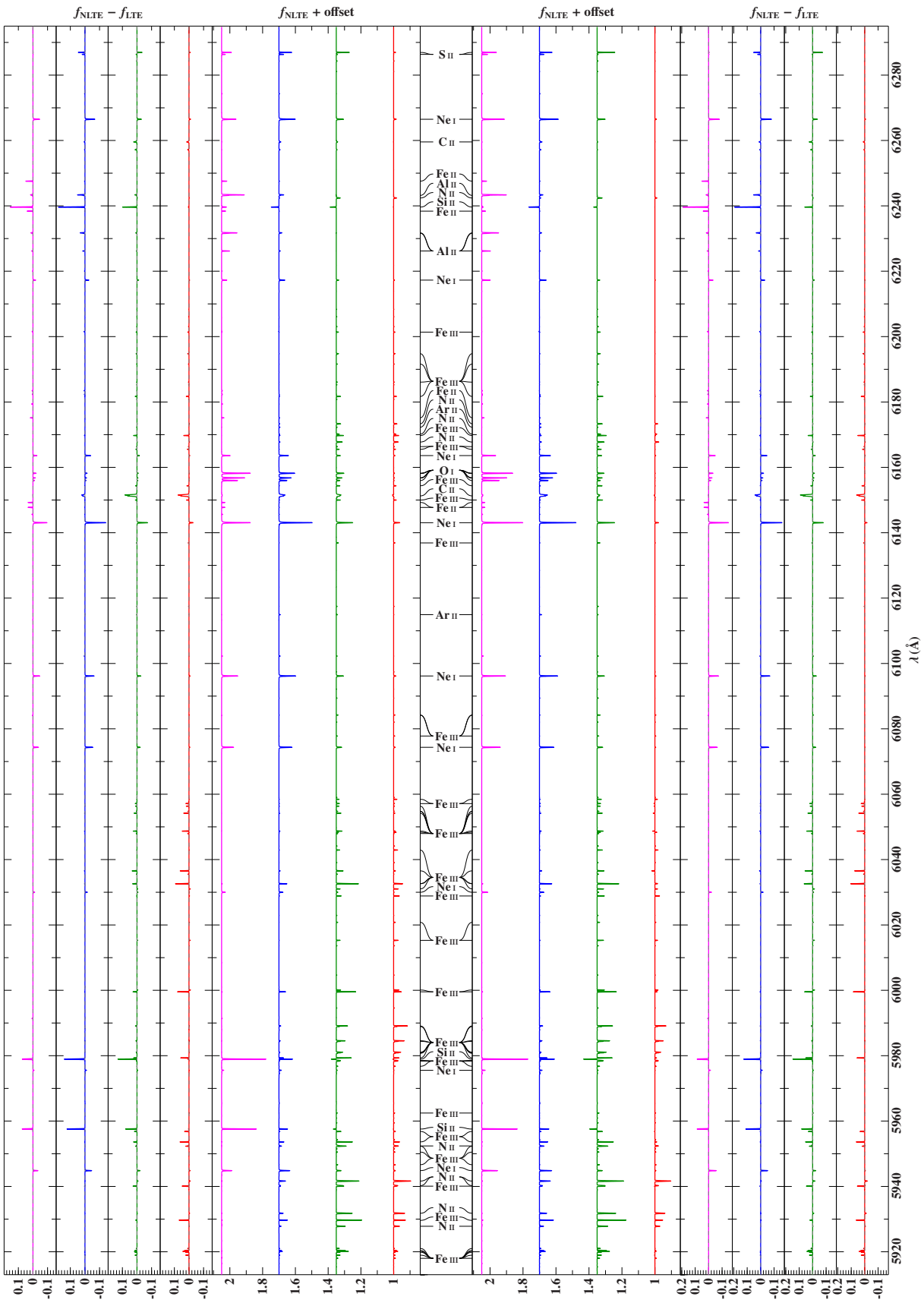

Figure C.1.1i: See Sect. C.1.

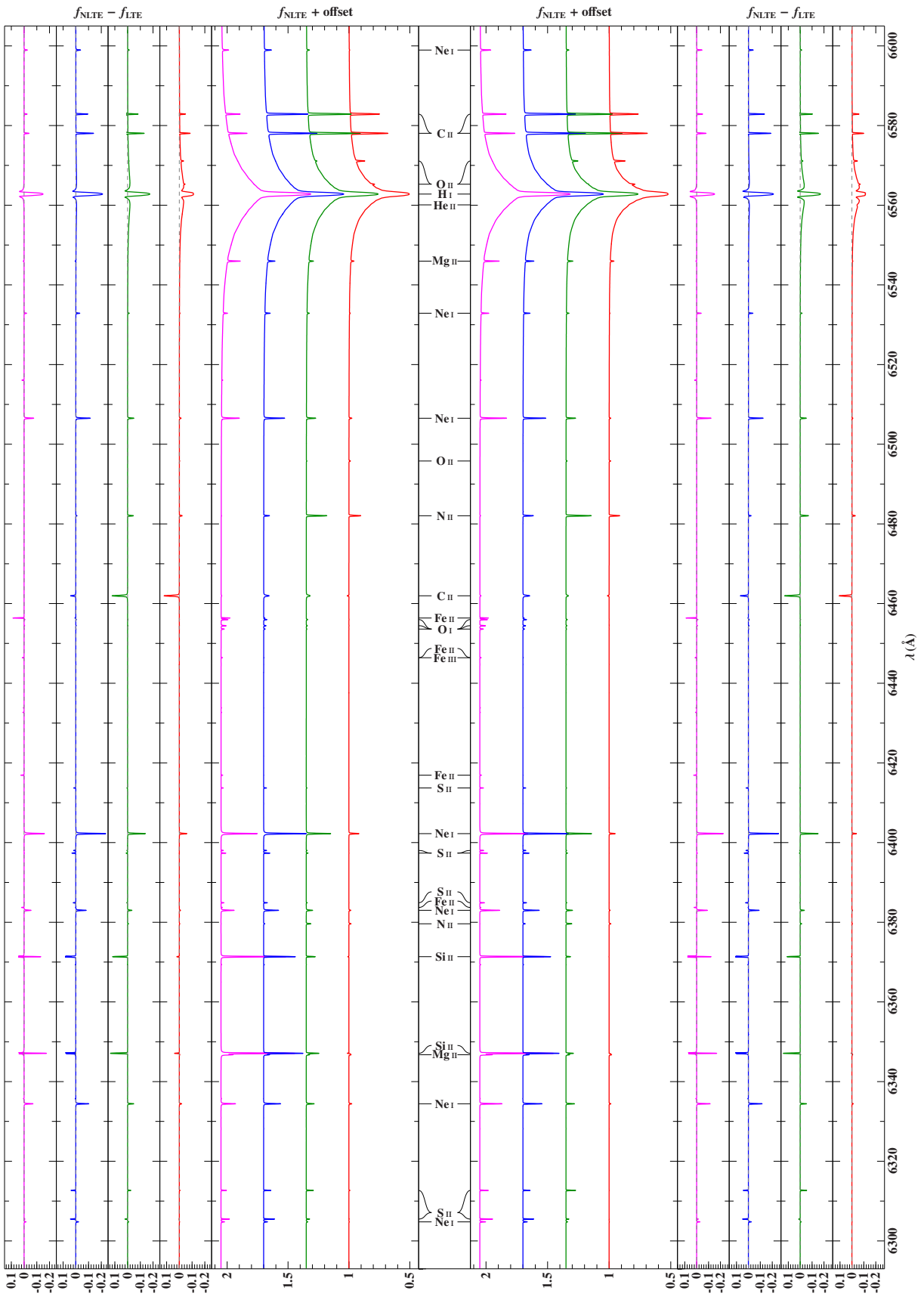

Figure C.1.1j: See Sect. C.1.

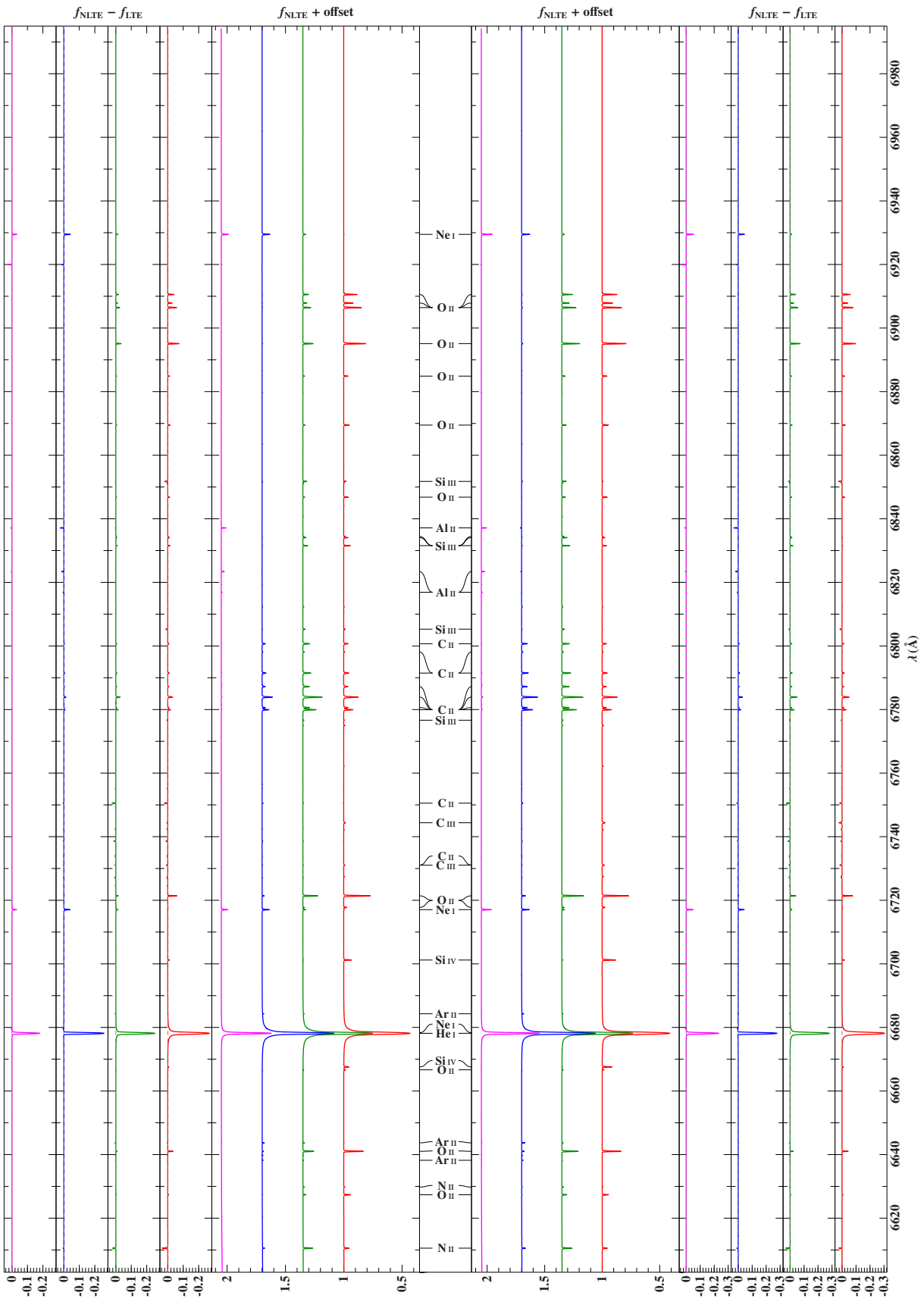

Figure C.1.1k: See Sect. C.1.

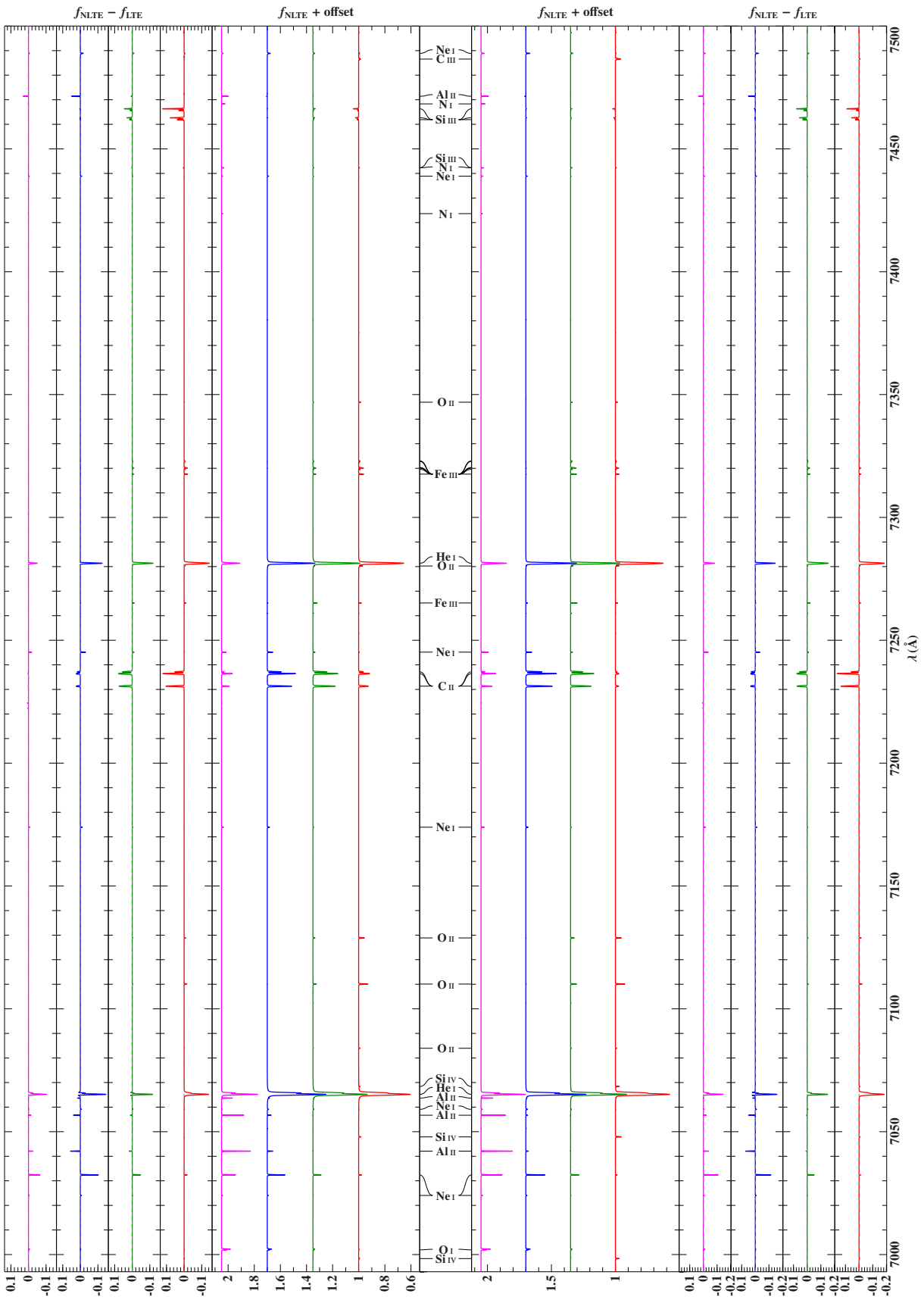

Figure C.1.1l: See Sect. C.1.

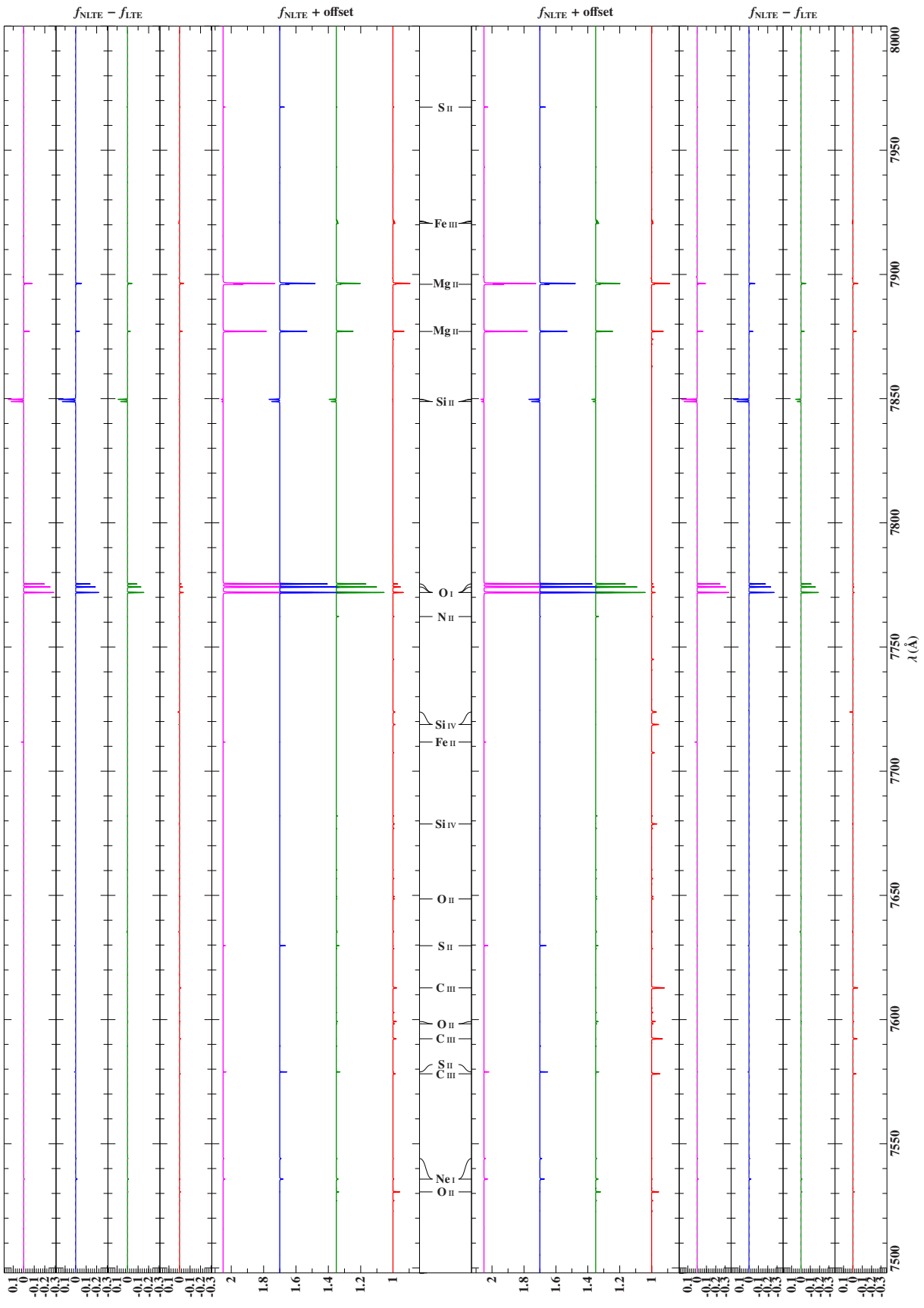

Figure C.1.1m: See Sect. C.1.

C.2 Model versus observation

Figures C.2.2a–C.2.2i show the comparison of the best-fitting model spectrum (red line) with the re-normalized observation (black line) for the stars HD 35912 (*right*), HD 35299 (*middle*), and HD 37042 (*left*) in the spectral range $\lambda\lambda$ 3940–6742 Å. Light colors mark regions that have been excluded from fitting due to the presence of features that are not (properly) included in our models. For the sake of clarity, only the strongest out of all lines that have been used in the analysis are labeled. The residuals χ are defined by the bracket in Eq. (5.2).

Figures C.2.3a–C.2.3i show the same comparison for the double-lined spectroscopic binary systems HD 119109 (*right*), HD 213420 (*middle*), and HD 75821 (*left*). Blue connection lines mark contributions of the secondary component.

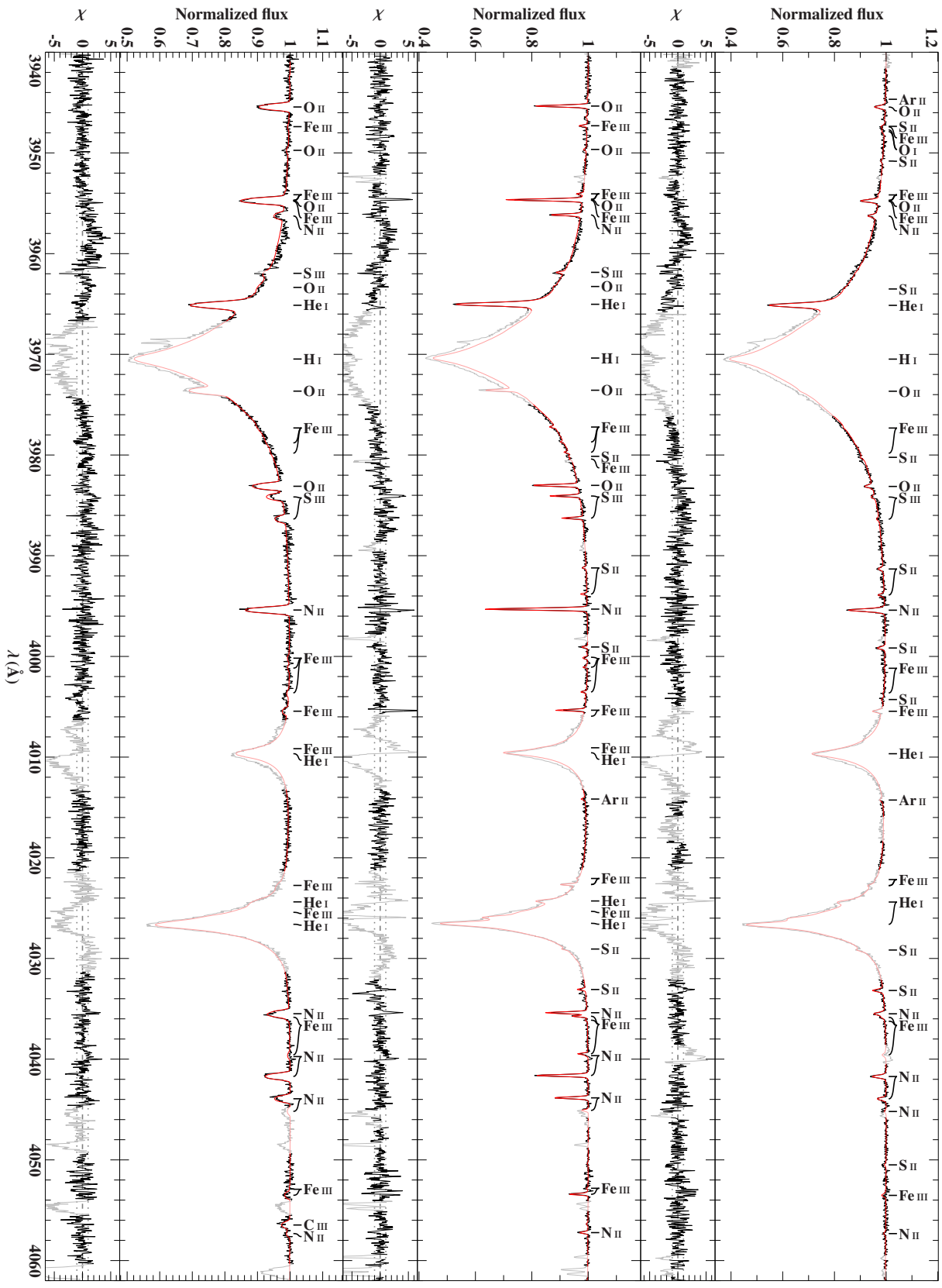

Figure C.2.2a: See Sect. C.2.

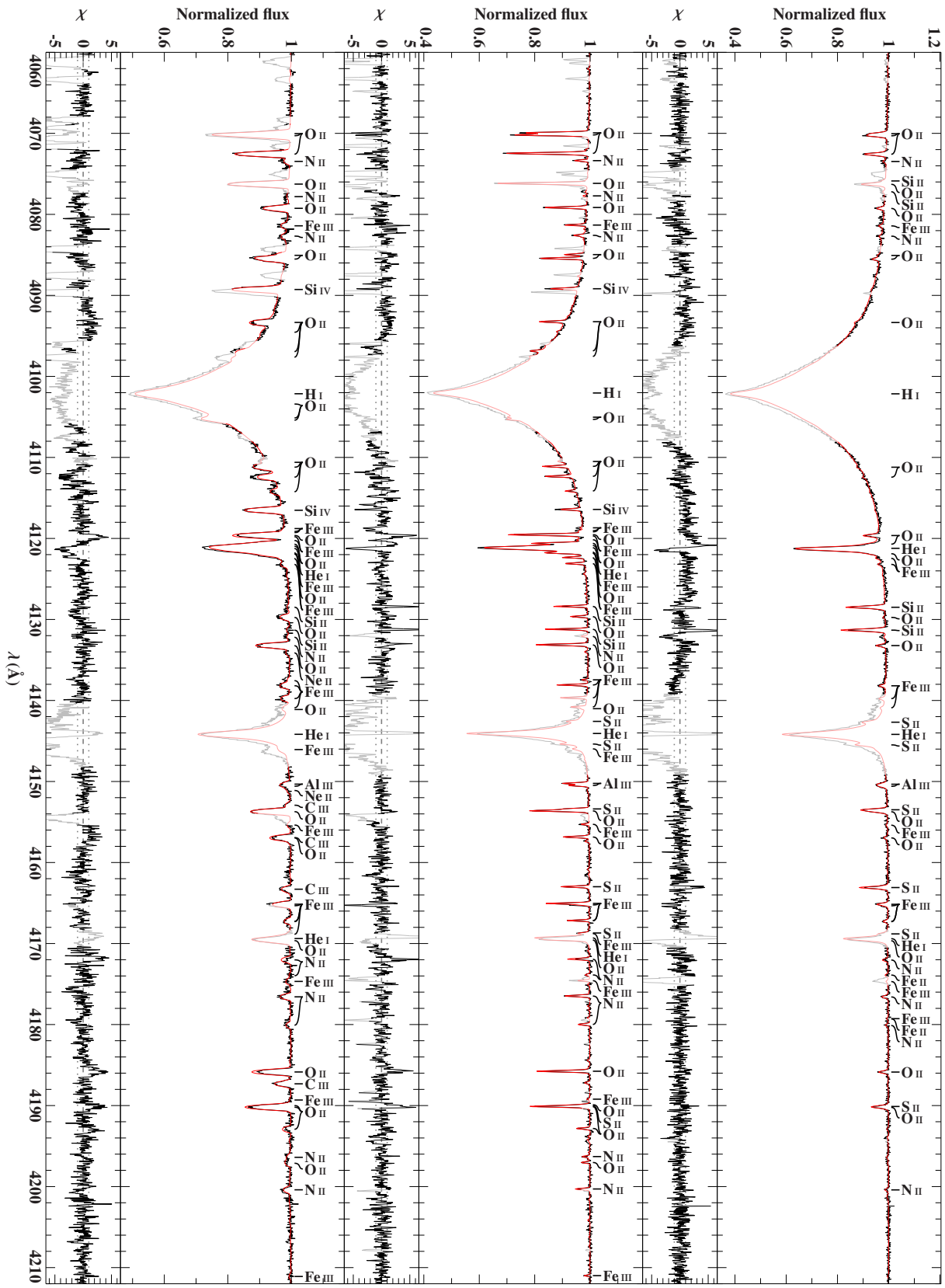

Figure C.2.2b: See Sect. C.2.

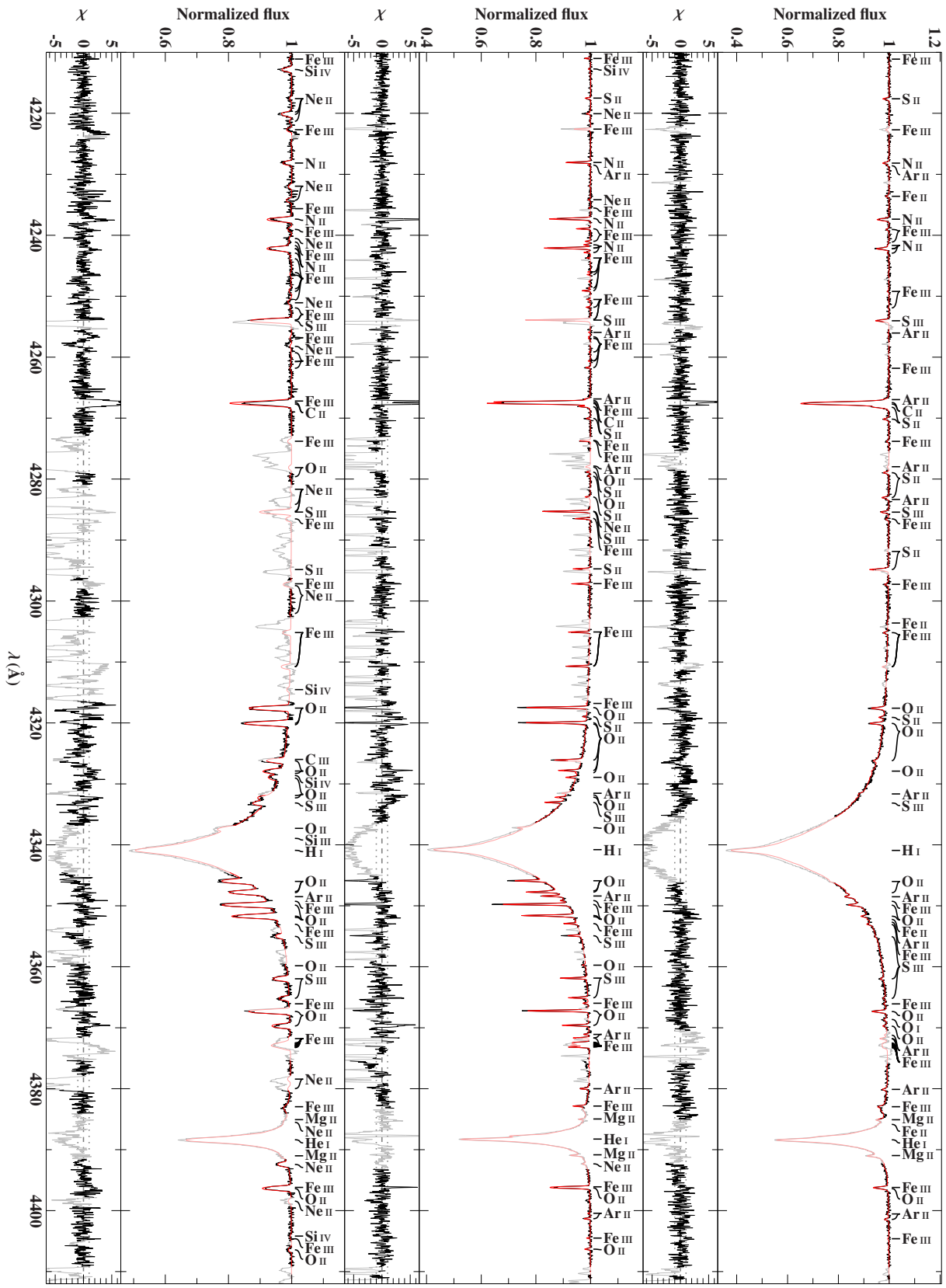

Figure C.2.2c: See Sect. C.2.

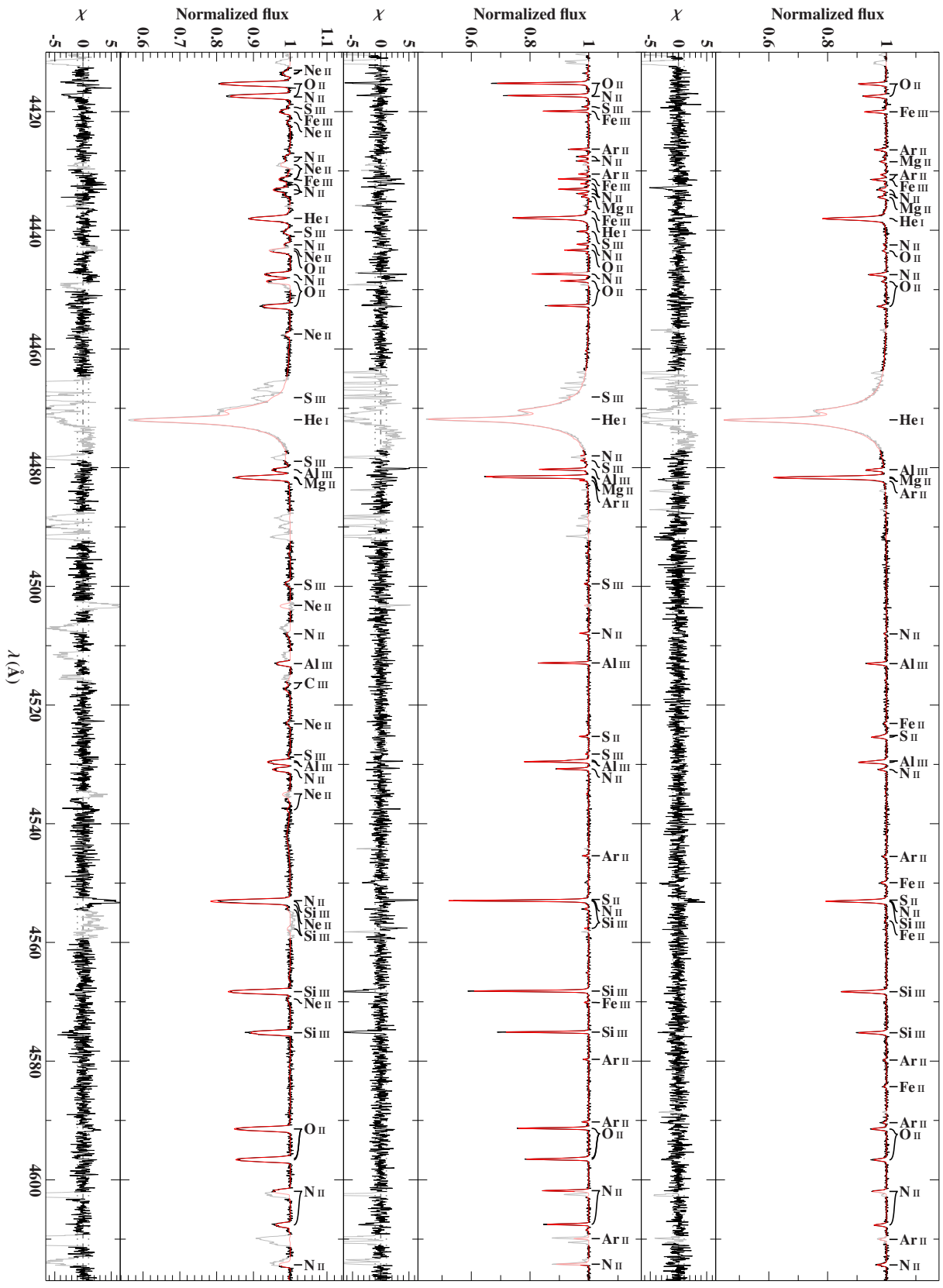

Figure C.2.2d: See Sect. C.2.

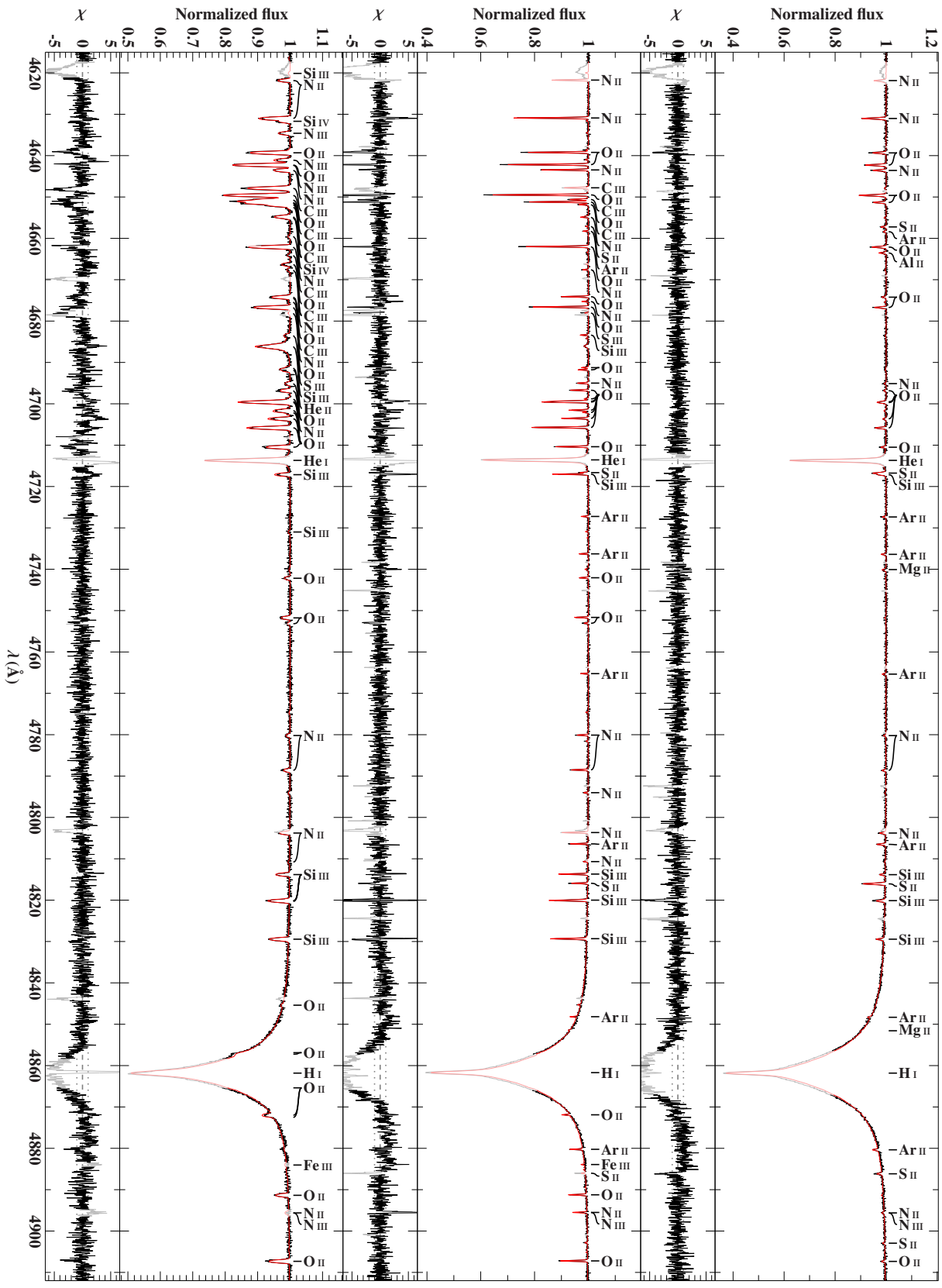

Figure C.2.2e: See Sect. C.2.

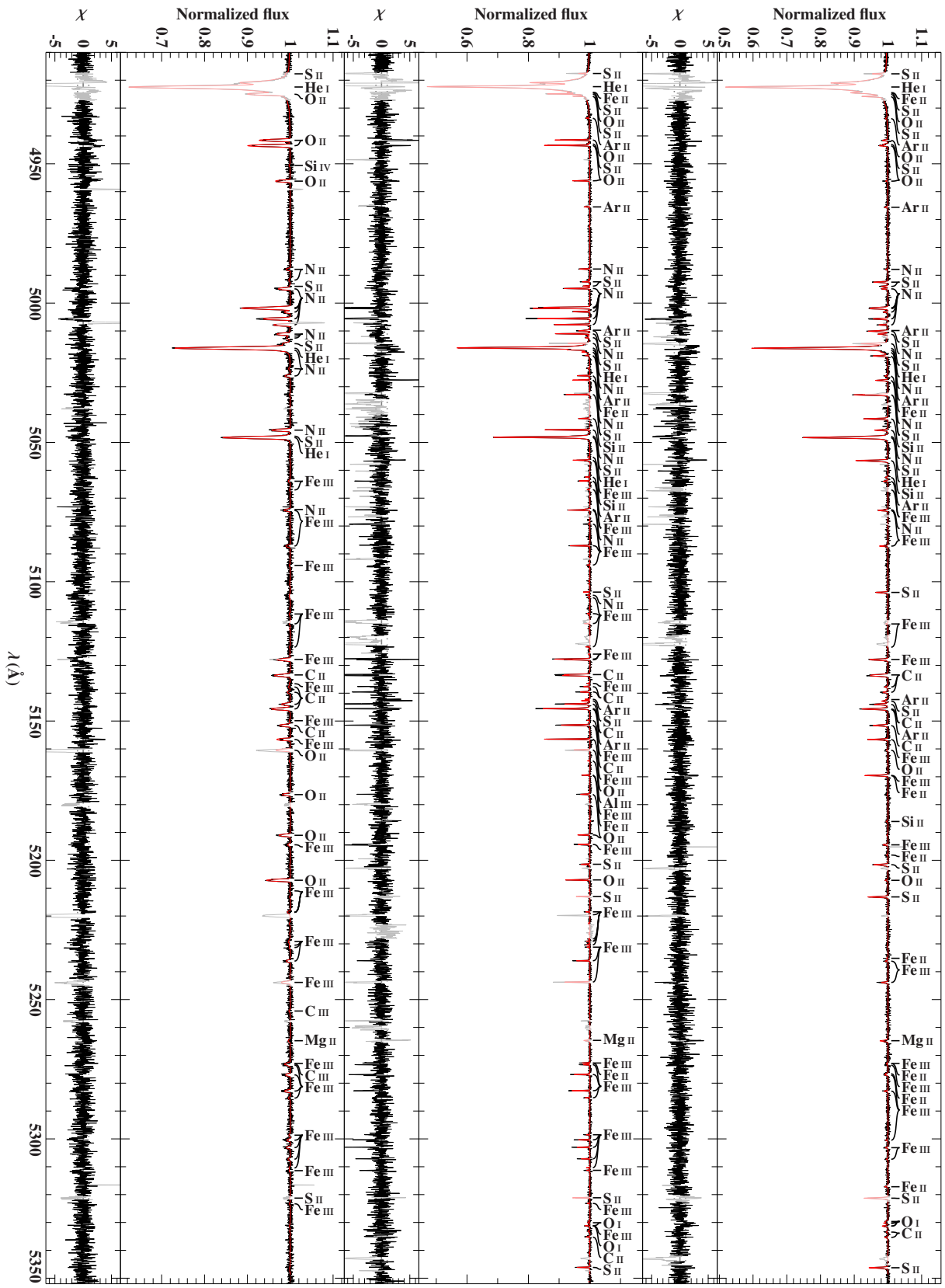

Figure C.2.2f: See Sect. C.2.

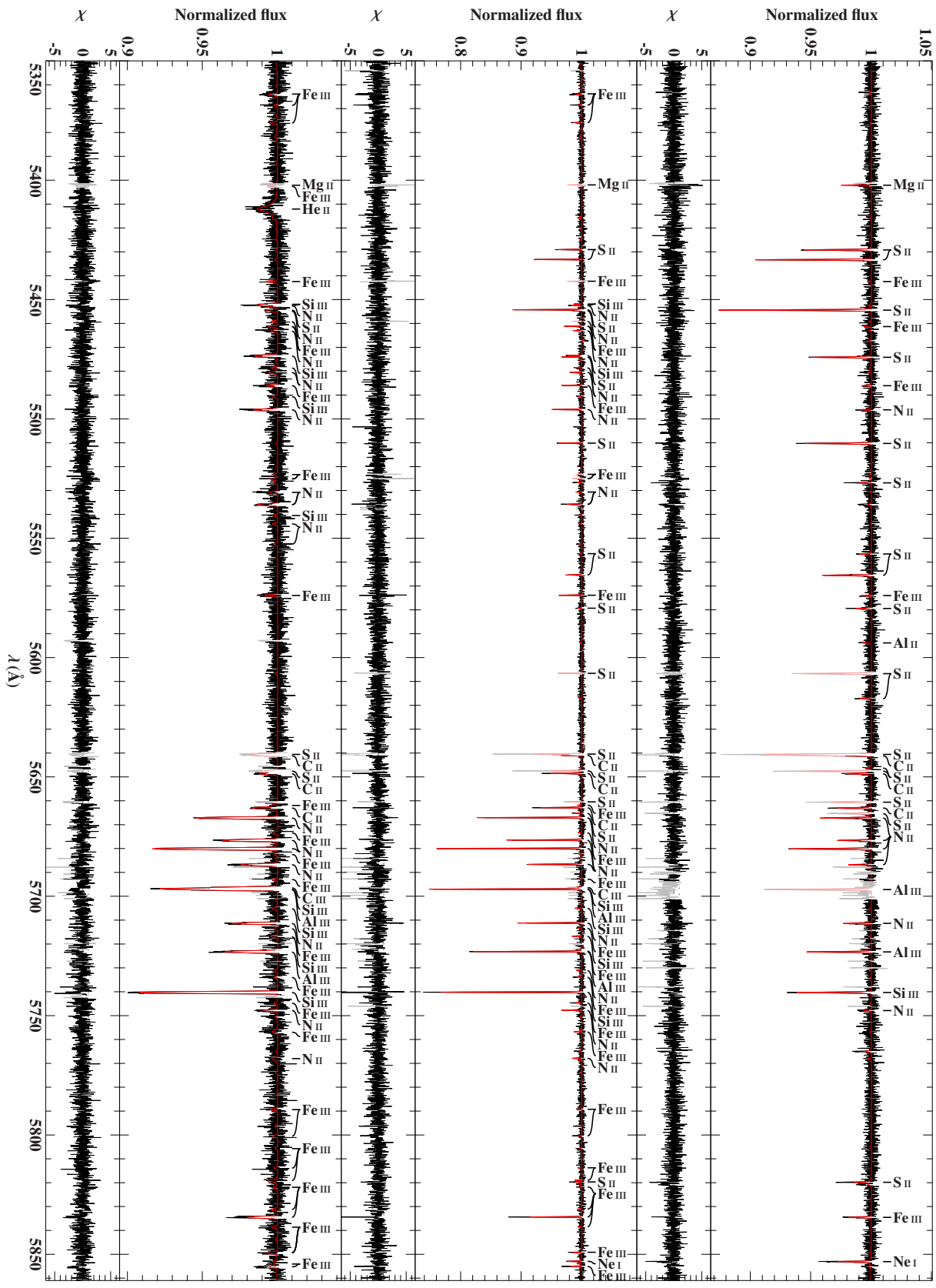

Figure C.2.2g: See Sect. C.2.

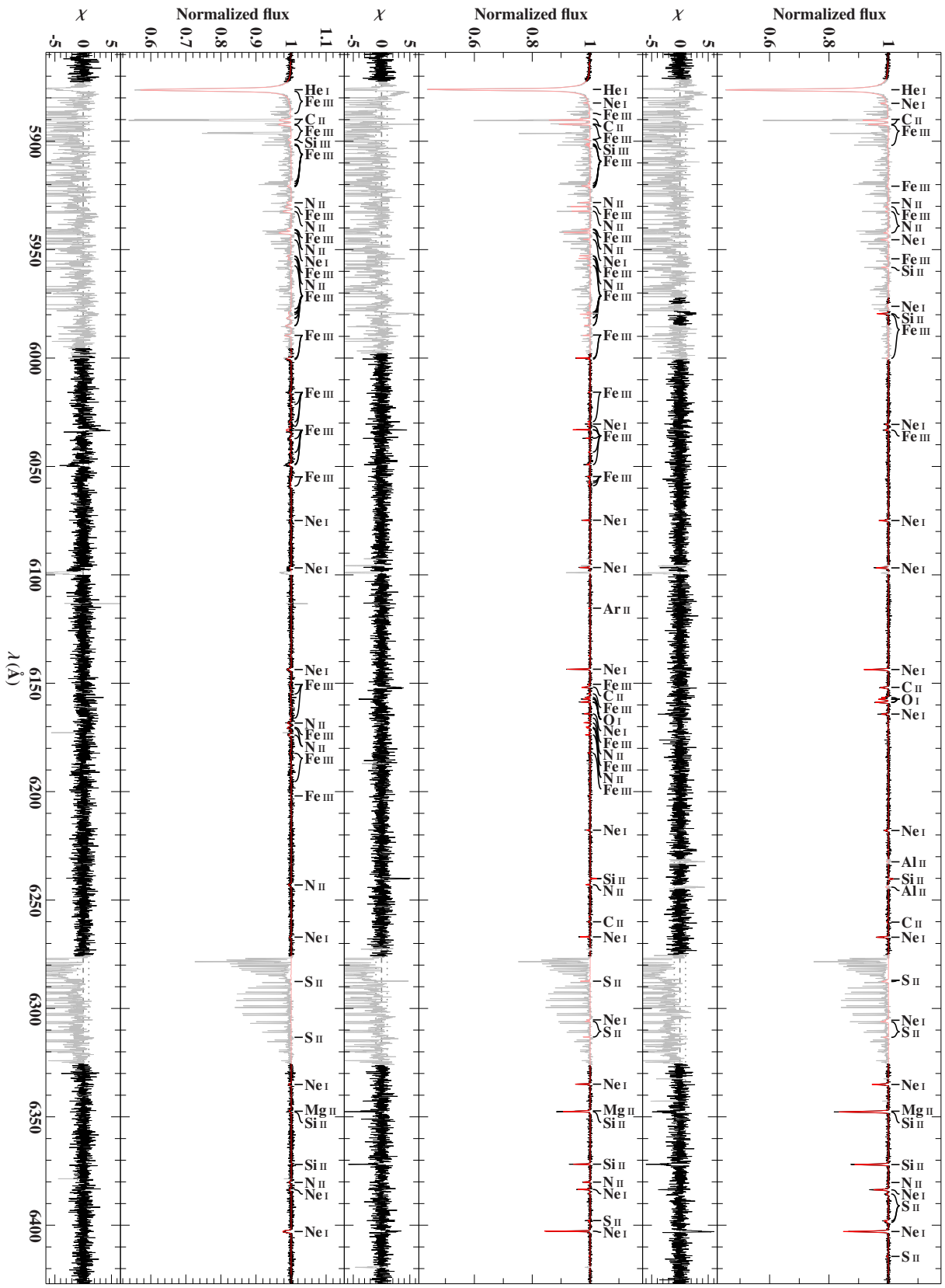

Figure C.2.2h: See Sect. C.2. Contamination with telluric lines.

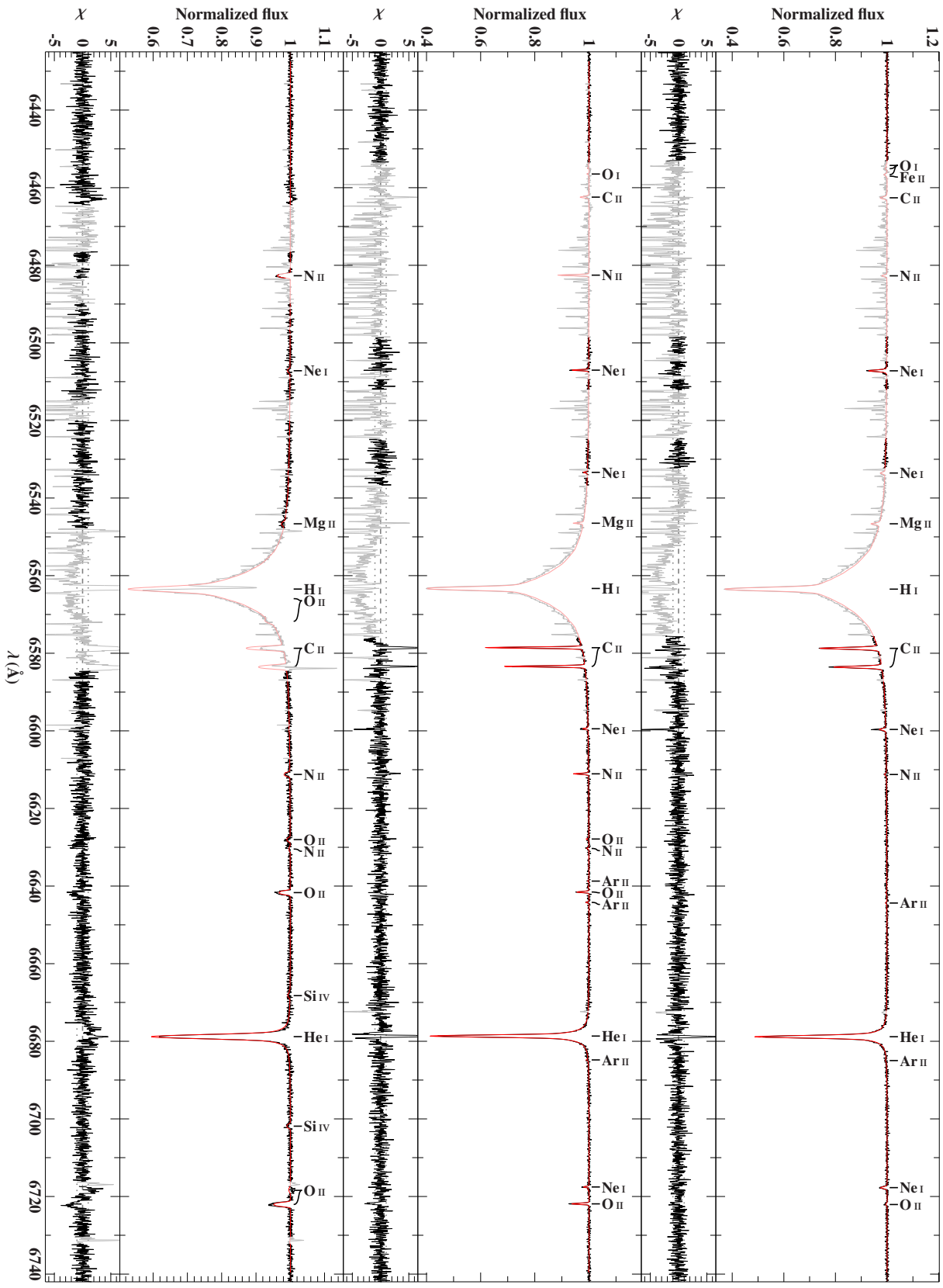

Figure C.2.2i: See Sect. C.2. Contamination with telluric lines. Nebula emission lines visible in HD 37042's spectrum (*left*).

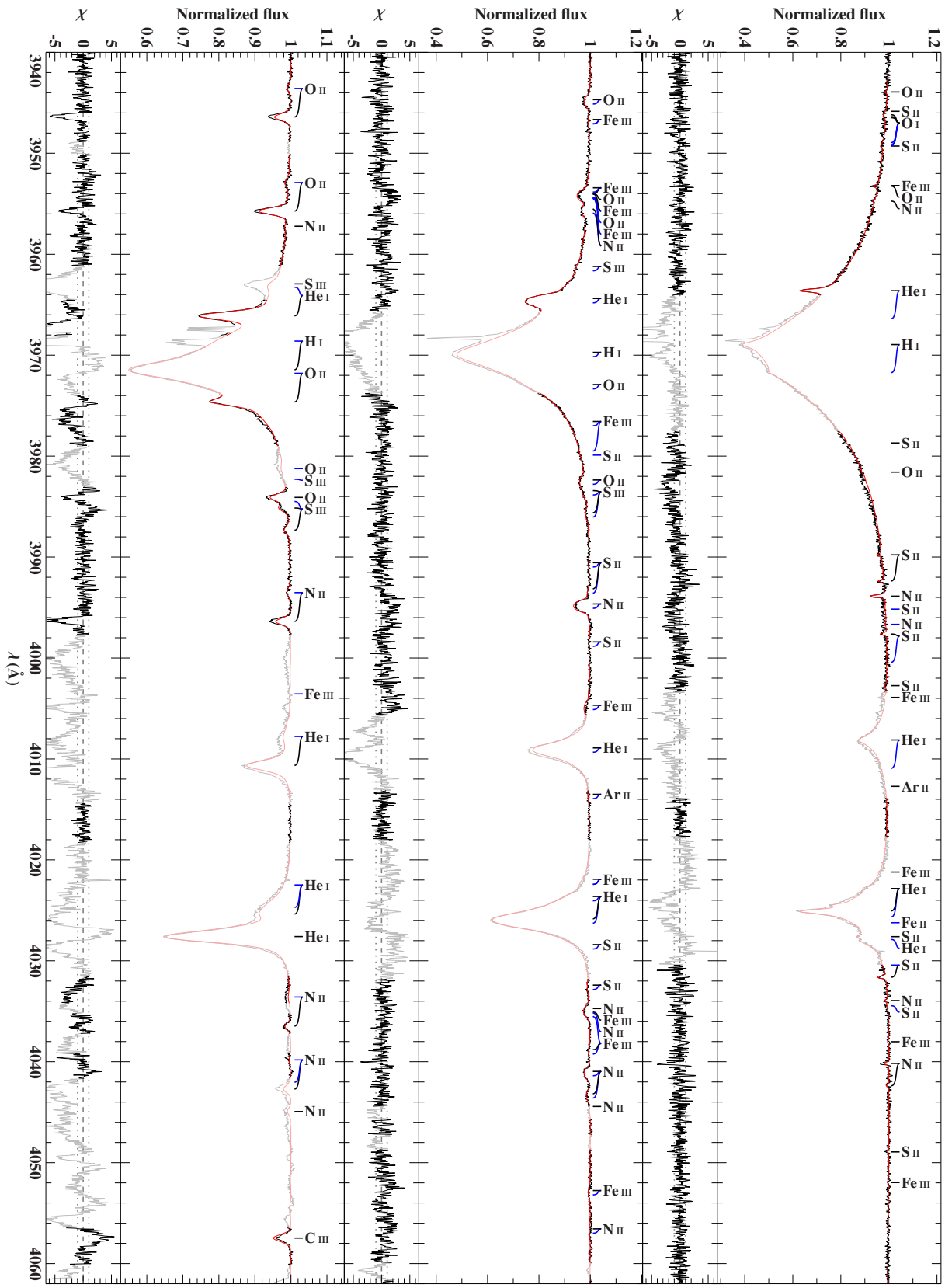

Figure C.2.3a: See Sect. C.2.

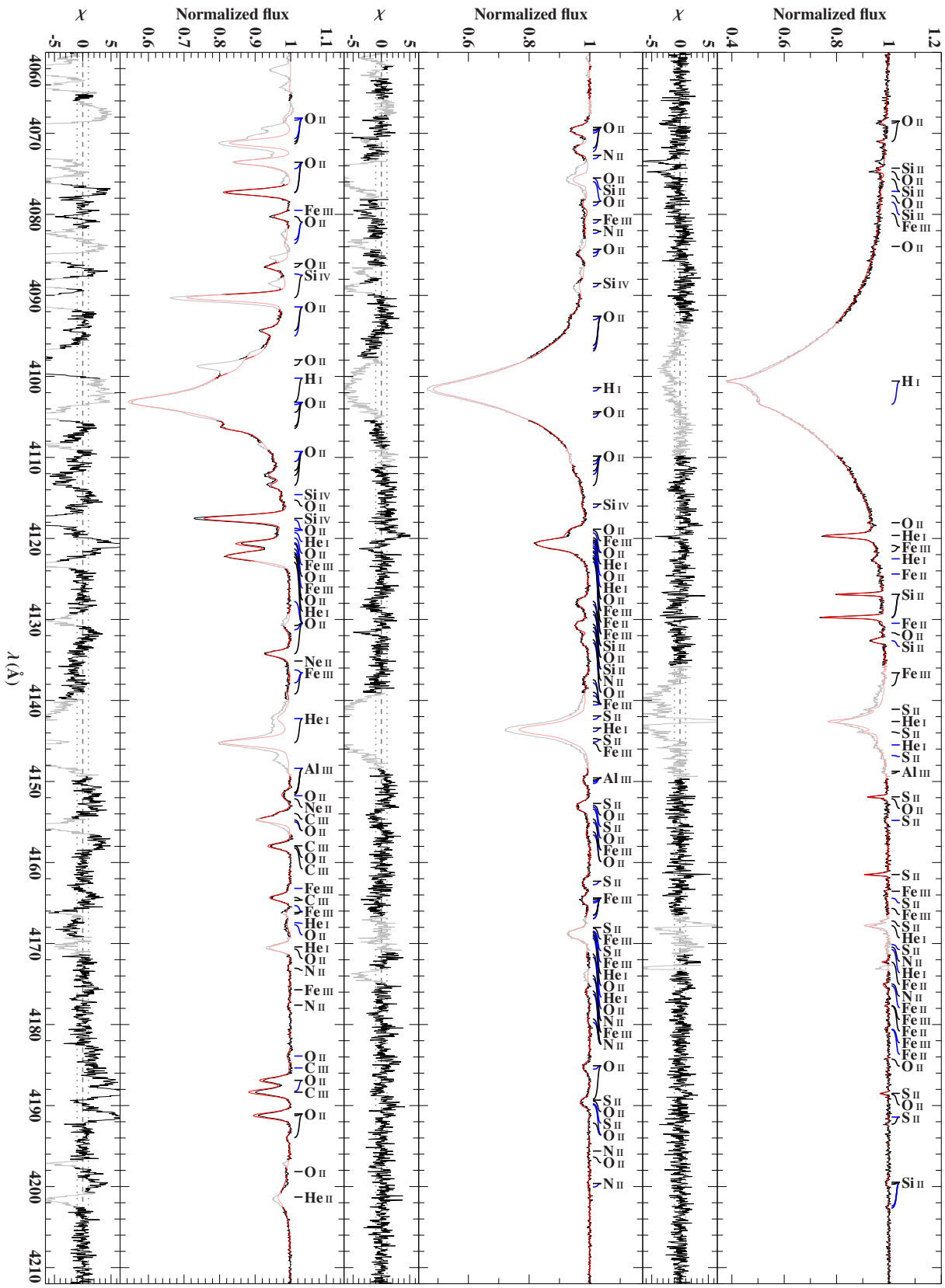

Figure C.2.3b: See Sect. C.2.

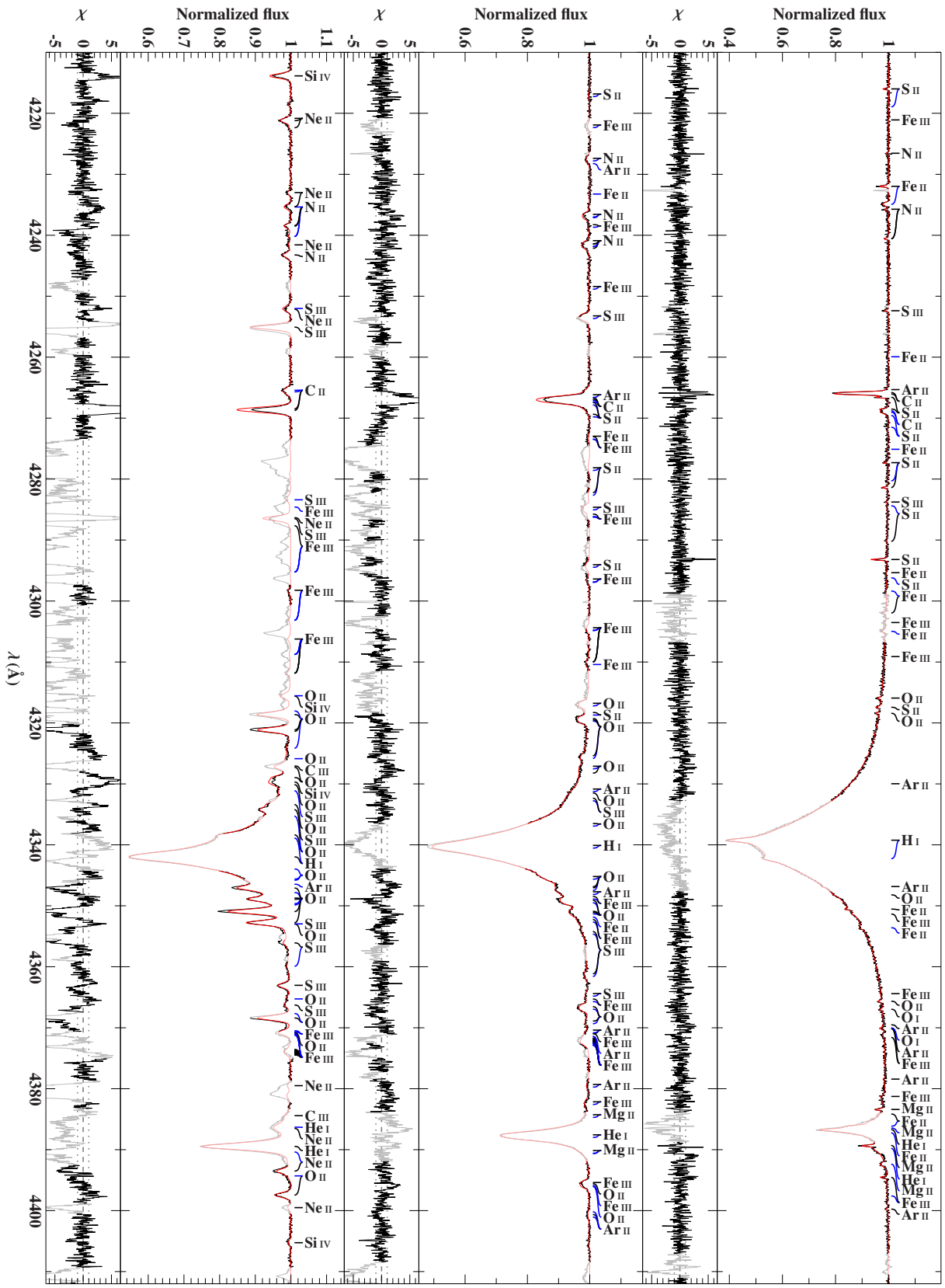

Figure C.2.3c: See Sect. C.2.

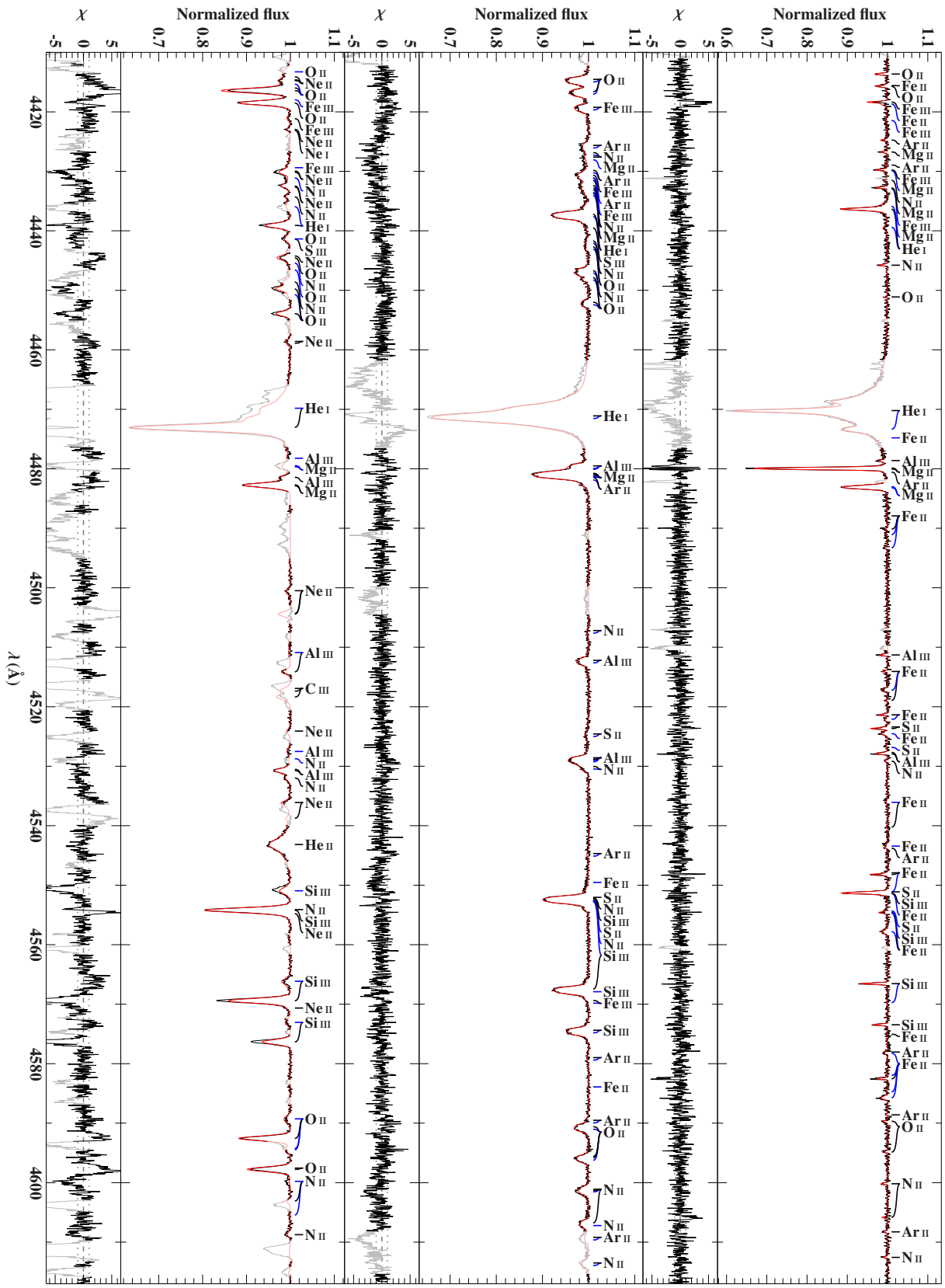

Figure C.2.3d: See Sect. C.2.

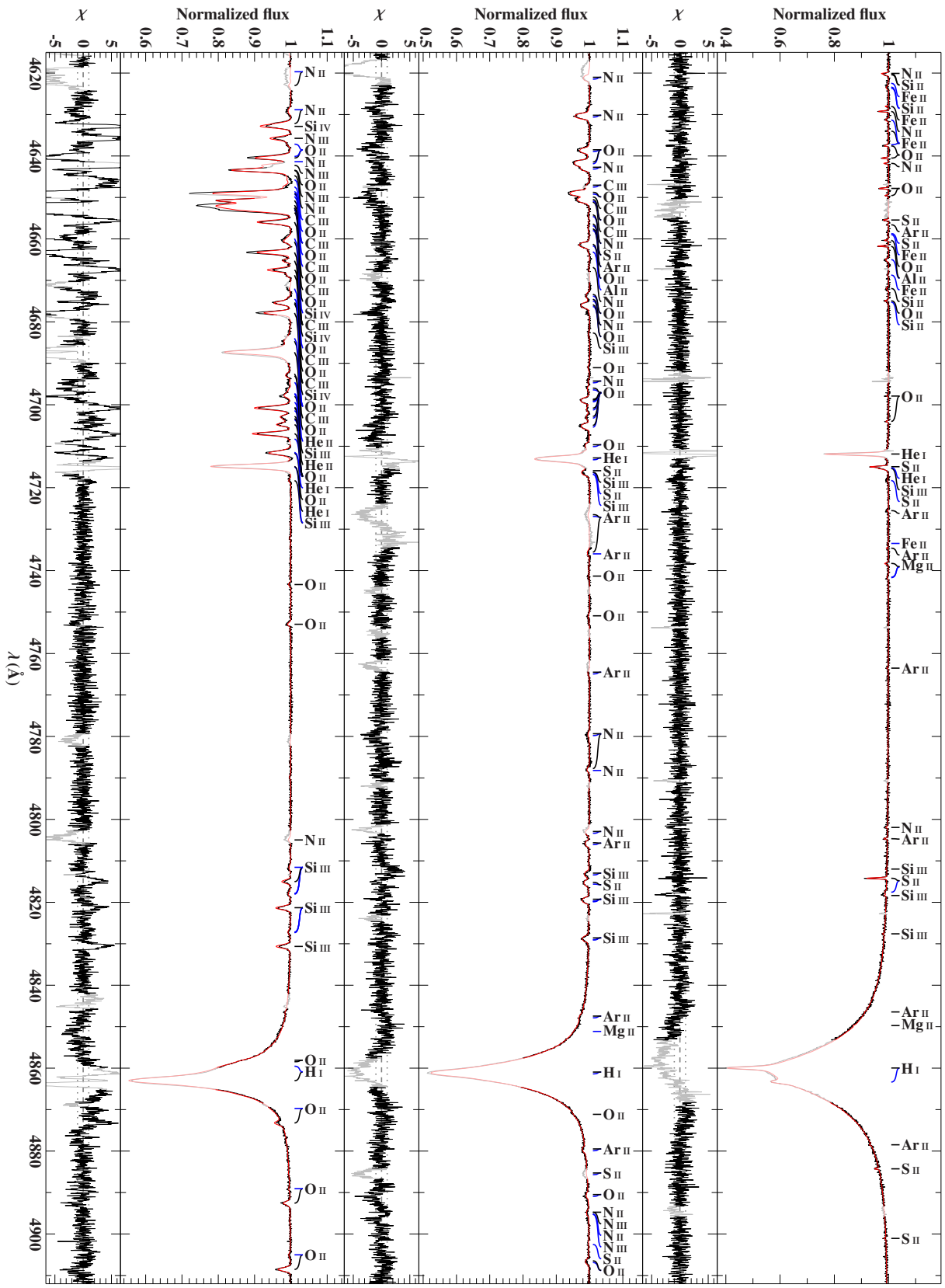

Figure C.2.3e: See Sect. C.2.

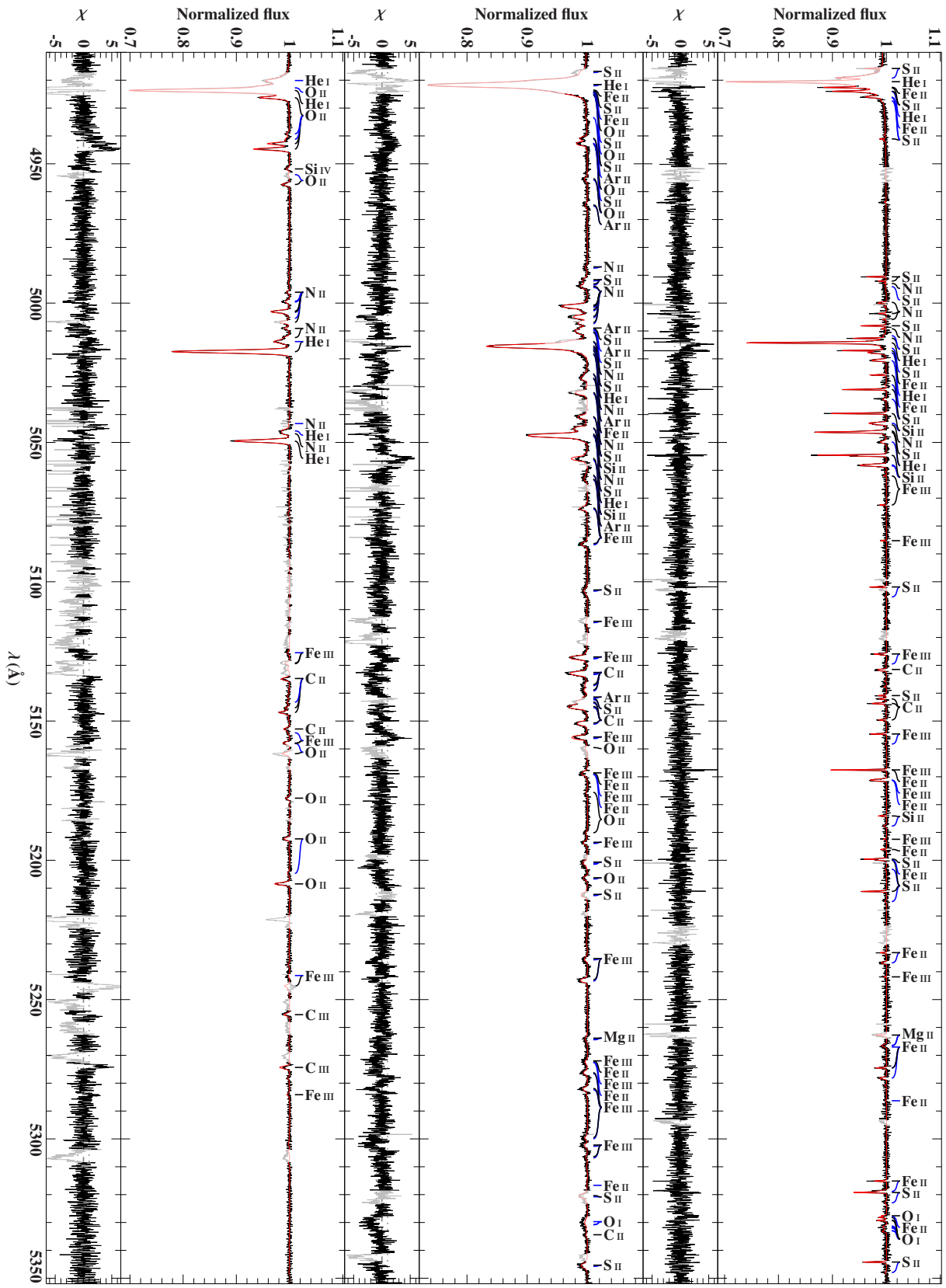

Figure C.2.3f: See Sect. C.2.

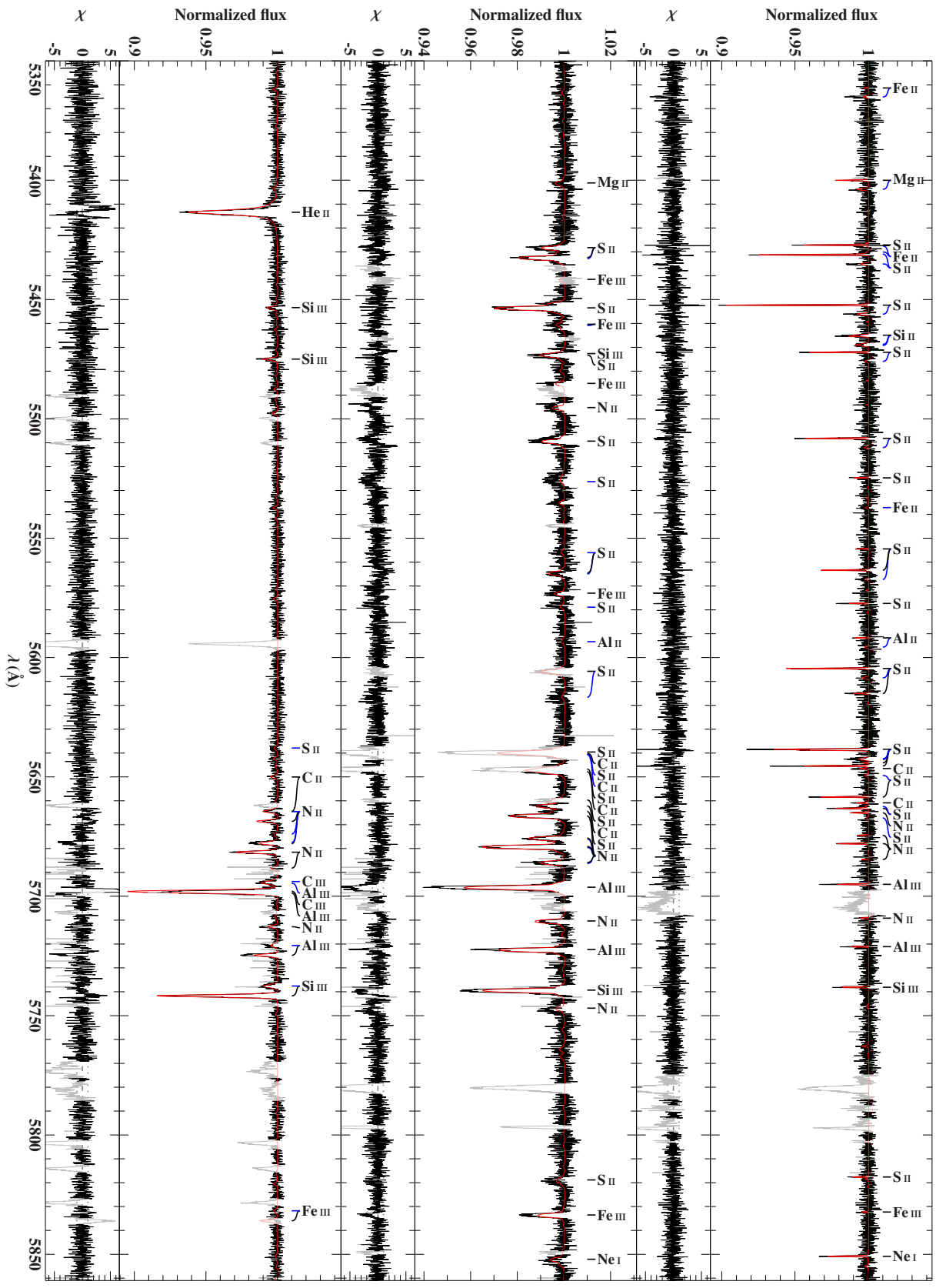

Figure C.2.3g: See Sect. C.2.

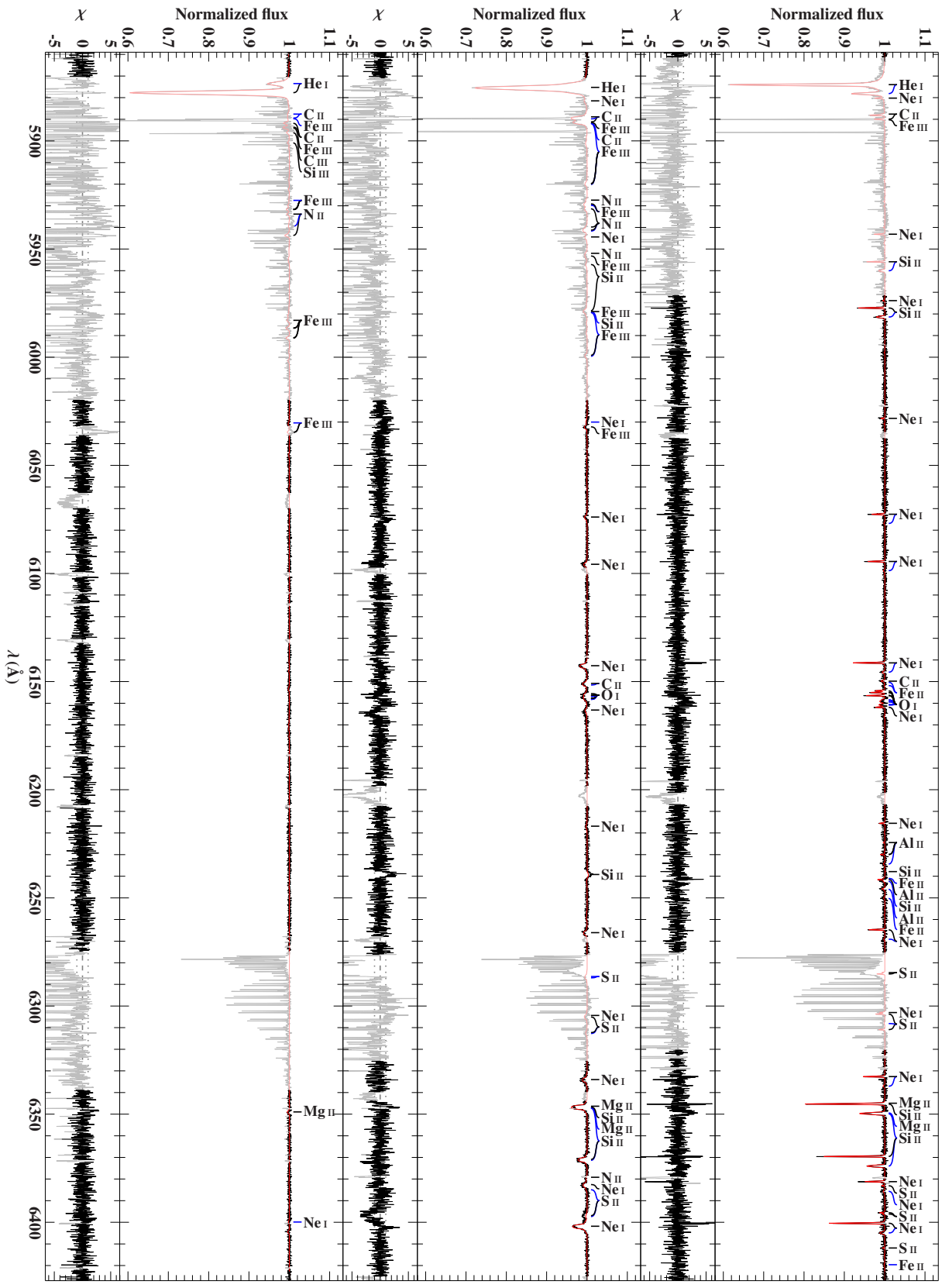

Figure C.2.3h: See Sect. C.2. Strong contamination with telluric lines.

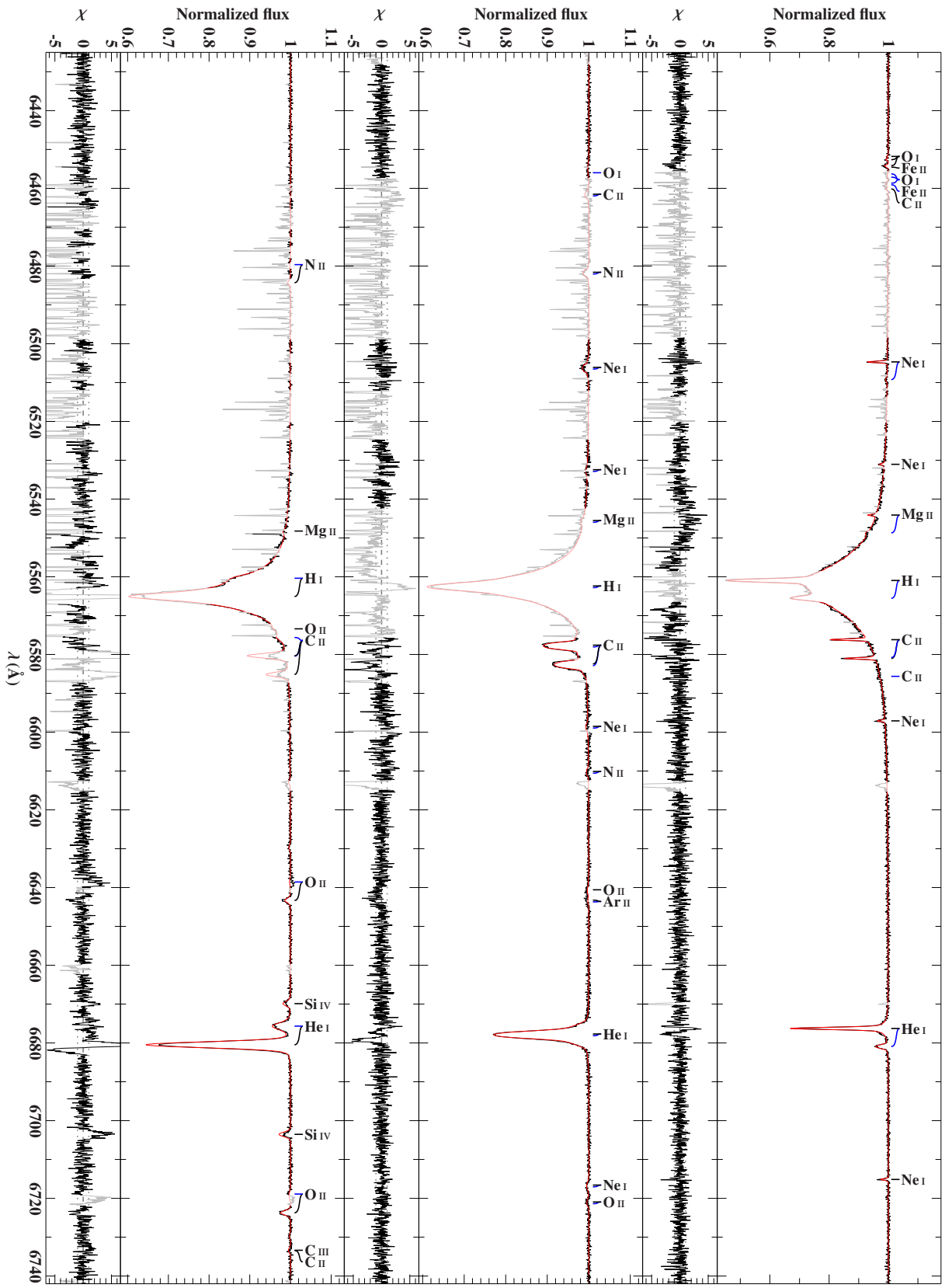

Figure C.2.3i: See Sect. C.2. Strong contamination with telluric lines.

D Tables

D.1 Astronomical units and constants

Table D.1: Astronomical units and constants (see, for instance, Karttunen et al. 2007).

Constant	Symbol	Numerical value	
		(SI)	(cgs)
Gravitational constant	G	$6.673 \times 10^{-11}\,\mathrm{m^3\,s^{-2}\,kg^{-1}}$	$6.673 \times 10^{-8}\,\mathrm{cm^3\,s^{-2}\,g^{-1}}$
Planck constant	h	$6.6261 \times 10^{-34}\,\mathrm{J\,s}$	$6.6261 \times 10^{-27}\,\mathrm{erg\,s}$
Mass of electron	m_e	$9.1094 \times 10^{-31}\,\mathrm{kg}$	$9.1094 \times 10^{-28}\,\mathrm{g}$
Boltzmann constant	k	$1.3807 \times 10^{-23}\,\mathrm{J\,K^{-1}}$	$1.3807 \times 10^{-16}\,\mathrm{erg\,K^{-1}}$
Stefan-Boltzmann constant	σ_SB	$5.6705 \times 10^{-8}\,\mathrm{J\,m^{-2}\,s^{-1}\,K^{-4}}$	$5.6705 \times 10^{-5}\,\mathrm{erg\,cm^{-2}\,s^{-1}\,K^{-4}}$
Speed of light	c	$299\,792\,458\,\mathrm{m\,s^{-1}}$	$29\,979\,245\,800\,\mathrm{cm\,s^{-1}}$
Parsec	pc	$3.0857 \times 10^{16}\,\mathrm{m}$	$3.0857 \times 10^{18}\,\mathrm{cm}$
Solar values			
Mass	$M_\odot$	$1.989 \times 10^{30}\,\mathrm{kg}$	$1.989 \times 10^{33}\,\mathrm{g}$
Radius	$R_\odot$	$6.96 \times 10^{8}\,\mathrm{m}$	$6.96 \times 10^{10}\,\mathrm{cm}$
Luminosity	$L_\odot$	$3.9 \times 10^{26}\,\mathrm{J\,s^{-1}}$	$3.9 \times 10^{33}\,\mathrm{erg\,s^{-1}}$

D.2 Reference stars

Table D.2: Differences, i.e., SH minus VCS based results, in atmospheric parameters obtained from fitting spectra of 63 mid B-type to late O-type stars with SH or VCS broadened Balmer lines, respectively.

#	$T_{\rm eff}$	$\log(g)$	$v_{\rm rad}$	$v\sin(i)$	ζ	ξ	$\log(n(x))$										
	(%)	(cgs)	($\rm km\,s^{-1}$)				He	C	N	O	Ne	Mg	Al	Si	S	Ar	Fe
1	$1.8^{+0.2}_{-0.2}$	$0.165^{+0.009}_{-0.022}$	$0.0^{+0.1}_{-0.1}$	$0.0^{+0.2}_{-0.0}$	$-0.4^{+0.6}_{-0.5}$	$0.11^{+0.06}_{-0.05}$	$-0.06^{+0.01}_{-0.01}$	$0.00^{+0.08}_{-0.07}$	$-0.01^{+0.09}_{-0.09}$	$0.04^{+0.01}_{-0.03}$	$-0.01^{+0.02}_{-0.04}$	$0.02^{+0.03}_{-0.01}$	$0.03^{+0.04}_{-0.04}$	$0.02^{+0.02}_{-0.02}$	$0.01^{+0.02}_{-0.02}$	...	$0.06^{+0.04}_{-0.01}$
2	$0.6^{+0.2}_{-0.3}$	$0.111^{+0.003}_{-0.004}$	$0.0^{+0.6}_{-0.5}$	$-1.1^{+0.0}_{-0.0}$	$5.1^{+3.4}_{-8.0}$	$-0.11^{+0.13}_{-0.15}$	$0.01^{+0.01}_{-0.01}$	$0.04^{+0.07}_{-0.07}$	...	$0.00^{+0.03}_{-0.03}$	$0.02^{+0.07}_{-0.07}$	$-0.02^{+0.02}_{-0.02}$	$0.02^{+0.07}_{-0.07}$	$0.00^{+0.02}_{-0.03}$	$0.03^{+0.04}_{-0.04}$	...	$0.02^{+0.02}_{-0.02}$
3	$1.9^{+0.4}_{-0.6}$	$0.160^{+0.005}_{-0.004}$	$0.0^{+0.4}_{-0.3}$	$-0.5^{+0.0}_{-0.0}$	$0.6^{+2.0}_{-2.1}$	$0.08^{+0.16}_{-0.17}$	$-0.05^{+0.02}_{-0.02}$	$-0.01^{+0.07}_{-0.07}$	...	$0.03^{+0.03}_{-0.03}$	$0.00^{+0.07}_{-0.07}$	$0.00^{+0.02}_{-0.02}$	$0.02^{+0.07}_{-0.07}$	$0.00^{+0.03}_{-0.02}$	$0.01^{+0.04}_{-0.04}$	...	$0.07^{+0.03}_{-0.04}$
4	$0.8^{+0.3}_{-0.4}$	$0.127^{+0.007}_{-0.013}$	$-0.1^{+0.4}_{-0.5}$	$-1.4^{+0.0}_{-0.0}$	$1.8^{+2.6}_{-2.7}$	$-0.07^{+0.16}_{-0.11}$	$0.00^{+0.01}_{-0.01}$	$0.01^{+0.06}_{-0.06}$	...	$0.01^{+0.03}_{-0.03}$	$0.02^{+0.06}_{-0.06}$	$-0.02^{+0.03}_{-0.03}$	$0.05^{+0.08}_{-0.07}$	$0.01^{+0.03}_{-0.03}$	$0.03^{+0.03}_{-0.03}$	...	$0.03^{+0.03}_{-0.02}$
5p	$0.5^{+0.5}_{-0.3}$	$0.084^{+0.010}_{-0.006}$	$0.1^{+0.3}_{-0.3}$	$-0.4^{+0.5}_{-0.6}$	$0.0^{+1.7}_{-2.2}$	$0.00^{+0.25}_{-0.25}$	$0.00^{+0.02}_{-0.02}$	$0.02^{+0.06}_{-0.06}$	...	$0.02^{+0.04}_{-0.04}$	$0.02^{+0.05}_{-0.06}$	$0.00^{+0.02}_{-0.03}$	$0.02^{+0.05}_{-0.05}$	$0.00^{+0.03}_{-0.03}$	$0.03^{+0.02}_{-0.02}$	...	$0.02^{+0.02}_{-0.03}$
6	$1.9^{+0.1}_{-0.2}$	$0.167^{+0.004}_{-0.004}$	$-0.1^{+0.6}_{-0.7}$	$-0.7^{+0.0}_{-0.0}$	$0.0^{+6.6}_{-6.0}$	$0.03^{+0.21}_{-0.21}$	$-0.05^{+0.01}_{-0.01}$	$-0.01^{+0.04}_{-0.05}$	...	$0.06^{+0.05}_{-0.04}$	$0.00^{+0.05}_{-0.05}$	$0.01^{+0.04}_{-0.04}$	$0.04^{+0.11}_{-0.11}$	$0.00^{+0.03}_{-0.03}$	$0.01^{+0.03}_{-0.03}$	...	$0.06^{+0.04}_{-0.03}$
7	$1.7^{+0.5}_{-0.4}$	$0.154^{+0.016}_{-0.013}$	$0.0^{+0.1}_{-0.1}$	$-0.1^{+0.3}_{-0.2}$	$-1.3^{+2.7}_{-1.2}$	$0.10^{+0.23}_{-0.18}$	$-0.03^{+0.02}_{-0.02}$	$0.01^{+0.04}_{-0.05}$	$0.00^{+0.04}_{-0.04}$	$0.03^{+0.03}_{-0.03}$	$0.01^{+0.02}_{-0.02}$	$0.01^{+0.03}_{-0.03}$	$0.03^{+0.04}_{-0.03}$	$0.00^{+0.03}_{-0.03}$	$0.02^{+0.02}_{-0.02}$	$0.02^{+0.08}_{-0.08}$	$0.05^{+0.02}_{-0.02}$
8	$2.1^{+0.4}_{-0.5}$	$0.190^{+0.013}_{-0.015}$	$-0.1^{+0.4}_{-0.4}$	$1.2^{+0.8}_{-2.2}$	$-1.7^{+1.7}_{-1.3}$	$0.29^{+0.24}_{-0.28}$	$-0.03^{+0.01}_{-0.01}$	$-0.01^{+0.03}_{-0.04}$	$0.00^{+0.06}_{-0.07}$	$0.03^{+0.04}_{-0.03}$	$0.01^{+0.02}_{-0.02}$	$-0.01^{+0.03}_{-0.03}$	$0.06^{+0.09}_{-0.09}$	$0.01^{+0.03}_{-0.04}$	$0.02^{+0.02}_{-0.02}$	...	$0.05^{+0.03}_{-0.03}$
9	$1.0^{+0.5}_{-0.4}$	$0.127^{+0.015}_{-0.015}$	$0.0^{+0.1}_{-0.1}$	$0.0^{+0.6}_{-0.4}$	$-0.6^{+0.8}_{-1.0}$	$-0.02^{+0.28}_{-0.25}$	$0.00^{+0.02}_{-0.02}$	$0.03^{+0.04}_{-0.04}$	$0.03^{+0.05}_{-0.04}$	$0.02^{+0.03}_{-0.03}$	$0.01^{+0.02}_{-0.02}$	$0.01^{+0.03}_{-0.03}$	$0.01^{+0.06}_{-0.06}$	$0.01^{+0.04}_{-0.04}$	$0.03^{+0.02}_{-0.02}$	$0.05^{+0.07}_{-0.07}$	$0.03^{+0.03}_{-0.02}$
10	$0.7^{+0.8}_{-0.5}$	$0.122^{+0.024}_{-0.014}$	$0.0^{+0.2}_{-0.2}$	$-0.2^{+0.8}_{-1.0}$	$-0.3^{+1.1}_{-1.1}$	$0.02^{+0.32}_{-0.30}$	$0.01^{+0.02}_{-0.03}$	$0.03^{+0.03}_{-0.05}$	$0.03^{+0.08}_{-0.08}$	$0.02^{+0.04}_{-0.04}$	$0.01^{+0.02}_{-0.03}$	$0.00^{+0.04}_{-0.03}$	$0.01^{+0.08}_{-0.07}$	$0.00^{+0.03}_{-0.03}$	$0.03^{+0.02}_{-0.02}$	...	$0.02^{+0.04}_{-0.03}$
11	$1.4^{+0.3}_{-0.6}$	$0.137^{+0.009}_{-0.013}$	$0.0^{+0.2}_{-0.2}$	$-0.3^{+0.7}_{-0.6}$	$-0.1^{+0.7}_{-0.6}$	$0.02^{+0.17}_{-0.17}$	$-0.02^{+0.02}_{-0.02}$	$0.01^{+0.02}_{-0.03}$	$0.03^{+0.03}_{-0.03}$	$0.02^{+0.03}_{-0.03}$	$0.01^{+0.02}_{-0.02}$	$0.01^{+0.03}_{-0.02}$	$0.02^{+0.07}_{-0.06}$	$0.01^{+0.03}_{-0.03}$	$0.02^{+0.01}_{-0.02}$	$0.06^{+0.08}_{-0.08}$	$0.04^{+0.02}_{-0.02}$
12p	$1.9^{+0.6}_{-0.6}$	$0.179^{+0.031}_{-0.035}$	$0.0^{+0.6}_{-0.4}$	$1.5^{+1.5}_{-1.2}$	$-1.7^{+2.7}_{-2.9}$	$-0.01^{+0.36}_{-0.35}$	$-0.02^{+0.02}_{-0.02}$	$0.01^{+0.05}_{-0.04}$	$0.02^{+0.04}_{-0.04}$	$0.01^{+0.02}_{-0.03}$	$0.01^{+0.02}_{-0.02}$	$0.00^{+0.04}_{-0.03}$	$0.02^{+0.04}_{-0.04}$	$0.01^{+0.04}_{-0.05}$	$0.03^{+0.02}_{-0.02}$	$0.03^{+0.05}_{-0.05}$	$0.03^{+0.02}_{-0.02}$
13p	$1.1^{+0.8}_{-0.9}$	$0.137^{+0.047}_{-0.052}$	$-0.5^{+0.5}_{-0.4}$	$0.1^{+0.8}_{-0.5}$	$0.0^{+1.0}_{-1.4}$	$0.13^{+0.41}_{-0.51}$	$-0.04^{+0.02}_{-0.02}$	$0.00^{+0.03}_{-0.04}$	$0.01^{+0.04}_{-0.04}$	$0.03^{+0.03}_{-0.03}$	$0.01^{+0.02}_{-0.02}$	$-0.01^{+0.03}_{-0.03}$	$0.04^{+0.08}_{-0.08}$	$-0.01^{+0.03}_{-0.03}$	$0.02^{+0.02}_{-0.02}$	$0.02^{+0.08}_{-0.08}$	$0.05^{+0.03}_{-0.03}$
14p	$1.2^{+1.0}_{-1.1}$	$0.126^{+0.045}_{-0.052}$	$-0.1^{+0.2}_{-0.2}$	$2.7^{+2.0}_{-2.9}$	$-4.1^{+3.9}_{-2.7}$	$-0.03^{+0.37}_{-0.41}$	$-0.02^{+0.04}_{-0.03}$	$0.01^{+0.06}_{-0.06}$	$0.01^{+0.07}_{-0.07}$	$0.01^{+0.05}_{-0.05}$	$0.00^{+0.03}_{-0.03}$	$0.01^{+0.05}_{-0.06}$	$0.01^{+0.09}_{-0.09}$	$0.00^{+0.05}_{-0.05}$	$0.01^{+0.04}_{-0.04}$	$0.02^{+0.14}_{-0.14}$	$0.03^{+0.05}_{-0.06}$
15	$2.4^{+0.5}_{-0.5}$	$0.177^{+0.016}_{-0.014}$	$-0.1^{+0.2}_{-0.2}$	$-0.3^{+0.6}_{-0.3}$	$-0.3^{+0.9}_{-1.0}$	$0.28^{+0.29}_{-0.26}$	$-0.06^{+0.02}_{-0.02}$	$-0.02^{+0.03}_{-0.04}$	$-0.01^{+0.04}_{-0.05}$	$0.03^{+0.04}_{-0.04}$	$0.02^{+0.03}_{-0.03}$	$0.01^{+0.03}_{-0.02}$	$0.04^{+0.08}_{-0.08}$	$-0.01^{+0.04}_{-0.04}$	$0.01^{+0.02}_{-0.02}$	$0.01^{+0.08}_{-0.11}$	$0.04^{+0.04}_{-0.04}$
16	$1.2^{+0.4}_{-0.4}$	$0.131^{+0.010}_{-0.011}$	$0.0^{+0.1}_{-0.1}$	$0.0^{+2.5}_{-2.0}$	$-0.3^{+0.5}_{-0.7}$	$0.14^{+0.25}_{-0.27}$	$-0.02^{+0.02}_{-0.02}$	$0.02^{+0.03}_{-0.03}$	$0.02^{+0.02}_{-0.02}$	$0.02^{+0.02}_{-0.02}$	$0.01^{+0.02}_{-0.02}$	$0.01^{+0.03}_{-0.03}$	$0.02^{+0.04}_{-0.03}$	$0.01^{+0.03}_{-0.03}$	$0.02^{+0.01}_{-0.01}$	$0.03^{+0.03}_{-0.03}$	$0.04^{+0.02}_{-0.02}$
17	$2.2^{+0.4}_{-0.4}$	$0.153^{+0.010}_{-0.009}$	$0.0^{+0.2}_{-0.2}$	$4.5^{+0.5}_{-1.0}$	$-6.3^{+0.4}_{-0.9}$	$0.08^{+0.15}_{-0.20}$	$-0.05^{+0.02}_{-0.01}$	$-0.02^{+0.03}_{-0.02}$	$-0.01^{+0.02}_{-0.02}$	$0.00^{+0.02}_{-0.02}$	$0.01^{+0.02}_{-0.02}$	$0.01^{+0.03}_{-0.02}$	$0.02^{+0.03}_{-0.03}$	$0.00^{+0.04}_{-0.02}$	$0.03^{+0.01}_{-0.01}$	$0.03^{+0.04}_{-0.04}$	$0.04^{+0.02}_{-0.02}$
18	$1.7^{+0.7}_{-0.8}$	$0.152^{+0.023}_{-0.021}$	$0.0^{+0.5}_{-0.6}$	$-0.1^{+0.9}_{-0.6}$	$-0.5^{+2.1}_{-2.8}$	$-0.01^{+0.77}_{-0.89}$	$-0.01^{+0.03}_{-0.04}$	$-0.02^{+0.07}_{-0.06}$	$0.04^{+0.07}_{-0.07}$	$0.02^{+0.06}_{-0.05}$	$0.02^{+0.05}_{-0.04}$	$0.01^{+0.06}_{-0.07}$	$0.02^{+0.09}_{-0.09}$	$0.02^{+0.09}_{-0.08}$	$0.03^{+0.04}_{-0.03}$	$0.05^{+0.12}_{-0.11}$	$0.05^{+0.07}_{-0.08}$
19	$1.8^{+0.6}_{-0.7}$	$0.152^{+0.017}_{-0.021}$	$0.0^{+0.1}_{-0.1}$	$0.3^{+1.2}_{-1.2}$	$-1.0^{+2.2}_{-2.3}$	$0.22^{+0.42}_{-0.52}$	$-0.03^{+0.03}_{-0.03}$	$0.00^{+0.06}_{-0.06}$	$0.01^{+0.04}_{-0.04}$	$0.01^{+0.04}_{-0.04}$	$0.02^{+0.03}_{-0.03}$	$0.01^{+0.05}_{-0.05}$	$0.01^{+0.04}_{-0.04}$	$0.01^{+0.07}_{-0.07}$	$0.02^{+0.03}_{-0.03}$	$0.03^{+0.06}_{-0.06}$	$0.04^{+0.04}_{-0.04}$
20	$1.7^{+0.6}_{-0.6}$	$0.152^{+0.013}_{-0.015}$	$0.0^{+0.7}_{-0.6}$	$0.8^{+1.5}_{-4.0}$	$-0.8^{+4.0}_{-4.1}$	$0.24^{+0.40}_{-0.40}$	$-0.05^{+0.03}_{-0.03}$	$0.00^{+0.05}_{-0.04}$	$0.02^{+0.04}_{-0.03}$	$0.04^{+0.04}_{-0.04}$	$0.02^{+0.05}_{-0.05}$	$-0.01^{+0.05}_{-0.05}$	$0.02^{+0.07}_{-0.07}$	$-0.01^{+0.05}_{-0.06}$	$0.01^{+0.03}_{-0.03}$	$0.02^{+0.10}_{-0.10}$	$0.05^{+0.05}_{-0.06}$
21	$1.0^{+0.4}_{-0.5}$	$0.124^{+0.009}_{-0.010}$	$0.0^{+0.1}_{-0.2}$	$-0.4^{+1.3}_{-0.5}$	$0.0^{+0.6}_{-0.7}$	$0.00^{+0.21}_{-0.22}$	$-0.01^{+0.01}_{-0.01}$	$0.02^{+0.03}_{-0.02}$	$0.03^{+0.02}_{-0.02}$	$0.02^{+0.02}_{-0.02}$	$0.01^{+0.03}_{-0.03}$	$0.01^{+0.03}_{-0.03}$	$0.02^{+0.03}_{-0.03}$	$0.02^{+0.05}_{-0.05}$	$0.02^{+0.02}_{-0.02}$	$0.03^{+0.03}_{-0.03}$	$0.04^{+0.03}_{-0.03}$
22	$1.5^{+0.5}_{-0.4}$	$0.148^{+0.011}_{-0.011}$	$0.0^{+0.1}_{-0.1}$	$0.5^{+0.8}_{-0.9}$	$-0.7^{+1.6}_{-1.2}$	$0.13^{+0.38}_{-0.25}$	$-0.03^{+0.02}_{-0.02}$	$0.01^{+0.04}_{-0.04}$	$0.02^{+0.03}_{-0.03}$	$0.01^{+0.03}_{-0.03}$	$0.02^{+0.03}_{-0.03}$	$0.00^{+0.04}_{-0.04}$	$0.01^{+0.04}_{-0.04}$	$0.00^{+0.04}_{-0.04}$	$0.02^{+0.02}_{-0.02}$	$0.03^{+0.05}_{-0.05}$	$0.04^{+0.03}_{-0.03}$
23	$0.9^{+0.6}_{-0.6}$	$0.133^{+0.015}_{-0.015}$	$-0.1^{+0.4}_{-0.5}$	$0.6^{+0.0}_{-0.0}$	$-3.7^{+7.5}_{-6.2}$	$-0.02^{+0.45}_{-0.53}$	$-0.02^{+0.02}_{-0.01}$	$0.01^{+0.03}_{-0.03}$	$0.04^{+0.02}_{-0.03}$	$0.02^{+0.03}_{-0.03}$	$0.02^{+0.05}_{-0.06}$	$0.00^{+0.05}_{-0.05}$	$0.02^{+0.05}_{-0.05}$	$0.02^{+0.04}_{-0.04}$	$0.02^{+0.04}_{-0.03}$	$0.05^{+0.08}_{-0.09}$	$0.05^{+0.05}_{-0.05}$
24p	$0.6^{+0.3}_{-0.2}$	$0.059^{+0.039}_{-0.009}$	$0.0^{+0.2}_{-0.2}$	$0.0^{+2.4}_{-2.4}$	$0.2^{+0.9}_{-1.2}$	$0.20^{+0.20}_{-0.23}$	$-0.02^{+0.01}_{-0.01}$	$0.02^{+0.02}_{-0.03}$	$0.01^{+0.02}_{-0.02}$	$0.00^{+0.03}_{-0.02}$	$0.01^{+0.03}_{-0.03}$	$-0.01^{+0.03}_{-0.04}$	$0.01^{+0.02}_{-0.03}$	$-0.01^{+0.04}_{-0.04}$	$0.01^{+0.02}_{-0.02}$	$0.04^{+0.05}_{-0.05}$	$0.01^{+0.03}_{-0.03}$
25	$1.0^{+0.6}_{-0.6}$	$0.120^{+0.013}_{-0.013}$	$0.0^{+0.1}_{-0.1}$	$0.7^{+1.4}_{-1.9}$	$-1.3^{+2.1}_{-1.4}$	$0.20^{+0.23}_{-0.22}$	$-0.02^{+0.02}_{-0.02}$	$0.01^{+0.03}_{-0.03}$	$0.02^{+0.02}_{-0.02}$	$0.02^{+0.03}_{-0.03}$	$0.01^{+0.03}_{-0.03}$	$-0.01^{+0.03}_{-0.04}$	$0.01^{+0.03}_{-0.03}$	$0.00^{+0.04}_{-0.04}$	$0.01^{+0.02}_{-0.02}$	$0.02^{+0.03}_{-0.03}$	$0.02^{+0.02}_{-0.02}$

Table D.2: continued.

#	$T_{\rm eff}$	$\log(g)$	$v_{\rm rad}$	$v\sin(i)$	ζ	ξ	$\log(n(x))$										
	(%)	(cgs)	($\rm km\,s^{-1}$)				He	C	N	O	Ne	Mg	Al	Si	S	Ar	Fe
26	$1.3^{+0.7}_{-0.6}$	$0.136^{+0.019}_{-0.018}$	$0.0^{+0.1}_{-0.1}$	$0.0^{+4.4}_{-4.3}$	$-0.2^{+2.4}_{-2.5}$	$0.01^{+0.45}_{-0.43}$	$-0.02^{+0.03}_{-0.02}$	$0.01^{+0.03}_{-0.03}$	$0.03^{+0.03}_{-0.03}$	$0.03^{+0.03}_{-0.03}$	$0.02^{+0.03}_{-0.03}$	$0.01^{+0.05}_{-0.05}$	$0.03^{+0.04}_{-0.04}$	$0.03^{+0.06}_{-0.06}$	$0.02^{+0.03}_{-0.03}$	$0.03^{+0.05}_{-0.05}$	$0.03^{+0.04}_{-0.04}$
27p	$1.2^{+0.4}_{-0.2}$	$0.112^{+0.009}_{-0.008}$	$0.0^{+0.4}_{-0.4}$	$0.0^{+0.0}_{-0.0}$	$0.7^{+3.5}_{-2.3}$	$-0.09^{+0.15}_{-0.17}$	$-0.04^{+0.01}_{-0.01}$	$-0.01^{+0.02}_{-0.03}$	$0.01^{+0.02}_{-0.02}$	$0.00^{+0.02}_{-0.02}$	$0.02^{+0.03}_{-0.03}$	$0.00^{+0.04}_{-0.04}$	$0.01^{+0.03}_{-0.04}$	$0.01^{+0.03}_{-0.02}$	$0.03^{+0.02}_{-0.02}$	$0.03^{+0.04}_{-0.04}$	$0.03^{+0.02}_{-0.03}$
28	$0.9^{+0.4}_{-0.4}$	$0.131^{+0.008}_{-0.011}$	$0.0^{+0.1}_{-0.1}$	$-0.3^{+0.3}_{-0.4}$	$-0.2^{+0.7}_{-0.6}$	$0.29^{+0.19}_{-0.21}$	$-0.04^{+0.01}_{-0.01}$	$0.01^{+0.02}_{-0.02}$	$0.02^{+0.02}_{-0.02}$	$0.02^{+0.02}_{-0.02}$	$0.01^{+0.03}_{-0.02}$	$-0.03^{+0.04}_{-0.04}$	$0.01^{+0.03}_{-0.03}$	$0.00^{+0.03}_{-0.04}$	$0.01^{+0.02}_{-0.02}$	$0.03^{+0.03}_{-0.03}$	$0.02^{+0.02}_{-0.02}$
29	$0.8^{+0.7}_{-0.7}$	$0.107^{+0.016}_{-0.016}$	$0.0^{+0.1}_{-0.1}$	$0.6^{+4.0}_{-3.9}$	$-0.7^{+2.4}_{-2.5}$	$0.30^{+0.45}_{-0.56}$	$-0.04^{+0.02}_{-0.02}$	$0.01^{+0.03}_{-0.03}$	$0.02^{+0.03}_{-0.03}$	$0.01^{+0.04}_{-0.03}$	$0.02^{+0.03}_{-0.03}$	$-0.01^{+0.05}_{-0.05}$	$0.02^{+0.03}_{-0.03}$	$0.00^{+0.05}_{-0.05}$	$0.01^{+0.02}_{-0.02}$	$0.03^{+0.04}_{-0.04}$	$0.02^{+0.03}_{-0.03}$
30	$1.2^{+0.7}_{-0.7}$	$0.142^{+0.017}_{-0.018}$	$0.0^{+0.1}_{-0.1}$	$0.2^{+1.1}_{-1.1}$	$-0.9^{+1.7}_{-1.7}$	$0.20^{+0.45}_{-0.30}$	$-0.03^{+0.02}_{-0.02}$	$0.02^{+0.03}_{-0.03}$	$0.02^{+0.03}_{-0.03}$	$0.01^{+0.04}_{-0.04}$	$0.02^{+0.03}_{-0.03}$	$0.00^{+0.04}_{-0.04}$	$0.01^{+0.04}_{-0.04}$	$0.00^{+0.05}_{-0.05}$	$0.02^{+0.03}_{-0.03}$	$0.03^{+0.04}_{-0.04}$	$0.03^{+0.03}_{-0.03}$
31	$1.9^{+0.6}_{-0.6}$	$0.100^{+0.006}_{-0.013}$	$0.2^{+0.6}_{-0.5}$	$-0.2^{+0.8}_{-0.0}$	$-3.9^{+3.5}_{-3.6}$	$-0.18^{+0.38}_{-0.30}$	$-0.02^{+0.02}_{-0.02}$	$0.02^{+0.04}_{-0.04}$	$0.01^{+0.02}_{-0.02}$	$-0.01^{+0.02}_{-0.02}$	$-0.06^{+0.08}_{-0.06}$	$-0.01^{+0.04}_{-0.04}$	$0.02^{+0.02}_{-0.02}$	$0.01^{+0.02}_{-0.02}$	$0.00^{+0.04}_{-0.04}$	...	$0.03^{+0.02}_{-0.02}$
32	$0.8^{+0.2}_{-0.2}$	$0.103^{+0.006}_{-0.004}$	$0.0^{+0.1}_{-0.1}$	$0.0^{+0.9}_{-0.8}$	$-0.3^{+0.0}_{-0.1}$	$0.05^{+0.12}_{-0.18}$	$-0.01^{+0.01}_{-0.01}$	$0.00^{+0.03}_{-0.03}$	$0.00^{+0.01}_{-0.01}$	$0.03^{+0.01}_{-0.01}$	$0.00^{+0.03}_{-0.03}$	$0.00^{+0.03}_{-0.03}$	$0.00^{+0.02}_{-0.02}$	$0.02^{+0.02}_{-0.01}$	$0.03^{+0.03}_{-0.03}$	$0.02^{+0.04}_{-0.04}$	$0.02^{+0.01}_{-0.01}$
33	$1.3^{+0.4}_{-0.4}$	$0.150^{+0.009}_{-0.012}$	$0.0^{+0.1}_{-0.1}$	$-0.4^{+0.3}_{-0.4}$	$0.1^{+0.5}_{-0.6}$	$0.18^{+0.23}_{-0.20}$	$-0.03^{+0.01}_{-0.01}$	$0.01^{+0.02}_{-0.02}$	$0.02^{+0.02}_{-0.01}$	$0.02^{+0.02}_{-0.02}$	$0.02^{+0.03}_{-0.03}$	$0.00^{+0.03}_{-0.03}$	$0.02^{+0.02}_{-0.02}$	$0.00^{+0.03}_{-0.03}$	$0.03^{+0.02}_{-0.02}$	$0.04^{+0.04}_{-0.04}$	$0.04^{+0.02}_{-0.02}$
34	$0.9^{+1.1}_{-1.1}$	$0.130^{+0.038}_{-0.038}$	$0.0^{+0.2}_{-0.2}$	$0.4^{+6.0}_{-6.3}$	$-0.5^{+4.2}_{-3.8}$	$0.27^{+0.94}_{-1.04}$	$-0.02^{+0.05}_{-0.04}$	$0.01^{+0.07}_{-0.07}$	$0.03^{+0.04}_{-0.04}$	$0.03^{+0.06}_{-0.06}$	$0.01^{+0.08}_{-0.08}$	$-0.01^{+0.11}_{-0.11}$	$0.02^{+0.06}_{-0.06}$	$0.01^{+0.09}_{-0.09}$	$0.02^{+0.07}_{-0.07}$	$0.04^{+0.14}_{-0.15}$	$0.03^{+0.06}_{-0.06}$
35	$1.9^{+0.2}_{-0.2}$	$0.142^{+0.007}_{-0.010}$	$0.0^{+0.6}_{-0.6}$	$1.8^{+0.0}_{-0.0}$	$-14.7^{+3.7}_{-5.9}$	$0.15^{+0.18}_{-0.18}$	$-0.02^{+0.02}_{-0.01}$	$0.03^{+0.03}_{-0.03}$	$0.02^{+0.01}_{-0.01}$	$0.00^{+0.01}_{-0.01}$	$0.00^{+0.05}_{-0.05}$	$0.00^{+0.03}_{-0.03}$	$0.03^{+0.03}_{-0.02}$	$0.00^{+0.02}_{-0.02}$	$0.03^{+0.04}_{-0.04}$	...	$0.02^{+0.02}_{-0.02}$
36	$0.9^{+0.4}_{-0.4}$	$0.142^{+0.010}_{-0.011}$	$0.0^{+0.1}_{-0.1}$	$0.0^{+0.5}_{-0.6}$	$-0.6^{+0.4}_{-0.4}$	$0.52^{+0.18}_{-0.34}$	$-0.03^{+0.01}_{-0.01}$	$0.01^{+0.02}_{-0.02}$	$0.02^{+0.01}_{-0.01}$	$0.03^{+0.02}_{-0.02}$	$0.01^{+0.02}_{-0.02}$	$-0.02^{+0.03}_{-0.04}$	$0.00^{+0.02}_{-0.02}$	$0.00^{+0.03}_{-0.02}$	$0.01^{+0.02}_{-0.02}$	$0.02^{+0.04}_{-0.04}$	$0.02^{+0.02}_{-0.02}$
37	$2.0^{+0.3}_{-0.5}$	$0.163^{+0.007}_{-0.012}$	$-0.8^{+0.5}_{-0.7}$	$-0.1^{+0.0}_{-0.0}$	$0.0^{+2.5}_{-1.3}$	$0.03^{+0.15}_{-0.20}$	$-0.02^{+0.01}_{-0.02}$	$0.01^{+0.05}_{-0.03}$	$0.02^{+0.02}_{-0.02}$	$0.02^{+0.02}_{-0.02}$	$0.03^{+0.10}_{-0.08}$	$0.01^{+0.05}_{-0.05}$	$0.03^{+0.03}_{-0.03}$	$0.02^{+0.03}_{-0.03}$	$0.06^{+0.04}_{-0.04}$	...	$0.03^{+0.02}_{-0.02}$
38	$0.8^{+0.5}_{-0.5}$	$0.126^{+0.014}_{-0.014}$	$0.0^{+0.1}_{-0.1}$	$-0.3^{+3.0}_{-4.4}$	$-0.3^{+3.1}_{-2.9}$	$0.23^{+0.34}_{-0.22}$	$-0.04^{+0.02}_{-0.02}$	$0.01^{+0.02}_{-0.02}$	$0.02^{+0.02}_{-0.02}$	$0.03^{+0.02}_{-0.02}$	$0.02^{+0.03}_{-0.03}$	$0.00^{+0.05}_{-0.05}$	$0.01^{+0.03}_{-0.03}$	$0.02^{+0.04}_{-0.04}$	$0.01^{+0.02}_{-0.02}$	$0.02^{+0.04}_{-0.04}$	$0.03^{+0.02}_{-0.02}$
39	$0.9^{+0.9}_{-0.4}$	$0.090^{+0.019}_{-0.015}$	$0.0^{+0.8}_{-0.8}$	$-0.3^{+0.4}_{-1.6}$	$0.8^{+3.7}_{-4.2}$	$0.04^{+0.48}_{-0.41}$	$-0.01^{+0.04}_{-0.02}$	$0.01^{+0.03}_{-0.04}$	$-0.01^{+0.03}_{-0.02}$	$0.01^{+0.02}_{-0.02}$	$0.01^{+0.07}_{-0.07}$	$-0.02^{+0.07}_{-0.07}$	$0.02^{+0.03}_{-0.03}$	$0.02^{+0.03}_{-0.03}$	$0.02^{+0.05}_{-0.05}$	...	$0.00^{+0.03}_{-0.03}$
40	$0.8^{+0.2}_{-0.2}$	$0.132^{+0.006}_{-0.007}$	$0.0^{+0.3}_{-0.3}$	$-0.4^{+0.0}_{-0.0}$	$0.0^{+2.9}_{-1.6}$	$0.19^{+0.14}_{-0.13}$	$-0.02^{+0.01}_{-0.01}$	$-0.01^{+0.04}_{-0.03}$	$0.03^{+0.02}_{-0.02}$	$0.03^{+0.01}_{-0.01}$	$0.02^{+0.05}_{-0.05}$	$-0.02^{+0.03}_{-0.03}$	$0.01^{+0.03}_{-0.03}$	$0.01^{+0.03}_{-0.03}$	$0.03^{+0.04}_{-0.05}$	...	$0.03^{+0.03}_{-0.03}$
41	$0.9^{+0.2}_{-0.2}$	$0.145^{+0.006}_{-0.012}$	$0.0^{+0.2}_{-0.2}$	$-0.1^{+0.0}_{-0.1}$	$-3.1^{+4.6}_{-1.4}$	$0.24^{+0.21}_{-0.17}$	$-0.02^{+0.01}_{-0.01}$	$0.01^{+0.03}_{-0.04}$	$0.02^{+0.01}_{-0.01}$	$0.03^{+0.01}_{-0.01}$	$0.01^{+0.05}_{-0.05}$	$-0.01^{+0.03}_{-0.03}$	$0.01^{+0.02}_{-0.02}$	$0.01^{+0.03}_{-0.03}$	$0.02^{+0.04}_{-0.04}$	$0.05^{+0.07}_{-0.08}$	$0.03^{+0.03}_{-0.02}$
42p	$0.0^{+1.0}_{-0.4}$	$0.036^{+0.066}_{-0.027}$	$2.3^{+0.7}_{-1.3}$	$-2.8^{+2.5}_{-2.3}$	$0.3^{+2.2}_{-1.7}$	$0.23^{+0.40}_{-0.52}$	$-0.01^{+0.01}_{-0.01}$	$0.01^{+0.02}_{-0.02}$	$0.01^{+0.01}_{-0.01}$	$0.02^{+0.01}_{-0.01}$	$0.02^{+0.03}_{-0.03}$	$0.00^{+0.02}_{-0.02}$	$0.01^{+0.02}_{-0.02}$	$0.02^{+0.02}_{-0.02}$	$0.04^{+0.03}_{-0.03}$	$0.07^{+0.05}_{-0.06}$	$0.02^{+0.01}_{-0.01}$
43	$0.9^{+1.2}_{-0.8}$	$0.110^{+0.024}_{-0.019}$	$0.1^{+0.6}_{-0.7}$	$-0.1^{+1.5}_{-0.8}$	$0.0^{+2.5}_{-3.4}$	$0.13^{+0.49}_{-0.49}$	$-0.01^{+0.04}_{-0.05}$	$0.01^{+0.05}_{-0.05}$	$0.00^{+0.03}_{-0.03}$	$0.03^{+0.02}_{-0.03}$	$0.00^{+0.08}_{-0.08}$	$-0.01^{+0.07}_{-0.07}$	$0.01^{+0.04}_{-0.04}$	$0.02^{+0.04}_{-0.03}$	$0.03^{+0.06}_{-0.06}$	...	$0.01^{+0.04}_{-0.03}$
44	$1.4^{+0.3}_{-0.3}$	$0.123^{+0.007}_{-0.005}$	$0.0^{+0.1}_{-0.1}$	$0.0^{+0.3}_{-0.3}$	$-0.4^{+1.4}_{-0.7}$	$0.21^{+0.12}_{-0.09}$	$0.00^{+0.01}_{-0.02}$	$0.01^{+0.03}_{-0.03}$	$0.01^{+0.01}_{-0.01}$	$0.02^{+0.01}_{-0.01}$	$0.00^{+0.04}_{-0.04}$	$0.01^{+0.02}_{-0.02}$	$0.01^{+0.03}_{-0.03}$	$0.02^{+0.02}_{-0.02}$	$0.03^{+0.02}_{-0.02}$	...	$0.01^{+0.01}_{-0.01}$
45	$0.6^{+0.2}_{-0.2}$	$0.135^{+0.006}_{-0.007}$	$-0.1^{+0.2}_{-0.2}$	$-0.2^{+0.0}_{-0.0}$	$0.0^{+0.5}_{-0.4}$	$0.19^{+0.13}_{-0.11}$	$-0.03^{+0.01}_{-0.01}$	$-0.01^{+0.03}_{-0.03}$	$0.02^{+0.01}_{-0.01}$	$0.04^{+0.01}_{-0.01}$	$0.01^{+0.04}_{-0.05}$	$-0.01^{+0.03}_{-0.03}$	$0.00^{+0.02}_{-0.02}$	$0.02^{+0.02}_{-0.02}$	$0.04^{+0.03}_{-0.04}$	$0.07^{+0.08}_{-0.09}$	$0.03^{+0.02}_{-0.02}$
46	$1.1^{+0.2}_{-0.3}$	$0.119^{+0.008}_{-0.005}$	$0.0^{+0.2}_{-0.2}$	$0.3^{+0.1}_{-0.8}$	$-1.0^{+0.5}_{-0.3}$	$0.02^{+0.17}_{-0.19}$	$-0.01^{+0.01}_{-0.01}$	$0.02^{+0.03}_{-0.03}$	$0.01^{+0.01}_{-0.01}$	$0.02^{+0.01}_{-0.01}$	$0.01^{+0.06}_{-0.06}$	$0.01^{+0.03}_{-0.03}$	$0.01^{+0.02}_{-0.02}$	$0.02^{+0.02}_{-0.02}$	$0.03^{+0.02}_{-0.02}$	$0.11^{+0.10}_{-0.12}$	$0.01^{+0.01}_{-0.01}$
47	$1.2^{+0.2}_{-0.2}$	$0.104^{+0.008}_{-0.008}$	$0.0^{+0.2}_{-0.2}$	$1.9^{+0.9}_{-1.1}$	$-2.2^{+1.8}_{-0.3}$	$0.06^{+0.27}_{-0.34}$	$-0.01^{+0.01}_{-0.01}$	$0.01^{+0.03}_{-0.03}$	$0.00^{+0.01}_{-0.01}$	$0.02^{+0.01}_{-0.01}$	$0.01^{+0.05}_{-0.05}$	$-0.01^{+0.03}_{-0.03}$	$0.00^{+0.03}_{-0.03}$	$0.02^{+0.02}_{-0.02}$	$0.02^{+0.03}_{-0.03}$	$0.08^{+0.14}_{-0.13}$	$0.00^{+0.01}_{-0.02}$
48	$0.9^{+0.4}_{-0.3}$	$0.134^{+0.013}_{-0.012}$	$0.0^{+0.1}_{-0.1}$	$-0.3^{+0.3}_{-0.2}$	$0.0^{+1.2}_{-1.3}$	$0.23^{+0.25}_{-0.25}$	$-0.02^{+0.02}_{-0.02}$	$0.00^{+0.03}_{-0.03}$	$0.02^{+0.01}_{-0.02}$	$0.03^{+0.02}_{-0.02}$	$0.02^{+0.04}_{-0.04}$	$-0.01^{+0.03}_{-0.03}$	$0.01^{+0.03}_{-0.03}$	$0.01^{+0.03}_{-0.03}$	$0.01^{+0.03}_{-0.03}$	$0.04^{+0.05}_{-0.05}$	$0.03^{+0.02}_{-0.02}$
49	$1.0^{+0.3}_{-0.3}$	$0.130^{+0.011}_{-0.011}$	$0.0^{+0.1}_{-0.1}$	$0.0^{+1.7}_{-1.6}$	$-0.3^{+0.3}_{-0.3}$	$0.17^{+0.20}_{-0.22}$	$-0.02^{+0.01}_{-0.01}$	$0.02^{+0.03}_{-0.03}$	$0.01^{+0.01}_{-0.01}$	$0.03^{+0.01}_{-0.02}$	$0.02^{+0.03}_{-0.03}$	$0.00^{+0.03}_{-0.03}$	$0.00^{+0.04}_{-0.04}$	$0.01^{+0.02}_{-0.02}$	$0.01^{+0.04}_{-0.04}$	$0.04^{+0.06}_{-0.06}$	$0.02^{+0.02}_{-0.02}$
50	$0.9^{+0.3}_{-0.3}$	$0.101^{+0.010}_{-0.009}$	$0.0^{+0.1}_{-0.1}$	$0.0^{+1.0}_{-1.3}$	$-0.1^{+0.3}_{-0.3}$	$0.06^{+0.11}_{-0.14}$	$0.00^{+0.02}_{-0.01}$	$0.01^{+0.03}_{-0.03}$	$0.02^{+0.01}_{-0.01}$	$0.02^{+0.01}_{-0.01}$	$0.01^{+0.03}_{-0.03}$	$0.00^{+0.05}_{-0.05}$	$0.01^{+0.02}_{-0.03}$	$0.02^{+0.02}_{-0.02}$	$0.03^{+0.03}_{-0.04}$	$0.03^{+0.11}_{-0.09}$	$0.01^{+0.02}_{-0.02}$
51	$1.1^{+0.6}_{-0.4}$	$0.120^{+0.022}_{-0.018}$	$0.0^{+0.2}_{-0.2}$	$0.0^{+1.6}_{-1.8}$	$-0.2^{+0.5}_{-0.4}$	$0.09^{+0.37}_{-0.41}$	$0.00^{+0.03}_{-0.03}$	$0.02^{+0.05}_{-0.05}$	$0.02^{+0.02}_{-0.02}$	$0.02^{+0.02}_{-0.02}$	$0.02^{+0.07}_{-0.07}$	$0.01^{+0.07}_{-0.07}$	$0.01^{+0.06}_{-0.06}$	$0.02^{+0.04}_{-0.04}$	$0.03^{+0.06}_{-0.06}$	...	$0.02^{+0.04}_{-0.04}$

Table D.2: continued.

#	$T_{\rm eff}$	$\log(g)$	$v_{\rm rad}$	$v\sin(i)$	ζ	ξ	$\log(n(x))$										
	(%)	(cgs)	($\mathrm{km\,s^{-1}}$)				He	C	N	O	Ne	Mg	Al	Si	S	Ar	Fe
52	$1.5^{+0.2}_{-0.2}$	$0.151^{+0.007}_{-0.008}$	$-0.2^{+0.4}_{-0.9}$	$-3.5^{+0.0}_{-0.0}$	$14.2^{+\ 3.2}_{-10.3}$	$-0.08^{+0.19}_{-0.19}$	$-0.04^{+0.02}_{-0.02}$	$0.02^{+0.05}_{-0.05}$	$0.01^{+0.02}_{-0.02}$	$0.04^{+0.02}_{-0.02}$	$0.01^{+0.10}_{-0.09}$	$0.02^{+0.06}_{-0.06}$	$0.01^{+0.05}_{-0.05}$	$0.04^{+0.03}_{-0.03}$	$0.08^{+0.09}_{-0.09}$	...	$0.03^{+0.04}_{-0.04}$
53	$1.0^{+0.3}_{-0.2}$	$0.128^{+0.012}_{-0.010}$	$0.0^{+0.2}_{-0.2}$	$0.1^{+0.0}_{-0.1}$	$0.0^{+\ 0.5}_{-\ 1.1}$	$0.09^{+0.21}_{-0.20}$	$-0.01^{+0.02}_{-0.02}$	$0.01^{+0.03}_{-0.03}$	$0.02^{+0.02}_{-0.02}$	$0.03^{+0.01}_{-0.01}$	$0.01^{+0.05}_{-0.05}$	$0.01^{+0.04}_{-0.04}$	$0.01^{+0.04}_{-0.04}$	$0.02^{+0.03}_{-0.03}$	$0.04^{+0.05}_{-0.05}$	...	$0.01^{+0.03}_{-0.03}$
54	$1.3^{+0.2}_{-0.2}$	$0.133^{+0.009}_{-0.008}$	$0.0^{+0.2}_{-0.2}$	$-0.5^{+0.4}_{-0.6}$	$0.0^{+\ 1.1}_{-\ 1.3}$	$0.17^{+0.19}_{-0.17}$	$-0.01^{+0.01}_{-0.01}$	$0.01^{+0.02}_{-0.02}$	$0.02^{+0.01}_{-0.01}$	$0.02^{+0.01}_{-0.01}$	$0.01^{+0.04}_{-0.04}$	$0.01^{+0.03}_{-0.03}$	$0.01^{+0.03}_{-0.03}$	$0.02^{+0.02}_{-0.02}$	$0.04^{+0.03}_{-0.03}$	...	$0.02^{+0.02}_{-0.02}$
55p	$1.3^{+0.1}_{-0.2}$	$0.099^{+0.008}_{-0.010}$	$0.1^{+0.1}_{-0.1}$	$-4.9^{+0.5}_{-0.7}$	$3.2^{+\ 0.5}_{-\ 0.6}$	$0.21^{+0.22}_{-0.22}$	$0.00^{+0.01}_{-0.01}$	$0.01^{+0.02}_{-0.02}$	$0.01^{+0.02}_{-0.02}$	$0.02^{+0.01}_{-0.01}$	$-0.01^{+0.03}_{-0.03}$	$0.03^{+0.03}_{-0.03}$	$0.01^{+0.04}_{-0.03}$	$0.03^{+0.01}_{-0.02}$	$0.05^{+0.03}_{-0.04}$	...	$-0.11^{+0.06}_{-0.05}$
56	$1.0^{+0.3}_{-0.4}$	$0.124^{+0.012}_{-0.012}$	$0.0^{+0.2}_{-0.2}$	$0.0^{+3.1}_{-3.3}$	$-0.3^{+\ 0.1}_{-\ 0.2}$	$0.10^{+0.32}_{-0.23}$	$-0.01^{+0.03}_{-0.03}$	$0.02^{+0.04}_{-0.04}$	$0.01^{+0.02}_{-0.02}$	$0.03^{+0.01}_{-0.01}$	$0.02^{+0.05}_{-0.05}$	$0.01^{+0.05}_{-0.05}$	$0.00^{+0.06}_{-0.06}$	$0.02^{+0.03}_{-0.03}$	$0.03^{+0.06}_{-0.06}$	...	$0.01^{+0.04}_{-0.04}$
57	$1.0^{+0.1}_{-0.2}$	$0.117^{+0.007}_{-0.007}$	$0.0^{+0.2}_{-0.2}$	$0.2^{+0.4}_{-0.7}$	$-0.6^{+\ 1.8}_{-\ 0.8}$	$0.20^{+0.20}_{-0.21}$	$0.00^{+0.01}_{-0.02}$	$0.01^{+0.02}_{-0.02}$	$0.01^{+0.01}_{-0.01}$	$0.02^{+0.01}_{-0.01}$	$0.02^{+0.03}_{-0.03}$	$0.01^{+0.02}_{-0.02}$	$0.00^{+0.02}_{-0.02}$	$0.01^{+0.02}_{-0.02}$	$0.04^{+0.04}_{-0.04}$	...	$0.01^{+0.03}_{-0.03}$
58	$1.0^{+0.3}_{-0.3}$	$0.121^{+0.014}_{-0.018}$	$0.0^{+0.4}_{-0.4}$	$0.0^{+0.0}_{-0.0}$	$0.0^{+\ 1.4}_{-\ 1.6}$	$0.20^{+0.26}_{-0.38}$	$-0.01^{+0.02}_{-0.02}$	$0.01^{+0.04}_{-0.03}$	$0.01^{+0.03}_{-0.02}$	$0.03^{+0.02}_{-0.02}$	$0.01^{+0.06}_{-0.06}$	$0.01^{+0.06}_{-0.06}$	$0.01^{+0.07}_{-0.06}$	$0.01^{+0.04}_{-0.04}$	$-0.01^{+0.08}_{-0.08}$	...	$0.02^{+0.07}_{-0.06}$
59	$0.8^{+0.2}_{-0.2}$	$0.078^{+0.006}_{-0.007}$	$0.0^{+0.2}_{-0.3}$	$-0.2^{+1.2}_{-1.8}$	$0.1^{+\ 0.0}_{-\ 0.4}$	$-0.09^{+0.31}_{-0.39}$	$-0.01^{+0.01}_{-0.01}$	$0.00^{+0.03}_{-0.03}$	$0.00^{+0.03}_{-0.03}$	$0.00^{+0.01}_{-0.01}$	$-0.01^{+0.03}_{-0.03}$	$0.00^{+0.02}_{-0.02}$	$0.00^{+0.05}_{-0.05}$	$0.01^{+0.02}_{-0.01}$	$0.00^{+0.05}_{-0.05}$	...	$0.00^{+0.08}_{-0.08}$
60	$1.2^{+0.3}_{-0.4}$	$0.171^{+0.017}_{-0.019}$	$-0.1^{+1.0}_{-0.9}$	$0.9^{+0.1}_{-0.8}$	$-8.9^{+15.9}_{-\ 3.7}$	$0.21^{+0.73}_{-0.53}$	$-0.01^{+0.03}_{-0.03}$	$0.02^{+0.06}_{-0.05}$	$0.02^{+0.06}_{-0.06}$	$0.03^{+0.03}_{-0.03}$	$0.02^{+0.15}_{-0.15}$	$0.01^{+0.14}_{-0.14}$	$0.02^{+0.16}_{-0.16}$	$0.02^{+0.07}_{-0.06}$	$0.03^{+0.12}_{-0.12}$	...	$0.00^{+0.15}_{-0.11}$
61	$1.0^{+0.1}_{-0.1}$	$0.121^{+0.005}_{-0.006}$	$0.0^{+0.0}_{-0.0}$	$-1.0^{+1.0}_{-0.2}$	$0.0^{+\ 0.0}_{-\ 2.1}$	$0.14^{+0.11}_{-0.09}$	$0.00^{+0.01}_{-0.01}$	$0.02^{+0.01}_{-0.01}$	$0.01^{+0.01}_{-0.01}$	$0.02^{+0.01}_{-0.01}$	$0.01^{+0.01}_{-0.01}$	$0.01^{+0.02}_{-0.02}$	$0.01^{+0.02}_{-0.02}$	$0.02^{+0.01}_{-0.01}$	$0.03^{+0.03}_{-0.03}$	...	$0.01^{+0.02}_{-0.02}$
62	$0.8^{+0.3}_{-0.4}$	$0.110^{+0.021}_{-0.022}$	$0.0^{+0.4}_{-0.4}$	$0.6^{+3.5}_{-3.1}$	$-0.8^{+\ 3.7}_{-\ 3.3}$	$0.13^{+0.71}_{-0.64}$	$-0.01^{+0.02}_{-0.02}$	$0.01^{+0.03}_{-0.04}$	$0.01^{+0.08}_{-0.06}$	$0.01^{+0.02}_{-0.03}$	$0.00^{+0.14}_{-0.14}$	$0.01^{+0.06}_{-0.06}$	$0.00^{+0.10}_{-0.10}$	$0.02^{+0.04}_{-0.04}$	$0.01^{+0.11}_{-0.11}$	...	$-0.01^{+0.13}_{-0.13}$
63	$1.0^{+0.2}_{-0.2}$	$0.120^{+0.014}_{-0.014}$	$0.0^{+0.2}_{-0.2}$	$-1.8^{+1.6}_{-1.6}$	$0.4^{+\ 1.5}_{-\ 2.0}$	$0.16^{+0.42}_{-0.48}$	$0.00^{+0.01}_{-0.01}$	$0.01^{+0.02}_{-0.02}$	$0.03^{+0.04}_{-0.03}$	$0.02^{+0.02}_{-0.02}$	$0.01^{+0.03}_{-0.03}$	$0.01^{+0.03}_{-0.03}$	$0.00^{+0.06}_{-0.06}$	$0.02^{+0.03}_{-0.03}$	$0.03^{+0.06}_{-0.06}$	...	$0.03^{+0.12}_{-0.14}$

Notes. Numbering according to Table 7.1. Primary components of a SB2 system are denoted by "p". Uncertainties are statistical 99%-confidence limits. The abundance $n(x)$ is given as fractional particle number of species x with respect to all elements. Lines of nitrogen and argon are not visible in all objects.

Table D.3: Atmospheric parameters of the reference stars.

#	$T_{\rm eff}$	log g	$v_{\rm rad}$	$v \sin(i)$	ζ	ξ	$A_{\rm eff,s}/A_{\rm eff,p}$	log($n(x)$)										
	(K)	(cgs)	(km s^{-1})					He	C	N	O	Ne	Mg	Al	Si	S	Ar	Fe
1	12 140	3.201	−1.5	15.7	4.3	1.03	…	−0.81	−3.63	−3.80	−3.38	−3.97	−4.69	−5.86	−4.41	−4.84	…	−4.61
Stat.	+10	+0.008	+0.1	+0.1	+0.5	+0.06	…	+0.01	+0.04	+0.05	+0.02	+0.03	+0.01	+0.03	+0.02	+0.01	…	+0.02
	−10	−0.003	−0.1	−0.2	−0.6	−0.06		−0.01	−0.05	−0.05	−0.02	−0.02	−0.02	−0.03	−0.01	−0.02		−0.01
Sys.	+250	+0.100	+0.1	+0.1	+0.2	+0.22	…	+0.13	+0.09	+0.10	+0.05	+0.09	+0.05	+0.02	+0.04	+0.06	…	+0.09
	−240	−0.100	−0.1	−0.1	−0.4	−0.20		−0.16	−0.09	−0.09	−0.05	−0.07	−0.06	−0.03	−0.04	−0.06		−0.08
2	13 220	3.911	−18.0	84.6	0.0	1.42	…	−0.94	−3.49	…	−3.26	−4.12	−4.54	−5.81	−4.31	−4.77	…	−4.44
Stat.	+30	+0.003	+0.3	+0.1	+4.0	+0.07	…	+0.01	+0.04	…	+0.02	+0.04	+0.01	+0.03	+0.02	+0.02	…	+0.02
	−20	−0.002	−0.3	−0.1	−0.0	−0.08		−0.01	−0.04		−0.02	−0.04	−0.02	−0.04	−0.01	−0.03		−0.02
Sys.	+270	+0.100	+0.3	+0.4	+2.8	+0.43	…	+0.16	+0.08	…	+0.04	+0.07	+0.04	+0.02	+0.05	+0.07	…	+0.08
	−270	−0.100	−0.2	−0.1	−0.0	−0.39		−0.17	−0.07		−0.04	−0.07	−0.05	−0.03	−0.04	−0.07		−0.08
3	13 360	4.025	20.7	52.5	17.6	1.31	…	−0.92	−3.44	…	−3.27	−4.09	−4.56	−5.77	−4.29	−4.82	…	−4.51
Stat.	+10	+0.001	+0.1	+0.1	+1.1	+0.09	…	+0.01	+0.04	…	+0.02	+0.04	+0.02	+0.03	+0.02	+0.03	…	+0.03
	−50	−0.003	−0.3	−0.1	−1.0	−0.08		−0.01	−0.04		−0.02	−0.04	−0.02	−0.04	−0.01	−0.02		−0.02
Sys.	+270	+0.100	+0.1	+0.2	+0.4	+0.45	…	+0.15	+0.08	…	+0.04	+0.07	+0.04	+0.02	+0.04	+0.08	…	+0.08
	−280	−0.100	−0.1	−0.1	−0.4	−0.39		−0.18	−0.07		−0.04	−0.07	−0.05	−0.03	−0.03	−0.06		−0.09
4	13 490	3.878	13.7	80.0	27.7	1.62	…	−0.83	−3.44	…	−3.31	−4.20	−4.60	−5.87	−4.36	−4.84	…	−4.63
Stat.	+30	+0.007	+0.3	+0.1	+1.4	+0.04	…	+0.01	+0.03	…	+0.02	+0.04	+0.02	+0.04	+0.02	+0.02	…	+0.01
	−20	−0.006	−0.3	−0.1	−1.4	−0.09		−0.01	−0.04		−0.02	−0.03	−0.02	−0.05	−0.02	−0.02		−0.02
Sys.	+270	+0.100	+0.1	+0.4	+0.5	+0.46	…	+0.13	+0.07	…	+0.04	+0.07	+0.05	+0.02	+0.05	+0.05	…	+0.09
	−280	−0.100	−0.2	−0.1	−1.2	−0.42		−0.13	−0.07		−0.05	−0.05	−0.06	−0.04	−0.05	−0.05		−0.09
5p	13 740	4.099	34.3	19.8	0.0	1.06	…	−0.84	−3.41	…	−3.34	−4.13	−4.71	−5.96	−4.39	−4.80	…	−4.65
Stat.	+20	+0.003	+0.2	+0.1	+2.3	+0.13	…	+0.01	+0.03	…	+0.02	+0.04	+0.01	+0.03	+0.02	+0.02	…	+0.01
	−20	−0.007	−0.2	−0.5	−0.0	−0.13		−0.01	−0.04		−0.03	−0.03	−0.02	−0.03	−0.02	−0.02		−0.02
Sys.	+280	+0.100	+0.2	+0.1	+0.2	+0.28	…	+0.07	+0.06	…	+0.04	+0.05	+0.04	+0.02	+0.03	+0.04	…	+0.09
	−280	−0.100	−0.2	−0.1	−0.0	−0.16		−0.07	−0.07		−0.05	−0.04	−0.04	−0.03	−0.03	−0.04		−0.09
5s	13 420	3.783	5.1	19.4	8.3	1.46	0.871	…	…	…	…	…	…	…	…	…	…	…
Stat.	+20	+0.005	+0.2	+0.2	+0.8	+0.13	+0.012	…	…	…	…	…	…	…	…	…	…	…
	−30	−0.007	−0.2	−0.4	−0.8	−0.13	−0.022											
Sys.	+350	+0.229	+0.3	+0.1	+1.6	+0.15	+0.035	…	…	…	…	…	…	…	…	…	…	…
	−320	−0.188	−0.2	−0.2	−0.7	−0.12	−0.033											
6	14 300	3.965	24.4	106.8	0.0	1.49	…	−0.84	−3.47	…	−3.38	−4.15	−4.71	−6.02	−4.43	−4.88	…	−4.76
Stat.	+20	+0.003	+0.4	+0.1	+6.0	+0.10	…	+0.01	+0.03	…	+0.02	+0.03	+0.02	+0.06	+0.02	+0.02	…	+0.02
	−20	−0.002	−0.4	−0.1	−0.0	−0.14		−0.01	−0.02		−0.03	−0.04	−0.03	−0.07	−0.03	−0.02		−0.03
Sys.	+290	+0.100	+0.2	+0.6	+3.6	+0.88	…	+0.12	+0.08	…	+0.05	+0.05	+0.05	+0.04	+0.11	+0.04	…	+0.08
	−290	−0.100	−0.3	−0.1	−0.0	−1.05		−0.14	−0.06		−0.05	−0.05	−0.06	−0.06	−0.10	−0.05		−0.09
7	15 050	3.776	−15.4	11.4	1.3	1.57	…	−0.94	−3.48	−4.10	−3.20	−4.01	−4.62	−5.85	−4.34	−4.84	−5.47	−4.54
Stat.	+40	+0.008	+0.1	+0.2	+1.3	+0.11	…	+0.02	+0.03	+0.03	+0.02	+0.02	+0.02	+0.02	+0.03	+0.01	+0.05	+0.02
	−40	−0.008	−0.1	−0.2	−1.3	−0.12		−0.01	−0.03	−0.03	−0.02	−0.01	−0.02	−0.03	−0.02	−0.01	−0.04	−0.02
Sys.	+310	+0.100	+0.1	+0.1	+0.7	+0.75	…	+0.13	+0.08	+0.08	+0.02	+0.05	+0.05	+0.05	+0.05	+0.04	+0.06	+0.06
	−300	−0.100	−0.1	−0.2	−1.3	−0.76		−0.16	−0.08	−0.09	−0.04	−0.03	−0.06	−0.05	−0.07	−0.04	−0.06	−0.08
8	15 310	3.800	21.6	42.2	42.6	0.90	…	−0.87	−3.47	−4.00	−3.30	−4.09	−4.71	−6.00	−4.42	−4.87	…	−4.66
Stat.	+40	+0.009	+0.2	+1.2	+0.7	+0.13	…	+0.01	+0.02	+0.03	+0.01	+0.02	+0.02	+0.05	+0.03	+0.01	…	+0.02
	−30	−0.004	−0.2	−0.5	−1.0	−0.13		−0.02	−0.02	−0.04	−0.03	−0.02	−0.02	−0.04	−0.02	−0.02		−0.02
Sys.	+310	+0.100	+0.2	+0.5	+0.3	+1.15	…	+0.12	+0.08	+0.08	+0.03	+0.02	+0.07	+0.06	+0.13	+0.02	…	+0.07
	−310	−0.100	−0.2	−0.3	−0.1	−0.90		−0.13	−0.08	−0.09	−0.05	−0.02	−0.07	−0.05	−0.15	−0.04		−0.08
9	15 400	3.522	−18.5	15.3	7.6	1.56	…	−1.00	−3.59	−4.21	−3.20	−4.08	−4.66	−5.87	−4.39	−4.94	−5.53	−4.65
Stat.	+40	+0.007	+0.1	+0.2	+0.4	+0.11	…	+0.02	+0.02	+0.03	+0.02	+0.01	+0.02	+0.03	+0.03	+0.02	+0.03	+0.01
	−50	−0.009	−0.1	−0.4	−0.4	−0.15		−0.01	−0.02	−0.03	−0.02	−0.02	−0.02	−0.04	−0.02	−0.01	−0.04	−0.02
Sys.	+310	+0.100	+0.1	+0.1	+0.5	+0.79	…	+0.14	+0.08	+0.09	+0.02	+0.01	+0.08	+0.04	+0.09	+0.03	+0.07	+0.05
	−310	−0.100	−0.1	−0.1	−0.5	−0.99		−0.14	−0.09	−0.08	−0.03	−0.02	−0.07	−0.06	−0.09	−0.03	−0.06	−0.06
10	15 680	3.945	−16.6	23.1	16.5	1.52	…	−1.02	−3.74	−4.40	−3.33	−4.23	−4.74	−6.01	−4.48	−5.05	…	−4.72
Stat.	+30	+0.005	+0.1	+0.5	+0.4	+0.15	…	+0.02	+0.03	+0.05	+0.02	+0.02	+0.02	+0.04	+0.03	+0.02	…	+0.02
	−80	−0.015	−0.2	−0.4	−0.7	−0.17		−0.02	−0.02	−0.05	−0.03	−0.02	−0.03	−0.04	−0.02	−0.01		−0.03
Sys.	+320	+0.100	+0.1	+0.3	+0.3	+0.92	…	+0.13	+0.07	+0.08	+0.03	+0.03	+0.07	+0.06	+0.09	+0.03	…	+0.06
	−320	−0.100	−0.1	−0.1	−0.7	−1.03		−0.13	−0.08	−0.08	−0.04	−0.03	−0.08	−0.06	−0.11	−0.03		−0.10
$\odot^{(a)}$								−1.06	−3.57	−4.17	−3.31	−4.07	−4.40	−5.55	−4.49	−4.88	−5.60	−4.50
								+0.01	+0.05	+0.05	+0.05	+0.10	+0.04	+0.03	+0.04	+0.03	+0.13	+0.04
								−0.01	−0.05	−0.05	−0.05	−0.10	−0.04	−0.03	−0.04	−0.03	−0.13	−0.04

Table D.3: continued.

#	$T_{\rm eff}$	log g	$v_{\rm rad}$	$v \sin(i)$	ζ	ξ	$A_{\rm eff,s}/A_{\rm eff,p}$	log($n(x)$)										
	(K)	(cgs)	(km s^{-1})					He	C	N	O	Ne	Mg	Al	Si	S	Ar	Fe
11	15 820	3.553	−22.9	24.8	21.1	1.94	…	−0.99	−3.54	−4.17	−3.23	−4.05	−4.67	−5.91	−4.45	−4.93	−5.55	−4.68
Stat.	+40	+0.007	+0.2	+0.2	+0.4	+0.10	…	+0.01	+0.02	+0.02	+0.02	+0.01	+0.02	+0.03	+0.02	+0.01	+0.04	+0.02
	−40	−0.006	−0.1	−0.8	−0.4	−0.13		−0.02	−0.02	−0.02	−0.02	−0.01	−0.02	−0.05	−0.02	−0.02	−0.05	−0.01
Sys.	+320	+0.100	+0.3	+0.2	+0.3	+0.81	…	+0.13	+0.07	+0.08	+0.01	+0.02	+0.08	+0.05	+0.13	+0.02	+0.09	+0.04
	−330	−0.100	−0.2	−0.1	−0.6	−1.23		−0.15	−0.09	−0.08	−0.04	−0.02	−0.08	−0.07	−0.17	−0.03	−0.11	−0.08
12p	16 120	3.213	−20.6	10.7	18.6	3.49	…	−1.02	−3.62	−4.26	−3.22	−4.02	−4.64	−5.76	−4.49	−4.90	−5.59	−4.66
Stat.	+40	+0.021	+0.2	+0.7	+1.7	+0.19	…	+0.01	+0.03	+0.02	+0.02	+0.01	+0.03	+0.02	+0.02	+0.01	+0.03	+0.02
	−60	−0.019	−0.3	−0.8	−1.0	−0.16		−0.02	−0.03	−0.02	−0.02	−0.01	−0.02	−0.03	−0.03	−0.01	−0.03	−0.01
Sys.	+320	+0.100	+0.2	+0.4	+0.2	+0.09	…	+0.03	+0.04	+0.04	+0.03	+0.01	+0.03	+0.01	+0.01	+0.01	+0.02	+0.01
	−330	−0.100	−0.3	−0.8	−0.1	−0.07		−0.03	−0.04	−0.05	−0.03	−0.01	−0.03	−0.02	−0.02	−0.01	−0.03	−0.01
12s	16 240	3.330	8.0	18.5	2.4	3.35	0.758	…	…	…	…	…	…	…	…	…	…	…
Stat.	+80	+0.030	+0.3	+0.8	+2.8	+0.20	+0.042	…	…	…	…	…	…	…	…	…	…	…
	−70	−0.028	−0.4	−0.6	−2.4	−0.19	−0.030											
Sys.	+330	+0.103	+0.2	+0.2	+2.3	+0.17	+0.064	…	…	…	…	…	…	…	…	…	…	…
	−330	−0.153	−0.4	−0.1	−2.4	−0.15	−0.038											
13p	16 440	4.058	42.8	16.4	0.0	1.79	…	−0.97	−3.57	−4.15	−3.28	−4.09	−4.73	−5.97	−4.46	−4.92	−5.50	−4.72
Stat.	+80	+0.035	+0.3	+0.1	+1.4	+0.25	…	+0.02	+0.02	+0.03	+0.02	+0.02	+0.02	+0.04	+0.02	+0.01	+0.04	+0.02
	−90	−0.036	−0.4	−0.3	−0.0	−0.30		−0.01	−0.03	−0.02	−0.02	−0.02	−0.02	−0.05	−0.02	−0.01	−0.04	−0.02
Sys.	+340	+0.100	+0.2	+0.2	+0.1	+0.29	…	+0.03	+0.03	+0.04	+0.01	+0.01	+0.02	+0.01	+0.01	+0.01	+0.03	+0.02
	−330	−0.100	−0.4	−0.1	−0.0	−0.51		−0.02	−0.03	−0.03	−0.01	−0.01	−0.02	−0.03	−0.01	−0.01	−0.02	−0.03
13s	16 180	4.127	27.5	6.9	13.2	1.11	0.796	…	…	…	…	…	…	…	…	…	…	…
Stat.	+120	+0.050	+0.3	+1.0	+1.2	+0.36	+0.062	…	…	…	…	…	…	…	…	…	…	…
	−100	−0.042	−0.3	−0.8	−2.7	−0.40	−0.054											
Sys.	+330	+0.100	+0.3	+0.8	+0.2	+0.57	+0.097	…	…	…	…	…	…	…	…	…	…	…
	−330	−0.165	−0.3	−0.3	−0.1	−0.46	−0.074											
14p	16 680	4.098	−84.7	7.9	11.4	2.10	…	−0.96	−3.55	−4.16	−3.25	−4.04	−4.73	−5.86	−4.45	−4.91	−5.58	−4.66
Stat.	+100	+0.027	+0.1	+1.9	+1.0	+0.17	…	+0.02	+0.03	+0.03	+0.02	+0.02	+0.04	+0.05	+0.03	+0.02	+0.06	+0.03
	− 90	−0.021	−0.2	−1.3	−2.2	−0.19		−0.02	−0.03	−0.04	−0.03	−0.03	−0.03	−0.04	−0.03	−0.03	−0.08	−0.03
Sys.	+330	+0.100	+0.1	+1.2	+0.5	+0.25	…	+0.06	+0.06	+0.06	+0.01	+0.01	+0.04	+0.03	+0.01	+0.02	+0.04	+0.04
	−340	−0.100	−0.1	−0.2	−1.7	−0.29		−0.06	−0.06	−0.06	−0.02	−0.02	−0.03	−0.03	−0.03	−0.03	−0.05	−0.05
14s	13 490	4.274	125.0	28.3	15.6	0.79	0.642	…	…	…	…	…	…	…	…	…	…	…
Stat.	+90	+0.030	+0.5	+1.1	+3.1	+0.32	+0.015	…	…	…	…	…	…	…	…	…	…	…
	−80	−0.025	−0.4	−1.5	−2.0	−0.31	−0.013											
Sys.	+270	+0.100	+0.1	+0.2	+1.6	+0.23	+0.027	…	…	…	…	…	…	…	…	…	…	…
	−280	−0.102	−0.2	−0.3	−0.7	−0.23	−0.028											
15	16 810	4.159	11.8	28.7	17.3	1.36	…	−0.97	−3.58	−4.07	−3.21	−4.10	−4.68	−5.84	−4.45	−4.90	−5.46	−4.68
Stat.	+60	+0.009	+0.2	+0.2	+0.6	+0.16	…	+0.01	+0.03	+0.03	+0.02	+0.02	+0.02	+0.05	+0.02	+0.01	+0.06	+0.03
	−40	−0.008	−0.1	−0.6	−0.7	−0.18		−0.02	−0.02	−0.03	−0.02	−0.02	−0.02	−0.04	−0.03	−0.02	−0.03	−0.02
Sys.	+340	+0.100	+0.1	+0.2	+0.4	+1.22	…	+0.10	+0.08	+0.08	+0.04	+0.01	+0.09	+0.03	+0.11	+0.03	+0.08	+0.05
	−340	−0.100	−0.1	−0.1	−0.4	−1.31		−0.12	−0.09	−0.08	−0.05	−0.01	−0.09	−0.04	−0.14	−0.04	−0.08	−0.09
16	17 540	3.741	−31.5	0.0	7.2	1.66	…	−1.02	−3.56	−4.17	−3.19	−3.99	−4.60	−5.69	−4.44	−4.85	−5.56	−4.64
Stat.	+40	+0.006	+0.1	+2.1	+0.2	+0.14	…	+0.01	+0.02	+0.01	+0.01	+0.01	+0.02	+0.02	+0.02	+0.01	+0.02	+0.02
	−40	−0.006	−0.1	−0.0	−0.4	−0.13		−0.02	−0.01	−0.02	−0.02	−0.02	−0.02	−0.02	−0.02	−0.02	−0.02	−0.01
Sys.	+360	+0.100	+0.1	+0.1	+0.5	+0.83	…	+0.12	+0.08	+0.08	+0.07	+0.02	+0.08	+0.06	+0.10	+0.02	+0.05	+0.01
	−350	−0.100	−0.1	−0.0	−1.0	−1.07		−0.12	−0.06	−0.08	−0.07	−0.03	−0.09	−0.07	−0.10	−0.03	−0.03	−0.02
17	17 760	3.277	−12.2	33.7	41.6	5.46	…	−1.07	−3.63	−4.20	−3.25	−4.02	−4.69	−5.66	−4.49	−4.87	−5.67	−4.67
Stat.	+40	+0.004	+0.2	+0.3	+0.6	+0.07	…	+0.01	+0.02	+0.01	+0.01	+0.02	+0.02	+0.02	+0.01	+0.01	+0.02	+0.02
	−40	−0.006	−0.2	−0.4	−0.2	−0.10		−0.02	−0.02	−0.02	−0.02	−0.01	−0.02	−0.02	−0.02	−0.01	−0.02	−0.01
Sys.	+360	+0.100	+0.2	+0.4	+0.4	+0.54	…	+0.18	+0.07	+0.09	+0.14	+0.04	+0.16	+0.03	+0.18	+0.05	+0.07	+0.03
	−360	−0.100	−0.2	−0.9	−0.1	−1.39		−0.14	−0.06	−0.08	−0.11	−0.03	−0.10	−0.04	−0.09	−0.04	−0.06	−0.02
18	17 780	3.647	−15.0	40.9	18.0	1.29	…	−1.06	−3.65	−4.29	−3.21	−4.09	−4.65	−5.75	−4.53	−4.88	−5.59	−4.73
Stat.	+100	+0.015	+0.3	+0.4	+1.2	+0.50	…	+0.03	+0.03	+0.04	+0.03	+0.03	+0.04	+0.05	+0.04	+0.02	+0.06	+0.05
	− 80	−0.015	−0.3	−0.3	−1.3	−0.28		−0.02	−0.04	−0.04	−0.03	−0.03	−0.04	−0.05	−0.05	−0.03	−0.07	−0.04
Sys.	+360	+0.100	+0.1	+0.3	+0.7	+1.10	…	+0.12	+0.08	+0.09	+0.08	+0.03	+0.12	+0.02	+0.12	+0.03	+0.08	+0.02
	−360	−0.100	−0.1	−0.1	−1.3	−1.29		−0.09	−0.07	−0.08	−0.09	−0.03	−0.11	−0.04	−0.10	−0.03	−0.08	−0.03
$\odot^{(a)}$								−1.06	−3.57	−4.17	−3.31	−4.07	−4.40	−5.55	−4.49	−4.88	−5.60	−4.50
								+0.01	+0.05	+0.05	+0.05	+0.10	+0.04	+0.03	+0.04	+0.03	+0.13	+0.04
								−0.01	−0.05	−0.05	−0.05	−0.10	−0.04	−0.03	−0.04	−0.03	−0.13	−0.04

Table D.3: continued.

#	$T_{\rm eff}$	log g	$v_{\rm rad}$	$v \sin(i)$	ζ	ξ	$A_{\rm eff,s}/A_{\rm eff,p}$	log($n(x)$)										
	(K)	(cgs)	($\rm km\,s^{-1}$)					He	C	N	O	Ne	Mg	Al	Si	S	Ar	Fe
19	17 810	3.643	−14.3	7.4	5.6	1.81	…	−1.03	−3.64	−4.27	−3.19	−4.06	−4.66	−5.70	−4.51	−4.90	−5.61	−4.66
Stat.	+70	+0.012	+0.1	+0.6	+0.9	+0.25	…	+0.02	+0.04	+0.03	+0.02	+0.02	+0.03	+0.03	+0.04	+0.02	+0.03	+0.02
	−60	−0.010	−0.1	−0.7	−1.2	−0.27		−0.02	−0.03	−0.03	−0.02	−0.02	−0.03	−0.02	−0.04	−0.02	−0.04	−0.03
Sys.	+360	+0.100	+0.1	+0.2	+0.5	+0.67	…	+0.10	+0.07	+0.08	+0.04	+0.03	+0.09	+0.05	+0.08	+0.03	+0.03	+0.01
	−370	−0.100	−0.1	−0.2	−1.2	−0.88		−0.09	−0.07	−0.08	−0.05	−0.02	−0.10	−0.06	−0.09	−0.04	−0.05	−0.03
20	18 600	3.845	−13.7	79.6	76.8	2.70	…	−1.15	−3.84	−4.10	−3.19	−4.18	−4.79	−5.82	−4.56	−4.88	−5.68	−4.75
Stat.	+70	+0.008	+0.3	+3.1	+1.9	+0.22	…	+0.02	+0.02	+0.02	+0.03	+0.03	+0.04	+0.04	+0.03	+0.02	+0.05	+0.03
	−60	−0.007	−0.4	−0.3	−2.0	−0.18		−0.01	−0.03	−0.03	−0.02	−0.03	−0.03	−0.04	−0.03	−0.02	−0.05	−0.04
Sys.	+370	+0.100	+0.3	+1.2	+6.2	+2.24	…	+0.14	+0.08	+0.10	+0.11	+0.04	+0.13	+0.05	+0.13	+0.05	+0.15	+0.02
	−380	−0.100	−0.2	−0.9	−2.9	−0.70		−0.15	−0.13	−0.11	−0.15	−0.04	−0.20	−0.08	−0.25	−0.09	−0.20	−0.06
21	19 090	3.597	18.5	25.2	17.8	2.53	…	−1.03	−3.70	−4.26	−3.22	−4.02	−4.58	−5.73	−4.53	−4.87	−5.58	−4.68
Stat.	+50	+0.005	+0.2	+0.1	+0.3	+0.12	…	+0.01	+0.02	+0.01	+0.02	+0.02	+0.01	+0.02	+0.03	+0.01	+0.02	+0.02
	−40	−0.005	−0.1	−1.1	−0.3	−0.10		−0.02	−0.02	−0.02	−0.02	−0.01	−0.02	−0.02	−0.02	−0.01	−0.02	−0.01
Sys.	+390	+0.100	+0.1	+0.2	+0.6	+1.08	…	+0.09	+0.08	+0.07	+0.10	+0.04	+0.09	+0.06	+0.14	+0.06	+0.04	+0.04
	−380	−0.100	−0.1	−0.1	−0.8	−1.18		−0.09	−0.07	−0.08	−0.12	−0.03	−0.12	−0.08	−0.15	−0.06	−0.05	−0.05
22	19 250	4.052	30.7	7.3	17.1	1.99	…	−1.00	−3.64	−4.23	−3.21	−4.06	−4.60	−5.71	−4.48	−4.89	−5.57	−4.63
Stat.	+60	+0.007	+0.2	+0.4	+0.5	+0.14	…	+0.01	+0.03	+0.02	+0.02	+0.02	+0.02	+0.03	+0.03	+0.02	+0.03	+0.02
	−50	−0.007	−0.1	−0.5	−1.1	−0.26		−0.02	−0.02	−0.02	−0.02	−0.02	−0.03	−0.02	−0.03	−0.01	−0.03	−0.02
Sys.	+390	+0.100	+0.1	+0.7	+0.2	+1.08	…	+0.08	+0.07	+0.08	+0.10	+0.03	+0.11	+0.06	+0.13	+0.05	+0.04	+0.01
	−390	−0.100	−0.1	−1.8	−0.1	−1.56		−0.09	−0.07	−0.08	−0.11	−0.03	−0.13	−0.07	−0.14	−0.05	−0.05	−0.03
23	19 910	4.005	26.3	84.1	3.7	1.02	…	−1.10	−3.73	−4.19	−3.10	−4.20	−4.65	−5.83	−4.47	−4.97	−5.67	−4.73
Stat.	+60	+0.007	+0.3	+0.1	+6.3	+0.25	…	+0.01	+0.02	+0.02	+0.02	+0.03	+0.03	+0.03	+0.03	+0.02	+0.05	+0.03
	−60	−0.008	−0.3	−0.1	−3.3	−0.24		−0.02	−0.02	−0.02	−0.02	−0.03	−0.03	−0.03	−0.02	−0.03	−0.04	−0.04
Sys.	+400	+0.100	+0.3	+0.3	+8.1	+2.42	…	+0.08	+0.06	+0.07	+0.10	+0.03	+0.10	+0.06	+0.11	+0.06	+0.14	+0.02
	−410	−0.100	−0.2	−0.1	−0.4	−1.02		−0.08	−0.10	−0.11	−0.19	−0.04	−0.16	−0.09	−0.25	−0.07	−0.17	−0.06
24p	20 110	4.216	23.6	0.0	21.5	2.37	…	−0.96	−3.64	−4.23	−3.24	−4.06	−4.61	−5.74	−4.54	−4.87	−5.53	−4.66
Stat.	+30	+0.004	+0.2	+2.4	+0.1	+0.16	…	+0.01	+0.02	+0.01	+0.01	+0.02	+0.03	+0.03	+0.03	+0.01	+0.03	+0.02
	−40	−0.004	−0.1	−0.0	−1.0	−0.09		−0.01	−0.02	−0.02	−0.02	−0.02	−0.02	−0.02	−0.02	−0.01	−0.03	−0.02
Sys.	+400	+0.100	+0.2	+3.0	+0.1	+0.27	…	+0.02	+0.02	+0.05	+0.06	+0.02	+0.03	+0.04	+0.05	+0.02	+0.01	+0.03
	−410	−0.100	−0.1	−0.0	−0.1	−0.23		−0.03	−0.03	−0.06	−0.07	−0.01	−0.02	−0.04	−0.05	−0.02	−0.02	−0.03
24s	17 380	4.202	31.9	32.2	0.0	0.08	0.707	…	…	…	…	…	…	…	…	…	…	…
Stat.	+60	+0.003	+0.3	+0.6	+5.0	+0.42	+0.029	…	…	…	…	…	…	…	…	…	…	…
	−60	−0.004	−0.4	−0.4	−0.0	−0.08	−0.026											
Sys.	+460	+0.124	+0.9	+0.3	+0.1	+0.51	+0.137	…	…	…	…	…	…	…	…	…	…	…
	−360	−0.161	−0.9	−0.1	−0.0	−0.08	−0.127											
25	20 450	3.631	29.0	7.9	9.9	2.95	…	−0.99	−3.67	−4.32	−3.29	−4.00	−4.59	−5.76	−4.57	−4.87	−5.57	−4.66
Stat.	+60	+0.007	+0.1	+0.9	+0.9	+0.12	…	+0.02	+0.02	+0.02	+0.02	+0.02	+0.03	+0.02	+0.02	+0.01	+0.02	+0.01
	−60	−0.007	−0.1	−1.0	−1.1	−0.11		−0.01	−0.02	−0.01	−0.02	−0.02	−0.02	−0.02	−0.03	−0.02	−0.02	−0.02
Sys.	+420	+0.100	+0.1	+0.4	+1.1	+0.87	…	+0.07	+0.04	+0.06	+0.11	+0.04	+0.12	+0.05	+0.13	+0.06	+0.03	+0.04
	−410	−0.100	−0.1	−0.5	−1.1	−0.72		−0.06	−0.04	−0.05	−0.10	−0.04	−0.11	−0.05	−0.12	−0.07	−0.03	−0.04
26	20 590	3.845	−10.9	0.0	6.5	2.07	…	−1.02	−3.76	−4.36	−3.30	−4.04	−4.68	−5.83	−4.69	−4.96	−5.63	−4.72
Stat.	+70	+0.008	+0.1	+4.4	+0.3	+0.17	…	+0.02	+0.02	+0.02	+0.02	+0.02	+0.03	+0.03	+0.04	+0.02	+0.03	+0.02
	−70	−0.009	−0.1	−0.0	−2.2	−0.28		−0.02	−0.02	−0.01	−0.02	−0.02	−0.03	−0.03	−0.04	−0.02	−0.03	−0.03
Sys.	+420	+0.100	+0.1	+0.7	+0.7	+0.71	…	+0.06	+0.03	+0.07	+0.07	+0.04	+0.12	+0.04	+0.09	+0.06	+0.02	+0.02
	−420	−0.100	−0.1	−0.0	−1.2	−1.19		−0.06	−0.04	−0.05	−0.07	−0.03	−0.10	−0.04	−0.08	−0.06	−0.02	−0.03
27p	20 590	3.485	−11.2	54.2	9.4	6.04	…	−1.02	−3.79	−4.38	−3.39	−4.02	−4.74	−5.87	−4.66	−4.98	−5.59	−4.78
Stat.	+30	+0.004	+0.3	+0.1	+0.1	+0.09	…	+0.01	+0.02	+0.01	+0.02	+0.02	+0.02	+0.02	+0.02	+0.01	+0.02	+0.02
	−40	−0.005	−0.2	−0.1	−2.2	−0.08		−0.02	−0.02	−0.02	−0.01	−0.02	−0.03	−0.02	−0.02	−0.02	−0.03	−0.02
Sys.	+420	+0.100	+0.1	+0.3	+1.7	+0.60	…	+0.01	+0.02	+0.02	+0.06	+0.02	+0.02	+0.02	+0.03	+0.01	+0.01	+0.02
	−410	−0.100	−0.1	−0.1	−3.2	−0.61		−0.02	−0.01	−0.03	−0.04	−0.01	−0.02	−0.03	−0.03	−0.03	−0.03	−0.02
27s	18 610	3.227	−9.1	134.0	59.5	2.90	0.936	…	…	…	…	…	…	…	…	…	…	…
Stat.	+50	+0.004	+1.1	+0.1	+4.3	+0.18	+0.014	…	…	…	…	…	…	…	…	…	…	…
	−70	−0.006	−1.0	−0.6	−4.7	−0.18	−0.015											
Sys.	+460	+0.148	+0.3	+0.5	+2.2	+0.96	+0.069	…	…	…	…	…	…	…	…	…	…	…
	−370	−0.130	−0.2	−0.8	−1.8	−0.82	−0.060											
$\odot^{(a)}$								−1.06	−3.57	−4.17	−3.31	−4.07	−4.40	−5.55	−4.49	−4.88	−5.60	−4.50
								+0.01	+0.05	+0.05	+0.05	+0.10	+0.04	+0.03	+0.04	+0.03	+0.13	+0.04
								−0.01	−0.05	−0.05	−0.05	−0.10	−0.04	−0.03	−0.04	−0.03	−0.13	−0.04

Table D.3: continued.

#	$T_{\rm eff}$	log g	$v_{\rm rad}$	$v \sin(i)$	ζ	ξ	$A_{\rm eff,s}/A_{\rm eff,p}$	log($n(x)$)										
	(K)	(cgs)	(km s^{-1})					He	C	N	O	Ne	Mg	Al	Si	S	Ar	Fe
28	21 060	3.760	0.4	11.8	16.6	2.56	...	−0.97	−3.79	−3.88	−3.26	−4.01	−4.53	−5.71	−4.51	−4.84	−5.55	−4.60
Stat.	+50	+0.005	+0.1	+0.1	+0.3	+0.10	...	+0.01	+0.02	+0.01	+0.02	+0.02	+0.02	+0.02	+0.03	+0.01	+0.02	+0.02
	−50	−0.006	−0.1	−0.3	−0.4	−0.11		−0.01	−0.01	−0.02	−0.02	−0.02	−0.03	−0.02	−0.02	−0.01	−0.02	−0.02
Sys.	+430	+0.100	+0.1	+0.4	+0.1	+0.76	...	+0.06	+0.04	+0.06	+0.08	+0.04	+0.09	+0.04	+0.10	+0.06	+0.05	+0.04
	−420	−0.100	−0.1	−0.7	−0.1	−0.76		−0.07	−0.03	−0.07	−0.11	−0.04	−0.09	−0.05	−0.11	−0.05	−0.04	−0.04
29	21 160	4.262	37.9	4.7	9.5	1.73	...	−1.00	−3.71	−4.29	−3.26	−4.02	−4.63	−5.80	−4.62	−4.90	−5.58	−4.68
Stat.	+70	+0.009	+0.1	+1.6	+1.1	+0.29	...	+0.01	+0.02	+0.02	+0.02	+0.02	+0.03	+0.03	+0.03	+0.02	+0.02	+0.02
	−70	−0.007	−0.1	−2.5	−1.3	−0.30		−0.02	−0.02	−0.02	−0.03	−0.02	−0.04	−0.02	−0.03	−0.02	−0.03	−0.02
Sys.	+430	+0.100	+0.1	+0.9	+0.6	+0.93	...	+0.06	+0.06	+0.07	+0.10	+0.04	+0.12	+0.06	+0.12	+0.05	+0.02	+0.02
	−430	−0.100	−0.1	−1.1	−0.9	−1.65		−0.06	−0.05	−0.06	−0.11	−0.03	−0.11	−0.05	−0.10	−0.06	−0.02	−0.04
30	21 950	4.206	22.5	9.7	8.2	2.02	...	−1.01	−3.70	−4.30	−3.25	−4.03	−4.59	−5.78	−4.62	−4.88	−5.58	−4.65
Stat.	+80	+0.009	+0.1	+0.6	+0.8	+0.15	...	+0.02	+0.02	+0.02	+0.02	+0.02	+0.03	+0.02	+0.03	+0.02	+0.03	+0.02
	−80	−0.008	−0.1	−0.7	−0.9	−0.31		−0.01	−0.02	−0.02	−0.03	−0.03	−0.03	−0.02	−0.03	−0.01	−0.02	−0.02
Sys.	+440	+0.100	+0.1	+0.3	+0.8	+0.71	...	+0.06	+0.04	+0.06	+0.09	+0.03	+0.11	+0.06	+0.09	+0.06	+0.05	+0.03
	−450	−0.100	−0.1	−0.3	−1.1	−1.32		−0.05	−0.03	−0.05	−0.11	−0.04	−0.10	−0.05	−0.09	−0.05	−0.03	−0.04
31	22 250	3.059	34.4	131.4	42.1	18.75	...	−1.32	−3.93	−4.47	−3.53	−4.09	−4.72	−5.83	−4.80	−5.22	...	−4.81
Stat.	+80	+0.007	+0.4	+0.1	+1.7	+0.13	...	+0.02	+0.03	+0.01	+0.01	+0.04	+0.02	+0.02	+0.02	+0.03		+0.02
	−70	−0.002	−0.3	−0.8	−1.7	−0.22		−0.02	−0.02	−0.02	−0.02	−0.04	−0.02	−0.02	−0.01	−0.02	...	−0.01
Sys.	+450	+0.100	+0.4	+0.4	+6.1	+1.25	...	+0.14	+0.02	+0.06	+0.05	+0.01	+0.07	+0.06	+0.04	+0.03		+0.06
	−450	−0.100	−0.3	−0.1	−7.2	−1.28		−0.13	−0.03	−0.05	−0.06	−0.02	−0.07	−0.05	−0.03	−0.02	...	−0.04
32	22 770	3.376	26.6	0.0	40.5	11.74	...	−1.14	−3.92	−4.01	−3.43	−4.04	−4.68	−5.75	−4.67	−5.04	−5.53	−4.73
Stat.	+30	+0.003	+0.2	+0.9	+0.1	+0.08	...	+0.01	+0.02	+0.01	+0.01	+0.02	+0.02	+0.02	+0.02	+0.02	+0.03	+0.01
	−10	−0.003	−0.1	−0.0	−0.1	−0.08		−0.01	−0.02	−0.01	−0.01	−0.02	−0.02	−0.01	−0.01	−0.02	−0.02	−0.01
Sys.	+470	+0.100	+0.2	+9.1	+0.4	+0.87	...	+0.11	+0.03	+0.05	+0.07	+0.01	+0.09	+0.06	+0.05	+0.01	+0.09	+0.03
	−460	−0.100	−0.1	−0.0	−0.1	−1.28		−0.09	−0.04	−0.03	−0.04	−0.03	−0.08	−0.05	−0.02	−0.01	−0.08	−0.03
33	22 790	4.192	22.1	16.4	11.8	1.96	...	−1.02	−3.74	−4.28	−3.28	−4.06	−4.58	−5.77	−4.61	−4.91	−5.58	−4.67
Stat.	+60	+0.007	+0.1	+0.3	+0.3	+0.13	...	+0.01	+0.01	+0.01	+0.02	+0.02	+0.02	+0.01	+0.02	+0.02	+0.02	+0.01
	−50	−0.006	−0.1	−0.2	−0.4	−0.13		−0.01	−0.02	−0.02	−0.01	−0.02	−0.02	−0.02	−0.02	−0.01	−0.02	−0.02
Sys.	+460	+0.100	+0.1	+0.1	+0.7	+0.84	...	+0.05	+0.02	+0.04	+0.09	+0.03	+0.10	+0.04	+0.09	+0.06	+0.06	+0.03
	−460	−0.100	−0.1	−0.1	−1.1	−1.63		−0.05	−0.02	−0.04	−0.10	−0.03	−0.09	−0.05	−0.09	−0.06	−0.06	−0.04
34	23 100	3.901	46.9	2.2	6.6	1.39	...	−0.96	−3.90	−4.12	−3.34	−4.09	−4.61	−5.86	−4.70	−4.95	−5.66	−4.72
Stat.	+130	+0.020	+0.2	+3.7	+0.8	+0.51	...	+0.03	+0.04	+0.02	+0.04	+0.04	+0.06	+0.03	+0.05	+0.04	+0.08	+0.04
	−140	−0.020	−0.1	−2.2	−3.3	−0.51		−0.03	−0.04	−0.03	−0.03	−0.05	−0.07	−0.04	−0.05	−0.04	−0.08	−0.03
Sys.	+460	+0.100	+0.1	+1.4	+0.9	+0.75	...	+0.04	+0.03	+0.03	+0.07	+0.03	+0.07	+0.01	+0.03	+0.04	+0.06	+0.04
	−470	−0.100	−0.1	−2.2	−0.5	−0.85		−0.05	−0.02	−0.02	−0.07	−0.05	−0.08	−0.01	−0.03	−0.06	−0.06	−0.02
35	23 280	3.595	41.1	153.7	33.1	7.91	...	−1.08	−3.87	−4.35	−3.48	−4.09	−4.67	−5.72	−4.71	−5.01	...	−4.83
Stat.	+30	+0.003	+0.4	+0.1	+3.2	+0.06	...	+0.01	+0.02	+0.02	+0.01	+0.03	+0.02	+0.02	+0.01	+0.03		+0.02
	−30	−0.003	−0.3	−0.1	−1.1	−0.08		−0.01	−0.02	−0.01	−0.01	−0.03	−0.03	−0.02	−0.02	−0.02	...	−0.01
Sys.	+470	+0.100	+1.0	+0.6	+5.9	+1.46	...	+0.11	+0.05	+0.05	+0.09	+0.03	+0.09	+0.05	+0.09	+0.06		+0.02
	−470	−0.100	−1.0	−0.1	−7.1	−1.37		−0.11	−0.06	−0.03	−0.10	−0.03	−0.09	−0.05	−0.08	−0.07	...	−0.01
36	23 620	4.062	19.8	12.5	8.0	1.63	...	−1.02	−3.75	−4.31	−3.28	−4.04	−4.57	−5.78	−4.62	−4.90	−5.58	−4.68
Stat.	+50	+0.006	+0.1	+0.2	+0.2	+0.26	...	+0.01	+0.01	+0.01	+0.01	+0.01	+0.02	+0.01	+0.01	+0.01	+0.02	+0.01
	−50	−0.005	−0.1	−0.4	−0.2	−0.10		−0.01	−0.02	−0.01	−0.01	−0.02	−0.03	−0.02	−0.02	−0.01	−0.02	−0.01
Sys.	+480	+0.100	+0.1	+0.1	+0.8	+0.97	...	+0.04	+0.01	+0.03	+0.08	+0.03	+0.10	+0.02	+0.08	+0.05	+0.06	+0.02
	−480	−0.100	−0.1	−0.1	−1.0	−1.50		−0.05	−0.02	−0.02	−0.08	−0.04	−0.10	−0.04	−0.08	−0.05	−0.07	−0.02
37	23 630	3.869	19.7	116.1	0.0	4.46	...	−1.13	−3.98	−4.37	−3.26	−4.23	−4.79	−5.84	−4.74	−4.93	...	−4.66
Stat.	+90	+0.010	+0.3	+0.1	+1.3	+0.12	...	+0.01	+0.02	+0.01	+0.01	+0.05	+0.03	+0.03	+0.02	+0.03		+0.01
	−40	−0.003	−0.4	−0.1	−0.0	−0.10		−0.02	−0.03	−0.01	−0.02	−0.04	−0.03	−0.02	−0.03	−0.03	...	−0.02
Sys.	+480	+0.100	+0.4	+0.1	+0.1	+1.70	...	+0.09	+0.04	+0.03	+0.13	+0.03	+0.05	+0.06	+0.12	+0.06		+0.03
	−480	−0.100	−0.4	−0.1	−0.0	−1.43		−0.11	−0.10	−0.04	−0.11	−0.03	−0.09	−0.06	−0.12	−0.07	...	−0.03
38	23 880	4.127	23.0	5.2	4.4	2.02	...	−0.98	−3.73	−4.30	−3.29	−4.00	−4.56	−5.79	−4.66	−4.88	−5.49	−4.71
Stat.	+70	+0.008	+0.1	+0.7	+2.0	+0.11	...	+0.01	+0.02	+0.01	+0.02	+0.02	+0.02	+0.01	+0.02	+0.02	+0.02	+0.02
	−70	−0.008	−0.1	−2.2	−0.7	−0.23		−0.02	−0.02	−0.01	−0.02	−0.02	−0.03	−0.02	−0.02	−0.01	−0.02	−0.02
Sys.	+480	+0.100	+0.1	+0.5	+0.8	+0.68	...	+0.04	+0.02	+0.03	+0.09	+0.04	+0.10	+0.03	+0.07	+0.06	+0.07	+0.03
	−480	−0.100	−0.1	−0.3	−1.5	−1.39		−0.06	−0.02	−0.02	−0.08	−0.04	−0.10	−0.03	−0.06	−0.06	−0.06	−0.02
$\odot^{(a)}$								−1.06	−3.57	−4.17	−3.31	−4.07	−4.40	−5.55	−4.49	−4.88	−5.60	−4.50
								+0.01	+0.05	+0.05	+0.05	+0.10	+0.04	+0.03	+0.04	+0.03	+0.13	+0.04
								−0.01	−0.05	−0.05	−0.05	−0.10	−0.04	−0.03	−0.04	−0.03	−0.13	−0.04

Table D.3: continued.

#	$T_{\rm eff}$	log g	$v_{\rm rad}$	$v \sin(i)$	ζ	ξ	$A_{\rm eff,s}/A_{\rm eff,p}$	log($n(x)$)										
	(K)	(cgs)		(km s^{-1})				He	C	N	O	Ne	Mg	Al	Si	S	Ar	Fe
39	23 890	3.233	37.3	100.1	39.3	14.81	…	−1.20	−3.92	−4.21	−3.50	−4.07	−4.68	−5.62	−4.71	−5.07	…	−4.63
Stat.	+ 60	+0.009	+0.5	+1.0	+2.1	+0.26	…	+0.01	+0.03	+0.01	+0.02	+0.04	+0.05	+0.02	+0.02	+0.03	…	+0.01
	−130	−0.012	−0.4	−0.4	−2.1	−0.27		−0.03	−0.02	−0.03	−0.01	−0.04	−0.04	−0.02	−0.02	−0.03		−0.02
Sys.	+490	+0.100	+0.2	+0.7	+2.9	+0.95	…	+0.12	+0.06	+0.05	+0.05	+0.01	+0.07	+0.06	+0.04	+0.03	…	+0.06
	−480	−0.100	−0.2	−0.1	−4.3	−0.95		−0.11	−0.07	−0.07	−0.03	−0.02	−0.06	−0.06	−0.03	−0.02		−0.06
40	24 150	4.185	25.2	68.7	0.0	2.23	…	−1.03	−3.80	−4.29	−3.30	−4.07	−4.67	−5.87	−4.74	−4.99	…	−4.76
Stat.	+30	+0.004	+0.2	+0.1	+1.7	+0.07	…	+0.01	+0.02	+0.02	+0.01	+0.03	+0.02	+0.02	+0.02	+0.03	…	+0.01
	−30	−0.004	−0.2	−0.1	−0.0	−0.07		−0.02	−0.02	−0.01	−0.01	−0.03	−0.02	−0.02	−0.02	−0.02		−0.02
Sys.	+490	+0.100	+0.1	+0.3	+1.5	+1.30	…	+0.06	+0.05	+0.04	+0.10	+0.02	+0.10	+0.02	+0.09	+0.06	…	+0.02
	−490	−0.100	−0.2	−0.1	−0.0	−2.22		−0.07	−0.08	−0.02	−0.10	−0.03	−0.10	−0.02	−0.08	−0.05		−0.03
40$^{(b)}$	23 840	4.147	25.2	68.9	0.0	2.84	…	−1.09	−3.85	−4.36	−3.30	−4.09	−4.73	−5.85	−4.73	−4.99	…	−4.84
Stat.	+20	+0.003	+0.2	+0.1	+2.8	+0.09	…	+0.01	+0.02	+0.01	+0.01	+0.04	+0.02	+0.02	+0.02	+0.03	…	+0.02
	−30	−0.002	−0.2	−0.1	−0.0	−0.06		−0.01	−0.02	−0.01	−0.01	−0.03	−0.02	−0.01	−0.02	−0.03		−0.02
Sys.	+480	+0.100	+0.1	+0.3	+0.4	+1.43	…	+0.06	+0.04	+0.04	+0.11	+0.03	+0.10	+0.04	+0.11	+0.06	…	+0.04
	−480	−0.100	−0.1	−0.1	−0.0	−1.97		−0.06	−0.04	−0.03	−0.12	−0.03	−0.11	−0.03	−0.11	−0.06		−0.03
41	24 370	4.249	27.9	35.2	3.2	2.50	…	−1.00	−3.82	−4.29	−3.30	−4.04	−4.65	−5.83	−4.68	−4.97	−5.63	−4.69
Stat.	+30	+0.003	+0.1	+0.1	+1.3	+0.09	…	+0.01	+0.02	+0.01	+0.02	+0.02	+0.02	+0.02	+0.02	+0.02	+0.05	+0.01
	−30	−0.004	−0.2	−0.1	−2.2	−0.10		−0.01	−0.03	−0.02	−0.01	−0.03	−0.02	−0.01	−0.02	−0.03	−0.05	−0.02
Sys.	+490	+0.100	+0.1	+0.2	+2.4	+1.13	…	+0.05	+0.04	+0.02	+0.10	+0.03	+0.08	+0.02	+0.07	+0.04	+0.10	+0.02
	−490	−0.100	−0.1	−0.1	−3.2	−0.50		−0.05	−0.06	−0.03	−0.10	−0.04	−0.10	−0.03	−0.09	−0.05	−0.11	−0.04
42p	24 990	3.800	−12.1	37.0	20.5	7.32	…	−1.10	−3.76	−4.30	−3.42	−4.05	−4.60	−5.70	−4.67	−5.04	−5.55	−4.61
Stat.	+ 40	+0.009	+0.7	+0.6	+0.7	+0.25	…	+0.01	+0.01	+0.01	+0.01	+0.02	+0.02	+0.01	+0.01	+0.02	+0.03	+0.01
	−110	−0.025	−0.2	−1.3	−1.2	−0.19		−0.01	−0.02	−0.01	−0.01	−0.02	−0.01	−0.02	−0.02	−0.02	−0.03	−0.01
Sys.	+500	+0.100	+0.9	+0.3	+0.7	+0.80	…	+0.01	+0.01	+0.01	+0.01	+0.01	+0.02	+0.01	+0.01	+0.01	+0.01	+0.01
	−510	−0.100	−0.7	−0.1	−1.6	−0.64		−0.01	−0.02	−0.02	−0.01	−0.01	−0.02	−0.02	−0.02	−0.01	−0.03	−0.01
42s	25 570	3.908	−39.4	21.7	29.5	6.27	0.813	…	…	…	…	…	…	…	…	…	…	…
Stat.	+100	+0.020	+0.5	+0.8	+2.7	+0.22	+0.074	…	…	…	…	…	…	…	…	…	…	…
	− 80	−0.014	−0.2	−0.4	−0.4	−0.27	−0.016											
Sys.	+520	+0.107	+0.7	+1.2	+0.2	+0.79	+0.108	…	…	…	…	…	…	…	…	…	…	…
	−520	−0.123	−0.2	−0.7	−0.1	−0.48	−0.060											
43	25 050	3.578	2.5	69.7	33.3	11.41	…	−1.17	−3.94	−4.23	−3.40	−4.03	−4.73	−5.62	−4.64	−4.98	…	−4.54
Stat.	+100	+0.011	+0.4	+0.4	+2.2	+0.25	…	+0.03	+0.03	+0.02	+0.03	+0.05	+0.04	+0.03	+0.02	+0.04	…	+0.02
	−240	−0.016	−0.3	−1.1	−1.5	−0.26		−0.03	−0.03	−0.02	−0.02	−0.05	−0.04	−0.02	−0.03	−0.03		−0.03
Sys.	+510	+0.100	+0.1	+0.2	+2.0	+0.84	…	+0.09	+0.04	+0.06	+0.06	+0.01	+0.05	+0.06	+0.05	+0.04	…	+0.06
	−500	−0.100	−0.1	−0.1	−2.0	−0.73		−0.09	−0.09	−0.06	−0.03	−0.02	−0.05	−0.06	−0.04	−0.01		−0.06
44	25 230	3.662	34.3	27.2	31.0	10.68	…	−1.15	−3.93	−4.33	−3.43	−4.11	−4.68	−5.70	−4.72	−5.08	…	−4.75
Stat.	+40	+0.002	+0.1	+0.3	+0.2	+0.04	…	+0.01	+0.02	+0.01	+0.01	+0.02	+0.02	+0.01	+0.01	+0.01	…	+0.01
	−50	−0.004	−0.1	−0.1	−1.4	−0.03		−0.02	−0.01	−0.01	−0.01	−0.03	−0.01	−0.02	−0.02	−0.02		−0.01
Sys.	+510	+0.100	+0.1	+1.2	+0.3	+1.08	…	+0.08	+0.01	+0.05	+0.05	+0.06	+0.07	+0.05	+0.06	+0.02	…	+0.06
	−510	−0.100	−0.1	−1.6	−0.1	−0.92		−0.10	−0.02	−0.05	−0.04	−0.09	−0.05	−0.07	−0.07	−0.02		−0.05
45	25 460	4.182	29.4	47.2	0.0	2.79	…	−1.05	−3.83	−4.31	−3.34	−4.07	−4.61	−5.81	−4.69	−4.94	−5.65	−4.72
Stat.	+20	+0.004	+0.1	+0.1	+0.4	+0.06	…	+0.01	+0.02	+0.01	+0.01	+0.03	+0.02	+0.02	+0.02	+0.03	+0.05	+0.01
	−40	−0.003	−0.2	−0.1	−0.0	−0.07		−0.02	−0.03	−0.01	−0.01	−0.02	−0.02	−0.01	−0.01	−0.02	−0.06	−0.02
Sys.	+510	+0.100	+0.1	+0.2	+0.1	+1.04	…	+0.04	+0.05	+0.03	+0.09	+0.02	+0.09	+0.05	+0.06	+0.03	+0.12	+0.02
	−520	−0.100	−0.1	−0.1	−0.0	−0.79		−0.05	−0.06	−0.03	−0.09	−0.02	−0.08	−0.04	−0.06	−0.04	−0.13	−0.03
45$^{(b)}$	25 500	4.185	29.7	47.5	0.0	2.70	…	−1.05	−3.85	−4.31	−3.33	−4.05	−4.61	−5.78	−4.69	−4.92	−5.69	−4.68
Stat.	+40	+0.009	+0.2	+0.1	+0.6	+0.14	…	+0.02	+0.03	+0.01	+0.01	+0.03	+0.03	+0.02	+0.01	+0.03	+0.06	+0.01
	−50	−0.004	−0.1	−0.1	−0.0	−0.11		−0.01	−0.02	−0.01	−0.02	−0.03	−0.02	−0.02	−0.02	−0.03	−0.07	−0.02
Sys.	+510	+0.100	+0.2	+0.2	+0.1	+1.02	…	+0.05	+0.06	+0.03	+0.07	+0.02	+0.08	+0.04	+0.05	+0.04	+0.11	+0.02
	−520	−0.100	−0.1	−0.1	−0.0	−0.70		−0.05	−0.06	−0.03	−0.09	−0.02	−0.07	−0.05	−0.07	−0.04	−0.10	−0.03
46	25 780	3.739	30.4	37.4	29.0	8.61	…	−1.09	−3.93	−4.00	−3.42	−4.15	−4.65	−5.68	−4.68	−5.05	−5.71	−4.69
Stat.	+50	+0.003	+0.1	+0.1	+0.3	+0.09	…	+0.01	+0.02	+0.01	+0.01	+0.03	+0.02	+0.02	+0.01	+0.01	+0.07	+0.01
	−30	−0.006	−0.1	−0.1	−0.3	−0.06		−0.01	−0.02	−0.01	−0.01	−0.04	−0.02	−0.01	−0.02	−0.02	−0.07	−0.01
Sys.	+520	+0.100	+0.1	+0.3	+1.0	+0.73	…	+0.08	+0.01	+0.05	+0.04	+0.05	+0.06	+0.06	+0.05	+0.02	+0.14	+0.05
	−520	−0.100	−0.1	−0.1	−1.7	−0.69		−0.07	−0.02	−0.06	−0.04	−0.07	−0.06	−0.06	−0.06	−0.03	−0.12	−0.06
$\odot^{(a)}$								−1.06	−3.57	−4.17	−3.31	−4.07	−4.40	−5.55	−4.49	−4.88	−5.60	−4.50
								+0.01	+0.05	+0.05	+0.05	+0.10	+0.04	+0.03	+0.04	+0.03	+0.13	+0.04
								−0.01	−0.05	−0.05	−0.05	−0.10	−0.04	−0.03	−0.04	−0.03	−0.13	−0.04

Table D.3: continued.

#	$T_{\rm eff}$	log g	$v_{\rm rad}$	$v \sin(i)$	ζ	ξ	$A_{\rm eff,s}/A_{\rm eff,p}$	log($n(x)$)										
	(K)	(cgs)	(km s^{-1})					He	C	N	O	Ne	Mg	Al	Si	S	Ar	Fe
47	26 040	3.502	−7.5	27.7	46.9	12.32	…	−1.10	−3.87	−4.00	−3.51	−4.20	−4.68	−5.67	−4.72	−5.09	−5.56	−4.66
Stat.	+30	+0.004	+0.2	+0.3	+0.2	+0.18	…	+0.01	+0.02	+0.01	+0.01	+0.03	+0.02	+0.01	+0.02	+0.02	+0.07	+0.01
	−20	−0.004	−0.2	−0.5	−1.6	−0.13		−0.01	−0.02	−0.01	−0.01	−0.03	−0.02	−0.02	−0.01	−0.02	−0.08	−0.02
Sys.	+530	+0.100	+0.1	+1.9	+0.3	+1.08	…	+0.09	+0.02	+0.06	+0.05	+0.02	+0.06	+0.05	+0.06	+0.06	+0.15	+0.07
	−530	−0.100	−0.1	−2.4	−0.1	−1.24		−0.08	−0.05	−0.07	−0.04	−0.03	−0.06	−0.07	−0.06	−0.04	−0.18	−0.08
48	26 070	4.310	27.5	10.7	0.0	2.51	…	−1.03	−3.73	−4.27	−3.33	−3.98	−4.55	−5.76	−4.67	−4.86	−5.50	−4.64
Stat.	+30	+0.007	+0.1	+0.2	+1.3	+0.14	…	+0.01	+0.02	+0.02	+0.02	+0.03	+0.02	+0.02	+0.02	+0.02	+0.03	+0.02
	−50	−0.007	−0.1	−0.2	−0.0	−0.13		−0.02	−0.02	−0.01	−0.01	−0.02	−0.02	−0.02	−0.02	−0.02	−0.03	−0.01
Sys.	+520	+0.100	+0.1	+0.5	+0.1	+0.89	…	+0.05	+0.02	+0.04	+0.07	+0.03	+0.07	+0.05	+0.04	+0.04	+0.08	+0.03
	−530	−0.100	−0.1	−0.7	−0.0	−0.51		−0.05	−0.02	−0.02	−0.06	−0.03	−0.09	−0.04	−0.05	−0.05	−0.07	−0.02
49	27 140	4.105	33.2	0.0	13.2	3.87	…	−1.04	−3.76	−4.27	−3.35	−4.00	−4.59	−5.73	−4.69	−5.00	−5.50	−4.63
Stat.	+50	+0.006	+0.1	+1.6	+0.2	+0.12	…	+0.01	+0.02	+0.01	+0.01	+0.02	+0.02	+0.03	+0.02	+0.03	+0.03	+0.01
	−50	−0.006	−0.1	−0.0	−0.2	−0.11		−0.01	−0.02	−0.01	−0.02	−0.01	−0.02	−0.02	−0.01	−0.02	−0.04	−0.02
Sys.	+550	+0.100	+0.1	+3.0	+0.5	+0.57	…	+0.05	+0.01	+0.06	+0.04	+0.01	+0.06	+0.07	+0.04	+0.03	+0.10	+0.06
	−550	−0.100	−0.1	−0.0	−1.0	−0.72		−0.04	−0.04	−0.04	−0.03	−0.01	−0.05	−0.05	−0.04	−0.02	−0.08	−0.04
50	27 150	3.790	37.8	0.0	12.9	4.86	…	−1.04	−3.77	−4.01	−3.42	−4.04	−4.61	−5.69	−4.62	−5.04	−5.60	−4.69
Stat.	+50	+0.005	+0.1	+1.4	+0.1	+0.08	…	+0.01	+0.02	+0.02	+0.01	+0.02	+0.03	+0.02	+0.02	+0.02	+0.05	+0.01
	−50	−0.007	−0.1	−0.0	−0.3	−0.06		−0.01	−0.02	−0.01	−0.01	−0.02	−0.03	−0.01	−0.01	−0.02	−0.07	−0.01
Sys.	+550	+0.100	+0.1	+3.6	+0.2	+0.22	…	+0.05	+0.01	+0.06	+0.02	+0.02	+0.04	+0.06	+0.02	+0.05	+0.10	+0.06
	−540	−0.100	−0.1	−0.0	−0.1	−0.36		−0.04	−0.04	−0.05	−0.01	−0.01	−0.04	−0.06	−0.01	−0.03	−0.12	−0.07
51	28 560	4.178	−15.5	0.0	17.6	3.86	…	−1.12	−3.74	−4.03	−3.37	−4.01	−4.53	−5.61	−4.56	−4.97	…	−4.57
Stat.	+70	+0.007	+0.1	+1.8	+0.2	+0.20	…	+0.02	+0.03	+0.01	+0.02	+0.05	+0.04	+0.03	+0.02	+0.03	…	+0.02
	−80	−0.009	−0.2	−0.0	−0.2	−0.21		−0.02	−0.03	−0.02	−0.01	−0.04	−0.04	−0.03	−0.03	−0.03		−0.03
Sys.	+570	+0.100	+0.1	+2.1	+0.2	+0.30	…	+0.04	+0.02	+0.06	+0.03	+0.02	+0.05	+0.06	+0.02	+0.05	…	+0.08
	−580	−0.100	−0.1	−0.0	−0.1	−0.50		−0.03	−0.04	−0.05	−0.01	−0.01	−0.05	−0.06	−0.02	−0.04		−0.07
52	29 130	4.099	36.8	147.3	0.2	4.11	…	−0.92	−4.07	−3.81	−3.63	−4.27	−4.48	−5.68	−4.67	−5.19	…	−4.55
Stat.	+30	+0.005	+0.5	+0.1	+5.3	+0.09	…	+0.01	+0.03	+0.01	+0.01	+0.05	+0.04	+0.03	+0.02	+0.05	…	+0.02
	−40	−0.005	−0.1	−0.1	−0.2	−0.10		−0.01	−0.03	−0.02	−0.01	−0.06	−0.03	−0.03	−0.02	−0.05		−0.02
Sys.	+580	+0.100	+0.7	+0.4	+13.7	+0.67	…	+0.06	+0.02	+0.05	+0.07	+0.03	+0.07	+0.05	+0.07	+0.16	…	+0.09
	−590	−0.100	−0.6	−0.1	− 0.2	−1.02		−0.06	−0.03	−0.06	−0.05	−0.03	−0.05	−0.06	−0.05	−0.12		−0.08
53	29 210	4.284	29.9	30.9	0.0	3.22	…	−1.04	−3.71	−4.13	−3.40	−4.01	−4.58	−5.73	−4.66	−4.97	…	−4.62
Stat.	+30	+0.006	+0.2	+0.1	+1.1	+0.10	…	+0.01	+0.02	+0.01	+0.02	+0.03	+0.02	+0.03	+0.03	+0.03	…	+0.02
	−50	−0.007	−0.1	−0.1	−0.0	−0.11		−0.02	−0.02	−0.01	−0.01	−0.03	−0.03	−0.02	−0.01	−0.03		−0.02
Sys.	+580	+0.100	+0.1	+0.2	+2.6	+0.47	…	+0.04	+0.01	+0.05	+0.04	+0.02	+0.05	+0.05	+0.04	+0.07	…	+0.08
	−590	−0.100	−0.1	−0.1	−0.0	−0.59		−0.04	−0.03	−0.05	−0.02	−0.02	−0.05	−0.05	−0.03	−0.05		−0.06
54	29 330	4.079	27.1	21.1	29.2	7.15	…	−1.09	−3.71	−4.36	−3.48	−4.07	−4.60	−5.65	−4.64	−4.95	…	−4.68
Stat.	+40	+0.003	+0.1	+0.3	+0.2	+0.09	…	+0.01	+0.02	+0.01	+0.01	+0.02	+0.02	+0.02	+0.02	+0.02	…	+0.01
	−30	−0.005	−0.2	−0.3	−1.0	−0.10		−0.01	−0.01	−0.01	−0.01	−0.02	−0.02	−0.02	−0.01	−0.02		−0.02
Sys.	+590	+0.100	+0.1	+0.9	+0.2	+0.58	…	+0.05	+0.02	+0.05	+0.05	+0.01	+0.04	+0.05	+0.03	+0.09	…	+0.08
	−590	−0.100	−0.1	−1.0	−0.1	−0.55		−0.05	−0.03	−0.05	−0.05	−0.01	−0.04	−0.05	−0.02	−0.07		−0.09
54$^{(b)}$	29 460	4.108	27.2	22.7	28.2	7.29	…	−1.09	−3.70	−4.33	−3.46	−4.02	−4.59	−5.63	−4.61	−4.93	…	−4.60
Stat.	+40	+0.005	+0.1	+0.3	+0.5	+0.09	…	+0.01	+0.02	+0.01	+0.01	+0.03	+0.02	+0.02	+0.02	+0.03	…	+0.02
	−40	−0.004	−0.1	−0.2	−0.4	−0.11		−0.01	−0.02	−0.01	−0.01	−0.03	−0.02	−0.02	−0.02	−0.02		−0.02
Sys.	+590	+0.100	+0.1	+0.8	+0.2	+0.55	…	+0.05	+0.03	+0.06	+0.06	+0.02	+0.05	+0.06	+0.02	+0.08	…	+0.10
	−600	−0.100	−0.1	−0.8	−0.1	−0.60		−0.04	−0.04	−0.05	−0.05	−0.02	−0.05	−0.05	−0.02	−0.08		−0.08
55p	29 710	3.669	104.0	23.7	41.2	14.92	…	−1.17	−3.76	−4.50	−3.59	−4.07	−4.61	−5.70	−4.71	−4.94	…	−4.69
Stat.	+40	+0.005	+0.2	+0.5	+0.4	+0.12	…	+0.01	+0.02	+0.02	+0.01	+0.02	+0.02	+0.02	+0.01	+0.02	…	+0.03
	−40	−0.004	−0.1	−0.5	−0.6	−0.12		−0.01	−0.01	−0.02	−0.01	−0.01	−0.02	−0.02	−0.01	−0.03		−0.03
Sys.	+600	+0.100	+0.1	+1.2	+0.1	+0.27	…	+0.03	+0.02	+0.06	+0.05	+0.02	+0.03	+0.04	+0.05	+0.07	…	+0.05
	−600	−0.100	−0.1	−1.5	−0.1	−0.24		−0.03	−0.01	−0.05	−0.05	−0.01	−0.03	−0.04	−0.05	−0.07		−0.06
55s	28 070	4.343	−110.9	35.5	62.6	6.04	0.218	…	…	…	…	…	…	…	…	…	…	…
Stat.	+140	+0.016	+0.8	+2.7	+3.5	+0.23	+0.003	…	…	…	…	…	…	…	…	…	…	…
	−170	−0.021	−1.0	−2.8	−3.4	−0.35	−0.002											
Sys.	+610	+0.310	+0.6	+2.6	+0.4	+0.78	+0.014	…	…	…	…	…	…	…	…	…	…	…
	−870	−0.434	−0.4	−1.9	−0.6	−0.80	−0.011											
$\odot^{(a)}$								−1.06	−3.57	−4.17	−3.31	−4.07	−4.40	−5.55	−4.49	−4.88	−5.60	−4.50
								+0.01	+0.05	+0.05	+0.05	+0.10	+0.04	+0.03	+0.04	+0.03	+0.13	+0.04
								−0.01	−0.05	−0.05	−0.05	−0.10	−0.04	−0.03	−0.04	−0.03	−0.13	−0.04

Table D.3: continued.

#	$T_{\rm eff}$	log g	$v_{\rm rad}$	$v \sin(i)$	ζ	ξ	$A_{\rm eff,s}/A_{\rm eff,p}$	log($n(x)$)										
	(K)	(cgs)	($\rm km\,s^{-1}$)					He	C	N	O	Ne	Mg	Al	Si	S	Ar	Fe
56	29 960	4.148	−7.2	0.0	31.0	5.96	...	−1.32	−3.87	−4.33	−3.52	−4.08	−4.70	−5.67	−4.64	−4.97	...	−4.63
Stat.	+70	+0.006	+0.1	+3.3	+0.2	+0.13	...	+0.02	+0.03	+0.02	+0.02	+0.02	+0.03	+0.04	+0.02	+0.04	...	+0.02
	−50	−0.008	−0.2	−0.0	−0.1	−0.18		−0.02	−0.03	−0.02	−0.01	−0.04	−0.03	−0.03	−0.02	−0.03		−0.02
Sys.	+610	+0.100	+0.1	+4.2	+0.3	+0.24	...	+0.06	+0.05	+0.07	+0.07	+0.01	+0.04	+0.06	+0.03	+0.10	...	+0.10
	−600	−0.100	−0.1	−0.0	−0.1	−0.48		−0.07	−0.06	−0.06	−0.04	−0.01	−0.04	−0.05	−0.02	−0.08		−0.08
57	30 200	4.190	19.1	25.3	28.3	7.33	...	−1.16	−3.68	−4.38	−3.48	−4.02	−4.57	−5.65	−4.62	−5.00	...	−4.67
Stat.	+30	+0.004	+0.1	+0.2	+0.2	+0.09	...	+0.02	+0.01	+0.01	+0.01	+0.01	+0.02	+0.02	+0.01	+0.02	...	+0.02
	−20	−0.003	−0.2	−0.3	−1.1	−0.07		−0.01	−0.02	−0.02	−0.01	−0.02	−0.01	−0.02	−0.02	−0.03		−0.01
Sys.	+610	+0.100	+0.1	+0.8	+0.2	+0.72	...	+0.07	+0.04	+0.05	+0.07	+0.01	+0.06	+0.06	+0.02	+0.10	...	+0.09
	−610	−0.100	−0.1	−1.0	−0.1	−0.62		−0.07	−0.05	−0.06	−0.07	−0.01	−0.05	−0.05	−0.02	−0.08		−0.08
58	30 290	4.316	39.2	50.9	0.0	2.74	...	−1.08	−3.70	−4.36	−3.48	−4.05	−4.60	−5.90	−4.78	−4.97	...	−4.71
Stat.	+60	+0.010	+0.2	+0.1	+1.7	+0.26	...	+0.02	+0.02	+0.02	+0.02	+0.03	+0.04	+0.04	+0.02	+0.05	...	+0.04
	−40	−0.009	−0.3	−0.1	−0.0	−0.13		−0.02	−0.02	−0.02	−0.02	−0.04	−0.03	−0.04	−0.03	−0.04		−0.04
Sys.	+610	+0.100	+0.1	+0.2	+1.9	+0.66	...	+0.05	+0.03	+0.05	+0.06	+0.01	+0.05	+0.05	+0.05	+0.11	...	+0.09
	−610	−0.100	−0.1	−0.1	−0.0	−0.63		−0.05	−0.04	−0.04	−0.05	−0.02	−0.05	−0.05	−0.07	−0.09		−0.10
59	30 680	3.646	26.8	16.1	49.4	15.51	...	−1.11	−3.91	−4.29	−3.76	−4.06	−4.70	−5.72	−4.84	−5.06	...	−4.71
Stat.	+30	+0.003	+0.2	+0.8	+0.1	+0.14	...	+0.01	+0.02	+0.02	+0.01	+0.02	+0.01	+0.03	+0.01	+0.03	...	+0.04
	−20	−0.002	−0.1	−0.9	−0.1	−0.12		−0.01	−0.02	−0.02	−0.01	−0.02	−0.02	−0.03	−0.01	−0.02		−0.05
Sys.	+620	+0.100	+0.3	+5.3	+0.4	+1.49	...	+0.08	+0.03	+0.08	+0.09	+0.05	+0.05	+0.06	+0.07	+0.11	...	+0.07
	−610	−0.100	−0.3	−8.2	−0.1	−2.04		−0.06	−0.02	−0.07	−0.08	−0.04	−0.05	−0.06	−0.04	−0.08		−0.09
60	31 230	4.384	−0.8	66.1	8.9	2.48	...	−1.13	−3.80	−4.37	−3.51	−4.22	−4.69	−5.83	−4.71	−4.84	...	−4.68
Stat.	+50	+0.009	+0.5	+0.2	+3.8	+0.26	...	+0.03	+0.03	+0.03	+0.02	+0.08	+0.08	+0.08	+0.03	+0.06	...	+0.06
	−60	−0.009	−0.6	−0.1	−7.3	−0.34		−0.02	−0.03	−0.04	−0.02	−0.08	−0.07	−0.09	−0.04	−0.06		−0.07
Sys.	+630	+0.100	+0.2	+0.4	+5.0	+0.86	...	+0.06	+0.02	+0.05	+0.07	+0.02	+0.06	+0.06	+0.05	+0.11	...	+0.11
	−630	−0.100	−0.1	−0.1	−5.1	−0.48		−0.06	−0.03	−0.05	−0.07	−0.02	−0.05	−0.05	−0.07	−0.11		−0.10
61	31 650	4.215	0.0	4.7	0.0	4.08	...	−1.02	−3.73	−3.90	−3.53	−3.94	−4.56	−5.67	−4.64	−4.99	...	−4.65
Stat.	+30	+0.004	+0.1	+0.2	+2.2	+0.07	...	+0.01	+0.01	+0.01	+0.01	+0.01	+0.01	+0.02	+0.02	+0.02	...	+0.01
	−20	−0.003	−0.0	−0.8	−0.0	−0.05		−0.01	−0.02	−0.01	−0.01	−0.01	−0.01	−0.02	−0.01	−0.02		−0.01
Sys.	+640	+0.100	+0.1	+1.0	+2.7	+0.34	...	+0.05	+0.05	+0.09	+0.09	+0.02	+0.05	+0.05	+0.03	+0.10	...	+0.09
	−640	−0.100	−0.0	−0.8	−0.0	−0.57		−0.05	−0.05	−0.08	−0.07	−0.01	−0.05	−0.05	−0.01	−0.10		−0.08
62	33 190	4.160	10.4	10.6	31.6	10.10	...	−1.11	−3.77	−4.38	−3.58	−4.19	−4.57	−5.60	−4.68	−4.95	...	−4.58
Stat.	+70	+0.012	+0.3	+1.6	+2.1	+0.31	...	+0.02	+0.02	+0.04	+0.02	+0.07	+0.04	+0.05	+0.03	+0.06	...	+0.07
	−60	−0.011	−0.2	−2.1	−1.5	−0.34		−0.01	−0.03	−0.05	−0.02	−0.08	−0.03	−0.06	−0.02	−0.06		−0.07
Sys.	+670	+0.100	+0.2	+3.4	+0.2	+0.91	...	+0.03	+0.03	+0.05	+0.08	+0.03	+0.05	+0.05	+0.06	+0.09	...	+0.09
	−670	−0.100	−0.1	−6.3	−0.1	−1.08		−0.03	−0.01	−0.06	−0.08	−0.04	−0.04	−0.06	−0.03	−0.09		−0.09
63	33 330	4.242	17.3	9.5	23.2	7.74	...	−1.05	−3.75	−4.41	−3.56	−3.93	−4.60	−5.77	−4.76	−4.85	...	−4.76
Stat.	+40	+0.007	+0.2	+0.6	+1.1	+0.23	...	+0.01	+0.02	+0.02	+0.02	+0.02	+0.02	+0.03	+0.02	+0.03	...	+0.07
	−40	−0.007	−0.1	−0.9	−0.5	−0.22		−0.01	−0.02	−0.02	−0.01	−0.02	−0.02	−0.04	−0.02	−0.03		−0.07
Sys.	+670	+0.100	+0.2	+2.8	+0.3	+1.23	...	+0.04	+0.03	+0.10	+0.11	+0.04	+0.05	+0.05	+0.07	+0.09	...	+0.09
	−670	−0.100	−0.2	−6.4	−0.1	−1.56		−0.03	−0.02	−0.10	−0.08	−0.03	−0.05	−0.05	−0.04	−0.08		−0.08
$\odot^{(a)}$								−1.06	−3.57	−4.17	−3.31	−4.07	−4.40	−5.55	−4.49	−4.88	−5.60	−4.50
								+0.01	+0.05	+0.05	+0.05	+0.10	+0.04	+0.03	+0.04	+0.03	+0.13	+0.04
								−0.01	−0.05	−0.05	−0.05	−0.10	−0.04	−0.03	−0.04	−0.03	−0.13	−0.04

Notes. Same as Table 5.2 Numbering according to Table 7.1. Argon and nitrogen lines are not visible for all temperatures. For the double-lined spectroscopic binary systems, the parameter $A_{\rm eff,s}/A_{\rm eff,p}$ is the ratio of effective surface areas (see Sect. 5.1.4 for details). Furthermore, abundances of the secondary components "s" are tied to the ones of the primaries "p" owing to the assumption of a homogeneous chemical composition. $^{(a)}$ Protosolar nebula values and uncertainties from Asplund et al. (2009). $^{(b)}$ Results obtained from a spectrum that was taken during a different observing run than the first one in order to estimate the influence of the instrument and the data reduction on the outcome of the analysis. Apart from this purpose, these data are not used in this work.

Table D.4: Stellar parameters and mass fractions of the reference stars.

#	M	τ	$\log(L/L_\odot)$	$R_\star$	d	$E(B-V)$	X	Y	Z
	($M_\odot$)	(Myr)		($R_\odot$)	(pc)	(mag)			
1	$5.4^{+0.2}_{-0.4}$	82^{+24}_{-5}	$3.26^{+0.07}_{-0.09}$	$9.7^{+1.2}_{-1.3}$	360^{+60}_{-60}	$0.027^{+0.022}_{-0.031}$	$0.570^{+0.098}_{-0.082}$	$0.418^{+0.083}_{-0.099}$	$0.012^{+0.002}_{-0.002}$
2	$3.9^{+0.2}_{-0.1}$	145^{+11}_{-16}	$2.56^{+0.09}_{-0.08}$	$3.6^{+0.6}_{-0.4}$	1080^{+170}_{-170}	$0.038^{+0.036}_{-0.022}$	$0.648^{+0.089}_{-0.097}$	$0.338^{+0.098}_{-0.091}$	$0.014^{+0.002}_{-0.002}$
3	$3.8^{+0.2}_{-0.1}$	130^{+16}_{-27}	$2.45^{+0.09}_{-0.08}$	$3.1^{+0.5}_{-0.4}$	1180^{+260}_{-200}	$-0.008^{+0.046}_{-0.060}$	$0.641^{+0.088}_{-0.092}$	$0.344^{+0.094}_{-0.089}$	$0.014^{+0.002}_{-0.002}$
4	$4.1^{+0.2}_{-0.1}$	136^{+9}_{-12}	$2.65^{+0.08}_{-0.08}$	$3.9^{+0.6}_{-0.5}$	160^{+30}_{-20}	$-0.018^{+0.020}_{-0.026}$	$0.583^{+0.078}_{-0.084}$	$0.405^{+0.085}_{-0.080}$	$0.012^{+0.002}_{-0.001}$
5p	$3.9^{+0.3}_{-0.2}$	100^{+18}_{-31}	$2.43^{+0.14}_{-0.11}$	$2.9^{+0.5}_{-0.4}$	170^{+40}_{-30}	$-0.030^{+0.018}_{-0.024}$	$0.594^{+0.038}_{-0.049}$	$0.394^{+0.049}_{-0.040}$	$0.012^{+0.002}_{-0.001}$
5s	$4.0^{+0.7}_{-0.1}$	163^{+28}_{-54}	$2.69^{+0.25}_{-0.15}$	$4.3^{+1.4}_{-1.1}$	… …	… …	… …	… …	… …
6	$4.3^{+0.3}_{-0.1}$	108^{+11}_{-19}	$2.68^{+0.09}_{-0.07}$	$3.6^{+0.5}_{-0.5}$	150^{+30}_{-30}	$-0.025^{+0.041}_{-0.052}$	$0.595^{+0.075}_{-0.084}$	$0.394^{+0.085}_{-0.076}$	$0.011^{+0.001}_{-0.001}$
7	$4.9^{+0.5}_{-0.1}$	95^{+11}_{-25}	$3.02^{+0.10}_{-0.05}$	$4.8^{+0.7}_{-0.5}$	370^{+70}_{-40}	$0.033^{+0.019}_{-0.018}$	$0.649^{+0.079}_{-0.077}$	$0.335^{+0.079}_{-0.080}$	$0.016^{+0.001}_{-0.002}$
8	$5.0^{+0.4}_{-0.2}$	90^{+18}_{-16}	$3.04^{+0.07}_{-0.07}$	$4.7^{+0.6}_{-0.6}$	440^{+70}_{-60}	$0.041^{+0.025}_{-0.030}$	$0.612^{+0.068}_{-0.076}$	$0.374^{+0.078}_{-0.067}$	$0.013^{+0.001}_{-0.001}$
9	$6.1^{+0.4}_{-0.3}$	54^{+6}_{-6}	$3.41^{+0.10}_{-0.09}$	$7.1^{+1.1}_{-0.9}$	470^{+90}_{-100}	$0.036^{+0.065}_{-0.052}$	$0.681^{+0.069}_{-0.077}$	$0.304^{+0.078}_{-0.068}$	$0.015^{+0.001}_{-0.001}$
10	$5.1^{+0.2}_{-0.2}$	71^{+6}_{-9}	$2.93^{+0.09}_{-0.08}$	$4.0^{+0.6}_{-0.5}$	1280^{+220}_{-200}	$0.004^{+0.035}_{-0.027}$	$0.699^{+0.058}_{-0.074}$	$0.290^{+0.075}_{-0.058}$	$0.011^{+0.001}_{-0.001}$
11	$6.4^{+0.4}_{-0.5}$	61^{+4}_{-15}	$3.44^{+0.09}_{-0.09}$	$7.0^{+1.0}_{-0.9}$	270^{+50}_{-40}	$0.014^{+0.019}_{-0.021}$	$0.679^{+0.071}_{-0.076}$	$0.306^{+0.077}_{-0.070}$	$0.014^{+0.001}_{-0.001}$
12p	$8.7^{+0.5}_{-1.2}$	29^{+14}_{-2}	$3.95^{+0.10}_{-0.17}$	$12.1^{+1.8}_{-2.1}$	530^{+110}_{-110}	$0.037^{+0.029}_{-0.023}$	$0.695^{+0.012}_{-0.013}$	$0.291^{+0.012}_{-0.013}$	$0.014^{+0.001}_{-0.001}$
12s	$7.7^{+1.0}_{-0.8}$	39^{+16}_{-10}	$3.79^{+0.18}_{-0.14}$	$9.9^{+2.7}_{-1.5}$	… …	… …	… …	… …	… …
13p	$5.2^{+0.3}_{-0.3}$	55^{+8}_{-15}	$2.91^{+0.12}_{-0.13}$	$3.5^{+0.6}_{-0.5}$	1560^{+430}_{-330}	$0.026^{+0.046}_{-0.045}$	$0.667^{+0.012}_{-0.014}$	$0.320^{+0.014}_{-0.012}$	$0.013^{+0.001}_{-0.001}$
13s	$4.9^{+0.4}_{-0.3}$	51^{+13}_{-23}	$2.79^{+0.18}_{-0.12}$	$3.2^{+0.8}_{-0.5}$	… …	… …	… …	… …	… …
14p	$5.2^{+0.2}_{-0.2}$	48^{+10}_{-16}	$2.90^{+0.09}_{-0.09}$	$3.4^{+0.5}_{-0.5}$	470^{+70}_{-60}	$0.156^{+0.018}_{-0.016}$	$0.660^{+0.031}_{-0.028}$	$0.327^{+0.028}_{-0.032}$	$0.014^{+0.001}_{-0.001}$
14s	$3.5^{+0.4}_{-0.2}$	49^{+47}_{-48}	$2.18^{+0.11}_{-0.13}$	$2.3^{+0.3}_{-0.4}$	… …	… …	… …	… …	… …
15	$5.1^{+0.2}_{-0.2}$	41^{+15}_{-21}	$2.84^{+0.09}_{-0.07}$	$3.1^{+0.5}_{-0.4}$	120^{+30}_{-20}	$0.000^{+0.043}_{-0.032}$	$0.669^{+0.058}_{-0.060}$	$0.317^{+0.060}_{-0.058}$	$0.014^{+0.001}_{-0.001}$
16	$6.9^{+0.3}_{-0.3}$	40^{+4}_{-2}	$3.46^{+0.09}_{-0.08}$	$5.9^{+0.8}_{-0.8}$	160^{+30}_{-30}	$0.011^{+0.026}_{-0.018}$	$0.695^{+0.056}_{-0.066}$	$0.289^{+0.066}_{-0.054}$	$0.016^{+0.002}_{-0.002}$
17	$9.2^{+0.5}_{-0.6}$	29^{+6}_{-3}	$4.07^{+0.09}_{-0.09}$	$11.5^{+1.7}_{-1.5}$	370^{+60}_{-60}	$0.070^{+0.015}_{-0.015}$	$0.721^{+0.060}_{-0.099}$	$0.265^{+0.097}_{-0.059}$	$0.014^{+0.003}_{-0.002}$
18	$6.9^{+0.4}_{-0.4}$	49^{+7}_{-7}	$3.58^{+0.09}_{-0.07}$	$6.5^{+1.0}_{-0.7}$	340^{+70}_{-50}	$0.090^{+0.048}_{-0.035}$	$0.714^{+0.044}_{-0.062}$	$0.271^{+0.062}_{-0.042}$	$0.014^{+0.002}_{-0.002}$
19	$7.1^{+0.3}_{-0.3}$	42^{+13}_{-5}	$3.60^{+0.08}_{-0.07}$	$6.7^{+0.8}_{-0.8}$	490^{+80}_{-80}	$0.176^{+0.050}_{-0.037}$	$0.697^{+0.043}_{-0.051}$	$0.288^{+0.052}_{-0.042}$	$0.015^{+0.001}_{-0.002}$
20	$6.9^{+0.3}_{-0.4}$	42^{+4}_{-4}	$3.46^{+0.08}_{-0.08}$	$5.2^{+0.7}_{-0.7}$	260^{+60}_{-50}	$0.024^{+0.058}_{-0.047}$	$0.755^{+0.061}_{-0.067}$	$0.231^{+0.065}_{-0.058}$	$0.014^{+0.003}_{-0.003}$
21	$8.5^{+0.6}_{-1.0}$	31^{+11}_{-3}	$3.85^{+0.10}_{-0.13}$	$7.7^{+1.2}_{-1.1}$	600^{+120}_{-100}	$0.025^{+0.035}_{-0.030}$	$0.702^{+0.040}_{-0.053}$	$0.284^{+0.051}_{-0.038}$	$0.014^{+0.002}_{-0.002}$
22	$6.7^{+0.3}_{-0.3}$	29^{+6}_{-8}	$3.30^{+0.08}_{-0.08}$	$4.0^{+0.6}_{-0.5}$	400^{+70}_{-70}	$0.006^{+0.047}_{-0.038}$	$0.685^{+0.042}_{-0.045}$	$0.301^{+0.043}_{-0.041}$	$0.014^{+0.002}_{-0.002}$
23	$7.1^{+0.4}_{-0.3}$	31^{+5}_{-8}	$3.43^{+0.09}_{-0.07}$	$4.4^{+0.6}_{-0.5}$	480^{+80}_{-80}	$0.021^{+0.040}_{-0.029}$	$0.735^{+0.036}_{-0.041}$	$0.249^{+0.039}_{-0.032}$	$0.016^{+0.003}_{-0.004}$
24p	$6.7^{+0.3}_{-0.4}$	14^{+10}_{-12}	$3.21^{+0.11}_{-0.13}$	$3.3^{+0.6}_{-0.4}$	400^{+90}_{-70}	$-0.010^{+0.018}_{-0.017}$	$0.663^{+0.014}_{-0.010}$	$0.324^{+0.011}_{-0.015}$	$0.013^{+0.002}_{-0.001}$
24s	$5.3^{+0.5}_{-0.3}$	30^{+20}_{-25}	$2.87^{+0.20}_{-0.12}$	$3.0^{+0.8}_{-0.5}$	… …	… …	… …	… …	… …
25	$9.2^{+0.4}_{-0.4}$	26^{+8}_{-4}	$3.97^{+0.08}_{-0.08}$	$7.7^{+0.9}_{-0.9}$	370^{+70}_{-60}	$0.017^{+0.048}_{-0.043}$	$0.677^{+0.034}_{-0.035}$	$0.310^{+0.034}_{-0.034}$	$0.013^{+0.002}_{-0.002}$
26	$8.4^{+0.4}_{-0.4}$	26^{+3}_{-2}	$3.72^{+0.10}_{-0.09}$	$5.7^{+0.9}_{-0.7}$	570^{+100}_{-90}	$0.063^{+0.038}_{-0.032}$	$0.697^{+0.029}_{-0.033}$	$0.291^{+0.033}_{-0.028}$	$0.012^{+0.001}_{-0.002}$
27p	$10.4^{+1.3}_{-1.2}$	20^{+10}_{-4}	$4.18^{+0.15}_{-0.15}$	$9.7^{+1.6}_{-1.6}$	510^{+110}_{-100}	$0.109^{+0.032}_{-0.028}$	$0.700^{+0.004}_{-0.005}$	$0.290^{+0.004}_{-0.006}$	$0.011^{+0.001}_{-0.001}$
27s	$11.1^{+0.5}_{-2.1}$	18^{+14}_{-2}	$4.29^{+0.12}_{-0.22}$	$13.4^{+2.4}_{-3.2}$	… …	… …	… …	… …	… …
28	$9.2^{+0.4}_{-0.5}$	23^{+6}_{-2}	$3.89^{+0.06}_{-0.09}$	$6.6^{+0.8}_{-0.8}$	200^{+30}_{-30}	$0.022^{+0.019}_{-0.014}$	$0.669^{+0.032}_{-0.032}$	$0.318^{+0.031}_{-0.033}$	$0.014^{+0.002}_{-0.002}$
29	$7.2^{+0.3}_{-0.4}$	7^{+11}_{-7}	$3.29^{+0.07}_{-0.09}$	$3.3^{+0.4}_{-0.4}$	470^{+80}_{-80}	$0.215^{+0.038}_{-0.032}$	$0.686^{+0.027}_{-0.032}$	$0.301^{+0.030}_{-0.026}$	$0.013^{+0.002}_{-0.002}$
30	$7.8^{+1.3}_{-0.4}$	11^{+8}_{-11}	$3.44^{+0.13}_{-0.07}$	$3.6^{+0.6}_{-0.4}$	380^{+70}_{-70}	$0.031^{+0.045}_{-0.033}$	$0.688^{+0.026}_{-0.029}$	$0.299^{+0.028}_{-0.025}$	$0.013^{+0.002}_{-0.002}$
31	$17.6^{+1.1}_{-2.6}$	10^{+4}_{-1}	$4.97^{+0.10}_{-0.16}$	$20.6^{+3.1}_{-3.5}$	1500^{+260}_{-280}	$0.242^{+0.024}_{-0.023}$	$0.826^{+0.038}_{-0.050}$	$0.165^{+0.050}_{-0.038}$	$0.009^{+0.001}_{-0.001}$
32	$14.0^{+1.0}_{-1.4}$	12^{+4}_{-2}	$4.59^{+0.11}_{-0.12}$	$12.7^{+2.1}_{-1.8}$	150^{+50}_{-50}	$0.055^{+0.104}_{-0.103}$	$0.754^{+0.036}_{-0.049}$	$0.235^{+0.049}_{-0.036}$	$0.011^{+0.001}_{-0.001}$
$\odot^{(a)}$							0.716	0.270	0.014

Table D.4: continued.

#	M	τ	$\log(L/L_\odot)$	$R_\star$	d	$E(B-V)$	X	Y	Z
	($M_\odot$)	(Myr)		($R_\odot$)	(pc)	(mag)			
33	$8.4^{+0.7}_{-0.3}$	10^{+7}_{-10}	$3.55^{+0.09}_{-0.07}$	$3.8^{+0.6}_{-0.4}$	330^{+60}_{-50}	$0.115^{+0.035}_{-0.028}$	$0.696^{+0.021}_{-0.025}$	$0.292^{+0.024}_{-0.022}$	$0.013^{+0.001}_{-0.002}$
34	$9.9^{+0.5}_{-0.5}$	18^{+1}_{-3}	$3.94^{+0.09}_{-0.10}$	$5.8^{+0.9}_{-0.7}$	2390^{+650}_{-540}	$0.423^{+0.085}_{-0.073}$	$0.663^{+0.025}_{-0.019}$	$0.326^{+0.020}_{-0.025}$	$0.011^{+0.001}_{-0.001}$
35	$11.9^{+0.2}_{-1.1}$	17^{+6}_{-1}	$4.34^{+0.07}_{-0.09}$	$9.1^{+1.1}_{-1.2}$	740^{+100}_{-100}	$0.147^{+0.019}_{-0.017}$	$0.729^{+0.049}_{-0.058}$	$0.262^{+0.058}_{-0.049}$	$0.009^{+0.001}_{-0.001}$
36	$9.4^{+0.4}_{-0.4}$	14^{+4}_{-5}	$3.80^{+0.08}_{-0.09}$	$4.7^{+0.7}_{-0.6}$	330^{+50}_{-50}	$0.006^{+0.029}_{-0.022}$	$0.698^{+0.021}_{-0.023}$	$0.290^{+0.023}_{-0.022}$	$0.013^{+0.001}_{-0.002}$
37	$10.3^{+0.5}_{-0.5}$	18^{+2}_{-3}	$4.03^{+0.08}_{-0.09}$	$6.2^{+0.8}_{-0.8}$	490^{+90}_{-60}	$0.072^{+0.026}_{-0.035}$	$0.751^{+0.044}_{-0.041}$	$0.237^{+0.040}_{-0.043}$	$0.012^{+0.003}_{-0.002}$
38	$9.3^{+0.5}_{-0.4}$	12^{+4}_{-7}	$3.75^{+0.08}_{-0.08}$	$4.4^{+0.6}_{-0.6}$	380^{+60}_{-60}	$0.012^{+0.029}_{-0.024}$	$0.677^{+0.024}_{-0.022}$	$0.311^{+0.022}_{-0.025}$	$0.012^{+0.002}_{-0.001}$
39	$17.8^{+1.0}_{-3.3}$	9^{+5}_{-1}	$4.92^{+0.10}_{-0.17}$	$17.0^{+2.4}_{-3.3}$	1290^{+270}_{-300}	$0.771^{+0.050}_{-0.046}$	$0.781^{+0.040}_{-0.052}$	$0.209^{+0.052}_{-0.040}$	$0.010^{+0.001}_{-0.001}$
40	$9.4^{+0.4}_{-0.5}$	8^{+7}_{-7}	$3.71^{+0.08}_{-0.08}$	$4.1^{+0.6}_{-0.5}$	410^{+80}_{-60}	$-0.009^{+0.037}_{-0.036}$	$0.704^{+0.031}_{-0.035}$	$0.284^{+0.035}_{-0.030}$	$0.012^{+0.001}_{-0.002}$
41	$9.3^{+1.2}_{-0.4}$	4^{+7}_{-4}	$3.66^{+0.11}_{-0.08}$	$3.8^{+0.5}_{-0.4}$	410^{+60}_{-60}	$0.031^{+0.023}_{-0.018}$	$0.686^{+0.025}_{-0.024}$	$0.302^{+0.025}_{-0.025}$	$0.012^{+0.001}_{-0.002}$
42p	$12.0^{+0.9}_{-0.7}$	14^{+2}_{-2}	$4.26^{+0.12}_{-0.13}$	$7.2^{+1.1}_{-1.0}$	650^{+160}_{-110}	$0.089^{+0.025}_{-0.024}$	$0.736^{+0.005}_{-0.002}$	$0.253^{+0.002}_{-0.005}$	$0.011^{+0.001}_{-0.001}$
42s	$11.8^{+0.9}_{-0.7}$	12^{+2}_{-2}	$4.19^{+0.14}_{-0.13}$	$6.3^{+1.3}_{-0.9}$	...	...	...	...	...
43	$14.3^{+1.1}_{-2.4}$	12^{+7}_{-1}	$4.56^{+0.12}_{-0.17}$	$10.2^{+1.5}_{-1.7}$	1960^{+520}_{-470}	$0.727^{+0.073}_{-0.066}$	$0.766^{+0.037}_{-0.039}$	$0.222^{+0.039}_{-0.037}$	$0.011^{+0.001}_{-0.001}$
44	$13.7^{+1.3}_{-1.9}$	12^{+5}_{-2}	$4.47^{+0.12}_{-0.12}$	$9.1^{+1.4}_{-1.2}$	150^{+40}_{-20}	$0.009^{+0.027}_{-0.023}$	$0.762^{+0.035}_{-0.037}$	$0.228^{+0.037}_{-0.035}$	$0.010^{+0.001}_{-0.001}$
45	$11.5^{+0.7}_{-1.5}$	0^{+12}_{-0}	$3.89^{+0.08}_{-0.12}$	$4.6^{+0.3}_{-0.8}$	400^{+80}_{-90}	$0.039^{+0.070}_{-0.059}$	$0.714^{+0.021}_{-0.021}$	$0.274^{+0.022}_{-0.020}$	$0.011^{+0.002}_{-0.001}$
46	$13.7^{+0.8}_{-1.8}$	11^{+5}_{-1}	$4.43^{+0.11}_{-0.10}$	$8.3^{+1.2}_{-1.1}$	520^{+120}_{-100}	$0.018^{+0.059}_{-0.050}$	$0.731^{+0.031}_{-0.035}$	$0.259^{+0.035}_{-0.031}$	$0.010^{+0.001}_{-0.001}$
47	$15.1^{+3.6}_{-0.6}$	12^{+1}_{-4}	$4.73^{+0.18}_{-0.09}$	$11.4^{+2.7}_{-1.4}$	550^{+150}_{-80}	$0.222^{+0.026}_{-0.020}$	$0.736^{+0.034}_{-0.040}$	$0.254^{+0.040}_{-0.033}$	$0.010^{+0.001}_{-0.001}$
48	$10.1^{+1.3}_{-0.5}$	0^{+4}_{-0}	$3.75^{+0.13}_{-0.07}$	$3.7^{+0.7}_{-0.2}$	330^{+110}_{-70}	$0.033^{+0.087}_{-0.076}$	$0.702^{+0.024}_{-0.026}$	$0.286^{+0.025}_{-0.025}$	$0.012^{+0.001}_{-0.001}$
49	$12.0^{+0.6}_{-0.6}$	8^{+2}_{-5}	$4.10^{+0.10}_{-0.09}$	$5.1^{+0.7}_{-0.6}$	390^{+80}_{-80}	$0.070^{+0.060}_{-0.050}$	$0.707^{+0.019}_{-0.024}$	$0.282^{+0.023}_{-0.020}$	$0.012^{+0.001}_{-0.001}$
50	$14.7^{+1.1}_{-1.0}$	9^{+2}_{-1}	$4.50^{+0.12}_{-0.11}$	$8.1^{+1.3}_{-1.1}$	410^{+90}_{-60}	$0.030^{+0.031}_{-0.026}$	$0.706^{+0.018}_{-0.022}$	$0.283^{+0.022}_{-0.019}$	$0.011^{+0.001}_{-0.001}$
51	$14.7^{+0.3}_{-2.3}$	0^{+8}_{-0}	$4.20^{+0.04}_{-0.15}$	$5.2^{+0.3}_{-0.9}$	1650^{+270}_{-390}	$0.438^{+0.064}_{-0.053}$	$0.745^{+0.013}_{-0.016}$	$0.242^{+0.016}_{-0.013}$	$0.013^{+0.001}_{-0.001}$
52	$14.2^{+0.6}_{-0.8}$	5^{+3}_{-3}	$4.30^{+0.09}_{-0.09}$	$5.6^{+0.7}_{-0.7}$	690^{+130}_{-110}	$0.026^{+0.043}_{-0.038}$	$0.644^{+0.031}_{-0.038}$	$0.348^{+0.037}_{-0.031}$	$0.008^{+0.002}_{-0.001}$
53	$12.9^{+2.0}_{-0.7}$	1^{+2}_{-1}	$4.08^{+0.14}_{-0.08}$	$4.3^{+0.9}_{-0.3}$	450^{+90}_{-60}	$0.175^{+0.014}_{-0.016}$	$0.709^{+0.016}_{-0.019}$	$0.279^{+0.020}_{-0.016}$	$0.012^{+0.001}_{-0.001}$
54	$14.3^{+0.6}_{-0.6}$	6^{+2}_{-3}	$4.34^{+0.10}_{-0.10}$	$5.7^{+0.8}_{-0.7}$	390^{+80}_{-70}	$0.021^{+0.048}_{-0.039}$	$0.734^{+0.018}_{-0.022}$	$0.255^{+0.023}_{-0.017}$	$0.010^{+0.002}_{-0.001}$
55p	$20.2^{+1.8}_{-1.5}$	7^{+1}_{-1}	$4.92^{+0.12}_{-0.12}$	$10.9^{+1.7}_{-1.6}$	960^{+240}_{-200}	$0.034^{+0.050}_{-0.048}$	$0.770^{+0.010}_{-0.011}$	$0.220^{+0.011}_{-0.010}$	$0.010^{+0.001}_{-0.002}$
55s	$11.5^{+2.0}_{-0.5}$	0^{+10}_{-0}	$3.93^{+0.42}_{-0.07}$	$3.9^{+2.9}_{-0.1}$	...	...	...	...	...
56	$14.5^{+0.5}_{-0.6}$	4^{+3}_{-3}	$4.31^{+0.09}_{-0.09}$	$5.3^{+0.7}_{-0.6}$	1210^{+360}_{-280}	$0.482^{+0.094}_{-0.082}$	$0.826^{+0.019}_{-0.019}$	$0.163^{+0.020}_{-0.019}$	$0.010^{+0.002}_{-0.001}$
57	$14.5^{+0.6}_{-0.5}$	3^{+3}_{-3}	$4.28^{+0.09}_{-0.09}$	$5.1^{+0.7}_{-0.7}$	290^{+50}_{-50}	$0.011^{+0.023}_{-0.018}$	$0.763^{+0.029}_{-0.028}$	$0.226^{+0.029}_{-0.030}$	$0.011^{+0.002}_{-0.001}$
58	$13.5^{+0.9}_{-0.5}$	0^{+3}_{-0}	$4.14^{+0.10}_{-0.06}$	$4.3^{+0.6}_{-0.2}$	460^{+120}_{-80}	$0.279^{+0.038}_{-0.039}$	$0.728^{+0.020}_{-0.021}$	$0.262^{+0.021}_{-0.020}$	$0.010^{+0.002}_{-0.001}$
59	$22.7^{+1.8}_{-1.6}$	6^{+1}_{-1}	$5.05^{+0.11}_{-0.11}$	$11.9^{+1.9}_{-1.7}$	1410^{+310}_{-250}	$0.083^{+0.039}_{-0.038}$	$0.744^{+0.026}_{-0.040}$	$0.248^{+0.039}_{-0.026}$	$0.008^{+0.002}_{-0.001}$
60	$14.3^{+0.6}_{-0.6}$	0^{+1}_{-0}	$4.20^{+0.05}_{-0.05}$	$4.4^{+0.2}_{-0.2}$	960^{+360}_{-250}	$0.396^{+0.120}_{-0.116}$	$0.749^{+0.026}_{-0.024}$	$0.241^{+0.025}_{-0.026}$	$0.010^{+0.001}_{-0.002}$
61	$15.9^{+0.6}_{-0.7}$	2^{+3}_{-2}	$4.38^{+0.08}_{-0.10}$	$5.2^{+0.6}_{-0.7}$	150^{+30}_{-30}	$0.043^{+0.029}_{-0.026}$	$0.698^{+0.023}_{-0.026}$	$0.291^{+0.026}_{-0.024}$	$0.011^{+0.002}_{-0.001}$
62	$18.2^{+0.8}_{-0.7}$	3^{+2}_{-3}	$4.58^{+0.10}_{-0.12}$	$5.9^{+0.9}_{-0.8}$	1680^{+350}_{-290}	$0.722^{+0.038}_{-0.035}$	$0.742^{+0.011}_{-0.012}$	$0.248^{+0.012}_{-0.010}$	$0.009^{+0.002}_{-0.001}$
63	$17.7^{+0.7}_{-0.9}$	1^{+3}_{-1}	$4.49^{+0.10}_{-0.09}$	$5.3^{+0.8}_{-0.5}$	370^{+80}_{-60}	$0.027^{+0.039}_{-0.034}$	$0.713^{+0.014}_{-0.019}$	$0.278^{+0.019}_{-0.016}$	$0.010^{+0.002}_{-0.002}$
$\odot^{(a)}$							0.716	0.270	0.014

Notes. Same as Table 5.7. Numbering according to Table 7.1. $^{(a)}$ Protosolar nebula values from Asplund et al. (2009).

D.3 Runaway stars

Table D.5: Stellar parameters and mass fractions of the runaway stars.

#	M	τ	$\log(L/L_\odot)$	$R_\star$	d	$E(B-V)$	X	Y	Z
	($M_\odot$)	(Myr)		($R_\odot$)	(pc)	(mag)			
1	$4.2^{+0.2}_{-0.2}$	102^{+17}_{-26}	$2.59^{+0.08}_{-0.08}$	$3.2^{+0.5}_{-0.4}$	6890^{+1000}_{-1200}	$0.077^{+0.061}_{-0.037}$	$0.741^{+0.047}_{-0.088}$	$0.232^{+0.089}_{-0.046}$	$0.027^{+0.001}_{-0.002}$
2	$6.4^{+0.4}_{-0.4}$	50^{+7}_{-6}	$3.48^{+0.10}_{-0.10}$	$8.3^{+1.4}_{-1.1}$	1560^{+320}_{-230}	$-0.019^{+0.025}_{-0.034}$	$0.608^{+0.081}_{-0.087}$	$0.385^{+0.087}_{-0.081}$	$0.008^{+0.001}_{-0.002}$
3	$4.9^{+0.2}_{-0.2}$	81^{+9}_{-13}	$2.89^{+0.08}_{-0.08}$	$3.9^{+0.6}_{-0.5}$	470^{+90}_{-90}	$-0.024^{+0.055}_{-0.046}$	$0.661^{+0.082}_{-0.082}$	$0.321^{+0.083}_{-0.083}$	$0.018^{+0.001}_{-0.001}$
4	$4.5^{+0.2}_{-0.2}$	72^{+12}_{-20}	$2.73^{+0.09}_{-0.08}$	$3.0^{+0.4}_{-0.4}$	6610^{+990}_{-850}	$0.020^{+0.025}_{-0.018}$	$0.755^{+0.048}_{-0.080}$	$0.236^{+0.081}_{-0.047}$	$0.008^{+0.001}_{-0.001}$
5p	$4.9^{+0.4}_{-0.3}$	53^{+11}_{-16}	$2.82^{+0.15}_{-0.15}$	$3.2^{+0.6}_{-0.4}$	5060^{+4300}_{-2160}	$-0.040^{+0.172}_{-0.171}$	$0.665^{+0.021}_{-0.021}$	$0.320^{+0.021}_{-0.020}$	$0.015^{+0.001}_{-0.001}$
5s	$4.8^{+0.5}_{-0.4}$	16^{+40}_{-16}	$2.66^{+0.32}_{-0.12}$	$2.6^{+1.3}_{-0.4}$	...	...	...	...	...
6	$5.2^{+0.2}_{-0.2}$	53^{+13}_{-19}	$2.89^{+0.08}_{-0.07}$	$3.4^{+0.5}_{-0.4}$	3320^{+1230}_{-860}	$0.005^{+0.127}_{-0.130}$	$0.667^{+0.069}_{-0.076}$	$0.309^{+0.076}_{-0.068}$	$0.024^{+0.002}_{-0.002}$
7	$5.8^{+0.2}_{-0.5}$	55^{+20}_{-5}	$3.16^{+0.08}_{-0.09}$	$4.6^{+0.5}_{-0.6}$	2370^{+430}_{-540}	$0.038^{+0.064}_{-0.053}$	$0.684^{+0.065}_{-0.076}$	$0.300^{+0.076}_{-0.065}$	$0.017^{+0.001}_{-0.001}$
8	$5.7^{+0.6}_{-0.3}$	7^{+10}_{-7}	$2.92^{+0.11}_{-0.08}$	$2.8^{+0.5}_{-0.3}$	1300^{+240}_{-190}	$-0.016^{+0.024}_{-0.016}$	$0.700^{+0.054}_{-0.068}$	$0.280^{+0.066}_{-0.051}$	$0.020^{+0.002}_{-0.004}$
9	$11.6^{+0.2}_{-0.8}$	17^{+4}_{-1}	$4.37^{+0.08}_{-0.10}$	$14.7^{+1.8}_{-2.0}$	$19\,920^{+4520}_{-4130}$	$0.084^{+0.075}_{-0.071}$	$0.763^{+0.076}_{-0.119}$	$0.230^{+0.117}_{-0.075}$	$0.007^{+0.002}_{-0.001}$
10	$6.2^{+0.4}_{-0.3}$	46^{+5}_{-7}	$3.30^{+0.10}_{-0.08}$	$4.0^{+0.7}_{-0.5}$	$12\,640^{+15\,790}_{-6\,930}$	$-0.283^{+0.384}_{-0.383}$	$0.728^{+0.054}_{-0.071}$	$0.266^{+0.069}_{-0.053}$	$0.007^{+0.002}_{-0.002}$
11	$7.2^{+0.4}_{-0.5}$	35^{+6}_{-6}	$3.47^{+0.10}_{-0.09}$	$4.8^{+0.8}_{-0.6}$	6770^{+2890}_{-2030}	$-0.083^{+0.138}_{-0.133}$	$0.768^{+0.056}_{-0.085}$	$0.221^{+0.082}_{-0.055}$	$0.011^{+0.004}_{-0.002}$
12	$7.0^{+0.4}_{-0.3}$	32^{+4}_{-7}	$3.41^{+0.09}_{-0.08}$	$4.4^{+0.7}_{-0.5}$	6640^{+1240}_{-1030}	$0.070^{+0.046}_{-0.042}$	$0.714^{+0.038}_{-0.045}$	$0.275^{+0.043}_{-0.036}$	$0.011^{+0.003}_{-0.002}$
13	$8.1^{+0.4}_{-0.4}$	28^{+3}_{-3}	$3.67^{+0.08}_{-0.08}$	$5.5^{+0.7}_{-0.7}$	4660^{+700}_{-660}	$-0.012^{+0.027}_{-0.021}$	$0.696^{+0.034}_{-0.038}$	$0.291^{+0.036}_{-0.033}$	$0.013^{+0.003}_{-0.002}$
14	$12.2^{+2.4}_{-0.6}$	18^{+2}_{-7}	$4.50^{+0.16}_{-0.10}$	$12.3^{+2.7}_{-1.6}$	2860^{+780}_{-460}	$0.050^{+0.037}_{-0.039}$	$0.741^{+0.054}_{-0.061}$	$0.244^{+0.061}_{-0.054}$	$0.015^{+0.001}_{-0.001}$
15	$8.2^{+1.0}_{-0.3}$	16^{+5}_{-16}	$3.58^{+0.07}_{-0.08}$	$4.2^{+0.5}_{-0.6}$	3100^{+770}_{-650}	$0.092^{+0.087}_{-0.081}$	$0.712^{+0.027}_{-0.032}$	$0.278^{+0.030}_{-0.027}$	$0.010^{+0.003}_{-0.001}$
16	$9.5^{+0.5}_{-0.4}$	21^{+2}_{-3}	$3.92^{+0.08}_{-0.08}$	$6.1^{+0.9}_{-0.8}$	7030^{+1260}_{-1270}	$0.031^{+0.054}_{-0.047}$	$0.681^{+0.034}_{-0.035}$	$0.297^{+0.036}_{-0.034}$	$0.021^{+0.003}_{-0.002}$
17	$10.8^{+0.7}_{-0.5}$	18^{+2}_{-2}	$4.16^{+0.10}_{-0.10}$	$7.2^{+1.0}_{-0.9}$	2320^{+510}_{-440}	$0.097^{+0.062}_{-0.052}$	$0.683^{+0.043}_{-0.048}$	$0.299^{+0.048}_{-0.044}$	$0.018^{+0.001}_{-0.001}$
18	$10.9^{+1.3}_{-0.5}$	9^{+4}_{-9}	$3.95^{+0.08}_{-0.08}$	$4.9^{+0.6}_{-0.5}$	3470^{+390}_{-280}	$-0.001^{+0.007}_{-0.005}$	$0.698^{+0.034}_{-0.035}$	$0.289^{+0.033}_{-0.033}$	$0.013^{+0.003}_{-0.002}$
$\odot^{(a)}$							0.716	0.270	0.014

Notes. Same as Table 5.7. Numbering according to Table 8.1. $^{(a)}$ Protosolar nebula values from Asplund et al. (2009).

Table D.6: Atmospheric parameters of the runaway stars.

#	$T_{\rm eff}$	log g	$v_{\rm rad}$	$v \sin(i)$	ζ	ξ	$A_{\rm eff,s}/A_{\rm eff,p}$	log($n(x)$)										
	(K)	(cgs)	($\rm km\,s^{-1}$)					He	C	N	O	Ne	Mg	Al	Si	S	Ar	Fe
1	14 300	4.043	250.1	85.0	35.8	2.03	…	−1.14	−2.97	…	−3.25	−4.16	−4.51	−5.52	−4.24	−4.63	…	−4.20
Stat.	+90	+0.011	+1.3	+1.7	+5.6	+0.18	…	+0.03	+0.08	…	+0.08	+0.12	+0.07	+0.12	+0.05	+0.07	…	+0.06
	−70	−0.009	−1.3	−1.4	−5.6	−0.28		−0.03	−0.08		−0.08	−0.11	−0.06	−0.14	−0.05	−0.07		−0.05
Sys.	+290	+0.100	+0.3	+0.7	+2.5	+0.48	…	+0.19	+0.10	…	+0.02	+0.07	+0.02	+0.02	+0.03	+0.06	…	+0.03
	−290	−0.100	−0.4	−1.1	−0.5	−0.61		−0.11	−0.09		−0.04	−0.04	−0.03	−0.03	−0.04	−0.05		−0.06
2	14 850	3.405	−121.4	108.9	12.3	0.01	…	−0.86	−3.65	…	−3.56	−4.27	−4.98	−6.21	−4.64	−5.22	…	−5.16
Stat.	+30	+0.007	+0.7	+0.2	+6.3	+0.41	…	+0.01	+0.05	…	+0.07	+0.05	+0.05	+0.14	+0.07	+0.06	…	+0.05
	−40	−0.014	−0.8	−0.1	−9.4	−0.01		−0.01	−0.06		−0.08	−0.06	−0.05	−0.15	−0.06	−0.04		−0.06
Sys.	+300	+0.100	+0.1	+0.5	+11.5	+2.20	…	+0.13	+0.05	…	+0.03	+0.03	+0.05	+0.05	+0.06	+0.04	…	+0.08
	−310	−0.100	−0.1	−0.1	− 4.3	−0.01		−0.15	−0.13		−0.08	−0.03	−0.17	−0.06	−0.26	−0.05		−0.09
3	15 360	3.941	148.0	146.9	26.9	2.13	…	−0.96	−3.41	…	−3.21	−4.04	−4.45	…	−4.22	−4.77	…	−4.46
Stat.	+ 60	+0.009	+0.9	+0.1	+7.7	+0.15	…	+0.02	+0.05	…	+0.04	+0.05	+0.04	…	+0.03	+0.03	…	+0.04
	−130	−0.005	−1.0	−0.3	−9.3	−0.12		−0.02	−0.06		−0.05	−0.04	−0.04		−0.04	−0.03		−0.04
Sys.	+310	+0.100	+0.6	+0.8	+6.0	+0.93	…	+0.14	+0.08	…	+0.04	+0.03	+0.09	…	+0.12	+0.04	…	+0.06
	−310	−0.100	−0.8	−0.2	−6.8	−1.25		−0.17	−0.10		−0.05	−0.02	−0.08		−0.14	−0.04		−0.07
4	16 140	4.142	112.8	20.2	15.5	0.98	…	−1.14	−3.97	−4.20	−3.57	−4.17	−4.99	…	−4.65	−5.30	…	−4.67
Stat.	+130	+0.020	+0.3	+1.7	+3.0	+0.41	…	+0.03	+0.06	+0.07	+0.07	+0.04	+0.04	…	+0.05	+0.03	…	+0.04
	−130	−0.019	−0.3	−1.8	−2.5	−0.38		−0.02	−0.06	−0.08	−0.07	−0.04	−0.05		−0.05	−0.04		−0.04
Sys.	+320	+0.100	+0.1	+0.1	+3.1	+1.84	…	+0.17	+0.08	+0.09	+0.02	+0.03	+0.06	…	+0.11	+0.03	…	+0.06
	−330	−0.100	−0.1	−1.5	−1.3	−0.98		−0.11	−0.10	−0.11	−0.06	−0.02	−0.09		−0.17	−0.05		−0.10
5p	16 280	4.112	135.4	18.2	5.8	1.94	…	−0.97	−3.56	−4.04	−3.24	−4.05	−4.66	−5.86	−4.40	−4.89	−5.48	−4.58
Stat.	+ 30	+0.014	+0.3	+0.3	+3.1	+0.28	…	+0.02	+0.03	+0.04	+0.03	+0.02	+0.03	+0.05	+0.02	+0.02	+0.07	+0.02
	−100	−0.020	−0.2	−0.4	−1.5	−0.21		−0.01	−0.03	−0.03	−0.03	−0.02	−0.03	−0.04	−0.02	−0.01	−0.07	−0.02
Sys.	+330	+0.100	+2.3	+2.9	+2.0	+0.44	…	+0.05	+0.05	+0.05	+0.02	+0.01	+0.02	+0.03	+0.01	+0.01	+0.04	+0.03
	−340	−0.100	−1.8	−3.6	−5.8	−0.58		−0.04	−0.05	−0.06	−0.02	−0.01	−0.03	−0.02	−0.02	−0.02	−0.04	−0.05
5s	16 640	4.292	119.0	1.5	0.0	1.90	0.491	…	…	…	…	…	…	…	…	…	…	…
Stat.	+ 60	+0.008	+0.3	+2.0	+3.5	+0.29	+0.035	…	…	…	…	…	…	…	…	…	…	…
	−120	−0.009	−0.2	−1.5	−0.0	−0.37	−0.012											
Sys.	+340	+0.153	+0.9	+2.3	+3.7	+0.57	+0.212	…	…	…	…	…	…	…	…	…	…	…
	−330	−0.302	−0.2	−1.5	−0.0	−0.74	−0.168											
6	16 520	4.083	263.6	135.1	21.4	1.65	…	−0.98	−3.27	−3.80	−3.02	−3.98	−4.33	−5.47	−4.06	−4.76	…	−4.40
Stat.	+30	+0.003	+0.9	+0.3	+ 8.5	+0.33	…	+0.03	+0.04	+0.05	+0.05	+0.05	+0.04	+0.07	+0.02	+0.04	…	+0.05
	−10	−0.013	−1.0	−0.8	−10.6	−0.27		−0.02	−0.05	−0.08	−0.05	−0.05	−0.04	−0.08	−0.04	−0.03		−0.05
Sys.	+340	+0.100	+0.3	+0.4	+8.4	+1.39	…	+0.13	+0.09	+0.08	+0.04	+0.01	+0.10	+0.01	+0.14	+0.06	…	+0.05
	−330	−0.100	−0.4	−0.1	−4.3	−1.65		−0.14	−0.11	−0.09	−0.05	−0.02	−0.11	−0.01	−0.19	−0.06		−0.07
7	16 550	3.868	−6.4	17.1	11.9	2.09	…	−1.00	−3.53	−4.05	−3.16	−4.01	−4.63	−5.77	−4.34	−4.84	−5.44	−4.56
Stat.	+40	+0.007	+0.1	+0.4	+0.3	+0.09	…	+0.01	+0.03	+0.02	+0.02	+0.01	+0.02	+0.04	+0.02	+0.02	+0.03	+0.01
	−50	−0.007	−0.1	−0.3	−0.7	−0.09		−0.02	−0.02	−0.03	−0.02	−0.01	−0.02	−0.04	−0.03	−0.01	−0.04	−0.02
Sys.	+330	+0.100	+0.1	+0.1	+0.2	+0.74	…	+0.13	+0.08	+0.09	+0.02	+0.01	+0.07	+0.03	+0.08	+0.02	+0.06	+0.03
	−340	−0.100	−0.1	−0.1	−0.5	−1.06		−0.14	−0.08	−0.08	−0.04	−0.02	−0.07	−0.05	−0.12	−0.03	−0.06	−0.06
8	18 510	4.295	98.4	82.2	52.1	2.10	…	−1.04	−3.48	−3.89	−3.08	−3.99	−4.42	−5.55	−4.33	−4.69	…	−4.63
Stat.	+30	+0.007	+0.4	+0.2	+1.0	+0.12	…	+0.02	+0.02	+0.02	+0.02	+0.02	+0.02	+0.04	+0.03	+0.02	…	+0.03
	−60	−0.008	−0.4	−0.5	−1.3	−0.10		−0.01	−0.01	−0.03	−0.01	−0.02	−0.03	−0.03	−0.03	−0.01		−0.03
Sys.	+380	+0.100	+0.2	+0.5	+1.5	+1.77	…	+0.13	+0.10	+0.10	+0.08	+0.03	+0.12	+0.04	+0.16	+0.06	…	+0.02
	−370	−0.100	−0.2	−0.1	−0.9	−2.10		−0.11	−0.11	−0.09	−0.11	−0.03	−0.15	−0.05	−0.22	−0.07		−0.05
9	18 630	3.168	442.5	127.0	21.6	6.52	…	−1.15	−4.01	−4.75	−3.61	−4.10	−4.92	−5.93	−4.80	−5.10	−6.00	−5.07
Stat.	+30	+0.003	+0.5	+0.1	+4.2	+0.02	…	+0.01	+0.02	+0.03	+0.01	+0.03	+0.02	+0.03	+0.02	+0.02	+0.04	+0.03
	−30	−0.004	−0.4	−0.1	−4.5	−0.22		−0.02	−0.03	−0.03	−0.02	−0.02	−0.02	−0.04	−0.02	−0.01	−0.01	−0.02
Sys.	+370	+0.100	+0.9	+0.9	+10.8	+2.66	…	+0.23	+0.10	+0.09	+0.22	+0.06	+0.17	+0.12	+0.31	+0.08	+0.08	+0.06
	−380	−0.100	−0.8	−0.1	−20.0	−2.69		−0.21	−0.10	−0.07	−0.14	−0.06	−0.17	−0.09	−0.16	−0.08	−0.01	−0.03
10	19 230	4.016	35.0	117.6	39.7	3.58	…	−1.07	−4.09	−4.52	−3.54	−4.34	−5.10	−5.99	−4.97	−5.32	…	−4.93
Stat.	+70	+0.012	+0.9	+0.2	+5.8	+0.31	…	+0.01	+0.05	+0.06	+0.05	+0.07	+0.06	+0.09	+0.03	+0.06	…	+0.08
	−50	−0.008	−1.1	−0.2	−6.6	−0.29		−0.03	−0.05	−0.06	−0.06	−0.07	−0.06	−0.09	−0.06	−0.06		−0.09
Sys.	+390	+0.100	+0.1	+1.2	+8.9	+2.42	…	+0.13	+0.17	+0.13	+0.16	+0.05	+0.24	+0.10	+0.28	+0.09	…	+0.02
	−390	−0.100	−0.2	−0.7	−9.4	−3.58		−0.13	−0.19	−0.11	−0.17	−0.04	−0.13	−0.09	−0.19	−0.07		−0.06
$\odot^{(a)}$								−1.06	−3.57	−4.17	−3.31	−4.07	−4.40	−5.55	−4.49	−4.88	−5.60	−4.50
								+0.01	+0.05	+0.05	+0.05	+0.10	+0.04	+0.03	+0.04	+0.03	+0.13	+0.04
								−0.01	−0.05	−0.05	−0.05	−0.10	−0.04	−0.03	−0.04	−0.03	−0.13	−0.04

Table D.6: continued.

#	$T_{\rm eff}$	log g	$v_{\rm rad}$	$v\sin(i)$	ζ	ξ	$A_{\rm eff,s}/A_{\rm eff,p}$	log($n(x)$)										
	(K)	(cgs)	($\rm km\,s^{-1}$)					He	C	N	O	Ne	Mg	Al	Si	S	Ar	Fe
11	19 380	3.925	142.6	241.4	42.0	5.76	…	−1.17	−3.82	−4.26	−3.32	−4.38	−4.76	−5.65	−4.93	−4.77	−5.59	−5.14
Stat.	+60	+0.007	+1.0	+0.4	+ 8.7	+0.33	…	+0.02	+0.03	+0.04	+0.04	+0.08	+0.05	+0.05	+0.05	+0.03	+0.07	+0.07
	−70	−0.012	−1.1	−0.9	−12.9	−0.23		−0.02	−0.04	−0.03	−0.03	−0.08	−0.06	−0.05	−0.04	−0.02	−0.10	−0.07
Sys.	+400	+0.100	+0.4	+1.0	+22.9	+2.27	…	+0.18	+0.17	+0.11	+0.21	+0.05	+0.18	+0.13	+0.26	+0.12	+0.15	+0.05
	−390	−0.100	−0.3	−0.3	−34.9	−2.87		−0.15	−0.13	−0.06	−0.14	−0.04	−0.14	−0.06	−0.12	−0.08	−0.25	−0.07
12	19 580	3.993	76.1	36.7	22.0	2.02	…	−1.05	−3.83	−4.35	−3.33	−4.13	−4.69	−5.86	−4.62	−4.98	−5.78	−4.73
Stat.	+100	+0.009	+0.3	+0.2	+1.1	+0.23	…	+0.01	+0.03	+0.02	+0.03	+0.03	+0.05	+0.02	+0.04	+0.02	+0.05	+0.03
	−100	−0.011	−0.2	−1.9	−0.8	−0.39		−0.02	−0.03	−0.03	−0.03	−0.03	−0.04	−0.03	−0.04	−0.02	−0.07	−0.03
Sys.	+400	+0.100	+0.2	+0.1	+1.3	+2.11	…	+0.08	+0.08	+0.07	+0.12	+0.05	+0.16	+0.06	+0.18	+0.06	+0.07	+0.02
	−390	−0.100	−0.1	−0.2	−0.6	−2.02		−0.08	−0.13	−0.10	−0.15	−0.04	−0.21	−0.10	−0.21	−0.07	−0.10	−0.05
13	20 460	3.870	90.8	36.1	7.4	2.13	…	−1.02	−3.69	−4.20	−3.26	−3.99	−4.65	−5.77	−4.59	−4.83	−5.55	−4.67
Stat.	+60	+0.005	+0.2	+0.2	+0.5	+0.11	…	+0.01	+0.01	+0.01	+0.02	+0.02	+0.02	+0.01	+0.01	+0.01	+0.03	+0.02
	−50	−0.005	−0.2	−0.4	−1.4	−0.06		−0.01	−0.02	−0.01	−0.02	−0.02	−0.03	−0.02	−0.02	−0.01	−0.02	−0.01
Sys.	+410	+0.100	+0.1	+0.2	+0.9	+1.37	…	+0.07	+0.06	+0.07	+0.14	+0.04	+0.11	+0.07	+0.16	+0.07	+0.04	+0.04
	−420	−0.100	−0.1	−0.1	−2.0	−1.98		−0.07	−0.07	−0.08	−0.14	−0.04	−0.11	−0.09	−0.16	−0.07	−0.03	−0.05
14	22 030	3.348	97.7	86.3	48.3	13.36	…	−1.12	−3.65	−4.06	−3.28	−3.89	−4.60	−5.68	−4.53	−4.80	−5.36	−4.65
Stat.	+30	+0.002	+0.3	+0.1	+0.3	+0.11	…	+0.02	+0.02	+0.01	+0.01	+0.03	+0.02	+0.01	+0.01	+0.03	+0.03	+0.02
	−30	−0.004	−0.3	−0.4	−1.1	−0.04		−0.02	−0.02	−0.01	−0.01	−0.03	−0.02	−0.02	−0.01	−0.02	−0.03	−0.01
Sys.	+450	+0.100	+0.2	+0.3	+1.8	+1.45	…	+0.13	+0.07	+0.04	+0.06	+0.02	+0.09	+0.04	+0.04	+0.03	+0.06	+0.03
	−440	−0.100	−0.3	−0.1	−2.5	−1.12		−0.13	−0.07	−0.02	−0.06	−0.03	−0.09	−0.03	−0.05	−0.02	−0.07	−0.02
15	22 230	4.118	87.7	23.1	7.9	2.14	…	−1.05	−3.87	−4.41	−3.36	−4.08	−4.71	−5.88	−4.73	−4.95	−5.65	−4.75
Stat.	+80	+0.007	+0.1	+0.3	+0.8	+0.15	…	+0.01	+0.02	+0.02	+0.02	+0.02	+0.03	+0.01	+0.02	+0.02	+0.03	+0.02
	−60	−0.007	−0.2	−0.2	−1.1	−0.13		−0.01	−0.02	−0.01	−0.03	−0.02	−0.03	−0.02	−0.03	−0.02	−0.03	−0.02
Sys.	+450	+0.100	+0.1	+0.1	+1.0	+1.40	…	+0.06	+0.05	+0.06	+0.13	+0.03	+0.12	+0.04	+0.13	+0.06	+0.08	+0.05
	−450	−0.100	−0.1	−0.1	−1.8	−2.11		−0.06	−0.06	−0.06	−0.13	−0.04	−0.12	−0.05	−0.14	−0.06	−0.07	−0.05
16	22 290	3.843	59.8	30.3	18.0	7.65	…	−1.00	−3.46	−3.78	−3.13	−3.72	−4.41	−5.46	−4.28	−4.52	−5.22	−4.40
Stat.	+60	+0.008	+0.1	+0.3	+0.4	+0.12	…	+0.01	+0.02	+0.02	+0.02	+0.02	+0.03	+0.03	+0.02	+0.02	+0.02	+0.01
	−60	−0.008	−0.2	−0.3	−0.9	−0.12		−0.02	−0.02	−0.01	−0.01	−0.02	−0.03	−0.03	−0.02	−0.02	−0.03	−0.02
Sys.	+450	+0.100	+0.1	+0.2	+1.0	+0.77	…	+0.06	+0.04	+0.05	+0.10	+0.02	+0.08	+0.02	+0.08	+0.02	+0.03	+0.02
	−450	−0.100	−0.1	−0.1	−1.5	−0.79		−0.08	−0.04	−0.03	−0.09	−0.04	−0.09	−0.02	−0.07	−0.07	−0.07	−0.02
17	23 540	3.759	−0.2	105.8	4.1	7.48	…	−1.00	−3.56	−3.93	−3.16	−3.83	−4.55	−5.52	−4.35	−4.54	−5.20	−4.57
Stat.	+40	+0.006	+0.3	+0.1	+5.3	+0.07	…	+0.02	+0.02	+0.02	+0.02	+0.03	+0.05	+0.02	+0.02	+0.02	+0.01	+0.02
	−30	−0.005	−0.4	−0.1	−4.1	−0.09		−0.02	−0.02	−0.01	−0.01	−0.03	−0.04	−0.02	−0.02	−0.03	−0.02	−0.01
Sys.	+480	+0.100	+0.2	+0.5	+7.1	+0.97	…	+0.09	+0.05	+0.04	+0.07	+0.03	+0.12	+0.03	+0.06	+0.04	+0.01	+0.01
	−470	−0.100	−0.1	−0.1	−4.1	−0.97		−0.09	−0.07	−0.03	−0.07	−0.03	−0.09	−0.04	−0.06	−0.05	−0.06	−0.01
18	25 460	4.101	263.2	163.4	59.8	2.99	…	−1.03	−3.88	−4.25	−3.26	−3.87	−4.53	−5.74	−4.65	−4.86	…	−4.67
Stat.	+60	+0.012	+0.7	+0.1	+3.7	+0.36	…	+0.02	+0.04	+0.03	+0.05	+0.05	+0.05	+0.04	+0.03	+0.05	…	+0.02
	−60	−0.011	−0.8	−0.1	−4.5	−0.27		−0.02	−0.03	−0.02	−0.03	−0.07	−0.05	−0.04	−0.04	−0.04		−0.03
Sys.	+510	+0.100	+0.2	+2.6	+ 8.7	+1.66	…	+0.07	+0.08	+0.04	+0.15	+0.01	+0.08	+0.04	+0.11	+0.08	…	+0.02
	−510	−0.100	−0.4	−0.1	−11.3	−0.99		−0.07	−0.11	−0.05	−0.14	−0.02	−0.10	−0.07	−0.14	−0.13		−0.04
$\odot^{(a)}$								−1.06	−3.57	−4.17	−3.31	−4.07	−4.40	−5.55	−4.49	−4.88	−5.60	−4.50
								+0.01	+0.05	+0.05	+0.05	+0.10	+0.04	+0.03	+0.04	+0.03	+0.13	+0.04
								−0.01	−0.05	−0.05	−0.05	−0.10	−0.04	−0.03	−0.04	−0.03	−0.13	−0.04

Notes. Same as Table 5.2 Numbering according to Table 8.1. Aluminum, argon, and nitrogen lines are not visible for all temperatures. For the double-lined spectroscopic binary systems, the parameter $A_{\rm eff,s}/A_{\rm eff,p}$ is the ratio of effective surface areas (see Sect. 5.1.4 for details). Furthermore, abundances of the secondary components "s" are tied to the ones of the primaries "p" owing to the assumption of a homogeneous chemical composition.
$^{(a)}$ Protosolar nebula values and uncertainties from Asplund et al. (2009).

Table D.7: Kinematic parameters of the runaway stars using Milky Way mass Model I.

#	x	y	z	v_x	v_y	v_z	v_{Grf}	$v_{\mathrm{Grf}} - v_{\mathrm{esc}}$	P_{b}	x_{d}	y_{d}	r_{d}	$v_{x,\mathrm{d}}$	$v_{y,\mathrm{d}}$	$v_{z,\mathrm{d}}$	$v_{\mathrm{Grf,d}}$	v_{ej}	τ_{flight}
	(kpc)			(km s^{-1})					(%)	(kpc)			(km s^{-1})					(Myr)
1	−10.5	−5.6	3.4	−190	90	130	260	−310	100	−5.1	−6.8	8.9	−280	20	170	360	240	22
Stat.	$^{+0.5}_{-0.3}$	$^{+1.0}_{-0.9}$	$^{+0.5}_{-0.7}$	$^{+230}_{-230}$	$^{+150}_{-140}$	$^{+210}_{-210}$	$^{+250}_{-200}$	$^{+250}_{-210}$	⋯	$^{+16.1}_{-5.3}$	$^{+8.5}_{-2.4}$	$^{+3.9}_{-7.8}$	$^{+250}_{-200}$	$^{+190}_{-330}$	$^{+200}_{-60}$	$^{+200}_{-180}$	$^{+280}_{-50}$	$^{+43}_{-13}$
2	−9.3	1.0	0.9	180	220	0	280	−320	100	−12.6	−7.2	14.5	0	180	30	180	120	39
Stat.	$^{+0.2}_{-0.2}$	$^{+0.2}_{-0.2}$	$^{+0.2}_{-0.2}$	$^{+30}_{-20}$	$^{+10}_{-20}$	$^{+20}_{-10}$	$^{+30}_{-20}$	$^{+30}_{-30}$	⋯	$^{+1.3}_{-0.9}$	$^{+1.9}_{-2.2}$	$^{+1.0}_{-0.8}$	$^{+70}_{-60}$	$^{+30}_{-40}$	$^{+20}_{-10}$	$^{+40}_{-30}$	$^{+40}_{-20}$	$^{+13}_{-10}$
3	−8.8	−0.2	0.2	−210	220	−90	320	−300	100	8.0	−5.1	9.5	−280	−70	80	300	220	51
Stat.	$^{+0.2}_{-0.1}$	$^{+0.1}_{-0.1}$	$^{+0.1}_{-0.1}$	$^{+20}_{-30}$	$^{+10}_{-10}$	$^{+40}_{-30}$	$^{+30}_{-30}$	$^{+40}_{-30}$	⋯	$^{+4.8}_{-3.7}$	$^{+0.2}_{-0.2}$	$^{+4.3}_{-2.9}$	$^{+50}_{-50}$	$^{+20}_{-10}$	$^{+10}_{-10}$	$^{+50}_{-40}$	$^{+10}_{-30}$	$^{+15}_{-11}$
4	−12.2	−3.0	4.5	−60	260	120	290	−280	100	−8.6	−10.3	13.7	−160	190	150	300	170	32
Stat.	$^{+0.6}_{-0.6}$	$^{+0.4}_{-0.5}$	$^{+0.7}_{-0.6}$	$^{+120}_{-120}$	$^{+160}_{-160}$	$^{+110}_{-110}$	$^{+180}_{-170}$	$^{+180}_{-170}$	⋯	$^{+10.0}_{-4.1}$	$^{+4.3}_{-5.2}$	$^{+2.5}_{-5.8}$	$^{+140}_{-120}$	$^{+180}_{-250}$	$^{+90}_{-40}$	$^{+160}_{-110}$	$^{+150}_{-50}$	$^{+30}_{-13}$
5	−6.3	−2.1	4.1	−60	50	110	140	−470	100	−2.9	−2.5	3.9	−230	−50	230	330	330	25
Stat.	$^{+1.7}_{-1.0}$	$^{+0.9}_{-1.9}$	$^{+3.6}_{-1.8}$	$^{+80}_{-150}$	$^{+90}_{-160}$	$^{+50}_{-70}$	$^{+110}_{-80}$	$^{+120}_{-80}$	⋯	$^{+5.2}_{-3.3}$	$^{+3.6}_{-1.6}$	$^{+3.1}_{-3.8}$	$^{+130}_{-180}$	$^{+140}_{-270}$	$^{+340}_{-80}$	$^{+360}_{-120}$	$^{+410}_{-130}$	$^{+12}_{-9}$
6	−9.1	0.5	3.2	−350	410	180	570	−30	78	−2.8	−5.8	6.6	−440	350	230	610	400	16
Stat.	$^{+0.2}_{-0.3}$	$^{+0.2}_{-0.2}$	$^{+1.2}_{-0.9}$	$^{+100}_{-130}$	$^{+80}_{-60}$	$^{+30}_{-40}$	$^{+110}_{-80}$	$^{+120}_{-80}$	⋯	$^{+5.5}_{-2.9}$	$^{+2.2}_{-3.7}$	$^{+3.2}_{-1.0}$	$^{+110}_{-110}$	$^{+60}_{-60}$	$^{+20}_{-20}$	$^{+80}_{-80}$	$^{+180}_{-70}$	$^{+7}_{-6}$
7	−9.9	0.0	−1.8	0	190	20	200	−400	100	−1.8	−7.2	8.1	−240	0	−80	260	100	56
Stat.	$^{+0.4}_{-0.3}$	$^{+0.1}_{-0.1}$	$^{+0.4}_{-0.4}$	$^{+70}_{-70}$	$^{+90}_{-90}$	$^{+60}_{-60}$	$^{+80}_{-90}$	$^{+80}_{-90}$	⋯	$^{+7.2}_{-7.5}$	$^{+4.0}_{-5.4}$	$^{+5.0}_{-4.6}$	$^{+150}_{-90}$	$^{+170}_{-150}$	$^{+30}_{-100}$	$^{+120}_{-80}$	$^{+130}_{-40}$	$^{+23}_{-23}$
8	−8.0	0.3	−1.2	−290	370	−160	490	−120	100	−5.8	−2.2	6.2	−350	360	−180	530	340	7
Stat.	$^{+0.1}_{-0.1}$	$^{+0.2}_{-0.1}$	$^{+0.2}_{-0.3}$	$^{+60}_{-70}$	$^{+30}_{-30}$	$^{+20}_{-30}$	$^{+70}_{-40}$	$^{+60}_{-50}$	⋯	$^{+0.8}_{-0.6}$	$^{+0.4}_{-0.5}$	$^{+0.5}_{-0.6}$	$^{+70}_{-70}$	$^{+30}_{-30}$	$^{+20}_{-20}$	$^{+70}_{-60}$	$^{+70}_{-50}$	$^{+1}_{-1}$
9	−6.4	−17.2	−9.8	−600	−140	−330	710	180	13	10.4	−12.1	17.1	−570	−210	−360	720	580	28
Stat.	$^{+0.5}_{-0.5}$	$^{+3.6}_{-3.9}$	$^{+2.1}_{-2.3}$	$^{+450}_{-500}$	$^{+190}_{-190}$	$^{+320}_{-330}$	$^{+480}_{-380}$	$^{+490}_{-380}$	⋯	$^{+62.8}_{-12.7}$	$^{+39.4}_{-7.6}$	$^{+60.6}_{-9.4}$	$^{+420}_{-500}$	$^{+230}_{-170}$	$^{+260}_{-310}$	$^{+460}_{-290}$	$^{+480}_{-260}$	$^{+91}_{-14}$
10	−15.0	7.0	−8.2	70	240	−110	290	−250	98	−15.0	−6.5	17.6	−70	220	−170	310	200	56
Stat.	$^{+3.7}_{-8.3}$	$^{+8.8}_{-3.9}$	$^{+4.5}_{-10.4}$	$^{+310}_{-200}$	$^{+200}_{-260}$	$^{+150}_{-270}$	$^{+310}_{-130}$	$^{+350}_{-120}$	⋯	$^{+21.5}_{-27.2}$	$^{+18.8}_{-49.1}$	$^{+45.8}_{-13.3}$	$^{+380}_{-290}$	$^{+190}_{-190}$	$^{+90}_{-230}$	$^{+260}_{-60}$	$^{+350}_{-80}$	$^{+137}_{-27}$
11	−5.5	1.8	−5.9	70	250	−130	300	−310	100	−5.4	−5.1	7.5	−90	190	−250	330	270	29
Stat.	$^{+1.3}_{-0.9}$	$^{+0.8}_{-0.6}$	$^{+1.8}_{-2.5}$	$^{+160}_{-160}$	$^{+140}_{-150}$	$^{+90}_{-100}$	$^{+110}_{-90}$	$^{+120}_{-80}$	⋯	$^{+3.9}_{-6.2}$	$^{+4.2}_{-8.4}$	$^{+9.4}_{-4.6}$	$^{+140}_{-140}$	$^{+100}_{-90}$	$^{+100}_{-150}$	$^{+150}_{-90}$	$^{+150}_{-60}$	$^{+23}_{-9}$
12	−9.8	5.2	−3.9	110	290	−100	330	−250	100	−11.1	−4.1	11.9	−30	300	−150	330	180	30
Stat.	$^{+0.3}_{-0.3}$	$^{+1.0}_{-0.9}$	$^{+0.6}_{-0.8}$	$^{+80}_{-70}$	$^{+50}_{-50}$	$^{+60}_{-70}$	$^{+50}_{-40}$	$^{+50}_{-40}$	⋯	$^{+2.7}_{-2.5}$	$^{+3.6}_{-6.5}$	$^{+3.7}_{-2.1}$	$^{+110}_{-100}$	$^{+20}_{-40}$	$^{+50}_{-50}$	$^{+30}_{-10}$	$^{+50}_{-30}$	$^{+17}_{-9}$
13	−8.7	1.0	−4.5	−160	150	−100	250	−350	100	−1.4	−2.9	3.4	−360	60	−240	430	290	28
Stat.	$^{+0.1}_{-0.1}$	$^{+0.2}_{-0.2}$	$^{+0.6}_{-0.8}$	$^{+130}_{-140}$	$^{+100}_{-100}$	$^{+30}_{-20}$	$^{+80}_{-70}$	$^{+90}_{-60}$	⋯	$^{+2.8}_{-3.5}$	$^{+2.6}_{-3.5}$	$^{+4.0}_{-2.8}$	$^{+150}_{-150}$	$^{+90}_{-130}$	$^{+70}_{-160}$	$^{+200}_{-120}$	$^{+240}_{-110}$	$^{+6}_{-4}$
14	−8.6	−1.8	−2.2	−160	180	−40	250	−360	100	−1.9	−5.5	5.8	−320	50	−120	340	150	27
Stat.	$^{+0.1}_{-0.1}$	$^{+0.3}_{-0.6}$	$^{+0.4}_{-0.6}$	$^{+30}_{-60}$	$^{+20}_{-20}$	$^{+20}_{-20}$	$^{+40}_{-30}$	$^{+50}_{-30}$	⋯	$^{+2.7}_{-1.8}$	$^{+0.5}_{-0.6}$	$^{+0.7}_{-0.6}$	$^{+40}_{-30}$	$^{+50}_{-80}$	$^{+20}_{-30}$	$^{+40}_{-30}$	$^{+30}_{-10}$	$^{+5}_{-5}$
15	−7.1	2.1	−1.9	170	240	−50	300	−320	100	−9.3	−4.0	10.2	10	230	−90	250	140	25
Stat.	$^{+0.3}_{-0.3}$	$^{+0.6}_{-0.5}$	$^{+0.5}_{-0.5}$	$^{+80}_{-70}$	$^{+40}_{-40}$	$^{+70}_{-60}$	$^{+50}_{-30}$	$^{+50}_{-30}$	⋯	$^{+1.5}_{-3.7}$	$^{+2.7}_{-7.1}$	$^{+6.4}_{-2.1}$	$^{+60}_{-50}$	$^{+20}_{-50}$	$^{+40}_{-50}$	$^{+30}_{-60}$	$^{+40}_{-20}$	$^{+30}_{-10}$
16	−5.6	2.4	−6.0	0	60	−150	170	−430	100	−3.5	0.2	3.8	−190	110	−300	370	380	26
Stat.	$^{+0.5}_{-0.6}$	$^{+0.5}_{-0.5}$	$^{+1.2}_{-1.1}$	$^{+120}_{-130}$	$^{+140}_{-140}$	$^{+80}_{-80}$	$^{+100}_{-30}$	$^{+90}_{-40}$	⋯	$^{+2.5}_{-3.3}$	$^{+3.6}_{-3.8}$	$^{+3.4}_{-2.5}$	$^{+130}_{-130}$	$^{+30}_{-110}$	$^{+80}_{-100}$	$^{+150}_{-120}$	$^{+180}_{-130}$	$^{+11}_{-6}$
17	−6.8	0.4	−1.7	−50	120	−80	160	−470	100	−5.1	−1.4	5.3	−190	110	−130	250	220	15
Stat.	$^{+0.4}_{-0.4}$	$^{+0.1}_{-0.1}$	$^{+0.4}_{-0.4}$	$^{+30}_{-30}$	$^{+40}_{-40}$	$^{+30}_{-30}$	$^{+20}_{-30}$	$^{+20}_{-30}$	⋯	$^{+0.7}_{-0.5}$	$^{+0.6}_{-0.7}$	$^{+0.6}_{-0.7}$	$^{+30}_{-20}$	$^{+30}_{-40}$	$^{+30}_{-40}$	$^{+30}_{-20}$	$^{+60}_{-60}$	$^{+3}_{-2}$
18	−8.7	−1.6	3.0	−50	290	320	440	−160	100	−8.0	−4.3	9.1	−100	280	340	450	350	9
Stat.	$^{+0.1}_{-0.1}$	$^{+0.1}_{-0.3}$	$^{+0.4}_{-0.2}$	$^{+60}_{-60}$	$^{+60}_{-50}$	$^{+40}_{-30}$	$^{+70}_{-60}$	$^{+60}_{-60}$	⋯	$^{+0.6}_{-0.6}$	$^{+0.6}_{-0.6}$	$^{+0.6}_{-0.6}$	$^{+60}_{-70}$	$^{+60}_{-60}$	$^{+30}_{-30}$	$^{+60}_{-60}$	$^{+40}_{-40}$	$^{+2}_{-1}$

Notes. Numbering according to Table 8.1. Results and statistical uncertainties (*"Stat." row*) are given as median values and 99%-confidence limits and are derived via a Monte Carlo simulation. The probability P_{b} is the fraction of Monte Carlo runs for which the star is bound to the Milky Way. See Section 8.2 for details.

Table D.8: Kinematic parameters of the runaway stars using Milky Way mass Model II.

#	x	y	z	v_x	v_y	v_z	$v_{\rm Grf}$	$v_{\rm Grf} - v_{\rm esc}$	$P_{\rm b}$	$x_{\rm d}$	$y_{\rm d}$	$r_{\rm d}$	$v_{x,{\rm d}}$	$v_{y,{\rm d}}$	$v_{z,{\rm d}}$	$v_{\rm Grf,d}$	$v_{\rm ej}$	$\tau_{\rm flight}$
	(kpc)			(km s^{-1})					(%)	(kpc)			(km s^{-1})					(Myr)
1	−10.5	−5.6	3.4	−190	90	130	260	−270	100	−5.2	−6.8	8.9	−280	20	170	360	240	22
Stat.	$^{+0.5}_{-0.3}$	$^{+1.0}_{-0.9}$	$^{+0.5}_{-0.7}$	$^{+230}_{-230}$	$^{+150}_{-150}$	$^{+210}_{-210}$	$^{+250}_{-200}$	$^{+250}_{-210}$	⋯	$^{+16.2}_{-5.2}$	$^{+8.5}_{-2.4}$	$^{+3.9}_{-7.8}$	$^{+250}_{-200}$	$^{+190}_{-340}$	$^{+200}_{-60}$	$^{+200}_{-180}$	$^{+290}_{-50}$	$^{+43}_{-13}$
2	−9.3	1.0	0.9	180	220	0	280	−280	100	−12.6	−7.1	14.5	10	180	30	180	130	39
Stat.	$^{+0.2}_{-0.2}$	$^{+0.2}_{-0.2}$	$^{+0.2}_{-0.2}$	$^{+30}_{-20}$	$^{+10}_{-20}$	$^{+20}_{-10}$	$^{+30}_{-20}$	$^{+30}_{-20}$	⋯	$^{+1.2}_{-1.0}$	$^{+1.9}_{-2.1}$	$^{+1.0}_{-0.8}$	$^{+60}_{-60}$	$^{+30}_{-40}$	$^{+20}_{-10}$	$^{+40}_{-30}$	$^{+30}_{-30}$	$^{+12}_{-10}$
3	−8.8	−0.2	0.2	−210	220	−90	320	−260	100	8.1	−5.0	9.5	−280	−70	80	300	220	51
Stat.	$^{+0.2}_{-0.1}$	$^{+0.1}_{-0.1}$	$^{+0.1}_{-0.1}$	$^{+20}_{-30}$	$^{+10}_{-10}$	$^{+40}_{-30}$	$^{+30}_{-30}$	$^{+40}_{-30}$	⋯	$^{+4.7}_{-3.6}$	$^{+0.2}_{-0.2}$	$^{+4.3}_{-2.8}$	$^{+50}_{-50}$	$^{+20}_{-10}$	$^{+10}_{-10}$	$^{+40}_{-40}$	$^{+10}_{-30}$	$^{+15}_{-10}$
4	−12.2	−3.0	4.5	−60	260	120	290	−230	100	−8.6	−10.3	13.7	−160	190	150	300	170	32
Stat.	$^{+0.6}_{-0.6}$	$^{+0.4}_{-0.5}$	$^{+0.7}_{-0.6}$	$^{+120}_{-120}$	$^{+150}_{-160}$	$^{+110}_{-110}$	$^{+180}_{-170}$	$^{+170}_{-170}$	⋯	$^{+9.9}_{-4.1}$	$^{+4.3}_{-5.2}$	$^{+2.5}_{-5.7}$	$^{+140}_{-120}$	$^{+180}_{-240}$	$^{+100}_{-40}$	$^{+160}_{-120}$	$^{+150}_{-50}$	$^{+30}_{-13}$
5	−6.3	−2.1	4.1	−60	50	110	140	−430	100	−2.9	−2.5	3.8	−230	−50	230	330	330	25
Stat.	$^{+1.7}_{-1.0}$	$^{+0.9}_{-1.9}$	$^{+3.6}_{-1.8}$	$^{+80}_{-150}$	$^{+90}_{-160}$	$^{+50}_{-70}$	$^{+110}_{-80}$	$^{+130}_{-80}$	⋯	$^{+5.2}_{-3.3}$	$^{+3.6}_{-1.5}$	$^{+3.2}_{-3.7}$	$^{+130}_{-200}$	$^{+140}_{-280}$	$^{+350}_{-80}$	$^{+370}_{-130}$	$^{+430}_{-130}$	$^{+12}_{-9}$
6	−9.1	0.5	3.2	−350	410	180	570	10	40	−2.8	−5.8	6.5	−440	350	230	610	400	16
Stat.	$^{+0.2}_{-0.3}$	$^{+0.2}_{-0.2}$	$^{+1.2}_{-0.9}$	$^{+100}_{-130}$	$^{+80}_{-60}$	$^{+30}_{-40}$	$^{+110}_{-80}$	$^{+120}_{-80}$	⋯	$^{+5.5}_{-2.9}$	$^{+2.2}_{-3.7}$	$^{+3.3}_{-0.9}$	$^{+110}_{-120}$	$^{+60}_{-60}$	$^{+10}_{-20}$	$^{+80}_{-80}$	$^{+180}_{-60}$	$^{+7}_{-6}$
7	−9.9	0.0	−1.8	0	190	20	190	−360	100	−2.0	−7.2	8.1	−240	0	−80	260	100	56
Stat.	$^{+0.4}_{-0.3}$	$^{+0.1}_{-0.1}$	$^{+0.4}_{-0.4}$	$^{+70}_{-70}$	$^{+90}_{-90}$	$^{+60}_{-60}$	$^{+90}_{-80}$	$^{+90}_{-90}$	⋯	$^{+7.3}_{-7.3}$	$^{+4.1}_{-5.4}$	$^{+5.0}_{-4.7}$	$^{+150}_{-90}$	$^{+170}_{-150}$	$^{+30}_{-90}$	$^{+120}_{-80}$	$^{+130}_{-40}$	$^{+22}_{-23}$
8	−8.0	0.3	−1.2	−290	360	−160	490	−80	100	−5.8	−2.2	6.2	−350	360	−180	530	340	7
Stat.	$^{+0.1}_{-0.1}$	$^{+0.2}_{-0.1}$	$^{+0.2}_{-0.3}$	$^{+60}_{-70}$	$^{+40}_{-20}$	$^{+20}_{-30}$	$^{+70}_{-50}$	$^{+60}_{-50}$	⋯	$^{+0.8}_{-0.6}$	$^{+0.4}_{-0.4}$	$^{+0.5}_{-0.6}$	$^{+70}_{-70}$	$^{+30}_{-30}$	$^{+20}_{-20}$	$^{+70}_{-60}$	$^{+70}_{-50}$	$^{+1}_{-1}$
9	−6.4	−17.2	−9.8	−600	−140	−330	710	230	7	10.4	−12.1	17.1	−570	−210	−360	720	580	28
Stat.	$^{+0.5}_{-0.5}$	$^{+3.6}_{-3.9}$	$^{+2.1}_{-2.3}$	$^{+450}_{-500}$	$^{+190}_{-190}$	$^{+320}_{-330}$	$^{+480}_{-380}$	$^{+480}_{-380}$	⋯	$^{+64.5}_{-12.7}$	$^{+40.2}_{-7.6}$	$^{+62.3}_{-9.4}$	$^{+420}_{-500}$	$^{+230}_{-170}$	$^{+260}_{-310}$	$^{+460}_{-290}$	$^{+490}_{-260}$	$^{+94}_{-14}$
10	−15.0	7.0	−8.2	70	230	−110	280	−210	97	−15.1	−6.4	17.8	−70	220	−170	300	200	56
Stat.	$^{+3.7}_{-8.3}$	$^{+8.8}_{-3.9}$	$^{+4.5}_{-10.4}$	$^{+310}_{-200}$	$^{+210}_{-250}$	$^{+150}_{-270}$	$^{+320}_{-120}$	$^{+360}_{-120}$	⋯	$^{+21.6}_{-27.6}$	$^{+18.9}_{-51.8}$	$^{+48.2}_{-13.4}$	$^{+390}_{-290}$	$^{+190}_{-200}$	$^{+100}_{-230}$	$^{+280}_{-50}$	$^{+350}_{-80}$	$^{+145}_{-27}$
11	−5.5	1.8	−5.9	70	250	−130	290	−270	100	−5.3	−5.1	7.5	−90	190	−250	330	270	29
Stat.	$^{+1.3}_{-0.9}$	$^{+0.8}_{-0.6}$	$^{+1.8}_{-2.5}$	$^{+160}_{-160}$	$^{+130}_{-150}$	$^{+90}_{-100}$	$^{+120}_{-80}$	$^{+120}_{-80}$	⋯	$^{+3.8}_{-6.4}$	$^{+4.2}_{-8.4}$	$^{+9.4}_{-4.6}$	$^{+140}_{-150}$	$^{+100}_{-90}$	$^{+100}_{-150}$	$^{+150}_{-90}$	$^{+150}_{-60}$	$^{+23}_{-9}$
12	−9.8	5.2	−3.9	110	290	−100	330	−210	100	−11.1	−4.1	12.0	−20	300	−150	330	180	30
Stat.	$^{+0.3}_{-0.3}$	$^{+1.0}_{-0.9}$	$^{+0.6}_{-0.8}$	$^{+80}_{-70}$	$^{+50}_{-50}$	$^{+60}_{-70}$	$^{+50}_{-40}$	$^{+60}_{-40}$	⋯	$^{+2.7}_{-2.6}$	$^{+3.6}_{-6.4}$	$^{+3.7}_{-2.2}$	$^{+100}_{-110}$	$^{+20}_{-40}$	$^{+50}_{-50}$	$^{+30}_{-10}$	$^{+50}_{-30}$	$^{+17}_{-9}$
13	−8.7	1.0	−4.5	−160	150	−100	250	−310	100	−1.4	−2.9	3.4	−360	60	−230	440	290	28
Stat.	$^{+0.1}_{-0.1}$	$^{+0.2}_{-0.2}$	$^{+0.6}_{-0.8}$	$^{+130}_{-140}$	$^{+100}_{-110}$	$^{+30}_{-20}$	$^{+80}_{-70}$	$^{+90}_{-60}$	⋯	$^{+2.8}_{-3.5}$	$^{+2.6}_{-3.4}$	$^{+4.0}_{-2.9}$	$^{+150}_{-160}$	$^{+90}_{-140}$	$^{+60}_{-180}$	$^{+190}_{-130}$	$^{+250}_{-110}$	$^{+6}_{-4}$
14	−8.6	−1.8	−2.2	−160	180	−40	250	−320	100	−1.9	−5.4	5.8	−320	50	−120	340	150	27
Stat.	$^{+0.1}_{-0.1}$	$^{+0.3}_{-0.6}$	$^{+0.4}_{-0.6}$	$^{+30}_{-60}$	$^{+20}_{-20}$	$^{+20}_{-20}$	$^{+40}_{-30}$	$^{+50}_{-30}$	⋯	$^{+2.7}_{-1.8}$	$^{+0.4}_{-0.7}$	$^{+0.6}_{-0.6}$	$^{+50}_{-30}$	$^{+50}_{-80}$	$^{+20}_{-20}$	$^{+40}_{-30}$	$^{+30}_{-10}$	$^{+6}_{-5}$
15	−7.1	2.1	−1.9	170	240	−50	300	−280	100	−9.4	−4.0	10.2	10	220	−90	240	140	25
Stat.	$^{+0.3}_{-0.3}$	$^{+0.6}_{-0.5}$	$^{+0.5}_{-0.5}$	$^{+80}_{-70}$	$^{+40}_{-50}$	$^{+70}_{-60}$	$^{+50}_{-40}$	$^{+50}_{-40}$	⋯	$^{+1.6}_{-3.6}$	$^{+2.7}_{-7.0}$	$^{+6.5}_{-2.1}$	$^{+60}_{-50}$	$^{+30}_{-40}$	$^{+40}_{-50}$	$^{+40}_{-50}$	$^{+40}_{-20}$	$^{+30}_{-10}$
16	−5.6	2.4	−6.0	0	60	−150	170	−390	100	−3.5	0.2	3.7	−200	100	−290	370	380	26
Stat.	$^{+0.5}_{-0.6}$	$^{+0.5}_{-0.5}$	$^{+1.2}_{-1.1}$	$^{+120}_{-130}$	$^{+140}_{-150}$	$^{+80}_{-80}$	$^{+100}_{-30}$	$^{+90}_{-40}$	⋯	$^{+2.6}_{-3.3}$	$^{+3.7}_{-3.8}$	$^{+3.5}_{-2.5}$	$^{+140}_{-140}$	$^{+50}_{-100}$	$^{+70}_{-110}$	$^{+160}_{-120}$	$^{+180}_{-130}$	$^{+11}_{-6}$
17	−6.8	0.4	−1.7	−50	120	−80	150	−430	100	−5.1	−1.4	5.3	−190	110	−130	250	220	15
Stat.	$^{+0.4}_{-0.4}$	$^{+0.1}_{-0.1}$	$^{+0.4}_{-0.4}$	$^{+30}_{-30}$	$^{+30}_{-40}$	$^{+30}_{-30}$	$^{+30}_{-20}$	$^{+20}_{-30}$	⋯	$^{+0.7}_{-0.5}$	$^{+0.6}_{-0.7}$	$^{+0.6}_{-0.8}$	$^{+30}_{-20}$	$^{+20}_{-40}$	$^{+30}_{-40}$	$^{+30}_{-20}$	$^{+60}_{-60}$	$^{+3}_{-2}$
18	−8.7	−1.6	3.0	−50	290	320	440	−120	100	−8.0	−4.3	9.1	−100	270	340	450	350	9
Stat.	$^{+0.1}_{-0.1}$	$^{+0.1}_{-0.3}$	$^{+0.4}_{-0.2}$	$^{+60}_{-60}$	$^{+60}_{-60}$	$^{+40}_{-30}$	$^{+60}_{-60}$	$^{+70}_{-60}$	⋯	$^{+0.6}_{-0.6}$	$^{+0.6}_{-0.6}$	$^{+0.6}_{-0.6}$	$^{+60}_{-70}$	$^{+70}_{-50}$	$^{+30}_{-30}$	$^{+60}_{-60}$	$^{+50}_{-40}$	$^{+2}_{-1}$

Notes. Same as Table D.7.

Table D.9: Kinematic parameters of the runaway stars using Milky Way mass Model III.

#	x	y	z	v_x	v_y	v_z	$v_{\rm Grf}$	$v_{\rm Grf} - v_{\rm esc}$	$P_{\rm b}$	$x_{\rm d}$	$y_{\rm d}$	$r_{\rm d}$	$v_{x,{\rm d}}$	$v_{y,{\rm d}}$	$v_{z,{\rm d}}$	$v_{\rm Grf,d}$	$v_{\rm ej}$	$\tau_{\rm flight}$
	(kpc)			(km s^{-1})					(%)	(kpc)			(km s^{-1})					(Myr)
1	−10.5	−5.6	3.4	−190	90	130	260	−520	100	−5.1	−6.8	8.9	−280	10	170	360	250	22
Stat.	$^{+0.5}_{-0.3}$	$^{+1.0}_{-0.9}$	$^{+0.5}_{-0.7}$	$^{+230}_{-230}$	$^{+150}_{-150}$	$^{+210}_{-210}$	$^{+250}_{-200}$	$^{+250}_{-210}$	⋯	$^{+16.4}_{-5.3}$	$^{+8.6}_{-2.3}$	$^{+3.9}_{-7.8}$	$^{+240}_{-190}$	$^{+200}_{-300}$	$^{+200}_{-60}$	$^{+200}_{-180}$	$^{+280}_{-60}$	$^{+44}_{-13}$
2	−9.3	1.0	0.9	180	220	0	280	−520	100	−12.5	−7.3	14.5	−10	170	30	170	120	40
Stat.	$^{+0.2}_{-0.2}$	$^{+0.2}_{-0.2}$	$^{+0.2}_{-0.2}$	$^{+30}_{-20}$	$^{+10}_{-20}$	$^{+20}_{-10}$	$^{+30}_{-20}$	$^{+30}_{-20}$	⋯	$^{+1.4}_{-1.0}$	$^{+2.0}_{-2.2}$	$^{+1.0}_{-0.8}$	$^{+70}_{-60}$	$^{+30}_{-40}$	$^{+10}_{-10}$	$^{+40}_{-20}$	$^{+40}_{-20}$	$^{+14}_{-11}$
3	−8.8	−0.2	0.2	−210	220	−90	320	−490	100	7.7	−5.3	9.3	−290	−60	90	300	220	50
Stat.	$^{+0.2}_{-0.1}$	$^{+0.1}_{-0.1}$	$^{+0.1}_{-0.1}$	$^{+20}_{-30}$	$^{+10}_{-10}$	$^{+40}_{-30}$	$^{+30}_{-30}$	$^{+30}_{-30}$	⋯	$^{+5.0}_{-3.8}$	$^{+0.2}_{-0.3}$	$^{+4.5}_{-2.9}$	$^{+60}_{-50}$	$^{+20}_{-10}$	$^{+10}_{-20}$	$^{+50}_{-50}$	$^{+10}_{-30}$	$^{+17}_{-11}$
4	−12.2	−3.0	4.5	−60	260	120	290	−480	100	−8.5	−10.1	13.5	−170	180	150	300	170	32
Stat.	$^{+0.6}_{-0.6}$	$^{+0.4}_{-0.5}$	$^{+0.7}_{-0.6}$	$^{+120}_{-120}$	$^{+150}_{-160}$	$^{+110}_{-110}$	$^{+180}_{-170}$	$^{+170}_{-170}$	⋯	$^{+10.0}_{-4.1}$	$^{+4.3}_{-5.1}$	$^{+2.5}_{-5.8}$	$^{+150}_{-110}$	$^{+180}_{-240}$	$^{+100}_{-40}$	$^{+150}_{-110}$	$^{+140}_{-50}$	$^{+29}_{-13}$
5	−6.3	−2.1	4.1	−60	50	110	140	−670	100	−3.0	−2.5	3.9	−220	−50	230	330	330	25
Stat.	$^{+1.7}_{-1.0}$	$^{+0.9}_{-1.9}$	$^{+3.6}_{-1.8}$	$^{+80}_{-150}$	$^{+90}_{-160}$	$^{+50}_{-70}$	$^{+110}_{-80}$	$^{+130}_{-70}$	⋯	$^{+5.4}_{-3.3}$	$^{+3.7}_{-1.6}$	$^{+3.1}_{-3.7}$	$^{+120}_{-170}$	$^{+140}_{-250}$	$^{+340}_{-80}$	$^{+350}_{-130}$	$^{+410}_{-130}$	$^{+13}_{-9}$
6	−9.1	0.5	3.2	−350	410	180	570	−230	100	−2.8	−5.8	6.6	−440	350	230	610	400	16
Stat.	$^{+0.2}_{-0.3}$	$^{+0.2}_{-0.2}$	$^{+1.2}_{-0.9}$	$^{+100}_{-130}$	$^{+80}_{-60}$	$^{+30}_{-40}$	$^{+110}_{-80}$	$^{+120}_{-80}$	⋯	$^{+5.5}_{-2.9}$	$^{+2.2}_{-3.7}$	$^{+3.2}_{-1.0}$	$^{+110}_{-110}$	$^{+60}_{-60}$	$^{+20}_{-20}$	$^{+80}_{-80}$	$^{+180}_{-70}$	$^{+7}_{-6}$
7	−9.9	0.0	−1.8	0	190	20	190	−600	100	−1.7	−7.2	8.0	−240	0	−80	260	100	57
Stat.	$^{+0.4}_{-0.3}$	$^{+0.1}_{-0.1}$	$^{+0.4}_{-0.4}$	$^{+70}_{-70}$	$^{+90}_{-90}$	$^{+60}_{-60}$	$^{+90}_{-80}$	$^{+80}_{-90}$	⋯	$^{+7.2}_{-7.5}$	$^{+4.0}_{-5.2}$	$^{+4.9}_{-4.5}$	$^{+140}_{-90}$	$^{+170}_{-140}$	$^{+30}_{-100}$	$^{+120}_{-80}$	$^{+130}_{-40}$	$^{+23}_{-24}$
8	−8.0	0.3	−1.2	−290	360	−160	490	−320	100	−5.8	−2.2	6.2	−340	360	−180	530	340	7
Stat.	$^{+0.1}_{-0.1}$	$^{+0.2}_{-0.1}$	$^{+0.2}_{-0.3}$	$^{+60}_{-70}$	$^{+40}_{-30}$	$^{+20}_{-30}$	$^{+70}_{-50}$	$^{+60}_{-50}$	⋯	$^{+0.8}_{-0.6}$	$^{+0.4}_{-0.4}$	$^{+0.5}_{-0.6}$	$^{+60}_{-80}$	$^{+30}_{-30}$	$^{+20}_{-20}$	$^{+60}_{-60}$	$^{+70}_{-50}$	$^{+1}_{-1}$
9	−6.4	−17.2	−9.8	−600	−140	−330	710	−30	57	10.3	−12.0	16.9	−570	−220	−360	720	570	27
Stat.	$^{+0.5}_{-0.5}$	$^{+3.6}_{-3.9}$	$^{+2.1}_{-2.3}$	$^{+450}_{-500}$	$^{+190}_{-190}$	$^{+320}_{-330}$	$^{+480}_{-370}$	$^{+480}_{-380}$	⋯	$^{+56.1}_{-12.6}$	$^{+36.8}_{-7.5}$	$^{+53.6}_{-9.4}$	$^{+420}_{-490}$	$^{+230}_{-170}$	$^{+250}_{-310}$	$^{+460}_{-280}$	$^{+470}_{-240}$	$^{+83}_{-13}$
10	−15.0	7.0	−8.2	70	230	−110	280	−470	100	−14.5	−6.2	17.1	−90	210	−180	310	200	55
Stat.	$^{+3.7}_{-8.3}$	$^{+8.8}_{-3.9}$	$^{+4.5}_{-10.4}$	$^{+310}_{-200}$	$^{+210}_{-250}$	$^{+150}_{-270}$	$^{+320}_{-120}$	$^{+350}_{-120}$	⋯	$^{+20.4}_{-25.4}$	$^{+18.3}_{-38.5}$	$^{+35.6}_{-12.9}$	$^{+380}_{-270}$	$^{+190}_{-170}$	$^{+90}_{-230}$	$^{+260}_{-60}$	$^{+350}_{-80}$	$^{+107}_{-26}$
11	−5.5	1.8	−5.9	70	240	−130	290	−510	100	−5.4	−5.1	7.6	−90	190	−250	330	270	29
Stat.	$^{+1.3}_{-0.9}$	$^{+0.8}_{-0.6}$	$^{+1.8}_{-2.5}$	$^{+160}_{-160}$	$^{+140}_{-140}$	$^{+90}_{-100}$	$^{+120}_{-80}$	$^{+120}_{-80}$	⋯	$^{+3.9}_{-6.3}$	$^{+4.2}_{-8.4}$	$^{+9.3}_{-4.6}$	$^{+140}_{-130}$	$^{+100}_{-90}$	$^{+100}_{-150}$	$^{+150}_{-90}$	$^{+150}_{-60}$	$^{+23}_{-9}$
12	−9.8	5.2	−3.9	110	290	−100	330	−460	100	−11.1	−4.1	11.9	−30	300	−150	330	180	30
Stat.	$^{+0.3}_{-0.3}$	$^{+1.0}_{-0.9}$	$^{+0.6}_{-0.8}$	$^{+80}_{-70}$	$^{+50}_{-50}$	$^{+60}_{-70}$	$^{+50}_{-40}$	$^{+60}_{-30}$	⋯	$^{+2.7}_{-2.5}$	$^{+3.6}_{-6.4}$	$^{+3.6}_{-2.1}$	$^{+100}_{-100}$	$^{+20}_{-40}$	$^{+50}_{-50}$	$^{+30}_{-10}$	$^{+40}_{-30}$	$^{+17}_{-9}$
13	−8.7	1.0	−4.5	−160	150	−100	250	−550	100	−1.5	−2.9	3.4	−350	60	−240	430	290	28
Stat.	$^{+0.1}_{-0.1}$	$^{+0.2}_{-0.2}$	$^{+0.6}_{-0.8}$	$^{+130}_{-140}$	$^{+100}_{-110}$	$^{+30}_{-20}$	$^{+80}_{-70}$	$^{+90}_{-70}$	⋯	$^{+2.8}_{-3.4}$	$^{+2.6}_{-3.5}$	$^{+4.0}_{-2.8}$	$^{+140}_{-150}$	$^{+100}_{-120}$	$^{+70}_{-170}$	$^{+200}_{-120}$	$^{+250}_{-110}$	$^{+6}_{-4}$
14	−8.6	−1.8	−2.2	−160	180	−40	250	−560	100	−1.9	−5.5	5.8	−310	50	−120	340	150	27
Stat.	$^{+0.1}_{-0.1}$	$^{+0.3}_{-0.6}$	$^{+0.4}_{-0.6}$	$^{+30}_{-60}$	$^{+20}_{-20}$	$^{+20}_{-20}$	$^{+40}_{-30}$	$^{+50}_{-30}$	⋯	$^{+2.7}_{-1.8}$	$^{+0.5}_{-0.6}$	$^{+0.7}_{-0.6}$	$^{+40}_{-40}$	$^{+50}_{-70}$	$^{+20}_{-30}$	$^{+30}_{-40}$	$^{+30}_{-10}$	$^{+6}_{-4}$
15	−7.1	2.1	−1.9	170	240	−50	300	−520	100	−9.4	−4.0	10.3	10	220	−90	240	140	25
Stat.	$^{+0.3}_{-0.3}$	$^{+0.6}_{-0.5}$	$^{+0.5}_{-0.5}$	$^{+80}_{-70}$	$^{+40}_{-50}$	$^{+70}_{-60}$	$^{+50}_{-40}$	$^{+50}_{-30}$	⋯	$^{+1.6}_{-3.6}$	$^{+2.7}_{-7.1}$	$^{+6.3}_{-2.2}$	$^{+60}_{-50}$	$^{+30}_{-50}$	$^{+40}_{-50}$	$^{+40}_{-60}$	$^{+40}_{-20}$	$^{+31}_{-10}$
16	−5.6	2.4	−6.0	0	60	−150	170	−630	100	−3.6	0.2	3.9	−180	100	−300	360	380	27
Stat.	$^{+0.5}_{-0.6}$	$^{+0.5}_{-0.5}$	$^{+1.2}_{-1.1}$	$^{+120}_{-130}$	$^{+130}_{-150}$	$^{+80}_{-80}$	$^{+100}_{-30}$	$^{+90}_{-30}$	⋯	$^{+2.5}_{-3.3}$	$^{+3.7}_{-3.8}$	$^{+3.4}_{-2.5}$	$^{+130}_{-130}$	$^{+40}_{-100}$	$^{+90}_{-100}$	$^{+160}_{-120}$	$^{+170}_{-140}$	$^{+10}_{-7}$
17	−6.8	0.4	−1.7	−50	120	−80	150	−670	100	−5.1	−1.4	5.3	−180	110	−130	250	220	15
Stat.	$^{+0.4}_{-0.4}$	$^{+0.1}_{-0.1}$	$^{+0.4}_{-0.4}$	$^{+30}_{-30}$	$^{+30}_{-40}$	$^{+30}_{-30}$	$^{+30}_{-20}$	$^{+30}_{-20}$	⋯	$^{+0.6}_{-0.5}$	$^{+0.6}_{-0.6}$	$^{+0.6}_{-0.7}$	$^{+20}_{-30}$	$^{+20}_{-40}$	$^{+30}_{-40}$	$^{+30}_{-20}$	$^{+60}_{-60}$	$^{+3}_{-2}$
18	−8.7	−1.6	3.0	−50	290	320	440	−360	100	−8.0	−4.2	9.1	−100	270	340	450	350	9
Stat.	$^{+0.1}_{-0.1}$	$^{+0.1}_{-0.3}$	$^{+0.4}_{-0.2}$	$^{+60}_{-60}$	$^{+60}_{-60}$	$^{+40}_{-30}$	$^{+60}_{-60}$	$^{+60}_{-60}$	⋯	$^{+0.6}_{-0.6}$	$^{+0.5}_{-0.7}$	$^{+0.6}_{-0.6}$	$^{+60}_{-70}$	$^{+60}_{-50}$	$^{+30}_{-30}$	$^{+60}_{-60}$	$^{+40}_{-40}$	$^{+2}_{-1}$

Notes. Same as Table D.7.

Bibliography

Abadi, M. G., Navarro, J. F., & Steinmetz, M. 2009, ApJ, 691, L63
Abt, H. A. & Cardona, O. 1984, ApJ, 285, 190
Abt, H. A., Gomez, A. E., & Levy, S. G. 1990, ApJS, 74, 551
Abt, H. A. & Levy, S. G. 1978, ApJS, 36, 241
Abt, H. A., Levy, S. G., & Gandet, T. L. 1972, AJ, 77, 138
Abt, H. A., Wang, R., & Cardona, O. 1991, ApJ, 367, 155
Aceituno, J., Sánchez, S. F., Grupp, F., et al. 2013, A&A, 552, A31
Acon, B. W., Stehlé, C., Zhang, H., & Montaser, A. 2001, Spectrochimica Acta, 56, 527
Aerts, C., Puls, J., Godart, M., & Dupret, M.-A. 2009, A&A, 508, 409
Allen, C. & Martos, M. A. 1986, Rev. Mex. Astron. Astrofis., 13, 137
Allen, C., Moreno, E., & Pichardo, B. 2008, ApJ, 674, 237
Allen, C. & Santillán, A. 1991, Rev. Mex. Astron. Astrofis., 22, 255
Altmann, M. & de Boer, K. S. 2000, A&A, 353, 135
Altmann, M., Edelmann, H., & de Boer, K. S. 2004, A&A, 414, 181
Asaki, Y., Deguchi, S., Imai, H., et al. 2010, ApJ, 721, 267
Asplund, M., Grevesse, N., Sauval, A. J., & Scott, P. 2009, ARA&A, 47, 481
Bagnulo, S., Landstreet, J. D., Fossati, L., & Kochukhov, O. 2012, A&A, 538, A129
Becker, S. R. 1998, ASP Conf. Ser., 131, 137
Becker, S. R. & Butler, K. 1988, A&A, 201, 232
Bessell, M. & Murphy, S. 2012, PASP, 124, 140
Bessell, M. S. 2011, PASP, 123, 1442
Bessell, M. S., Castelli, F., & Plez, B. 1998, A&A, 333, 231
Bevington, P. R. & Robinson, D. K. 1992, Data reduction and error analysis for the physical sciences, 2nd edn. (New York: McGraw-Hill)
Blaauw, A. 1961, Bull. Astron. Inst. Neth., 15, 265
Boylan-Kolchin, M., Bullock, J. S., Sohn, S. T., Besla, G., & van der Marel, R. P. 2013, ApJ, 768, 140
Briquet, M., Aerts, C., Baglin, A., et al. 2011, A&A, 527, A112
Brissaud, A. & Frisch, U. 1971, J. Quant. Spec. Radiat. Transf., 11, 1767
Brown, A. & Kilkenny, D. 1979, MNRAS, 187, 823
Brown, W. R., Anderson, J., Gnedin, O. Y., et al. 2010, ApJ, 719, L23
Brown, W. R., Geller, M. J., Kenyon, S. J., & Kurtz, M. J. 2005, ApJ, 622, L33
Burbidge, E. M., Burbidge, G. R., Fowler, W. A., & Hoyle, F. 1957, Reviews of Modern Physics, 29, 547
Burton, W. B. & Gordon, M. A. 1978, A&A, 63, 7
Butler, K. & Giddings, J. R. 1985, in Newsletter of Analysis of Astronomical Spectra, No. 9 (Univ. London)
Caffau, E., Ludwig, H.-G., Steffen, M., Freytag, B., & Bonifacio, P. 2011, Sol. Phys., 268, 255
Cameron, A. G. W. 1957, AJ, 62, 9
Cantiello, M., Langer, N., Brott, I., et al. 2009, A&A, 499, 279
Cardenoso, V. & Gigosos, M. 1997, J. Phys. B: At. Mol. Phys., 30, 3361
Carigi, L., Peimbert, M., Esteban, C., & García-Rojas, J. 2005, ApJ, 623, 213
Carroll, B. W. & Ostlie, D. A. 1996, An Introduction to Modern Astrophysics, 1st edn. (Reading, Massachusetts et al.: Addison-Wesley)
Castro, N., Urbaneja, M. A., Herrero, A., et al. 2012, A&A, 542, A79
Chieffi, A. & Limongi, M. 2013, ApJ, 764, 21
Chini, R., Hoffmeister, V. H., Nasseri, A., Stahl, O., & Zinnecker, H. 2012, MNRAS, 424, 1925
Claret, A. & Bloemen, S. 2011, A&A, 529, A75
Clayton, D. D. 1983, Principles of Stellar Evolution and Nucleosynthesis, 1st edn. (Chicago and London: The University of Chicago Press)
Clemens, D. P. 1985, ApJ, 295, 422
Conlon, E. S., Brown, P. J. F., Dufton, P. L., & Keenan, F. P. 1988, A&A, 200, 168
Conlon, E. S., Dufton, P. L., Keenan, F. P., & Leonard, P. J. T. 1990, A&A, 236, 357
Conlon, E. S., Dufton, P. L., Keenan, F. P., McCausland, R. J. H., & Holmgren, D. 1992, ApJ, 400, 273
Cowley, C. R. 1958, AJ, 63, 484

Cowley, C. R. & Castelli, F. 2002, A&A, 387, 595
Cunha, K. & Lambert, D. L. 1994, ApJ, 426, 170
de Boer, K. S., Richtler, T., & Heber, U. 1988, A&A, 202, 113
Dehnen, W. & Binney, J. 1998, MNRAS, 294, 429
Dekker, H., D'Odorico, S., Kaufer, A., Delabre, B., & Kotzlowski, H. 2000, in SPIE Conf. Ser. 4008, eds. M. Iye, & A. F. Moorwood, 534
Donati, J.-F., Howarth, I. D., Jardine, M. M., et al. 2006, MNRAS, 370, 629
Ducati, J. R. 2002, VizieR Online Data Catalog, 2237
Edelmann, H., Napiwotzki, R., Heber, U., Christlieb, N., & Reimers, D. 2005, ApJ, 634, L181
Eggleton, P. P. & Tokovinin, A. A. 2008, MNRAS, 389, 869
Ekström, S., Georgy, C., Eggenberger, P., et al. 2012, A&A, 537, A146
Esteban, C., García-Rojas, J., Peimbert, M., et al. 2005, ApJ, 618, L95
Evans, C. J., Lennon, D. J., Smartt, S. J., & Trundle, C. 2006, A&A, 456, 623
Feige, J. 1958, ApJ, 128, 267
Feinstein, A. 1967, ApJ, 149, 107
Firnstein, M. 2010, PhD thesis, University of Erlangen-Nuremberg
Fitzpatrick, E. L. 1999, PASP, 111, 63
Frandsen, S. & Lindberg, B. 1999, Astrophysics with the NOT, 71
Freedman, W. L., Madore, B. F., Gibson, B. K., et al. 2001, ApJ, 553, 47
Fuhrmann, K. 2008, MNRAS, 384, 173
Georgy, C., Ekström, S., Granada, A., et al. 2013, A&A, 553, A24
Giddings, J. R. 1981, PhD thesis, University of London
Gies, D. R. & Lambert, D. L. 1992, ApJ, 387, 673
Gigosos, M. & Cardenoso, V. 1996, J. Phys. B: At. Mol. Phys., 29, 4795
Gillessen, S., Eisenhauer, F., Trippe, S., et al. 2009, ApJ, 692, 1075
Gnedin, O. Y., Brown, W. R., Geller, M. J., & Kenyon, S. J. 2010, ApJ, 720, L108
Goeppert Mayer, M. 1964, Science, 145, 999
Gray, D. F. 2005, The Observation and Analysis of Stellar Photospheres, 3rd edn. (Cambridge: Cambridge University Press)
Grevesse, N. & Sauval, A. J. 1998, Space Sci. Rev., 85, 161
Griffin, R. E., Gray, R. O., & Corbally, C. J. 2012, A&A, 547, A8
Gvaramadze, V. V. 2009, MNRAS, 395, L85
Hadrava, P. 1995, A&AS, 114, 393
Hambly, N. C., Conlon, E. S., Dufton, P. L., et al. 1993, ApJ, 417, 706
Hambly, N. C., Kilkenny, D., Keenan, F. P., et al. 1994, MNRAS, 267, 1103
Hauck, B. & Mermilliod, M. 1998, A&AS, 129, 431
Heber, U., Edelmann, H., Napiwotzki, R., Altmann, M., & Scholz, R.-D. 2008, A&A, 483, L21
Heger, A. & Langer, N. 2000, ApJ, 544, 1016
Hempel, M. & Holweger, H. 2003, A&A, 408, 1065
Hill, P. W. 1970, MNRAS, 150, 23
Hills, J. G. 1988, Nature, 331, 687
Hirota, T., Ando, K., Bushimata, T., et al. 2008a, PASJ, 60, 961
Hirota, T., Bushimata, T., Choi, Y. K., et al. 2008b, PASJ, 60, 37
Hirsch, H. A., Heber, U., O'Toole, S. J., & Bresolin, F. 2005, A&A, 444, L61
Hirschi, R., Meynet, G., & Maeder, A. 2005, A&A, 433, 1013
Høg, E., Fabricius, C., Makarov, V. V., et al. 2000, A&A, 355, L27
Holmberg, J. & Flynn, C. 2000, MNRAS, 313, 209
Holmberg, J. & Flynn, C. 2004, MNRAS, 352, 440
Holmgren, D. E., McCausland, R. J. H., Dufton, P. L., Keenan, F. P., & Kilkenny, D. 1992, MNRAS, 258, 521
Honma, M., Hirota, T., Kan-Ya, Y., et al. 2011, PASJ, 63, 17
Hoogerwerf, R., de Bruijne, J. H. J., & de Zeeuw, P. T. 2001, A&A, 365, 49
Hooper, C. 1968, Phys. Rev., 165, 215
Houck, J. C. & Denicola, L. A. 2000, in Astronomical Data Analysis Software and Systems IX, eds. N. Manset, C. Veillet, & D. Crabtree, ASP Conf. Ser., 216, 591

Huang, W., Gies, D. R., & McSwain, M. V. 2009, ApJ, 703, 81
Hubrig, S., Briquet, M., De Cat, P., et al. 2009, Astronomische Nachrichten, 330, 317
Hubrig, S., Briquet, M., Schöller, M., et al. 2006, MNRAS, 369, L61
Irrgang, A., Butler, K., Przybilla, N., & Heber, U. 2014a, A&A, submitted
Irrgang, A., Przybilla, N., Heber, U., et al. 2014b, A&A, 565, A63
Irrgang, A., Przybilla, N., Heber, U., Nieva, M. F., & Schuh, S. 2010, ApJ, 711, 138
Irrgang, A., Wilcox, B., Tucker, E., & Schiefelbein, L. 2013, A&A, 549, A137
Israelian, G., Rebolo, R., Basri, G., Casares, J., & Martín, E. L. 1999, Nature, 401, 142
Jerzykiewicz, M. & Sterken, C. 1977, Acta Astron., 27, 365
Jerzykiewicz, M. & Sterken, C. 1993, MNRAS, 260, 826
Jilinski, E., Ortega, V. G., Drake, N. A., & de la Reza, R. 2010, ApJ, 721, 469
Kaempf, T. A., de Boer, K. S., & Altmann, M. 2005, A&A, 432, 879
Kallivayalil, N., van der Marel, R. P., Alcock, C., et al. 2006, ApJ, 638, 772
Karttunen, H., Kröger, P., Oja, H., Poutanen, M., & Donner, K. 2007, Fundamental Astronomy, 5th edn. (Berlin Heidelberg New York: Springer Verlag)
Kaufer, A., Stahl, O., Tubbesing, S., et al. 1999, The Messenger, 95, 8
Keenan, F. P., Brown, P. J. F., Conlon, E. S., Dufton, P. L., & Lennon, D. J. 1987, A&A, 178, 194
Keenan, F. P., Brown, P. J. F., & Lennon, D. J. 1986a, A&A, 155, 333
Keenan, F. P., Dufton, P. L., & McKeith, C. D. 1982, MNRAS, 200, 673
Keenan, F. P., Lennon, D. J., Brown, P. J. F., & Dufton, P. L. 1986b, ApJ, 307, 694
Kenyon, S. J., Bromley, B. C., Geller, M. J., & Brown, W. R. 2008, ApJ, 680, 312
Kilian, J. 1992, A&A, 262, 171
Kilkenny, D., O'Donoghue, D., Koen, C., Stobie, R. S., & Chen, A. 1997, MNRAS, 287, 867
Kilkenny, D. & Stone, L. E. 1988, MNRAS, 234, 1011
Kilkenny, K., Hill, P. W., & Brown, A. 1977, MNRAS, 178, 123
Kroupa, P. & Bastian, U. 1997, New Astron., 2, 77
Kudritzki, R.-P. & Puls, J. 2000, ARA&A, 38, 613
Kurucz, R. 1993a, CD-ROM No. 2–12 (Cambridge, Mass: SAO)
Kurucz, R. 1993b, CD-ROM No. 13 (Cambridge, Mass: SAO)
Kurucz, R. L. 1996, in Model Atmospheres and Spectrum Synthesis, ed. S. J. Adelman, F. Kupka, & W. W. Weiss (San Francisco: ASP), 160
Lane, R. R., Küpper, A. H. W., & Heggie, D. C. 2012, MNRAS, 423, 2845
Lefever, K., Puls, J., & Aerts, C. 2007, A&A, 463, 1093
Lefever, K., Puls, J., Morel, T., et al. 2010, A&A, 515, A74
Lemasle, B., François, P., Genovali, K., et al. 2013, A&A, 558, A31
Leonard, P. J. T. & Duncan, M. J. 1988, AJ, 96, 222
Lépine, S., Koch, A., Rich, R. M., & Kuijken, K. 2011, ApJ, 741, 100
Lindroos, K. P. 1985, A&AS, 60, 183
Lodders, K., Palme, H., & Gail, H.-P. 2009, Landolt Börnstein, 44
Lynn, B. B., Keenan, F. P., Dufton, P. L., et al. 2004, MNRAS, 353, 633
Maciel, W. J. & Köppen, J. 1994, A&A, 282, 436
Maeder, A., Przybilla, N., Nieva, M.-F., et al. 2014, A&A, 565, A39
Magee, H. R. M., Dufton, P. L., Keenan, F. P., et al. 2001, MNRAS, 324, 747
Maitzen, H. M., Paunzen, E., Pressberger, R., Slettebak, A., & Wagner, R. M. 1998, A&A, 339, 782
Martin, J. C. 2004, AJ, 128, 2474
Martin, J. C. 2006, AJ, 131, 3047
Massey, R. 2010, MNRAS, 409, L109
Mayer, P., Drechsel, H., & Irrgang, A. 2014, A&A, 565, A86
Mayer, P., Lorenz, R., & Drechsel, H. 1997, A&A, 320, 109
McConnachie, A. W. 2012, AJ, 144, 4
McMillan, P. J. 2011, MNRAS, 414, 2446
McMillan, P. J. & Binney, J. J. 2010, MNRAS, 402, 934
Mermilliod, J. C. 1991, Catalogue of Homogeneous Means in the UBV System, Institut d'Astronomie, Universite de Lausanne

Meynet, G. & Maeder, A. 2000, A&A, 361, 101
Miyamoto, M. & Nagai, R. 1975, PASJ, 27, 533
Mokiem, M. R., de Koter, A., Puls, J., et al. 2005, A&A, 441, 711
Morel, M. & Magnenat, P. 1978, A&AS, 34, 477
Morel, T. & Butler, K. 2008, A&A, 487, 307
Morel, T., Butler, K., Aerts, C., Neiner, C., & Briquet, M. 2006, A&A, 457, 651
Morel, T., Hubrig, S., & Briquet, M. 2008, A&A, 481, 453
Morrell, N. & Levato, H. 1991, ApJS, 75, 965
Navarro, J. F., Frenk, C. S., & White, S. D. M. 1997, ApJ, 490, 493
Neiner, C., Geers, V. C., Henrichs, H. F., et al. 2003, A&A, 406, 1019
Nieva, M.-F. 2013, A&A, 550, A26
Nieva, M. F. & Przybilla, N. 2006, ApJ, 639, L39
Nieva, M. F. & Przybilla, N. 2007, A&A, 467, 295
Nieva, M. F. & Przybilla, N. 2008, A&A, 481, 199
Nieva, M.-F. & Przybilla, N. 2010, EAS Publ. Ser., 43, 167
Nieva, M.-F. & Przybilla, N. 2012, A&A, 539, A143
Nieva, M.-F. & Przybilla, N. 2014, A&A, in press, DOI: 10.1051/0004-6361/201423373
Nieva, M.-F. & Simón-Díaz, S. 2011, A&A, 532, A2
Niinuma, K., Nagayama, T., Hirota, T., et al. 2011, PASJ, 63, 9
Nomoto, K., Tominaga, N., Umeda, H., Kobayashi, C., & Maeda, K. 2006, Nuclear Physics A, 777, 424
Odenkirchen, M., Brosche, P., Geffert, M., & Tucholke, H.-J. 1997, New Astron., 2, 477
Olchawa, W., Olchawa, R., & Grabowski, B. 2004, European Physical Journal D, 28, 119
Oort, J. H. 1932, Bull. Astron. Inst. Neth., 6, 249
Oudmaijer, R. D. & Parr, A. M. 2010, MNRAS, 405, 2439
Palate, M. & Rauw, G. 2012, A&A, 537, A119
Palate, M., Rauw, G., Koenigsberger, G., & Moreno, E. 2013, A&A, 552, A39
Pauli, E.-M., Napiwotzki, R., Altmann, M., et al. 2003, A&A, 400, 877
Pauli, E.-M., Napiwotzki, R., Heber, U., Altmann, M., & Odenkirchen, M. 2006, A&A, 447, 173
Pavlovski, K. & Southworth, J. 2013, EAS Publ. Ser., 64, 29
Pereira, C. B., Jilinski, E., Drake, N. A., et al. 2012, A&A, 543, A58
Perets, H. B. 2009, ApJ, 698, 1330
Perryman, M. A. C. & ESA. 1997, The Hipparcos and TYCHO catalogues. Astrometric and photometric star catalogues derived from the ESA Hipparcos Space Astrometry Mission, ESA SP, 1200
Pfeiffer, M. J., Frank, C., Baumueller, D., Fuhrmann, K., & Gehren, T. 1998, A&AS, 130, 381
Pichardo, B., Martos, M., & Moreno, E. 2004, ApJ, 609, 144
Pichardo, B., Martos, M., Moreno, E., & Espresate, J. 2003, ApJ, 582, 230
Pigulski, A. & Pojmański, G. 2008, A&A, 477, 917
Pourbaix, D., Tokovinin, A. A., Batten, A. H., et al. 2004, A&A, 424, 727
Poveda, A., Ruiz, J., & Allen, C. 1967, Bol. Obs. Tonantzintla Tacubaya, 4, 86
Przybilla, N. 2005, A&A, 443, 293
Przybilla, N. 2008, Rev. Mod. Astron., 20, 323
Przybilla, N. & Butler, K. 2001, A&A, 379, 955
Przybilla, N. & Butler, K. 2004, ApJ, 609, 1181
Przybilla, N., Butler, K., Becker, S. R., & Kudritzki, R. P. 2001, A&A, 369, 1009
Przybilla, N., Butler, K., Becker, S. R., & Kudritzki, R. P. 2006, A&A, 445, 1099
Przybilla, N., Butler, K., Becker, S. R., Kudritzki, R. P., & Venn, K. A. 2000, A&A, 359, 1085
Przybilla, N., Firnstein, M., Nieva, M. F., Meynet, G., & Maeder, A. 2010a, A&A, 517, A38
Przybilla, N., Nieva, M.-F., & Butler, K. 2008a, ApJ, 688, L103
Przybilla, N., Nieva, M.-F., & Butler, K. 2011, Journal of Physics Conference Series, 328, 012015
Przybilla, N., Nieva, M. F., Heber, U., & Butler, K. 2008b, ApJ, 684, L103
Przybilla, N., Nieva, M. F., Heber, U., et al. 2008c, A&A, 480, L37
Przybilla, N., Tillich, A., Heber, U., & Scholz, R.-D. 2010b, ApJ, 718, 37
Ramspeck, M., Heber, U., & Moehler, S. 2001, A&A, 378, 907
Reid, M. J. & Brunthaler, A. 2004, ApJ, 616, 872

Reid, M. J., Menten, K. M., Zheng, X. W., et al. 2009, ApJ, 700, 137
Rolleston, W. R. J., Hambly, N. C., Dufton, P. L., et al. 1997, MNRAS, 290, 422
Rolleston, W. R. J., Hambly, N. C., Keenan, F. P., Dufton, P. L., & Saffer, R. A. 1999, A&A, 347, 69
Rufener, F. & Bartholdi, P. 1982, A&AS, 48, 503
Ryans, R. S. I., Hambly, N. C., Dufton, P. L., & Keenan, F. P. 1996, MNRAS, 278, 132
Ryans, R. S. I., Keenan, F. P., Rolleston, W. R. J., Sembach, K. R., & Davies, R. D. 1999, MNRAS, 304, 947
Rybicki, G. B. & Hummer, D. G. 1991, A&A, 245, 171
Rygl, K. L. J., Brunthaler, A., Reid, M. J., et al. 2010, A&A, 511, A2
Sakamoto, T., Chiba, M., & Beers, T. C. 2003, A&A, 397, 899
Sana, H., de Mink, S. E., de Koter, A., et al. 2012, Science, 337, 444
Sandstrom, K. M., Peek, J. E. G., Bower, G. C., Bolatto, A. D., & Plambeck, R. L. 2007, ApJ, 667, 1161
Sato, M., Hirota, T., Reid, M. J., et al. 2010, PASJ, 62, 287
Schönrich, R., Binney, J., & Dehnen, W. 2010, MNRAS, 403, 1829
Schuster, W. J., Moreno, E., Nissen, P. E., & Pichardo, B. 2012, A&A, 538, A21
Sigut, T. A. A. 1996, ApJ, 473, 452
Sigut, T. A. A. 1999, ApJ, 519, 303
Silva, M. D. V. & Napiwotzki, R. 2011, MNRAS, 411, 2596
Silva, M. D. V. & Napiwotzki, R. 2013, MNRAS, 431, 502
Silvester, J., Neiner, C., Henrichs, H. F., et al. 2009, MNRAS, 398, 1505
Simon, K. P. & Sturm, E. 1994, A&A, 281, 286
Simón-Díaz, S. 2010, A&A, 510, A22
Simón-Díaz, S., Castro, N., Garcia, M., Herrero, A., & Markova, N. 2011a, Bulletin de la Societe Royale des Sciences de Liege, 80, 514
Simón-Díaz, S., Castro, N., Herrero, A., et al. 2011b, Journal of Physics Conference Series, 328, 012021
Smith, J. A., Tucker, D. L., Kent, S., et al. 2002, AJ, 123, 2121
Smith, K. C. 1996, Ap&SS, 237, 77
Smith, M. C., Ruchti, G. R., Helmi, A., et al. 2007, MNRAS, 379, 755
Sohn, S. T., Besla, G., van der Marel, R. P., et al. 2013, ApJ, 768, 139
Stankov, A. & Handler, G. 2005, ApJS, 158, 193
Stehlé, C. & Hutcheon, R. 1999, A&AS, 140, 93
Stickland, D. J. & Lloyd, C. 2000, The Observatory, 120, 141
Telting, J. H., Schrijvers, C., Ilyin, I. V., et al. 2006, A&A, 452, 945
Tenjes, P., Einasto, J., Maitzen, H. M., & Zinnecker, H. 2001, A&A, 369, 530
Tetzlaff, N., Neuhäuser, R., & Hohle, M. M. 2011, MNRAS, 410, 190
Tillich, A., Heber, U., Geier, S., et al. 2011, A&A, 527, A137
Tobin, W. 1986, A&A, 155, 326
van der Marel, R. P., Alves, D. R., Hardy, E., & Suntzeff, N. B. 2002, AJ, 124, 2639
van Leeuwen, F. 2007, *Hipparcos*, the New Reduction of the Raw Data (Berlin: Springer), Astrophys. Space Sci. Lib. 350
Vidal, C. R., Cooper, J., & Smith, E. W. 1971a, NBS Monograph, 120
Vidal, C. R., Cooper, J., & Smith, E. W. 1971b, J. Quant. Spec. Radiat. Transf., 11, 263
Vidal, C. R., Cooper, J., & Smith, E. W. 1973, ApJS, 25, 37
Vrancken, M., Butler, K., & Becker, S. R. 1996, A&A, 311, 661
Waelkens, C., Aerts, C., Kestens, E., Grenon, M., & Eyer, L. 1998, A&A, 330, 215
Waelkens, C. & Rufener, F. 1988, A&A, 201, L5
Walker, M. F. 1969, ApJ, 155, 447
Wallerstein, G., Iben, Jr., I., Parker, P., et al. 1997, Reviews of Modern Physics, 69, 995
Wallerstein, G., Vanture, A. D., Jenkins, E. B., & Fuller, G. M. 1995, ApJ, 449, 688
Wesemael, F., Fontaine, G., Bergeron, P., Lamontagne, R., & Green, R. F. 1992, AJ, 104, 203
Wilkinson, M. I. & Evans, N. W. 1999, MNRAS, 310, 645
Woosley, S. E. & Weaver, T. A. 1995, ApJS, 101, 181
Wu, Z.-Y., Ma, J., Zhou, X., & Du, C.-H. 2011, AJ, 141, 104
Xue, X. X., Rix, H. W., Zhao, G., et al. 2008, ApJ, 684, 1143
Yanny, B., Rockosi, C., Newberg, H. J., et al. 2009, AJ, 137, 4377

Zacharias, N., Finch, C. T., Girard, T. M., et al. 2013, AJ, 145, 44

Acknowledgements

I am deeply grateful to my supervisors Uli Heber and Norbert Przybilla for giving me the opportunity to work on an exciting scientific topic, for enabling me to attend international conferences and to spend a research stay abroad, for allowing me to follow my own ideas, for never putting pressure on me, and, quite generally, for their strong support throughout the last couple of years.

Moreover, I would like to thank my colleagues from the Dr. Karl Remeis-Observatory, in particular my former and current office mates, for the pleasant working atmosphere. My special thanks goes to Moritz Böck, Manfred Hanke, and Markus Firnstein, who helped me really a lot, especially in the early stages of this thesis. I am also very grateful to Thomas Dauser, Ingo Kreykenbohm, and Fritz-Walter Schwarm for maintaining and improving the Remeis computer cluster which was extensively used for this study. Thanks to Irmela Bues for proof-reading the thesis and to Horst Drechsel for keeping things going at our beautiful observatory.

Mahalo nui loa to Rolf-Peter Kudritzki, Miguel Urbaneja, and the University of Hawai'i for their great hospitality during my research stay at the Institute for Astronomy and to the German Academic Exchange Service (DAAD) as well as to the Physics Advanced study program for financial support of this stay.

Many thanks to the summer students Natasa Dragovic, Lucas Schiefelbein, Evan Tucker, and Benjamin Wilcox for their contributions to this study. Their research internships were made possible by support from the MIT-Germany Program and from the DAAD's RISE program. I am very grateful to Lucas Schiefelbein and Sara Nagelberg for helping me to create the runaway animations with the free open source tool Blender.

I thank Maria-Fernanda Nieva for giving me the opportunity to present my work in the SAGA seminar at the Planck Institute for Astrophysics (MPA) and for fruitful discussions. Furthermore, I appreciate valuable feedback on paper drafts by Keith Butler.

I am very grateful to • the European Southern Observatory (ESO), • the MPA, • the Observing Programs Committee of the Nordic Optical Telescope, and • the Time Allocation Committee of the Centro Astronómico Hispano Alemán (CAHA) for granting valuable observing time for this study. Travels to the CAHA (Calar Alto, Spain) and to the ESO Observatory (La Silla, Chile) were supported by the German Research Foundation (DFG) under grants PR685/6-1 and PR685/7-1.

Financially, I acknowledge • the funding from a research scholarship by the Elite Network of Bavaria (BayEF), • subsequent funding by the DFG through grant He1356/45-2, • funding of my participation in the "WE-Heraeus Summer School" by the Wilhelm and Else Heraeus Foundation, • support for my participation in the "11th Symposium on Nuclei in the Cosmos" by the German Astronomical Society, • funding of my participation in the summer school "Stars and Supernovae in galaxies" by the BayEF, • funding of my participation in the "Annual Meeting of the German Astronomical Society 2012" by the BayEF, • grants for and funding of my participation in the "Nuclear Physics in Astrophysics VI" conference by the organizers, the ExtreMe Matter Institute, and the Physics Advanced study program, • funding of my participation in the "Massive stars: From α to Ω" conference by the Physics Advanced study program, and • a grant for my participation in the summer school "GREAT-ITN school: The Galaxy, Stellar Compositions and Dynamics" by the organizers.

Finally, I thank John E. Davis for the development of the SLXFIG module and Till Tantau for the development of the PGF/TikZ TEX package used to prepare most of the figures in this

thesis. This research has made use of NASA's Astrophysics Data System Bibliographic Services as well as of the SIMBAD database, operated at CDS, Strasbourg, France.